Journal of Applied Mechanics

Published Bimonthly by ASME

VOLUME 76 • NUMBER 6 • NOVEMBER 2009

Transactions of the ASME, Journal of Applied Mechanics (ISSN 0021-8936) is published bimonthly (Jan., Mar., May, July, Sept., Nov.) by The American Society of Mechanical Engineers, Three Park Avenue, New York, NY 10016. Periodicals postage paid at New York, NY and additional mailing offices. POSTMASTER: Send address changes to Transactions of the ASME, Journal of Applied Mechanics, c/o THE AMERICAN SOCIETY OF MECHANICAL ENGINEERS, 22 Law Drive, Box 2300, Fairfield, NJ 07007-2300. **CHANGES OF ADDRESS** must be received at Society headquarters seven weeks before they are to be effective. Please send old label and new address. **STATEMENT from By-Laws.** The Society shall not be responsible for statements or opinions advanced in papers or printed in its publications (B7.1, Para. 3).

RESEARCH PAPERS

(Contents continued on inside back cover)

The ASME Journal of Applied Mechanics is abstracted and indexed in the following:

Alloys Index, Aluminum Industry Abstracts, Applied Science & Technology Index, Ceramic Abstracts, Chemical Abstracts, Civil Engineering Abstracts, Compendex (The electronic equivalent of Engineering Index), Computer & Information Systems Abstracts, Corrosion Abstracts, Current Contents, EEA (Earthquake Engineering Abstracts Database), Electronics & Communications Abstracts Journal, Engineered Materials Abstracts, Engineering Index, Environmental Engineering Abstracts, Environmental Science and Pollution Management, Fluidex, Fuel & Energy Abstracts, GeoRef, Geotechnical Abstracts, INSPEC, International Aerospace Abstracts, Journal of Ferrocement, Materials Science Citation Index, Mechanical Engineering Abstracts, METADEX (The electronic equivalent of Metals Abstracts and Alloys Index), Metals Abstracts, Nonferrous Metals Alert, Polymers Ceramics Composites Alert, Referativnyi Zhurnal, Science Citation Index, SciSearch (Electronic equivalent of Science Citation Index), Shock and Vibration Digest, Solid State and Superconductivity Abstracts, Steels Alert, Zentralblatt MATH

Dynamic Analysis of Laminated Composite Coated Beams Carrying Multiple Accelerating Oscillators Using a Coupled Finite Element-Differential Quadrature Method

S. A. Eftekhari
Department of Mechanical Engineering,
K. N. Toosi University,
Tehran 19395, Iran

M. Farid
Department of Mechanical Engineering,
Shiraz University,
Shiraz, Iran

M. Khani
Department of Civil Engineering,
Shiraz University,
Shiraz, Iran

In this paper, a numerical algorithm using a coupled finite element-differential quadrature (DQ) method is proposed for the dynamic analysis of laminated composite coated beams subjected to a stream of accelerating oscillators. The finite element method with cubic Hermitian interpolation functions is used to discretize the spatial domain. The DQ method is then employed to discretize the time domain. The resulting set of algebraic equations can be solved by either direct methods or iterative methods. It is revealed that the DQ method stands out in numerical accuracy, as well as in computational efficiency, over the well-known standard finite difference schemes, such as the Newmark, Wilson θ, Houbolt, and central difference methods, for the cases considered. Furthermore, in the numerical examples, the effects of various parameters having something to do with the title problem, such as lamina thickness, orientation of the coats, arrival time intervals, velocities, and accelerations of the oscillators on the dynamic behavior of the system, are investigated. The technique presented in this investigation is general and can be easily applied to any time-dependent problem. [DOI: 10.1115/1.3114969]

1 Introduction

The problem of calculating the dynamic response of structures excited by one or more moving oscillators is an interesting topic of considerable engineering importance. The use of composite materials in modern engineering has increased rapidly in recent years due to their light weight and high strength. Furthermore, laminated composite may be utilized as a coating to improve the behavior of dynamic systems, such as reduction in vibrations and noise and increase in total internal damping of the system [1]. Many analytical and numerical methods have been proposed in the past to study the dynamics of isotropic structures under the influence of moving loads [2–10]. But little attention has been paid to dynamics of laminated composite structures, besides, most researchers have focused on the multimoving forces and masses with constant speed and consequently constant arrival time intervals. Hence, the aim of this work focuses on the influence of properties of laminated composite and oscillators' accelerations and arrival time intervals on the dynamics of the system. Esmailzadeh and Ghorashi [11] analyzed the effects of shear deformation and rotary inertia on the vibration of the Timoshenko beam subjected to a traveling mass. In addition, Wang [12] investigated the forced vibration of multispan Timoshenko beams due to a moving force. The dynamic response of unsymmetric orthotropic laminated composite beams subjected to a moving force was studied by Kadivar and Mohebpour [13,14]. Lee and Yhim [15] analyzed the dynamics of composite plates under the action of multimoving loads based on a third order theory. The goal of this work is to develop a numerical procedure for calculating the dynamic response of a laminated composite coated beam, subjected to an arbitrary number of oscillators traveling along the beam at arbitrary speeds and accelerations. The finite element (FE) method is used for the spatial discretization, while the differential quadrature (DQ) method is used for the temporal discretization. The resulting set of algebraic equations can be solved by either direct methods (such as the Gaussian elimination method) or iterative methods (such as the Gauss–Seidel method). This paper also provides a comprehensive comparative study of various time integration methods in context of the finite element formulation of moving load problems. It is revealed that the DQ method gives much more accurate solutions than the traditional time step methods using a considerably smaller number of time points and therefore requiring relatively little computational effort.

2 Differential Quadrature Method

The DQ method is based on the idea that the derivative of a function at the any discrete point is approximated by a weighted linear sum of all the functional values in the whole domain [16]. For example the first- and second-order derivatives of function $f(t)$ at time point t_i can be expressed as

$$\left.\frac{df}{dt}\right|_{t=t_i} = \sum_{j=1}^{m} A_{ij}^{(1)} f(t_j) \tag{1}$$

$$\left.\frac{d^2f}{dt^2}\right|_{t=t_i} = \sum_{j=1}^{m} A_{ij}^{(2)} f(t_j) \tag{2}$$

where t_i are the discrete time points, $f(t_i)$ are the function values at these points, $A_{ij}^{(1)}$ and $A_{ij}^{(2)}$ are the weighting coefficients associated with the first- and second-order derivatives, respectively, and m is

Contributed by the Applied Mechanics Division of ASME for publication in the Journal of Applied Mechanics. Manuscript received December 27, 2006; final manuscript received November 18, 2008; published online July 21, 2009. Review conducted by Sanjay Govindjee.

the number of discrete time points. The weighting coefficients of the first-order derivative are given by [17]

$$A_{ik}^{(1)} = \begin{cases} \dfrac{M^{(1)}(t_i)}{(t_i - t_k)M^{(1)}(t_k)} & i \neq k, \quad i,k = 1,2,\ldots,m \\ -\displaystyle\sum_{j=1, j\neq i}^{m} A_{ij}^{(1)} & i = k, \quad i = 1,2,\ldots,m \end{cases} \tag{3}$$

where $M^{(1)}\ (t)$ is defined as

$$M^{(1)}(t_i) = \prod_{j=1, j\neq i}^{m} (t_i - t_j) \tag{4}$$

The weighting coefficients of the second-order derivative can be obtained from the following recurrence relationship [18]:

$$A_{ik}^{(2)} = \begin{cases} 2\left[A_{ii}^{(1)}A_{ik}^{(1)} - \dfrac{A_{ik}^{(1)}}{t_i - t_k}\right] & i \neq k, \quad i,k = 1,2,\ldots,m \\ -\displaystyle\sum_{j=1, j\neq i}^{m} A_{ij}^{(2)} & i = k, \quad i = 1,2,\ldots,m \end{cases} \tag{5}$$

In this work, the sampling time points are obtained from following equations ($0 \leq t \leq T$):

$$t_1 = 0, \quad t_2 = \delta \times T, \quad t_i = T/2\left[1 - \cos\left(\frac{(i-2)\pi}{m-2}\right)\right], \quad i = 3,4,\ldots,m \tag{6}$$

where t_2 is a time discrete point very close to the initial point (δ-point), and T is the time span.

3 Problem Formulation

To simplify the problem formulation, a symmetrical laminated beam with three layers is considered (Fig. 35). The top and bottom layers consist of composite material. This simple model was also used by several authors [1,19,20], and is very suitable for studying the dynamic behavior of laminated composite beams, subjected to a set of moving oscillators. Let q oscillators arrive at the left end of the beam, rested on visco-elastic foundation, at $T_1 = 0, T_2, \ldots, T_q$. If there are no external forces acting on the system, the equations governing its vibration can be written in the form

$$(EI)_{\text{eq}}\frac{\partial^4 w}{\partial x^4} + \rho_{\text{eq}}\frac{\partial^2 w}{\partial t^2} + C_0\frac{\partial w}{\partial t} + K_0 w = -\sum_{k=1}^{q}(M_k g + f_k(t))[h(t - T_k) - h(t - (T_k + T_{Tk}))]\delta(x - x_k(t)) \tag{7}$$

$$M_k \ddot{z}_k = f_k(t), \quad k = 1,2,\ldots,q, \quad T_k \leq t \leq T_k + T_{Tk} \tag{8}$$

where $(EI)_{\text{eq}}$ and ρ_{eq} are the equivalent bending stiffness and equivalent mass per unit length of the beam, respectively, $w(x,t)$ is the transverse deflection of the beam, C_0 and K_0 are the foundation parameters, M_k is the mass of the kth oscillator, $h(t)$ is the Heaviside unit-step function, $\delta(x)$ is the Dirac delta function, $z_k(t)$ is the deflection of the kth oscillator, T_{Tk} is the time required for the kth oscillator to traverse the beam, $x_k(t)$ is the position coordinate of the kth oscillator, and $f_k(t)$ is the interaction force between the beam and the kth oscillator. $x_k(t)$ and $f_k(t)$ are given by

$$x_k(t) = v_k(t - t_k) + \tfrac{1}{2}a_k(t - t_k)^2 \tag{9}$$

$$f_k(t) = K_k(w(x_k(t),t) - z_k(t)) + C_k(\dot{w}(x_k(t),t) - \dot{z}_k(t)) \tag{10}$$

where v_k and a_k are the arrival velocity and the acceleration of the kth oscillator, while K_k and C_k are stiffness and damping coefficients of the kth oscillator suspension. To obtain a FE model, the beam is divided into n number of elements. Using the weak formulation and finite element approximation, Eq. (7) can be written as

$$[M^e]\{\ddot{w}^e\} + [C_{fn}^e]\{\dot{w}^e\} + ([K_{fn}^e] + [K^e])\{w^e\} = \{F^e\} + \{Q^e\} \tag{11}$$

where

$$K_{ij}^e = (EI)_{\text{eq}}\int_{x_e}^{x_{e+1}} \frac{d^2\psi_i^e}{dx^2}\frac{d^2\psi_j^e}{dx^2}dx, \quad i,j = 1,2,3,4 \tag{12}$$

$$M_{ij}^e = \rho_{\text{eq}}\int_{x_e}^{x_{e+1}} \psi_i^e\psi_j^e dx, \quad C_{fn_{ij}}^e = C_0\int_{x_e}^{x_{e+1}} \psi_i^e\psi_j^e dx, \quad K_{fn_{ij}}^e = K_0\int_{x_e}^{x_{e+1}} \psi_i^e\psi_j^e dx \tag{13}$$

$$w^e(x,t) = \sum_{j=1}^{4} w_j^e(t)\psi_j^e(x) \tag{14}$$

$$F_i^e(t) = -\sum_{k=1}^{q}(M_k g + f_k(t))[h(t - t_{in,k}^e) - h(t - t_{in,k}^e + t_{tk}^e)]\psi_i^e(x_k(t)), \quad x_e \leq x_k(t) \leq x_{e+1}, \quad k = 1,2,\ldots,q \tag{15}$$

where ψ_i^e are the Hermit cubic interpolation functions, $t_{in,k}^e$ is the time at which the kth oscillator arrives at left-hand side of the eth element, and t_{tk}^e is the traveling time of the kth oscillator for eth element. One can easily see from Eq. (15) that all nodal forces of the beam are equal to zero except those of the beam element on which the moving loads are applied. For the differential quadrature solution, consider m sampling points in the time domain, $0 \leq t \leq t_T$, where t_T is the total traveling time of all oscillators. From Eqs. (1) and (2), the first- and second-order derivatives of $z_k(t)$ and $w(x_k(t),t)$ may be written in matrix notation as

$$\{\dot{z}_k\} = [A]^{(1)}\{z_k\}, \quad \{\ddot{z}_k\} = [A]^{(2)}\{z_k\} \tag{16}$$

$$\{\dot{w}_{d,k}\} = [A]^{(1)}\{w_{d,k}\} \tag{17}$$

where

$$\{z_k\} = [z_k(t_1) \quad z_k(t_2) \quad \cdots \quad z_k(t_m)]^T \tag{18}$$

$$\{w_{d,k}\} = [w(x_k(t_1),t_1) \quad w(x_k(t_2),t_2) \quad \cdots \quad w(x_k(t_m),t_m)]^T \tag{19}$$

Now, the quadrature analog of Eq. (8) can be written in matrix notation as

$$(M_k[A]^{(2)} + C_k[A]^{(1)} + K_k[I])\{z_k\} = (C_k[A]^{(1)} + K_k[I])\{w_{d,k}\} \tag{20}$$

Applying the initial conditions of the kth oscillator, Eq. (20) can be written in the following form:

$$\{z_k\} = [B_k]\{w_{d,k}\} + \{N_k\} \tag{21}$$

In the case of zero initial conditions for the kth oscillator, Eq. (21) is reduced to

$$\{z_k\} = [B_k]\{w_{d,k}\} \tag{22}$$

In order to simplify the calculation of components of load vector of each element in which the kth oscillator is traveling, the following definitions are introduced:

$$\{\psi_{i,k}^e\} = \begin{cases} \psi_i^e(x_k(t_j)), & x_e \leq x_k(t_j) \leq x_{e+1} \\ 0, & x_k(t_j) < x_e \quad \text{or} \quad x_k(t_j) > x_{e+1} \end{cases}, \quad i = 1,2,3,4, \quad j = 1,2,\ldots,m \tag{23}$$

$$[\psi^e_{i,k}] = \text{diag}\{\psi^e_{i,k}\} \tag{24}$$

Using Eqs. (23) and (24) and

$$w^e(x_k(t_i),t_i) = \sum_{j=1}^{4} w^e_j(t_i)\psi^e_j(x_k(t_i)) \tag{25}$$

The vector $\{w_{d,k}\}$ would be written as

$$\{w_{d,k}\} = \sum_{e=1}^{n} ([\psi^e_{1,k}]\{w^e_1\} + [\psi^e_{2,k}]\{w^e_2\} + [\psi^e_{3,k}]\{w^e_3\} + [\psi^e_{4,k}]\{w^e_4\})$$
$$= \sum_{e=1}^{n}\sum_{j=1}^{4} [\psi^e_{j,k}]\{w^e_j\} \tag{26}$$

where

$$\{w^e_j\} = [w^e_j(t_1) \quad w^e_j(t_2) \quad \cdots \quad w^e_j(t_m)^T] \tag{27}$$

Now, consider the first equation of the system of equations (11), the quadrature analog of this equation may be written in matrix notation as

$$(M^e_{11}[A]^{(2)} + C_{fn_{11}}[A]^{(1)} + (K^e_{11} + K_{fn_{11}})[I])\{w^e_1\} + (M^e_{12}[A]^{(2)} + C_{fn_{12}}[A]^{(1)} + (K^e_{12} + K_{fn_{12}})[I])\{w^e_2\} + (M^e_{13}[A]^{(2)} + C_{fn_{13}}[A]^{(1)} + (K^e_{13} + K_{fn_{13}})[I])\{w^e_3\} + (M^e_{14}[A]^{(2)} + C_{fn_{14}}[A]^{(1)} + (K^e_{14} + K_{fn_{14}})[I])\{w^e_4\} = \{F^e_1\} + \{Q^e_1\} \tag{28}$$

where

$$\{F^e_1\} = [F^e_1(t_1) \quad F^e_1(t_2) \quad \cdots \quad F^e_1(t_m)^T] \tag{29}$$

$$\{Q^e_1\} = [Q^e_1(t_1) \quad Q^e_1(t_2) \quad \cdots \quad Q^e_1(t_m)^T] \tag{30}$$

The force vector in right side of Eq. (28) can be written as

$$\{F^e_1\} = \sum_{k=1}^{q} (-M_k g\{\psi^e_{1,k}\} + [\psi^e_{1,k}]([K_k]([B_k] - [I])\{w_{d,k}\} + C_k[A] \times ([B_k] - [I])\{w_{d,k}\})) \tag{31}$$

Equation (31) can also be rewritten as

$$\{F^e_1\} = \sum_{k=1}^{q} (-M_k g\{\psi^e_{1,k}\} + [\psi^e_{1,k}][D_k]\{w_{d,k}\}) = \{F^e_1\}_g + \{F^e_1\}_{\text{int}} \tag{32}$$

Using $[D_k]$ as

$$[D_k] = (C_k[A]^{(1)} + K_k[I])([B_k] - [I]) \tag{33}$$

From Eqs. (26) and (32) one can obtain

$$\{F^e_1\}_{\text{int}} = \sum_{k=1}^{q} [\psi^e_{1,k}][D_k]\sum_{e=1}^{n}\sum_{j=1}^{4} [\psi^e_{j,k}]\{w^e_j\} \tag{34}$$

Applying the above procedure to the remaining three equations of the system of equations (11) yields

$$[K^e_{\text{exp}}]\{w'\} = \{F^e_{\text{exp}}\} + \{Q^e_{\text{exp}}\} \tag{35}$$

The subscript "exp" means that the associated matrix or vector is written in the global coordinate system, and $\{w'\}$ is the global nodal vector as

$$\{w'\} = \{\{w_1\}^T \quad \{w_2\}^T \quad \cdots \quad \{w_{2n+2}\}^T\}^T \tag{36}$$

The assembled matrices can be easily obtained as

$$[K'] = \sum_{e=1}^{n} K^e_{\text{exp}}, \quad \{F'\} = \sum_{e=1}^{n} F^e_{\text{exp}}, \quad \{Q'\} = \sum_{e=1}^{n} Q^e_{\text{exp}} \tag{37}$$

and finally

$$[K']\{w'\} = \{F'\} + \{Q'\} \tag{38}$$

where $[K']$ is the $(2n+2)m \times (2n+2)m$ matrix and $\{w'\}$, $\{f'\}$, and $\{Q'\}$ are the $(2n+2)m \times 1$ vectors.

4 Solution of Resulting Algebraic Equations

By using the proposed mixed methodology we finally obtained a large system of algebraic equations for the nodal values containing both discretized space and time points (Eq. (38)). After applying the initial and boundary conditions to this equation, one can easily solve the resulting equations by using the direct methods or iterative methods for unknown displacements. In this work the Gaussian elimination method is used to solve the resulting algebraic equations. Before solving Eq. (38), and after applying the boundary conditions to this equation, it is better to rewrite this equation in the standard partitioned form

$$\begin{bmatrix} [K'_{ii}] & [K'_{id}] \\ [K'_{di}] & [K'_{dd}] \end{bmatrix} \begin{bmatrix} \{w'_i\} \\ \{w'_d\} \end{bmatrix} = \begin{bmatrix} \{F'_i\} \\ \{F'_d\} \end{bmatrix} \tag{39}$$

In this matrix equation, the subscripts i and d indicate the sample time points used for writing the quadrature analog of the initial conditions and the ordinary differential equations, respectively. By eliminating the column vector $\{w'_i\}$, the matrix equation (39) is reduced to the following algebraic equation:

$$[K'']\{w'_d\} = \{F''\} \tag{40}$$

where

$$[K''] = [K'_{dd}] - [K'_{di}][K'_{ii}]^{-1}[K'_{id}] \tag{41}$$

$$\{F''\} = \{F'_d\} - [K'_{di}][K'_{ii}]^{-1}\{F'_i\} \tag{42}$$

After solving Eq. (40) for displacements, one can use the Lagrange interpolation scheme to obtain the solutions at all the time domain.

5 Numerical Stability

Numerical stability is a crucial issue for a computational method. It is of great importance to know whether a numerical algorithm is stable or not. The DQ method approximates the partial derivative of a function with respect to a space/time variable at a given discrete point as a weighted linear sum of the function values at all discrete points. This is in contrast to the standard finite difference method (FDM) in which a solution value at a point is a function of values at adjacent points only. Actually, the DQ method is an extension of the FDM [18]. It is also shown that when the grid points are chosen to be Chebyshev collocation points, the DQ method is identical to the Chebyshev collocation method [18]. As we know, the FDM and Chebyshev collocation method are stable. Hence due to the natural equivalence between the DQ method and these methods, it is expected that the DQ method to be also stable. The stability of the DQ method for solving various static problems was shown in Ref. [16] and the references therein. However, to obtain accurate and stable results the number of sample points cannot be too large. In other words, the resulting DQ discretization matrix tends to become ill-conditioned when a very large number of sample points are used. To overcome this difficulty one should carefully select the ordering of sample points to get a well-conditioned DQ discretization matrix. For example, for the present problem, the use of equally spaced sample points may result in ill-conditioned matrix $[K']$. This ill-conditioning can be removed by using the nonuniform sample points. But when the number of time points is very large, it is better to use this type of points with an adjacent δ-point (Eq. (6)). Note that the δ-technique, as proposed in Ref. [16], is not used in this work. The derivative initial conditions are exactly satisfied at initial points and therefore the numerical solutions do not depend on the choice of δ-value. We only use this type of points to calculate the weighting coefficients.

However, it is evident that when the proposed formulation is applied to multidimensional problems, the dimension of resulting matrix $[K']$ is too large. Hence the virtual storage required increases considerably. Furthermore, this may lead to difficulties in obtaining the solution or even worse, reduce the accuracy of the solutions. This may also affect the stability of the scheme. These difficulties can be overcome by using the multidomain DQ technique. In this technique, the time domain is decomposed into several time elements. For each time element, a procedure similar to a single time domain, as stated before, can be repeated. Since the time domain is not bounded, this procedure can be performed independently for each time element. Note that the initial conditions of the $(i+1)$th time element can be obtained using the solutions of the ith time element. The solution procedure is summarized bellow for use in a computer program. It is assumed that the time domain is divided into n_T equal DQM time elements with an equal number of sample time points.

For Part A: initial calculations,

1. form element matrices $[M^e]$, $[C^e]$, and $[K^e]$
2. select n_T (number of time elements) and m (number of time points per element)
3. form weighting coefficient matrices $[A]^{(1)}$ and $[A]^{(2)}$
4. form matrix $[K'']$

For Part B: for each time element,

1. form vector $\{f''\}$
2. solve Eq. (40) by either direct methods (such as the Gaussian elimination method) or iterative methods (such as the Gauss–Seidel method) for unknown displacements
3. evaluate the derivative initial conditions of the next time element

6 Numerical Accuracy

Consider a function $f(t)$, which is approximated by the Lagrange interpolation polynomial of degree $(m-1)$. The error for the rth order derivative approximation of this function at point t_i can be obtained as [18]

$$E^{(r)}[f(t_i)] = \frac{f^{(m)}(\xi)\cdot M^{(r)}(t_i)}{m!}, \quad i=1,2,\ldots,m \tag{43}$$

where

$$M(t) = \prod_{j=1}^{m}(t-t_j) \tag{44}$$

It may be seen that very high accuracy can be achieved even if the number of sample points, m, is not too large. Also the accuracy of DQ method is proportional to m or its power.

7 Numerical Results and Discussion

Before studying the title problem, two numerical examples are presented, and the superiority of the DQ method over the classical implicit step methods, such as the Newmark, Wilson θ, Houbolt, and central difference methods, is demonstrated. Parameters $\alpha=0.25$ and $\delta=0.5$ are taken in the Newmark scheme and $\theta=1.4$ in the Wilson θ method [21].

7.1 Example 1: Vibration of a Simply Supported Beam Due to a Moving Point Load.

Consider a concentrated load moving with a constant speed on a simply supported beam. The parameters used in this numerical example are as follows:

$$EI/\rho = 10^4 \ \mathrm{m^4/s^2}, \quad M/\rho L = 0.001, \quad L=50 \ \mathrm{m}, \quad T_f = 50/\pi \ \mathrm{s}$$

This problem has an analytical solution [22], and the accuracy of the proposed mixed methodology is demonstrated by comparing the calculated results with those of analytical solutions.

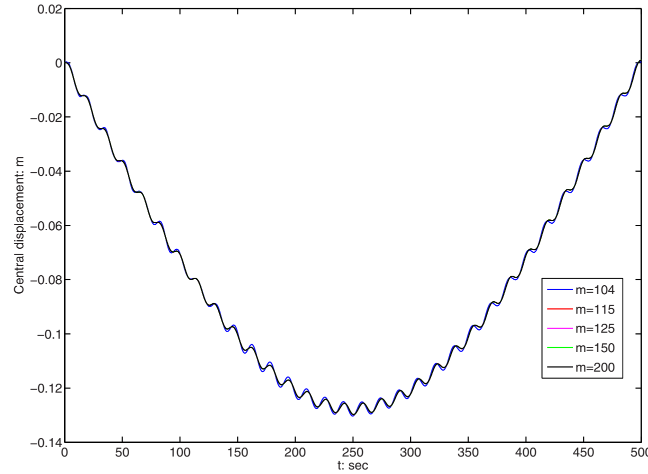

Fig. 1 Convergence of solutions with respect to the number of sample time points for $v=0.1$ m/s ($n=4$)

The central displacements of the beam are calculated for different values of v (velocity of moving load). Figures 1–3 present the convergence of solutions with respect to the number of sample time points for $v=0.1$, 0.2, and 0.75 m/s, respectively. Note that the central displacement values at all the time domain (i.e., $0\le t$

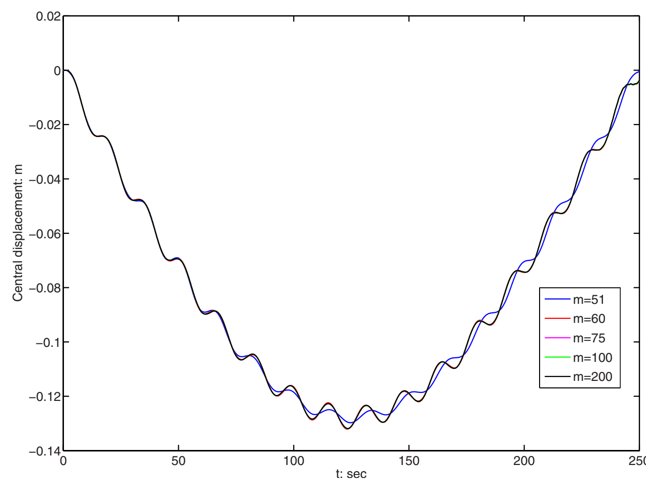

Fig. 2 Convergence of solutions with respect to the number of sample time points for $v=0.2$ m/s ($n=4$)

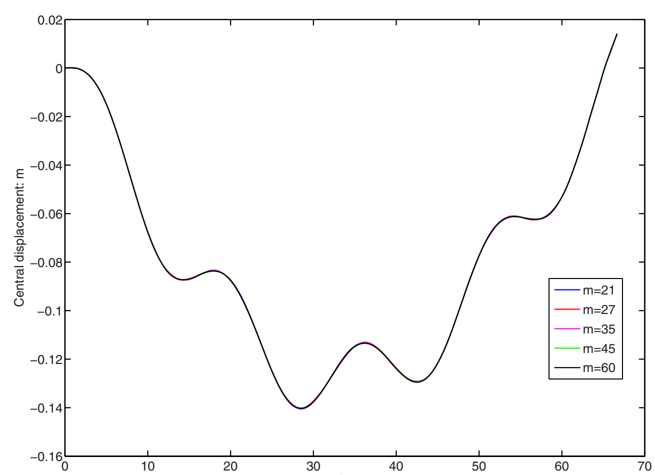

Fig. 3 Convergence of solutions with respect to the number of sample time points for $v=0.75$ m/s ($n=4$)

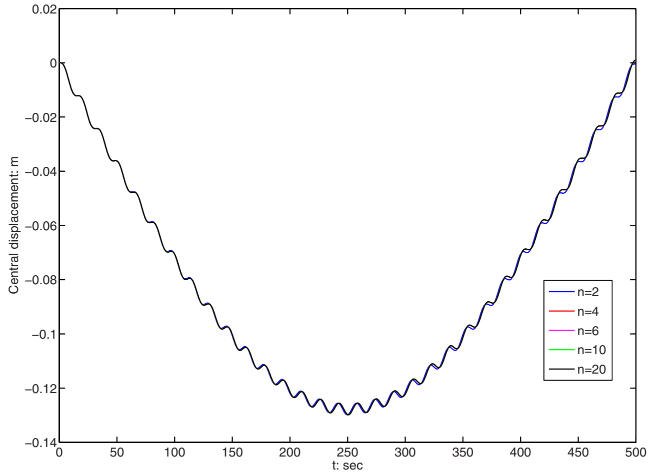

Fig. 4 Convergence of solutions with respect to the number of finite elements for $v=0.1$ m/s ($m=115$)

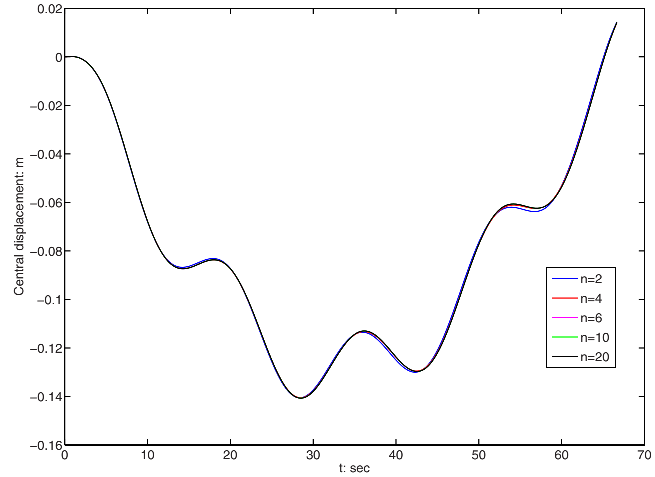

Fig. 6 Convergence of solutions with respect to the number of finite elements for $v=0.75$ m/s ($m=21$)

$\leq T$ where $T=L/v$) are obtained by the Lagrange interpolation from the quadrature solution results at discrete time points. It can be seen that the converging trend of solutions is excellent. The solution convergence behaviors according to the number of finite elements for $v=0.1$, 0.2, and 0.75 m/s are shown in Figs. 4–6, respectively. A very good convergence behavior is observed. Figures 7 and 8 present the central displacement of the simply supported beam for $v=0.1$ m/s. As it can be seen, the DQ method gives better accuracy than other finite difference schemes using a smaller number of time points. Numerical results for $v=0.2$ m/s are shown in Figs. 9 and 10. It is seen that the DQ method can obtain more accurate solutions than other schemes using a considerably smaller number of sample time points. Figures 11 and 12 illustrate the results for $v=0.75$ m/s. Again, the DQ method shows high accuracy and efficiency. From Figs. 7, 9, and 11 it is seen that all the time step methods have a great loss of accuracy when a small number of grid time points are used for time discretization. From Fig. 13, one sees that the solutions obtained by various direct integration schemes are not acceptable in accuracy, while the DQ method presents high accuracy. When a large number of time points are used for time discretization, Fig. 14 illustrates the results for $v=2.5$ m/s. As seen, all the finite difference schemes provide the exact solution using a sufficiently large number of time points. From Fig. 15, it is seen that except for the DQ method, all other schemes have a great loss of accuracy. When a larger number of time points are used, Fig. 16 shows distinct performance of various time step schemes. It is seen that all methods provide the exact solution. From the DQM solutions shown in the Figs. 1–16, it is found that the number of time points required to achieve accurate solutions only depends on the shape of dynamic responses (the value of v, in this case). As the velocity

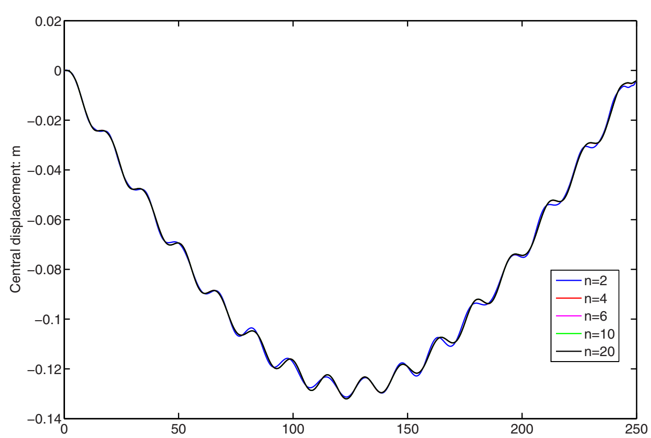

Fig. 5 Convergence of solutions with respect to the number of finite elements for $v=0.2$ m/s ($m=60$)

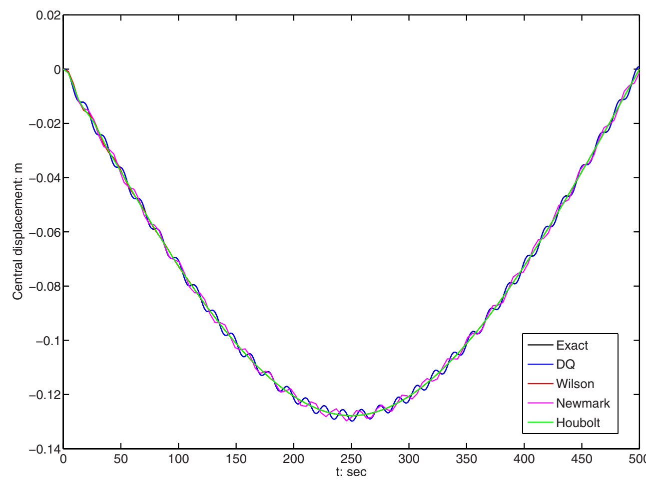

Fig. 7 Central displacement of a simply supported beam subjected to a moving point load ($v=0.1$ m/s, $n=4$, and $m=115$)

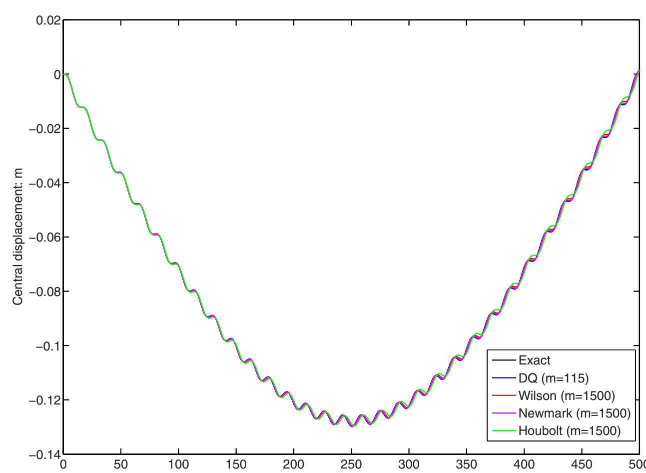

Fig. 8 Central displacement of a simply supported beam subjected to a moving point load ($v=0.1$ m/s and $n=4$)

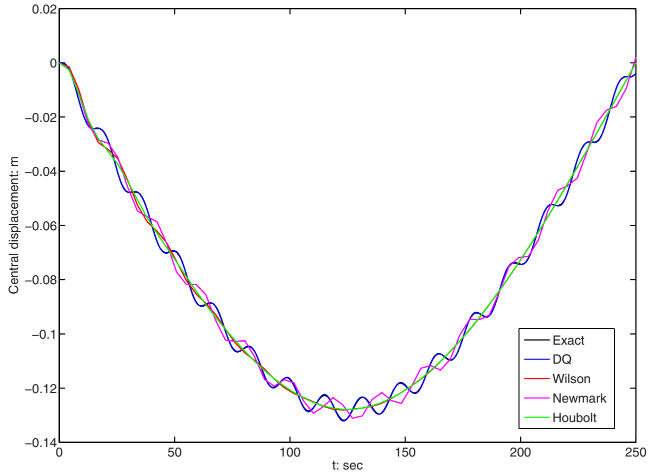

Fig. 9 Central displacement of a simply supported beam subjected to a moving point load ($v=0.2$ m/s, $n=4$, and $m=60$)

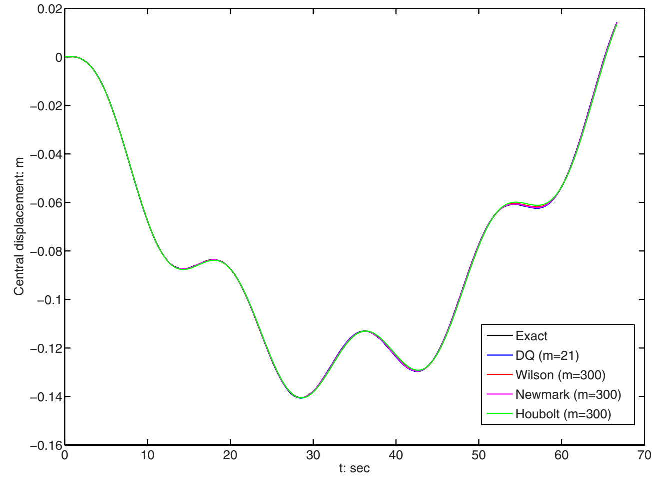

Fig. 12 Central displacement of a simply supported beam subjected to a moving point load ($v=0.75$ m/s and $n=6$)

of the moving point load increases, the shape of dynamic responses becomes smoother, hence the number of time points required to obtain accurate results decreases, since the DQ method is basically based on polynomial interpolation and derivation. To demonstrate the rate of convergence of the presented mixed methodology, the percent errors in displacements (defined as $(w_{\text{numerical}}-w_{\text{exact}})/w_{\text{exact}}\times 100$) are calculated for different values of v and m. In Figs. 17–20, the percent error in solutions is plotted against the number of time points. As seen, the rate of convergence and accuracy of the DQM are superior over the traditional

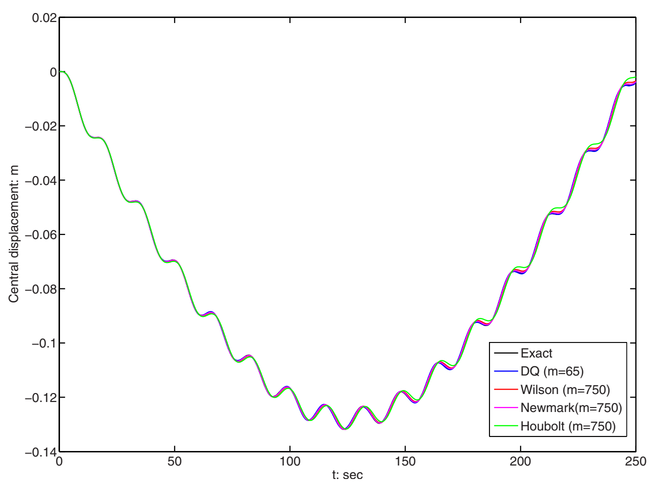

Fig. 10 Central displacement of a simply supported beam subjected to a moving point load ($v=0.2$ m/s, and $n=4$)

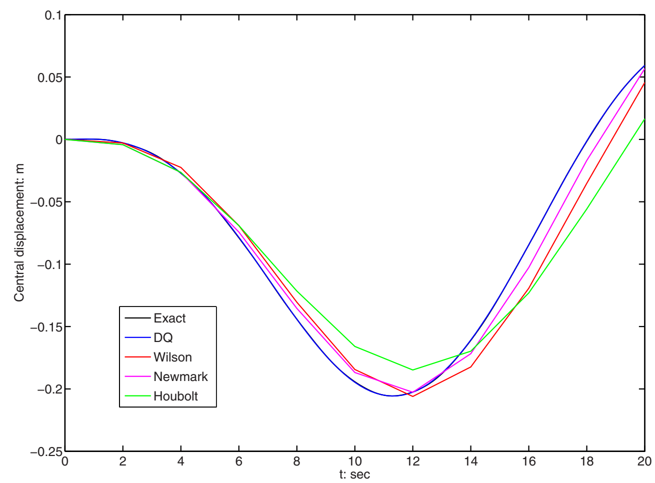

Fig. 13 Central displacement of a simply supported beam subjected to a moving point load ($v=2.5$ m/s, $n=4$, and $m=11$)

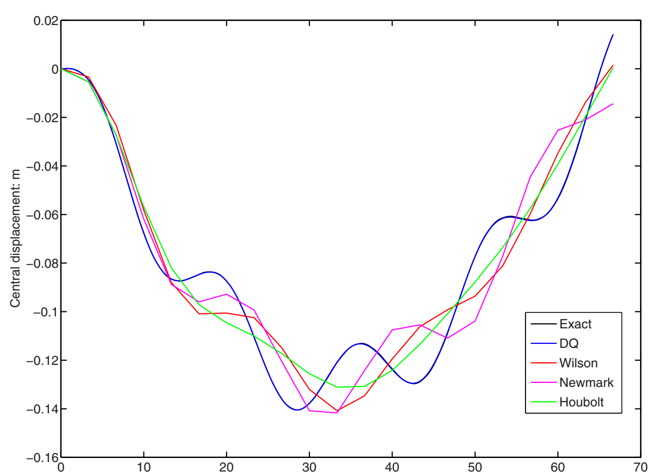

Fig. 11 Central displacement of a simply supported beam subjected to a moving point load ($v=0.75$ m/s, $n=6$, and $m=21$)

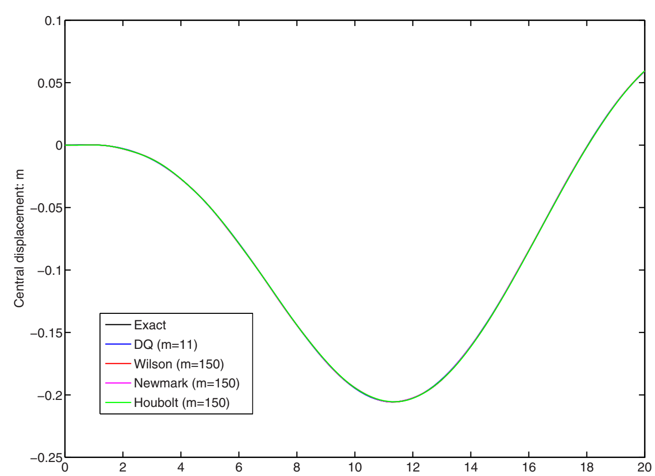

Fig. 14 Central displacement of a simply supported beam subjected to a moving point load ($v=2.5$ m/s and $n=4$)

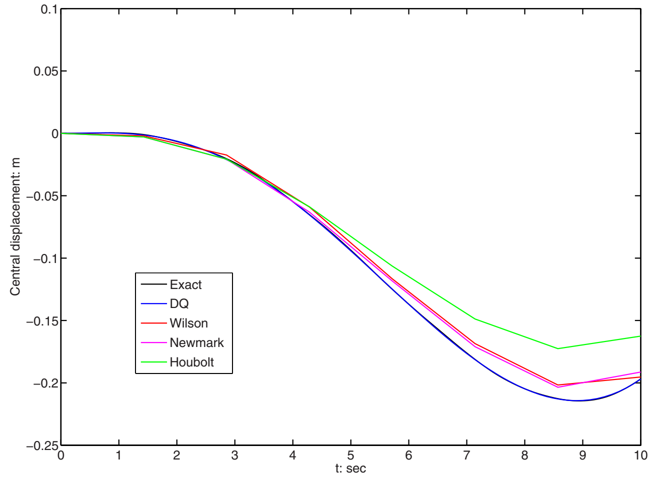

Fig. 15 Central displacement of a simply supported beam subjected to a moving point load ($v=5$ m/s, $n=4$, and $m=8$)

time step methods. To investigate the effect of δ-value on accuracy and stability of numerical results, numerical experiments are carried out for different values of δ and the results are shown in Figs. 21 and 22. It can be seen clearly from Figs. 21 and 22 that the accuracy and stability of results do not depend on the choice

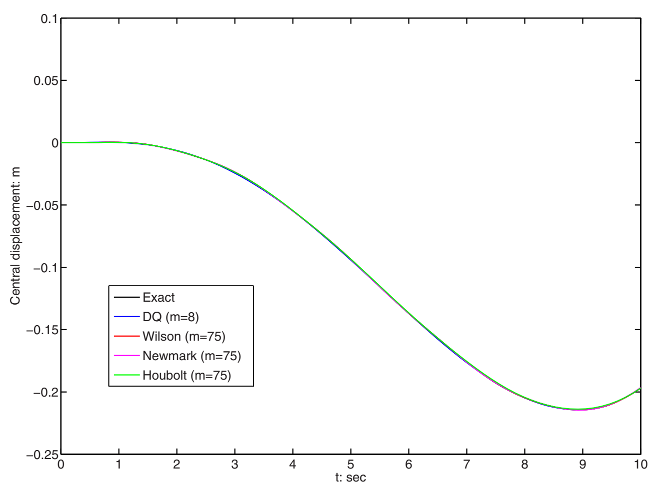

Fig. 16 Central displacement of a simply supported beam subjected to a moving point load ($v=5$ m/s and $n=4$)

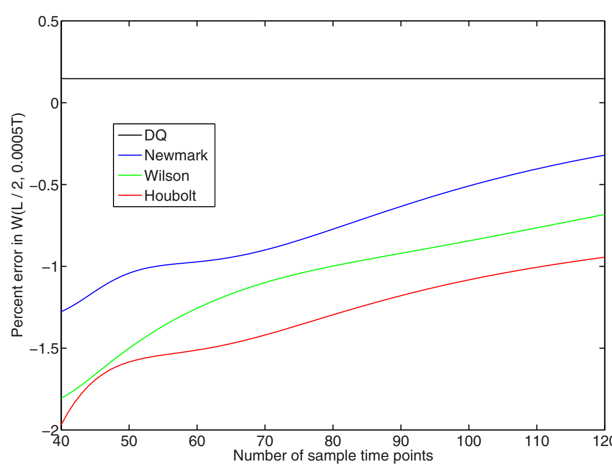

Fig. 17 Convergence of solutions with respect to the number of sample time points for $v=0.05$ m/s ($n=8$)

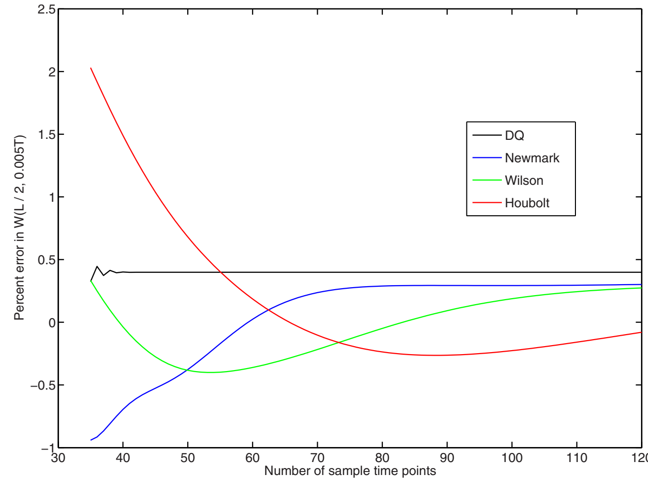

Fig. 18 Convergence of solutions with respect to the number of sample time points for $v=0.25$ m/s ($n=6$)

of δ-value. In Figs. 23 and 24, the percent error in solutions is plotted against the number of time points without and with δ-point. The results of other time step methods are also included for comparison. It can be observed from Figs. 23 and 24 that when the δ-point is used better accuracy and convergence are achieved. To test the accuracy, convergence, and stability of mixed FE and

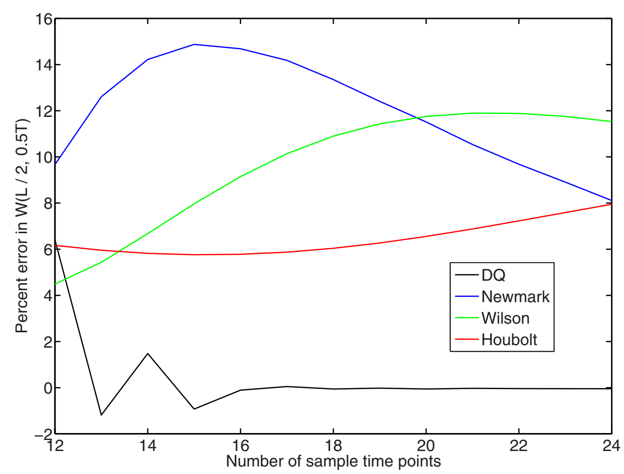

Fig. 19 Convergence of solutions with respect to the number of sample time points for $v=0.5$ m/s ($n=4$)

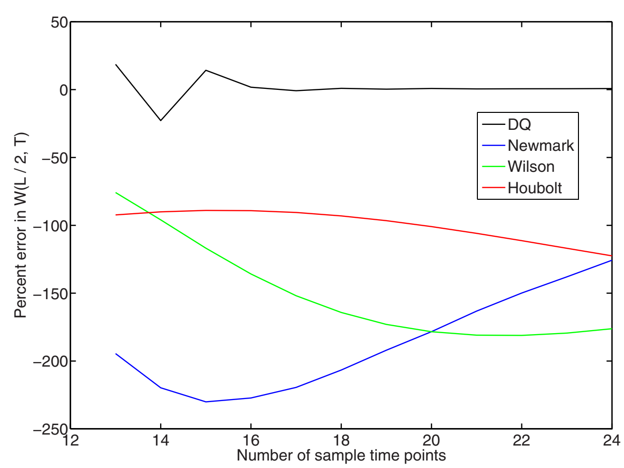

Fig. 20 Convergence of solutions with respect to the number of sample time points for $v=1$ m/s ($n=6$)

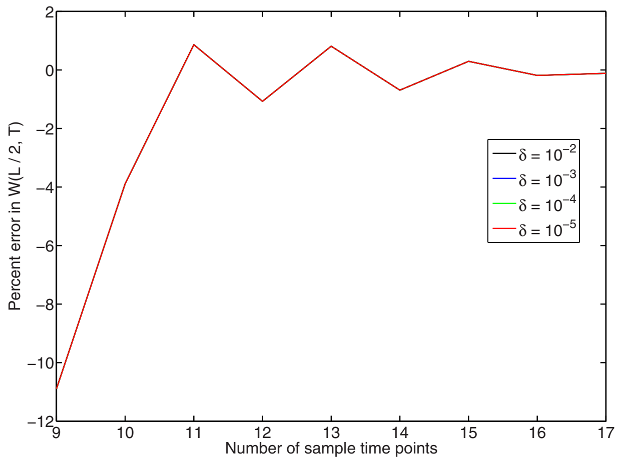

Fig. 21 Effect of δ-value on accuracy and stability of numerical results ($v=2$ m/s and $n=4$)

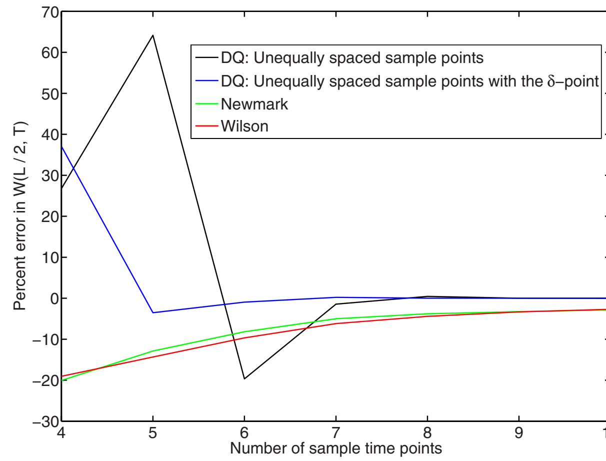

Fig. 24 Convergence of solutions with respect to the number of sample time points for $v=7$ m/s ($n=4$)

multidomain DQ techniques, the present numerical example is considered. Figures 25 and 26 present the convergence behavior of solutions with respect to the number of time elements (n_T). It is observed that the solutions have excellent accuracies without instability for an increase in the number of time elements. Also, the total number of time points ($M_{\text{tot}}=n_T(m-1)+1$) required to achieve accurate solutions is minimum when a single time element is used.

7.2 Example 2: Vibration of an Elastic Beam Carrying Moving Linear Oscillator.

Consider an elastic beam subjected to a moving oscillator. The beam and oscillator parameters are given

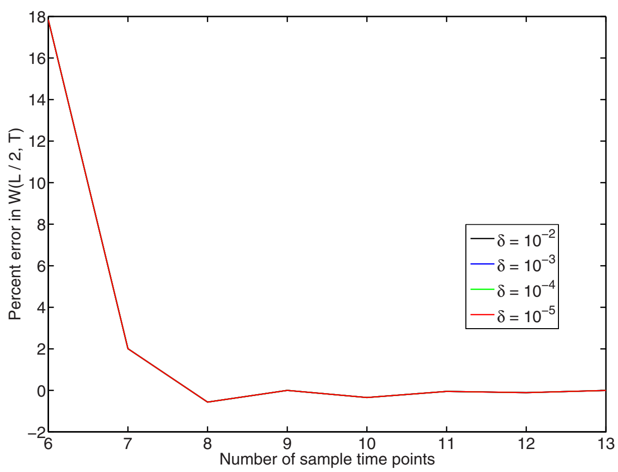

Fig. 22 Effect of δ-value on accuracy and stability of numerical results ($v=4$ m/s and $n=6$)

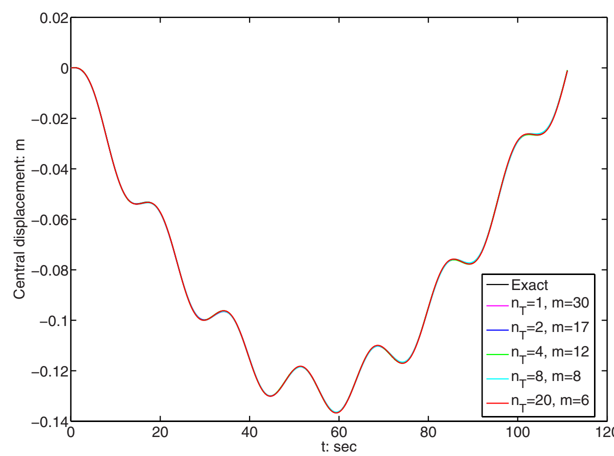

Fig. 25 Convergence of solutions with respect to the number of time elements for $v=0.45$ m/s ($n=4$)

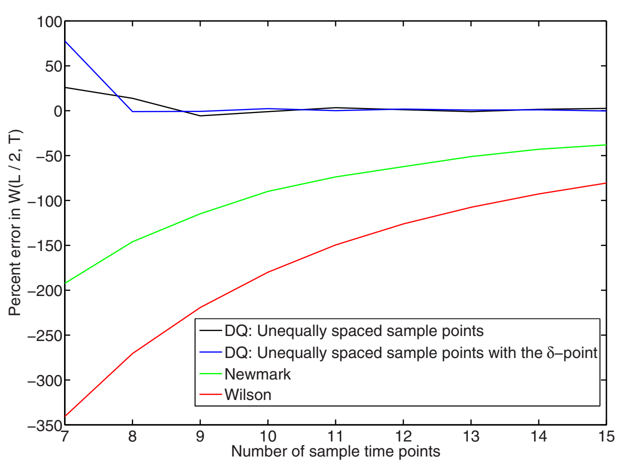

Fig. 23 Convergence of solutions with respect to the number of sample time points for $v=3$ m/s ($n=4$)

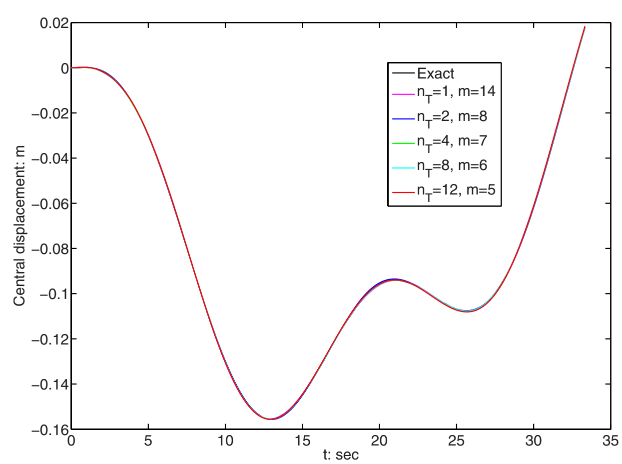

Fig. 26 Convergence of solutions with respect to the number of time elements for $v=1.5$ m/s ($n=4$)

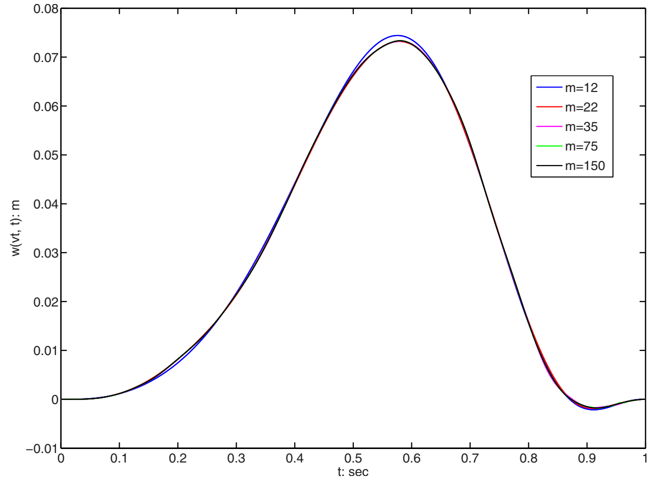

Fig. 27 Convergence of solutions with respect to the number of sample time points for $v=6$ m/s ($n=6$)

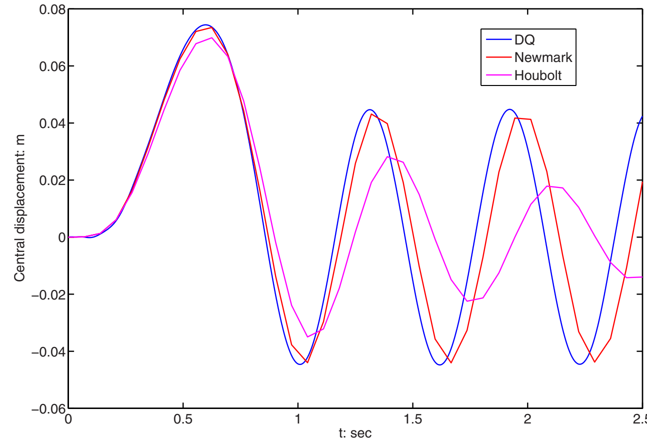

Fig. 29 Central displacement of a clamped-clamped beam subjected to a moving oscillator ($v=6$ m/s, $n=6$, and $m=37$)

by $EI/\rho=275.4408\ \mathrm{m^4/s^2}$, $M/\rho L=0.2$, $K=2000$ N/m, and $L=6$ m [23].

To be consistent with the cited work, the negative response $[-w(x,t)]$ is shown in the figures.

Figures 27 and 28 demonstrate the solutions' convergence behavior for the clamped-clamped beam subjected to a moving linear oscillator with respect to the number of sample time points and finite elements, respectively. The convergence behavior of solutions is excellent, and it is evident that only 22 sample time points is sufficient for this case. The results are also in good agreement with those found in Ref. [23]. Figures 29 and 30 present the midspan deflection of the clamped-clamped beam for $v=6$ m/s. As seen, when a small number of time points are used for time discretization the solutions of the conventional time step methods encounter a sharp drop of accuracy in long-term response, while the DQ method exhibits high accuracy and efficiency. Figures 31 and 32 present the midspan displacement of the simply supported beam for $v=6$ m/s. As it can be seen, the solutions of the Newmark and Houbolt methods have visible phase shift and a great loss of accuracy in long-term response. Figures 33 and 34 show the central displacement of the simply supported beam for $v=6$ m/s. Again, the DQ method gives better accuracy than other methods using a smaller number of time points. From Figs. 29, 31, and 33 one can also observe the numerical damping of the Houbolt method. Figures 30, 32, and 34 also show that the central difference method produces accurate results only when a very large number of sample points are used for time discretization (i.e., a very small time step need to be used).

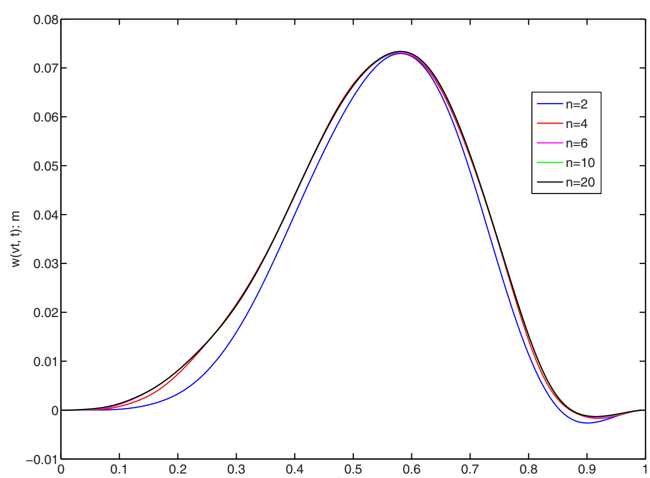

Fig. 28 Convergence of solutions with respect to the number of finite elements for $v=6$ m/s ($m=25$)

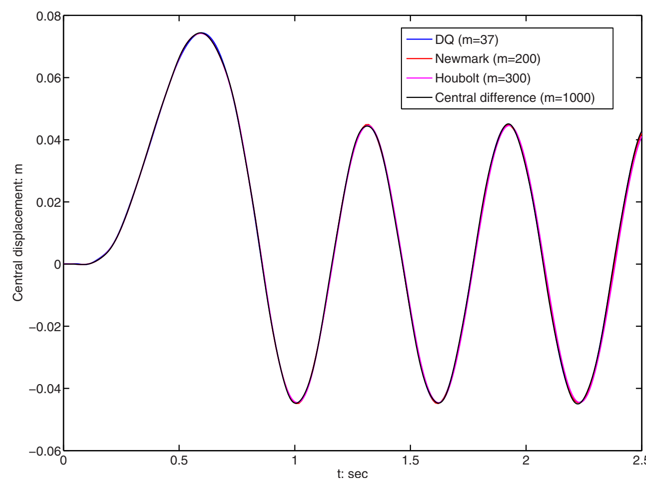

Fig. 30 Central displacement of a clamped-clamped beam subjected to a moving oscillator ($v=6$ m/s and $n=6$)

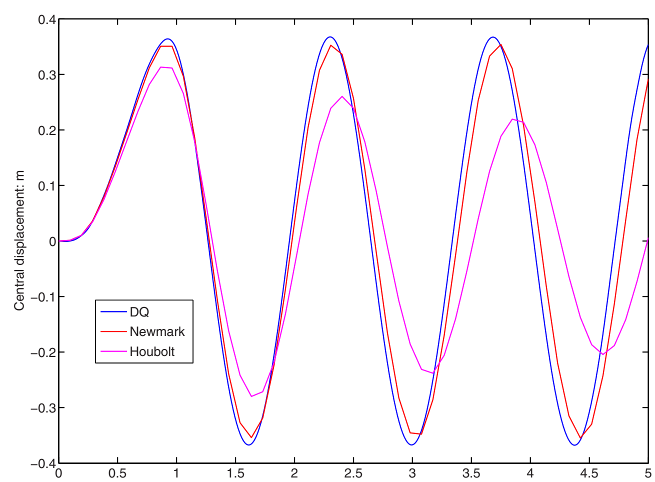

Fig. 31 Central displacement of a simply supported beam subjected to a moving oscillator ($v=6$ m/s, $n=6$, and $m=53$)

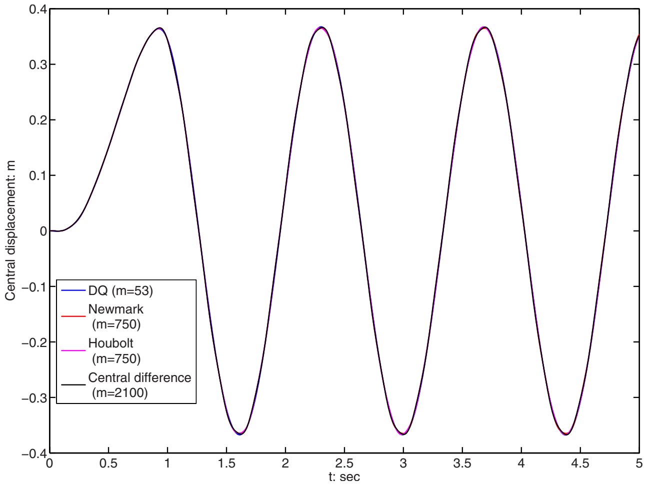

Fig. 32 Central displacement of a simply supported beam subjected to a moving oscillator (v=6 m/s and n=6)

7.3 Forced Vibration of a Laminated Composite Coated Beam Due to a Moving Oscillator. Figure 35 shows the cross section of a laminated composite coated beam and associated parameters, h and H. In this figure h and H are the half thickness of the core and the half thickness of the laminated coated beam, respectively. It is assumed that the core is made from steel and the faces are made from glass-epoxy composite material. In this numerical example, the following data for the laminated composite coated beam and oscillator are used:

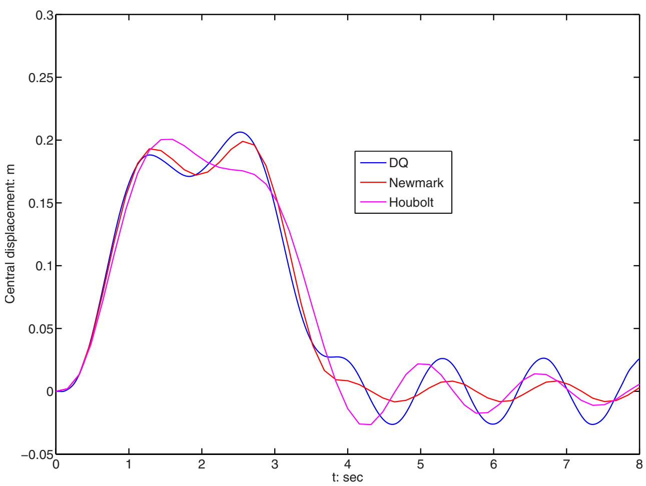

Fig. 33 Central displacement of a simply supported beam subjected to a moving oscillator (v=1.5 m/s, n=6, and m=51)

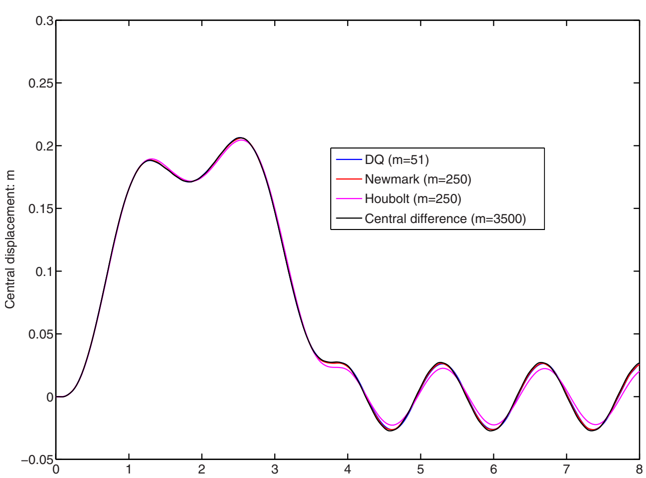

Fig. 34 Central displacement of a simply supported beam subjected to a moving oscillator (v=1.5 m/s and n=6)

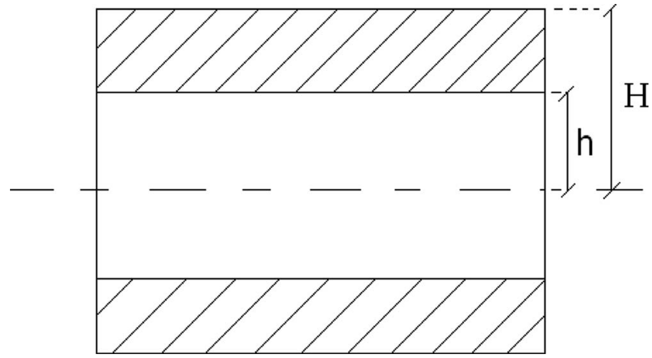

Fig. 35 Laminated composite coated beam cross section

$$E_{11} = 38.6 \text{ GPa}, \quad E_{22} = 8.27 \text{ GPa}, \quad G_{12} = 4.14 \text{ GPa},$$

$$E_c = 200 \text{ GPa}$$

$$\upsilon_{12} = 0.26, \quad H = 1 \text{ m}, \quad \rho_f = 1759 \text{ Kg/m}^3,$$

$$\rho_c = 7850 \text{ Kg/m}^3, \quad L = 30 \text{ m}$$

$$M = 4 \times 10^4 \text{ kg}, \quad K = 9 \times 10^6 \text{ N/m}, \quad C = 8 \times 10^4 \text{ Ns/m},$$

$$b = 2 \text{ m}$$

where E_c, ρ_f, ρ_c, and b are the core Young's modulus, the density of the beam faces, the density of the core, and the beam width, respectively. Figures 36 and 37 show the effects of parameters h/H and orientation of the coats, θ, on the dynamic magnification factor. In the results shown in Figs. 36 and 37 the velocity of the oscillator is assumed to be constant and equals to 30 m/s. From these figures, one sees that the shape of curves become smoother as the h/H increases or θ decreases. In Figs. 38 and 39, the dynamic magnification factor versus the velocity of moving oscillator for different values of θ and h/H is presented. From Fig. 38, it can be seen that the critical velocity (the velocity at which the maximum dynamic central deflection appears) first decreases and then increases when the h/H increases. As seen in Fig. 39, the

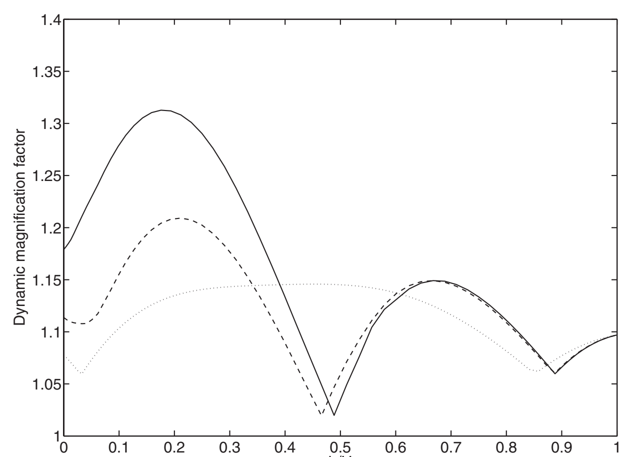

Fig. 36 Effects of parameters h/H and θ on the dynamic magnification factor, v=30 m/s; θ=0 (dotted line), θ=45 (dashed line), and θ=90 (solid line)

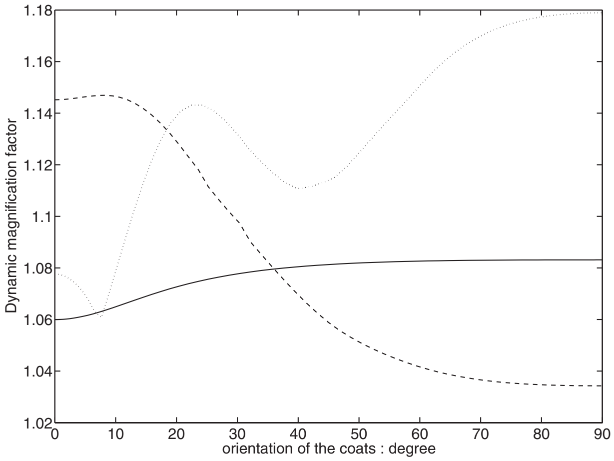

Fig. 37 Effects of parameters h/H and θ on the dynamic magnification factor, v=30 m/s; h/H=0 (dotted line), h/H=0.5 (dashed line), and h/H=0.85 (solid line)

critical velocity decreases as the θ increases because the beam is stiffer when the coats orientate at θ=0. It is evident that the dynamic magnification factor can be controlled by choosing the proper fiber orientation or lamina thickness. From Fig. 39 it is seen that at high speeds the dynamic magnification factor for glass-epoxy beam is considerably lower than that for steel beam, in spite of the fact that the weight of composite beam is approximately 4.46 times less than that of the steel beam. Also the critical velocity for both materials is approximately the same. In Fig. 40, the variation in dynamic magnification factor versus the equivalent bending stiffness of the composite laminated beam is shown for different values of v. As it can be seen, the dynamic magnification factor first both increases and decreases with decreasing $(EI)_{\mathrm{eq}}$ and takes its maximum value (This maximum value depends on the velocity of the moving oscillator.) After that, the dynamic magnification factor decreases rapidly with decreasing $(EI)_{\mathrm{eq}}$ and approaches zero.

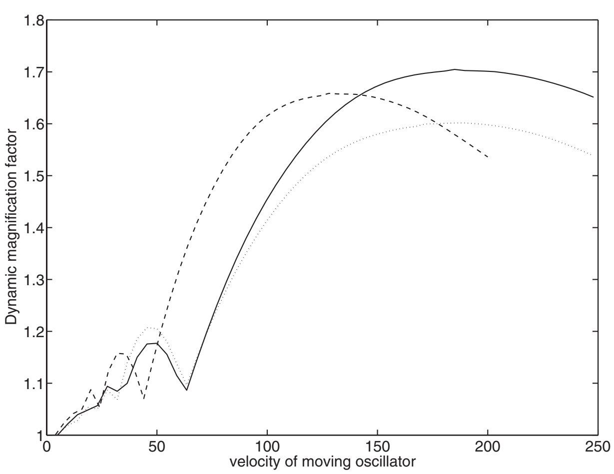

Fig. 38 Influence of h/H and velocity of moving oscillator on the dynamic magnification factor, θ=0; h/H=0 (dotted line), h/H=0.5 (dashed line), and h/H=1 (solid line)

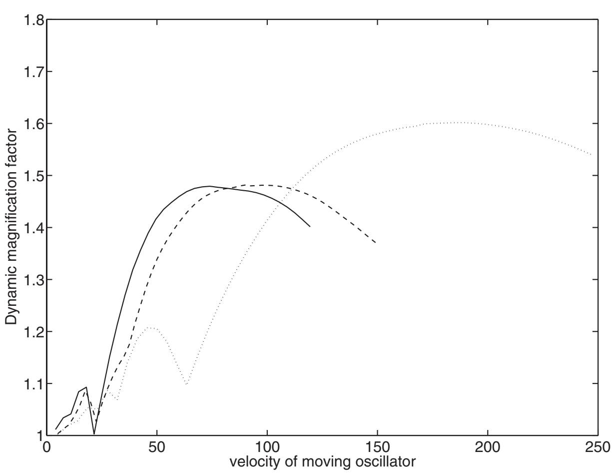

Fig. 39 Influence of θ and velocity of moving oscillator on the dynamic magnification factor, h/H=0; θ=0 (dotted line), θ=45 (dashed line), and θ=90 (solid line)

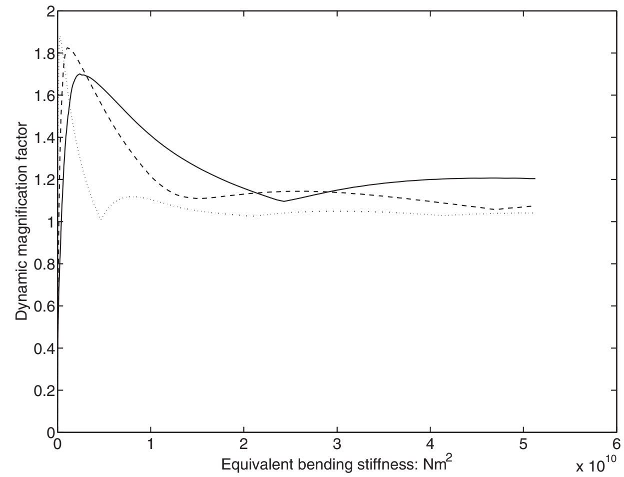

Fig. 40 Variation in dynamic magnification factors versus the equivalent bending stiffness of the beam; v=15 m/s (dotted line), v=30 m/s (dashed line), and v=45 m/s (solid line)

7.4 Forced Vibration of a Simply Supported Laminated Composite Coated Beam Due to a Stream of Accelerating Oscillators. In this section, several numerical experiments are presented in order to study the effects of moving oscillators' velocities, accelerations, and decelerations on the beam vibration. We consider the case where two identical oscillators (i.e., $M_1 = M_2$, $K_1 = K_2$, and $C_1 = C_2$) traverse a simply supported laminated composite coated beam. The parameters for the beam and oscillators are the same as those employed in Sec. 7.3. Also h/H=0.5 and θ=45 are considered. Figures 41 and 42 show the effects of moving oscillators' velocities and arrival time interval, $\Delta T = T_2$

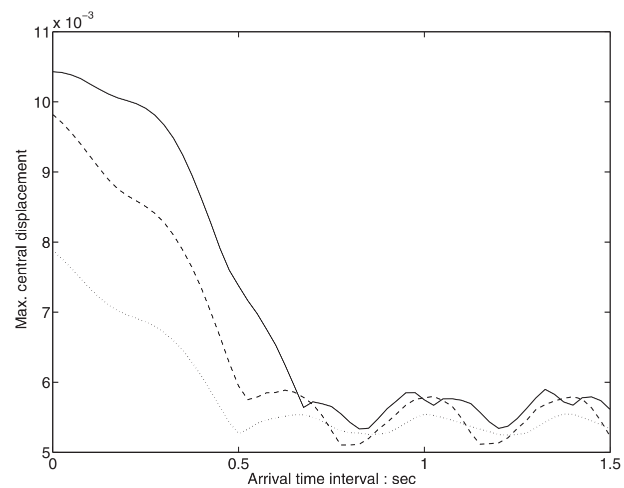

Fig. 41 Maximum central deflections of the beam due to two oscillators for $v_2 \leq v_1$, v_1=30 m/s; v_2=10 m/s (dotted line), v_2=20 m/s (dashed line), and v_2=30 m/s (solid line)

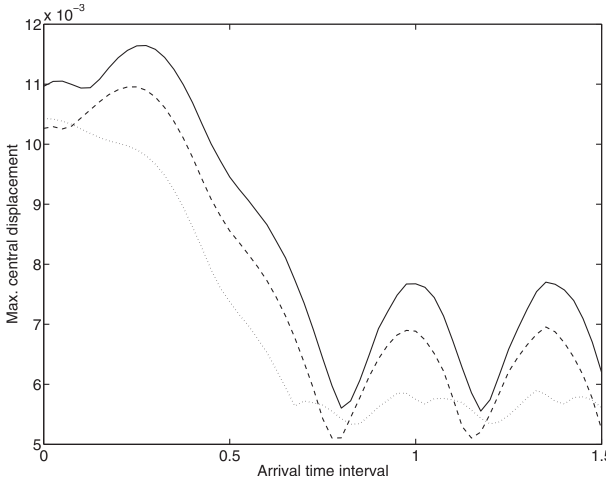

Fig. 42 Maximum central deflections of the beam due to two oscillators for $v_2 \geq v_1$, $v_1 = 30$ m/s; $v_2 = 30$ m/s (dotted line), $v_2 = 40$ m/s (dashed line), and $v_2 = 50$ m/s (solid line)

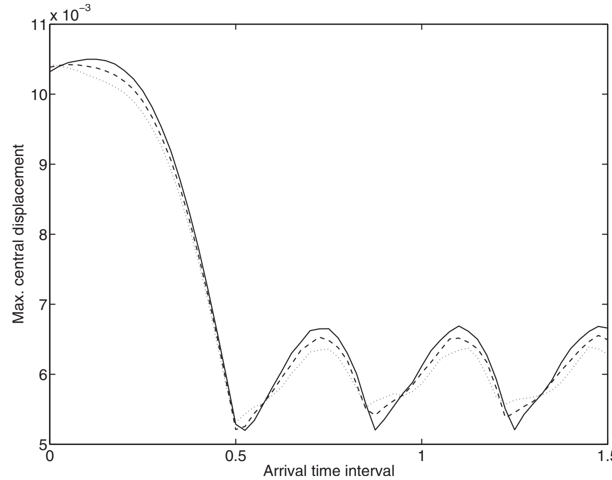

Fig. 44 Maximum central deflections of the beam due to two oscillators for $a_2 \geq a_1$, $a_1 = 20$ m/s^2; $a_2 = 20$ m/s^2 (dotted line), $a_2 = 30$ m/s^2 (dashed line), and $a_2 = 40$ m/s^2 (solid line) ($v_1 = v_2 = 30$ m/s)

$-T_1$, on the maximum central deflection for two cases: $v_2 \leq v_1$ and $v_2 \geq v_1$. As it can be seen, the maximum value of maximum central displacements increases when the velocity of second oscillator increases. From these figures one can conclude that for $v_2 \leq v_1$, the maximum magnitude of maximum central deflection occurs when ΔT is zero, i.e., they start at the same time to move, and for $v_2 \geq v_1$ it occurs at certain value of ΔT, which depends on the velocities of the oscillators and natural frequency of the beam. From Fig. 42 one also sees that the magnitude of ΔT, at which the maximum central deflection occurs, and the corresponding deflection increase as the velocity of the second oscillator increases. From these figures one also sees that after a certain value of ΔT, the maximum central deflection behaves as a periodic function of ΔT. This trend of maximum central deflection also is seen in the accelerating and decelerating motion of oscillators (see Figs. 43–46).To investigate the influence of moving oscillator acceleration and arrival time interval, ΔT on the maximum central deflection, the arrival velocity of two oscillators is set to $v_1 = v_2 = 30$ m/s, and two cases are considered: $a_2 \leq a_1$ and $a_2 \geq a_1$. Figures 43 and 44 illustrate the results for these cases. As can be seen, the maximum central deflection increases as the acceleration of the second oscillator increases. In Figs. 45 and 46 the influence of moving oscillators' deceleration and arrival time interval on the maximum central deflection, for two cases: $|a_2| \leq |a_1|$ and $|a_2| \geq |a_1|$, are shown. In these cases the arrival velocity of two oscillators is set to: $v_1 = v_2 = 50$ m/s. As seen, the maximum central deflection only slightly changes as the second oscillator deceleration varies from 0 m/s^2 to -40 m/s^2.

8 Conclusions

An efficient coupled *FE-DQM* is introduced and developed to analyze the dynamics of laminated composite coated beams carrying a set of accelerating oscillators. The finite element method is used to discretize the spatial domain. The DQ method is then employed to discretize the time domain. The stability, rate of convergence, and accuracy of the presented mixed methodology are demonstrated by different numerical examples. It is shown that the DQ method gives much more accurate solutions than the standard time step methods, such as the Newmark, Wilson θ, Houbolt, and central difference methods, using a considerably smaller number of time points (i.e., using a bigger time steps) and therefore

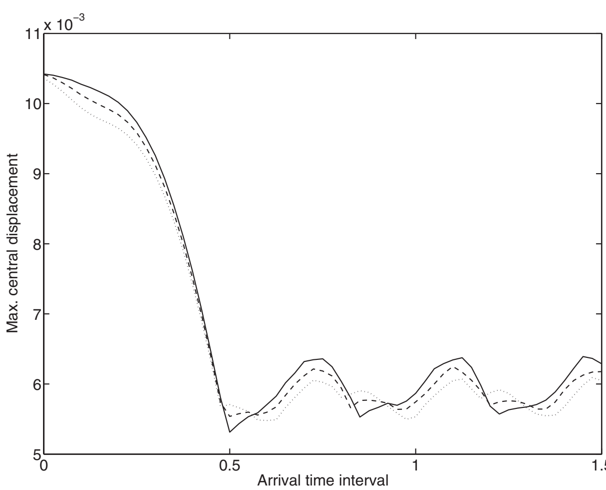

Fig. 43 Maximum central deflections of the beam due to two oscillators for $a_2 \leq a_1$, $a_1 = 20$ m/s^2; $a_2 = 0$ m/s (dotted line), $a_2 = 10$ m/s^2 (dashed line), and $a_2 = 20$ m/s^2 (solid line) ($v_1 = v_2 = 30$ m/s)

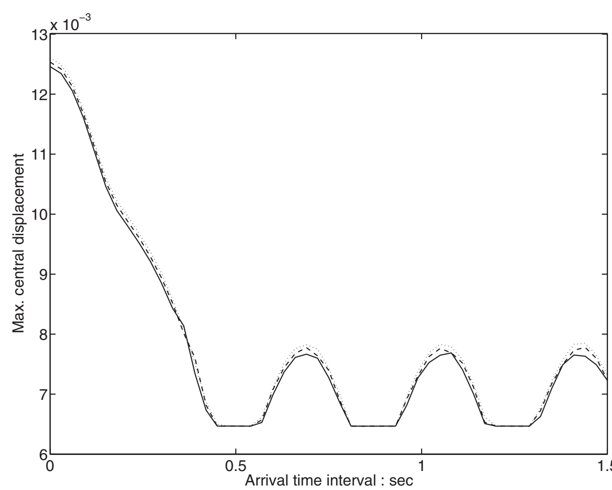

Fig. 45 Maximum central deflections of the beam due to two oscillators for $|a_2| \leq |a_1|$, $a_1 = -20$ m/s^2; $a_2 = 0$ (dotted line), $a_2 = -10$ m/s^2 (dashed line), and $a_2 = -20$ m/s^2 (solid line) ($v_1 = v_2 = 50$ m/s)

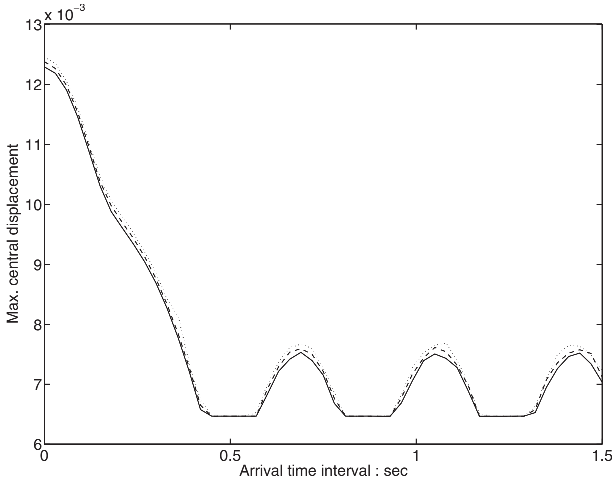

Fig. 46 Maximum central deflections of the beam due to two oscillators for $|a_2| \geq |a_1|$, $a_1=-20$ m/s^2; $a_2=-20$ m/s^2 (dotted line), $a_2=-30$ m/s^2 (dashed line), and $a_2=-40$ m/s^2 (solid line) ($v_1=v_2=50$ m/s)

requiring relatively little computational effort. In the numerical examples the effects of various parameters, such as velocities, accelerations, decelerations, and arrival time intervals of oscillators, as well as lamina thickness, and orientation of the coats on the dynamic behavior of the system, are studied. It is shown that all the above-mentioned parameters have significant influence on the dynamic behavior of the system. The proposed algorithm is general and can be easily used to solve various time-dependent problems.

References

[1] Zibdeh, H. S., and Abu-Hilal, M., 2003, "Stochastic Vibration of Laminated Composite Coated Beam Traversed by a Random Moving Load," Eng. Struct., **25**, pp. 397–404.

[2] Fryba, L., 1972, *Vibration of Solids and Structures Under Moving Loads*, Noordhoff International, the Netherlands.

[3] Katz, R., Lee, C. W., Ulsoy, A. G., and Scott, R. A., 1987, "Dynamic Stability and Response of a Beam Subjected to a Deflection Dependent Moving Load," ASME J. Vib., Acoust., Stress, Reliab. Des., **109**, pp. 361–365.

[4] Rao, G. V., 2000, "Linear Dynamics of an Elastic Beam Under Moving Loads," ASME J. Vibr. Acoust., **122**, pp. 281–289.

[5] Lin, Y.-H., and Trethewey, M. W., 1990, "Finite Element Analysis of Elastic Beams Subjected to Moving Dynamic Loads," J. Sound Vib., **136**, pp. 323–342.

[6] Lin, Y.-H., Trethewey, M. W., Reed, H. M., Shawley, J. D., and Sager, S. J., 1990, "Dynamic Modeling and Analysis of a High Speed Precision Drilling Machine," ASME J. Vibr. Acoust., **112**, pp. 355–365.

[7] Saigal, S., 1986, "Dynamic Behavior of Beam Structures Carrying Moving Masses," ASME J. Appl. Mech., **53**, pp. 222–224.

[8] Benedetti, G. A., 1974, "Dynamic Stability of a Beam Loaded by a Sequence of Moving Mass Particles," ASME J. Appl. Mech., **41**, pp. 1069–1071.

[9] Nelson, H. D., and Conover, R. A., 1971, "Dynamic Stability of a Beam Carrying Moving Masses," ASME J. Appl. Mech., **38**, pp. 1003–1006.

[10] Pesterev, A. V., and Bergman, L. A., 1998, "Response of a Nonconservative Continuous System to a Moving Concentrated Load," ASME J. Appl. Mech., **65**, pp. 436–444.

[11] Esmailzadeh, E., and Ghorashi, M., 1997, "Vibration Analysis of a Timoshenko Beam Subjected to a Traveling Mass," J. Sound Vib., **199**, pp. 615–628.

[12] Wang, R. T., 1997, "Vibration of Multi-Span Timoshenko Beams to a Moving Force," J. Sound Vib., **207**, pp. 731–742.

[13] Kadivar, M. H., and Mohebpour, S. R., 1998, "Forced Vibration of Unsymmetric Laminated Composite Beams Under the Action of Moving Loads," Compos. Sci. Technol., **58**, pp. 1675–1684.

[14] Kadivar, M. H., and Mohebpour, S. R., 1998, "Finite Element Analysis of Unsymmetric Laminated Composite Beams With Shear Effect and Rotary Inertia Under the Action of Moving Loads," Finite Elem. Anal. Des., **29**, pp. 259–273.

[15] Lee, S. Y., and Yhim, S. S., 2004, "Dynamic Analysis of Composite Plates Subjected to Multi-Moving Loads Based on a Third Order Theory," Int. J. Solids Struct., **41**, pp. 4457–4472.

[16] Bert, C. W., and Malik, M., 1996, "Differential Quadrature Method in Computational Mechanics: A Review," Appl. Mech. Rev., **49**, pp. 1–28.

[17] Quan, J. R., and Chang, C. T., 1989, "New Insights in Solving Distributed System Equations by the Quadrature Methods, Part I: Analysis," Comput. Chem. Eng., **13**, pp. 779–788.

[18] Shu, C., 2000, *Differential Quadrature and Its Application in Engineering*, Springer, New York.

[19] Teboub, Y., and Hajela, P., 1995, "Free Vibrations of Generally Layered Composite Beams Using Symbolic Computations," Compos. Struct., **33**, pp. 123–134.

[20] Hamada, A., 1995, "Vibration and Damping Analysis of Beams With Composite Coats," Compos. Struct., **32**, pp. 33–38.

[21] Bathe, K. J., and Wilson, E. L., 1976, *Numerical Methods in Finite Element Analysis*, Prentice-Hall, Englewood Cliffs, NJ.

[22] Meirovitch, L., 1967, *Analytical Methods in Vibrations*, Macmillan, New York.

[23] Pesterev, A. V., and Bergman, L. A., 1997, "Response of Elastic Continuum Carrying Moving Linear Oscillator," J. Eng. Mech., **123**, pp. 878–88.

Elasticity Approach to Load Transfer in Cord-Composite Materials

Anthony J. Paris
Mechanical Engineering,
University of Alaska Anchorage,
3211 Providence Drive,
Anchorage, AK 99508
e-mail: afajp@uaa.alaska.edu

An elasticity approach to the mechanics of load transfer in cord-reinforced composite materials is developed. Finite cords embedded in an elastic matrix and subjected to axial loading is considered, and the extension-twist coupling of the cords is taken into account. Closed form solutions for the axial force and twisting moment in the cord, the shear stresses at the cord-matrix interface in the axial and circumferential directions, the effective axial modulus of the cord, and the apparent modulus of the cord composite are presented. An example of a cord composite typical of what can be found in steel-belted-radial tires is used to illustrate the results. It was found that large shear stresses occur at the cord-matrix interface in both the axial and circumferential directions at the cord ends and that the effective modulus of the cords may be greatly reduced. As a result, the apparent modulus of the composite may be significantly less than that found by a conventional application of the rule-of-mixtures approach. [DOI: 10.1115/1.3130442]

1 Introduction

The mechanics of load transfer from the matrix to the cords in cord-reinforced composite materials is considered. Cord-composite materials are used in a wide variety of applications including automobile and truck tires and hoses. The desire to model cord-composite materials using the bulk properties of the composite indicates the need for a mathematical model of the mechanics of load transfer and the development of an apparent modulus for the composite.

In the literature on fiber-reinforced composite materials, investigators took analytical, experimental, and numerical approaches to better understand the mechanics of load transfer in composite systems ranging from paper to Kevlar/epoxy. Many authors used the analytical results of Cox [1] and Dow [2] as the benchmarks to which they compare their results.

Cox [1] presented an approximate analytical model for load transfer in fiber-reinforced composite materials consisting of finite fibers embedded in an elastic matrix. The study primarily focused on the behavior of paper. Cox analyzed the effect of fiber geometry and orientation on the stiffness and strength of fiber-reinforced composite materials. A model for load transfer from the matrix to the fiber was developed. It was assumed that the matrix and fiber are elastic, that the matrix and fiber are perfectly bonded, that load transfer occurs through shear stresses at the fiber-matrix interface, and that no load transfer occurs on the fiber ends. Cox concluded that using a reduced value for the elastic modulus of the fibers represents the effect of short fibers. Cox compared the model with experimental results and found moderately good agreement.

Outwater [3,4] developed an analytical model for the mechanics of load transfer for short fibers embedded in resin. Resin shrinkage, yielding of the resin, debonding of the ends and sides of the fibers from the resin, and friction between the resin and the fibers along the debonded surfaces were taken into account. The system considered in the paper was glass fiber-reinforced polyester. The study yielded expressions for the modulus of a fiber-reinforced composite material. Outwater found that until debonding occurred, the modulus of elasticity of the composite is approximately equal to the product of the fiber volume fraction and the fiber modulus. After the ends of the fibers are debonded from the resin, the composite modulus is reduced. Outwater qualitatively compared his model for load transfer favorably with the load-deformation plots for two specimens from a previous experimental study by Freas [5].

Dow [2] conducted an analytical study of the stresses near a discontinuity in fiber-reinforced composite materials and developed both an elastic model and a model that takes plasticity of the matrix into account. Stresses were calculated and plotted for an aluminum oxide whiskers/pure aluminum composite material system. Dow concluded that high shear stresses near discontinuities must be accommodated to take advantage of the properties of high-strength fibers and that there is a filament length required for effectiveness. Rosen et al. [6] investigated the mechanical properties of fibrous composites used in aerospace vehicles and included an analysis of the effect of fiber length on those properties. Their model consists of a finite cylindrical fiber that is embedded in a concentric cylindrical binder of the same length that is embedded in the composite. An estimate of the fiber stress, matrix shear stress, and shear stress distribution along the fiber/matrix interface is given, and the effects of both an elastic matrix and an elastic-plastic matrix are considered. Short fibers are taken into account by defining the fiber efficiency and an ineffective fiber length in determining composite strength. They fabricated, analyzed, and tested glass/plastic composite systems and favorably compared the analytical results with the experimental results. Rosen [7] presented a refined mathematical model and the experimental results of the tensile failure of fibrous composites. Studies by Dow and Rosen [8] and Rosen [9] that included a similar treatment of the stresses near the ends of discontinuous fibers in an elastic matrix followed.

Schuster and Scala [10] studied the mechanical interaction of sapphire whiskers with a birefringent matrix using photoelastic techniques. They concluded that the interfacial stresses found experimentally agreed well with those found analytically with the model developed by Dow [2].

Tyson and Davies [11] conducted a photo-elastic study of the shear stresses associated with the transfer of stress from the matrix to the fiber reinforcement and compared their experimental results with the models developed by Cox [1] and Dow [2]. They used an Araldite CT200 with hardener HT 901/Dural matrix/fiber system. Near the fiber end, the shear stresses at the fiber/matrix interface parallel to the fiber axis found experimentally were much larger

Contributed by the Applied Mechanics Division of ASME for publication in the Journal of Applied Mechanics. Manuscript received December 26, 2006; final manuscript received March 24, 2009; published online July 21, 2009. Review conducted by Matthew R. Begley.

than the theoretically determined values. Tyson and Davies attributed the difference between the experimental and theoretical values to the square corner of the fiber end. The experimental results show that the models of Cox and Dow predict the shear stresses reasonably accurately two or more fiber diameters from the end of the fiber.

Allison and Hollaway [12] conducted further tests to determine the stresses in fiber-reinforced materials using the photoelastic method with an Araldite CT200 with hardener HY901/Dural matrix/fiber system. The complete stresses around an isolated fiber surrounded by an elastic matrix subjected to uniaxial tension were found. The stresses for fibers with square ends and round ends were investigated. They concluded that the stresses around fibers with round ends are greater than the stresses around fibers with square ends. No direct comparisons were made between the photo-elastic results and the results of Cox [1] or Dow [2].

Carrara and McGarry [13] used finite element analysis to study the matrix and the interface stresses in single filament glass/resin and sapphire/resin composites for various filament-tip geometries. They found that matrix stresses depend strongly on the fiber tip geometry. They compared their results favorably with those of the Cox [1] model for a fiber with a blunt end.

Smith and Spencer [14] developed an approximate solution to the interfacial tractions between the fiber and the matrix using the theory of elasticity. They compared their results for the shear stress at the interface with those of Dow [2] and found good agreement for the silica fiber/aluminum matrix system they considered.

Galiotis et al. [15] experimentally determined the fiber strain by resonance Raman spectroscopy and compared their results with those of the Cox [1] model. They found that for high matrix strains, the Cox model described well the strain distribution along the fiber for a composite system consisting of one polydiacetylene single crystal fiber in an epoxy resin. In a related paper, Robinson et al. [16] studied polydiacetylene/epoxy composites and the effect of resin shrinkage experimentally using Raman spectroscopy to determine the fiber strain and found good agreement between their experimental results and those of the Cox model.

Whitney and Drzal [17] used elasticity theory to develop an approximate solution for the stress distribution around an isolated fiber fragment. They found good agreement between the predicted and experimentally determined values for the critical fiber lengths for AS-4 graphite fibers embedded in an epoxy matrix and to a lesser extent good agreement for Kevlar 49 aramid fibers embedded in an epoxy Epon 828 with the stoichiometric amount of metaphenylenediamine (mPDA) matrix.

Termonia [18,19] used the finite difference method to develop a computer model for the elastic properties of short fiber and particulate filled polymers. The numerical results were successfully verified with experimental data available in the literature for the composite modulus for glass fibers in a polyester resin, silica particles in an epoxy resin, and other composite systems.

Nairn [20] used a variational mechanics approach to the problem of stresses around breaks in embedded fibers. The results were compared with those found by using the solution of Cox [1] and by the finite element method for a carbon fiber/epoxy matrix composite system. It was found that there were significant differences between the variational mechanics approach and the Cox method results and good agreement between the variational mechanics approach and the FEM results.

Related studies in the literature include fiber pullout, fiber pushout, fiber debonding, interfacial debonding, matrix cracking, fiber breaking, fracture, and damage modeling of composite materials.

In the literature on cord-reinforced composite materials, Paris et al. [21] presented an analytical model of the load-deformation behavior of cord-reinforced composites consisting of infinitely long cords embedded in an elastic matrix, where the extension-twist coupling of the cords was taken into account. In three papers, Shield and Costello [22–24] reported on studies of the behavior of cord-composite plates. In two papers, Paris and Costello [25,26] presented an analysis of cord-composite cylindrical shells. In each of these studies, it was assumed that the end effects of the cords could be neglected, and load transfer through shear stresses at the cord-matrix interface was not considered.

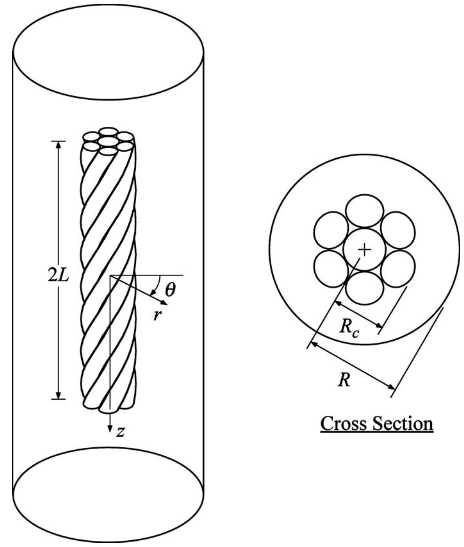

Fig. 1 Cord-composite material model

Velinsky et al. [27] developed the theory that is used to model the axial response of the cords. The book by Costello [28] reviews the theory developed in that paper as well as other issues related to wire rope. In those works, it was found that the cord extension and twist are coupled; the cord axial force and twisting moment are linearly proportional to the axial strain and twist of the cord. Prakash et al. [29] and Velinsky [30] considered the compression of a cord and found that cords are bimodular and behave differently in tension than in compression. In the following analysis, the bimodular characteristics of the cords are neglected.

The matrix is modeled as linear-elastic. Relations between stress and strain are found in the book by Love [31]. It is assumed that the cords are perfectly bonded to the matrix. Approximate solutions for the axial force and twisting moment in the cord, the shear stresses at the cord-matrix interface in the axial and circumferential directions, the effective axial modulus of the cord, and the apparent modulus of the cord-reinforced composite material are presented. An example of a cord-composite material typical of what can be found in steel-belted-radial tires is used to illustrate the results. The conventional treatment of the mechanics of composite materials such as the rule of mixtures or rule-of-averages can be found in the book by Hull and Clyne [32].

2 Formulation

Consider a cord-composite material that consists of parallel cords of length $2L_c$ and radius R_c with an average spacing $2R$ embedded in a matrix that is subjected to an average axial strain ε and rate of twist τ. Figure 1 shows the cord-composite material model representative volume element. Cylindrical coordinates are denoted by r, θ, and z, where the origin is at the center of the cord and the z axis is parallel to the axis of the cord. The displacements are u_r, u_θ, and u_z, the normal strains are ε_r, ε_θ, and ε_z, the shear strains are $\gamma_{r\theta}$, $\gamma_{\theta z}$, and γ_{rz}, the normal stresses are σ_r, σ_θ, and σ_z, the shear stresses are $\tau_{r\theta}$, $\tau_{\theta z}$, and τ_{rz}, the cord axial force is F_c, the twisting moment is M_{tc}, and the interfacial shear stresses are $\tau_{r\theta i}$ and τ_{rzi}.

Figure 2 shows an element of the cord, where dz is the length of the element in the axial direction. Only the axial and circumferential components of the stresses acting on the elements are shown. The equilibrium equations for the cord element yield

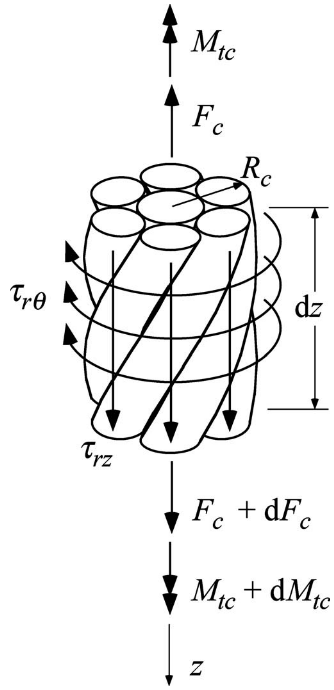

Fig. 2 An element of the cord

$$\frac{dF_c}{dz} + 2\pi R_c \tau_{rzi} = 0 \quad \text{and} \quad \frac{dM_{tc}}{dz} + 2\pi R_c^2 \tau_{r\theta i} = 0 \tag{1}$$

For the matrix, the equilibrium equations in cylindrical coordinates [31] yield

$$\frac{\partial \sigma_r}{\partial r} + \frac{1}{r}\frac{\partial \tau_{r\theta}}{\partial \theta} + \frac{\partial \tau_{rz}}{\partial z} + \frac{\sigma_r - \sigma_\theta}{r} + f_r = 0$$

$$\frac{\partial \tau_{r\theta}}{\partial r} + \frac{1}{r}\frac{\partial \sigma_\theta}{\partial \theta} + \frac{\partial \tau_{\theta z}}{\partial z} + \frac{2\tau_{r\theta}}{r} + f_\theta = 0 \tag{2}$$

$$\frac{\partial \tau_{rz}}{\partial r} + \frac{1}{r}\frac{\partial \tau_{\theta z}}{\partial \theta} + \frac{\partial \sigma_z}{\partial z} + \frac{\tau_{rz}}{r} + f_z = 0$$

Figure 3 shows an axially loaded cord, where F_c is the axial force, M_{tc} is the twisting moment, R_1 is the radius of the inner wire, R_2 is the radius of the outer wires, R_c is the outside radius of the cord, m is the number of outer wires, and α is the helix angle of the outer wires. Velinsky et al. [27] and Costello [28] showed that F_c and M_{tc} may be expressed as

$$\frac{F_c}{A_c E_c} = C_1 \varepsilon_c + C_2 R_c \tau_c \quad \text{and} \quad \frac{M_{tc}}{E_c R_c^3} = C_3 \varepsilon_c + C_4 R_c \tau_c \tag{3}$$

where $A_c = \Sigma_N \pi R_i^2$ is the metallic cross sectional area, N is the total number of wires, E_c is the modulus of elasticity of the material, ε_c is the axial strain, τ_c is the rate of twist, and C_1, C_2, C_3, and C_4 are constants that can be determined analytically from the cord geometry and Poisson's ratio of the cord material ν_c.

The matrix is modeled as a linear-elastic material [31]. The elastic modulus is denoted by E_m, the Poisson ratio is denoted by ν_m, and the shear modulus is denoted by G_m, where

$$G_m = \frac{E_m}{2(1+\nu_m)} \tag{4}$$

The matrix strain-stress relations are

$$\varepsilon_r = \frac{1}{E_m}[\sigma_r - \upsilon_m(\sigma_\theta + \sigma_z)]$$

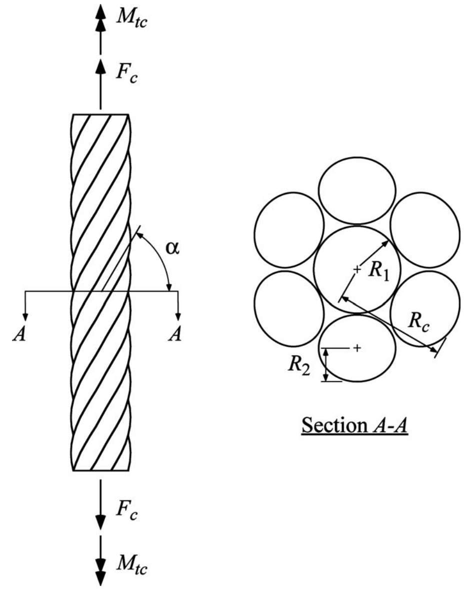

Fig. 3 An axially loaded cord

$$\varepsilon_\theta = \frac{1}{E_m}[\sigma_\theta - \upsilon_m(\sigma_r + \sigma_z)]$$

$$\varepsilon_z = \frac{1}{E_m}[\sigma_z - \upsilon_m(\sigma_r + \sigma_\theta)]$$

$$\gamma_{rz} = \frac{\tau_{rz}}{G_m}, \quad \gamma_{r\theta} = \frac{\tau_{r\theta}}{G_m}, \quad \gamma_{\theta z} = \frac{\tau_{\theta z}}{G_m} \tag{5}$$

The strain-displacement relations in cylindrical coordinates are

$$\varepsilon_r = \frac{\partial u_r}{\partial r}, \quad \varepsilon_\theta = \frac{1}{r}\frac{\partial u_\theta}{\partial \theta} + \frac{u_r}{r}, \quad \varepsilon_z = \frac{\partial u_z}{\partial z}$$

$$\gamma_{r\theta} = \frac{1}{r}\frac{\partial u_r}{\partial \theta} + \frac{\partial u_\theta}{\partial r} - \frac{u_\theta}{r} \tag{6}$$

$$\gamma_{rz} = \frac{\partial u_z}{\partial r} + \frac{\partial u_r}{\partial z}$$

$$\gamma_{\theta z} = \frac{\partial u_\theta}{\partial z} + \frac{1}{r}\frac{\partial u_z}{\partial \theta}$$

Since the cord-composite material model chosen is symmetric, all derivatives with respect to θ are zero.

The axial strains and the rates of twist of the cord and the composite can be expressed as

$$\varepsilon_c = \frac{du_z(r=R_c)}{dz}, \quad \varepsilon = \frac{du_z(r=R)}{dz}$$

$$\tau_c = \frac{1}{R_c}\frac{du_\theta(r=R_c)}{dz}, \quad \tau = \frac{1}{R}\frac{du_\theta(r=R)}{dz} \tag{7}$$

where ε is the axial strain and τ is the rate of twist of the composite.

It is assumed that load transfer occurs between the cords and the matrix primarily through shear stresses at the cord/matrix interface, and load transfer between the cords and the matrix due to stresses acting at the cord/matrix interface on the ends of the cord is neglected. Thus, the boundary conditions for the cord are $F_c = 0$ and $M_{tc} = 0$ at $z = \pm L_c$.

3 Results

An approximate solution is achieved by neglecting small terms. Equations (1)–(7) yield two coupled, second order, linear, nonhomogeneous, ordinary differential equations for the cord axial force and twisting moment,

$$\frac{d^2F_c}{dz^2} - a_{11}F_c + a_{12}M_{tc} = -f_1$$
$$\frac{d^2M_{tc}}{dz^2} + a_{21}F_c - a_{22}M_{tc} = -f_2 \qquad (8)$$

where

$$a_{11} = \frac{2\pi C_4 G_m}{A_c C E_c \ln\left(\frac{R}{R_c}\right)}, \quad a_{12} = \frac{2\pi C_2 G_m}{C E_c R_c^3 \ln\left(\frac{R}{R_c}\right)}$$

$$a_{21} = \frac{4\pi C_3 G_m R_c^2}{A_c C E_c R_c\left[1 - \left(\frac{R_c}{R}\right)^2\right]}, \quad a_{22} = \frac{4\pi C_1 G_m R_c^2}{C E_c R_c^4\left[1 - \left(\frac{R_c}{R}\right)^2\right]}$$

$$f_1 = \frac{2\pi G_m}{\ln\left(\frac{R}{R_c}\right)}\varepsilon, \quad f_2 = \frac{4\pi G_m R_c^2}{1 - \left(\frac{R_c}{R}\right)^2}\tau, \quad C = C_1C_4 - C_2C_3$$

Equation (8) has the general solution

$$F_c = d_1\cosh(\lambda_1 z) + d_2\cosh(\lambda_2 z) + d_3\sinh(\lambda_1 z) + d_4\sinh(\lambda_2 z) + F_{cp}$$
$$M_{tc} = k_1 d_1\cosh(\lambda_1 z) + k_2 d_2\cosh(\lambda_2 z) + k_1 d_3\sinh(\lambda_1 z) + k_2 d_4\sinh(\lambda_2 z) + M_{tcp} \qquad (9)$$

where

$$\lambda_{1,2} = \sqrt{\frac{a_{11} + a_{22} \pm \sqrt{(a_{11}+a_{22})^2 - 4(a_{11}a_{22} - a_{12}a_{21})}}{2}}$$

$$k_1 = \frac{a_{11} - \lambda_1^2}{a_{12}} = \frac{a_{21}}{a_{22} - \lambda_1^2}, \quad k_2 = \frac{a_{11} - \lambda_2^2}{a_{12}} = \frac{a_{21}}{a_{22} - \lambda_2^2}$$

$$F_{cp} = \frac{a_{22}f_1 + a_{12}f_2}{a_{11}a_{22} - a_{12}a_{21}} = A_c E_c(C_1\varepsilon + C_2 R_c\tau)$$

$$M_{tcp} = \frac{a_{21}f_1 + a_{11}f_2}{a_{11}a_{22} - a_{12}a_{21}} = E_c R_c^3(C_3\varepsilon + C_4 R_c\tau)$$

Applying the boundary conditions $F_c = 0$ and $M_{tc} = 0$ at $z = \pm L_c$ yields

$$d_1 = \frac{k_2 F_{cp} - M_{tcp}}{(k_1 - k_2)\cosh(\lambda_1 L_c)}, \quad d_2 = -\frac{k_1 F_{cp} - M_{tcp}}{(k_1 - k_2)\cosh(\lambda_2 L_c)}$$

$$d_3 = 0, \quad d_4 = 0$$

Equations (1) and (9) yield

$$\tau_{rzi} = \frac{-1}{2\pi R_c}[d_1\lambda_1\sinh(\lambda_1 z) + d_2\lambda_2\sinh(\lambda_2 z)]$$
$$\tau_{r\theta i} = \frac{-1}{2\pi R_c^2}[k_1 d_1\lambda_1\sinh(\lambda_1 z) + k_2 d_2\lambda_2\sinh(\lambda_2 z)] \qquad (10)$$

The average axial force and twisting moment in the cord are defined as

$$(F_c)_{\text{average}} = \frac{1}{2L_c}\int_{z=-L_c}^{L_c} F_c dz \quad \text{and} \quad (M_{tc})_{\text{average}} = \frac{1}{2L_c}\int_{z=-L_c}^{L_c} M_{tc} dz \qquad (11)$$

Substituting Eq. (9) into Eq. (11) and evaluating the integrals yield

$$\frac{(F_c)_{\text{average}}}{A_c E_c} = C_1\left\{1 - \frac{1}{L_c(k_1 - k_2)}\left[\frac{\tanh(\lambda_1 L_c)}{\lambda_1}\left(\frac{a_{21}}{a_{22}} - k_2\right) - \frac{\tanh(\lambda_2 L_c)}{\lambda_2}\left(\frac{a_{21}}{a_{22}} - k_1\right)\right]\right\}\varepsilon + C_2\left\{1 - \frac{1}{L_c(k_1 - k_2)}\left[\frac{\tanh(\lambda_1 L_c)}{\lambda_1}\left(\frac{a_{11}}{a_{12}} - k_2\right) - \frac{\tanh(\lambda_2 L_c)}{\lambda_2}\left(\frac{a_{11}}{a_{12}} - k_1\right)\right]\right\}R_c\tau \qquad (12)$$

and

$$\frac{(M_{tc})_{\text{average}}}{E_c R_c^3} = C_3\left\{1 - \frac{1}{L_c(k_1 - k_2)}\left[\frac{k_1\tanh(\lambda_1 L_c)}{\lambda_1}\left(1 - \frac{a_{22}}{a_{21}}k_2\right) - \frac{k_2\tanh(\lambda_2 L_c)}{\lambda_2}\left(1 - \frac{a_{22}}{a_{21}}k_1\right)\right]\right\}\varepsilon + C_4\left\{1 - \frac{1}{L_c(k_1 - k_2)}\left[\frac{k_1\tanh(\lambda_1 L_c)}{\lambda_1}\left(1 - \frac{a_{12}}{a_{11}}k_2\right) - \frac{k_2\tanh(\lambda_2 L_c)}{\lambda_2}\left(1 - \frac{a_{12}}{a_{11}}k_1\right)\right]\right\}R_c\tau$$

In the mathematical limit as $L_c \to 0$, Eqs. (9) and (10) yield $F_c \to 0$, $M_{tc} \to 0$, $\tau_{rzi} \to 0$, and $\tau_{r\theta i} \to 0$. In the mathematical limit as $L_c \to \infty$, Eq. (12) yields $(F_c)_{\text{average}} \to F_{cp}$ and $(M_{tc})_{\text{average}} \to M_{tcp}$. Thus, shorter cords have smaller axial force and twisting moment and shear stresses, while longer cords have higher force and twisting moment and shear stresses. As the cord length approaches infinity, away from the ends of the cord, the cord axial force and twisting moment approach the axial force and twisting moment of a cord subjected to the composite average axial strain and rate of twist. These results are consistent with the proposed material model.

The effective modulus of the cord is defined by the equation

$$\frac{(E_c)_{\text{effective}}}{E_c} = \frac{(F_c)_{\text{average}}}{A_c E_c} \qquad (13)$$

For many applications of cord-composite materials, the twisting of the composite will be constrained, and the rate of twist τ of the composite will be zero. In that case, the effective modulus of the cord $(E_c)_{\text{effective}}$ can be expressed as

$$\frac{(E_c)_{\text{effective}}}{E_c} = C_1\left\{1 - \frac{1}{L_c(k_1 - k_2)}\left[\frac{\tanh(\lambda_1 L_c)}{\lambda_1}\left(\frac{a_{21}}{a_{22}} - k_2\right) - \frac{\tanh(\lambda_2 L_c)}{\lambda_2}\left(\frac{a_{21}}{a_{22}} - k_1\right)\right]\right\} \qquad (14)$$

and the apparent modulus of the composite E can be expressed using the rule-of-mixtures or rule-of-averages [32] as

$$E = V_c(E_c)_{\text{effective}} + (1 - V_c)E_m \qquad (15)$$

where

$$V_c = \frac{A_c}{\pi R^2}$$

is the cord volume fraction.

To illustrate the results, consider a steel-belted-radial tire, where steel cords are embedded in a rubber matrix. Take the dimensions and material properties of the cord, the matrix, and the composite to be $R_1=0.150$ mm, $R_2=0.140$ mm, $m=6$, $\alpha=81.4$ deg, $R_c=0.430$ mm, $A_c=0.440$ mm^2, $E_c=200$ GPa, $\nu_c=0.25$, $C_1=0.967$, $C_2=0.0828$, $C_3=0.187$, $C_4=0.0723$, $E_m=10$ MPa, $\nu_m=0.499$, and $R_m=4R_c$. The composite is subjected to $\varepsilon=0.001$ and $\tau=0$. Figure 4 shows $F_c/(A_cE_c)$ and τ_{rzi}/E_c versus $z/(R_cs)$, Fig. 5 shows $M_{tc}/(E_cR_c^3)$ and $\tau_{r\theta i}/E_c$ versus $z/(R_cs)$, and Fig. 6 shows $(E_c)_{\text{effective}}/E_c$ versus s, where $s=L_c/R_c$ is the cord aspect ratio.

4 Discussion

Figure 4 shows the cord axial force and axial shear stress at the cord-matrix interface versus position along the axis of the cord. The cord axial force is zero at the ends of the cord. The axial shear stress and the rate of change of the cord axial force are greatest near the ends of the cord and decrease to zero at the center of the cord. The maximum cord axial force occurs at the center of the cord and is significantly greater for long cords than for short ones, and the maximum axial shear stress at the cord/matrix interface occurs at the ends of the cord and is greater for long cords than it is for short ones. As the length of the cord increases, the value of the cord axial force approaches the value of the axial force of a cord subjected to the composite average axial strain and rate of twist. The results presented in Fig. 4 are consistent with the hypothesis that axial load is transferred from the matrix to the cords through shear stresses at the cord-matrix interface.

Figure 5 shows the cord axial twisting moment and circumferential shear stresses at the cord-matrix interface versus position along the cord and is similar in appearance to Fig. 4. The cord axial twisting moment is zero at the ends of the cord. The circumferential shear stress and the rate of change of the cord axial twisting moment are greatest near the ends of the cord and decrease to zero at the center of the cord. The maximum cord axial twisting moment occurs at the center of the cord and is significantly greater for long cords than for short ones, and the circumferential shear stress at the cord/matrix interface occurs at the ends of the cord and is greater for long cords than it is for short ones. As the length of the cord increases, the value of the cord axial twisting moment approaches the value of the twisting moment of a cord subjected to the composite average axial strain and rate of twist. The results presented in Fig. 5 are consistent with the hypothesis that axial load is transferred from the matrix to the cords through shear stresses at the cord-matrix interface. It is concluded from Figs. 4 and 5 that greater load, both axial force and twisting moment, is transferred to long cords and lesser load is transferred to short ones. Shear stresses at the cord/matrix interface, both axial and circumferential, are greatest at the ends of the cord and diminish to zero at the center of the cord and are greater for long cords than they are for short ones. It is noted that the maximum value of the circumferential shear stress at the cord-matrix interface $\tau_{r\theta i}$ is approximately one order of magnitude less than the maximum value of the axial shear stress at the cord-matrix interface τ_{rzi}.

Figure 6 shows the cord effective modulus versus the cord length. For short cords, the effective modulus is small. As the cord length increases, the effective cord modulus increases. For long cords, the effective cord modulus approaches the value of the effective cord modulus for a cord where the rotation of the ends is prevented. We conclude that the effective modulus of long cords is much greater than the effective modulus of short ones due to greater load transfer to long cords and lesser load transfer to short ones—greater shear stresses act over greater lengths for long cords, and lesser shear stresses act over lesser lengths for short cords. Finally, the effective axial modulus of the cords may be significantly less than the modulus of a cord where rotation of the ends is prevented.

It is noted that the terms that were neglected in Eqs. (1)–(7) to arrive at the differential equations given by Eq. (8) and the solution given by Eqs. (9) and (10) may not be small near the ends of the cords where $z/(R_cs)$ approaches ±1. Thus, Eqs. (9) and (10) and Figs. 4 and 5 may not be accurate for values of $z/(R_cs)$ approaching ±1. However, the solution given for the cord axial force and twisting moment given by Eq. (9) and the shear stresses at the cord-matrix interface given by Eq. (10) are believed to be accurate to one or two cord diameters from the end of the cord as the end effects decay exponentially. Also, the average values of the cord axial force and twisting moment given by Eq. (12), the

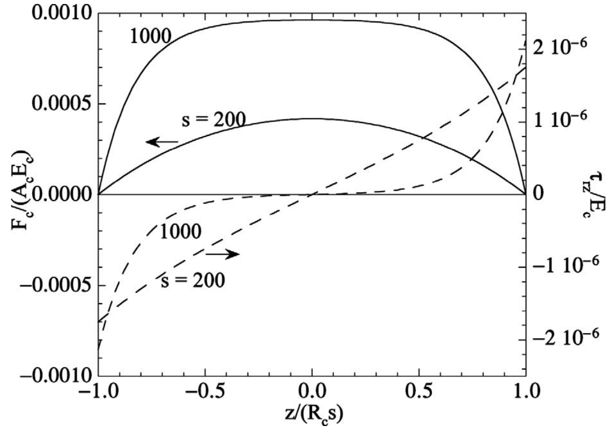

Fig. 4 $F_c/(A_cE_c)$ **versus** $z/(R_cs)$

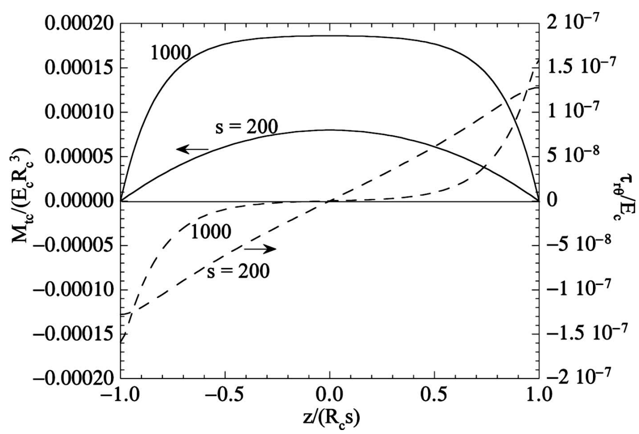

Fig. 5 $M_{tc}/(E_cR_c^3)$ **versus** $z/(R_cs)$

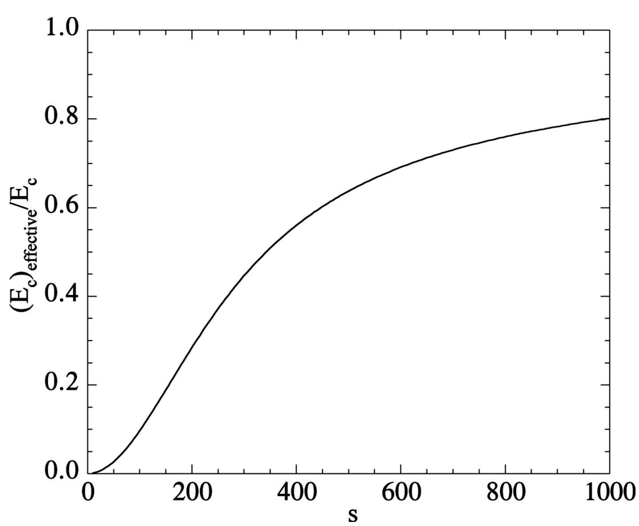

Fig. 6 $(E_c)_{\text{effective}}/E_c$ **versus** s

cord effective modulus given by Eq. (14), and the apparent modulus of the composite given by Eq. (15) are believed to be accurate since the neglected terms will contribute little to the integrals defined by Eq. (11). The apparent modulus of the composite is found by substituting the value for the effective modulus of the cord given by Eq. (14) into the rule-of-averages or rule-of-mixtures equation given by Eq. (15).

5 Summary and Conclusions

The results of an elasticity approach to the mechanics of load transfer in cord-reinforced composite materials were presented. A cord-composite material consisting of finite cords embedded in an elastic matrix and subjected to axial loading was considered. The extension-twist coupling of the cords was taken into account. Solutions for the axial force and twisting moment in the cord, the shear stresses at the cord-matrix interface in the axial and circumferential directions, the effective axial modulus of the cord, and the apparent modulus of the cord-reinforced composite material were presented. An example of a cord-composite material typical of what can be found in steel-belted-radial tires was used to illustrate the results, where the modulus of the material of the steel cords is much higher than the modulus of the rubber matrix.

It was found that when a cord-reinforced composite material consisting of finite cords embedded in an elastic matrix is axially loaded, significant shear stresses occur near the ends of the cords at the cord/matrix interface in the axial and circumferential directions. While the shear stresses at the ends of long cords are greater than those for short cords, greater load is transferred from the matrix to long cords than is transferred from the matrix to short ones. For short cords, the effective axial modulus of the cords may be significantly less than the modulus of the cord material. With an effective modulus of the cord significantly less than the modulus of the cord material, the apparent modulus of the cord-composite material will be significantly less than that predicted by a conventional application of a rule-of-mixtures approach.

Acknowledgment

The author wishes to thank Sarah E. Zeller for our discussions regarding the solution to the differential equations for the cord axial force and twisting moment.

References

[1] Cox, H. L., 1952, "The Elasticity and Strength of Paper and Other Fibrous Materials," Br. J. Appl. Phys., **3**, pp. 72–79.
[2] Dow, N. F., 1963, "Study of Stresses Near a Discontinuity in a Filament-Reinforced Composite Metal," General Electric, Missile and Space Division, Mechanics Section, Space Sciences Laboratory, Technical Information Series No. R63SD61.
[3] Outwater, J. O., Jr., 1956, "The Mechanics of Plastics Reinforcement in Tension," Mod. Plast., **33**(7), pp. 156–162.
[4] Outwater, J. O., Jr., 1956, "The Mechanics of Plastics Reinforcement in Tension," Mod. Plast., **33**(7), pp. 247–248.
[5] Freas, A. D., 1953, "Effect of Preloading and Fatigue on Mechanical Properties of Glass-Cloth Plastic Laminates," Trans. ASME, **75**, pp. 621–633.
[6] Rosen, B. W., Dow, N. F., and Hashin, Z., 1964, "Mechanical Properties of Fibrous Composites," General Electric Company, Report No. NASA CR-31.
[7] Rosen, B. W., 1964, "Tensile Failure of Fibrous Composites," AIAA J., **2**(11), pp. 1985–1991.
[8] Dow, N. F., and Rosen, B. W., 1964, "Evaluations of Filament-Reinforced Composites for Aerospace Structural Applications," General Electric Company, Report No. NASA CR-207.
[9] Rosen, B. W., 1965, "Fiber Composite Materials," Papers Presented at a Seminar of the American Society for Metals, American Society for Metals, Metals Park, OH, Chap. 3, pp. 37–75.
[10] Schuster, D. M., and Scala, E., 1964, "The Mechanical Interaction of Sapphire Whiskers With a Birefringent Matrix," Trans. Metall. Soc. AIME, **230**, pp. 1635–1640.
[11] Tyson, W. R., and Davies, G. J., 1965, "A Photoelastic Study of the Shear Stresses Associated With the Transfer of Stress During Fibre Reinforcement," Br. J. Appl. Phys., **16**, pp. 199–205.
[12] Allison, I. M., and Hollaway, L. C., 1967, "Stresses in Fiber-Reinforced Materials," Br. J. Appl. Phys., **18**, pp. 979–989.
[13] Carrara, A. S., and McGarry, F. J., 1968, "Matrix and Interface Stresses in a Discontinuous Fiber Composite Model," J. Compos. Mater., **2**(2), pp. 222–243.
[14] Smith, G. E., and Spencer, A. J. M., 1970, "Interfacial Tractions in a Fibre-Reinforced Elastic Composite Material," J. Mech. Phys. Solids, **18**, pp. 81–100.
[15] Galiotis, C., Young, R. J., Yeung, P. H. J., and Batchelder, D. N., 1984, "The Study of Model Polydiacetylene/Epoxy Composites–Part 1 The Axial Strain in the Fibre," J. Mater. Sci., **19**, pp. 3640–3648.
[16] Robinson, I. M., Young, R. J., Galiotis, C., and Batchelder, D. N., 1987, "The Study of Model Polydiacetylene/Epoxy Composites–Part 2 Effect of Resin Shrinkage," J. Mater. Sci., **22**, pp. 3642–3646.
[17] Whitney, J. M., and Drzal, L. T., 1987, "Axisymmetric Stress Distribution Around an Isolated Fiber Fragment," *Toughened Composites*, N. J. Johnston, ed., American Society for Testing and Materials, Philadelphia, ASTM STP No. 937, pp. 179–196.
[18] Termonia, Y., 1987, "Computer Model for the Elastic Properties of Short Fibre and Particulate Filled Polymers," J. Mater. Sci., **22**, pp. 1733–1736.
[19] Termonia, Y., 1987, "Theoretical Study of the Stress Transfer in Single Fiber Composites," J. Mater. Sci., **22**, pp. 504–508.
[20] Nairn, J. A., 1992, "A Variational Mechanics Analysis of the Stresses Around Breaks in Embedded Fibers," Mech. Mater., **13**, pp. 131–154.
[21] Paris, A. J., Lin, C. C., and Costello, G. A., 1992, "Simple Cord Composites," J. Eng. Mech., **118**(9), pp. 1939–1948.
[22] Shield, C. K., and Costello, G. A., 1994, "The Effect of Wire Rope Mechanics on the Mechanical Response of Cord Composite Laminates: An Elasticity Approach," ASME J. Appl. Mech., **61**, pp. 1–8.
[23] Shield, C. K., and Costello, G. A., 1994, "The Effect of Wire Rope Mechanics on the Mechanical Response of Cord Composite Laminates: An Energy Approach," ASME J. Appl. Mech., **61**, pp. 9–15.
[24] Shield, C. K., and Costello, G. A., 1994, "Bending of Cord Composite Plates," J. Eng. Mech., **120**, pp. 876–892.
[25] Paris, A. J., and Costello, G. A., 2000, "Bending of Cord Composite Cylindrical Shells," ASME J. Appl. Mech., **67**, pp. 117–127.
[26] Paris, A. J., and Costello, G. A., 2003, "Bending of Cord Composite Laminate Cylindrical Shells," ASME J. Appl. Mech., **70**, pp. 364–373.
[27] Velinsky, S. A., Anderson, G. L., and Costello, G. A., 1984, "Wire Rope With Complex Cross Sections," J. Eng. Mech., **110**, pp. 380–391.
[28] Costello, G. A., 1997, *Theory of Wire Rope*, 2nd ed., Springer-Verlag, New York.
[29] Prakash, A., Conway, T. A., and Costello, G. A., 1991, "Compression of a Cord," ASME J. Appl. Mech., **59**, pp. 5213–5216.
[30] Velinsky, S. A., 2004, "Compressive Loading of Stiffened, Wire-Strand Based Structures," Mech. Based Des. Struct. Mach., **32**(1), pp. 101–113.
[31] Love, A. E. H., 1934, *A Treatise on the Mathematical Theory of Elasticity*, 4th ed., Cambridge University, Cambridge.
[32] Hull, D., and Cline, T. W., 1996, *An Introduction to Composite Materials*, 2nd ed., Cambridge University, Cambridge.

The Damage Tolerance of a Sandwich Panel Containing a Cracked Honeycomb Core

I. Quintana Alonso

N. A. Fleck[1]
e-mail: naf1@cam.ac.uk

Department of Engineering,
Cambridge University,
Trumpington Street,
Cambridge CB2 1PZ, UK

The tensile fracture strength of a sandwich panel, with a center-cracked core made from an elastic-brittle diamond-celled honeycomb, is explored by analytical models and finite element simulations. The crack is on the midplane of the core and loading is normal to the faces of the sandwich panel. Both the analytical models and finite element simulations indicate that linear elastic fracture mechanics applies when a K-field exists on a scale larger than the cell size. However, there is a regime of geometries for which no K-field exists; in this regime, the stress concentration at the crack tip is negligible and the net strength of the cracked specimen is comparable to the unnotched strength. A fracture map is developed for the sandwich panel with axes given by the sandwich geometry. The effect of a statistical variation in the cell-wall strength is explored using Weibull theory, and the consequences of a stochastic strength upon the fracture map are outlined.
[DOI: 10.1115/1.2912995]

Keywords: finite element analysis, fracture, toughness, elastic behaviour, lattice materials

1 Introduction

Ceramic honeycombs are used in catalytic converters and diesel particulate filters for automobiles, in filters of continuous casting plant, in plates for gas burners, and in medical prosthetic implants. Glass honeycombs have been used as lightweight supports for space mirrors as, for example, in the Hubble telescope. In most of these applications, the ceramic lattices are chosen for their multifunctional properties, such as high thermal shock resistance, high chemical stability, and high stiffness. They are loaded in a sandwich panel configuration with stiff and strong face sheets. The flaw sensitivity of the tensile strength of these honeycombs is of concern and is the motivation for the present study: We shall explore the tensile fracture strength of a sandwich panel, with a center-cracked core made from an elastic-brittle diamond-celled honeycomb. The crack is on the midplane, with loading normal to the face of the sandwich panel, see Fig. 1. The strength is determined both by finite element simulations and by simple analytical models. It will be shown that the tensile strength is dictated by the Mode I fracture toughness of the honeycomb for a limited regime of sandwich panel geometries. Accordingly, we begin by reviewing the fracture toughness of brittle honeycombs.

1.1 Fracture Toughness of Brittle Honeycombs. The fracture toughness of brittle hexagonal honeycombs has been modeled by relating the crack tip elastic fields of an equivalent continuum to the stress state within the lattice [1,2]. It was assumed that the macroscopic fracture toughness is set by local tensile failure when the maximum stress in any strut of the lattice attains the fracture strength σ_f of the cell-wall material. It is shown that the fracture toughness of the hexagonal honeycomb scales linearly with σ_f, quadratically with relative density and with the square root of cell size (as demanded by dimensional analysis).

Numerical and analytical predictions for the fracture toughness of several honeycomb topologies are now available. Fleck and Qiu [3] have determined the fracture behavior of isotropic lattices of deterministic fracture strength: hexagonal, triangular, and Kagome. Orthotropic lattices with square cells have also been examined [4]. An analytical model of the fracture toughness of the diamond-celled honeycomb shown in Fig. 2 has been developed and validated by finite element calculations [5]. The diamond-celled honeycomb is remarkably tough: Its Mode I fracture toughness scales as

$$K_{IC} = \beta \sigma_f \bar{t} \sqrt{\ell} \tag{1}$$

where $\bar{t}$ is the ratio of cell-wall thickness t to cell size ℓ, and the numerical constant is $\beta = 0.44$ [4]. Limited experimental studies of the fracture toughness of honeycombs have been found in the literature. Measurements on notched three point bend specimens of cordierite honeycombs have been carried out by Huang and Gibson [6]. Their data suggest that Eq. (1) gives an adequate description of the fracture toughness of the diamond-celled honeycomb.

Microstructural imperfections, such as wavy struts and displaced joints, are expected to have a knockdown effect on the fracture properties of elastic-brittle honeycombs. The sensitivity of fracture toughness to imperfections in the form of displaced joints has been explored by Romijn and Fleck [4]. They found that the nodal connectivity of the lattice dictates the response. A connectivity of four struts per joint, as in the diamond-celled lattice, is the transition case: The behavior of these structures can be bending-dominated or stretching-dominated depending on the

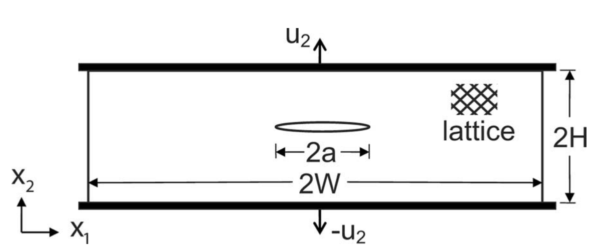

Fig. 1 Center-cracked sandwich plate made from a diamond-celled honeycomb and subjected to uniaxial tension

[1]Corresponding author.

Contributed by the Applied Mechanics Division of ASME for publication in the JOURNAL OF APPLIED MECHANICS. Manuscript received July 30, 2007; final manuscript received October 23, 2007; published online July 21, 2009. Review conducted by Robert M. McMeeking.

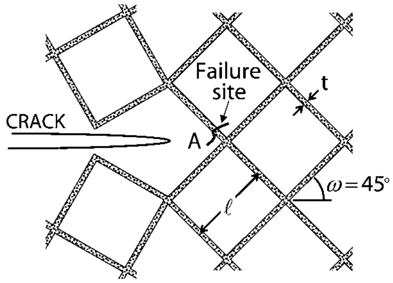

Fig. 2 Crack morphology

level of imperfection. Consequently, the fracture toughness of the diamond-celled topology is imperfection sensitive.

Brittle solids exhibit a scatter of failure strengths: Variable flaw sizes and a random orientation within the brittle cell walls lead to variations in the tensile strength of the solid material σ_f. Huang and Gibson [6] and later Huang and Chou [7] have included statistical effects in the fracture toughness of hexagonal and square honeycombs by assuming that the strength of the cell walls follows a Weibull distribution. They concluded that the fracture toughness K_{IC} increases with cell size if the Weibull modulus m is greater than 4, is insensitive to cell size if m equals 4, and it decreases with cell size if m is less than 4. We shall reassess this result for the diamond-celled honeycomb.

1.2 Statement of the Problem. In the present study, we investigate the tensile fracture response of a center-cracked sandwich panel made from a diamond-celled honeycomb (Fig. 1). This is a common test geometry and is representative of practical applications. The sandwich panel is of width $2W$ and height $2H$, and contains a crack of length $2a$. Fixed grip load conditions are applied by prescribing remote displacements, as shown in Fig. 1.

The diamond-celled lattice, sketched in Fig. 2, is characterized by its cell size ℓ, wall thickness t, and core angle ω. However, only orthogonal honeycombs of $\omega=45$ deg are considered in this study. The cell-wall material is linear elastic to fracture. It has Young's modulus E_s, Poisson's ratio ν_s, and a deterministic tensile fracture strength σ_f. Later in our study, we shall modify this by considering a Weibull distribution of strength. The relative density of the diamond-celled honeycomb is defined by the density of the lattice divided by that of the of the cell-wall material, and is related to $\bar{t}\equiv t/\ell$ by

$$\bar{\rho}=\bar{t}(2-\bar{t}) \tag{2}$$

Classical beam theory suffices to analyze the stress state within the sandwich core in the absence of a crack. Straightforward analysis reveals that the sandwich panel has an out-of-plane unnotched tensile strength σ_u, which scales with the tensile fracture strength of the solid material σ_f and with $\bar{t}$ according to

$$\sigma_u=\frac{\bar{t}}{1+3\bar{t}}\sigma_f \tag{3}$$

This expression takes into account both bending and stretching of the cell walls. Upon neglecting the bending contribution, it reduces to

$$\sigma_u=\bar{t}\sigma_f \tag{4}$$

The approximation (4) is acceptable at low relative densities: At $\bar{t}=0.05$, it leads to an error of 15% in Eq. (3). Henceforth, we shall assume that the unnotched strength is given by Eq. (4).

Now introduce a macroscopic crack into the honeycomb. We write σ^{∞} as the remote gross stress required to initiate crack growth under uniaxial loading. Then σ^{∞}/σ_f depends on the four nondimensional groups $\bar{t}$, a/ℓ, H/ℓ, and H/W. In the current study, we shall limit attention to practical sandwich geometries for which H/W is small.

1.3 Scope of the Study. The structure of this paper is as follows. First, simple analytical models are used to obtain the deterministic fracture strength of the center-cracked panels. These predictions are used to construct a fracture map with axes given by the sandwich beam geometry. The map is validated by selected finite element (FE) simulations. The statistics of brittle fracture are then considered, and the effect of a Weibull distribution of strength on the regimes of dominance of the fracture map is explored.

2 Analytic Description

Consider the center-cracked sandwich panel shown in Fig. 1. The failure strength for any given geometry is determined from a series of simple analytical models. We shall show that the effect of geometry on strength is adequately captured by the two nondimensional groups ℓ/a and $\ell/(\bar{t}H)$. These groups are used to define the axes of a failure mechanism map, and each analytical model of failure has a *regime* of dominance on the map.

We argue that there exists a Regime I of specimen geometries for which the stresses are uniform throughout the lattice. The stress concentration at the crack tip is negligible and the net strength of the cracked panel equals the unnotched strength: The panel is damage tolerant. However, there exist other geometries for which a K-field develops around the crack tip, on a scale larger than the cell size. We call this Regime II if the crack is long compared to the height of the sandwich panel, and Regime III if it is short. A detailed analysis for each regime is now given.

2.1 Regime I. A schematic representation of the stress state within the sandwich core for Regime I is shown in Fig. 3(*a*). Elastic shear regions partition zones of uniform stress state within the sandwich panel: equibiaxial stress, uniaxial stress, and zero stress, see Fig. 3(*a*).

A simple physical model can be developed for the macroscopic strength [8]. It is assumed that only bars that connect one face sheet to the other carry load. Bars that end on the crack faces or on the side edges of the sandwich panel are unloaded. The remaining bars connect both face sheets and are subjected to an axial stress on the bar cross section of

$$\sigma_a=\frac{u_2}{2H}E_s \tag{5}$$

The number n of load carrying bars is given by

$$n=\frac{4(W-H-a)}{\ell\sqrt{2}} \tag{6}$$

Equilibrium in the vertical x_2-direction of Fig. 3(*a*) gives the relation between the macroscopic gross stress σ^{∞} and the local tensile stress in the bars σ_a as

$$\sigma^{\infty}=n\frac{t\sqrt{2}}{4W}\sigma_a \tag{7}$$

Failure occurs when the axial stress in the bars, σ_a, attains the tensile strength of the solid material, σ_f. The gross-section strength of the sandwich panel follows as

$$\sigma^{\infty}=\left(1-\frac{H}{W}-\frac{a}{W}\right)\bar{t}\sigma_f \tag{8}$$

The net-section strength is defined by $\sigma_n=\sigma^{\infty}/(1-a/W)$ and in nondimensional form it reads

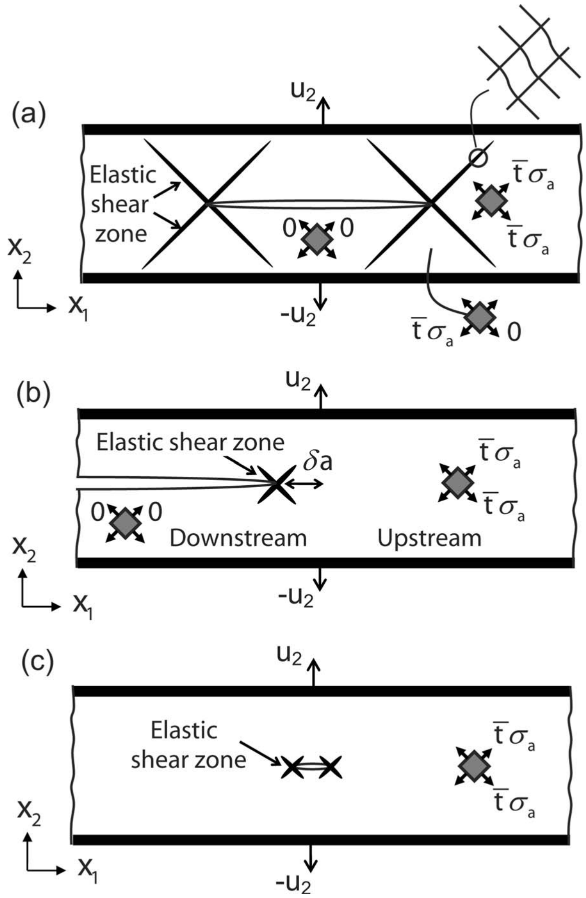

Fig. 3 (***a***) **Regime I: uniform stress with practically no stress concentration at the crack tip. (*b*) Regime II: *K*-field exists. Strength is independent of crack length. (*c*) Regime III: *K*-field exists. Strength scales with crack length as $a^{-1/2}$. In all three regimes, the effective stress far ahead of the crack tip is equibiaxial, and of magnitude $\bar{t}\sigma_a$ upon neglecting the contribution from beam bending.**

$$\bar{\sigma} \equiv \frac{\sigma_n}{\sigma_u} = \frac{\sigma^\infty}{\left(1-\frac{a}{W}\right)\sigma_u} \tag{9}$$

Now limit attention to the case $H/W \ll 1$. Substitution of Eq. (8) into Eq. (9) gives $\bar{\sigma}=1$ since $\sigma_u=\bar{t}\sigma_f$ according to expression (4). We emphasize that the nondimensional parameter $\bar{\sigma}$ compares the net-section strength of the cracked sandwich panel to the unnotched strength. It is therefore a measure of the damage tolerance of the sandwich panel.

2.2 Regime II. Assume that the crack is sufficiently long compared to the height $2H$ of the sandwich panel that the core behaves as an orthotropic elastic strip with a semi-infinite crack, see Fig. 3(*b*). Upstream of the crack tip, a biaxial state of stress prevails while downstream the core is unloaded. In the intermediate zone, a crack tip *K*-field exists on a length scale larger than that of the cell size. The Mode I stress intensity factor K_I at the crack tip is given by the steady state solution as follows.

First, calculate the energy release rate G_I by advancing the crack tip a virtual increment δa. The energy released $G_I\delta a$ equals the difference in stored elastic energy within a strip of width δa and height $2H$ upstream and downstream of the crack tip. Treat the lattice as an effective medium, subjected to a uniform stress state far ahead of the crack tip and far behind the crack tip. Material elements downstream of the crack tip are unloaded. Upstream, material elements are subjected to the macroscopic strain state $\varepsilon_{11}=\varepsilon_{12}=0$ and $\varepsilon_{22}=u_2/H$. The macroscopic stress component σ_{22} is [4]

$$\sigma_{22} = \frac{1}{2}E_s(\bar{t}+\bar{t}^3)\varepsilon_{22} \tag{10}$$

with $\sigma_{12}=0$. Consequently, an energy balance reads

$$G_I\delta a = \frac{1}{2}\sigma_{22}\varepsilon_{22}2H\delta a = \frac{2H\sigma_{22}^2}{E_s(\bar{t}+\bar{t}^3)}\delta a \tag{11}$$

It remains to determine the stress intensity factor K_I in terms of G_I.

The energy release rate G_I and the stress intensity factor K_I in an orthotropic material in plane stress are related through the expression

$$G_I = C_I K_I^2 \tag{12}$$

where the elastic coefficient C_I is a function of the elastic moduli, see, for example, Tada et al. [9]. For the orthotropic honeycomb under consideration, C_I is given by

$$C_I = \frac{\sqrt{\bar{t}^2+1}}{\sqrt{2}}\frac{1}{\bar{t}^2E_s} \tag{13}$$

The stress intensity factor K_I follows as

$$K_I = \frac{2^{3/4}\bar{t}\sigma_{22}\sqrt{H}}{(\bar{t}+\bar{t}^3)^{1/2}(\bar{t}^2+1)^{1/4}} \tag{14}$$

We modify this expression to account for the case of a finite crack. Since σ_{22} is the net-section stress, the remote gross stress σ^∞ reads

$$\sigma^\infty = (1-a/W)\sigma_{22}, \tag{15}$$

Also assume that $\bar{t}$ is much less than unity. Then Eqs. (14) and (15) simplify to

$$K_I = F_I\sigma^\infty\sqrt{H} \tag{16}$$

where the calibration function F_I is

$$F_I = \frac{2^{3/4}\sqrt{\bar{t}}}{(1-a/W)} \tag{17}$$

Recall that Mode I fracture toughness K_{IC} of the diamond-celled lattice has already been given by Eq. (1) in terms of a single numerical constant $\beta=0.44$, as calibrated by FE simulations [4]. Failure occurs when $K_I=K_{IC}$. Consequently, the gross-section strength of the sandwich panel is

$$\sigma^\infty = \frac{K_{IC}}{F_I\sqrt{H}} = 2^{-3/4}\beta\sqrt{\bar{t}}\left(\frac{\ell}{H}\right)^{1/2}\left(1-\frac{a}{W}\right)\sigma_f \tag{18}$$

and the nondimensional net-section strength reads

$$\bar{\sigma} \equiv \frac{\sigma^\infty}{\left(1-\frac{a}{W}\right)\sigma_u} = 2^{-3/4}\beta\left(\frac{\ell}{H\bar{t}}\right)^{1/2} \tag{19}$$

We mention in passing that the calibration factor F_I derived here is in excellent agreement with that obtained by Georgiadis and Papadopoulos [10] using Fourier transforms and the Wiener–Hopf technique. Additional FE simulations have been performed for a cracked strip made from an orthotropic continuum. They confirm the accuracy of Eq. (19) for finite a/W, and are omitted here for the sake of brevity.

2.3 Regime III. Regime III is schematically depicted in Fig. 3(*c*). Now, the crack is much smaller than the height and width of the sandwich panel. The *K*-calibration for an orthotropic panel containing a short central crack of length $2a$ is approximately

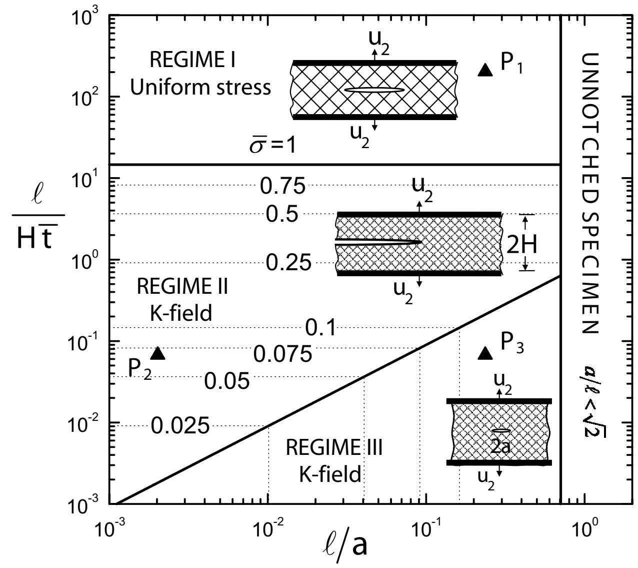

Fig. 4 Fracture map for a panel containing a center crack and subjected to prescribed displacements. The sample geometries P_1, P_2, and P_3 are explored in detail in Sec. 3 to illustrate the response within each regime.

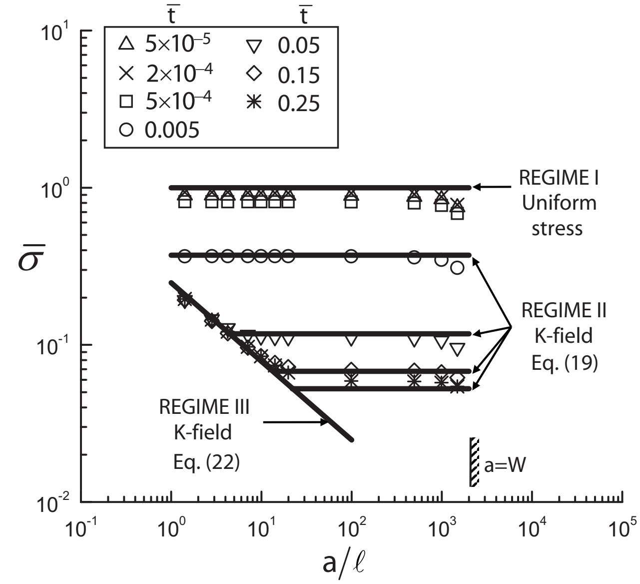

Fig. 5 Normalized net strength as a function of crack size. The width of the sandwich panel is much larger than its height (W/H=20), and its height is much larger than the cell size ($H/\ell=70\sqrt{2}$). The solid lines denote analytic predictions.

$$K_I = \frac{\sigma^\infty\sqrt{\pi a}}{\left(1-\dfrac{a}{W}\right)} \tag{20}$$

A more precise calibration can be found in the literature [11]. However, the approximate relation (20) is adequate for our purposes and it leads to a major simplification of subsequent algebra.

Failure occurs when the stress intensity factor K_I reaches the critical value, K_{IC}. The gross-section strength of the sandwich panel is given by

$$\sigma^\infty = \frac{\left(1-\dfrac{a}{W}\right)K_{IC}}{\sqrt{\pi a}} = \frac{\beta}{\sqrt{\pi}}\bar{t}\left(\frac{\ell}{a}\right)^{1/2}\left(1-\frac{a}{W}\right)\sigma_f \tag{21}$$

and the normalized net-section strength is

$$\bar{\sigma} \equiv \frac{\sigma^\infty}{\left(1-\dfrac{a}{W}\right)\sigma_u} = \frac{\beta}{\sqrt{\pi}}\left(\frac{\ell}{a}\right)^{1/2} \tag{22}$$

2.4 Construction of the Fracture Map. The above three analytical models can be used to construct a fracture map, with suitably chosen axes in terms of the sandwich geometry. The nondimensional net-section strength $\bar{\sigma}$ equals unity in Regime I, depends on $\ell/\bar{t}H$ in Regime II, and depends on ℓ/a in Regime III. Consequently, we construct a fracture map with axes $(\ell/a, \ell/\bar{t}H)$, as shown in Fig. 4. The boundaries between regimes are obtained by equating the expressions for the strength within each regime. The boundary between Regimes I and II is given by $\ell/\bar{t}H=14.6$ upon taking $\bar{\sigma}=1$ in Eq. (19). Likewise, the boundary between Regimes II and III is obtained by equating $\bar{\sigma}$ from Eq. (19) with $\bar{\sigma}$ from Eq. (22), to give $\ell/\bar{t}H=0.9\ell/a$. A physical constraint on the minimum crack length is also imposed on the map: The minimum crack length in the lattice is $a/\ell=\sqrt{2}$. It is straightforward to add contours of nondimensional strength $\bar{\sigma}$ to the map, upon making use of $\bar{\sigma}=1$ in Regime I, and relations (19) and (22) in Regimes II and III, respectively. We emphasize that the fracture map is universal for all relative densities and for all geometries of sandwich panel, provided W/H is sufficiently large. It remains to perform a series of FE simulations to validate the map.

3 Numerical Calculations

Selected FE simulations have been carried out to determine the gross-section fracture strength σ^∞ of centrally cracked sandwich panels made from an elastic-brittle, diamond-celled honeycomb. It is assumed that the honeycomb fails when the maximum tensile principal stress anywhere in the lattice attains a critical value σ_f.

The linear elastic calculations were performed using the commercial FE code ABAQUS (version 6.5-3). Each strut in the lattice was modeled as a two-noded Euler–Bernoulli beam element (type $B23$ in ABAQUS notation): This element uses cubic interpolation functions and allows for both stretching and bending deformations but neglects shear deformation.

The symmetries of the geometry and loading were such that a FE mesh was generated for one-quarter of the sandwich panel. The crack in the lattice was defined by splitting the joints along the cracking plane while keeping intact the struts on each face of the crack (Fig. 2). The face sheets were not explicitly modeled in the FE simulations. Rather, all lattice joints attached to the face sheets were subjected to the same prescribed vertical displacement, with zero transverse displacement and zero rotation.

The FE mesh of the sandwich core comprised 1400 cells in the x_1 direction by 70 cells in the x_2 direction. Throughout this numerical study, two aspect ratios were held constant: $H/\ell=70\sqrt{2}$ and $H/W=1/20$. We investigated the sensitivity of the fracture strength of the sandwich panel to crack length a/ℓ and to relative density as parametrized by $\bar{t}\equiv t/\ell$.

3.1 Verification of the Regimes of Behavior. A series of FE calculations has been performed for selected values of $\bar{t}$ in the range 5×10^{-5} to 0.25 and a/ℓ between $\sqrt{2}$ and $1050\sqrt{2}$. The results are given in Fig. 5 in the form of a plot of $\bar{\sigma}$ versus a/ℓ, together with the analytic prediction $\bar{\sigma}=1$ for all $\bar{t}$ in Regime I, the prediction (19) for selected values of $\bar{t}$ in Regime II, and the prediction (22) for all in $\bar{t}$ Regime III. Good agreement between the analytical formulas and numerical predictions is noted for all

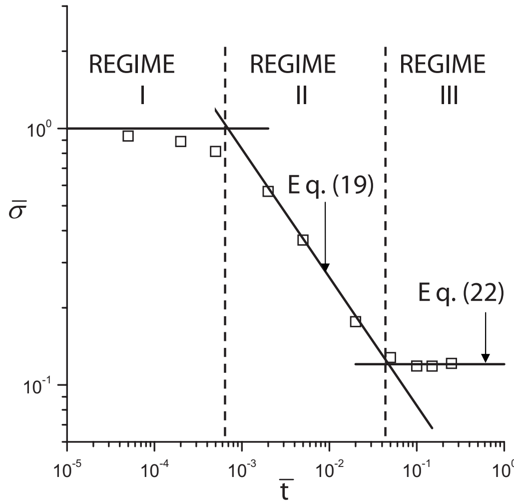

Fig. 6 Net strength as a function of relative density for a sandwich panel made from a lattice, which contains a central crack of length $a/\ell=3\sqrt{2}$. The panel has aspect ratios $W/H=20$ and $H/\ell=70\sqrt{2}$.

three regimes. For $\bar{t}$ below a transition value of $\beta^2\ell/2\sqrt{2}H=6.9\times10^{-4}$, the response lies within Regime I: The FE simulations confirm that $\bar{\sigma}\approx1$. For $\bar{t}$ above this transition value, the strength of the sandwich panel is toughness controlled and $\bar{\sigma}$ is below the unnotched value. In Regime II, the strength of the panel is independent of crack length and scales with relative density according to $\bar{\sigma}\propto(\bar{t}H/\ell)^{-1/2}$, recall Eq. (19). In Regime III, the nondimensional strength of the panel is independent of relative density and scales with crack length as $\bar{\sigma}\propto(a/\ell)^{-1/2}$.

Additional insight is obtained by plotting in Fig. 6 the normalized net-section strength $\bar{\sigma}$ as a function of $\bar{t}$; this is done by cross plotting the seven data points of Fig. 5 at fixed $a/\ell=3\sqrt{2}$. Three additional simulations were run and added to Fig. 6 in order to present a more complete comparison between FE results and analytical estimates. At small $\bar{t}$, the response lies within Regime I: No stress concentration exists and the unnotched strength is maintained, $\bar{\sigma}=1$. With increasing $\bar{t}$, the response switches to Regime II and $\bar{\sigma}$ scales as $\bar{t}^{-1/2}$ in accordance with Eq. (19). At large $\bar{t}$, Regime III exists such that $\bar{\sigma}$ is insensitive to $\bar{t}$, as stated in Eq. (22). It is remarkable that the simple estimates of Sec. 2, based on linear elastic fracture mechanics for a continuum, capture the response in Regimes II and III despite the fact that the lattices of Fig. 6 contain only a few broken cells.

3.2 Normal Traction Directly Ahead of the Crack Tip. Consider the forces in the joints of the lattice directly ahead of the crack tip. These forces are used to construct a traction distribution on the crack plane directly ahead of the crack tip, in order to make comparisons with the stress state in a cracked continuum. This traction distribution has been obtained for the geometries P_1, P_2, and P_3, as defined in Fig. 4. These geometries are taken to be representative of the response for each of the three regimes.

(i) The traction distribution for geometry P_1 (representative of Regime I) is uniform at $\sigma_{22}\approx\sigma^\infty$, see Fig. 7(*a*). This implies that no *K*-field exists.

(ii) The traction $\sigma_{22}(r)$ for geometry P_2 of Regime II is compared to the asymptotic crack tip field $\sigma_{22}=K_I/\sqrt{2\pi r}$ in Fig. 7(*a*), where *r* is the distance ahead of the crack tip. Note that Eq. (16) is used for K_I. It is clear that the traction in the discrete lattice is consistent with the *K*-field of a continuum.

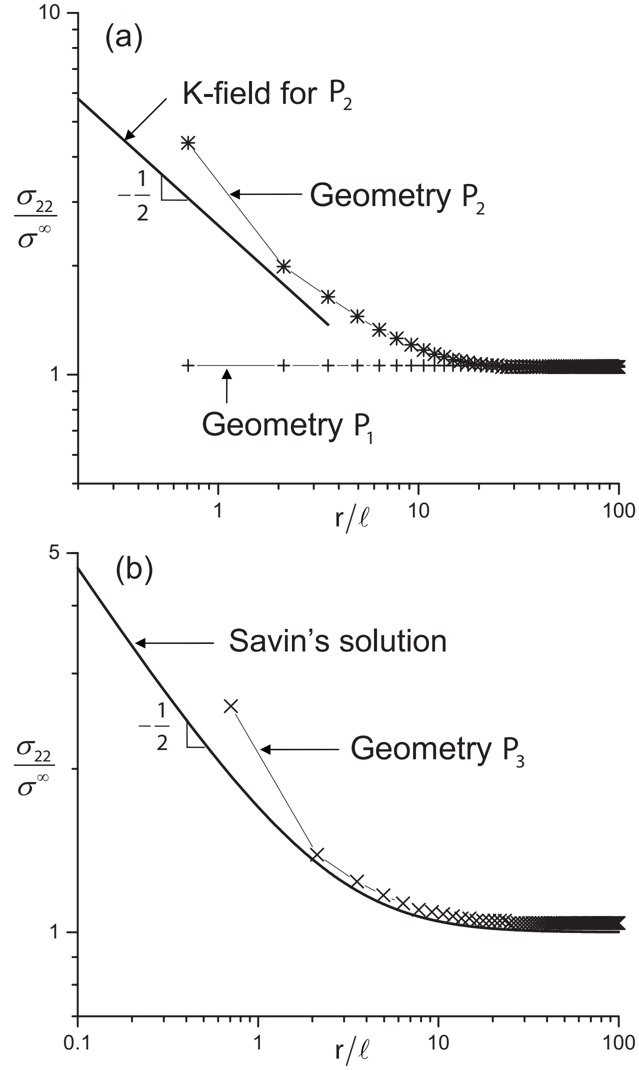

Fig. 7 Normal tractions directly ahead of the crack tip. The geometries are specified by P_1: $\bar{t}=5\times10^{-5}$, $a/\ell=3\sqrt{2}$; P_2: $\bar{t}=0.15$, $a/\ell=350\sqrt{2}$, and P_3: $\bar{t}=0.15$, $a/\ell=3\sqrt{2}$.

(iii) Finally, consider geometry P_3 of Regime III. The traction within the discrete lattice is plotted in Fig. 7(*b*) along with the Savin [12] solution for an infinite orthotropic panel containing a center crack. It is clear that the traction ahead of the crack tip in the lattice is adequately represented by the continuum solution. The agreement is remarkably close given the fact that the crack in the lattice is short, $a/\ell=3\sqrt{2}$.

The comparisons made in Fig. 7 support the applicability of linear elastic fracture mechanics in Regimes II and III: K_{IC} serves as a useful fracture parameter to describe the local conditions near the crack tip of the lattice.

4 Statistics of Brittle Failure

Brittle solids, such as engineering ceramics, contain a random distribution of flaws of stochastic length. Consequently, the solid cell walls of a brittle honeycomb exhibit a statistical distribution of tensile fracture strength σ_f. Weibull statistics are commonly used to model this scatter in strength: the survival probability P_s of a brittle solid of volume V subjected to a maximum principal tensile stress σ_1 is given by

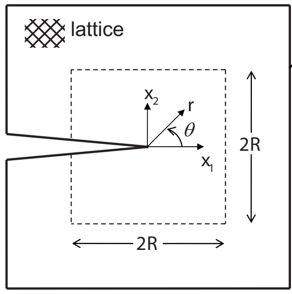

Fig. 8 FE model used to assess the fracture toughness of the lattice

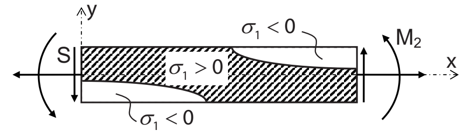

Fig. 9 Maximum principal stress distribution for a typical strut in the lattice

$$P_s(\sigma_1) = \exp\left[-\int_V \left(\frac{\sigma_1}{\sigma_0}\right)^m \frac{dV}{V_0} \right] \tag{23}$$

where m is the Weibull modulus and σ_0 is a reference fracture strength for a reference volume V_0. The magnitude of the Weibull modulus is a measure of the variability in strength: The lower the value of m, the greater the variability in strength.

We proceed to include the statistical component of cell-wall strength in our analysis of the cracked sandwich panel. Strength-controlled failure (Regime I) and toughness-controlled failure (Regimes II and III) are treated in turn.

4.1 Strength-Controlled Regime I. In Regime I, the deterministic net-section strength of the cracked panel is adequately predicted by the unnotched strength $\sigma_u = \bar{t}\sigma_f$. It is straightforward to modify this analysis for a statistical distribution of strength. Assume that the cell walls are uniaxially loaded. Then, the maximum principal tensile stress σ_1 can be written in terms of the remote applied net-section stress σ_n as $\sigma_1 = \sigma_n / \bar{t}$. The Weibull distribution (23) now takes the form

$$P_s(\sigma_n) = \exp\left[-\left(\frac{\sigma_n}{\bar{t}\sigma_0}\right)^m \frac{V}{V_0} \right] \tag{24}$$

The average net-section strength $(\sigma_n)_{\text{mean}}$ immediately follows as

$$(\sigma_n)_{\text{mean}} = \int_0^\infty P_s(\sigma_n) d\sigma_n = \sigma_0 \bar{t} \left(\frac{V_0}{V}\right)^{1/m} \Gamma\left(\frac{m+1}{m}\right) \tag{25}$$

where $\Gamma(1+1/m)$ is the gamma function and $V = 4H(W-a)\bar{\rho}$ is the total volume of cell-wall material per unit depth.

4.2 Statistics of Fracture Toughness. So far, we have used a deterministic value of fracture toughness; however, statistical variations in the strength of the solid cell walls lead to variations in the fracture toughness of the lattice. We proceed to use Weibull theory to predict the variability in fracture toughness in terms of m, σ_0, and V_0.

4.2.1 Weibull Analysis for a Crack Tip Field. Consider the problem of a diamond-celled lattice containing a long crack, as sketched in Fig. 8. The polar coordinates (r, θ) are centered on the crack tip and are defined in the usual manner, see Fig. 8. We subject the outer boundary of the lattice to the displacement field **u** associated with the macroscopic crack tip K-field for an orthotropic elastic solid [13].

Write the maximum principal tensile stress σ_1 within the cell walls of the lattice in the form

$$\sigma_1 = \frac{K_I}{\bar{t}\sqrt{\ell}} g(r/\ell, \theta, \bar{t}) \tag{26}$$

where K_I is Mode I stress intensity factor and the function g gives the dependence on position within the lattice and on the bar stubbiness $\bar{t}$.

According to Weibull theory, the probability of survival of the lattice subjected to a stress intensity K_I is found by substituting Eq. (26) into Eq. (23):

$$\begin{aligned} P_s(K_I) &= \exp\left[-\int_V \left(\frac{K_I g}{\sigma_0 \bar{t}\sqrt{\ell}}\right)^m \frac{dV}{V_0} \right] \\ &= \exp\left[-\left(\frac{K_I}{\sigma_0 \bar{t}\sqrt{\ell}}\right)^m \int_V g^m \frac{dV}{V_0} \right] \end{aligned} \tag{27}$$

The average fracture toughness of the lattice follows as

$$(K_{IC})_{\text{mean}} = \int_0^\infty P_s(K_I) dK_I = \bar{K}\sigma_0 \bar{t}\sqrt{\ell} \tag{28}$$

where

$$\bar{K} \equiv \frac{(K_{IC})_{\text{mean}}}{\sigma_0 \bar{t}\sqrt{\ell}} = \Gamma\left(\frac{m+1}{m}\right) \left[\int_V g^m \frac{dV}{V_0} \right]^{-1/m} \tag{29}$$

4.2.2 Finite Element Simulations. We shall now evaluate $\bar{K}$ from FE simulations. A square mesh of the diamond-celled lattice was created using ABAQUS (version 6.5-3). Each strut of the lattice was modeled as an Euler–Bernoulli beam element. The square mesh was of side 600 unit cells and contained a traction-free edge crack along the negative x_1-axis (Fig. 8). Loading was applied by imposing the displacement field corresponding to the K-field on the boundary of the mesh [13]. A mesh convergence study based on the maximum local tensile stress in the lattice revealed that the mesh suffices for the present investigation.

$\bar{K}$ is calculated as follows. The maximum principal tensile stress σ_1 within the cell walls of the lattice is determined from the FE simulations. These stresses are used to obtain the function g as defined in Eq. (26). Note that only the maximum principal tensile stress σ_1 enters the calculation. Figure 9 shows a typical strut in the lattice with the zone of tensile stress. Introduce a local Cartesian reference frame (x, y) for each strut such that x is the distance along the strut and y is the distance from the neutral section. The stress distribution $\sigma_1(x,y) = F/t + 12My/t^3$ is obtained from the bending moment along the strut $M(x) = M_1 + (M_2 - M_1)x/\ell$ and the axial force F. By setting $\sigma_1(x,y) = 0$, we locate the position of the neutral axis as a function of the distance x along the beam, $y_{NA}(x) = -Ft^2/12M(x)$. The integral within expression (29) then reads

$$\int_V g^m(r/\ell, \theta, \bar{t}) \frac{r dr d\theta}{V_0} = \left(\frac{\ell^2}{V_0}\right) \left(\frac{\bar{t}\sqrt{\ell}}{K_I}\right)^m \int_V \sigma_1^m(\xi, \theta, \bar{t}) \xi d\xi d\theta \tag{30}$$

where $\xi = r/\ell$ is used as a dummy variable. This integral is calculated over a square region of side $2R$ centered at the crack tip (Fig. 8). As the size of the square region increases, the volume integral

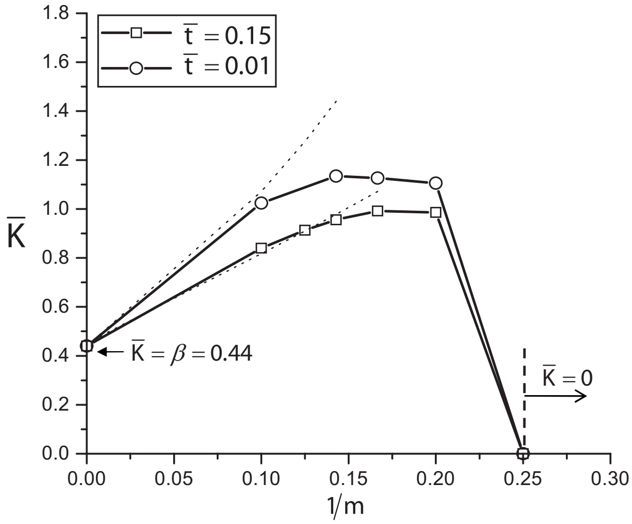

Fig. 10 Dependence of $\bar{K}$ on the Weibull modulus. The dotted lines denote the analytical estimate of Eq. (33) for large *m*.

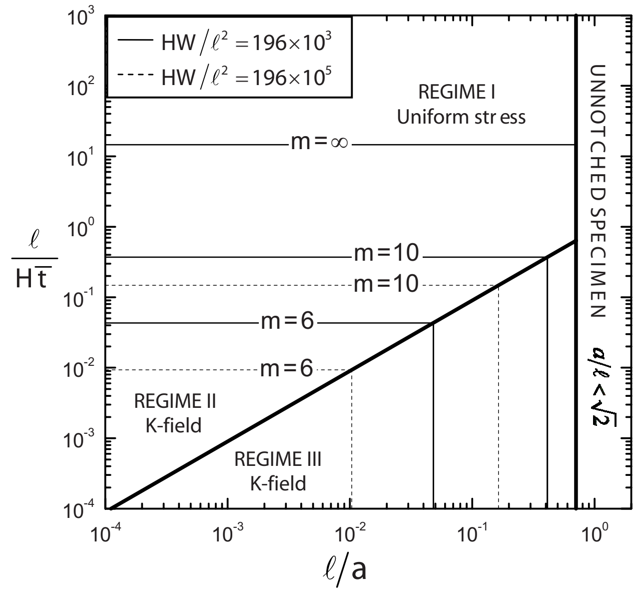

Fig. 11 Fracture map for a honeycomb core sandwich panel where the statistical variability of the cell-wall strength is included

in Eq. (30) converges to a constant value. The higher the Weibull modulus *m*, the faster the convergence is achieved.

The dependence of $\bar{K} \equiv (K_{IC})_{\text{mean}}/\sigma_0\bar{t}\sqrt{\ell}$ on Weibull modulus is plotted in Fig. 10 for the two values of cell-wall stubbiness, $\bar{t}=0.15$ and $\bar{t}=0.01$, with the arbitrary volume V_0 taken to be $V_0=\ell^2$. The plots display a peak value of fracture toughness for m about equal to 6. A large Weibull modulus m implies small variations in cell-wall strength, and deterministic fracture toughness, $\bar{K}=\beta=0.44$. However, at low m, the effect of a stochastic strength is significant. There exists a limit $m=4$ below which $\bar{K}$ drops to zero. A scaling argument can be used to explain this. Conventional linear elastic fracture mechanics suggests that the nondimensional function g scales with distance r from the crack tip as $g\propto r^{-1/2}$. Therefore, the integral within Eq. (29) has the following scaling:

$$\int_V g^m dV \propto \int_V r^{-m/2} r\,d\theta\,dr \propto \int_\delta^\infty r^{2-m/2}dr \approx \frac{2}{4-m}[r^{4-m/2}]_{r=\delta}^{r=\infty} \tag{31}$$

where the lower limit of integration δ is on the order of the cell size of the lattice ℓ. Note that this integral has a finite value for $m>4$; however, for $m\leq 4$ the integral is unbounded at the outer limit and $\bar{K}$ equals zero. We conclude from Eq. (28) that the fracture toughness of the lattice tends to zero for $m\leq 4$. The physical interpretation is the following: The variability in strength is sufficiently great for $m\leq 4$ that struts remote from the crack tip fail and the effective "stressed volume" is unbounded.

4.2.3 Analytical Estimate of the Mean Fracture Toughness. For large values of Weibull modulus m, failure always occurs near the crack tip. An estimate for the mean fracture toughness is found by considering only the critical strut directly ahead of the crack tip (Fig. 2). Assume that this critical strut deforms as a built-in beam, as sketched in Fig. 3(*a*). Ignore the tensile stress caused by axial and shear forces so that only the tensile stress due to bending is taken into account. The survival probability is given in terms of the maximum local bending stress in the built-in beam σ_A by [14]

$$P_s = \exp\left[-\frac{1}{2(m+1)^2}\left(\frac{V}{V_0}\right)\left(\frac{\sigma_A}{\sigma_0}\right)^m\right] \tag{32}$$

Here, the volume V per unit depth is equal to $2\ell t$ since only two struts are critical: the one containing the fracture site A, as shown in Fig. 2, and its mirror image about the cracking plane. Numerical investigations [4] have revealed that the maximum local bending stress σ_A in the beam reads $\sigma_A=K_I/0.44\bar{t}\sqrt{\ell}$. Substitution of this value into Eq. (32) provides

$$\bar{K} \equiv \frac{(K_{IC})_{\text{mean}}}{\sigma_0\bar{t}\sqrt{\ell}} = \Gamma\left(\frac{m+1}{m}\right)\left[0.44^m(1+m)^2\left(\frac{V_0}{\ell^2}\right)\frac{1}{\bar{t}}\right]^{1/m} \tag{33}$$

Equation (33) is plotted in Fig. 10 as a dotted line for the two values of $\bar{t}$ considered in the numerical calculation of the previous section. As expected, the estimate is valid only for large m. For example, for $m>10$, the error is less than 4%. However, the analytical estimate considerably deviates from the numerical calculation of $\bar{K}$ as the Weibull modulus is decreased.

4.3 Implications of Weibull Statistics on the Fracture Map. The variability in cell-wall strength leads to a variability in strength of the cracked sandwich panel in Regime I of the fracture map, recall Eq. (8). Likewise, the variability in fracture toughness leads to a variability in strength of the cracked sandwich panel, recall Eqs. (18) and (21) for Regimes II and III, respectively.

The implications of cell-wall strength variability on the fracture map are now examined. We make use of expressions (25) and (33) in order to derive analytical estimates for the boundaries between regimes.

First, consider the boundary between Regimes I and II. Upon equating the mean strength (25) in Regime I with the mean strength in Regime II, as specified by Eqs. (18) and (33), we obtain

$$\frac{\ell}{H\bar{t}} = \frac{2\sqrt{2}}{\beta^2}\left[\frac{1}{2(1+m)^2}\left(\frac{\ell^2}{2HW}\right)\right]^{2/m} \tag{34}$$

Second, the boundary between Regimes I and III is obtained via Eqs. (25), (21), and (33), giving

$$\frac{\ell}{a} = \frac{\pi}{\beta^2}\left[\frac{1}{2(1+m)^2}\left(\frac{\ell^2}{2HW}\right)\right]^{2/m} \tag{35}$$

Third, the boundary between Regimes II and III is obtained by equating the strengths as specified by Eqs. (18) and (21); Note that this boundary is insensitive to the value of m.

The effect m on the boundaries of the fracture map is shown in Fig. 11. Boundaries are plotted for selected values of $m=10$ and

$m=6$ together with the deterministic result $m=\infty$. It is clear that as the Weibull modulus decreases the regimes of fracture toughness control shrink in favor of the strength-governed Regime I.

Boundaries are given in Fig. 11 for two values of HW/ℓ^2. One choice corresponds to the geometry considered in the FE analysis of the present study such that $W/H=20$ and $H/\ell=70\sqrt{2}$, giving $HW/\ell^2=196\times 10^3$. A second choice assumes a much larger structure such that $W/H=20$ and $H/\ell=700\sqrt{2}$, giving $HW/\ell^2=196\times 10^5$. It is clear from Fig. 11 that for finite m Regime I expands with increasing volume of panel, for a given cell size ℓ.

Engineering ceramics have a wide range of m value from 3 to 20 depending on the processing route. For example, cordierite in catalytic converters has approximately $m=6$ [6]. Thus, it is necessary to include statistical effects on the strength of the sandwich panel.

5 Concluding Remarks

In this study, it is shown that the fracture strength of a center-cracked sandwich panel made from a brittle diamond-celled honeycomb depends on the relative density of the lattice, the crack size, and the geometric dimensions of the panel. The FE method has been used to investigate the damage tolerance of the structure. A fracture map has been constructed with axes $(\ell/a, \ell/\bar{t}H)$ given by the sandwich geometry. Three regimes of behavior have been observed. Simple analytical models of each regime are able to capture the mechanical response of the sandwich panel.

Statistical variations in the cell-wall strength have been quantified by assuming that it follows a Weibull distribution. The effect of specimen geometry and Weibull modulus on the fracture map has been explored. As expected, a large sandwich panel is more likely to be strength controlled, for a given cell size of the honeycomb. It is also found that the domain of toughness-controlled fracture shrinks as the Weibull modulus m is decreased. For $m\leq 4$, the fracture toughness of the honeycomb falls to zero and failure is strength governed.

The results presented above give the fracture toughness of the lattice K_{IC} in terms of the tensile strength σ_f of the cell-wall material. However, σ_f derives from the fracture toughness K_s of the cell wall and the intrinsic flaw size c within the cell walls

$$\sigma_f \approx \frac{K_s}{\sqrt{\pi c}} \tag{36}$$

Substition of Eq. (36) into Eq. (1) gives

$$\frac{K_{IC}}{K_s} = 0.23\bar{t}\left(\frac{\ell}{c}\right)^{1/2} \tag{37}$$

This alternative presentation of the fracture toughness K_{IC} suggests that improved processing techniques, which reduce c, will lead to an enhanced toughness of the lattice.

The current study is also of relevance to the fatigue strength of *metallic* lattices. Following Gibson and Ashby [2] and Huang and Lin [15], we argue that fatigue failure of the cracked lattice is due to the cyclic failure of the most heavily loaded strut. Now limit attention to the fatigue limit of the lattice. At infinite fatigue life, this critical strut is subjected to local stress of amplitude equal to the endurance limit σ_e of the solid. The map shown in Fig. 4 can be reinterpreted as a fatigue fracture map for infinite life once we rewrite $\bar{\sigma}$ as amplitude of net-section fatigue loading normalized by σ_e. Also, the stress intensity range for fatigue crack growth in the metallic lattice ΔK_{th} can be directly stated from Eq. (1) as

$$\Delta K_{\mathrm{th}} = 2\beta\sigma_e\bar{t}\sqrt{\ell} \tag{38}$$

The authors are unaware of any experiments in the literature, which support or refute Eq. (38). Formulas similar to Eq. (38) have been developed for open-cell metallic foams and polymeric foams, see Gibson and Ashby [2], Olurin et al. [16], and Burman and Zenkert [17]. These experimental and theoretical studies support the idea that the fatigue crack growth threshold ΔK_{th} is dependent on the cyclic fatigue strength σ_e of the cell wall and on the cell size ℓ. The authors are unaware of any experimental studies, which can be used to validate the fracture and fatigue maps presented here. It is suggested that such validation is a topic for future study.

Acknowledgment

The authors are grateful for the support provided by the EPSRC and by the European Community's Human Potential Programme HPRN-CT-2002-00198 (RTN-DEFINO).

References

[1] Ashby, M. F., 1983, "The Mechanical Properties of Cellular Solids," Metall. Trans. A, **14A**, pp. 1755–1783.
[2] Gibson, L. J., and Ashby, M. F., 1999, *Cellular Solids: Structure and Properties*, 2nd ed., Pergamon, Oxford.
[3] Fleck, N. A., and Qiu, X., 2007, "The Damage Tolerance of Elastic-Brittle, Two Dimensional Isotropic Lattices," J. Mech. Phys. Solids, **55**(3), pp. 562–588.
[4] Romijn, N. E., and Fleck, N. A., 2007, "The Fracture Toughness of Planar Lattices: Imperfection Sensitivity," J. Mech. Phys. Solids, **55**(12), pp. 2538–2564.
[5] Quintana Alonso, I., and Fleck, N. A., 2007, "Damage Tolerance of an Elastic-Brittle Diamond-Celled Honeycomb," Scr. Mater., **56**(8), pp. 693–696.
[6] Huang, J. S., and Gibson, L. J., 1991, "Fracture Toughness of Brittle Honeycombs," Acta Metall. Mater., **39**(7), pp. 1617–1626.
[7] Huang, J. S., and Chou, C. Y., 1999, "Survival Probability for Brittle Honeycombs Under In-Plane Biaxial Loading," J. Mater. Sci., **34**(20), pp. 4945–4954.
[8] Zupan, M., Deshpande, V. S., and Fleck, N. A., 2004, "The Out-of-Plane Compressive Behaviour of Woven-Core Sandwich Plates," Eur. J. Mech. A/Solids, **23**(3), pp. 411–421.
[9] Tada, H., Paris, P. C., and Irwin, G. R., 1985, *The Stress Analysis of Cracks Handbook*, St. Louis, MO.
[10] Georgiadis, H. G., and Papadopoulos, G. A., 1988, "Cracked Orthotropic Strip With Clamped Boundaries," J. Appl. Math. Phys., **39**(4), pp. 573–578.
[11] Bowie, O. L., and Freese, C. E., 1972, "Central Crack in Plane Orthotropic Rectangular Sheet," Int. J. Fract. Mech., **8**(1), pp. 49–57.
[12] Savin, G. N., 1961, *Stress Concentration Around Holes*, Pergamon, Oxford.
[13] Sih, G. C., Paris, P. C., and Irwin, G. R., 1965, "On Cracks in Rectilinearly Anisotropic Bodies," Int. J. Fract. Mech., **1**(3), pp. 189–203.
[14] Jayatilaka, A. de S., 1979, *Fracture of Engineering Brittle Materials*, Applied Science, London.
[15] Huang, J. S., and Lin, J. Y., 1996, "Fatigue of Cellular Materials," Acta Mater., **44**(1), pp. 289–296.
[16] Olurin, O. B., McCullough, K. Y. G., Fleck, N. A., and Ashby, M. F., 2001, "Fatigue Crack Propagation in Aluminium Alloy Foams," Int. J. Fatigue, **23**, pp. 375–382.
[17] Burman, M., and Zenkert, D., 1997, "Fatigue of Foam Core Sandwich Beams," Int. J. Fatigue, **19**(7), pp. 551–578.

The Through-Thickness Compressive Strength of a Composite Sandwich Panel With a Hierarchical Square Honeycomb Sandwich Core

F. Côté

B. P. Russell

V. S. Deshpande

N. A. Fleck

Department of Engineering,
University of Cambridge,
Cambridge CB2 1PZ, UK

Sandwich panels with aluminum alloy face sheets and a hierarchical composite square honeycomb core have been manufactured and tested in out-of-plane compression. The prismatic direction of the square honeycomb is aligned with the normal of the overall sandwich panel. The cell walls of the honeycomb comprise sandwich plates made from glass fiber/epoxy composite faces and a polymethacrylimide foam core. Analytical models are presented for the compressive strength based on three possible collapse mechanisms: elastic buckling of the sandwich walls of the honeycomb, elastic wrinkling, and plastic microbuckling of the faces of the honeycomb. Finite element calculations confirm the validity of the analytical expressions for the perfect structure, but in order for the finite element simulations to achieve close agreement with the measured strengths it is necessary to include geometric imperfections in the simulations. Comparison of the compressive strength of the hierarchical honeycombs with that of monolithic composite cores shows a substantial increase in performance by using the hierarchical topology.
[DOI: 10.1115/1.3086436]

Keywords: honeycombs, composite, strength, sandwich panels

1 Introduction

[1]The concept of a thick and light core sandwiched between two strong thin facings has been used to produce stiff and lightweight panels since the 19th century [1]. The underlying theory and design methods for sandwich constructions are well known [2,3]. For example, it is generally recognized that the stiffness and strength of a sandwich panel under macroscopic loading (bending, end loading, and torsion) are sensitive to the thickness of the core and to the in-plane properties of the face sheets.

Stochastic foam and periodic lattice materials are two broad classes of core increasingly employed in sandwich construction [4]. Closed cell foams behave as a continuous core and provide a continuous interface for bonding to the faces, but they possess a low specific stiffness and strength. In contrast, lattice materials have a high specific stiffness and strength due to their high nodal connectivity [5]. Three categories of periodic lattice materials have been developed: (i) prismatic cores, (ii) 3D trusses, and (iii) honeycombs. In this study we shall explore the properties of a *hierarchical sandwich core* in the form of a square honeycomb.

Hexagonal honeycombs made from Nomex or from aluminum alloy are extensively employed in sandwich construction due to their high specific stiffness and strength in out-of-plane compression and in longitudinal shear. However, these hexagonal honeycombs have low values of in-plane stiffness and strength due to a nodal connectivity of only 3 [6]. Square honeycombs have a higher nodal connectivity of 4, and thereby have enhanced in-plane properties. Further, the out-of-plane properties of the square honeycomb are comparable to those of the hexagonal honeycombs, see, for example, recent measurements of out-of-plane compressive strength [7] and of longitudinal shear strength [8].

It is of interest to explore sandwich panel cores that possess a high stiffness and strength yet have a low density. Honeycomb cores made from monolithic composite sheets have a higher specific stiffness and strength than many metallic honeycombs. The out-of-plane compressive strength of sandwich panels with a composite or metallic honeycomb core is limited by the elastic buckling of the cell walls when the core has a low relative density ($\bar{\rho}<0.05$). Here, we shall explore a strategy for increasing the elastic buckling strength of the cell walls by employing sandwich construction for the cell walls [9]. The microstructure is *hierarchical* in topology: The *macroscopic* sandwich panel comprises aluminum alloy face sheets and a square honeycomb core, with the cell walls of the core made from *mesoscopic* sandwich panels (see Fig. 1(*a*)). These mesoscopic panels comprise a polymethacrylimide (PMI) foam sandwiched between woven glass fiber/epoxy composite faces.

The outline of this paper is as follows. First, competing collapse mechanisms are considered for the out-of-plane compressive strength of a sandwich panel with a square honeycomb core. Analytical expressions are taken from the literature for each mechanism, and the dominant collapse mechanism is plotted on a map with geometry as axes. Second, an experimental investigation is conducted to probe the accuracy of the analytical predictions. Third, the measurements and analytical predictions are compared with three-dimensional (3D) finite element (FE) simulations, and the role of geometric imperfection in dictating compressive strength is assessed. Finally, the measured and predicted compressive strengths are compared with that of monolithic composite square honeycombs.

[1]Trade name of Dupont referring to an aramid paper impregnated with epoxy resin.

Contributed by the Applied Mechanics Division of ASME for publication in the Journal of Applied Mechanics. Manuscript received August 9, 2007; final manuscript received January 11, 2009; published online July 23, 2009. Review conducted by Kenneth M. Liechti.

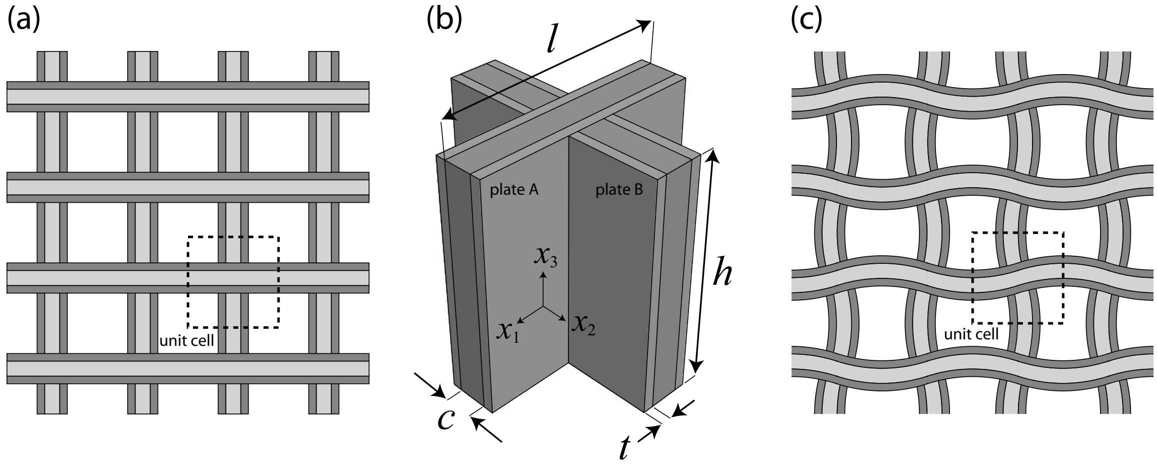

Fig. 1 (***a***) **Sketch of a square honeycomb core with the cell walls of the core made from a mesoscopic sandwich panels, (*b*) schematic of the unit cell and geometrical parameters employed in the analytical model and finite element analysis, and (*c*) torsional-axial buckling mode of square honeycomb core**

2 Analytical Models for the Competing Collapse Modes

2.1 Geometry of Core and the Imposed Loading. Consider a square honeycomb core perfectly bonded to rigid face sheets. The core has sandwich walls with square cells of side-length l and height h, and the prismatic direction of the honeycomb core is aligned with the out-of-plane direction of the overall honeycomb (Fig. 1(*b*)). The sandwich walls comprise an isotropic foam of thickness c and density ρ_c bonded between two orthotropic elastic faces, each of thickness t and density ρ_f. This representation is appropriate for the material system studied herein: woven glass fiber/epoxy faces and a PMI foam core.

The macroscopic sandwich panel is subjected to an out-of-plane compressive stress σ; consequently, each cell wall is subjected to a line load P per unit length where

$$P = \sigma\frac{l}{2} \tag{1}$$

while the effective density ρ of the square honeycomb core is

$$\rho = 2\frac{t}{l}\left(2 - \frac{(2t+c)}{l}\right)\rho_f + \frac{c}{l}\left(2 - \frac{(2t+c)}{l}\right)\rho_c \tag{2}$$

Three collapse mechanisms are considered: (i) elastic buckling of the square honeycomb, (ii) elastic face wrinkling of the mesoscopic sandwich panels that make up the cell walls of the square honeycomb, and (iii) plastic microbuckling of the composite face sheets of the mesoscopic sandwich panels. The out-of-plane compressive strength of the macroscopic sandwich panel is dictated by the collapse mechanism that has the lowest value of line load $P_{\rm cr}$ for any given set of geometric and material parameters. The compressive strengths for mechanisms (i) and (ii) above are sensitive to the elastic moduli of the foam core in the mesoscopic sandwich panels. We proceed by summarizing the elastic moduli for a closed-cell foam.

2.2 Elastic Properties of Closed-Cell Foams. Gibson and Ashby [4] extensively reviewed the mechanical properties of open- and closed-cell foams. They showed that Young's modulus E_c and the shear modulus G_c of an isotropic, closed-cell foam are directly related to the relative density $\bar{\rho} \equiv \rho_c/\rho_s$, where ρ_s is the density of the parent, solid polymer, such that

$$\frac{E_c}{E_s} \approx \phi^2\left(\frac{\rho_c}{\rho_s}\right)^2 + (1-\phi)\left(\frac{\rho_c}{\rho_s}\right) \tag{3}$$

and

$$G_c \approx \tfrac{3}{8}E_c \tag{4}$$

Here, E_s is Young's modulus of the solid polymer and ϕ is the volume fraction of cell wall material contained within the cell edges. For the PMI foam investigated in Sec. 3 of the present study, we assume that $E_s = 3600$ MPa, $\rho_s = 1250$ kg m^{-3}, and $\phi = 0.6$ [4].

2.3 Elastic Buckling of the Square Honeycomb Core. A recent experimental study [7] on the compressive collapse of square honeycombs made from type 304 stainless steel suggests that the elastic buckling mode resembles torsional-axial buckling of a square tube (i.e., local buckling of the walls) with built-in top and bottom edges, as sketched in Fig. 1(*c*). Finite element simulations reported later in the current study confirm this mode of elastic buckling for the sandwich-walled square honeycomb. This buckling mode is modeled by the buckling of a single plate with fully clamped top and bottom edges and simply supported sides. Ericksen and March [10] analyzed this reduced problem for a sandwich plate made from orthotropic faces and an orthotropic core, and we make direct use of their analytical results. The bifurcation line load reads

$$P_{\rm buck} = \frac{K\pi^2 D}{l^2} \tag{5}$$

where K is a buckling coefficient as prescribed by Ericksen and March [10] and D is the bending stiffness of the sandwich plate. In our problem, we consider a sandwich plate made from orthotropic composite faces of identical thickness t. Upon neglecting the contribution from the foam core to the overall bending stiffness D we have

$$D = \frac{\sqrt{E_{1f}E_{3f}}}{1 - \nu_{13f}\nu_{31f}}\frac{t(c+t)^2}{2} \tag{6}$$

where E_{if} and ν_{ijf} are Young's modulus and Poisson's ratios of the orthotropic faces along the $x_i = (x_1, x_3)$ directions, as defined in Fig. 1(*b*). (For the composite faces considered below Young's moduli are equal along directions x_1 and x_3.)

The formula for the buckling coefficient K is explicit but lengthy and is omitted here. They are functions of geometry (c, t, l, and h as defined in Fig. 1(*b*)), of the enforced boundary conditions along the edges of the plate, of Young's modulus E_c and shear modulus G_c for the isotropic core, as well as of the shear modulus, Young's moduli, and Poisson ratios of the faces in the $x_1 - x_3$ plane.

Table 1 Measured properties of the woven glass fiber/epoxy faces and a PMI foam core

Material	Density (kg m^{-3})	Compressive strength (MPa)	Young's modulus (GPa)	Shear modulus (GPa)	Poisson's ratio (−)
GFRP	$\rho_f=1957$	$\sigma_f=525$	$E_{3f}=32$	$G_{31f}=4$	$\nu_{31f}=0.15$
PMI foam	$\rho_c=75$	1.45	$E_c=0.089$	$G_c=0.038$	$\nu_c=0.16$

2.4 Elastic Face Wrinkling. The sandwich plates in the walls of the square honeycomb can collapse by an alternative mechanism to those considered by Ericksen and March [10]: elastic wrinkling of the faces of the sandwich plate. This wrinkling mode is a local instability associated with short wave buckling of the faces of the mesoscopic sandwich plate and occurs when a compressive stress within the faces attains a critical value, see, for example, Ref. [3]. Assume that the sandwich plate is loaded along the x_3-direction. Then, the critical line load P_{wrink} in the sandwich plate depends on Young's modulus E_{3f} in the face and on the moduli (E_c, G_c) of the core such that

$$P_{\text{wrink}} = 1.7t(E_{3f}E_cG_c)^{1/3} \tag{7}$$

This formula gives the bifurcation stress for the perfect structure in the absence of geometric imperfection. It is appreciated that the presence of imperfections knocks down this strength by a factor of about 2 for most practical sandwich structures [3].

2.5 Plastic Face Microbuckling. It is generally recognized that the composite faces of a sandwich plate can fail by plastic microbuckling, particularly when the composite has wavy fibers due to its woven construction, see Ref. [11] for details on plastic microbuckling. Here, we treat the microbuckling strength σ_f as an intrinsic material property. Consequently, the microbuckling line load in the x_3-direction on the sandwich plates of the square honeycomb reads

$$P_{\text{mb}} = 2t\sigma_f \tag{8}$$

where we neglect any contribution from the compression of the core.

2.6 Collapse Mechanism Map. In the remainder of this study we shall limit our attention to the practical case of square honeycombs with aspect ratio $h/l=1$, thereby reducing the number of independent geometric variables. The regimes of dominance of the collapse modes can then be illustrated in a collapse mechanism map, with axes t/c and l/c. In construction of the map, it is assumed that the operative collapse mode is the one associated with the lowest line load for any given geometry.

A collapse mechanism map has been constructed for the materials used in the experimental study, as listed in Table 1. This map is plotted in Fig. 2(*a*); it assumes a foam core of relative density $\bar{\rho}=6\%$ as used in the experiments. In addition, a map is shown in Fig. 2(*b*) for a higher relative density of foam core $\bar{\rho}=20\%$ for comparison purposes. Although such high density PMI foams exist, they are more expensive and less available than the $\bar{\rho}=6\%$ and so no experiments were conducted on the higher density foam. Contours of nondimensional compressive strength $\bar{\sigma}\equiv P_{\text{cr}}/P_{\text{mb}}$ have been added to the maps, upon treating the microbuckling line load as an intrinsic reference property of the sandwich plates, independent of (c, l, h).

The collapse mechanism map of Fig. 2(*a*) ($\bar{\rho}=6\%$) displays two failure modes: Core buckling dominates the map with a much smaller regime of face wrinkling. The dominance of core buckling can be traced to the fact that this mechanism is sensitive to a low value of shear modulus in the foam core. Now increase $\bar{\rho}$ to 20%. The buckling load and face wrinkling loads increase, and microbuckling replaces face wrinkling as an active mechanism, see Fig. 2(*b*).

The accuracy of the failure map given in Fig. 2(*a*) has been partially assessed by conducting a series of experiments on the geometries shown in the map. It was not practical to cover a much larger regime of the map due to manufacturing and testing constraints. These experiments are now reported.

3 Experimental Investigation

A series of compressive tests was performed on square honeycombs with cell walls made from glass fiber/epoxy composite face sheets and a $\bar{\rho}=6\%$ foam core.

3.1 Manufacturing Technique. The sandwich cores were made from a closed-cell PMI foam of relative density $\bar{\rho}\approx 6\%$ (trade name Rohacell 71 IG) and thickness $c=5.7$ mm. This foam

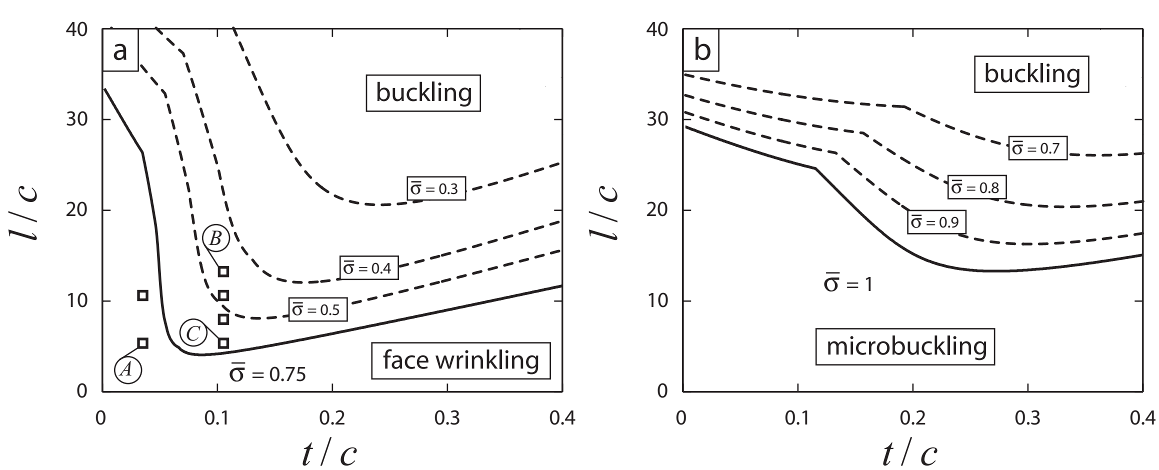

Fig. 2 Collapse mechanism map and contours of normalized strength $\bar{\sigma}\equiv P_{\text{cr}}/P_{\text{mb}}$ of the hierarchical square honeycomb made from elastic face and polymeric foam core of relative density (*a*) $\bar{\rho}=0.06$ and (*b*) $\bar{\rho}=0.20$. The six tested geometries are marked on the map (*a*).

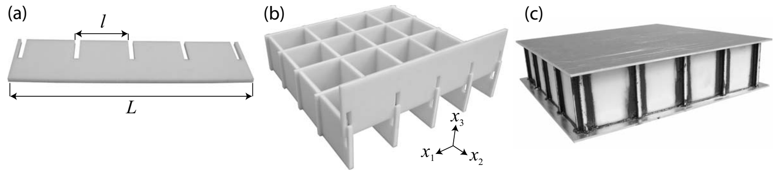

Fig. 3 Photographs a specimen with $l=75$ mm and $t=0.6$ mm demonstrating the manufacturing technique: (*a*) a waterjet machined panel, (*b*) the assembling technique, and (*c*) the final product

was selected for its low density ($\rho_c=75$ kg m^{-3}) and its capacity to sustain a pressure up to 0.35 MPa at 125°C, allowing autoclave curing.

The faces were made from one to three stacked plies of eight harness satin weave 7781 E-glass pre-impregnated (42 wt % of resin before curing) in a toughened epoxy matrix resin (trade name ACG MTM28/GF0100). This prepreg was selected for its low curing temperature of 120°C, high damage tolerance, and ability to bond directly to the PMI foam without additional adhesive. After curing, each ply has a thickness of 0.2 mm, a volume fraction of 55% glass fibers, and a density of $\rho_f=1957$ kg m^{-3}. The manufacturing sequence of the macroscopic square honeycomb is as follows.

(i) The PMI foam was dried for 2 h in a furnace at 100°C in order to reduce the moisture content. Layers of prepreg were placed symmetrically on each side of the foam, and the 0–9 deg orientations of the laminate were aligned with the x_1 and x_3 directions (see Fig. 1). Air pockets between each composite layer were removed by debulking the panel at room temperature under vacuum for 3 min.

(ii) The sandwich panel was then cured in an autoclave for 1 h at 120°C and a gauge pressure of 0.25 MPa, with the usual vacuum bagging technique.

(iii) The sandwich panel was cropped by a waterjet cutting machine into long strips of height $h=l$ and length $L=4l+2\Delta L$, where ΔL is a small overhang length set at 5 mm, see Fig. 3(*a*). Cross-slots were waterjet cut into the strips. These slots were of spacing l and of width $(c+2t+e)$, where e is a clearance of 0.1 mm to provide a sufficiently tight fit during honeycomb assembly.

(iv) Structural adhesive (trade name 3M Scotch-Weld DP490) was applied over the slot areas, and the honeycomb was assembled by slotting together the strips (Fig. 3(*b*)). Finally, the honeycomb was bonded to two 2014-T3 aluminum alloy face sheets of thickness 3 mm using the same structural adhesive as for the core (Fig. 3(*c*)).

A series of compression tests was performed on the macroscopic sandwich panels. Each specimen comprised 4×4 cells with a cell size l varying from 30 mm to 75 mm and a face thickness t between 0.2 mm and 0.6 mm. Consequently, the core density ρ varied from 38 kg m^{-3} to 167 kg m^{-3}. The cell sizes and densities of the tested specimens are listed in Table 2.

3.2 Material Properties of the Composite-Foam Sandwich Plates of the Square Honeycomb. The in-plane microbuckling strength σ_f, Young's modulus $E_{1f}=E_{3f}$, and Poisson ratio ν_{13} of

Table 2 Geometry, predicted compressive strength, and measured compressive strength of the macroscopic sandwich panels with a square honeycomb core

t (mm)	l (mm)	ρ (kg m^{-3})	Predicted strength (MPa) Wrinkling	Microbuckling	Buckling	First eigenvalue	Measured strength (MPa)
0.2	60	38	5.4	7.2	8.0	5.2	3.1
0.2	30	73	10.8	14.4	17.1	9.8	4.3
0.6	75	71	13.0	17.3	8.4	8.4	7.8
0.6	60	75	16.3	21.7	11.1	11.2	10.9
0.6	45	116	21.7	28.9	16.3	16.4	11.7
0.6	30	167	32.5	43.3	29.1	32.4	15.8

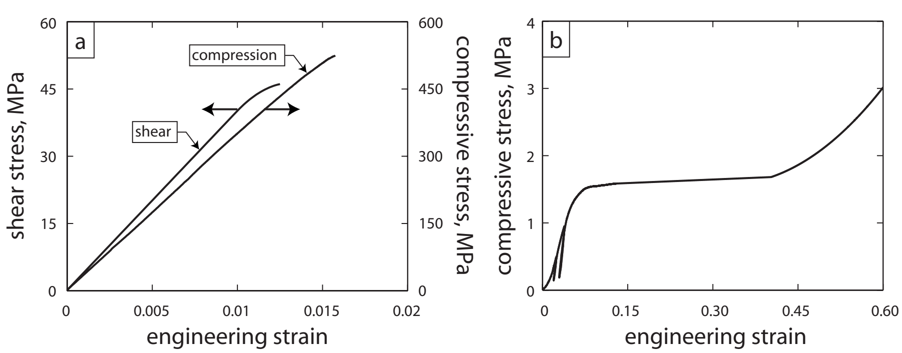

Fig. 4 (*a*) The measured compressive and shear responses of the eight harness satin weave 7781 E-glass/epoxy composite and (*b*) the measured uniaxial compressive response of the PMI foam (Rohacell 71 IG) used for the mesoscopic sandwich panel

the composite face sheet were measured by compressing the 0–90 deg composite along the x_3-direction within a Celanese test rig [12] at a nominal strain rate of $10^{-4}\ \mathrm{s}^{-1}$. The Celanese tests were performed on specimens of width 10 mm, thickness 2 mm, and gauge length 8 mm. Strain gauge rosettes were adhered to both faces of the specimen and confirmed that the degree of macroscopic bending in the tests was negligible. The measured compressive stress versus strain response is shown in Fig. 4(*a*); the measured axial Young's modulus is $E_{3f}=32$ GPa, the Poisson's ratio is $\nu_{31f}=0.15$, and the microbuckling strength is $\sigma_f=525$ MPa. These values are of the order expected from the specification given by the manufacturer.

The shear elastic properties of the composite faces were measured via a uniaxial tensile test on ± 45 deg material [13]. We denote the applied tensile stress as σ_x, and the corresponding axial strain and transverse strain as ε_x and ε_y, respectively. Then, the shear stress τ versus shear strain γ relation is obtained via the connections $\tau=\sigma_x/2$ and $\gamma=\varepsilon_x-\varepsilon_y$. The shear modulus G_{31f} follows immediately as the initial slope of the τ versus γ response. These uniaxial tensile tests were conducted on specimens of width 20 mm, thickness 0.4 mm, and gauge length 50 mm at a nominal strain rate of $10^{-4}\ \mathrm{s}^{-1}$. Strain gauge rosettes were used on both sides of the coupons, and the measured shear modulus was $G_{31f}=4.0$ GPa. The derived shear stress and strain response is included in Fig. 4(*a*).

The uniaxial compressive response of the Rohacell 71 IG foam core was measured by compressing cylindrical specimens of diameter 50 mm and height 6 mm between lubricated flat platens at an applied nominal strain rate of $10^{-3}\ \mathrm{s}^{-1}$. The nominal stress was estimated from the load cell of the test machine while the applied strain was deduced from the relative displacement of the top and bottom platens using a laser extensometer. The measured response is plotted in Fig. 4(*b*) and displays an initial elastic response and plateau strength of approximately 1.5 MPa and densification of the foam commences at a nominal compressive strain of 0.45. The elastic modulus of the foam was determined by conducting an unloading/reloading cycle, as shown in Fig. 4(*b*). However, difficulties in adhering strain gauges to the foam specimens mean that elastic Poisson's ratio was unable to be extracted from these compression tests.

We measured the elastic properties of the Rohacell 71 IG foam core using a vibro-acoustic technique based on Chaldni's law [14]. For an isotropic material, the method consists of identifying the x-mode resonance frequency f_x and ring mode resonance frequency f_o of square plates with free edges. This technique is simple and requires basic equipment, as discussed in Ref. [14]. The square plate is simply supported by soft blocks of foam and excited by a loudspeaker mounted beneath it. The loudspeaker is driven by a sinusoidal wave generator, and the frequency is adjusted to resonance. Chaldni's patterns are revealed by sprinkling a light powder on the surface. Once the f_x and f_o frequencies have been measured, both Young's modulus E_c and Poisson's ratio ν_c are determined via the prescriptions

$$\nu_c \approx 1.48\left[\frac{f_o{}^2 - f_x{}^2}{f_o{}^2 + f_x{}^2}\right] \tag{9}$$

$$E_c \approx 0.46(1-\nu_c{}^2)(f_o{}^2 + f_x{}^2)\rho_c a^4/c^2 \tag{10}$$

where a is the square plate length, ρ_c is the plate density, and c is the plate thickness.

In these measurements, a Rohacell 71 IG foam square plate of dimension $a=315$ mm, $\rho_c=75\ \mathrm{kg\,m^{-3}}$, and $c=5.7$ mm was employed. The resonance frequencies f_x and f_o were found to be 61.9 Hz and 68.6 Hz, respectively, leading to $\nu_c=0.16$ and $E_c=89$ MPa. These values are within a few percent given by Eq. (3) and the textbook values $E_s=3600$ MPa, $\rho_s=1250\ \mathrm{kg\,m^{-3}}$, and $\phi=0.6$ [4].

3.3 Measured Compressive Response of the Macroscopic Sandwich Panel With Square Honeycomb Core. Compression tests were performed on the macroscopic sandwich panels using a 1000 kN servohydraulic frame test machine and an applied macroscopic nominal strain rate of $10^{-4}\ \mathrm{s}^{-1}$. The macroscopic compressive stress σ on the core was inferred from the load cell of the test machine while the average through-thickness compressive strain ε was deduced from the relative displacement of the top and bottom faces of the sandwich panel, upon making used of two laser extensometers.

The measured out-of-plane compressive response of each sandwich panel is plotted in Fig. 5. All display an initial elastic response, with a peak load at a strain level $\varepsilon<0.02$ followed by a catastrophic drop in load. Each test was terminated after the drop in load, and the specimens were then visually examined to determine the collapse mechanism. It was not possible to use visual evidence to distinguish between the three anticipated collapse modes of elastic buckling, face wrinkling, and plastic microbuckling: In all cases the composite faces of the square honeycomb creased in bending, with no evidence of the initial cause of the failure.

The analytical predictions of compressive strength (Eqs. (1), (5), (7), and (8)) for the three competing collapse modes have been added to Fig. 5. In most cases all three analytical predictions are substantially higher than the measured strength. The tests reported in Figs. 5(*c*) and 5(*d*) are the exceptions to this observation: In these cases the elastic buckling strength is comparable to the measured strength. Note that these two geometries lie remote from the elastic buckling/face wrinkling boundary, as plotted in Fig. 2(*a*). In order to improve the accuracy of prediction, finite element simulations are performed, and the imperfection sensitivity is assessed.

4 Finite Element Modeling

4.1 Model Details. Finite element calculations of the through-thickness compressive response of the sandwich panels with a square honeycomb core were performed using the finite element package ABAQUS standard (Hibbitt, Karlsson & Sorensen, Inc. (HKS)). All simulations reported here are performed on the unit cell shown in Fig. 1(*b*) in the form of a cruciform section, including the nonlinear effects of large displacements.

The unit cell of the square honeycomb was modeled using linear 3D brick elements, i.e., C3D8R following ABAQUS notation. Typically, the model comprised four brick elements through the thickness of each composite face sheet and five to ten brick elements through the depth of the foam core. In order to avoid excessive distortion, the element aspect ratio was kept below 5 for all simulations. One exception is that the specimen with $t=0.2$ mm and $l=60$ mm was modeled with an aspect ratio of 10 in order to reduce the model size. This meshing rule assures convergence but leads to large models, for example, the model with $t=0.6$ mm and $l=75$ mm contains over 10^6 degrees of freedom.

In order to capture the torsional-axial buckling mode (Fig. 1(*c*)) and the face wrinkling mode, antiperiodic boundary conditions were imposed on the outer plate edges of the cruciform section. All nodes on the top and bottom of the unit cell were fully clamped. Loading was specified by prescribing an increasing relative vertical displacement δ between the top and bottom faces.

The PMI foam was modeled as an isotropic elastic-ideally plastic solid, using the properties values presented in Sec. 3. The post-yield behavior was modeled with the crushable foam formulation available in ABAQUS using an associated flow rule. The ratio of the uniaxial compressive strength to the hydrostatic strength was set to $\sqrt{3}$, and the tensile and compressive hydrostatic strengths were assumed to be equal. With these assumptions the crushable foam model in ABAQUS reduces to the Deshpande and Fleck [15] foam model with plastic Poisson's ratio of 0. Mild

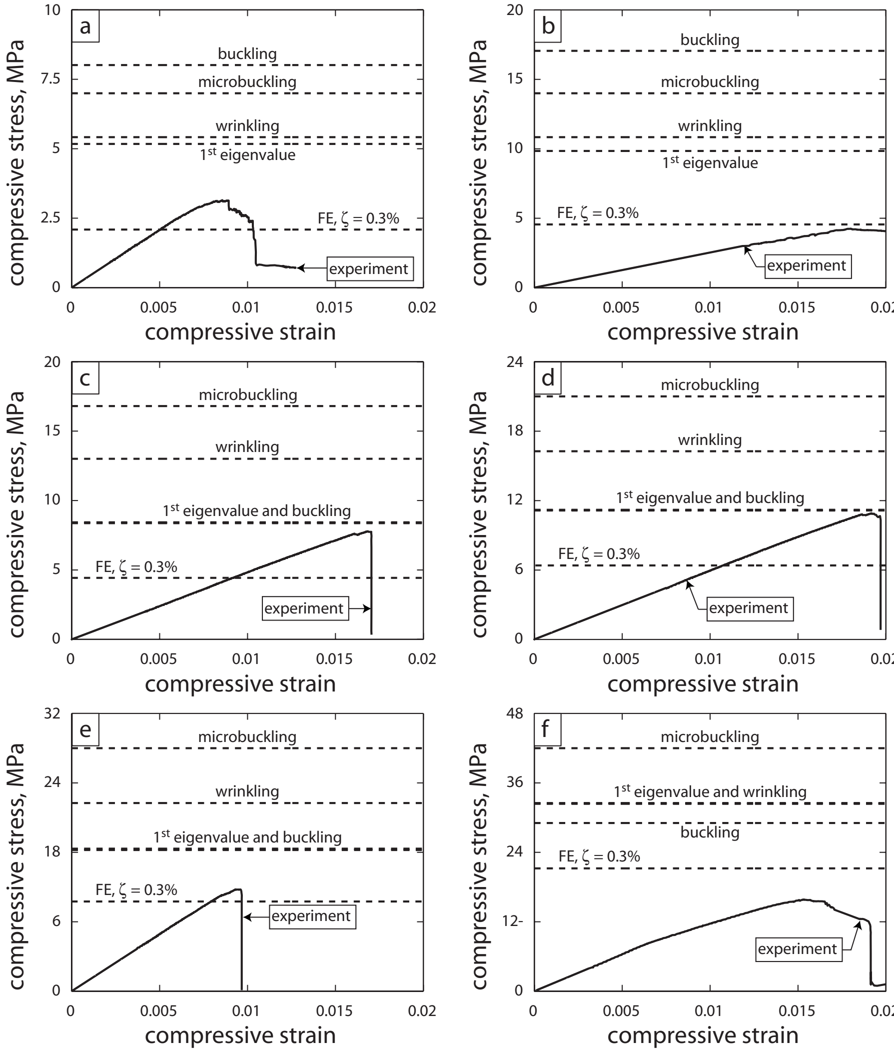

Fig. 5 The measured compressive response of square honeycomb specimens with (*a*) l=60 mm and t=0.2 mm, (*b*) l=30 mm and t=0.2 mm, (*c*) l=75 mm and t=0.6 mm, (*d*) l=60 mm and t=0.6 mm, (*e*) l=45 mm and t=0.6 mm, and (*f*) l=30 mm and t=0.6 mm. Also added in the figure is the compressive strength predicted by analytical models, FE buckling analysis, and FE static analysis with an imperfection of $\varsigma \equiv w/l = 0.3\%$.

volumetric hardening of the plastic response of the foam was included in order to assure numerical stability.

The woven glass fiber/epoxy composite was treated as an orthotropic solid with the in-plane measured properties stated in Sec. 3. Consider the representative sandwich plate A, as shown in Fig. 1(*b*). The properties in the direction normal to that of the composite plates were taken as E_2=7.5 GPa, G_{12}=G_{32}=4.0 GPa, and ν_{12}=ν_{32}=0.15. In order to mimic plastic microbuckling, it was assumed that the composite was modeled as an elastic-ideally plastic solid. J2 flow-theory was adopted with a yield strength equals to the microbuckling strength (σ_f=525 MPa) and a mild isotropic hardening to assure numerical stability. Although this description is only approximate it suffices to capture the onset of microbuckling for the in-plane uniaxial stress state imposed on the composite layers.

4.2 Elastic Buckling Analysis. The FE method has been used to determine the lowest buckling load (the first eigenvalue). The compressive strength is compared with the analytical models and the measured response in Fig. 5 and in Table 2. In general, the predicted first eigenvalues are in good agreement with the lowest collapse load predicted analytically by the three competing mechanisms. There is one exception: The analytical model underestimates the compressive strength of the specimen with t=0.6 mm and l=30 mm. It is argued that this is due to the fact that the analytical buckling model is inaccurate for stubby plates, $l/c<6$. The predicted eigenmode resembles the assumed buckling mode of elastic bucking model and resembles the face wrinkling mode, depending on the geometry considered. Consider, for example, the geometry as specified by t/c=0.035 and l/c=5.25 and label this specimen A in Fig. 2(*a*). This specimen undergoes elastic face wrinkling according to both the analytical model and the FE simulation, see Fig. 6(*a*) for the observed eigenmode. Second, consider specimens with t/c=0.105, and l/c=10.5 and l/c=5.25, and label them B and C in Fig. 2(*a*). The lowest FE eigenmode for these two specimens is given in Figs. 6(*b*) and 6(*c*), respectively. Plainly the modes are elastic buckling of the sandwich plates, and these modes are in agreement with the modes predicted by the analytical model of Ericksen and March [10].

4.3 Imperfection Sensitivity. The discrepancy between measured compressive strength and the extracted eigenvalues indicates a possible sensitivity to geometric imperfection. This sensitivity was scoped by FE calculations of the collapse response for sandwich plates with initial imperfections in the shape of the first elastic eigenmode. The magnitude of the initial imperfection is

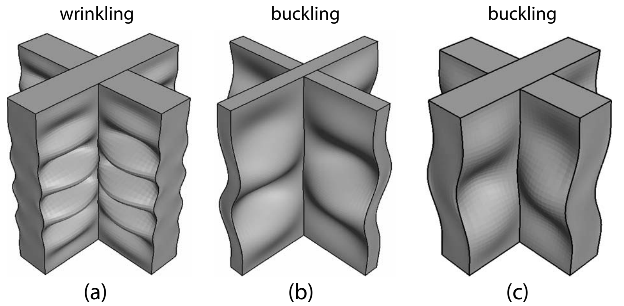

Fig. 6 Finite element predictions of the first eigenmode extracted for the specimen with (*a*) *l*=30 mm and *t*=0.2 mm, (*b*) *l*=75 mm and *t*=0.6 mm, and (*c*) *l*=30 mm and *t*=0.6 mm

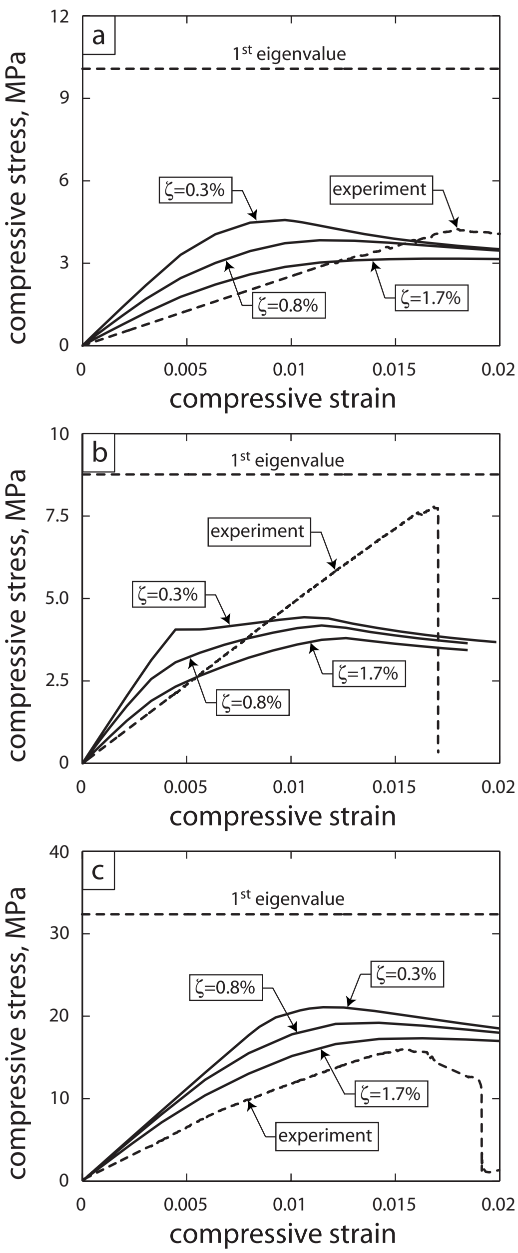

Fig. 7 FE predictions of the compressive response of specimens with (*a*) *l*=30 mm and *t*=0.2 mm, (*b*) *l*=75 mm and *t*=0.6 mm, and (*c*) *l*=30 mm and *t*=0.6 mm. Imperfections in the first eigenmode with maximum amplitude $\varsigma \equiv w/l$ are specified.

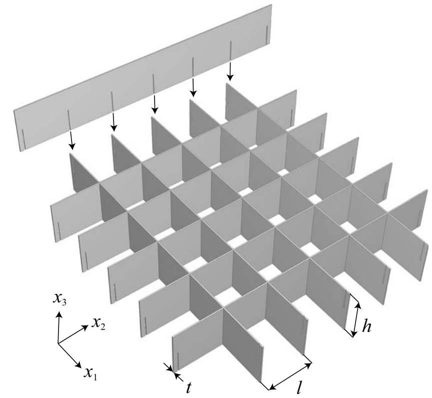

Fig. 8 Sketch of a conventional monolithic square honeycomb showing the geometrical parameters along with the manufacturing technique of the monolithic square honeycomb

defined as follows. The maximum transverse deflection of the walls of the honeycomb is set to $w=\zeta l$, where ζ is in the range of 0–1.7%.

The FE predictions of the compressive stress versus strain responses of the geometries labeled A, B, and C in Fig. 2 are plotted in Fig. 7. (These predictions correspond to the measured responses plotted in Figs. 5(*b*), 5(*d*), and 5(*f*), respectively.) The FE calculations clearly show that the peak stress is sensitive to the magnitude of initial imperfection, and an initial imperfection on the order of $\zeta=0.3\%$ is needed to reproduce the qualitative shape of the measured collapse response.

The finite element predictions of the peak compressive strength of the square honeycombs with $\zeta=0.3\%$ are included in Fig. 5. Mixed agreement is obtained with the measured values. The discrepancy between the measurements and FE predictions is largest for the specimens with $l \geq 60$ mm. For these specimens it would be necessary to consider a smaller imperfection in order to obtain the measured value of peak load. A quantification of the actual imperfections within the macroscopic sandwich panel is difficult to achieve in view of the 3D nature of the structure. This is suggested as a topic of future study using, for example, a computed axial tomography (CAT) scan machine but is not pursued further here.

5 Comparison of the Measured Compressive Strength for Square Honeycombs With Sandwich Walls and With Monolithic Walls

It is instructive to explore the degree to which a hierarchical sandwich construction is advantageous over a more conventional honeycomb. Here, we compare the through-thickness compressive strength of a macroscopic sandwich panel with a square honeycomb core made from monolithic plates with the compressive strength of a macroscopic sandwich panel with a square honeycomb core made from sandwich plates. An additional series of compressive tests has been performed for square honeycombs made from a monolithic, woven glass fiber/epoxy composite. The architecture is identical to that reported above for the foam-cored sandwich plates, but now the square honeycomb is constructed with the foam core absent. It is unclear a priori whether the presence of the foam core elevates or depresses the compressive strength: The presence of a foam core raises the bending stiffness D in Eq. (6) but it lowers the shear stiffness of the section.

Monolithic square honeycombs with 6×6 cells were manufactured from eight harness satin weave E-glass laminate of thickness $t=0.4$ mm using micromilling machining and epoxy bonding, see Fig. 8 for details of the geometric parameters and a sketch of the manufacturing route. The cell aspect ratio of the specimens was maintained at $h/l=1$. The cell size l was varied from 10.4 mm to

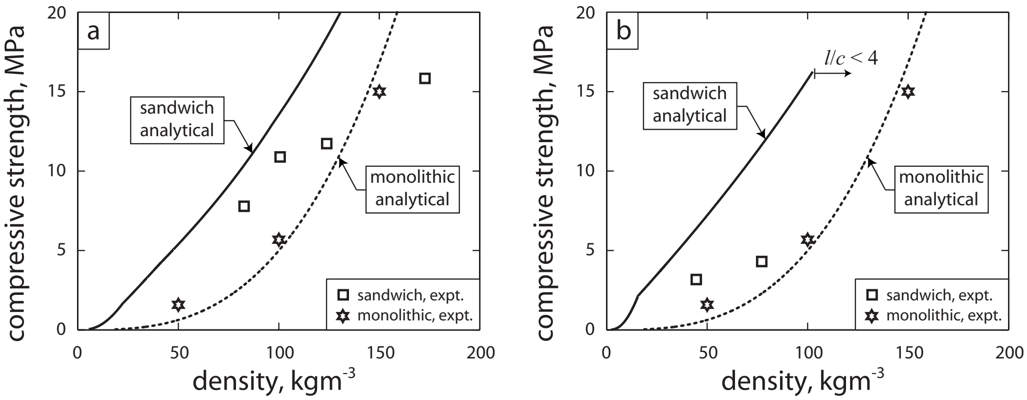

Fig. 9 Comparison between the measured and predicted compressive strength of square honeycombs made from monolithic GFRP laminates and sandwich walls with face sheets of (*a*) $t=0.6$ mm and (*b*) $t=0.2$ mm

31.3 mm in order to obtain three core densities of 50 kg m^{-3}, 100 kg m^{-3}, and 150 kg m^{-3}. Again, aluminum alloy face sheets of thickness 3 mm were bonded to the top and bottom of the square honeycomb using the structural adhesive 3M Scotch-Weld DP490.

Three nominally identical specimens were tested for each core density, and the measured strength varied by only 10% for a given core density. A postmortem visual examination of the failed specimens suggested that each failed by elastic buckling of the honeycomb walls. The average compressive strengths are compared with those of the hierarchical square honeycombs of face thickness $t=0.6$ mm in Fig. 9(*a*). Likewise, the average compressive strengths are compared with those of the hierarchical square honeycombs of face thickness $t=0.2$ mm in Fig. 9(*b*).

The analytical predictions of elastic buckling strength (Eq. (5)) for the monolithic and hierarchical honeycombs have been added to Fig. 9. For the monolithic honeycomb, the analytical model of Ericksen and March [10] is again employed but with

$$D = \frac{\sqrt{E_{1f}E_{3f}}}{1-\nu_{13f}\nu_{31f}}\frac{t^3}{12} \tag{11}$$

This prediction is in good agreement with the measured strengths. As already noted, bifurcation calculation of Ericksen and March [10] is nonconservative for the hierarchical honeycombs.

We note from Fig. 9 that there is a small advantage in using the hierarchical honeycomb over the monolithic honeycomb at sufficiently low core densities. But this comparison is for the case of a foam core of low modulus. As discussed in Sec. 2, additional structural advantages are expected by considering a hierarchical honeycomb for the choice of a stiffer foam core.

6 Concluding Remarks

The hierarchical sandwich panel with a square honeycomb core introduced in this study shows promise as it has a substantially higher through-thickness compressive strength than an equivalent sandwich panel with a monolithic composite core. The compressive strength of the hierarchical sandwich panel is dictated by a set of competing failure modes and these are best illustrated in the form of a collapse map, with geometry as axes. Analytic models are presented here for the competing collapse modes; these have limited accuracy due to the presence of geometric imperfections. Finite element simulations can give improved accuracy but these require as input the level of imperfection. A characterization of the imperfections remains a challenging task.

Acknowledgment

The authors are grateful to the Engineering and Physical Sciences Research Council, UK for financial support.

References

[1] Fairbairn, W., 1849, *An Account of the Construction of the Britannia and Conway Tubular Bridges*,Weale, London, UK.
[2] Allen, H. G., 1969, *Analysis and Design of Structural Sandwich Panels*, Pergamon, Oxford, UK.
[3] Zenkert, D., 1995, *An Introduction to Sandwich Construction*, EMAS, London, UK.
[4] Gibson, L. J., and Ashby, M. F., 1997, *Cellular Solids, Structure and Properties*, 2nd ed., Cambridge University Press, Cambridge, UK.
[5] Deshpande, V. S., Fleck, N. A., and Ashby, M. F., 2001, "Effective Properties of the Octet-Truss Lattice Material," J. Mech. Phys. Solids, **49**, pp. 1747–1769.
[6] Zhang, J., and Ashby, M. F., 1992, "The Out-Of-Plane Properties of Honeycombs," Int. J. Mech. Sci., **34**, pp. 475–489.
[7] Côté, F., Deshpande, V. S., Fleck, N. A., and Evans, A. G., 2004, "The Out-Of-Plane Compressive Behavior of Metallic Honeycombs," Mater. Sci. Eng., A, **380**, pp. 272–280.
[8] Côté, F., Deshpande, V. S., and Fleck, N. A., 2006, "The Shear Response of Metallic Square-Honeycombs," J. Mech. Mater. Struct., **1**, pp. 1281–1299.
[9] Budiansky, B., 1999, "On the Minimum Weights of Compression Structures," Int. J. Solids Struct., **36**, pp. 3677–3708.
[10] Ericksen, W. S., and March, H. W., 1958, "Effects of Shear Deformation in the Core of a Flat Rectangular Sandwich Panel. Compressive Buckling of Sandwich Panels Having Dissimilar Facings of Unequal Thickness," US Forest Product Laboratory, Report No. 1583-B.
[11] Fleck, N. A., 1997, "Compressive Failure of Fiber Composites," Adv. Appl. Mech., **33**, pp. 43–117.
[12] ASTM D3410/D3410M-03, Standard Test Method for Compressive Properties of Polymer Matrix Composite Materials With Unsupported Gage Section by Shear.
[13] Khashaba, U. A., 2004, "In-Plane Shear Properties of Cross-Ply Composite Laminates With Different Off-Axis Angles," Compos. Struct., **65**, pp. 167–177.
[14] McIntyre, M. E., and Woodhouse, J., 1988, "On Measuring the Elastic and Damping Constants of Orthotropic Sheet Materials," Acta Metall., **36**, pp. 1397–1416.
[15] Deshpande, V. S., and Fleck, N. A. J., 2000, "Isotropic Constitutive Models for Metallic Foams," J. Mech. Phys. Solids, **48**, pp. 1253–1283.

One-Way and Two-Way Coupling Analyses on Three Phase Flows in Hydrocyclone Separator

S. M. Mousavian

M. Ahmadvand

A. F. Najafi

School of Energy Engineering,
Power and Water University of Technology,
16765-1719 Tehran, Iran

The flow behavior in hydrocyclones is quite complex. The computational fluid dynamics method was used to simulate the flow fields inside a hydrocyclone in order to investigate its separation efficiency. In the computational fluid dynamics study of hydrocyclones, the air-core dimension is a key to predicting the mass split between the underflow and overflow. In turn, the mass split influences the prediction of the size classification curve. Generally in hydrocyclone simulations, assuming low particle volume fractions, the discrete phase effects on the continuous phase have been excluded; therefore, one-way coupling method has been used. Due to high particle consistencies, regions in some cases, especially in underflow areas, excluding discrete phase effects on continuous phase may be ineligible. In this study for an example case by consisting discrete phase effects and using two-way coupling method, simulation accuracy noticeably has been improved. Three models, the $k-\varepsilon$ model, the Reynolds stress model (RSM) without considering air core, and Reynolds stress turbulence model with volume of fluid multiphase model for simulating air core, were compared for the predictions of velocity, axial, and tangential velocity distributions and separation proportion. Results by the RSM with air-core simulation and two-way coupling model, since it produces some detailed features of the turbulence and discrete phase mode effects, are clearly closer in predicting the experimental data than the other two. [DOI: 10.1115/1.3130445]

Keywords: hydrocyclone, VOF multiphase, Lagrangian approach, particles trajectory, air core, one-way coupling, two-way coupling

1 Introduction

In the past 50 years, use of hydrocyclones has had a rapid growth in the chemical, mineral, coal and powder-processing industries. The reasons for this popularity lie in the design and operational simplicity, high capacity, low maintenance and operating costs, and the compact size of the device.

A typical hydrocyclone consists of a cylindrical section with a central tube connected to a conical section with a discharge tube. An inlet tube is attached to the top section of the cylinder, as shown in Fig. 1. The fluid is injected tangentially into hydrocyclone, which causes swirling and thus generates centrifugal force within the device. This centrifugal force field brings about a rapid classification of particulate material from the medium in which it is suspended. Various investigations have been performed to describe and improve design of hydrocyclone.

The first patent on hydrocyclones was published by Bretney [1]. Despite this, it took half a century before they were extensively used. Since 1950, a range of papers has been published concerning the operation of hydrocyclones and some mathematical models describing velocity profiles, the pressure drop, and the separation efficiency of hydrocyclone [2–9]. A first systematic and detailed experimental work was performed by Kelsall [2]; his measurements of radial, axial, and tangential velocity profiles served as a benchmark for many subsequent investigations.

Computational fluid dynamics (CFD) provides a means of predicting velocity profiles under a wide range of design and operating conditions. The numerical treatment of the Navier–Stokes equations, the basis of any CFD technique, crept into analysis of the cyclone in the early 1980s. This resulted from the rapid improvement in computers and a better understanding of the numerical treatment of turbulence. A successful model, especially based on computational fluid dynamics, would be a useful tool for studying design dimensions. More importantly, alternative geometries may be rapidly examined.

In this paper, the aim of modeling was to predict the separation effectiveness and to compare the performed simulations based on three models (the $k-\varepsilon$ model, the Reynolds stress model without considering air core, and Reynolds stress turbulence model with volume of fluid (VOF) multiphase model for simulating air core) with experimental results, with respect to the predictions of separation effectiveness, and axial and tangential velocity distributions. The RSM with air-core simulation model, since it produces some detailed features of the turbulence and multi phase, is clearly closer in predicting the experimental data than the other two.

2 Hydrocyclone CFD Simulation: Literature Review

2.1 Turbulence Modeling. Industrial hydrocyclones typically operate at velocities where the flow is turbulent. However, the strong swirl, the flow reversal, and the flow separation near the underflow introduce anisotropy and strain into the turbulence. Most hydrocyclones in mineral processing applications develop an air-core and the free surface between the air and the water introduces further turbulence anisotropy. These characteristics make modeling hydrocyclones using CFD difficult and the addition of solids adds even more complexity.

Rajamani and Devulapalli [10] modeled hydrocyclones using a 2D axisymmetric grid where the air core was not resolved and the air/water interface was treated using a shear free boundary condition. Turbulence anisotropy was incorporated into the model by using a modified mixing length turbulence model where a different mixing length constant was used for each component of the momentum equation. Although the model required calibration was

Contributed by the Applied Mechanics Division of ASME for publication in the Journal of Applied Mechanism. Manuscript received August 1, 2007; final manuscript received August 1, 2007; published online July 23, 2009. Review conducted by Arif Masud.

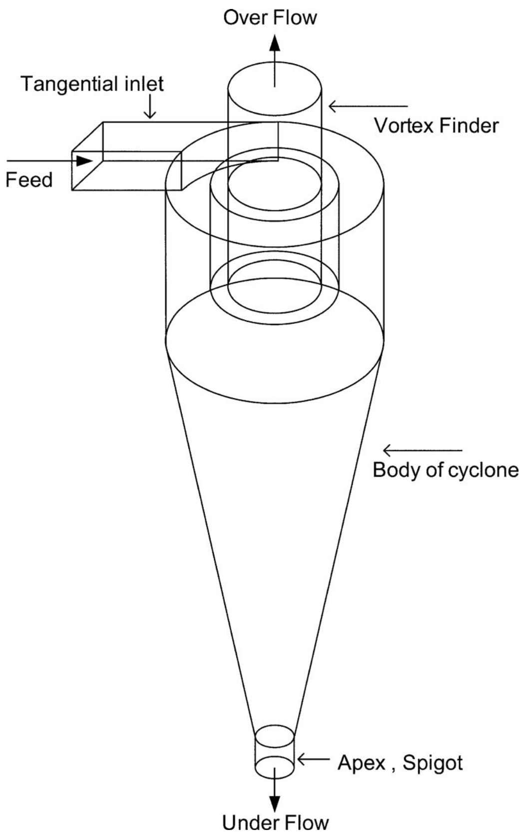

Fig. 1 Schematic of conventional hydrocyclone

able to predict velocities measured by these authors using laser Doppler anemometry with reasonable accuracy. $k-\varepsilon$ models intrinsically make the assumption that the turbulence is isotropic because only one scalar velocity fluctuation is modeled. Further the Bousinessq approximation on which the eddy viscosity relies intrinsically implies equilibrium between stress and strain. This would suggest that $k-\varepsilon$ models are not suitable for modeling turbulence in hydrocyclones and this has been shown to be the case by Ma et al. [11] and others. However, Dyakowski and Williams [12] suggested that the $k-\varepsilon$ model can be used on small (below 44 mm radius) hydrocyclones. To address this, other authors used the $k-\varepsilon$ renormalization group (RNG) model with the swirl correction [13–17]. However, Suasnabar [15] found that the swirl constant in the RNG model needed to be increased to improve predictions but beyond a certain point, further increases caused numerical instability. As an alternative, Suasnabar [15] adjusted the constants in the standard $k-\varepsilon$ model but acknowledged that this approach was limited. Stress transport models, in particular, the full differential Reynolds stress model (RSM), such as that developed by Launder et al. [18] solve transport equations for each individual Reynolds stress. This enables stress transport models to model anisotropic turbulence and strained flows where the Bousinessq approximation is known to be flawed. While more computationally intensive than $k-\varepsilon$ models, stress transport models are being used to model turbulence in hydrocyclones. Boysan et al. [19] used an algebraic stress model but the full RSM has been used in a more recent work. Cullivan et al. [20], Suasnabar [15], Slack et al. [21], and Brennan et al. [22] all used variants of the Launder et al. [18] model. However even here, the predictions are not what they could be and there is a debate about appropriate modeling options, even if Slack et al. [21] found that the RSM gave good predictions of velocities in gas cyclones.

We found that the RSM, where the air-core was being resolved with the VOF model, gives better cut size predictions in comparison with simulation of Narasimha [17] 100 mm hydrocyclone. Cut size is defined as a reference size, which at least 50% of particles with dimensions above it separated from the flow. Here d_{50} is defined as diameter, which is equal to this reference size [23]. However, this model cannot predict air-core dimension well. It can be seen that prediction error is about 50%.

2.2 Air-Core Modeling in Hydrocyclones. There is no doubt that a stable flow field in cyclones is a prerequisite for effective performance. The stability of the flow field is, to a great extent, dependent on parameters such as the feed pressure, the feed concentration, and so on, but the internal structure of the flow field itself also has an important effect.

One of the most important internal structures is the air-core generated inside the cyclone. At start up, a low-pressure region develops causing the formation of an air-core along the central axis. The classical literature on hydrocyclones makes very little reference to the air core, although in the 1990s some investigations were made of its role by Barrientos et al. [9], Castro and Concha [24], Concha et al. [25], and Dyakowsky and Williams [12].

In spite of its simple geometry and operation, explaining the detailed mechanism of the cyclone is extremely complicated. One difficulty in finding the actual flow in cyclones is the necessity of specifying the form and location of the air-core surface. In the usual models applied to a cyclone, the interface that bounds the air core is modeled as a fixed cylindrical surface, which greatly simplifies the problem. Many researchers developed theoretical models to approximate the air-core radius, for example, Barrientos et al. [9], Steffens et al. [26], Davidson [27], and Dyakowsky and Williams [12].

Numerical modeling of the air-core for liquid-phase cyclones has been dealt with in a number of ways. Before the work of Romero and Sampaio [28], most authors assumed that the air-core had a fixed diameter and applied a slip boundary condition at the interface, for example, Hsieh and Rajamani [29] and Malhotra et al. [30]. This is computationally advantageous but means that the CFD code cannot predict the air core in any way. Predictions of the air-core diameter have been provided through: application of Bernoulli's equation applied with a minimization procedure [31], the use of an effective air-core interface viscosity [12], and through application of Young–Laplace's relation [32]. Notably, the latter approaches offer the potential to account for asymmetric air-core geometry.

Pericleous and Rhodes [33] used the algebraic slip mixture (ASM) model, while Suasnabar [15], Cullivan et al. [20,34], and Brennan et al. [35] used the volume of fluid model. Both of these models are implemented in the commercial CFD code FLUENT and are similar in that they both solve an additional transport equation for the volume fraction of each additional phase. The ASM model is designed for dispersed two phase flows and Pericleous and Rhodes [33] used this model mainly to simulate the slurry phase, but it is interesting to note that it worked for the air core as well. The VOF model is simpler in that it does not have a drift calculation and assumes that the two phases do not interpenetrate, so it is probably a better model if the slurry phase is not to be modeled in detail.

2.3 Particle Fluid Model. The goal of a CFD simulation of a classifying hydrocyclone is to predict classification and if this goal is to be achieved then the interactions between the particulate phases and the fluid must be modeled. In CFD there are two approaches to simulating particulate phases in fluid systems; these are the Lagrangian and Eulerian approaches.

A Lagrangian simulation runs "on top" of a single phase CFD simulation and simulates the paths of individual particles through the fluid by a double integration of the particle acceleration, which is calculated from a force balance on the particle. The particle force balance includes drag, buoyancy forces, and other body forces and the drag force is calculated from the local fluid velocity as predicted by the single phase CFD calculation. The particle path calculation starts from an initial position, which is usually the feed boundary condition and terminates when the particle has left the domain via an outlet boundary condition or reaches a stagnant zone.

Hsieh [36] used the Lagrangian approach to predict classification of limestone in a 75 mm hydrocyclone. Hsieh [36] used the mean velocity field from his 2D axisymmetric CFD calculation of the water phase and did not incorporate any effects due to the turbulence. The Tromp (or cyclone efficiency) curve was constructed from repeated simulations for different particle sizes [37]. Hsieh's [36] simulations predicted the d_{50} of the 75 mm cyclone for limestone very well, but the short circuiting of large particles was not predicted and the cut above the d_{50} was not evaluated well compared when it was measured. Here d_{50} defined as Hsieh [36] attributed this shortcoming to the 2D axisymmetric grid equivalent to a ring inlet and Hsieh [36] suggested that the effects of turbulence and particle/particle interactions should be incorporated in the simulation. Devulapalli et al. [38–40] extended Hsieh's Lagrangian approach and incorporated the effects of turbulence by using a Lagrangian cloud model developed by Baxter and Smith [41], where the mean position of a cloud of particles is calculated and where the cloud was released from the cyclone inlet. The spread of the cloud about the mean position is calculated by a probability distribution function (defined as a function of the turbulence) as the cloud moves through the domain. Devulapalli [40] used the Lagrangian cloud approach to predict Tromp curves for a variety of 250 mm hydrocyclones (using several different vortex finders and spigots) passing limestone and copper ore. Again the d_{50} was predicted well, but again the cut above the d_{50} was not evaluated well compared when it was observed from real experiments using a cyclone of the same geometry. Devullapalli [40] suggested that a full 3D grid of the cyclone, with better turbulence models and other particle effects, was needed to improve these predictions.

The Lagrangian approach has been used to model multiphase flows using large eddy simulation for the continuous fluid phase [42–44]. These studies have focused on simulating the damping of the turbulence by small dense suspended particles and have used two-way coupling where the momentum exchange with the particles by drag is incorporated as a source term in the fluid phase momentum equation. The studies by Portela and Oliemans [43] and Millelli et al. [44] have also modeled the effect of the dispersed phases on the large eddy simulation (LES) subgrid scale model.

Eulerian CFD techniques treat the dispersed phases as a pseudocontinuum and solve transport equations for the phase concentrations. Flows containing dispersed solid phases at high concentrations and where interparticle collisions result in additional stresses can be simulated using a full Eulerian granular flow approach [45,46], where momentum and continuity equations are solved for both the dispersed phases and the continuous phases. The full Eulerian granular flow approach also solves transport equations for the continuous-phase turbulence and also solves transport equations for the granular temperature and granular pressure, which are used to calculate effective viscous stresses in the dispersed phase momentum equation.

Mixture model is a simplified aspect of Eulerian approach [47] where the momentum and continuity equations are only solved for the mixture and a transport equation, which contains an equilibrium slip velocity that is solved for the volume fraction of each phase.

The Eulerian approach has been used to simulate medium segregation in dense medium cyclones by Suasnabar [15]. Both the full Eulerian multiphase granular flow model [45,46] and the simplified Mixture model [47] were used to model the medium, and a single medium particle size was used. The Eulerian granular flow model and the mixture model predicted similar velocities and medium concentrations. The Eulerian granular flow model was felt to be more fundamentally correct but the mixture model was computationally more economical.

The advantage of the Lagrangian multiphase approach is that particle-particle and particle-fluid interactions are calculated dynamically for every particle present in the system based on the instantaneous velocity of the particle. By comparison the Eulerian approach only calculates a phase velocity, a phase volume fraction, and overall stresses associated with the average behavior of an ensemble of phase particles in each finite volume in the CFD grid. Thus the Eulerian approach innately involves averaging of some sort, which implies more modeling.

3 Simulation Overview

3.1 Governing Equation. The model used for flow simulation solves the conservation equations for mass (or continuity) and momentum. The turbulence in the system is solved through additional transport equations. Navier–Stokes equations for incompressible flows along with appropriate turbulence model are adopted for flow predictions. Under steady-state conditions, the equations for mass and momentum in a general form are as follows:

$$\nabla \,.\, \rho v = 0 \tag{1}$$

$$\nabla \,.\, (\rho \boldsymbol{v}\boldsymbol{v}) = -\nabla p + \nabla \,.\, (\bar{\tau}) + \rho \boldsymbol{g} \tag{2}$$

$$\bar{\tau} = \mu_{\text{effective}} \left[(\nabla \boldsymbol{v}) - \frac{2}{3} \nabla \,.\, \rho \boldsymbol{v} \boldsymbol{I} \right]$$

$$\mu_{\text{effective}} = \mu + \mu_t \tag{3}$$

3.1.1 The Standard $k-\varepsilon$ Model. The standard $k-\varepsilon$ model is a semi-empirical model based on model transport equations for the turbulent kinetic energy (k) and turbulent dissipation rate (ε) that are given by

$$\frac{\partial(\rho k)}{\partial t} + \frac{\partial(\rho k u_i)}{\partial x_i} = \frac{\partial}{\partial x_j}\left[\left(\left(\mu + \frac{\mu_t}{\sigma_k}\right)\frac{\partial k}{\partial x_j}\right)\right] + G_k - \rho\varepsilon \tag{4}$$

$$\frac{\partial(\rho \varepsilon)}{\partial t} + \frac{\partial(\rho \varepsilon u_i)}{\partial x_i} = \frac{\partial}{\partial x_j}\left[\left(\left(\mu + \frac{\mu_t}{\sigma_\varepsilon}\right)\frac{\partial k}{\partial x_j}\right)\right] - C_{1\varepsilon}\frac{\varepsilon}{k}(G_k) - C_{2\varepsilon}\frac{\varepsilon^2}{k} \tag{5}$$

$$G_k = -\overline{u_i' u_j'}\frac{\partial \overline{u_i}}{\partial x_j} \tag{6}$$

The "eddy" or turbulent viscosity, μ_t, defined in Eqs. (2) and (3) can be computed by combining k and ε as follows:

$$\mu_t = \rho C_\eta \frac{k^2}{\varepsilon} \tag{7}$$

The model constants $C_{1\varepsilon}$, $C_{2\varepsilon}$, C_η, σ_k, and σ_ε were assumed to have the following values: $\sigma_\varepsilon = 1.3$, $\sigma_k = 1.0$, $C_{2\varepsilon} = 1.92$, $C_{1\varepsilon} = 1.44$. For further details about $k-\varepsilon$ model, see Refs. [48,49].

3.1.2 RSM. For steady-state, the RSM relies on the following transport equations for the Reynolds stresses:

$$\frac{\partial}{\partial t}(\rho\overline{u_i' u_j'}) + \frac{\partial}{\partial x_k}(\rho\overline{u_k' u_i' u_j'}) = P_{ij} + F_{ij} + D_{Tij} + \phi_{ij} - \varepsilon_{ij} \tag{8}$$

$$P_{ij}(\text{stress production}) = -\rho\left(\overline{u_i' u_k'}\frac{\partial u_j}{\partial x_k} + \overline{u_j' u_k'}\frac{\partial u_i}{\partial x_k}\right) \tag{9}$$

$$F_{ij}(\text{rotation production}) = -2\rho\Omega_k(\overline{u_j' u_m'}\varepsilon_{ikm} + \overline{u_i' u_m'}\varepsilon_{jkm}) \tag{10}$$

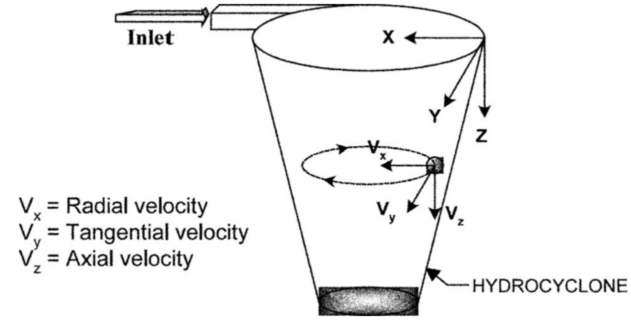

Fig. 2 Velocity components in hydrocyclone

$$D_{T,ij}(\text{turbulent diffusion}) = -\frac{\partial}{\partial x_k}[\rho\overline{u_i'u_j'u_k'} + p(\delta_{kj}u_i' + \delta_{ik}u_j')] \tag{11}$$

$$\phi_{ij}(\text{pressure strain}) = \left(\overline{\frac{\partial u_i'}{\partial x_j}} + \overline{\frac{\partial u_j'}{\partial x_i}}\right) \tag{12}$$

$$\varepsilon_{ij}(\text{dissipation}) = -2\mu\overline{\frac{\partial u_i'}{\partial x_k}\frac{\partial u_j'}{\partial x_k}} \tag{13}$$

For further details refer to Ref. [49].

3.1.3 Multiphase Model. The air-core is modeled with the VOF model. The fraction of fluid in each cell is defined as α_p. The transport equations for the air/water interface are defined in Eqs. (14) and (15). The VOF model locates the interface between air and fluid depending on the value of α_p, which varies between 0 and 1. The model equations are

$$\frac{\partial \alpha_P}{\partial t} + \alpha_P\frac{\partial u_i}{\partial x_i} = 0 \tag{14}$$

$$\frac{\partial(\rho u_i)}{\partial t} + \frac{\partial(\rho u_i u_j)}{\partial x_j} = -\frac{\partial p}{\partial x_j} + \frac{\partial}{\partial x_j}\left(\mu\left(\frac{\partial u_i}{\partial x_j} + \frac{\partial u_j}{\partial x_i}\right)\right) + \rho g_i \tag{15}$$

Based on the local value of α_p, the appropriate properties and variables will be assigned to each control volume within the domain. For more details, see Ref. [50].

3.1.4 Mathematical Modeling of Particle Trajectory. Prediction of solid separation in the hydrocyclone requires two additional modeling concepts beyond the basic CFD. They are the drag force acting on the particle and the diffusion of particles due to fluid turbulence. The movement of a particle is computed by Lagrangian tracking of particles upon the Eulerian continuous-phase predictions (Fig. 2).

The force balance on the particle, written in a Lagrangian reference frame, is a balance between drag, gravity, buoyancy, lift, and centrifugal forces, given as

$$\rho_d\vartheta_d\frac{d\boldsymbol{V}_d}{dt} = \boldsymbol{F}_B + \boldsymbol{F}_S \tag{16}$$

where $\vartheta_d=4\pi a^3/3$ is the particle volume.

The only body force that we consider here is the gravity. Therefore,

$$\boldsymbol{F}_B = \rho_d\vartheta_d\boldsymbol{g} \tag{17}$$

In this case the surface forces acting up on the particle are

$$\boldsymbol{F}_S = \boldsymbol{F}_L + \boldsymbol{F}_D + \boldsymbol{F}_M + \boldsymbol{F}_P \tag{18}$$

$\boldsymbol{F}_P$ is the action of the pressure gradient:

$$\boldsymbol{F}_P = \rho_c\vartheta_d\left(\frac{D\boldsymbol{V}_c}{Dt} - \boldsymbol{g}\right) \tag{19}$$

$\boldsymbol{F}_M$ denotes the added mass:

$$\boldsymbol{F}_M = -C_M\rho_c\vartheta_d\frac{D}{Dt}(\boldsymbol{V}_d - \boldsymbol{V}_c) \tag{20}$$

where $C_a=1/2$ is the added-mass coefficient of a sphere in an inviscid fluid.

$\boldsymbol{F}_D$ is the drag:

$$\boldsymbol{F}_D = -(1/2)\rho_c C_D\pi a^2(\boldsymbol{V}_d - \boldsymbol{V}_c)|\boldsymbol{V}_d - \boldsymbol{V}_c| \tag{21}$$

where $C_D=C_d(\mathrm{Re}_d)$ denotes the drag coefficient, which depends on the Reynolds number of the particle $\mathrm{Re}_d=2a|\boldsymbol{V}_d-\boldsymbol{V}_c|/\nu_c$, where the value of C_d for a wide range of Reynolds numbers is obtained from correlations given in Ref. [51].

$\boldsymbol{F}_L$ is the lift force, which is given by Auton [52].

$$\boldsymbol{F}_L = C_L\rho_c\vartheta(\boldsymbol{V}_c - \boldsymbol{V}_d)\times\boldsymbol{\Omega} \tag{22}$$

where $\boldsymbol{\Omega}=\nabla\times\boldsymbol{V}_c$ and $C_L=1/2$ is the lift coefficient, see Ref. [52].

By writing $\gamma=\rho_d/\rho_c$, one obtains

$$\frac{d\boldsymbol{V}_d}{dt} = \frac{1+C_M}{\gamma+C_M}\frac{D\boldsymbol{V}_c}{Dt} - \frac{1-\gamma}{\gamma+C_M}\boldsymbol{g} - \frac{3}{8}\frac{C_D}{a(\gamma+C_M)}(\boldsymbol{V}_d-\boldsymbol{V}_c)|\boldsymbol{V}_d-\boldsymbol{V}_c| - \frac{C_L}{\gamma+C_M}(\boldsymbol{V}_d-\boldsymbol{V}_c)\times\boldsymbol{\Omega} \tag{23}$$

3.1.5 Two-Way Coupling Model. As the trajectory of a particle is computed, track of the momentum gained or lost by the particle stream has been kept in which these quantities can be incorporated in the subsequent continuous-phase calculations. Thus, while the continuous phase always impacts the discrete phase, it is possible to incorporate the effect of the discrete phase trajectories on the continuum. This two-way coupling is accomplished by alternately solving the discrete and continuous-phase equations until the solutions in both phases have stopped changing. For more details See Ref. [53].

The momentum transfer from the continuous phase to the discrete phase is computed by examining the change in momentum of a particle as it passes through each control volume in the model. This momentum change is computed as

$$\boldsymbol{F} = \sum\left(\frac{18\mu C_D\,\mathrm{Re}}{\rho_P d_P^2 24}(\boldsymbol{u}_P - \boldsymbol{u}) + \boldsymbol{F}_{\text{other}}\right)\dot{m}_P\Delta t \tag{24}$$

Re is the relative Reynolds number, $\dot{m}_p$ defied as mass flow rate particles, and $\boldsymbol{F}_{\text{other}}$ would be the other interaction forces. This momentum exchange appears as a momentum sink in the continuous-phase momentum balance in any subsequent calculations of the continuous-phase flow field. Particle concentration effects have been influenced as mass transfer from a cell to another using a concentration coefficient in continuity equation.

3.2 Description and Geometry of Hydrocyclone Simulated. Hsieh's [36] experimental results were used to validate the simulation of velocity profiles. In this study, a single-channel dual-beam, 35 m W He–Ne laser-Doppler velocity meter was used. Since the air core blocked the scattered light as it passed through the liquid/air interface, the backscatter alignment was chosen. The frequency shifter permitted the detection of flow direction, as well as the measurement of low velocity flow. At every location, 1024 data points were collected and the average velocity and turbulence intensity was recorded. Also, the experimental results of Narasimha et al. [17] were used to validate the simulation of particle-size classification. The particle-size classification experiment was conducted in a standard sump-pump recirculation system. A diluted sand-water mixture was prepared and pumped through the same 100 mm hydrocyclone. Both underflow and

Table 1 Design details of 75 and 100 mm hydrocyclone

Dimensions	Cyclone Hsieh	Cyclone Narasimha	Cyclone Udaya
Cyclone diameter, mm	75	100	50
Cylindrical length, mm	75	85	85
Vortex finder diameter, mm	25	35	14.3
Vortex finder length, mm	50	50	50
Feed inlet dimensions, mm	25×20	25×12.5	7×7
Cone angle, deg	20	20	10
Spigot diameter, mm	12.5	10	3.2

overflow streams were sampled, and the size distribution was determined by a Microtrac particle-size analyzer. The experimental data of Udaya et al. [54] have been used in surveying the one-way and two-way coupling methods performance. Feed slurry consisting of flyash material at different solids consistency was pumped into the cyclone body through the pipeline connected to the pump. The other end of the pipeline was connected to the inlet opening of hydrocyclone in study. The pressure drop inside the cyclone was maintained at required level with the help of by-pass arrangement actuated through a control valve on the pipeline. The pressure drop in the cyclone was measured with the help of a diaphragm type pressure gauge fitted near the feed inlet. The hydrocyclone was positioned upright above the slurry tank.

The dimensions of the 75 mm, 100 mm, and 50 mm hydrocyclone used in the experimental work are shown in Table 1.

Cyclone 1 is the Hsieh [36] base case to validate velocity distribution, cyclone 2 is the base case of Narasimha et al. [17] to validate and study the separation effectiveness, and cyclone 3 is the base case of Udaya et al. [54], which has been used in comparison the one-way and two-way coupling methods.

3.3 Simulation. The simulations carried out on hydrocyclone were assumed to be operating with an air core. Solution of the model governing equations has been carried out by using the FLUENT code. The Cartesian coordinate system was used for numerical simulations. Flow simulation was carried out using a 3D double precision, steady state, and segregated solver. In this method, the governing Navier–Stokes equations are solved sequentially using iterative methods until the defined values of convergence are met.

A velocity inlet boundary condition was applied at the inlet and the overflow and underflow used pressure outlet boundary conditions with an air back-flow volume fraction of one. The feed air volume fraction was set to zero. The physical constants of the liquid primary phase were set to those of water; the second phase constants were those of air.

Initially, the properties of the water were used along with the pressure and face mass fluxes for calculating the momentum equations and further update the velocity field. Pressure staggered option (PRESTO), a pressure interpolation scheme that was reported to be useful for predicting highly swirling flow characteristics prevailing inside the cyclone body, was adopted. For turbulence calculations $k-\varepsilon$, RSM was independently used to evaluate the comparative simulation results. To obtain the pressure field inside the system, semi-implicit pressure linked equations algorithm (SIMPLE) scheme, which uses a combination of continuity and momentum equations to derive an equation for pressure, was used. Interpolation of field variables from cell centers to faces of the control volumes was opted with higher-order quadratic upwind interpolation (QUICK) spatial discretization scheme as it was reported to be useful for swirling flows. Simulations were carried out for about 10,000 incremental steps where in general a preset value of convergence criteria of 1×10^{-6} was achieved.

The following strategy was evolved because it could obtain, with reasonable reliability, a case study with steady flow and a stable air core. Other approaches were tried but the cases invariably diverged:

1. The case was initialized with a cyclone full of water with the backflow air volume fraction set to zero on overflow and underflow boundary conditions.
2. The case was run using the steady solver and the standard k-1 model for approximately 200 iterations.
3. The DRSM with the linear pressure strain (LPS) option was then enabled and the case ran for about 25 iterations using the steady solver and then the unsteady solver (fixed time step) was enabled and the simulation was ran as a time in-

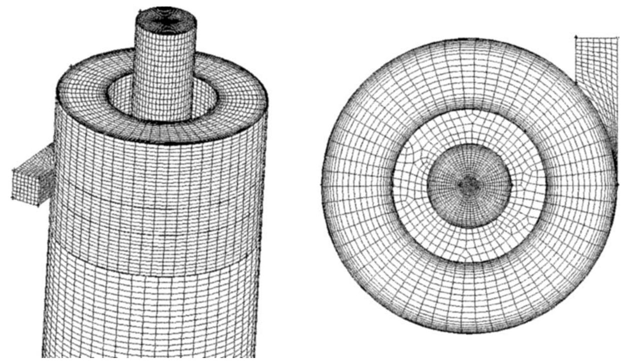

Fig. 3 One of the used meshes in CFD calculations

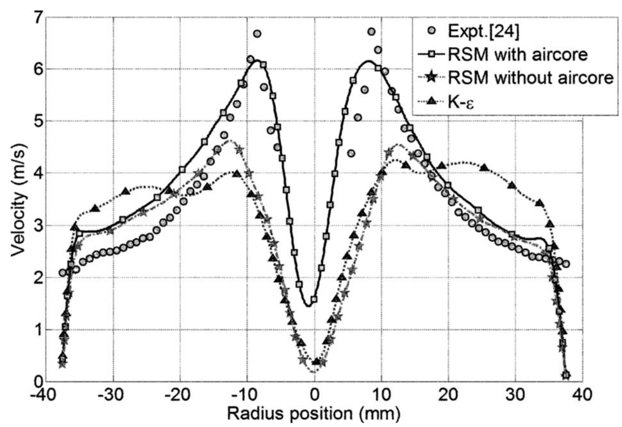

Fig. 4 Predicted versus experimental tangential velocities

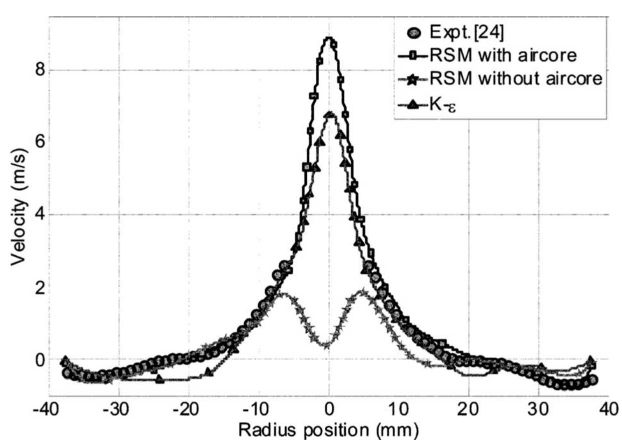

Fig. 5 Predicted versus experimental axial velocities at 0 deg

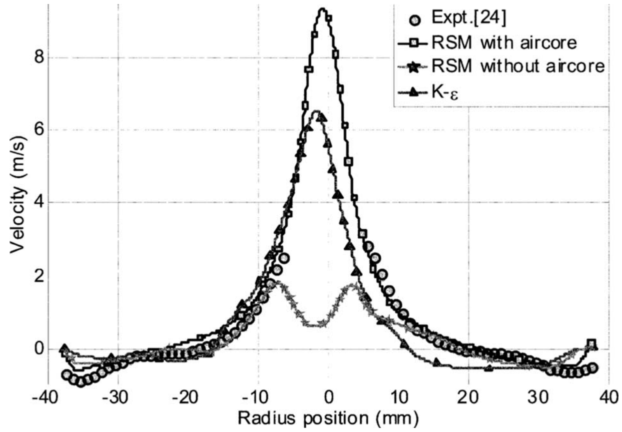

Fig. 6 Predicted versus experimental axial velocities at 90 deg

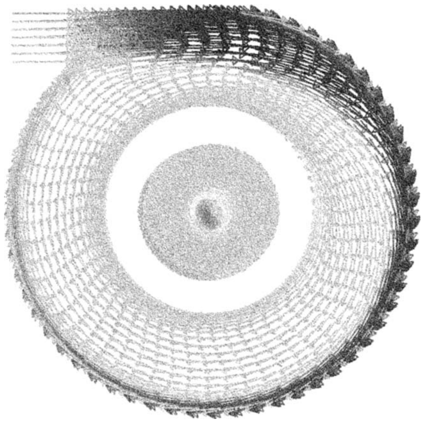

Fig. 7 Flow injection area

tegration until a central axial core of negative pressure formed, which led to a reversed flow on the overflow and underflow boundary conditions.

4. The back flow air volume fraction on both the overflow and underflow boundary conditions was then set to 1 and the simulation was run using the unsteady solver until the air core was fully developed and overflow and underflow mass flow rates matched the feed flow rate. The steady case study using DRSM/LPS/VOF was saved as a base case and was used as the starting case for other case studies using other model options.

The methodology (steps (1)–(4)) does not realistically represent the actual dynamics of air-core development because in reality the back flow air volume fraction is 1 from start up. However, perturbations of the final steady cases always saw the case stabilize back to the same flow split and velocities and hence the predictions should be independent on how the case was first evolved.

For achieving the particle separation behavior inside the cyclone, discrete phase modeling (DPM) technique was adopted. This method simulates the particle trajectory in a Lagrangian frame of reference. In slurries with dilute concentrations of solids (particle concentration below 10% by weight, see Ref. [55]), particle distribution behavior can be simulated using Lagrangian particle tracking approach. Thus in the present study particle tracking is carried out using the above methodology. Stochastic tracking model was adopted for the dispersion of particles due to turbulence in the primary phase. The discrete phase formulation used a

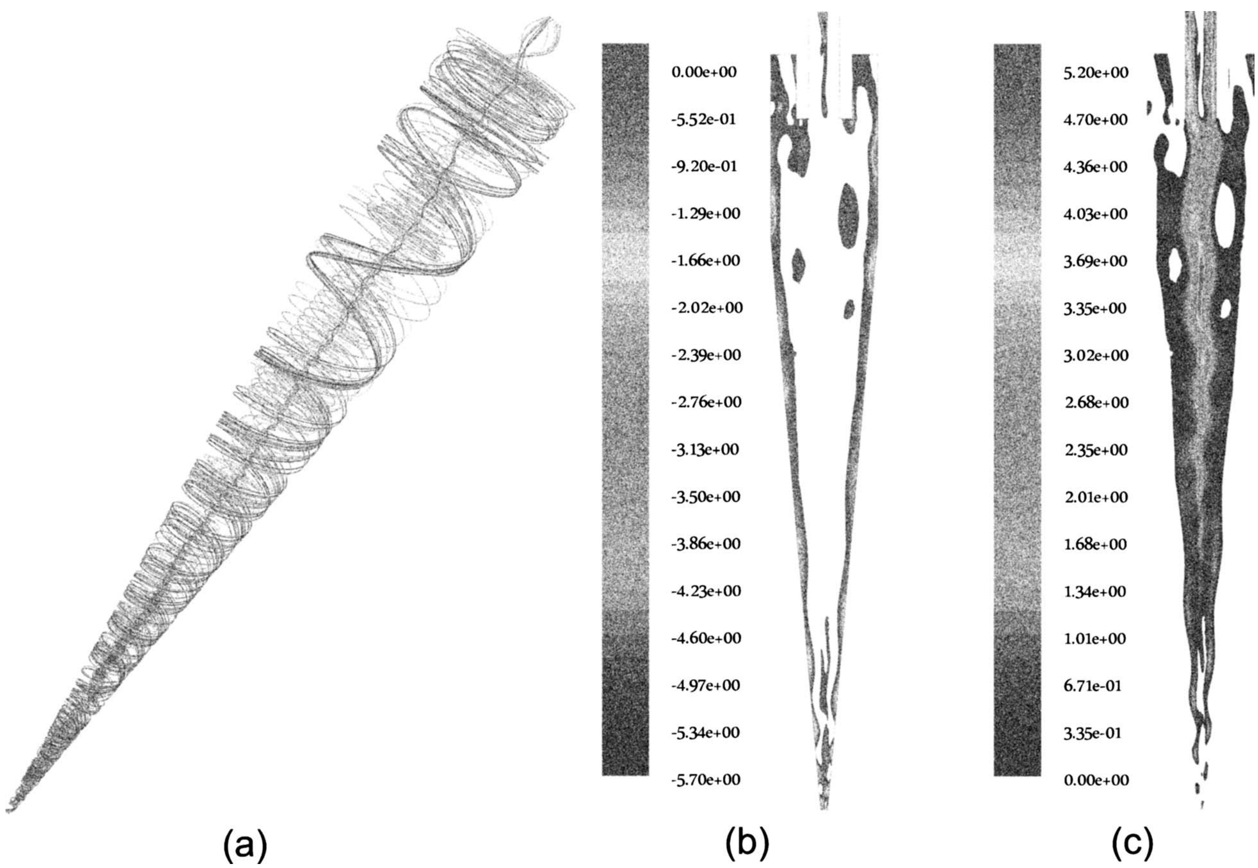

Fig. 8 Flow filed: (*a*) flow path lines, (*b*) downward velocity field, and (*c*) upward velocity field

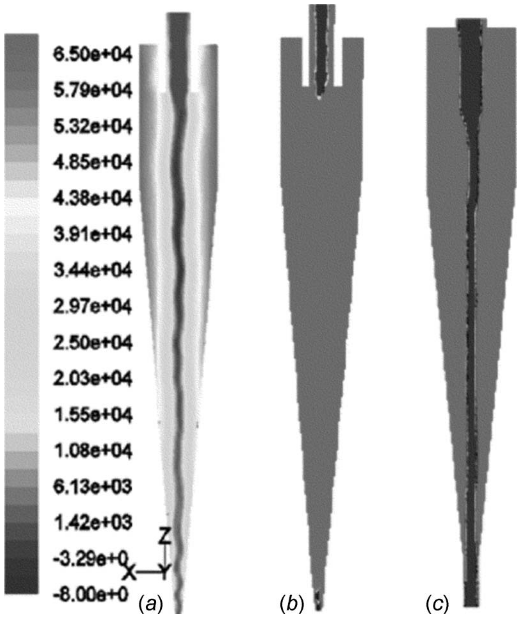

Fig. 9 (***a***) **Pressure field,** (***b***) **shaping the air core via air suction, and** (***c***) **completed air core**

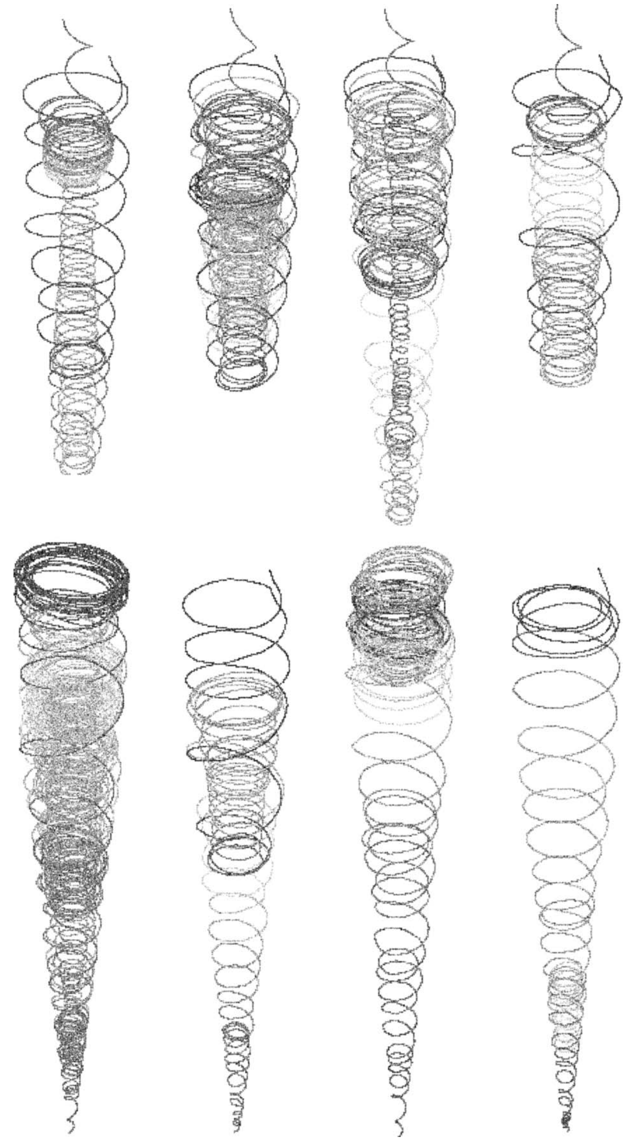

Fig. 10 Some obtained trajectory of particles, leaving the hydrocyclone: (up) from under flow and (down) from over flow

fourth-order Runge–Kutta scheme to obtain the numerical solution of the differential equations. Here, two methods that contain one-way and or two-way coupling have been used. In low particle concentration, one-way coupling can be used while it is better to use two-way at higher particle concentration. One-way coupling contains the assumption that the second phase is sufficiently diluted that particle-particle interactions and the effects of the particle volume fraction on the primary phase are negligible. In two-way coupling, particle effects on continues phase are be in accounted using appropriate source terms in continuity and momentum equations.

3.4 Meshing Scheme. Hydrocyclones truly cannot be modeled in a 2D plane due to nonaxisymmetric nature at the feed inlet opening. Earlier reports also indicated that the results using a 3D model are better matching with the experimental data compared with the results with axisymmetric geometry. The present computational model is based on 3D geometry. Triangular mesh, which can fit into small acute angles in the geometry, is used to mesh the face that joins the inlet to the cylindrical cyclone body. This triangular mesh is then extruded in the vertical direction to give rise to wedge shaped control volumes in the tangential inlet region. The rest of the cyclone is meshed using unstructured hexahedral mesh, which is known to be less diffusive compared with other types of meshes such as tetrahedral. A boundary layer mesh is generated adjacent to the outer wall of the cyclone. In order to capture the low-pressure central air-core, block-structured mesh is generated in that region. Additional care is taken to generate mesh near the spigot region where maximum aspect ratio is restricted to about 10. This is important to capture the back flow through spigot opening. Grid independence study was carried out with five different mesh densities with mesh sizes varying from 750,000 to 2,000,000. Water distribution studies have indicated that better predictions are obtained at higher mesh densities. A mesh density of 1,500,000 cells, as displayed in Fig. 3, is optimal for good predictions and reasonable computational time for simulations.

4 Results and Discussion

4.1 Model Validations. It is necessary to validate the model before its application for numerical experiment. Figures 4–6 show the experimental and predicted tangential and axial velocities for a cylindrical section of the hydrocyclone. In the experiment [24], the tangential velocity component was measured at one angle (0 deg), while the axial velocity component was measured at two angles (0 deg and 90 deg), as shown in Figs. 5 and 6. The simulation results predicted with RSM with air-core model are in good agreement with the experimental results, particularly for the axial velocities. Moreover, the comparison between the experimental results [17] and numerical results has also been made for other variables in the hydrocyclone, such as the cut size shown in Figs. 8–11.

4.2 Flow Patterns and Particle Size Classification. In order to establish the swirling flow field, fluid tangentially injected in cylindrical part (Fig. 7). Induced swirling flow field moved to down while after passing certain distance, an internal vortex flow has been shaped, which moved toward up. Figures 8(*a*)–8(*c*) separately represent areas in which flow tends to move up and or down. In swirling motion, due to rotational movement, pressure distribution increased in radial direction. Hence a low-pressure area has been made in cyclone central area. This results in reverse flow at both exit areas— underflow and overflow—which lead to produce throughout and or small air cores (Fig. 9).

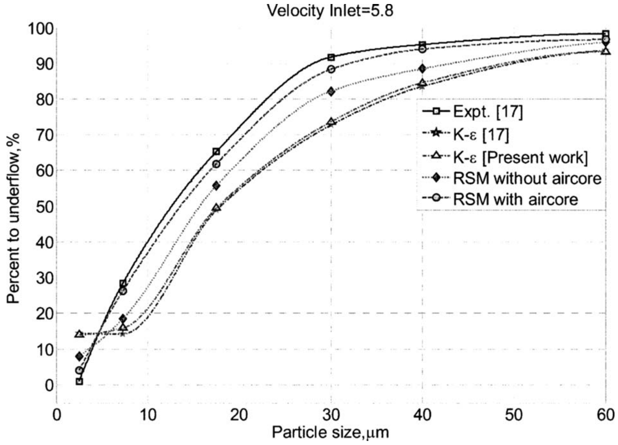

Fig. 11 Comparison of separation efficiency at 5.8 m/s inlet velocity

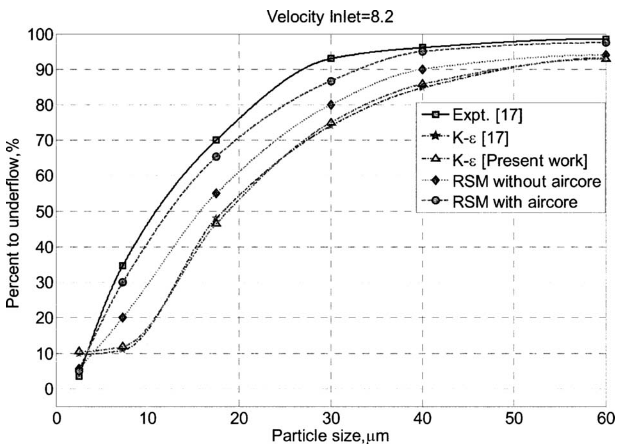

Fig. 12 Comparison of separation efficiency at 8.2 m/s inlet velocity

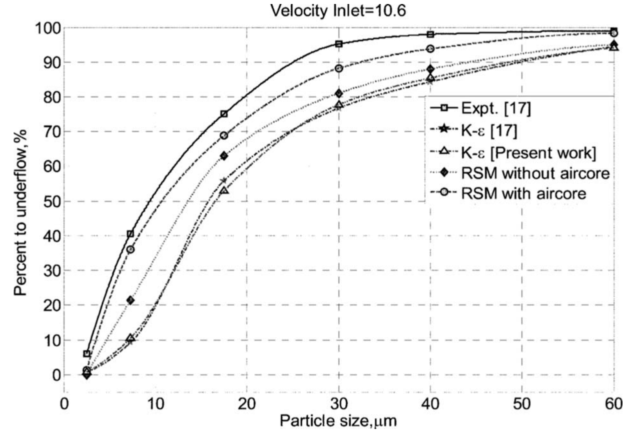

Fig. 13 Comparison of separation efficiency at 10.6 m/s inlet velocity

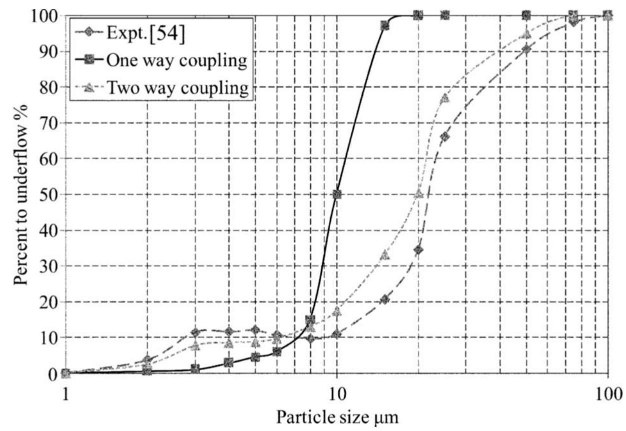

Fig. 14 Comparison of separation efficiency by one-way and two-way coupling methods

The particle-size classification was simulated by injecting a number of particles of each size class over the cross section of the inlet and tracking their exit via the underflow (Fig. 10(*a*)) or overflow streams (Fig. 10(*b*)). The outlet stream in which each particle was reported was noted and the separation characteristics of the cyclone were determined. In one-way coupling method, each run was repeated five times and the average value was noted. During each run, 1500 particles of same size were injected simultaneously. The density of the material is maintained constant at $2600\ \mathrm{kg/m^3}$, which corresponds to the density of sand. Simulation runs were repeated for sand particles of different sizes. These data were then used to generate the partition curve of the cyclone. These calculations are independent of the velocity field calculation. Since the volume percentage of solids in the feed was less the 5%, there is no need for momentum coupling between the solid phase and water phase. Figures 11–13 demonstrate that the separation of particles by size in the hydrocyclone is closely tracked by the RSM calculations. For high solid contents, one would have to resort to multiphase-flow models, which are not yet established [56]. Particle densities were 2300 in two-way coupling method, which their inlet volume fraction was fixed on 10%. Particles entered the hydrocyclone via unsteady treat, which has been continued to obtain steady-state condition (equals particle number at the inlet and outlet). Each discrete phase solution has been done after one continuum phase solution and each step of particle entering has been done after 50 iterations of continuum phase solution.

4.3 Comparison of Separation Efficiency Among Various CFD Models and Experimental Results

4.3.1 Study of Various Turbulence Models Together With Air Core. Simulation of flow fields in hydrocyclone without considering air core and by using $k-\varepsilon$ or RNG $k-\varepsilon$ turbulence models has been performed by many researchers [13–17]. In the present work, flow field in hydrocyclone was simulated by using the $k-\varepsilon$, RSM without air core, and RSM with air-core models. The comparison of the simulation results with respect to the experimental and $k-\varepsilon$ models results, which have been presented by Narasimha et al. [17], shows that the separation efficiency predicted with $k-\varepsilon$ model are in good agreement with that obtained by Narasimha et al. [17].

Considering the RSM and $k-\varepsilon$ turbulence models (shown in Figs. 11–13), it can be seen that the RSM is more precise than $k-\varepsilon$ model. This is due to observing isotropic condition for eddy viscosity in $k-\varepsilon$ model, since eddy viscosity is anisotropic in turbulent swirling flow. Also, with comparison between the simulations that consider the air core and simulations that ignore it, it is certain that including the air core makes the numerical results closer to the experimental results.

It is the result of the decreased accuracy of some turbulence models for an increased turbulence intensity and of the increased diameter of air core that increases the effect of it on the continuous flow field. Consequently, the use of RSM with air core will be

Table 2 Comparison of predicted water splits

Inlet velocity (m/s)	Inlet flow rate (kg/s)	Experimental values: OF flow rate (kg/s)	Experimental values: Water split into OF (%)	Predicted values for RSM with air core: O.F flow rate (kg/s)	Predicted values for RSM with air core: Water split in OF (%)	RSM with air core: Error for water split in OF (%)	$k-\varepsilon$ without air core: Error for water split in OF (%)
5.8	1.844	1.4250	77.28	1.4077	76.34	1.217	2.1345
8.2	2.574	2.1338	82.90	2.1094	81.95	1.1436	2.614
10.6	3.347	2.8893	86.33	2.8550	85.30	1.1873	2.9381

Table 3 Comparison of predicted water splits in one-way and two-way coupling

Flow	Inlet velocity (m/s)	Experimental values: Inlet water flow rate (kg/s)	Experimental values: OF flow water rate (kg/s)	Experimental values: Water split into OF (%)	Predicted values: Inlet water flow rate (kg/s)	Predicted values: OF water flow rate (kg/s)	Predicted values: Water split into OF (%)
Water	9.2	0.45	0.4334	96.3	0.45	0.4370	97.1
Mixture (one-way coupling)	9.2	-	-	-	0.45	0.4370	97.1
Mixture (two-way coupling)	9.2	-	-	-	0.45	0.4424	98.3

more reasonable at high inlet velocities. Table 2 shows the results of fluid splits predicted by CFD modeling and their deviation compare with experimental data.

4.3.2 Comparison of One-Way and Two-Way Coupling Methods. In order to study the discreet phase effects on the continuous phase and increase the simulation accuracy in study a cyclone with 10% inlet volume fraction, both one-way and two-way coupling methods have been utilized, which results have been compared with experimental data. In Fig. 14, clearly, it can be seen that results by two-way method be in closer criteria with experimental data. Because most of particles with large diameter tend to exit from the cone apex, a high thick region of particles established there. This particle closeness changes the flow division ratios as flow from the apex has been decreased while it carried less particles. Also the flow division area moved up and so the effective separation length forced to decrease which causes to lessen the separation efficiency. Because these subjects are not to be in account for one-way coupling, separation efficiency by this method evaluated in a larger criteria. Whereas in two-way method, particle interaction has been accounted, which clearly affects the underflow flow rate so more accurate results have been expected, which is clearly shown in Table 3.

5 Conclusion

In order to understand the effects of operation conditions such as inlet velocity and particle size on hydrocyclone performance, the CFD model proposed in the current work was used to quantify the flow and particle fields in hydrocyclones. The $k-\varepsilon$ model without considering air core and Reynolds stress model with and without considering air core was used to model continuous-phase flow in hydrocyclone. On this basis, a stochastic Lagrangian model was used to track the particles in the cyclones. For modeling the discontinuous phase, discrete phase model in one-way and two-way coupling modes has been utilized.

Eventually, by using the volume of fluid multiphase model and RSM, which observe air core and anisotropic turbulent flow, respectively, the prediction results will be closer to the experimental results. Also, in studied high volume fractions, two-way coupling method represents more accurate results compared with one way.

Nomenclature

$C_{1\varepsilon}$, $C_{2\varepsilon}$, C_η
$k-\varepsilon$ = model constants
C_L = lift coefficient
C_D = drag coefficient
$\boldsymbol{F}_B$ = body forces
$\boldsymbol{F}_s$ = surface forces
G_k = generation of turbulent kinetic energy due to the mean velocity gradients
g = gravitational force
k = turbulent kinetic energy
v = velocity component
V_d = particle velocity
P = pressure
u_i' = velocity fluctuation component
x_i = dimensional component

Greek Symbols

ρ = density
Ω = angular velocity
α_p = volume fraction
ν_c = kinematic viscosity
σ_k, σ_ε = turbulent Prandtl numbers for k and ε, respectively
$\bar{\tau}$ = stress tensor
$\mu_{\text{effective}}$ = effective viscosity
μ = molecular viscosity of the fluid
μ_t = turbulent eddy viscosity
ε = viscous dissipation rate

References

[1] Bretney, E., 1891, "Water Purifier," U.S. Patent No. 543 105.
[2] Kelsall, D. F., 1952, "A Study of the Motion of Solid Particles in a Hydraulic Cyclone," Trans. Inst. Chem. Eng., **30**, pp. 87–108.
[3] Kelsall, D. F., 1953, "A Further Study on the Hydraulic Cyclone," Chem. Eng. Sci., **2**, pp. 254–272.
[4] Bradley, D., 1965, *The Hydrocyclone*, Pergamon, London.
[5] Bloor, M. I. G., and Ingham, D. B., 1973, "Theoretical Investigation of the Flow in a Conical Hydrocyclone," Trans. Inst. Chem. Eng., **51**, pp. 36–41.
[6] Bloor, M. I. G., and Ingham, D. B., 1973, "On the Efficiency of the Industrial Cyclone," Trans. Inst. Chem. Eng., **51**, pp. 173–176.
[7] Bloor, M. I. G., and Ingham, D. B., 1975, "Turbulent Spin in a Cyclone," Trans. Inst. Chem. Eng., **53**, pp. 1–46.
[8] Svarovsky, L., 1984, *Hydrocyclones*, 1st ed., Holt, Rinehart and Winston, London.
[9] Barrientos, A., Sampaio, R., and Concha, F., 1993, "Effect of the Air Core on the Performance of a Hydrocyclone," *Proceedings of the XVIII International Mineral Processing Congress*, pp. 267–270.
[10] Rajamani, R. K., and Devulapalli, B., 1994, "Hydrodynamic Modeling of Swirling Flow and Particle Classification in Large-Scale-Hydrocyclones," Kona, **12**, pp. 95–104.

[11] Ma, L., Ingham, D. B., and Wen, X., 2000, "Numerical Modelling of the Fluid and Particle Penetration Through Small Sampling Cyclones," J. Aerosol Sci., **31**(9), pp. 1097–1119.
[12] Dyakowski, T., and Williams, R. A., 1995, "Prediction of Air-Core Size and Shape in a Hydrocyclone," Int. J. Min. Process., **43**, pp. 1–14.
[13] Fraser, S. M., Abdel Rasek, A. M., and Abdullah, M. Z., 1997, "Computational and Experimental Investigations in a Cyclone Dust Separator," Proc. Inst. Mech. Engrs., Part E: J. Process Mech. Eng., **211**, pp. 247–257.
[14] He, P., Salcudean, M., and Gartshore, I. S., 1999, "A Numerical Simulation of Hydrocyclones," Trans. Inst. Chem. Eng., **77**, pp. 429–441.
[15] Suasnabar, D. J., 2000, "Dense Medium Cyclone Performance, Enhancements Via Computational Modeling of the Physical Process," Ph.D. thesis, University of New South Wales, Sydney.
[16] Schuetz, S., Mayer, G., Bierdel, M., and Piesche, M., 2004, "Investigations on the Flow and Separation Behaviour of Hydrocyclones Using Computational Fluid Dynamics," Int. J. Min. Process., **73**, pp. 229–23717.
[17] Narasimha, M., Sripriya, R., and Banerjee, P. K., 2005, "CFD Modelling of Hydrocyclone—Prediction of Cut-Size," Int. J. Min. Process., **75**(1-2), pp. 53–68.
[18] Launder, B. E., Reece, G. J., and Rodi, W., 1975, "Progress in the Development of as Reynolds-Stress Turbulence Closure," J. Fluid Mech., **68**, pp. 537–566.
[19] Boysan, F., Ayers, W. H., and Swithenbank, J., 1982, "A Fundamental Mathematical Modelling Approach to Cyclone Design," Trans. Inst. Chem. Eng., **60**, pp. 222–230.
[20] Cullivan, J. C., Williams, R. A., and Cross, C. R., 2003, "Understanding the Hydrocyclone Separator Through Computational Fluid Dynamics," Chem. Eng. Res. Des., **81**, pp. 455–465.
[21] Slack, M. D., Prasad, R. O., Bakker, A., and Boysan, F., 2000, "Advances in Cyclone Modeling Using Unstructured Grids," Trans. IChemE, Part C, **78**, pp. 1098–1104.
[22] Brennan, M. S., Subramanian, V. J., Rong, R., Holtham, P. N., Lyman, G. J., and Napier-Munn, T. J., 2003, "Towards a New Understanding of the Cyclone Separator," *Proceedings of XXII International Mineral Processing Congress*, Cape Town, South Africa, Sept. 29–Oct. 3.
[23] Mousavian, S. M., and Najafi, A. F., 2008, "Numerical Simulations of Gas–Liquid–Solid Flows in a Hydrocyclone Separator," Arch. Appl. Mech., **79**, pp. 395–409
[24] Castro, O., and Concha, F., 1996, "Air Core Modeling for an Industrial Hydrocyclone," International Conference on Hydrocyclones '96, Cambridge, UK, Apr. 2–4, pp. 229–240.
[25] Concha, F., Barrientos, A., Montero, J., and Sampio, R., 1996, "Air Core and Roping in Hydrocyclones," Int. J. Min. Process., **44-45**, pp. 743–749.
[26] Steffens, P. R., Whiten, W. J., Appleby, S., and Hitchins, J., 1993, "Prediction of Air Core Diameters for Hydrocyclones," Int. J. Min. Process., **39**, pp. 61–74.
[27] Davidson, M. R., 1994, "A Numerical Model of Liquid–Solid Flow in a Hydrocyclone With High Solids Fraction," International Symposium Numerical Methods in Multiphase Flows, ASME FED-185, pp. 29–39.
[28] Romero, J., and Sampaio, R., 1999, "A Numerical Model for Prediction of the Air-Core Shape of Hydrocyclone Flow," Mech. Res. Commun., **26**(3), pp. 379–384.
[29] Hsieh, K. T., and Rajamani, R. K., 1991, "Mathematical Model of the Hydrocyclone Based on the Physics of Fluid Flow," AIChE J., **37**, pp. 735–746.
[30] Malhotra, A., Branion, R. M. R., and Hauptmann, E. G., 1994, "Modeling the Flow in a Hydrocyclone," Can. J. Chem. Eng., **72**, pp. 953–960.
[31] Davidson, M. R., 1988, "Similarity Solutions for Flow in Hydrocyclones," Chem. Eng. Sci., **43**(7), pp. 1499–1505.
[32] Concha, F., Castro, B., Ovalle, E., and Romero, J., 1998, "Numerical Simulation of the Flow Pattern in a Hydrocyclone" International Conference Innovation in Physical Separation Technology, Falmouth, UK, Jun. 4–5, pp. 35–60.
[33] Pericleous, K. A., and Rhodes, N., 1986, "The Hydrocyclone Classifier—A Numerical Approach," Int. J. Min. Process., **17**, pp. 23–43.
[34] Cullivan, J. C., Williams, R. A., and Cross, C. R., 2000, "Verification of Theoretical 3D-Flow in a Hydrocyclone Using Tomography," Fourth World Congress for Particle Technology, Sydney, pp. 1–9.
[35] Brennan, M. S., Holtham, P. N., Rong, R., and Lyman, G. J., 2002, "Computational Fluid Dynamic Simulation of Dense Medium Cyclones," *Proceedings of the Ninth Australian Coal Preparation Conference*, Yeppoon, Australia, Oct. 13–17, Paper No. B3.
[36] Hsieh, K. T., 1988. "A Phenomenological Model of the Hydrocyclone," Ph.D. thesis, University of Utah, Salt Lake, UT.
[37] Speziale, C. G., Sarkar, S., and Gatski, T. B., 1991, "Modelling the Pressure-Strain Correlation of Turbulence: An Invariant Dynamical Systems Approach," J. Fluid Mech., **227**, pp. 245–274.
[38] Devulapalli, B., and Rajamani, R. K., 1994, "Application of LDV to the Modelling of Particle Size Classification in Industrial Hydrocyclones," *Parallel Computing in Multiphase Flow Systems Simulations*, Vol. 191, ASME, New York, pp. 41–48.
[39] Devulapalli, B., and Rajamani, R. K., 1996, "A Comprehensive CFD Model for Particle Size Classification in Industrial Hydrocyclones," Hydrocyclones '96, Cambridge, UK, pp. 83–104.
[40] Devulapalli, B., 1997, "Hydrodynamic Modelling of Solid-Liquid Flows in Large Scale Hydrocyclones," Ph.D. thesis, University of Utah, Salt Lake, UT.
[41] Baxter, L. L., and Smith, P. J., 1993, "Turbulent Dispersion of Particles," Energy Fuels, **7**, pp. 852–859.
[42] Boivin, M., Simonin, O., and Squires, K. D., 2000, "On the Prediction of Gas-Solid Flows With Two-Way Coupling Using Large Eddy Simulation," Phys. Fluids, **12**, pp. 2080–2090.
[43] Portela, L. M., and Oliemans, R. V. A., 2001, "Direct and Large Eddy Simulation of Particle-Laden Flows Using the Point Particle Approach," *Direct and Large Eddy Simulation IV*, B. J. Geurts, ed., Kluwer Academic, Dordrecht, pp. 53–460.
[44] Millelli, M., Smith, B. L., and Lakehal, D., 2001, "Large-Eddy Simulation of Turbulent Shear Flows Laden With Bubbles," *Direct and Large Eddy Simulation IV*, B. J. Geurts, ed., Kluwer Academic, Dordrecht, pp. 61–470.
[45] Ding, J., and Gidaspow, D., 1990, "A Bubbling Fluidization Model Using Kinetic Theory of Granular Flow," AIChE J., **36**, pp. 523–528.
[46] Gidaspow, D., Bezburuah, R., and Ding, J., 1992, "Hydrodynamics of Circulating Fluidized Beds, Kinetic Theory Approach," *Fluidization VII, Proceedings of the Seventh Engineering Foundation Conference on Fluidization*, pp. 75–82.
[47] Roco, M. C., 1993, *Particulate Two-Phase Flow* (Butterworth-Heinemann Series in Chemical Engineering), Butterworth-Heinemann, Boston.
[48] Launder, B. E., and Spalding, D. B., 1972, *Lectures in Mathematical Models of Turbulence*, Academic, London, England.
[49] Gatski, T. B., Hussaini, M. Y., and Lumley, J. L., 1996, *Simulation and Modeling of Turbulent Flows*, Oxford University Press, New York.
[50] Ishii, M., and Hibiki, T., 2005, *Thermo-Fluid Dynamics of Two-Phase Flow*, Springer-Verlag, New York.
[51] Clift, R., Grace, J. R., and Weber, M. E., 1978, *Bubbles, Drops and Particles*, Academic, New York.
[52] Auton, T. R., 1987, "The Lift Force on a Spherical Body in a Rotational Flow," J. Fluid Mech., **183**, pp. 199–218.
[53] Crowe, C., Sommerfeld, M., Tsuji, Y., 1998, *Multiphase Flows With Droplets and Particles*, CRC, Boca Raton, FL.
[54] Udaya Bhaskar, K., Rama Murthy, Y., Ramakrishnan, N., Srivastava, J. K., Supriya, S., and Vimal, K., 2007, "CFD Validation for Flyash Particle Classification in Hydrocyclones," Minerals Eng., **20**, pp. 290–302.
[55] Stovin, V. R., and Saul, A. J., 1998, "A Computational Fluid Dynamics (CFD) Particle Tracking Approach to Efficiency Prediction," Water Sci. Technol., **37**(1), pp. 285–293.
[56] Nowakowski, A. F., Cullivan, J. C., Williams, R. A., and Dyakowski, T., 2004, "Application of CFD to Modelling of the Flow in Hydrocyclones. Is This a Realizable Option or Still a Research Challenge?," Minerals Eng., **17**, pp. 661–669.

Flow of a Biomagnetic Visco-Elastic Fluid in a Channel With Stretching Walls

J. C. Misra[1]
School of Medical Science and Technology,
Indian Institute of Technology,
Kharagpur-721302, India
e-mail: misrajc@rediffmail.com
e-mail: jcm@maths.iitkgp.ernet.inphys

G. C. Shit
Department of Mathematics,
Jadavpur University,
Kolkata-70032, India
e-mail: gcs@math.jdvu.ac.in

The flow of a visco-elastic fluid in a channel with stretching walls under the action of an externally applied magnetic field generated by a magnetic dipole was studied in this paper. As per an experimental report, the variation in magnetization M of the fluid with temperature T was approximated as a linear equation of state $M = K_1 T$, where K_1 is a constant called the pyromagnetic coefficient. In this investigation the model used is that of Walter's liquid B fluid, which includes the effect of fluid visco-elasticity. By introducing appropriate nondimensional variables, the problem is reduced to solving a coupled nonlinear system of ordinary differential equations subject to a set of boundary conditions. The problem is solved by developing a suitable numerical technique based on finite difference approach. Computational results concerning the variation in the velocity, pressure and temperature fields, skin friction and the rate of heat transfer with magnetic field strength, Prandtl number, and blood visco-elasticity are presented graphically. The results presented reveal that the velocity of blood in the normal physiological state can be lowered by applying a magnetic field of sufficient intensity. The study bears the promise of important applications in controlling the flow of blood during surgery and also during treatment of cancer by therapeutic means when it involves magnetic drug targeting (hyperthemia). [DOI: 10.1115/1.3130448]

Keywords: biomagnetic fluid, non-Newtonian model, visco-elasticity, stretching walls

1 Introduction

The study of biomagnetic fluid dynamics (BFD) has attracted the interest of many researchers in view of its important applications in bio-engineering and biomedical technology. The primary object of this emerging area of fluid dynamics is to investigate the dynamical behavior of biological fluids in the presence of magnetic fields generated by the action of magnetic dipoles. Higashi et al. [1] reported that hemoglobin is a form of iron oxide. Since blood is a suspension of erythrocytes in an aqueous solution called plasma and since erythrocytes contain hemoglobin molecules, blood is a characteristic example of a biomagnetic fluid. They [1] further suggested that the erythrocytes orient their disk plane parallel to the magnetic field. Pauling and Cryell [2] observed that blood, when oxygenated, possesses the properties of a diamagnetic material and when deoxygenated, it exhibits the properties of a paramagnetic material with magnetic susceptibility equal to 3.5×10^{-6}.

Mathematical modeling of biomagnetic fluid flow is performed by using the principles of ferrohydrodynamics (FHD). In this formulation, blood is considered as an electrically nonconducting magnetic fluid, and it is assumed that the flow is affected by the magnetization of the fluid. This formulation is different from that of magnetohydrodynamics (MHD), which deals with electrically conducting fluids. In the case of a magnetohydrodynamic flow, the force that comes into the picture is the so called Lorentz force, where the effects of magnetization and polarization are ignored. In the case of blood, it was reported that Lorentz force is sufficiently small, in comparison to the effects of magnetization and polarization [3–6]. Haik et al. [3] developed a magnetic device that separates red blood cells from the whole blood on a continuous basis. The importance of the device lies in the fact that certain cancer treatments require separation of white cells from the whole blood. In their experimental study, the magnetic field was varied from −5 T to +5 T. Haik et al. [7] also carried out another study on human blood at the National High Magnetic Field Laboratory. They reported that there is a marked reduction in the flow rate of blood as the magnetic field strength is increased. The experimental studies of Haik et al. [4] further shows that for an applied magnetic field of strength up to 8 T, the flow rate of human blood in a tube is reduced by 30%. The magnetic particles and magnets were used in the development of new therapeutic and clinical techniques. Perry [8] proposed the use of magnetic fluids as a method for reducing blood flow during surgeries, the basic purpose being to maintain a magnetic field permanently across a vein or an artery in the vicinity of a surgical procedure. Hiergeist et al. [9] developed an experimental setup for applying magnetic ferrofluids in the treatment of hyperthemia. Voltairas et al. [10] introduced the concept of magnetic drug targeting. It may be mentioned that efficient drug targeting plays a vital role for the medical treatment of various cardiovascular diseases such as stenosis and thrombosis.

A couple of studies in the field of biomagnetic fluids were made by Tzirtzilakis and co-workers [11–15]. Tzirtzilakis and Kafoussias [11] considered the flow of a heated ferrofluid over a linearly stretching sheet under the action of a magnetic field generated by the presence of a magnetic dipole. This study indicates that the temperature of a biomagnetic fluid increases with an increase in Prandtl number, as well as ferromagnetic induction. They reported these observations on the basis of their computational study that made use of the physical data for human blood. Loukopoulas and Tzirtzilakis [12] investigated the problem of biomagnetic channel flow under the influence of an applied magnetic field. In their study, they considered that magnetization of the fluid varies linearly with temperature, as well as with the intensity of the magnetic field. The results presented by them indicate that the local skin friction and the rate of heat transfer increase with the increase in the magnetic field strength. Papadopoulos and Tzirtzilakis [13]

[1]Corresponding author.

Contributed by the Applied Mechanics Division of ASME for publication in the Journal of Applied Mechanics. Manuscript received October 4, 2007; final manuscript received March 25, 2009; published online July 23, 2009. Review conducted by Arif Masud.

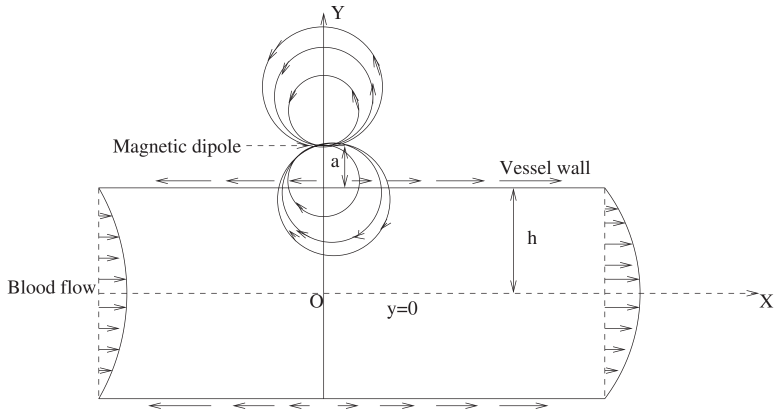

Fig. 1 Physical sketch of the problem

conducted a study of the laminar incompressible fully developed biomagnetic flow of blood in a curved square duct subject to the action of an applied magnetic field. Recently Tzirtzilakis et al. [14] dealt with a problem of turbulent biomagnetic fluid flow in a rectangular channel under the action of a localized magnetic field. Their study shows that the flow field is mainly affected by the formation of two vortices in the vicinity of the area where the magnetic field is applied. They formulated a model by using the principles of both FHD and MHD, that is, by considering the effects of magnetization and that of electrical conductivity of blood. The concept of this mathematical model of BFD was proposed earlier in Ref. [15]. Andersson and Valnes [16] studied the flow of a heated ferrofluid over a stretching sheet in the presence of a magnetic dipole. They observed that the primary effect of the magnetic field is to decelerate the fluid motion, as a result of which the skin friction of the sheet increases. It may, however, be mentioned that all the studies referred to above are restricted to the consideration of homogeneous Newtonian fluids.

Misra and Shit [17] investigated the flow and heat transfer of a visco-elastic electrically conducting fluid under the action of a magnetic field. Misra et al. [18,19] also studied the steady flow of an incompressible second-grade electrically conducting fluid in a channel permeated by a uniform transverse magnetic field. All the said studies performed by Misra et al. [17–19] are motivated toward different possible applications in the field of biomedical engineering. MHD flow of a viscous fluid over a linearly stretching sheet was studied by several investigators by considering visco-elastic non-Newtonian models [20–24]. Some similar studies for power law fluids were also reported in scientific literatures [25–27].

Exchange of heat take place between living tissues and blood in the circulatory system. The extent of heat exchange, however, depends on the geometry of the vessel through which blood flows. It is reported in Ref. [28] that blood flow affects the thermal response of living tissues. Craciunescu and Clegg [29] studied the effect of oscillatory flow upon the resulting temperature distribution of blood and convective heat transfer in rigid vessels. The importance of different types of blood vessels in the process of bioheat transfer was intensively studied by Weinbaun et al. [30].

Of concern in the present investigation is a problem of blood flow through a channel with stretching walls under the action of a localized magnetic field. Blood is treated here as a biomagnetic fluid obeying the Walter's liquid B model that takes care of the non-Newtonian visco-elastic behavior of blood. The problem is first treated analytically and then suitable numerical techniques were employed in order to derive the final solution of the problem. For this purpose, a suitable iterative finite difference scheme was developed. The results depicting the effects of magnetization and blood visco-elasticity on velocity profile, skin friction, and the rate of heat transfer at the channel wall were presented through graphs/tables. The study bears the potential of significant applications in biomedical technologies such as controlling the blood flow during surgery and also in the treatment of cancer that involves drug targeting to the affected cells.

2 Mathematical Formulation of the Problem

Let us consider the two-dimensional viscous incompressible flow of a biomagnetic fluid (e.g., blood) in a parallel plate channel bounded by the planes $y=\pm h$ in the presence of an applied magnetic field generated by a magnetic dipole. The flow is considered to be driven by the stretching of the channel walls such that the surface velocity of each wall is proportional to the axial coordinate x (see Fig. 1). The problem pertains to a situation where a magnetic dipole is located at a distance a above the channel wall, and the wall is kept at a constant temperature T_w.

The fluid under consideration is taken to be electrically nonconducting and governed by Walter's liquid B equations [31,32]:

$$\frac{\partial u}{\partial x}+\frac{\partial v}{\partial y}=0 \tag{1}$$

$$\begin{aligned}\rho\left(u\frac{\partial u}{\partial x}+v\frac{\partial u}{\partial y}\right)&=-\frac{\partial p}{\partial x}+\mu\nabla^2 u-k_0\Bigg[\left(u\frac{\partial}{\partial x}+v\frac{\partial}{\partial y}\right)\nabla^2 u-\frac{\partial u}{\partial x}\nabla^2 u\\&\quad-\frac{\partial u}{\partial y}\nabla^2 v-2\left\{\frac{\partial u}{\partial x}\frac{\partial^2 u}{\partial x^2}+\frac{\partial v}{\partial y}\frac{\partial^2 u}{\partial y^2}\right.\\&\quad\left.+\left(\frac{\partial u}{\partial y}+\frac{\partial v}{\partial x}\right)\frac{\partial^2 u}{\partial x\,\partial y}\right\}\Bigg]+\mu_0 M\frac{\partial H}{\partial x}\end{aligned} \tag{2}$$

$$\begin{aligned}\rho\left(u\frac{\partial v}{\partial x}+v\frac{\partial v}{\partial y}\right)&=-\frac{\partial p}{\partial y}+\mu\nabla^2 v-k_0\Bigg[\left(u\frac{\partial}{\partial x}+v\frac{\partial}{\partial y}\right)\nabla^2 v-\frac{\partial v}{\partial x}\nabla^2 u\\&\quad-\frac{\partial v}{\partial y}\nabla^2 v-2\left\{\frac{\partial u}{\partial x}\frac{\partial^2 v}{\partial x^2}+\frac{\partial v}{\partial y}\frac{\partial^2 v}{\partial y^2}\right.\\&\quad\left.+\left(\frac{\partial u}{\partial y}+\frac{\partial v}{\partial x}\right)\frac{\partial^2 v}{\partial x\,\partial y}\right\}\Bigg]+\mu_0 M\frac{\partial H}{\partial y}\end{aligned} \tag{3}$$

$$\begin{aligned}&\rho c_p\left(u\frac{\partial T}{\partial x}+v\frac{\partial T}{\partial y}\right)+\mu_0 T\frac{\partial M}{\partial T}\left(u\frac{\partial H}{\partial x}+v\frac{\partial H}{\partial y}\right)\\&\quad=k\left(\frac{\partial^2 T}{\partial x^2}+\frac{\partial^2 T}{\partial y^2}\right)+\mu\left[2\left(\frac{\partial u}{\partial x}\right)^2+2\left(\frac{\partial v}{\partial y}\right)^2+\left(\frac{\partial v}{\partial x}+\frac{\partial u}{\partial y}\right)^2\right]\\&\qquad-k_0\left(\frac{\partial u}{\partial y}\right)\frac{\partial}{\partial y}\left(u\frac{\partial u}{\partial x}+v\frac{\partial u}{\partial y}\right)\end{aligned} \tag{4}$$

The boundary conditions applicable to the flow problem may be mathematically described as

$$\frac{\partial u}{\partial y}=0, \quad v=0, \quad \frac{\partial T}{\partial y}=0 \quad \text{at} \quad y=0 \tag{5}$$

$$u=cx, \quad v=0, \quad T=T_w, \quad p+\tfrac{1}{2}\rho(u^2+v^2)=0 \quad \text{at} \quad y=h \tag{6}$$

In the above equations u and v are the (dimensional) velocity components of the fluid in x and y directions, respectively, p is the pressure, ρ is the biomagnetic fluid density, μ is the dynamic viscosity, μ_0 is the magnetic permeability, c_p is the specific heat at constant pressure, k is the thermal conductivity, H is the magnetic field strength, and k_0 is the measure of the visco-elasticity of the biomagnetic fluid. The terms $\mu_0 M\,\partial H/\partial x$ and $\mu_0 M\,\partial H/\partial y$ in the right hand side of Eqs. (2) and (3), respectively, represent the component of magnetic force per unit volume. The second term on the left hand side of the thermal energy equation (4) represents the thermal power per unit volume due to magnetization that takes place as an adiabatic process. It may be noted that during the motion of a visco-elastic fluid, a certain amount of energy is stored in the fluid as strain energy, while some portion of the energy is lost due to viscous dissipation. The second and the third terms on the right hand side of Eq. (4) represent the terms due to viscous dissipation and strain energy, respectively.

The biomagnetic fluid flow is affected by the magnetic field generated by the presence of a magnetic dipole, where the magnetic scalar potential is given by

$$\phi=\frac{\gamma}{2\pi}\cdot\frac{x}{x^2+(y-d)^2} \tag{7}$$

with $d=a+h$, and γ being the magnetic field strength at the source $(0,d)$.

The corresponding magnetic field H has the components

$$H_x=-\frac{\partial\phi}{\partial x}=\frac{\gamma}{2\pi}\cdot\frac{x^2-(y-d)^2}{[x^2+(y-d)^2]^2} \tag{8}$$

$$H_y=-\frac{\partial\phi}{\partial y}=\frac{\gamma}{2\pi}\cdot\frac{2x(y-d)}{[x^2+(y-d)^2]^2} \tag{9}$$

Thus the magnitude of the magnetic field intensity $H=|\boldsymbol{H}|$ is given by

$$H(x,y)=\sqrt{H_x^2+H_y^2}=\frac{\gamma}{2\pi}\cdot\frac{1}{x^2+(y-d)^2} \tag{10}$$

Hence

$$\begin{aligned}\frac{\partial H}{\partial x}&=-\frac{\gamma}{2\pi}\frac{2x}{[x^2+(y-d)^2]^2}=-\frac{\gamma}{2\pi}\cdot\frac{2x}{(y-d)^4}\left[1+\left(\frac{x}{y-d}\right)^2\right]^{-2}\\&=-\frac{\gamma}{2\pi}\cdot\frac{2x}{(y-d)^4}\left[1-\frac{2x^2}{(y-d)^2}+\frac{3x^4}{(y-d)^4}-\cdots\right]\\&=-\frac{\gamma}{2\pi}\cdot\frac{2x}{(y-d)^4}\quad [\text{neglecting } x^3 \text{ and higher powers of } x]\end{aligned} \tag{11}$$

Proceeding in a similar manner, we get

$$\frac{\partial H}{\partial y}=\frac{\gamma}{2\pi}\cdot\left[-\frac{2}{(y-d)^3}+\frac{4x^2}{(y-d)^5}\right] \tag{12}$$

We consider a state of equilibrium. According to the principle of FHD, the magnetization M is a function of temperature T. In the present formulation, in conformity to the experimental observation reported in Ref. [33], magnetization M is considered to vary with temperature T linearly. Thus we write $M=K_1T$, where K_1 is a constant called the pyromagnetic constant. Now we introduce the following nondimensional variables:

$$\psi(\xi,\eta)=h^2c\xi f(\eta) \tag{13}$$

$$P(\xi,\eta)=\frac{p}{c\mu}=-P_1(\eta)-\xi^2P_2(\eta) \tag{14}$$

$$\theta(\xi,\eta)=\frac{T}{T_w}=\theta_1(\eta)+\xi^2\theta_2(\eta) \tag{15}$$

$$\xi(x)=\frac{x}{h} \tag{16}$$

$$\eta(y)=\frac{y}{h} \tag{17}$$

where $\psi(\xi,\eta)$, $P(\xi,\eta)$, and $\theta(\xi,\eta)$ are the stream function, pressure, and temperature variables, respectively.

In terms of these dimensionless variables, the velocity components u and v can be obtained by using the formulas

$$u=\frac{\partial\psi}{\partial y}=cxf'(\eta) \tag{18}$$

$$v=-\frac{\partial\psi}{\partial x}=-chf(\eta) \tag{19}$$

Clearly u and v satisfy the continuity equation (1). Substituting Eqs. (13)–(19) into Eqs. (2)–(4) and then equating the coefficients of ξ and ξ^2, we get the following set of ordinary differential equations:

$$f'''+ff''-f'^2+K[ff^{iv}-2f'f'''+f''^2)]+2P_2-\frac{2B\theta_1}{(\eta-\alpha)^4}=0 \tag{20}$$

$$P_1'-f''-ff'-K(ff'''-3f'f'')-\frac{2B\theta_1}{(\eta-\alpha)^3}=0 \tag{21}$$

$$P_2'-\frac{2B\theta_2}{(\eta-\alpha)^3}+\frac{4B\theta_1}{(\eta-\alpha)^5}=0 \tag{22}$$

$$\theta_1''+Prf\theta_1'-\frac{2\lambda B\theta_1 f}{(\eta-\alpha)^3}+2\theta_2+4\lambda f'^2=0 \tag{23}$$

and

$$\begin{aligned}\theta_2''-Pr(2f'\theta_2-f\theta_2')-\frac{2\lambda Bf\theta_2}{(\eta-\alpha)^3}+\lambda B\theta_1\left[\frac{2f'}{(\eta-\alpha)^4}+\frac{4f}{(\eta-\alpha)^5}\right]\\+\lambda f''^2-\lambda K(f'f''^2-ff''f''')=0,\end{aligned} \tag{24}$$

while the boundary conditions (5) and (6) get transformed to

$$f=f''=0, \quad \theta_1'=\theta_2'=0 \quad \text{at} \quad \eta=0 \tag{25}$$

$$f=0, \quad f'=\theta_1=1, \quad \theta_2=0, \quad P_1=0, \quad P_2=\frac{1}{2} \quad \text{at} \quad \eta=1 \tag{26}$$

The five nondimensional parameters that appear in the Eqs. (20)–(24) are defined by

$$\mathrm{Pr}=\frac{\mu c_p}{k}$$

$$\lambda=\frac{c\mu^2}{\rho kT_w}$$

$$B=\left(\frac{\gamma}{2\pi}\right)\cdot\frac{\mu_0 kT_w\rho}{\mu^2}$$

$$\alpha = \frac{d}{h}$$

$$K = \frac{k_0 c}{\mu}$$

3 Perturbation Analysis

Since Eq. (20) is highly nonlinear and the visco-elastic parameter K is considered to be small, in order to solve the Eq. (20), we expand f in a power series in K as

$$f(\eta) = f_0(\eta) + K f_1(\eta) + K^2 f_2(\eta) + \cdots \tag{27}$$

K being taken as the perturbation parameter. Substituting Eq. (27) into Eq. (20), equating like powers of K and ignoring squares and higher powers, we obtain

$$f_0''' + f_0 f_0'' - f_0'^2 - \frac{2B\theta_1}{(\eta - \alpha)^4} + 2P_2 = 0 \tag{28}$$

and

$$f_1''' + f_0 f_1'' - 2f_0' f_1' + f_0'' f_1 = 2f_0' f_0''' - f_0''^2 - f_0 f_0^{iv} \tag{29}$$

Further, using Eq. (27) in Eqs. (25) and (26), the boundary conditions for f_0 and f_1 are found as

$$f_0 = f_1 = 0, \quad f_0'' = f_1'' = 0 \quad \text{at} \quad \eta = 0 \tag{30}$$

and

$$f_0 = f_1 = 0, \quad f_0' = 1, \quad f_1' = 0 \quad \text{at} \quad \eta = 1 \tag{31}$$

In Sec. 4, we will develop a numerical scheme for solving Eqs. (28) and (29) subject to the boundary conditions (30) and (31).

4 Numerical Method

The set of coupled differential equations (20)–(24) along with the boundary conditions (25) and (26) forms a nonlinear two point boundary value problem. To solve this we developed a suitable computational procedure. According to Eq. (14), $P = -P_1 - \xi^2 P_2$. It is noted that the pressure variable P_1 appears only in Eq. (21), while Eqs. (20) and (22)–(24) are all independent of P_1. This is why one can keep P_1 away from any further consideration, in case the object is to study the velocity field.

When the ferrohydrodynamic parameter $B=0$ and also the visco-elastic parameter $K=0$, the flow problem becomes decoupled from the thermal energy problem. In this case, the analytical solution for P_1 was put forward by Crane [34]. Following Newton's method of linearization, we now proceed to solve the nonlinear equation (28) subject to the boundary conditions (30) and (31). Substituting $f_0' = F$ in Eqs. (28), (30), and (31), we get

$$F'' + f_0 F' - F^2 = \frac{2B\theta_1}{(\eta - \alpha)^4} - 2P_2 \tag{32}$$

$$F'(0) = 0, \quad F(1) = 1 \tag{33}$$

Using central difference scheme for the derivatives with respect to η, we can write

$$(F')_i = \frac{F_{i+1} - F_{i-1}}{2\delta\eta} + O((\delta\eta)^2) \tag{34}$$

and

$$(F'')_i = \frac{F_{i+1} - 2F_i + F_{i-1}}{(\delta\eta)^2} + O((\delta\eta)^2) \tag{35}$$

where i is the grid index in η-direction with $\eta_i = i\delta\eta$; $i = 0, 1, 2, \ldots, m (=1/\delta\eta)$, and $\delta\eta$ is the increment along the η-axis. When the values of the dependent variables at the nth iteration are known, the corresponding values of these variables at the next iteration are obtained by using the relation

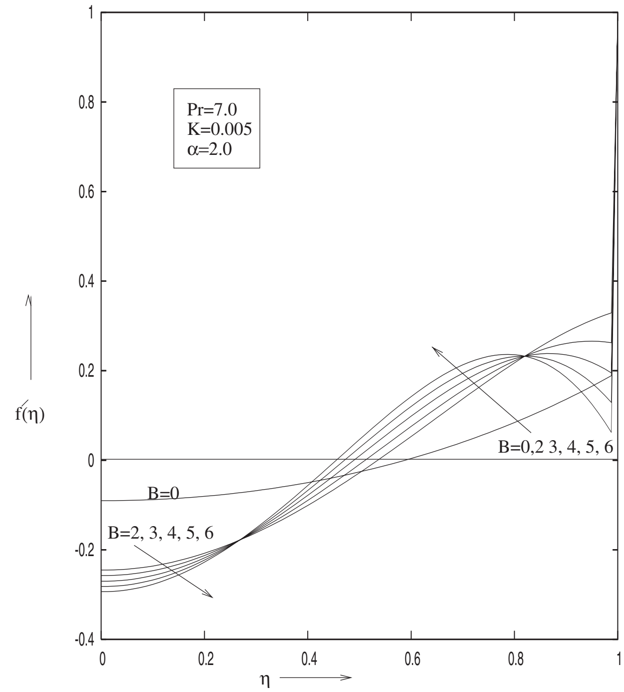

Fig. 2 Variation of $f'(\eta)$ for different values of B

$$F_i^{n+1} = F_i^n + (\Delta F_i)^n \tag{36}$$

where $(\Delta F_i)^n$ represents the error at the nth iteration, $i = 0, 1, 2, \ldots, m$. Here it is worthwhile to mention that the error $(\Delta F_i)^n$ at the boundary is zero because the values of F_i at the boundary are known.

Since Eq. (20) is highly nonlinear, it had to be solved for f by using the numerical solution of Eqs. (28) and (29), together with the use of Eq. (27). After having determined f numerically, we solved Eqs. (22)–(24) subject to the boundary conditions (25) and (26) using a suitable finite difference scheme that we have developed for this purpose.

5 Results and Discussion

We have determined theoretical estimates of the effects of the externally applied magnetic field generated by the magnetic dipole and also that of blood visco-elasticity on velocity, temperature, pressure, skin friction, and the rate of heat transfer in the flow of an electrically nonconducting fluid in a channel whose walls are stretchable.

As an illustrative example, we take up the case where the fluid is the representative of blood for which $\rho = 1050$ kg m^{-3} and $\mu = 3.2 \times 10^{-3}$ kg m^{-1} s^{-1}. The numerical investigation was carried out with an aim to examine the variations of various quantities (relevant to the present study) for different cases, by using the data: B in unit of $T = 0, 2, 3, 4, 5, 6$; $K = 0.0, 0.005, 0.01, 0.05$; $\alpha = 2.0, 2.5, 3.0$; and the Prandtl number Pr=7, 14, 21; $\lambda = 0.01$ [11,16,23], where $\lambda = 0.01$ corresponds to a situation in which the source term due to viscous dissipation in the energy equation (4) is of marginal importance compared with the conduction and convection terms. The computational work was carried out by taking $\delta\eta = 0.0125$ with 81 grid points. It was noted that further reduction in the value of $\delta\eta$ does not bring about any significant change in the computed values.

The variation in the dimensionless velocity components $f'(\eta) (=u/cx)$ and $v = -f(\eta)$ is shown in Figs. 2–7 for a given cross section of the channel. It reveals from Figs. 2 and 4 that in the vicinity of the central line of the channel, the axial velocity u decreases as the value of the ferromagnetic interaction parameter

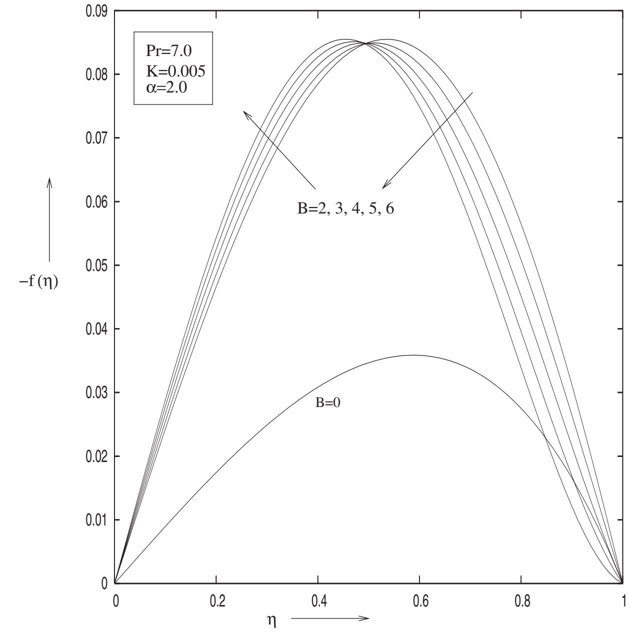

Fig. 3 Variation of $-f(\eta)$ for different values of B

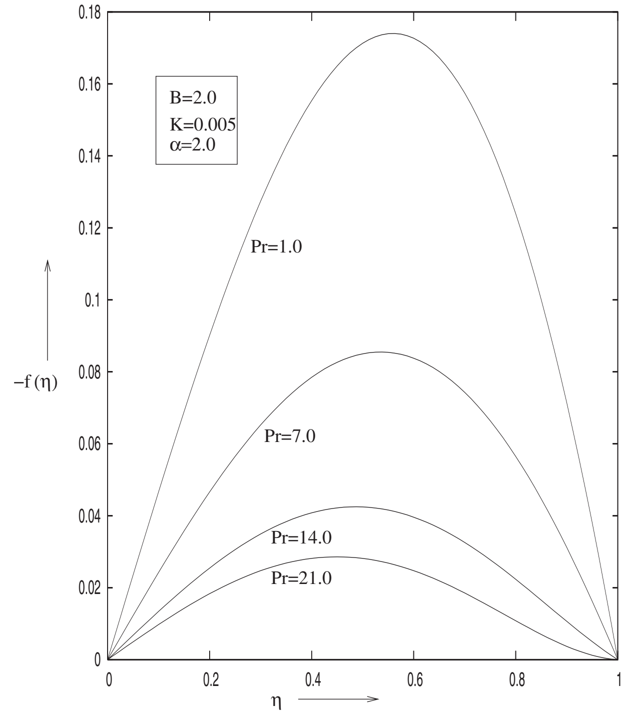

Fig. 5 Variation of $-f(\eta)$ for different values of Pr

B increases. It is, however, found that the velocity u in the axial direction of the channel increases in the vicinity of the channel wall. Figure 2 further reveals that u vanishes at different locations of the channel height for different values of B, and the point at which it vanishes can be shifted to the origin or eliminated altogether by applying a sufficiently strong magnetic field. Figure 4 indicates that u increases at the central line of the channel with the increase in the Prandtl number Pr but the trend is reversed near the channel wall.

It was shown in Ref. [4] that under the action of a magnetic field due to a magnetic dipole, the blood cells orient their disk plane parallel to the applied magnetic field. This orientation of blood cells creates an additional viscosity, which in turn causes a reduction in blood velocity. Our results presented in Fig. 2 agree with Ref. [4] to the extent that in the vicinity of the central line of the channel, the axial velocity u decreases with the increase in ferromagnetic interaction B.

Figure 6 gives the corresponding results for various locations of the magnetic dipole along the height of the channel wall. It may be noted that the axial velocity near the channel wall decreases with increasing distance α. Figures 3, 5, and 7 illustrate the variation in the velocity normal to the channel wall. Figures 5 and 7 show that the normal velocity decreases with the increase in Prandtl number, as well as the distance, while from Fig. 3 we find

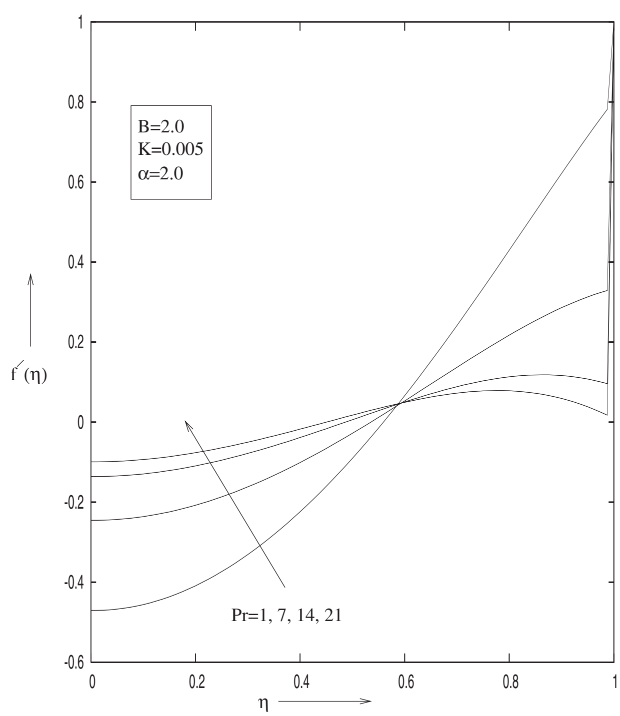

Fig. 4 Variation of $f'(\eta)$ for different values of Pr

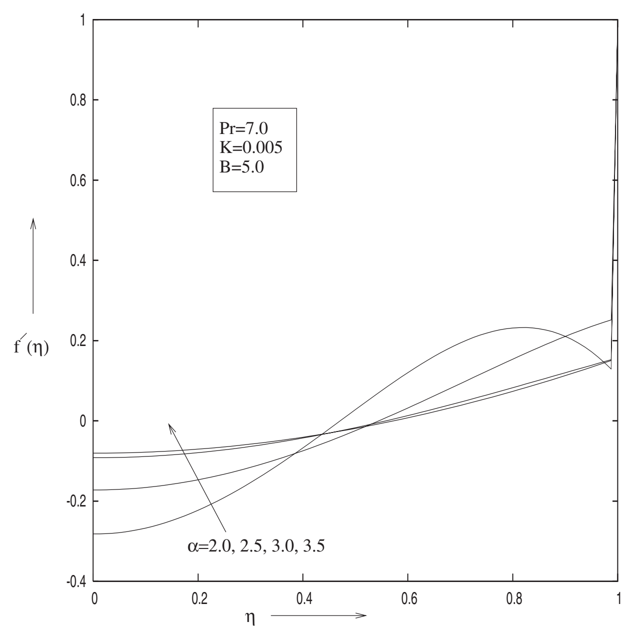

Fig. 6 Variation of $f'(\eta)$ for different values of α

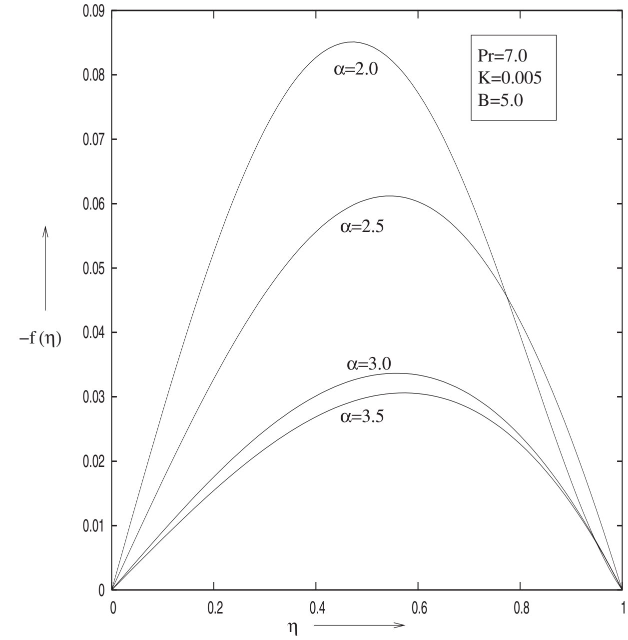

Fig. 7 Variation of $-f(\eta)$ for different values of α

that the normal velocity initially increases and after certain height of the channel, it decreases monotonically with the increase in the value of the ferromagnetic interaction parameter *B*.

Figures 8 and 9 depict some characteristic temperature profiles $\theta_1(\eta)$ for different values of the ferromagnetic interaction parameter *B* and Prandtl number Pr, respectively. It is observed from Fig. 8 that the temperature increases with the increase in ferromagnetic interaction. Figure 9 indicates that temperature also increases as the Prandtl number increases. Figures 10 and 11 give the pressure distribution for different values of *B* and Pr. From these two figures we find that the pressure decreases as the magnetic parameter *B* as well as the Prandtl number Pr increases.

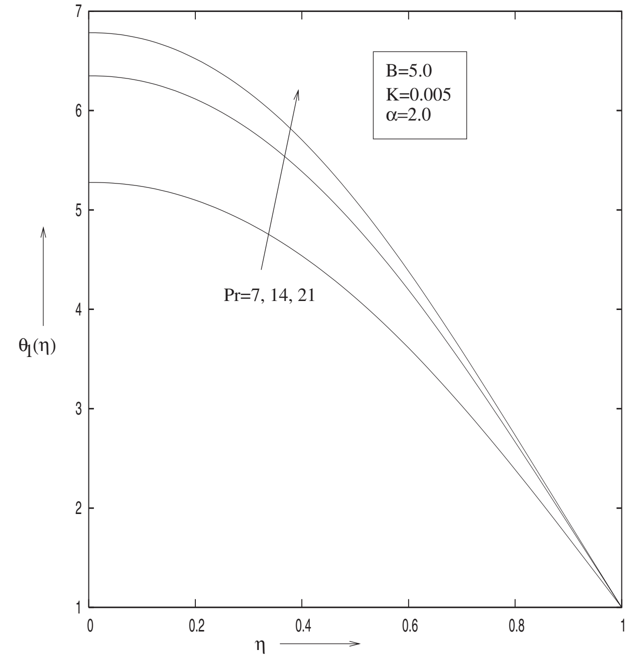

Fig. 9 Variation in temperature $\theta_1(\eta)$ for different values of Pr

The results presented in Fig. 8 have an important application in treatment of tumors/cancer therapy because the objective of hyperthemia in cancer therapy is to raise the temperature of cancerous tissues above a therapeutic value 42°C. When the temperature of blood rises above 42°C, irreversible damage occurs in plasma protein. Also the computational results presented in Fig. 10 are of considerable interest in clinical treatment related to controlling the blood pressure by the application of a magnetic field of sufficient intensity.

Other important characteristics of the present study are the local skin friction coefficient and the local rate of heat transfer defined as

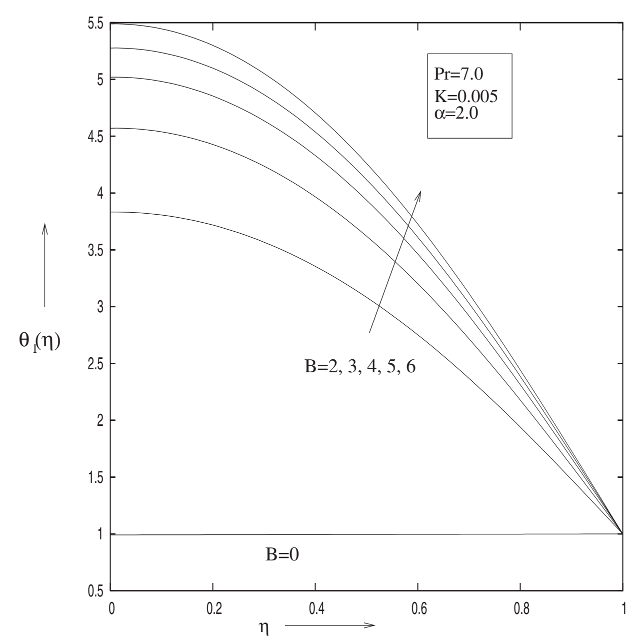

Fig. 8 Distribution of temperature (nondimensional) $\theta_1(\eta)$ for different values of *B*

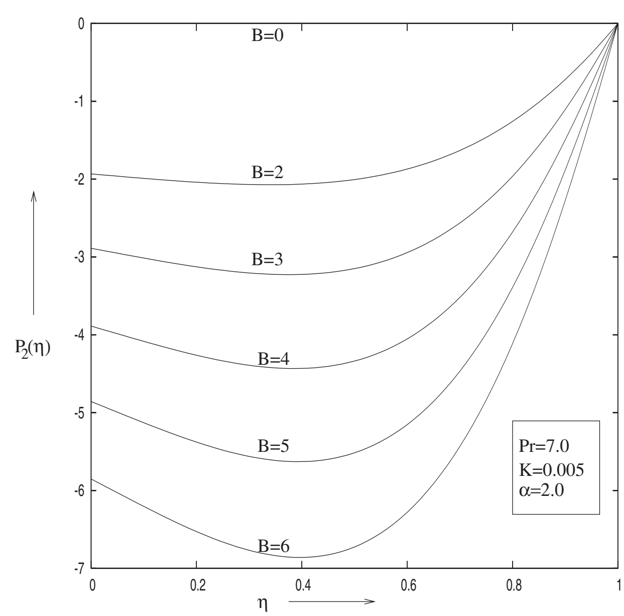

Fig. 10 Distribution of pressure (nondimensional) $P_2(\eta)$ with η for different values of *B*

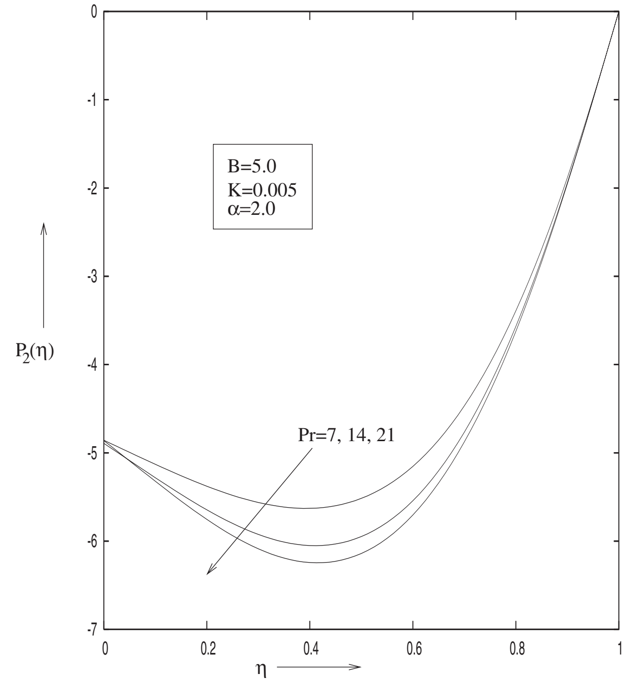

Fig. 11 Variation in pressure $P_2(\eta)$ for different values of Pr

$$C_{f_x} = \frac{2\tau_w}{\rho(cx)^2} = -\frac{2f''(1)}{\sqrt{\mathrm{Re}}}$$

and

$$\mathrm{Nu} = \frac{x}{T_w}\cdot\frac{\partial T}{\partial y}\Big|_{y=h} = [\theta_1'(1) + \xi^2\theta_2'(1)]\sqrt{\mathrm{Re}}$$

where $\tau_w = -\mu[\partial u/\partial y]_{y=h}$, $f''(1)$ is the local skin friction coefficient, and $[\theta_1'(1)+\xi^2\theta_2'(1)]$ is the dimensionless heat transfer at the wall. The rate of heat transfer at the channel wall can be measured by the ratio $\theta^*(1)=\theta_1'(1)/[\theta_1'(1)]_{B=0}$ because in the absence of ferromagnetic interaction, the pressure P_2 reduces to zero.

Table 1 gives the distribution of the local skin friction coefficient for different values of the parameters B, Pr, α, and K. From this table, one may observe that the skin friction increases with the increase in ferromagnetic interaction in a moderate range of values of the Prandtl number Pr. But when the Prandtl number is low, the skin friction initially decreases up to a certain value of B between 1 and 2, and then gradually increases with B. The skin friction also increases when the Prandtl number Pr increases. From the third row of Table 1, one may observe that for fixed values of Pr, α, and K, the skin friction coefficient increases with the increase in B. However, it decreases with the increase in blood visco-elasticity K when $B \leq 3$ and the trend reverses when $B \geq 4$. The skin friction coefficient decreases as the distance from the

Table 1 Distribution of local skin friction coefficient $-f''(1)$

Parameters		$B=0$	$B=1$	$B=2$	$B=4$	$B=5$	$B=6$
$\alpha=2.0$	Pr=7	−77.395994	−179.52341	−133.0739	−76.94855	−49.39606	−21.38254
$K=0.005$	Pr=14	−77.395994	−66.54988	−38.00444	−9.70572	45.49459	72.14398
	Pr=21	−77.395994	−34.73359	−5.76167	48.98430	74.81407	99.49153
$\alpha=2.0$	Pr=7	−82.046115	−181.91357	−139.54189	−82.18622	−53.27919	−24.546
$K=0.05$	Pr=14	−82.046115	−70.62743	−41.81759	18.85658	48.24579	77.06626
	Pr=21	−82.046115	−36.97695	−6.67133	52.55596	80.65434	107.75107
$\alpha=2.0$	$K=0.0$	−76.87867	−34.48445	−5.70979	48.53943	74.09306	98.47642
Pr=14	$K=0.005$	−77.39599	−34.73359	−5.76167	48.98430	74.81407	99.49153
	$K=0.05$	−82.046115	−36.97695	−6.67133	52.55596	80.65434	107.75107
	$K=0.1$	−87.20932	−39.49470	−7.53375	55.61875	85.69259	115.02139
Pr=21	$\alpha=2.0$	−76.87867	−34.48445	−5.70979	48.53943	74.09306	98.47642
$K=0.0$	$\alpha=2.5$	−76.87867	−58.52331	−52.56325	−42.63779	−37.60269	−32.64152
	$\alpha=3.0$	−76.87867	−62.29329	−59.92367	−55.18691	−52.81845	−50.38870

Table 2 Distribution of the heat transfer rate $\theta^*(1)=\theta_1'(1)/[\theta_1'(1)]_{B=0}$

		$B=0$	$B=2$	$B=3$	$B=4$	$B=5$	$B=6$
$\alpha=2.0$	Pr=7	1.0	−530.6556	−662.32774	−736.00279	−775.26103	−804.66786
$K=0.005$	Pr=14	1.0	−709.57064	−726.56335	−731.68992	−732.37450	−733.57310
	Pr=21	1.0	99.584556	96.688486	94.43694	92.295367	90.199851
$\alpha=2.0$	Pr=7	1.0	−422.1321	−535.22578	−590.46311	−624.04110	−644.91701
$K=0.05$	Pr=14	1.0	−512.08002	−532.88775	−537.76108	−537.94351	−538.02681
	Pr=21	1.0	200.70255	195.44699	190.79503	186.23810	181.865284
$\alpha=2.0$	$K=0.0$	1.0	92.927687	90.243765	88.147436	86.158125	84.208094
Pr=21	$K=0.005$	1.0	99.584556	96.688486	94.436945	92.295367	90.199850
	$K=0.05$	1.0	200.70255	195.44699	190.79503	186.23810	181.86528
	$K=0.1$	1.0	1049.4293	1019.7875	994.18145	968.13026	944.88598
Pr=21	$\alpha=2.0$	1.0	99.584556	96.688486	94.43694	92.295367	90.19985
$K=0.005$	$\alpha=2.5$	1.0	17.062519	15.118195	13.527832	12.82493	12.34450
	$\alpha=3.0$	1.0	9.132042	5.7278654	4.028502	3.011554	2.3477542

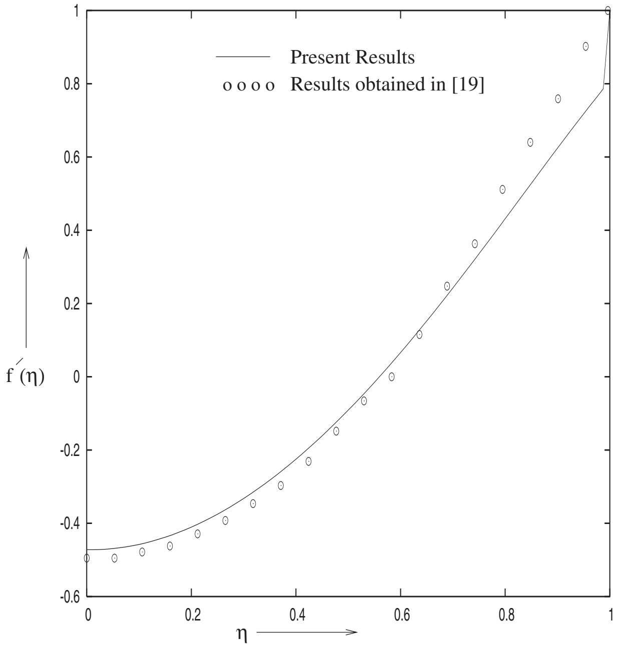

Fig. 12 Variation of $f'(\eta)$ with η when $B=0$, $K=0.005$, and Pr =1 in the present study

channel wall increases. It is also important to note from Table 1 that when $B=0$, the skin friction is the same for all values of the parameters Pr and α. However, the magnitude of the skin friction increases with the increase in the visco-elastic parameter K.

Table 2 gives the distribution of the heat transfer rate at the channel wall for different values of the various physical parameters. It is worthwhile to observe that for any particular values of Pr, K, and α, the rate of heat transfer decreases gradually as the ferromagnetic interaction increases. But the heat transfer rate increases with the increase in visco-elastic parameter K as well as with the Prandtl number Pr, while it decreases with distance (α). It may be noted that in a lower range of values of Pr (Pr<14), the heat transfer rate decreases with an increase in Prandtl number, but when Pr>14, the trend is reversed. This observation is valid only when the ferromagnetic parameter $B \leq 3$. It may also be noted that the heat transfer rate maintains a constant value, viz., 1.0 in the absence of ferromagnetic induction.

6 Conclusions

Of concern in this paper was the flow of a biomagnetic visco-elastic fluid (with special reference to blood) in a channel whose walls are stretchable, under the action of a magnetic field generated by a magnetic dipole. All the numerical results presented in Sec. 5 were computed for the flow of blood (as a representation of biomagnetic fluid) and the use of experimental data for blood reported in the existing literature was made in the computational work. The results reported here correspond to a mathematical model of BFD, which is based on the principles of FHD. An attempt was made to validate our results by comparing them with those presented in a previous work. Figure 12 shows very clearly that the results of the present study are in good conformity to those reported in Ref. [19]. The departure of the results of these two studies may be attributed to the coupling of temperature and velocity fields considered in the present study. In Fig. 12, the results presented correspond to the case when there is no applied magnetic field, both for Ref. [19] and for the present study. It is worthwhile to point out here that the physics of the study reported in Ref. [19] is identical to that of the present investigation. The difference is that Ref. [19] considers the channel flow of a magnetohydrodynamic fluid, while the fluid considered in the present study is a biomagnetic fluid. For the purpose of comparison, both studies were reduced to the case where the magnetic parameter is zero. It may be mentioned here that because of the variance of the two studies, the different physical parameters involved in one are different from those in the other, and comparison of the results for nonvanishing values of B was not possible. However, the results of Ref. [19] were compared with another previous study and the conformity was reported. In the scientific literature, no other similar study is available for the purpose of comparison for nonzero values of B.

The present analysis bears the potential to examine the complex flow behavior of blood, under the influence of the five physical parameters: B, Pr, K, α, and λ. The study reveals that the flow reversal can be eliminated, and the temperature of the vessel wall can be controlled by applying a magnetic field of sufficient strength. It also provides the information that the temperature increases gradually with the increase in ferromagnetic interaction. This observation is of paramount clinical importance in the process of hyperthemia (used in the treatment of cancer by therapeutic procedures).

Acknowledgment

The authors sincerely thank the referees for their kind words of appreciation about the work. Sincere thanks are also due to both of them for their very useful suggestions based on which the original manuscript has been revised to the present form. J.C.M. is thankful to the Council of Scientific and Industrial Research, New Delhi, while G.C.S. is thankful to the UGC, New Delhi for the financial support during this investigation.

Appendix

In derivation of Eqs. (20)–(26),

$$\frac{\partial u}{\partial x} = \frac{\partial u}{\partial \xi}\frac{\partial \xi}{\partial x} + \frac{\partial u}{\partial \eta}\frac{\partial \eta}{\partial x} = cf', \quad \frac{\partial^2 u}{\partial x^2} = \frac{\partial}{\partial x}\left(\frac{\partial u}{\partial x}\right) = 0, \quad \frac{\partial^3 u}{\partial x^3} = 0,$$

$$\frac{\partial u}{\partial y} = c\xi f'', \quad \frac{\partial^2 u}{\partial y^2} = \frac{c\xi}{h} f''', \quad \frac{\partial^2 u}{\partial x\,\partial y} = \frac{c}{h} f'',$$

$$\frac{\partial^3 u}{\partial x\,\partial y^2} = \frac{c}{h^2} f''', \quad \frac{\partial^2 u}{\partial x\,\partial y} = \frac{c}{h} f'', \quad \frac{\partial^3 u}{\partial x^2\,\partial y} = 0, \quad \frac{\partial^3 u}{\partial y^3} = \frac{c\xi}{h^2} f^{iv}$$

Similarly,

$$\frac{\partial v}{\partial x} = 0, \quad \frac{\partial v}{\partial y} = -cf', \quad \frac{\partial^2 v}{\partial x^2} = 0, \quad \frac{\partial^2 v}{\partial y^2} = -\frac{c}{h} f''$$

Also,

$$\frac{\partial T}{\partial x} = T_w \frac{\partial}{\partial \xi}(\theta_1 + \xi^2\theta_2)\frac{1}{h} = \frac{2\xi T_w}{h}\theta_2, \quad \frac{\partial^2 T}{\partial x^2} = \frac{2T_w}{h}\theta_2,$$

$$\frac{\partial T}{\partial y} = T_w \frac{\partial}{\partial \eta}(\theta_1 + \xi^2\theta_2)\frac{1}{h} = \frac{T_w}{h}(\theta_1' + \xi^2\theta_2'),$$

$$\frac{\partial^2 T}{\partial y^2} = \frac{T_w}{h^2}(\theta_1'' + \xi^2\theta_2'') \quad \text{and} \quad \frac{\partial M}{\partial T} = K_1, \quad \text{since} \quad M = K_1 T$$

Substituting all these in Eqs. (2)–(6), then equating the coefficients of ξ and ξ^2, and finally setting $\mu = c\rho h^2$, we obtain Eqs. (20)–(26).

References

[1] Higashi, T., Yamagishi, A., Takeuchi, T., Kawaguchi, N., Sagawa, S., Onishi, S., and Date, M., 1993, "Orientation of Erythrocytes in a Strong Static Magnetic Field," Blood, **82**, pp. 1328–1334.

[2] Pauling, L., and Cryell, C. D., 1936, "The Magnetic Properties and Structure of Hemoglobin," Proc. Natl. Acad. Sci. U.S.A., **22**, pp. 210–216.

[3] Haik, Y., Pai, V., and Chen, C. J., 1999, "Development of Magnetic Device for Cell Separation," J. Magn. Magn. Mater., **194**, pp. 254–261.

[4] Haik, Y., Pai, V., and Chen, C. J., 2001, "Apparent Viscosity of Human Blood

in a High Static Magnetic Field," J. Magn. Magn. Mater., **225**, pp. 180–186.
[5] Rosensweig, R. E., 1985, *Ferrohydrodynamics*, Cambridge University, Cambridge.
[6] Neuringer, J. L., and Rosensweig, R. E., 1964, "Ferrohydrodynamics," Phys. Fluids, **7**, pp. 1927–1937.
[7] Haik, Y., Chen, J. C., and Pai, V. M., 1996, "Development of Biomagnetic Fluid Dynamics," *Proceedings of the Ninth International Symposium on Transport Properties in Thermal Fluid Engineering*, S. H., Winoto, Y. T., Chew, and N. E., Wijeysundera, eds., HI, Jun. 25–28, pp. 121–126.
[8] Perry, M. P., 1972, "Thermomechanics," *Proceedings of the International Advanced Courses and Workshop*, pp. 219.
[9] Hiergeist, R., Andra, W., Buske, N., Hergt, R., Hilger, I., Richter, U., and Kaiser, W., 1999, "Application of Magnetic Ferrofluids for Hyperthemia," J. Magn. Magn. Mater., **201**, pp. 420–422.
[10] Voltairas, P. A., Fotiadis, D. I., and Michalis, L. K., 2002, "Hydrodynamics of Magnetic Drug Targeting," J. Biomech., **35**, pp. 813–821.
[11] Tzirtzilakis, E. E., and Kafoussias, N. G., 2003, "Biomagnetic Fluid Flow Over a Stretching Sheet With Non-Linear Temperature Dependent Magnetization," ZAMP, **54**, pp. 551–565.
[12] Loukopoulos, V. C., and Tzirtzilakis, E. E., 2004, "Biomagnetic Channel Flow in Spatially Varying Magnetic Field," Int. J. Eng. Sci., **42**, pp. 571–590.
[13] Papadopoulos, P. K., and Tzirtzilakis, E. E., 2004, "Biomagnetic Flow in a Curved Square Duct Under the Influence of an Applied Magnetic Field," Phys. Fluids, **16**, pp. 2952–2962.
[14] Tzirtzilakis, E. E., Xenos, M., Loukopoulos, V. C., and Kafoussias, N. G., 2006, "Turbulent Biomagnetic Fluid Flow in a Rectangular Channel Under the Action of a Localized Magnetic Field," Int. J. Eng. Sci., **44**, pp. 1205–1224.
[15] Tzirtzilakis, E. E., 2005, "A Mathematical Model for Blood Flow in Magnetic Field," Phys. Fluids, **17**, p. 077103.
[16] Andersson, H. I., and Valnes, O. A., 1998, "Flow of a Heated Ferrofluid Over a Stretching Sheet in the Presence of a Magnetic Dipole," Acta Mech., **128**, pp. 39–47.
[17] Misra, J. C., Shit, G. C., and Rath, H. J., 2008, "Flow and Heat Transfer of a MHD Viscoelastic Fluid in a Channel With Stretching Walls: Some Applications to Haemodynamics," Comput. Fluids, **37**, pp. 1–11.
[18] Misra, J. C., Pal, B., and Gupta, A. S., 1998, "Hydromagnetic Flow of a Second-Grade Fluid in a Channel—Some Applications to Physiological Systems," Math. Models Meth. Appl. Sci., **8**, pp. 1323–1342.
[19] Misra, J. C., and Pal, B., 1999, "Hydromagnetic Flow of a Viscoelastic Fluid in a Parallel Plate Channel With Stretching Walls," Indian J. Math., **41**, pp. 231–247.
[20] Andersson, H. I., 1992, "MHD Flow of a Viscoelastic Fluid Past a Stretching Surface," Acta Mech., **95**, pp. 227–230.
[21] Datti, P. S., Prasad, K. V., Abel, M. S., and Joshi, A., 2004, "MHD Viscoelastic Fluid Flow Over a Non-Isothermal Stretching Sheet," Int. J. Eng. Sci., **42**, pp. 935–946.
[22] Cortell, R., 2006, "A Note on Flow and Heat Transfer of a Viscoelastic Fluid Over a Stretching Sheet," Int. J. Non-Linear Mech., **41**, pp. 78–85.
[23] Rajagopal, K. R., Na, T. Y., and Gupta, A. S., 1984, "Flow of a Viscoelastic Fluid Over a Stretching Sheet," Rheol. Acta, **23**, pp. 213–215.
[24] Dandapat, B. S., and Gupta, A. S., 1989, "Flow and Heat Transfer in a Viscoelastic Fluid Over a Stretching Sheet," Int. J. Non-linear Mech., **24**, pp. 215–219.
[25] Andersson, H. I., Bech, K. H., and Dandapat, B. S., 1992, "Magnetohydrodynamic Flow of a Power-Law Fluid Over a Stretching Sheet," Int. J. Non-linear Mech., **27**, pp. 929–936.
[26] Mahmoud, M. A. A., and Mahmoud, M. A.-E., 2006, "Analytical Solutions of Hydromagnetic Boundary Layer Flow of a Non-Newtonian Power-Law Fluid Past a Continuously Moving Surface," Acta Mech., **181**, pp. 83–89.
[27] Andersson, H. I., and Dandapat, B. S., 1991, "Flow of a Power-Law Fluid Over a Stretching Sheet," Stability Appl. Anal. Continuous Media (SAACM) Italy, **1**, pp. 339–347.
[28] Dewhirst, M. W., and Samulski, T. V., 1988, "*Hyperthemia in the Treatment for Cancer*," Upjhon, Kalanazoo, MI.
[29] Craciunescu, O. I., and Clegg, S. T., 2001, "Pulsatile Blood Flow Effects on Temperature Distribution and Heat Transfer in Rigid Vessels," ASME J. Biomech. Eng., **123**, pp. 500–505.
[30] Weinbaun, S., Jiji, L. M., and Lemons, D. E., 1984, "Theory and Experiment for the Effect of Vascular Microstructure on Surface Tissue Heat Transfer—Part-I: Anatomical Foundation and Model Conceptualization," ASME J. Biomech. Eng., **106**, pp. 321–330.
[31] Beard, B. W., and Walters, K., 1964, "Elastico-Viscous Boundary Layer Flows," Proc. Cambridge Philos. Soc., **60**, pp. 667–6674.
[32] Labropulu, F., and Chinichian, M., 2004, "Unsteady Oscillatory Stagnation-Point Flow of a Viscoelastic Fluid," Int. J. Eng. Sci., **42**, pp. 625–633.
[33] Matsuki, H., Yamasawa, K., and Murakami, K., 1977, "Experimental Considerations on a New Automatic Cooling Device Using Temperature-Sensitive Magnetic Fluid," IEEE Trans. Magn., **13**, pp. 1143–1145.
[34] Crane, L. J., 1970, "Flow Past a Stretching Plate," Z. Angew. Math. Phys., **21**, pp. 645–647.

Theory of Images in Spherical-Layered Axisymmetric Viscous Hydrodynamics

K. Aderogba
Department of Mathematics,
University of Lagos,
Lagos 23401, Nigeria
e-mail: kanmiaderogba@yahoo.com

A spherical drop of viscosity $\mu^{(1)}$ and radius a_1 is surrounded by a spherical shell of viscosity $\mu^{(2)}$, internal radius a_1, and external radius a_2, beyond which there is an unbounded matrix fluid of viscosity $\mu^{(3)}$. An arbitrary axisymmetric singularity acts inside or outside the viscous spherical shell. It is established that the Stokes' stream function induced in this heterogeneous medium is explicitly expressible solely in terms of the corresponding stream function for the unperturbed homogeneous unbounded medium. As an application of the general solution, it is shown that there exists a homogeneous spherical drop of viscosity μ and radius a_2, which is equivalent to the spherical drop of viscosity $\mu^{(1)}$ and radius a_1, surrounded by the spherical shell of viscosity $\mu^{(2)}$ and outer radius a_2. A new formula is also established for the effective viscosity of a multiphase medium comprising an incompressible fluid of viscosity $\mu^{(3)}$ in which are embedded N small identical spherical drops of viscosity $\mu^{(1)}$, surrounded by spherical shells of viscosity $\mu^{(2)}$, assuming that the interference effects of these coated spherical drops are negligible, and that their arrangement is axisymmetrical. The corresponding two-dimensional results are also presented, by slightly modifying the three-dimensional results. [DOI: 10.1115/1.3130450]

Keywords: spherical drops, spherical shells, incompressible fluids, heterogeneous medium, Stokes' stream function

1 Introduction

The hydrodynamic circle theorem of Milne-Thomson [1] connects the complex potential due to the presence of an arbitrary two-dimensional singularity in an infinite inviscid fluid in the presence of a fixed rigid circular cylinder with the corresponding complex potential in the absence of the rigid cylinder, thus paving the way for a substantial reduction in effort in the calculation of field quantities. The theorem is essentially a method of images, which requires the specification of appropriate fictitious singularities at the images of an influencing point in a continuum with a given boundary, and which are then superposed on the initial influencing singularity in order to satisfy the required boundary conditions.

The three-dimensional counterpart of this circle theorem is the sphere theorem of Weiss [2], which expresses the velocity potential induced in an infinite inviscid fluid perturbed by a fixed rigid sphere in terms of the corresponding velocity potential in the absence of the rigid sphere, again when the influencing three-dimensional singularity is arbitrary. An axisymmetrical version of Weiss' sphere theorem has been furnished by Butler [3], using Stokes' stream function.

The present paper is a generalization of a mathematically analogous theorem of Collins [4], which also explicitly expresses the stream function of Stokes [5] due to the presence of an arbitrary axisymmetric singularity in an incompressible infinite viscous fluid disturbed by a fixed rigid sphere in terms of the corresponding stream function in the absence of the fixed rigid sphere.

Specifically, we assume that a spherical drop of viscosity $\mu^{(1)}$ is surrounded by a concentric spherical shell of viscosity $\mu^{(2)}$, beyond which there is an infinite incompressible homogeneous fluid of viscosity $\mu^{(3)}$. An arbitrary axisymmetric singularity, such as a source or an axial Stokeslet, acts inside or outside the viscous spherical shell. It is desired to express the induced Stokes' stream function in this heterogeneous medium *solely* in terms of the corresponding stream function for the unperturbed homogeneous infinite medium. The determination of the precise form of this unique dependence is facilitated by a complete theory of hydrodynamical images in the special case of two incompressible immiscible viscous fluids separated by a spherical surface, under the influence of an arbitrary axisymmetric singularity located in the interior of one of them. A systematic stepwise application of this theory at the two concentric spherical interfaces in the original three-phase fluid problem then yields the desired unique relationship between the disturbed and undisturbed stream functions.

The origin of this repeated reflection method belongs to Maxwell ([6], p. 443) in his elegant concise treatment of electrical conduction through a thick dielectric plate separating two other dissimilar semi-infinite dielectric media. Although his most important achievement appears to be his extension and mathematical formulation of Michael Faraday's theories of electricity and magnetic lines of force, he ([6], p. 438) also considered the analogous problem of electrical conduction through a thick dielectric spherical shell separating two other dissimilar dielectric media, but expressed the desired three electrostatic potentials in series of spherical harmonics of positive and negative degrees. His series expansion method of solution to this particular problem, instead of his powerful method of images, must have been prompted, if we are not missing something, by the fact that while his aforementioned case of three plane-layered dielectric materials requires only the process of simple superposition of singularities of the *same* type, involving no differentiation or integration, the generalized case of a composite comprising any number of strata bounded by concentric spherical interfaces, including even the special case of two spherical-layered media, requires the two operations of differentiation and integration, because unpredictable singularities of *different* types now have to be superposed. However, as shown by Maxwell ([6], p. 266), the case of two *uninsu-*

Contributed by the Applied Mechanics Division of ASME for publication in the JOURNAL OF APPLIED MECHANICS. Manuscript received November 19, 2007; final manuscript received February 9, 2009; published online July 23, 2009. Review conducted by Nesreen Ghaddar.

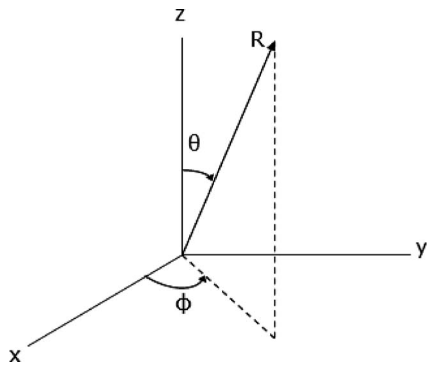

Fig. 1 Spherical polar coordinates

lated concentric spherical surfaces, subject to the induction of an electrified point placed between them, requires no differention or integration in the application of the method of repeated reflection. Therefore, the application of the method of repeated reflection appears to be inextricably tied not only to the conditions that must be fulfilled at the surface of separation between two media, but also on the geometry of the interface.

Perhaps it may be mentioned that Aderogba [7,8] recently considered two elastostatic counterparts of the present problem when the two concentric spherical interfaces are replaced with two parallel planes.

2 Formulation

Let x, y, and z be the three-dimensional rectangular Cartesian coordinates, which are connected with the spherical polar coordinates R, θ, and ϕ through the relations $x=R\sin\theta\cos\phi$, $y=R\sin\theta\sin\phi$, and $z=R\cos\theta$, as shown in Fig. 1.

We suppose that the three regions $0<R<a_1$, $a_1<R<a_2$, and $a_2<R<\infty$ are occupied by incompressible immiscible fluids of viscosities $\mu^{(1)}$, $\mu^{(2)}$, and $\mu^{(3)}$, respectively, the interfaces $R=a_1$ and $R=a_2$ being assumed to be permanently spherical, due to the action of surface tension.

In the usual indicial notation and summation convention, with $x=x_1$, $y=x_2$, and $z=x_3$, the equations governing the motion of each fluid are

$$U_{i,i}=0 \tag{1}$$

$$\sigma_{ij}=-P\delta_{ij}+\mu(U_{i,j}+U_{j,i}) \tag{2}$$

$$\mu\nabla^2U_i=P_{,i} \tag{3}$$

where U_i, σ_{ij}, and P are the velocity, stress, and pressure fields, respectively, while ∇^2 and δ_{ij} stand for the Laplacian operator and Kronecker delta.

When the motion of the multiphase medium is axisymmetrical, the foregoing equations are to be accompanied by the continuity conditions

$$\begin{gathered} U_R{}^{(1)}=0, \quad U_R{}^{(2)}=0 \\ U_\theta{}^{(1)}=U_\theta{}^{(2)}, \quad \sigma_{R\theta}{}^{(1)}=\sigma_{R\theta}{}^{(2)} \end{gathered} \tag{4}$$

at $R=a_1$, for all θ, and the similar conditions

$$\begin{gathered} U_R{}^{(2)}=0, \quad U_R{}^{(3)}=0 \\ U_\theta{}^{(2)}=U_\theta{}^{(3)}, \quad \sigma_{R\theta}{}^{(2)}=\sigma_{R\theta}{}^{(3)} \end{gathered} \tag{5}$$

at $R=a_2$, again for all θ, the superscripts 1, 2, and 3 in round brackets being used to distinguish between the fluids occupying $0<R<a_1$, $a_1<R<a_2$, and $a_2<R<\infty$, respectively. Generally, for axisymmetrical motion,

$$\begin{gathered} U_R=\frac{1}{R^2}\frac{\partial\Psi}{\partial q}, \quad U_\theta=\frac{1}{R(1-q^2)^{1/2}}\frac{\partial\Psi}{\partial R} \\ \sigma_{RR}=2\mu\frac{\partial U_R}{\partial q}-P, \quad \sigma_{\theta\theta}=2\mu\left[U_R-(1-q^2)^{1/2}\frac{\partial U_\theta}{\partial q}\right]\frac{1}{R}-P \\ \sigma_{\phi\phi}=2\mu\left[U_R+q(1-q^2)^{-1/2}U_\theta\right]\frac{1}{R}-P \\ \sigma_{R\theta}=-\mu\left[1/R(1-q^2)^{1/2}\frac{\partial U_R}{\partial q}-\frac{\partial U_\theta}{\partial R}+\frac{1}{R}U_\theta\right] \end{gathered} \tag{6}$$

where $q=\cos\theta=z/R$, while Stokes' stream function Ψ satisfies the equation

$$\Delta^4\Psi=\left[\frac{\partial^2}{\partial R^2}+\frac{1}{R^2}(1-q^2)\frac{\partial^2}{\partial q^2}\right]^2\Psi=0 \tag{7}$$

Henceforth, in the interest of brevity and consistency, it is helpful at the outset to introduce the contractions

$$\alpha^{(ij)}=\mu^{(i)}/(\mu^{(i)}+\mu^{(j)}), \quad \lambda=(a_1/a_2)^2 \tag{8}$$

as well as the *differential operators*

$$\begin{gathered} L^{(21)}(R)=[-1+\alpha^{(12)}L_1(R)](R/a_1)^3, \quad \pounds^{(21)}(R)=\alpha^{(21)}L_1(R) \\ L^{(23)}(R)=[-1+\alpha^{(32)}L_2(R)](R/a_2)^3, \quad \pounds^{(23)}(R)=\alpha^{(23)}L_2(R) \\ L^{(32)}(R)=\alpha^{(32)}L_2(R), \quad \pounds^{(32)}(R)=[-1+\alpha^{(23)}L_2(R)](R/a_2)^3 \\ L_i(R)=\left(1-\frac{R^2}{a_i{}^2}\right)\left[\frac{3}{2}-R\frac{\partial}{\partial R}-\frac{1}{4}(a_i{}^2-R^2)\Delta^2\right], \quad i=1,2 \end{gathered} \tag{9}$$

which facilitate the routine generation of additional stream functions from a given stream function.

Specifically, if any function $G(R,\theta)$ satisfies the equation $\Delta^4G(R,\theta)=0$, then the functions $L^{(21)}(R)G(a_1{}^2/R,\theta)$, $\pounds^{(21)}(R)G(R,\theta)$, $L^{(23)}(R)G(a_2{}^2/R,\theta)$, $L^{(32)}(R)G(R,\theta)$, $\pounds^{(23)}(R)G(R,\theta)$, and $\pounds^{(32)}(R)G(a_2{}^2/R,\theta)$ also satisfy the same equation.

This new theorem is analogous to Kelvin's transformation theorem of generating additional harmonic functions from a given harmonic function, and to the corresponding biharmonic analogy that *the biharmonicity of a three-dimensional function* $F(R,\theta,\Phi)$ implies the biharmonicity of the functions

$$RF\left(\frac{a^2}{R},\theta,\Phi\right),(R^2-a^2)\left[1-2R\frac{\partial}{\partial R}+\frac{1}{2}(R^2-a^2)\nabla^2\right]F(R,\theta,\Phi)$$

$$(R^2-a^2)\left[F(R,\theta,\Phi)-\frac{1}{4}(R^2-a^2)R^{-3/2}\int R^{1/2}\nabla^2F(R,\theta,\Phi)dR\right]$$

The theorem leads directly to a fundamental theorem in axisymmetric viscous flow, which will be repeatedly invoked in deriving all subsequent formulas; it may be stated as follows.

If there is a general axisymmetrical flow of an incompressible homogeneous viscous unbounded fluid, with *no* disturbing obstacles, characterized by the stream function $\Psi(R,\theta)$, all of whose singularities are at a distance greater than a_1 from the origin, then on introducing a different immiscible incompressible viscous fluid into the region $R<a_1$, so that the continuity conditions (4) are

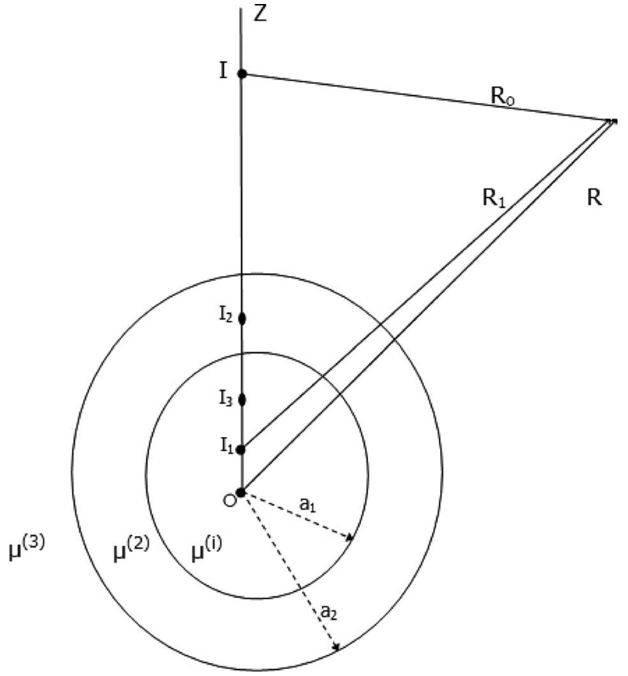

Fig. 2 Geometry of problem with singularity in third medium

satisfied at the interface $R=a_1$; the new stream functions for the two phases are

$$\begin{aligned}\Psi^{(1)} &= \pounds^{(21)}(R)\Psi(R,\theta)\\ \Psi^{(2)} &= \Psi(R,\theta) + L^{(21)}(R)\Psi\left(\frac{a_1{}^2}{R},\theta\right)\end{aligned} \tag{10}$$

where $\pounds^{(21)}(R)$ and $L^{(21)}(R)$ are given by Eq. (9), while it is assumed that the fluid occupying the region $0<R<a_1$ is of viscosity $\mu^{(i)}$, whereas the fluid occupying the region $a_1<R<\infty$ is of viscosity $\mu^{(2)}$.

The hydrodynamical current at any point of the first medium is thus the same as would have been produced by a combination of appropriate singularities placed at the influencing point I if the first medium had been infinite, while the current at any point of the second medium is the same as would have been produced by the influencing singularity at I, *together* with a combination of another group of appropriate singularities placed at the image point I_1 of I in $R=a_1$ if the second medium had been infinite.

If we suppose the first medium is a gas, then $\mu^{(1)}=0$, and the hydrodynamical action in the space occupied by the gas is less than it would otherwise be, whatever be the nature of the influencing singularity in the matrix medium, because we then simply have $\Psi^{(1)}=L_1(R)\Psi(R,\theta)$.

If we suppose the first medium is rigid, then $\mu^{(1)}=\infty$, and we readily recover from Eq. (10) Collin's [4] formula for an arbitrary axisymmetrical viscous flow past a fixed rigid spherical solid.

In passing, we must emphasize again that, here and henceforth, $L^{(ij)}$ and $\pounds^{(ij)}$ are envisaged as differential operators in manipulations, and not as functions.

3 Singularities in Outer Medium

We shall first consider the exterior problem in which an unbounded matrix fluid of viscosity $\mu^{(3)}$ is under the influence of an arbitrary axisymmetric singularity, which in an unperturbed infinite fluid is characterized by Stokes' stream function $\Psi(R,\theta)$. The singularity is located at I, as shown in Fig. 2, with I_1 standing for its image in $R=a_1$, while I_2 designates its image in $R=a_2$. I_3 is the image of I_2 in $R=a_1$, and vice-versa, and so on.

We wish to determine the induced stream functions $\Psi^{(1)}$, $\Psi^{(2)}$, and $\Psi^{(3)}$ in the three regions $0\le R\le a_1$, $a_1\le R\le a_2$, and $a_2\le R\le\infty$, respectively, consistent with the continuity conditions (4) and (5). We shall accomplish this seemingly tedious task in a systematic stepwise fashion, by disregarding each interface $R=a_1$ and $R=a_2$ in turn.

First, we discountenance the interface $R=a_1$ and invoke Eq. (10) to confirm that the continuity conditions (5) are completely satisfied when $R=a_2$ if we select the construction

$$\begin{aligned}\Psi^{(2)} &= L^{(32)}(R)\Psi(R,\theta)\\ \Psi^{(3)} &= \Psi(R,\theta) + \pounds^{(32)}(R)\Psi\left(\frac{a_2{}^2}{R},\theta\right)\end{aligned} \tag{11}$$

where $L^{(32)}$ and $\pounds^{(32)}$ are once again given by Eq. (9).

Next, we disregard the interface $R=a_2$, adopt Eq. (11) as the inducing field, and again invoke Eq. (10) to confirm that the continuity conditions (4) at the interface $R=a_1$ are completely satisfied by the second construction

$$\begin{aligned}\Psi^{(1)} &= \pounds^{(21)}(R)L^{(32)}(R)\Psi(R,\theta)\\ \Psi^{(2)} &= L^{(32)}(R)\Psi(R,\theta) + L^{(21)}(R)L^{(32)}\left(\frac{a_1{}^2}{R}\right)\Psi\left(\frac{a_1{}^2}{R},\theta\right)\end{aligned} \tag{12}$$

This second construction, in turn, upsets the continuity conditions (5) at the second interface $R=a_2$, and therefore demands a modification of our construction, guided again by the fact that Stokes' stream function in the outer medium must vanish at an infinite distance from the origin, leading to the third construction

$$\begin{aligned}\Psi^{(2)} &= L^{(32)}(R)\Psi(R,\theta) + L^{(21)}(R)L^{(32)}\left(\frac{a_1{}^2}{R}\right)\Psi\left(\frac{a_1{}^2}{R},\theta\right)\\ &\quad + L^{(23)}(R)L^{(21)}\left(\frac{a_2{}^2}{R}\right)L^{(32)}(\lambda R)\Psi(\lambda R,\theta)\\ \Psi^{(3)} &= \Psi(R,\theta) + \pounds^{(32)}(R)\Psi\left(\frac{a_2{}^2}{R},\theta\right) + \pounds^{(23)}(R)L^{(21)}(R)L^{(32)}\\ &\quad \times\left(\frac{a_1{}^2}{R}\right)\Psi\left(\frac{a_1{}^2}{R},\theta\right)\end{aligned} \tag{13}$$

where λ is once again given by Eq. (8).

This straightforward stepwise process of satisfying the continuity conditions at the concentric spherical interfaces can obviously be continued indefinitely.

If we put

$$\begin{aligned}L^{(n)}(R) &= L^{(21)}(R)L^{(23)}\left(\frac{a_1{}^2}{R}\right)L^{(21)}\left(\frac{R}{\lambda}\right)\cdots L^{(23)}\left(\frac{a_1{}^2\lambda^{n-2}}{R}\right)L^{(21)}\\ &\quad \times\left(\frac{R}{\lambda^{n-1}}\right)\end{aligned} \tag{14}$$

so that $L^{(1)}(R)=L^{(21)}(R)$, $L^{(2)}(R)=L^{(21)}(R)L^{(23)}(a_1{}^2/R)L^{(21)}(R/\lambda)$, and so on, then we find that the desired complete stream functions in the three media admit the structured series representations

$$\begin{aligned}\Psi^{(1)} = \pounds^{(21)}(R)\Bigg[& L^{(32)}(R)\Psi(R,\theta) + L^{(23)}(R)\sum_{n=1}^{\infty} L^{(n)}\left(\frac{a_2{}^2}{R}\right)L^{(32)}\\ & \times(\lambda^n R)\Psi(\lambda^n R,\theta)\Bigg]\end{aligned}$$

$$\Psi^{(2)} = L^{(32)}(R)\Psi(R,\theta) + \sum_{n=1}^{\infty} L^{(n)}(R)L^{(32)}\left(\frac{a_1{}^2\lambda^{n-1}}{R}\right)\Psi\left(\frac{a_1{}^2\lambda^{n-1}}{R},\theta\right) + L^{(23)}(R)\sum_{n=1}^{\infty} L^{(n)}\left(\frac{a_2{}^2}{R}\right)L^{(32)}(\lambda^n R)\Psi(\lambda^n R,\theta) \quad (15)$$

$$\Psi^{(3)} = \Psi(R,\theta) + \pounds^{(32)}(R)\Psi\left(\frac{a_2{}^2}{R},\theta\right) + \pounds^{(23)}(R)\sum_{n=1}^{\infty} L^{(n)}(R)L^{(32)} \times\left(\frac{a_1{}^2\lambda^{n-1}}{R}\right)\Psi\left(\frac{a_1{}^2\lambda^{n-1}}{R},\theta\right)$$

Collin's [4] case of a fixed rigid sphere disturbing an arbitrary axisymmetric flow may be deduced from Eq. (15) by making $a_1=0$ and $\mu^{(2)}=\infty$, and the stream functions then become

$$\Psi^{(1)} = 0, \quad \Psi^{(2)} = 0$$

$$\Psi^{(3)} = \Psi(R,\theta) - \left[1 - \left(1 - \frac{R^2}{a_2{}^2}\right)\left\{\frac{3}{2} - R\frac{\partial}{\partial R} - \frac{1}{4}(a_2{}^2 - R^2)\Delta^2\right\}\right] \times\left(\frac{R}{a_2}\right)^3\Psi\left(\frac{a_2{}^2}{R},\theta\right)\Bigg\}$$

which ensure the satisfaction of the no-slip condition at the spherical surface.

$R=a_2$. Alternatively, we can simply say that if the spherical shell is *more* viscous than the rest of the multiphase medium, then it has the effect of annulling the stream function all round the inner sphere.

The case when the space occupied by the concentric spherical shell is filled with gas may also be deduced from Eq. (15) by setting $\mu^{(2)}=0$, yielding the results

$$\Psi^{(1)} = 0$$

$$\Psi^{(2)} = L_2(R)\Psi(R,\theta) + \sum_{n=1}^{\infty} \pounds^{(n)}(R)L_2\left(\frac{a_1{}^2\lambda^{n-1}}{R}\right)\Psi\left(\frac{a_1{}^2\lambda^{n-1}}{R},\theta\right) + [L_2(R) - 1](R/a_2)^3\sum_{n=1}^{\infty} \pounds^{(n)}\left(\frac{a_2{}^2}{R}\right)L_2(\lambda^n R)\Psi(\lambda^n R,\theta,) \quad (16)$$

$$\Psi^{(3)} = \Psi(R,\theta) - (R/a_2)^3\Psi\left(\frac{a_2{}^2}{R},\theta\right)$$

where, for any positive integer n,

$$\pounds^{(n)}(R) = \pounds_1(R)\pounds_2\left(\frac{a_1{}^2}{R}\right)\pounds_1\left(\frac{R}{\lambda}\right)\cdots\pounds_2\left(\frac{a_1{}^2\lambda^{n-2}}{R}\right)\pounds_1(R\lambda^{1-n})$$

$$\pounds_1(R) = [-1 + L_1(R)](R/a_1)^3, \quad \pounds_2(R) = [-1 + L_2(R)](R/a_2)^3 \quad (17)$$

It follows from an examination of Eq. (16); therefore, that if the space $a_1 \le R \le a_2$ occupied by the spherical shell is filled with gas, then it tends to prevent hydrodynamical currents from reaching the inner spherical drop at all, and the hydrodynamical action in the outer medium is less than it would otherwise be, whatever be the physical nature of the influencing singularity.

4 Singularities in Inner Medium

Maxwell's method of repeated reflection is also readily applicable to the case when the arbitrary axisymmetric influencing singularity is operative inside the inner spherical drop of viscosity $\mu^{(1)}$. Again, let this singularity be characterized in an unbounded and undisturbed homogeneous fluid by $\Psi(R,\theta)$, and let us put

$$L^{(12)}(R) = \alpha^{(12)}L_1(R), \quad \pounds^{(12)}(R) = [-1 + \alpha^{(21)}L_1(R)](R/a_1)^3 \quad (18)$$

$$\Omega^{(n)}(R) = L^{(23)}(R)L^{(21)}\left(\frac{a_2{}^2}{R}\right)L^{(23)}(\lambda R)\ldots L^{(21)}\left(\frac{a_2{}^2\lambda^{2-n}}{R}\right)L^{(23)} \times(\lambda^{n-1}R)$$

Then, it may be readily established by repeated imaging that the stream functions induced in the three media by the arbitrary axisymmetric singularity located in the inner spherical medium are given by

$$\Psi^{(1)} = \Psi(R,\theta) + \pounds^{(12)}(R)\Psi\left(\frac{a_1^2}{R},\theta\right) + \pounds^{(21)}(R)\sum_{n=1}^{\infty}\Omega^{(n)}(R)L^{(12)} \times\left(\frac{a_2^2\lambda^{1-n}}{R}\right)\Psi\left(\frac{a_2^2\lambda^{1-n}}{R},\theta\right)$$

$$\Psi^{(2)} = L^{(12)}(R)\Psi(R,\theta) + \sum_{n=1}^{\infty}\Omega^{(n)}(R)L^{(12)}\left(\frac{a_2{}^2\lambda^{1-n}}{R}\right)\Psi\left(\frac{a_2{}^2\lambda^{1-n}}{R},\theta\right) + L^{(21)}(R)\sum_{n=1}^{\infty}\Omega^{(n)}\left(\frac{a_1{}^2}{R}\right)L^{(12)}\left(\frac{R}{\lambda^n}\right)\Psi\left(\frac{R}{\lambda^n},\theta\right) \quad (19)$$

$$\Psi^{(3)} = \pounds^{(23)}(R)\left[L^{(12)}(R)\Psi(R,\theta) + L^{(21)}(R)\sum_{n=1}^{\infty}\Omega^{(n)}\left(\frac{a_1{}^2}{R}\right)L^{(12)} \times\left(\frac{R}{\lambda^n}\right)\Psi\left(\frac{R}{\lambda^n},\theta\right)\right]$$

where the *differential* operators $L^{(ij)}$ and $\pounds^{(ij)}$ are as previously defined.

The special case when the intervening space $a_1 \le R \le a_2$ is occupied by gas ($\mu^{(2)}=0$) therefore reduces the stream functions (19) to

$$\Psi^{(1)} = \Psi(R,\theta) - (R/a_1)^3\Psi\left(\frac{a_1{}^2}{R},\theta\right)$$

$$\Psi^{(2)} = L_1(R)\Psi(R,\theta) + \sum_{n=1}^{\infty}\Omega_o^{(n)}(R)L_1\left(\frac{a_2^2\lambda^{1-n}}{R}\right)\Psi\left(\frac{a_2^2\lambda^{1-n}}{R},\theta\right) + \pounds_1(R)\sum_{n=1}^{\infty}\Omega_o^{(n)}\left(\frac{a_1^2}{R}\right)L_1\left(\frac{R}{\lambda^n}\right)\Psi\left(\frac{R}{\lambda^n},\theta\right) \quad (20)$$

$$\Psi^{(3)} = o$$

where $L_1(R)$ takes its value in Eq. (9), while

$$\Omega_o^{(n)}(R) = \pounds_2(R)\pounds_1\left(\frac{a_2{}^2}{R}\right)\pounds_2(\lambda R)\cdots\pounds_1\left(\frac{a_2{}^2\lambda^{2-n}}{R}\right)\pounds_2(\lambda^{n-1}R) \quad (21)$$

Thus, we see again from Eqs. (19) and (20), by virtue of the definitions of $L_1(R)$, $\pounds_1(R)$, $L^{(12)}(R)$, and $L^{(21)}(R)$, that whether the spherical shell is less or more viscous than the rest of the multiphase medium, the hydrodynamical action in the space occupied by the viscous concentric spherical shell is less than it would otherwise be.

It also follows from Eq. (19) that the dominant distant effect in the outer medium due to the presence of an arbitrary axisymmetric singularity in the inner medium is

$$\Psi_\infty^3 = \alpha^{(12)}\alpha^{(23)}L_2(R)L_1(R)\Psi(R,\theta)$$

It, therefore, appears that if there are $n+1$ spherical layers, with interfaces $R=a_1$, $R=a_2, \ldots, R=a_n$, the dominant distant effect in the outer medium of viscosity $\mu^{(n+1)}$ due to the specification of an arbitrary axisymmetric singularity in the inner medium of viscosity $\mu^{(1)}$ will be

$$\Psi_{\infty}^{(n+1)} = \alpha^{(12)}\alpha^{(23)}\alpha^{(34)}\cdots\alpha^{n(n+1)}L_n(R)L_{n-1}(R)\cdots L_1(R)\Psi(R,\theta)$$

5 Singularities in Interface Spherical Shell

We shall, finally, consider the case when an arbitrary axisymmetric singularity acts inside the fluid occupying the interface space $a_1 \le R \le a_2$, subject again to the assumption that this singularity in a homogeneous hydrodynamic medium of infinite extent is given by $\Psi(R,\theta)$. The singularity will form two infinite series of images, lying on the same radius as the influencing point, none of which lie within the spherical shell.

If we therefore proceed as in Sec. 2, then we will find that the induced stream functions are

$$\Psi^{(1)} = \pounds^{(21)}(R)\left[\Psi(R,\theta) + \sum_{n=1}^{\infty}\Omega^{(n)}(R)\left\{\Psi\left(\frac{a_2^2\lambda^{1-n}}{R},\theta\right) + L^{(21)}\left(\frac{a_2^2\lambda^{1-n}}{R}\right)\Psi(\lambda^n R,\theta)\right\}\right]$$

$$\begin{aligned}\Psi^{(2)} = {}& \Psi(R,\theta) + L^{(21)}(R)\Psi\left(\frac{a_1^2}{R},\theta\right) + \sum_{n=1}^{\infty}\Omega^{(n)}(R)\left[\Psi\left(\frac{a_2^2\lambda^{1-n}}{R},\theta\right)\right.\\ & \left. + L^{(21)}\left(\frac{a_2^2\lambda^{1-n}}{R}\right)\Psi(\lambda^n R,\theta)\right] + L^{(21)}(R)\sum_{n=1}^{\infty}\Omega^{(n)}\left(\frac{a_1^2}{R}\right)\\ & \times\left[\Psi\left(\frac{R}{\lambda^n},\theta\right) + L^{(21)}\left(\frac{R}{\lambda^n}\right)\Psi\left(\frac{a_1^2\lambda^n}{R},\theta\right)\right]\end{aligned} \tag{22}$$

$$\begin{aligned}\Psi^{(3)} = {}& \pounds_{23}(R)\left[\Psi(R,\theta) + L^{(21)}(R)\Psi\left(\frac{a_1^2}{R},\theta\right) + L^{(21)}(R)\sum_{n=1}^{\infty}\Omega^{(n)}\left(\frac{a_1^2}{R}\right)\right.\\ & \left.\times\left\{\Psi\left(\frac{R}{\lambda^n},\theta\right) + L^{(21)}\left(\frac{R}{\lambda^n}\right)\Psi\left(\frac{a_1^2\lambda^n}{R},\theta\right)\right\}\right]\end{aligned}$$

The case of an arbitrary axisymmetric singularity acting in a viscous fluid flowing between two no-slip concentric spherical surfaces may be deduced from Eq. (22) by making $\mu^{(1)}=\infty$ and $\mu^{(3)}=\infty$, yielding

$$\Psi^{(1)} = 0, \quad \Psi^{(3)} = 0$$

$$\begin{aligned}\Psi^{(2)} = {}& \Psi(R,\theta) + \pounds_1(R)\Psi\left(\frac{a_1^2}{R},\theta\right) + \sum_{n=1}^{\infty}\Omega_o^{(n)}(R)\left[\Psi\left(\frac{a_2^2\lambda^{1-n}}{R},\theta\right)\right.\\ & \left. + \pounds_1\left(\frac{a_2^2\lambda^{1-n}}{R}\right)\Psi(\lambda^n R,\theta)\right] + \pounds_1(R)\sum_{n=1}^{\infty}\Omega_o^{(n)}\left(\frac{a_1^2}{R}\right)\left[\Psi\left(\frac{R}{\lambda^n},\theta\right)\right.\\ & \left. + \pounds_1\left(\frac{R}{\lambda^n}\right)\Psi\left(\frac{a_1^2\lambda^n}{R},\theta\right)\right]\end{aligned} \tag{23}$$

where $\pounds_1(R)$ and $\Omega_o^{(n)}(R)$ are given by Eqs. (17) and (21), respectively.

6 Applications

An important application of the analysis in this paper is to the case of a spherical drop of viscosity $\mu^{(1)}$ and radius a_1, surrounded by a spherical shell of viscosity $\mu^{(2)}$, internal radius a_1, and external radius a_2 beyond which there is a matrix fluid of viscosity $\mu^{(3)}$ flowing uniformly at infinity with velocity $(0,0,-W)$. In this case, the stream function for the undisturbed uniform flow is

$$\Psi = \tfrac{1}{2}WR^2\sin^2\theta \tag{24}$$

If we now put

$$\begin{aligned}A = {}& \frac{\mu^{(1)}(1-\lambda^{1/2})(1+2\lambda^{1/2}+8\lambda+4\lambda^{3/2}) + 2\mu^{(2)}(1+\lambda^{1/2}+\lambda+\lambda^{3/2}+\lambda^2)}{[\mu^{(1)}(1-\lambda^{1/2})(1+3\lambda^{1/2}+\lambda)\{1-2\lambda^{1/2}-\alpha^{(32)}\lambda^{1/2}(1-2\lambda)\}}\\ & + \mu^{(1)}(1-\lambda^{1/2})(1+2\lambda^{1/2}+8\lambda+4\lambda^{3/2})\left\{1-\tfrac{1}{2}\alpha^{(32)}\lambda^{1/2}(1+\lambda^{1/2})\right\}\\ & + \mu^{(2)}\left\{2(1+\lambda^2+\lambda+\lambda^{3/2}+\lambda^2)\left(1-\tfrac{1}{2}\alpha^{(32)}\lambda^{1/2}(1+\lambda^{1/2})\right)\right.\\ & \left. - \alpha^{(32)}\lambda^{3/2}(1-\lambda^{1/2})(1+3\lambda^{1/2}+\lambda)\right\}\end{aligned} \tag{25a}$$

then the substitution of Eq. (24) into Eq. (14) shows that the stream function induced in the matrix medium of viscosity $\mu^{(3)}$ assumes the form

$$\Psi^{(3)} = \tfrac{1}{4}W[2R^2 - a_2R(2+A\alpha^{(23)}) + A{a_2}^3\alpha^{(23)}R^{-1}]\sin^2\theta \tag{25b}$$

which physically represents a combination of the direct effect of the applied uniform field with the effects of a Stokeslet in the z-direction and a point source, both singularities being located at the origin, outside the outer medium.

On the other hand, if a single spherical drop of viscosity μ_0 and radius a_2 is embedded in a matrix fluid of viscosity $\mu^{(3)}$ flowing uniformly at infinity with velocity $(0,0,-W)$, then the stream function induced in the matrix fluid is

$$\Psi^{(3)} = \tfrac{1}{2}W\left[R^2 - a_2R\left(1+\tfrac{1}{2}\alpha^{(03)}\right) + \tfrac{1}{2}\alpha^{(03)}({a_2}^3/R)\right]\sin^2\theta \tag{26}$$

It is therefore easy to show from Eqs. (25a), (25b), and (26) that the case of an embedded spherical drop of viscosity $\mu^{(1)}$, surrounded by a spherical shell of viscosity $\mu^{(2)}$, is the same as that of a homogeneous single spherical drop of the radius a_2 of the outer surface of the spherical shell, and of viscosity μ_0, provided that

$$\mu_0 = \frac{A\mu^{(2)}\mu^{(3)}}{(1-A)\mu^{(2)}+\mu^{(3)}} \tag{27}$$

By making $a_1=\mu^{(1)}=0$ in Eq. (25a), we deduce the expected result

$$\mu_0 = \mu^{(2)} \tag{28}$$

for the case of an embedded uncoated spherical drop of radius a_2.

Next, we suppose that there are N identical spherical drops of radius a_1 and viscosity $\mu^{(1)}$, each surrounded by a spherical shell of internal radius a_1 and external radius a_2 and viscosity $\mu^{(2)}$, placed in an incompressible medium of viscosity $\mu^{(3)}$, at such distances from each other that their interaction effects in disturbing the applied uniform flow $(0,0,-W)$ may be taken as independent of one another. Let all these surrounded spherical drops be enclosed within a sphere of radius a_3. Then, from Eq. (25b), the stream function induced in the matrix fluid of $\mu^{(3)}$ will be of the form

$$\Psi^{(3)} = \tfrac{1}{4}W[2R^2 - N\{a_2R(2+A\alpha^{(23)}) - A{a_2}^2\alpha^{(23)}R^{-1}\}]\sin^2\theta \tag{29}$$

If we put the ratio of the volume of the N small surrounded spherical drops to that of the sphere of radius a_3, which encloses them as

$$K = N(a_2/a_3)^3 \tag{30}$$

then the stream function (29) may be rewritten in the form

$$\Psi^{(3)} = \tfrac{1}{4}W[2R^2 - K{a_3}^3\{(R/{a_2}^2)(2+A\alpha^{(23)}) - A\alpha^{(23)}R^{-1}\}]\sin^2\theta \tag{31}$$

Now, if the enveloping sphere of radius a_3 had been composed of an incompressible fluid of viscosity $\mu^{(4)}$, then we should have had

$$\Psi^{(3)} = \tfrac{1}{4}W[2R^2 - a_3R(2+\alpha^{(43)}) + \alpha^{(43)}(a_3{}^3/R\ ]\sin^2\theta \quad (32)$$

Expression (31) may therefore be taken as equivalent to Eq. (32) if

$$\mu^{(4)} = \frac{AK\mu^{(2)}\mu^{(3)}}{(1-AK)\mu^{(2)}+\mu^{(3)}} \quad (33)$$

This $\mu^{(4)}$, therefore, is the effective viscosity of a multiphase medium comprising a fluid of viscosity $\mu^{(3)}$ in which are embedded, axisymmetrically, N small spherical drops of viscosity $\mu^{(1)}$ and radius a_1, surrounded by identical spherical shells of viscosity $\mu^{(2)}$, internal radius a_1, and external radius a_2, the ratio of the volume of the coated spherical drops to that of the whole being K.

The special case of a multiphase medium in which the matrix contains uncoated spherical drops, arranged axisymmetrically, may be obtained from Eq. (34) by making $a_1=0$, thereby obtaining

$$\mu^{(4)} = \frac{K\mu^{(2)}\mu^{(3)}}{(1-K)\mu^{(2)}+\mu^{(3)}} \quad (34)$$

while the further special case in which the dispersed spherical drops are rigid may also be deduced by making $\mu^{(2)}=\infty$, thereby obtaining

$$\mu^{(4)} = \frac{K}{1-K}\mu^{(3)} \quad (35)$$

7 Two-Dimensional Analogy

It is a straightforward exercise to pass from the solution of the foregoing three-dimensional problem to the solution of the corresponding two-dimensional problem.

Thus, let r and ϕ be the plane polar coordinates, which are connected with the rectangular Cartesian coordinates x and y through the relations $x=r\cos\phi$ and $y=r\sin\phi$. We suppose that the three regions $0<R<a_1$, $a_1<R<a_2$, and $a_2<r<\infty$ are occupied by immiscible incompressible fluids of viscosities $\mu^{(1)}$, $\mu^{(2)}$, and $\mu^{(3)}$, respectively, the interfaces $r=a_1$ and $r=a_2$ being assumed to be permanently circularly cylindrical, so that, at $r=a_1$, and for all ϕ,

$$U_r{}^{(1)}=0, \quad U_r{}^{(2)}=0$$
$$U_\phi{}^{(1)}=U_\phi{}^{(2)}, \quad \sigma_{r\phi}{}^{(1)}=\sigma_{r\phi}{}^{(2)} \quad (36)$$

and at $r=a_2$, and again for all ϕ,

$$U_r{}^{(2)}=0, \quad U_r{}^{(3)}=0$$
$$U_\phi{}^{(2)}=U_\phi{}^{(3)}, \quad \sigma_{r\phi}{}^{(2)}=\sigma_{r\phi}{}^{(3)} \quad (37)$$

It is well known that, in this two-dimensional case, a general solution of Eqs. (1) and (3) admits the representation

$$(u_1,u_2) = \left(-\frac{\partial\psi}{\partial y}, \frac{\partial\psi}{\partial x}\right)$$
$$P = \mu\int \nabla^2\frac{\partial\psi}{\partial x}dy \quad (38)$$

provided that

$$\nabla^4\Psi = 0, \quad \nabla^2 = \frac{\partial^2}{\partial x^2}+\frac{\partial^2}{\partial y^2} \quad (39)$$

Ψ being known now as Lagrange's stream function.

Also, apart from multiplicative constants, the functions

$$\left(f_1\frac{\partial}{\partial y} - f_2\frac{\partial}{\partial x}\right)r^2\log r, \quad \tan^{-1}(y/x), \quad \log r$$

represent, respectively, in a viscous fluid of infinite extent, the fundamental singularities, through the origin, corresponding to a line force (f_1,f_2), a line source, and a semi-infinite plane of source doublets.

Henceforth, the differential operators $L^{(n)}(r)$, $\Omega^{(n)}(r)$, $\pounds^{(ij)}(r)$, $L_i(r)$, and $L^{(ij)}(r)$ are redefined as follows:

$$\pounds^{(12)}(r) = [-1+\alpha^{(21)}L_1(r)](r/a_1)^2, \quad L^{(12)}(r) = \alpha^{(12)}L_1(r)$$
$$\pounds^{(21)}(r) = \alpha^{(21)}L_1(r), \quad L^{(21)}(r) = [-1+\alpha^{(12)}L_1(r)](r/a_1)^2$$
$$\pounds^{(23)}(r) = \alpha^{(23)}L_2(r), \quad L^{(23)}(r) = [-1+\alpha^{(32)}L_2(r)](r/a_2)^2$$
$$\pounds^{(32)}(r) = [-1+\alpha^{(23)}L_2(r)](r/a_2)^2, \quad L^{(32)}(r) = \alpha^{(32)}L_2(r) \quad (40)$$

$$L_i(r) = \left(1-\frac{r^2}{a_i{}^2}\right)\left[1 - r\frac{\partial}{\partial r} - \frac{1}{4}(a_i{}^2 - r^2)\nabla^2\right], \quad i=1,2$$

$$L^{(n)}(r) = L^{(21)}(r)L^{(23)}\left(\frac{a_1{}^2}{r}\right)L^{(21)}\left(\frac{r}{\lambda}\right)\cdots L^{(23)}\left(\frac{a_1{}^2\lambda^{n-2}}{r}\right)L^{(21)}(r\lambda^{1-n})$$

$$\Omega^{(n)}(r) = L^{(23)}(r)L^{(21)}\left(\frac{a_2{}^2}{r}\right)L^{(23)}(\lambda r)\cdots L^{(21)}\left(\frac{a_2{}^2\lambda^{2-n}}{r}\right)L^{(23)}(r\lambda^{n-1})$$

Then, as in the case of three-dimensional axisymmetrical flow, we can state a *basic* theorem whose function is to split into two parts in an invariant manner Lagrange's stream function induced by an arbitrary two-dimensional singularity operative in the interior of one of two incompressible immiscible viscous fluids separated by a permanently circular cylindrical surface. The statement of the theorem is as follows.

If there is a general two-dimensional flow of an incompressible homogeneous viscous infinite fluid, with *no* disturbing obstacles, characterized by Lagrange's stream function $\Psi(r,\phi)$ all of whose singularities are at a distance greater than a_1 from the origin, then on introducing a different incompressible immiscible viscous fluid into the region $r<a_1$, so that the conditions (36) are satisfied at the interface $r=a_1$, the new stream functions for the two phases are given by

$$\Psi^{(1)}(r,\phi) = \pounds^{(21)}(r)\Psi(r,\phi)$$
$$\Psi^{(2)}(r,\phi) = \Psi(r,\phi) + L^{(21)}(r)\Psi\left(\frac{a_1{}^2}{r},\phi\right) \quad (41)$$

where $\pounds^{(21)}(r)$ and $L^{(21)}(r)$ assume their values in Eq. (40). This theorem is mathematically analogous to the circle theorem of Aderogba [9] in extensional elasticity.

The circulation produced in the circular cylindrical drop by a line Stokeslet (f_1,o) applied at the point (o,h) in the matrix medium is therefore given by

$$\Psi^{(1)} = K_1\alpha^{(21)}\left(1-\frac{r^2}{a_i{}^2}\right)\left[y-h+2h\log r_1 + (a_1{}^2-h^2)\frac{\partial}{\partial y}\log r_1\right]$$

where K_1 is a constant and $r_1{}^2=x^2+(y-h)^2$, while the circulation produced in the circular cylindrical drop by a line Stokeslet (o,f_2) applied at the same point (o,h) in the matrix medium is given by

$$\Psi^{(1)} = K_2\alpha^{(21)}\left(1-\frac{r^2}{a_i{}^2}\right)\left[x + (a_1{}^2-h^2)\frac{\partial}{\partial y}\log r_1\right]$$

where K_2 is another constant. Thus, there is a fundamental difference in the stream function and associated velocity field due to a line force acting tangentially to the circular cylindrical interface than those due to a line force acting normally to the circular cylindrical interface.

As before, it may now be readily established by repeated imaging that the following representation law holds.

If Lagrange's stream function $\Psi(r,\phi)$ due to the specification of an arbitrary two-dimensional singularity in an incompressible viscous fluid of infinite extent is known, then the stream functions $\Psi^{(1)}$, $\Psi^{(2)}$, and $\Psi^{(3)}$ induced in the three regions $0<r<a_1$, $a_1<r<a_2$, and $a_2<r<\infty$, respectively, occupied by incompressible immiscible fluids due to the specification of the same arbitrary singularity in the inner medium $0<r<a_1$ are explicitly determinable in terms of $\Psi(r,\phi)$ in accordance with the relations

$$\Psi^{(1)} = \Psi(r,\phi) + \pounds^{(12)}(r)\Psi\left(\frac{a_1^2}{r},\phi\right) + \pounds^{(21)}(r)\sum_{n=1}^{\infty}\Omega^{(n)}(r)L^{(12)}\times\left(\frac{a_2^2\lambda^{1-n}}{r}\right)\Psi\left(\frac{a_2^2\lambda^{1-n}}{r},\phi\right)$$

$$\Psi^{(2)} = L^{(12)}(r)\Psi(r,\phi) + \sum_{n=1}^{\infty}\Omega^{(n)}(r)L^{(12)}\left(\frac{a_2^2\lambda^{1-n}}{r}\right)\Psi\left(\frac{a_2^2\lambda^{1-n}}{r}\right) + L^{(21)}(r)\sum_{n=1}^{\infty}\Omega^{(n)}\left(\frac{a_1^2}{r}\right)L^{(12)}\left(\frac{r}{\lambda^n}\right)\Psi\left(\frac{r}{\lambda^n},\phi\right) \quad (42)$$

$$\Psi^{(3)} = \pounds^{(23)}(r)\left[L^{(12)}(r)\Psi(r,\phi) + L^{(21)}(r)\sum_{n=1}^{\infty}\Omega^{(n)}\left(\frac{a_1^2}{r}\right)L^{(12)}\times\left(\frac{r}{\lambda^n}\right)\Psi\left(\frac{r}{\lambda^n},\phi\right)\right]$$

which may be deduced from Eq. (19), by replacing R with r, θ with ϕ, and remembering the new definitions in Eq. (40).

In a similar manner, it may be deduced that if the outer fluid of viscosity $\mu^{(3)}$ is under the influence of an arbitrary singularity, which in a fluid of infinite extent is characterized by $\Psi(r,\phi)$, then the induced stream functions in the three phases are given by

$$\Psi^{(1)} = \pounds^{(21)}(r)\left[L^{(32)}(r)\Psi(r,\phi) + L^{(23)}(r)\sum_{n=1}^{\infty}L^{(n)}\left(\frac{a_2^2}{r}\right)L^{(32)}\times(\lambda^n r)\Psi(\lambda^n r,\phi)\right],$$

$$\Psi^{(2)} = L^{(32)}(r)\Psi(r,\phi) + \sum_{n=1}^{\infty}L^{(n)}(r)L^{(32)}\left(\frac{a_1^2\lambda^{n-1}}{r}\right)\Psi\left(\frac{a_1^2\lambda^{n-1}}{r},\phi\right) + L^{(32)}(r)\sum_{n=1}^{\infty}L^{(n)}\left(\frac{a_2^2}{r}\right)L^{(32)}(\lambda^n r)\Psi(\lambda^n r,\phi) \quad (43)$$

$$\Psi^{(3)} = \Psi(r,\phi) + \pounds^{(32)}(r)\Psi\left(\frac{a_2^2}{r},\phi\right) + \pounds^{(23)}(r)\sum_{n=1}^{\infty}L^{(n)}(r)L^{(32)}\times\left(\frac{a_1^2\lambda^{n-1}}{r}\right)\Psi\left(\frac{a_1^2\lambda^{n-1}}{r},\phi\right)$$

where $L^{(21)}(r)$, $L^{(23)}(r)$, $\pounds^{(21)}(r)$, $\pounds^{(23)}(r)$, and $L_i(r)$ assume their values in Eq. (40).

It therefore follows from Eq. (43) that if the interface circular cylindrical tube $a_1<r<a_2$ is occupied by gas, then it tends to prevent hydrodynamical currents from reaching the inner circular cylindrical drop $0<r<a_1$ at all, and the hydrodynamical action in the outer medium $a_2<r<\infty$ is less than it would otherwise be, whatever be the nature of the influencing singularity in this outer medium. Indeed, whether the viscous cylindrical tube transmits singularities better or worse than the rest of the multiphase medium, the hydrodynamical action in the space occupied by the tube is less than it would otherwise be.

In a similar manner, it may be established that if Lagrange's stream function $\Psi(r,\phi)$ due to the specification of an arbitrary two-dimensional singularity in an incompressible infinite viscous fluid is known, then the stream functions $\Psi^{(1)}$, $\Psi^{(2)}$, and $\Psi^{(3)}$ induced in the three domains $0<r<a_1$, $a_1<r<a_2$, and $a_2<r<\infty$, respectively, due to the specification of the same singularity in the interface medium $a_1<r<a_2$ are explicitly determinable in terms of $\Psi(r,\phi)$ in accordance with the relations

$$\Psi^{(1)} = \pounds^{(21)}(r)\left[\Psi(r,\phi) + \sum_{n=1}^{\infty}\Omega^{(n)}(r)\left\{\Psi\left(\frac{{a_2}^2\lambda^{1-n}}{r},\phi\right) + L^{(21)}\times\left(\frac{{a_2}^2\lambda^{1-n}}{r}\right)\Psi(\lambda^n r,\phi)\right\}\right],$$

$$\Psi^{(2)} = \Psi(r,\phi) + L^{(21)}(r)\Psi\left(\frac{{a_1}^2}{r},\phi\right) + \sum_{n=1}^{\infty}\Omega^{(n)}(r)\left[\Psi\left(\frac{{a_2}^2\lambda^{1-n}}{r},\phi\right) + L^{(21)}\left(\frac{{a_2}^2\lambda^{1-n}}{r}\right)\Psi(\lambda^n r,\phi)\right] + L^{(21)}(r)\sum_{n=1}^{\infty}\Omega^{(n)}\left(\frac{{a_1}^2}{r}\right)\times\left[\Psi\left(\frac{r}{\lambda^n},\phi\right) + L^{(21)}\left(\frac{r}{\lambda^n}\right)\Psi\left(\frac{{a_1}^2\lambda^n}{r},\phi\right)\right] \quad (44)$$

$$\Psi^{(3)} = \pounds^{(23)}(r)\left[\Psi(r,\phi) + L^{(21)}(r)\Psi\left(\frac{{a_1}^2}{r},\phi\right) + L^{(21)}(r)\sum_{n=1}^{\infty}\Omega^{(n)}\times\left(\frac{{a_1}^2}{r}\right)\left\{\Psi\left(\frac{r}{\lambda^n},\phi\right) + L^{(21)}\left(\frac{r}{\lambda^n}\right)\Psi\left(\frac{{a_1}^2\lambda^n}{r},\phi\right)\right\}\right]$$

where the differential operators assume their values in Eq. (40).

A simple application of the foregoing two-dimensional results is afforded by the case of a circular cylindrical drop of viscosity $\mu^{(1)}$ and radius a_1, surrounded by a circular cylindrical tube of viscosity $\mu^{(2)}$, internal radius a_1, and external radius a_2, beyond which there is an infinite immiscible fluid of viscosity $\mu^{(3)}$, which flows at infinity with the shear velocity $V(-x,y)$, where V is a constant. In this case, the undisturbed Lagrange's stream function is

$$\Psi(r,\phi) = \tfrac{1}{2}vr^2\sin 2\phi \quad (45)$$

The substitution of this into formula (44) shows that the stream function induced in the incompressible matrix fluid of viscosity $\mu^{(3)}$ is

$$\Psi^{(3)} = \frac{1}{2}v\left[r^2 - {a_2}^2\left\{1 + \left(1 - \frac{{a_2}^2}{r^2}\right)B\alpha^{(23)}\right\}\right]\sin 2\phi \quad (46)$$

where

$$B=\frac{(1-\lambda)(\alpha^{(21)}-\lambda\alpha^{(12)}\alpha^{(32)})}{[\alpha^{(21)}(1-\lambda-\lambda\alpha^{(32)})-\lambda\alpha^{(12)}\{(1+\lambda)(1-2\lambda)+\alpha^{(32)}(1-2\lambda+\lambda^2+2\lambda^3)\}]} \tag{47}$$

Equation (46) represents the combination of the effect of the influencing stream function $(1/2)vr^2\sin 2\phi$ with the effects of a force doublet whose axis is parallel to the y-axis and a source multiplet whose axis is also parallel to the y-axis, with both line singularities passing through the origin.

If there are N such similarity coated noninteracting circular cylindrical drops placed in a matrix medium of viscosity $\mu^{(3)}$, then if these coated cylindrical drops are all contained within a circular cylinder of radius a_3, the stream function induced in the matrix medium may be taken as

$$\Psi^{(3)}=\frac{1}{2}v\left[r^2-ka_3{}^2\left\{1+\left(1-\frac{a_2{}^2}{r^2}\right)B\alpha^{(23)}\right\}\right]\sin 2\phi \tag{48}$$

where

$$k=N(a_2/a_3)^2 \tag{49}$$

and represents the ratio of the cross-sectional area of the N small coated cylinders to that of the cylinder, which encloses them.

Now, if the whole enclosing circular cylinder of radius a_3 had been occupied by a fluid of viscosity μ_0, then we should have had

$$\Psi^{(3)}=\frac{1}{2}v\left[r^2-a_3{}^2\left\{1+\left(1-\frac{a_3{}^2}{r^2}\right)\alpha^{(03)}\right\}\right]\sin 2\phi \tag{50}$$

Therefore, far away, Eq. (48) will be equivalent to Eq. (50) provided that

$$\mu_0=\frac{k\{(1+B)\mu^{(2)}+\mu^{(3)}\}-\mu^{(2)}-\mu^{(3)}}{2(\mu^{(2)}+\mu^{(3)})-k\{(1+B)\mu^{(2)}+\mu^{(3)}\}}\mu^{(3)} \tag{51}$$

With B given by Eq. (47), this μ_0 is the effective viscosity of a multiphase medium comprising an incompressible viscous medium of viscosity $\mu^{(3)}$ in which are embedded N small noninteracting incompressible circular cylindrical drops of viscosity $\mu^{(1)}$ and radius a_1, surrounded by incompressible circular cylindrical tubes of viscosity $\mu^{(2)}$, internal radius a_1, and external radius a_2.

The case of a multiphase medium comprising a medium containing uncoated circular cylindrical drops may be obtained from Eq. (51) by making $a_1=0$, which reduces Eq. (47) to $B=1$, thus finally obtaining, in this case,

$$\mu_0=\frac{k(2\mu^{(2)}+\mu^{(3)})-\mu^{(2)}-\mu^{(3)}}{2(\mu^{(2)}+\mu^{(3)})-k(2\mu^{(2)}+\mu^{(3)})}\mu^{(3)} \tag{52}$$

In the interest of completeness, if we suppose that the radii of the circular cylindrical interfaces in this section become infinite, then the case becomes that of three incompressible immiscible fluids of viscosities $\mu^{(1)}$, $\mu^{(2)}$, and $\mu^{(3)}$ occupying the three regions $(|x|<\infty,-\infty<y<0)$, $(|x|<\infty,0<y<H)$, and $(|x|<\infty,H<y<\infty)$, respectively, the fluids being infinite in the z-direction, while the interfaces $(|x|<\infty,\ y=0)$ and $(|x|<\infty,\ y=H)$ are assumed to be permanently flat.

In this case, it may again be readily established by repeated reflection that the following representation law holds.

If Lagrange's stream function $\Psi(x,y)$ due to the specification of an arbitrary two-dimensional singularity in an incompressible infinite viscous fluid is known, then the stream functions $\Psi^{(1)}$, $\Psi^{(2)}$, and $\Psi^{(3)}$ induced in the three regions $-\infty<y<0$, $0<y<H$, and $H<y<\infty$, respectively, occupied by incompressible immiscible viscous fluids due to the specification of the same singularity in the first medium $-\infty<y<0$ are explicitly determinable solely in terms $\Psi(x,y)$ in accordance with the relations

$$\Psi^{(1)}=\Psi(x,y)+\pounds^{(12)}(y)\Psi(x,-y)+\pounds^{(21)}(y)\sum_{n=1}^{\infty}L^{(n)}(y)L^{(12)}(2nH-y)\Psi(x,2nH-y)$$

$$\Psi^{(2)}=L^{(12)}\Psi(x,y)+\sum_{n=1}^{\infty}L^{(n)}(y)L^{(12)}(2nH-y)\Psi(x,2nH-y)+L^{(21)}(y)\sum_{n=1}^{\infty}L^{(n)}(-y)L^{(12)}(2nH+y)\Psi(x,2nH+y) \tag{53}$$

$$\Psi^{(3)}=\pounds^{(23)}(H-y)\left[L^{(12)}(y)\Psi(x,y)+L^{(21)}(y)\sum_{n=1}^{\infty}L^{(n)}(-y)L^{(12)}(2nH+y)\Psi(x,2nH+y)\right]$$

where

$$\begin{aligned}L^{(12)}(y)&=\alpha^{(12)}\pounds(y),\quad \pounds^{(12)}(y)=[-1+\alpha^{(21)}\pounds(y)],\quad \pounds(y)=y\left(2\frac{\partial}{\partial y}-y\nabla^2\right)\\ L^{(21)}(y)&=[-1+\alpha^{(12)}\pounds(y)],\quad \pounds^{(21)}(y)=\alpha^{(21)}\pounds(y)\\ L^{(23)}(y)&=[-1+\alpha^{(32)}\pounds(y)],\quad \pounds^{(23)}(y)=\alpha^{(23)}\pounds(y)\end{aligned} \tag{54}$$

$$L^n(y)=L^{(23)}(H-y)L^{(21)}(2H-y)L^{(23)}(3H-y)\cdots L^{(21)}[2(n-1)H-y]L^{(23)}[(2n-1)H-y]$$

Let us now suppose that the first fluid is the same as the third $(\mu^{(3)}=\mu^{(1)})$, so that the case is that of a viscous thick layer of viscosity $\mu^{(2)}$ separating a semi-infinite upper fluid of viscosity $\mu^{(1)}$ from a semi-infinite lower fluid of the same viscosity $\mu^{(1)}$. Then,

$$\Psi^{(2)}=\alpha^{(12)}\left[\pounds(y)\Psi(x,y)+\sum_{n=1}^{\infty}\pounds^{(n)}(y)\pounds(2nH-y)\Psi(x,2nH-y)+\{-1+\alpha^{(12)}\pounds(y)\}\sum_{n=1}^{\infty}\pounds^{(n)}(-y)\pounds(2nH+y)\Psi(x,2nH+y)\right] \tag{55}$$

where

$$\pounds^{(n)}(y)=L^{(21)}(H-y)L^{(21)}(2H-y)L^{(21)}(3H-y)\cdots L^{(21)}[(2n-1)H-y] \tag{56}$$

Since the operator $\pounds(y)$ must first be applied in each term of expression (55), It follows that whether the embedded thick layer is less or more viscous than the matrix medium, the hydrodynamical action in the embedded layer is physically different from what it would otherwise be, whatever be the nature of the inducing singularity in the matrix.

Finally, as in the cases of spherical-layered and circularly cylindrical-layered fluids, it may be established that the effective viscosity μ_0 of a multiphase medium comprising a medium of viscosity $\mu^{(1)}$ and thickness H_1 in which are embedded N small plane layers, each viscosity $\mu^{(2)}$ and thickness H_2, the ratio of the thickness of all the small plane layers to that of the whole being K, is given by

$$\frac{\mu_0+\mu^{(1)}}{(\mu^{(2)}+\mu^{(1)})^2}=\frac{1\pm[1-4K\mu^{(1)}\mu^{(2)}/(\mu^{(1)}+\mu^{(2)})^2]^{1/2}}{2K\mu^{(2)}} \quad (57)$$

In order that the action of these plane layers may not produce effects depending on their interference, their thickness must be small compared with their distances from one another, and therefore K, which is equal to NH_2/H_1, must be a small fraction.

8 Closure

It has been established with the help of Maxwell's method of repeated reflection that if we know the stream function due to the presence of an arbitrary singularity in an unbounded incompressible viscous fluid, with no disturbing obstacles, then the corresponding stream functions for three immiscible incompressible viscous fluids occupying the entire space and separated by either two concentric spherical or circular cylindrical surfaces are determined solely and compactly by the known stream function for the unbounded and unperturbed homogeneous fluids. The precise form of the unique dependence is facilitated by the known theory for the special case of two media separated by either a spherical or a circular cylindrical surface.

It is clear that we can apply the analysis presented to the case of three plane-layered fluids in three-dimensional axisymmetrical flow, because we know the corresponding fundamental theory of images in the case of two incompressible immiscible viscous fluids separated by a flat surface. Specifically, if there is a general axisymmetrical motion of an incompressible viscous fluid of infinite extent, with *no* disturbing obstacles, characterized by the stream function $\Psi(r,z)$, all of whose singularities are in the upper half-space $z>o$ of viscosity $\mu^{(2)}$, then on introducing a different immiscible fluid into the lower half-space $z<0$, of viscosity $\mu^{(1)}$, so that the flat surface conditions hold at the interface $z=0$, the new stream functions are given by

$$\begin{aligned}\Psi^{(1)}&=z\alpha^{(21)}\left[2\frac{\partial}{\partial z}-z\nabla^2\right]\Psi(r,z),\\ \Psi^{(2)}&=\Psi(r,z)-\left[1-z\alpha^{(12)}\left\{2\frac{\partial}{\partial z}-z\nabla^2\right\}\right]\Psi(r,-z)\end{aligned} \quad (58)$$

The proof of this theorem is analogous to that leading to Eq. (10). The theorem shows that an axial Stokeslet $(0,0,f_3)$ applied at the point $(0,0,h)$ in the half-space fluid of viscosity $\mu^{(2)}$ induces in the half-space fluid of viscosity $\mu^{(1)}$ the stream function

$$\Psi^{(1)}=K_3\alpha^{(21)}\left[\frac{hr^2}{R_1^3}-\frac{\partial}{\partial_z}\left(\frac{r^2}{R_1}\right)\right] \quad (59)$$

where K_3 is a constant, while ${R_1}^2=r^2+(z-h)^2$. Physically, Eq. (59) represents a combination, at the influencing point $(0,0,h)$, of a source and a Stokeslet doublet whose axis is parallel to the z-axis. The repeated application of the theorem to the general case of three plane-layered fluids is now a routine exercise.

Perhaps it will prove possible to extend the present paper to the more versatile case of three incompressible immiscible fluids separated by two confocal triaxial ellipsoidal surfaces, guided by the creative and original pioneering papers of Eshelby [10,11] on ellipsoidal inhomogeneities.

In this connection, it may be noted that a complete general solution of the governing equations (1) and (3) is

$$2\mu u_i=\nabla^2 G_i-\frac{\partial^2 G_j}{\partial X_j\,\partial X_j}, \quad P=-\frac{1}{2}\nabla^2 G_{i,i} \quad (60)$$

provided that $\nabla^4 G_i=0$.

References

[1] Milne-Thomson, L. M., 1940, "On Hydrodynamical Images," Proc. Cambridge Philos. Soc., **36**, pp. 246–248.
[2] Weiss, P., 1944, "Arbitrary Irrotational Flow Disturbed by a Sphere," Proc. Cambridge Philos. Soc., **40**, pp. 259–263.
[3] Butler, S. E. J., 1953, "A Note for Stokes' Stream Function for Motion With a Spherical Boundary," Proc. Cambridge Philos. Soc., **49**, pp. 169–171.
[4] Collins, W. D., 1958, "Viscous Stokes Flow Past a Rigid Sphere," Mathematika, **5**, pp. 118–124.
[5] Stokes, G. G., 1851, "On the Effect of the Internal Friction of Fluids on the Motion of Pendulums," Trans. Cambridge Philos. Soc., **9**, pp. 8–96.
[6] Maxwell, J. C., 1873, *A Treatise on Electricity and Magnetism*, Vol. 1, Dover, New York, pp. 244–450.
[7] Aderogba, K., 2003, "An Image Treatment of Elastostatic Transmission From an Interface Layer," J. Mech. Phys. Solids, **51**, pp. 267–279.
[8] Aderogba, K., 2007, "Theory of Images in Plane-Layered Axisymmetric Elastostatics," Int. J. Solids Struct., **44**, pp. 3920–3927.
[9] Aderogba, K., 1972, "Some Results for Two-Phase Elastic Plates," Proc. R. Soc. Edinburgh, Sect. A: Math. Phys. Sci., **71**, pp. 21–35.
[10] Eshelby, J. D., 1957, "The Determination of the Elastic Field of an Ellipsoidal Inhomogeneity and Related Problems," Proc. R. Soc. London, Ser. A, **241**, pp. 376–396.
[11] Eshelby, J. D., 1961, "Inclusions and Inhomogeneities," Progress in Solid Mechanics, **2**, pp. 89–140.

Gang Liu
Baohua Ji[1,2]
e-mail: bhji@bit.edu.cn
bhji@mail.tsinghua.edu.cn

Department of Engineering Mechanics,
Tsinghua University,
Beijing 100084, China

Haitao Chen
Marine Design and Research Institute of China,
Shanghai 200011, China

Diankui Liu[1]
School of Civil Engineering,
Harbin Engineering University,
Harbin 150001, China
e-mail: dkliu@yahoo.cn

Antiplane Harmonic Elastodynamic Stress Analysis of an Infinite Wedge With a Circular Cavity

In this paper, the antiplane harmonic dynamics stress of an infinite isotropic wedge with a circular cavity is analyzed for the first time by using a novel method with Green's function, complex functions, and multipolar coordinates. A basic solution for the displacement field of an elastic half-space containing a circular cavity subjected to antiplane harmonic point force is employed as the Green's function. Based on the Green's function, the infinite wedge problem is equivalently transformed into the problem of a half-space divided by a semi-infinite traction free line. The equivalent problem is solved numerically to determine the dynamic stress field in the wedge at different apex angles and cavity locations. We show that the wedge angle, cavity location, and incident angle and frequency of the external load have significant effect on the dynamic stress of the cavity surface. The dynamic stress concentration factor on the cavity surface becomes singular when the cavity is close to the boundary of the wedge.
[DOI: 10.1115/1.3130451]

Keywords: infinite wedge, circular cavity, Green's function, complex functions, multipolar coordinates, dynamic stress concentration

1 Introduction

Stress analysis in a wedge is of practical importance in engineering design. Engineering materials and structures often have wedgelike parts of which the geometry or materials are discontinuous. Shahani [1,2] studied the antiplane deformation of an anisotropic wedge of finite radius with different boundary conditions and studied the model III stress intensity factor (SIF) of edge-cracked circular shafts, bonded half planes, bonded wedges, and double cantilever beams of isotropic and anisotropic materials. Later on, Shahani [3,4] studied the antiplane shear deformation of two edge-bonded dissimilar isotropic wedges of both finite and infinite radii, and obtained the explicit expression for the stress intensity factor. The problem of wedgelike structure containing cavities, especially close to its vertex, is of particularly interest to the practical engineering (e.g., a dam with tunnel). In fact, the seismic wave scattering in the dam has been an important subject in the field of seismology for a long time, especially in the field of earthquake engineering and strong motion seismology. This provides a strong impetus to the understanding of the response of the wedge with interior cavity under external dynamic load. However, how to solve the dynamic problem of an infinite wedge with interior cavity is a big challenge.

The static analysis of a wedge with infinite or finite radius has been considered by various studies. Tranter [5] solved the plane elasticity problem of an isotropic wedge with Airy stress function and Mellin transform. Williams [6] studied the stress singularities at the wedge apex by using eigenfunction expansion method. Later on, Dempsey and Sinclair [7] examined the stress singularity at the wedge apex under different loading conditions. Dempsey [8] solved the paradox (the stress in the wedge becomes infinite when the wedge angle satisfies $\tan 2\varphi = 2\varphi$) in a classical two-dimensional solution given by Lévy [9] with an Airy stress function. Ting [10,11] further discussed the paradox existed in the elementary solution of Lévy by using an expansion form of the harmonic eigenfunctions. Kargmovin and Shahani [12] used finite Mellin transforms to obtain the displacement and stress components in an isotropic wedge with finite radius under antiplane deformation. 10 years later, Shahani [13] expanded his previous work [12] by giving a closed form solution for the stress distribution in the wedge and applied it to calculate the stress intensity factors of a circular shaft containing an edge crack. Faal et al. [14] obtained an analytical solutions for the antiplane static stress field of an infinite isotropic wedge with multiple cracks and later gave an analytical solutions for a finite wedge weakened by cavities [15].

Compared with the full space or half-space problems, the infinite wedge problems are much more difficult. In addition, most works in this direction are focused on antiplane static analysis, but few works are dedicated to antiplane dynamics stress. Achenbach [16,17] studied the shear horizontal (SH)-wave propagation in an elastic wedge as one of the earliest works on the elastic dynamics analysis of wedges. Demendjian [18] studied the behavior of wave propagation in an elastic wedge-shaped medium with an arbitrary shaped canyon at its vertex with Hankel function by adjusting the rank of Hankel function to satisfy the governing equation and boundary conditions. Liu and Liu [19] used the same idea of the "fractional Hankel function" in studying the ground motion of a half-space with an isosceles triangular hill and a subsurface cavity under incident SH waves, and they gave an analytical solution for the displacement field in the half-space.

This paper aims to study the problem of a plane SH-waves propagating through an infinite wedge with a cavity under antiplane shear loading by using the Green's function method to calculate the antiplane dynamic displacement and stresses field, as well as the dynamic stress concentration factors (DSCFs) on the cavity. The Green's function is obtained by solving the displace-

[1]Corresponding authors.
[2]Present address: Department of Applied Mechanics, Beijing Institute of Technology, Beijing 100081, China.
Contributed by the Applied Mechanics Division of ASME for publication in the Journal of Applied Mechanics. Manuscript received November 29, 2007; final manuscript received February 10, 2009; published online July 23, 2009. Review conducted by Professor Sridhar Krishnaswamy.

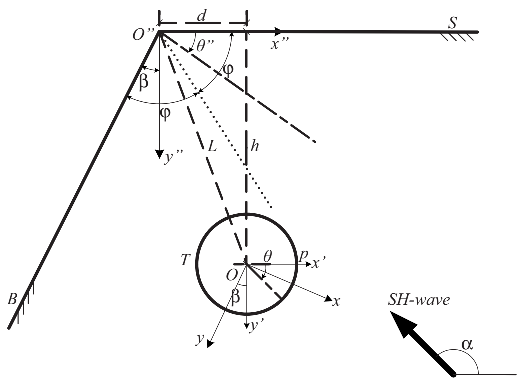

Fig. 1 The scattering model of the infinite wedge with a circular cavity

ment field of an elastic half-space containing a circular cavity subjected to an antiplane harmonic point force. Base on the Green's function method, the wedge problem can be equivalently transformed into a problem of a half-space divided by a semi-infinite traction free line. Combined with the method of complex functions and multipolar coordinate method proposed by Liu et al. [20,21], the infinite wedge problem are solved numerically to determine the dynamic displacement and stress field in the wedge.

2 The Model

The infinite wedge with a circular cavity is shown in Fig. 1. We denote the vertex of the wedge as O'', the center of the cavity as O, the surface of the cavity as T, the horizontal surface of the wedge as S, and the oblique surface as B. a is the radius of the cavity, and the distance between O'' and O and that between O and the horizontal surfaces are L and h, respectively. d is the projection of the distance OO'' on x'' axis. The position of any point on the surface of the cavity is defined by angle θ clockwise with respect to point p on x' axis. α is the incident angle, and β is the angle between the oblique surface B and y'' axis $(0 \leq \beta \leq 90$ deg). In this work, we will transform this infinite wedge problem equivalently into the problem of a half-space divided by a semi-infinite traction free line using the Green's function method.

3 Governing Equation

Supposing harmonic response and neglecting body force, the governing equation for the antiplane shear problem is the elastodynamic equation of motion as

$$\frac{\partial^2 W}{\partial x^2} + \frac{\partial^2 W}{\partial y^2} + k^2 W = 0 \tag{1}$$

where $k=\omega/c_s$, $c_s=\sqrt{\mu/\rho}$, ω is the circular frequency of the displacement $W(x,y,t)$, c_s is the shear wave velocity, and ρ and μ are the mass density and the shear modulus of the medium in the wedge, respectively.

Equation (1) written in the polar coordinate system (r,θ) is

$$\frac{\partial^2 W}{\partial r^2} + \frac{1}{r}\frac{\partial W}{\partial r} + \frac{1}{r^2}\frac{\partial^2 W}{\partial \theta^2} + k^2 W = 0 \tag{2}$$

and the corresponding stresses are given by

$$\tau_{xz} = \mu\frac{\partial W}{\partial x}, \quad \tau_{yz} = \mu\frac{\partial W}{\partial y} \tag{3}$$

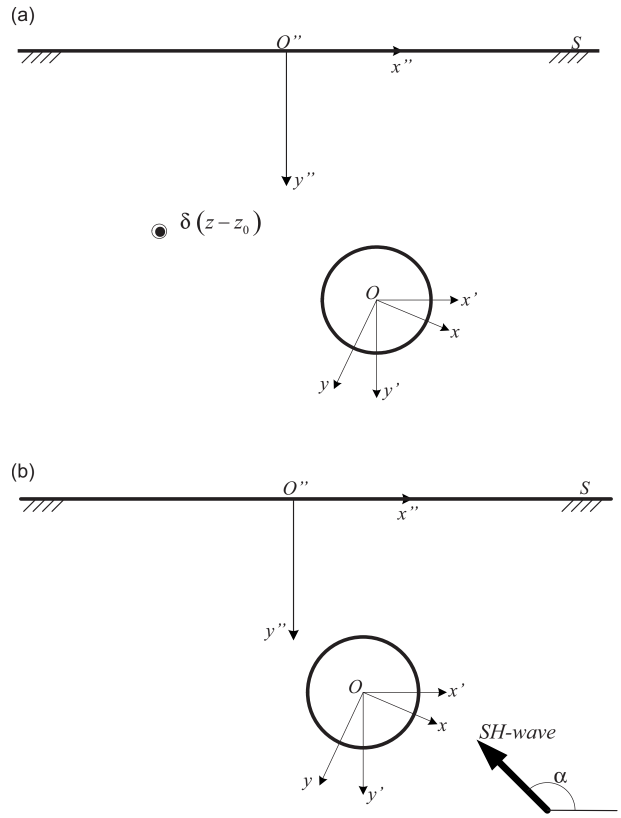

Fig. 2 (*a*) A half-space with a circular cavity loaded by a point force $\delta(z-z_0)$. (*b*) A half-space with a cavity loaded by an external force with an incident angle α.

$$\tau_{rz} = \mu\frac{\partial W}{\partial r}, \quad \tau_{\theta z} = \frac{\mu}{r}\frac{\partial W}{\partial \theta} \tag{4}$$

In complex-plane $(z,\bar{z})$, where $z=x+yi=r\cdot e^{i\theta}$ and $\bar{z}=x-yi=r\cdot e^{-i\theta}$, the stress functions are changed into

$$\tau_{xz} = \mu\left(\frac{\partial W}{\partial z} + \frac{\partial W}{\partial \bar{z}}\right), \quad \tau_{yz} = i\mu\left(\frac{\partial W}{\partial z} - \frac{\partial W}{\partial \bar{z}}\right) \tag{5}$$

$$\tau_{rz} = \mu\left(\frac{\partial W}{\partial z}e^{i\theta} + \frac{\partial W}{\partial \bar{z}}e^{-i\theta}\right), \quad \tau_{\theta z} = i\mu\left(\frac{\partial W}{\partial z}e^{i\theta} - \frac{\partial W}{\partial \bar{z}}e^{-i\theta}\right) \tag{6}$$

4 Green's Function

4.1 Governing Equation and Boundary Condition. The Green's function used in this paper is defined as the displacement response of the elastic half-space containing a cylindrical cavity to an antiplane harmonic point force at any point of the elastic plane, as shown in Fig. 2(*a*). In the polar coordinate system, the governing equation of displacement function G is written as follows:

$$\frac{\partial^2 G}{\partial r^2} + \frac{1}{r}\frac{\partial G}{\partial r} + \frac{1}{r^2}\frac{\partial^2 G}{\partial \theta^2} + k^2 G = \delta(\boldsymbol{r} - \boldsymbol{r_0}) \tag{7}$$

where $\boldsymbol{r}_0$ stands for the position of the point force, $\boldsymbol{r}_0=r_0\cdot e^{i\theta_0}$, and $\boldsymbol{r}$ stands for the position of the arbitrary point $\boldsymbol{r}=r\cdot e^{i\theta}$, in polar coordinates.

In complex plane $(z,\bar{z})$, Eq. (7) is transformed into

$$\frac{\partial^2 G}{\partial z\,\partial \bar{z}} + \frac{1}{4}k^2 G = \delta(z - z_0) \tag{8}$$

where z_0 stands for the position of the point force, $z_0=r_0\cdot e^{i\theta_0}$, and z stands for the position of an arbitrary point, $z=r\cdot e^{i\theta}$, in the complex plane. The boundary conditions can be expressed as

$$\tau_{\theta' z}=0, \quad \text{at} \quad \theta'=0 \quad \text{and} \quad \theta'=\pi/2+\beta \tag{9}$$

$$\tau_{rz}=0 \quad \text{at} \quad |z|=a \tag{10}$$

4.2 Derivation of the Green's Function. The basic solution that satisfies the governing equation (8) and the boundary conditions (9) and (10) should include the disturbance of the antiplane point force and the scattering wave incited by the cavity. The wave displacement of the full space due to the point force $\delta(z-z_0)$ loaded on an arbitrary position of the plane (as shown in Fig. 2(*a*)) is derived as follows. The solution of Eq. (7) is [22]

$$G^{(i)}=\frac{i}{4\mu}H_0^{(1)}(k(\boldsymbol{r}-\boldsymbol{r}_0)) \tag{11}$$

If we rewrite Eq. (11) in the complex plane $(z'',\overline{z''})$, we can obtain the wave displacement due to the point force in the complex plane $(z'',\overline{z''})$,

$$G^{(i)}=\frac{i}{4\mu}H_0^{(1)}(k|z''-z_0''|) \tag{12}$$

where $|z''-z_0''|=\boldsymbol{r}-\boldsymbol{r}_0$, $H_0^{(1)}(*)$ is the first kind of Hankel function of zero order [23].

According to the "symmetry theory," which was developed by Lee et al. [24], the reflected wave $G^{(r)}$ can be written as

$$G^{(r)}=\frac{i}{4\mu}H_0^{(1)}(k|z''-\overline{z_0''}|) \tag{13}$$

The stress induced by the summation of incident wave and reflect wave $G^{(i+r)}=G^{(i)}=G^{(r)}$ (the disturbance of the antiplane linear source force) satisfies the stress free condition on the horizontal surface of the wedge, i.e.,

$$G_{\theta'' z}^{(i+r)}=0 \quad \text{at} \quad \theta''=0 \quad \text{and} \quad \theta''=\pi \tag{14}$$

Then, we need to construct a wave function $G^{(s)}$ scattered by cavity to satisfy the stress free condition on the horizontal surface, as shown in Fig. 2(*a*).

The scattering wave of the cavity in an infinite full space is

$$G_1^{(s)}=\sum_{m=-\infty}^{\infty}A_mH_m^{(1)}(k|z''-\xi|)\cdot\left(\frac{z''-\xi}{|z''-\xi|}\right)^m \tag{15}$$

However, this wave function does not satisfy the traction free boundary condition at the surface of the half-space. We then construct an equivalent problem with the mirror image method [24] as follows: consider an unbound medium (a full space) and suppose there is another identical cylindrical cavity of the same radius with origin at $\bar{\xi}=d-hi$, which is the conjugate of the real cavity $\xi=d+hi$. The scattering wave of the imaginary cavity is

$$G_2^{(s)}=\sum_{m=-\infty}^{\infty}A_mH_m^{(1)}(k|z''-\bar{\xi}|)\cdot\left(\frac{z''-\bar{\xi}}{|z''-\bar{\xi}|}\right)^{-m} \tag{16}$$

The additional wave $G_2^{(s)}$ is a "mirror image" of the scattered wave $G_1^{(s)}$ with the line of symmetry being the surface of the half-space. This symmetry resulted in the sum of the functions $G_1^{(s)}+G_2^{(s)}$ having zero slope at the line of symmetry. In other words, the total displacement field of scattering wave $G^{(s)}=G_1^{(s)}+G_2^{(s)}$ satisfies the traction free condition on the horizontal surface,

$$G^{(s)}=\sum_{m=-\infty}^{\infty}A_m\left[H_m^{(1)}(k|z''-\xi|)\cdot\left(\frac{z''-\xi}{|z''-\xi|}\right)^m + H_m^{(1)}(k|z''-\bar{\xi}|)\cdot\left(\frac{z''-\bar{\xi}}{|z''-\bar{\xi}|}\right)^{-m}\right] \tag{17}$$

where ξ is the complex coordinate of point O with origin at O'', and $\xi=d+hi$. $\bar{\xi}$ is the conjugate of ξ, and A_m is the unknown coefficient.

The total displacement field G of this problem can be obtained by combining Eq. (12), (13), and (17),

$$G=G^{(i)}+G^{(r)}+G^{(s)}=\frac{i}{4\mu}[H_0^{(1)}(k|z''-z_0''|)+H_0^{(1)}(k|z''-\overline{z_0''}|)] + \sum_{m=-\infty}^{\infty}A_m\left[H_m^{(1)}(k|z''-\xi|)\cdot\left(\frac{z''-\xi}{|z''-\xi|}\right)^m + H_m^{(1)}(k|z''-\bar{\xi}|)\cdot\left(\frac{z''-\bar{\xi}}{|z''-\bar{\xi}|}\right)^{-m}\right] \tag{18}$$

It is obvious that Eq. (18) satisfies the traction free condition on the horizontal surface, and the unknown coefficient A_m can be determined by the stress free condition on the cavity.

5 Displacement Field of the Half-Space With Cavity

First, we consider the incidence of a SH-wave $W^{(i)}$ in the infinite half-space containing a cavity, as shown in Fig. 2(*b*). There will be a reflect wave $W^{(r)}$, which is induced by the surface of the half-space. In the complex plane $(z'',\overline{z''})$, the wave functions are

$$W^{(i)}=W_0\cdot e^{ik/2(z''e^{i\alpha}+\overline{z''}e^{-i\alpha})} \tag{19}$$

$$W^{(r)}=W_0\cdot e^{ik/2(z''e^{-i\alpha}+\overline{z''}e^{i\alpha})} \tag{20}$$

where W_0 is the amplitude of the wave, and always taken as unit 1 in the paper. Similarly, the stress induced by the summation of incident wave and reflect wave, $W^{(i+r)}=W^{(i)}+W^{(r)}$, satisfies the stress free conditions on the horizontal surface, i.e.,

$$\tau_{\theta'' z}^{(i+r)}=0 \quad \text{at} \quad \theta''=0 \quad \text{and} \quad \theta''=\pi \tag{21}$$

The scattered wave $W^{(s)}$ is constructed based on the mirror image method [24],

$$W^{(s)}=\sum_{m=-\infty}^{\infty}B_m\left[H_m^{(1)}(k|z''-\xi|)\cdot\left(\frac{z''-\xi}{|z''-\xi|}\right)^m + H_m^{(1)}(k|z''-\bar{\xi}|)\cdot\left(\frac{z''-\bar{\xi}}{|z''-\bar{\xi}|}\right)^{-m}\right] \tag{22}$$

At last, the total displacement field of the half-space W can be obtained as

$$W=W^{(i)}+W^{(r)}+W^{(s)}=W_0\cdot e^{ik/2(z''e^{i\alpha}+\overline{z''}e^{-i\alpha})}+W_0\cdot e^{ik/2(z''e^{-i\alpha}+\overline{z''}e^{i\alpha})} + \sum_{m=-\infty}^{\infty}B_m\left[H_m^{(1)}(k|z''-\xi|)\cdot\left(\frac{z''-\xi}{|z''-\xi|}\right)^m + H_m^{(1)}(k|z''-\bar{\xi}|)\cdot\left(\frac{z''-\bar{\xi}}{|z''-\bar{\xi}|}\right)^{-m}\right] \tag{23}$$

We can see that Eq. (23) also satisfies the stress free condition on the horizontal surface of the wedge. The unknown coefficient B_m can be determined by the stress free condition on the surface of the cavity in the same way of solving A_m.

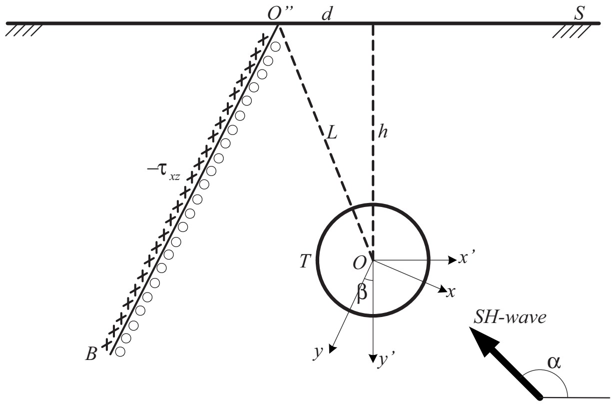

Fig. 3 Illustration of the construction of the infinite wedge problem by using Green's function method and the division technique

6 Infinite Wedge Problem

Based on the Green's function and above displacement field constructed for the elastic half-space containing a cavity (including incident field and scattered field), an infinite wedge model is obtained by using the division method. That is, we first calculate the stress field $\tau_{xz}=\mu(\partial W/\partial x)$ on the semi-infinite line B in half-space (shown in Fig. 3) based on the solution for the displacement of the elastic half-space with a cavity given in Sec. 5. Then, an opposite antiplane stress $\hat{\tau}_{xz}=-\tau_{xz}$ is applied on line B; therefore, the resultant force on line B is equal to zero, i.e., a traction free surface B is constructed. As a result, the right part of the half-space from the surface B is equivalent to an infinite wedge.

6.1 Wave Functions in Local Coordinates. In order to calculate the unknown coefficients A_m, B_m and load stress on the surface B conveniently, we need to describe them in the local coordinates (x,y). Introduce the complex coordinates $z=x+yi$ and $\bar{z}=x-yi$, where the relation between the local complex coordinate $(z,\bar{z})$ and the intermediate coordinate $(z',\overline{z'})$ and $(z'',\overline{z''})$ is

$$z''=z'+\xi=ze^{i\beta}+\xi \tag{24}$$

The position of point force z_0'' is shown as

$$z_0''=z_0'+\xi=z_0e^{i\beta}+\xi \tag{25}$$

$$\overline{z_0''}=\overline{z_0'}+\bar{\xi}=\overline{z_0}e^{-i\beta}+\bar{\xi} \tag{26}$$

where ξ is the complex coordinate of origin O of local coordinate in the original coordinate $(z'',\overline{z''})$, and $\xi=d+hi$. $\bar{\xi}$ is the conjugate of ξ, and β is the rotated angle from complex plane $(z',\overline{z'})$ to $(z,\bar{z})$, as shown in Fig. 1.

In the complex plane $(z,\bar{z})$, the expressions (12), (13), and (17) of the displacement induced by point force change into

$$G^{(i)}=\frac{i}{4\mu}H_0^{(1)}(k|z-z_0|) \tag{27}$$

$$G^{(r)}=\frac{i}{4\mu}H_0^{(1)}(k|ze^{i\beta}-\overline{z_0}e^{-i\beta}+2hi|) \tag{28}$$

$$G^{(s)}=\sum_{m=-\infty}^{\infty}A_m\left[H_m^{(1)}(k|z|)\cdot\left(\frac{ze^{i\beta}}{|z|}\right)^m + H_m^{(1)}(k|ze^{i\beta}+2hi|)\cdot\left(\frac{ze^{i\beta}+2hi}{|ze^{i\beta}+2hi|}\right)^{-m}\right] \tag{29}$$

Similarly, in the complex plane $(z,\bar{z})$, the displacement expressions (19), (20), and (22) excited by incident SH wave change into

$$W^{(i)}=W_0\cdot e^{ik/2[(ze^{i\beta}+\xi)e^{i\alpha}+(\bar{z}e^{-i\beta}+\bar{\xi})e^{-i\alpha}]} \tag{30}$$

$$W^{(r)}=W_0\cdot e^{ik/2[(ze^{i\beta}+\xi)e^{-i\alpha}+(\bar{z}e^{-i\beta}+\bar{\xi})e^{i\alpha}]} \tag{31}$$

$$W^{(s)}=\sum_{m=-\infty}^{\infty}B_m\left[H_m^{(1)}(k|z|)\cdot\left(\frac{ze^{i\beta}}{|z|}\right)^m + H_m^{(1)}(k|ze^{i\beta}+2hi|)\cdot\left(\frac{ze^{i\beta}+2hi}{|ze^{i\beta}+2hi|}\right)^{-m}\right] \tag{32}$$

6.2 Stress Functions in Local Coordinates. At first, substitute Eq. (27) into Eq. (6) to obtain the stress functions $G_{rz}^{(i)}$ and $G_{\theta z}^{(i)}$ of unit source force:

$$G_{rz}^{(i)}=\mu\left(\frac{\partial G^{(i)}}{\partial z}e^{i\theta}+\frac{\partial G^{(i)}}{\partial \bar{z}}e^{-i\theta}\right) = -\frac{ik}{8}\left\{H_1^{(1)}(k|z-z_0|)\cdot\frac{|z-z_0|}{z-z_0}\cdot e^{i\theta} + H_1^{(1)}(k|z-z_0|)\cdot\frac{z-z_0}{|z-z_0|}\cdot e^{-i\theta}\right\} \tag{33}$$

$$G_{\theta z}^{(i)}=i\mu\left(\frac{\partial G^{(i)}}{\partial z}e^{i\theta}-\frac{\partial G^{(i)}}{\partial \bar{z}}e^{-i\theta}\right) = \frac{k}{8}\left\{H_1^{(1)}(k|z-z_0|)\cdot\frac{|z-z_0|}{z-z_0}\cdot e^{i\theta} - H_1^{(1)}(k|z-z_0|)\cdot\frac{z-z_0}{|z-z_0|}\cdot e^{-i\theta}\right\} \tag{34}$$

and substituting Eq. (28) into Eq. (6), we obtain the stress functions $G_{rz}^{(r)}$ and $G_{\theta z}^{(r)}$:

$$G_{rz}^{(r)}=\mu\left(\frac{\partial G^{(r)}}{\partial z}e^{i\theta}+\frac{\partial G^{(r)}}{\partial \bar{z}}e^{-i\theta}\right) = -\frac{ik}{8}\left\{H_1^{(1)}(k|ze^{i\beta}-\overline{z_0}e^{-i\beta}+2hi|)\cdot\frac{|ze^{i\beta}-\overline{z_0}e^{-i\beta}+2hi|}{ze^{i\beta}-\overline{z_0}e^{-i\beta}+2hi}\cdot e^{i(\beta+\theta)} + H_1^{(1)}(k|ze^{i\beta}-\overline{z_0}e^{-i\beta}+2hi|)\cdot\frac{ze^{i\beta}-\overline{z_0}e^{-i\beta}+2hi}{|ze^{i\beta}-\overline{z_0}e^{-i\beta}+2hi|}\cdot e^{-i(\beta+\theta)}\right\} \tag{35}$$

$$G_{\theta z}^{(r)}=i\mu\left(\frac{\partial G^{(r)}}{\partial z}e^{i\theta}-\frac{\partial G^{(r)}}{\partial \bar{z}}e^{-i\theta}\right) = \frac{k}{8}\left\{H_1^{(1)}(k|ze^{i\beta}-\overline{z_0}e^{-i\beta}+2hi|)\cdot\frac{|ze^{i\beta}-\overline{z_0}e^{-i\beta}+2hi|}{ze^{i\beta}-\overline{z_0}e^{-i\beta}+2hi}\cdot e^{i(\beta+\theta)} - H_1^{(1)}(k|ze^{i\beta}-\overline{z_0}e^{-i\beta}+2hi|)\cdot\frac{ze^{i\beta}-\overline{z_0}e^{-i\beta}+2hi}{|ze^{i\beta}-\overline{z_0}e^{-i\beta}+2hi|}\cdot e^{-i(\beta+\theta)}\right\} \tag{36}$$

and substituting Eq. (29) into Eq. (6), we obtain the stress functions $G_{rz}^{(s)}$ and $G_{\theta z}^{(s)}$:

$$G_{rz}^{(s)} = \mu\left(\frac{\partial G^{(s)}}{\partial z}e^{i\theta} + \frac{\partial G^{(s)}}{\partial \bar{z}}e^{-i\theta}\right) = \frac{1}{2}\mu k \sum_{m=-\infty}^{\infty} A_m \Bigg\{ H_{m-1}^{(1)}(k|z|) \cdot \left(\frac{z}{|z|}\right)^{m-1} \cdot e^{i(m\beta+\theta)} - H_{m+1}^{(1)}(k|z|) \cdot \left(\frac{z}{|z|}\right)^{m+1} \cdot e^{i(m\beta-\theta)} + H_{m-1}^{(1)}(k|ze^{i\beta}+2hi|) \cdot \left(\frac{ze^{i\beta}+2hi}{|ze^{i\beta}+2hi|}\right)^{-m+1} \cdot e^{-i(\beta+\theta)} - H_{m+1}^{(1)}(k|ze^{i\beta}+2hi|) \cdot \left(\frac{ze^{i\beta}+2hi}{|ze^{i\beta}+2hi|}\right)^{-m-1} \cdot e^{i(\beta+\theta)} \Bigg\} \quad (37)$$

$$G_{\theta z}^{(s)} = i\mu\left(\frac{\partial G^{(s)}}{\partial z}e^{i\theta} - \frac{\partial G^{(s)}}{\partial \bar{z}}e^{-i\theta}\right) = \frac{i}{2}\mu k \sum_{m=-\infty}^{\infty} A_m \Bigg\{ H_{m-1}^{(1)}(k|z|) \cdot \left(\frac{z}{|z|}\right)^{m-1} \cdot e^{i(m\beta+\theta)} + H_{m+1}^{(1)}(k|z|) \cdot \left(\frac{z}{|z|}\right)^{m+1} \cdot e^{i(m\beta-\theta)} - H_{m-1}^{(1)}(k|ze^{i\beta}+2hi|) \cdot \left(\frac{ze^{i\beta}+2hi}{|ze^{i\beta}+2hi|}\right)^{-m+1} \cdot e^{-i(\beta+\theta)} - H_{m+1}^{(1)}(k|ze^{i\beta}+2hi|) \cdot \left(\frac{ze^{i\beta}+2hi}{|ze^{i\beta}+2hi|}\right)^{-m-1} \cdot e^{i(\beta+\theta)} \Bigg\} \quad (38)$$

Then, in a similar way, substitute Eq. (30) into Eqs. (5) and (6), respectively, to obtain the corresponding stress functions $\tau_{xz}^{(i)}$, $\tau_{rz}^{(i)}$ and $\tau_{\theta z}^{(i)}$:

$$\tau_{xz}^{(i)} = \mu\left(\frac{\partial W^{(i)}}{\partial z} + \frac{\partial W^{(i)}}{\partial \bar{z}}\right) = i\mu k W_0 \cdot e^{ik/2[(ze^{i\beta}+\xi)e^{i\alpha}+(\bar{z}e^{-i\beta}+\bar{\xi})e^{-i\alpha}]}\cos(\alpha+\beta) \quad (39)$$

$$\tau_{rz}^{(i)} = \mu\left(\frac{\partial W^{(i)}}{\partial z}e^{i\theta} + \frac{\partial W^{(i)}}{\partial \bar{z}}e^{-i\theta}\right) = i\mu k W_0 \cdot e^{ik/2[(ze^{i\beta}+\xi)e^{i\alpha}+(\bar{z}e^{-i\beta}+\bar{\xi})e^{-i\alpha}]}\cos(\alpha+\beta+\theta) \quad (40)$$

$$\tau_{\theta z}^{(i)} = i\mu\left(\frac{\partial W^{(i)}}{\partial z}e^{i\theta} - \frac{\partial W^{(i)}}{\partial \bar{z}}e^{-i\theta}\right) = -i\mu k W_0 \cdot e^{ik/2[(ze^{i\beta}+\xi)e^{i\alpha}+(\bar{z}e^{-i\beta}+\bar{\xi})e^{-i\alpha}]}\sin(\alpha+\beta+\theta) \quad (41)$$

and substituting Eq. (31) into Eqs. (5) and (6), respectively, we then obtain the stress functions $\tau_{xz}^{(r)}$, $\tau_{rz}^{(r)}$, and $\tau_{\theta z}^{(r)}$:

$$\tau_{xz}^{(r)} = \mu\left(\frac{\partial W^{(r)}}{\partial z} + \frac{\partial W^{(r)}}{\partial \bar{z}}\right) = i\mu k W_0 \cdot e^{ik/2[(ze^{i\beta}+\xi)e^{-i\alpha}+(\bar{z}e^{-i\beta}+\bar{\xi})e^{i\alpha}]}\cos(\alpha-\beta) \quad (42)$$

$$\tau_{rz}^{(r)} = \mu\left(\frac{\partial W^{(r)}}{\partial z}e^{i\theta} + \frac{\partial W^{(r)}}{\partial \bar{z}}e^{-i\theta}\right) = i\mu k W_0 \cdot e^{ik/2[(ze^{i\beta}+\xi)e^{-i\alpha}+(\bar{z}e^{-i\beta}+\bar{\xi})e^{i\alpha}]}\cos(\beta-\alpha+\theta) \quad (43)$$

$$\tau_{\theta z}^{(r)} = i\mu\left(\frac{\partial W^{(r)}}{\partial z}e^{i\theta} - \frac{\partial W^{(r)}}{\partial \bar{z}}e^{-i\theta}\right) = -i\mu k W_0 \cdot e^{ik/2[(ze^{i\beta}+\xi)e^{-i\alpha}+(\bar{z}e^{-i\beta}+\bar{\xi})e^{i\alpha}]}\sin(\beta-\alpha+\theta) \quad (44)$$

At last, substituting Eq. (32) into Eqs. (5) and (6), respectively, we obtain the stress functions $\tau_{xz}^{(s)}$, $\tau_{rz}^{(s)}$ and $\tau_{\theta z}^{(s)}$:

$$\tau_{xz}^{(s)} = \mu\left(\frac{\partial W^{(s)}}{\partial z} + \frac{\partial W^{(s)}}{\partial \bar{z}}\right) = \frac{1}{2}\mu k W_0 \sum_{m=-\infty}^{\infty} B_m \Bigg\{ H_{m-1}^{(1)}(k|z|) \cdot \left(\frac{z}{|z|}\right)^{m-1} \cdot e^{im\beta} - H_{m+1}^{(1)}(k|z|) \cdot \left(\frac{z}{|z|}\right)^{m+1} \cdot e^{im\beta} + H_{m-1}^{(1)}(k|ze^{i\beta}+2hi|) \cdot \left(\frac{ze^{i\beta}+2hi}{|ze^{i\beta}+2hi|}\right)^{-m+1} \cdot e^{-i\beta} - H_{m+1}^{(1)}(k|ze^{i\beta}+2hi|) \cdot \left(\frac{ze^{i\beta}+2hi}{|ze^{i\beta}+2hi|}\right)^{-m-1} \cdot e^{i\beta} \Bigg\} \quad (45)$$

$$\tau_{rz}^{(s)} = \mu\left(\frac{\partial W^{(s)}}{\partial z}e^{i\theta} + \frac{\partial W^{(s)}}{\partial \bar{z}}e^{-i\theta}\right) = \frac{1}{2}\mu k W_0 \sum_{m=-\infty}^{\infty} B_m \Bigg\{ H_{m-1}^{(1)}(k|z|) \cdot \left(\frac{z}{|z|}\right)^{m-1} \cdot e^{i(m\beta+\theta)} - H_{m+1}^{(1)}(k|z|) \cdot \left(\frac{z}{|z|}\right)^{m+1} \cdot e^{i(m\beta-\theta)} + H_{m-1}^{(1)}(k|ze^{i\beta}+2hi|) \cdot \left(\frac{ze^{i\beta}+2hi}{|ze^{i\beta}+2hi|}\right)^{-m+1} \cdot e^{-i(\beta+\theta)} - H_{m+1}^{(1)}(k|ze^{i\beta}+2hi|) \cdot \left(\frac{ze^{i\beta}+2hi}{|ze^{i\beta}+2hi|}\right)^{-m-1} \cdot e^{i(\beta+\theta)} \Bigg\} \quad (46)$$

$$\tau_{\theta z}^{(s)} = i\mu\left(\frac{\partial W^{(s)}}{\partial z}e^{i\theta} - \frac{\partial W^{(s)}}{\partial \bar{z}}e^{-i\theta}\right) = \frac{i}{2}\mu k W_0 \sum_{m=-\infty}^{\infty} B_m \Bigg\{ H_{m-1}^{(1)}(k|z|) \cdot \left(\frac{z}{|z|}\right)^{m-1} \cdot e^{i(m\beta+\theta)} + H_{m+1}^{(1)}(k|z|) \cdot \left(\frac{z}{|z|}\right)^{m+1} \cdot e^{i(m\beta-\theta)} - H_{m-1}^{(1)}(k|ze^{i\beta}+2hi|) \cdot \left(\frac{ze^{i\beta}+2hi}{|ze^{i\beta}+2hi|}\right)^{-m+1} \cdot e^{-i(\beta+\theta)} - H_{m+1}^{(1)}(k|ze^{i\beta}+2hi|) \cdot \left(\frac{ze^{i\beta}+2hi}{|ze^{i\beta}+2hi|}\right)^{-m-1} \cdot e^{i(\beta+\theta)} \Bigg\} \quad (47)$$

6.3 Displacement and Stress Field of the Wedge. The unknown coefficients A_m and B_m in the displacement expressions can be determined by the stress free conditions on the surface of the cavity as follows:

$$G_{rz}^{(i)} + G_{rz}^{(r)} + G_{rz}^{(s)} = 0 \quad \text{at} \quad r = a \quad (48)$$

$$\tau_{rz}^{(i)} + \tau_{rz}^{(r)} + \tau_{rz}^{(s)} = 0 \quad \text{at} \quad r = a \quad (49)$$

Using Fourier expansion, we can obtain

$$\sum_{n=-\infty}^{\infty} \zeta_n = \sum_{n=-\infty}^{\infty}\sum_{m=-\infty}^{\infty} A_m \cdot \mathrm{s}_{nm} \quad \text{at} \quad r = a \quad (50)$$

$$\sum_{n=-\infty}^{\infty} \chi_n = \sum_{n=-\infty}^{\infty}\sum_{m=-\infty}^{\infty} B_m \cdot \lambda_{nm} \quad \text{at} \quad r = a \quad (51)$$

where

$$\zeta_n = \frac{1}{2\pi}\int_0^{2\pi} (G_{rz}^{(i)} + G_{rz}^{(r)}) \cdot e^{-in\theta} d\theta$$

$$\mathrm{s}_{nm} = -\frac{1}{2\pi}\int_0^{2\pi} G_{rz}^{(s)} \cdot e^{-in\theta} d\theta$$

$$\chi_n = \frac{1}{2\pi}\int_0^{2\pi} (\tau_{rz}^{(i)} + \tau_{rz}^{(r)}) \cdot e^{-in\theta} d\theta$$

$$\lambda_{nm} = -\frac{1}{2\pi}\int_0^{2\pi} \tau_{rz}^{(s)} \cdot e^{-in\theta} d\theta$$

Therefore, the unknown coefficients A_m and B_m can be obtained by solving the linear algebraic equations (50) and (51), respectively.

Based on the wave functions (27)–(32), and considering the effect of the stress $\hat{\tau}_{xz}=-\tau_{xz}$ that loaded on the surface B, we can get the antiplane displacement of the infinite wedge with a circular cavity as

$$W^{(t)} = (W^{(i)} + W^{(r)} + W^{(s)}) - \int_{y_1}^{y_2} \tau_{xz} \cdot (G^{(i)} + G^{(r)} + G^{(s)}) \cdot idy \tag{52}$$

where $\tau_{xz}=\tau_{xz}^{(i)}+\tau_{xz}^{(r)}+\tau_{xz}^{(s)}$, at $x=-L\sin(\beta+\arctan(d/h))$ and $y \in (y_1,+\infty)$, y_1 is the y position of the initial point of surface B. Then, the stress field in the wedge is

$$\tau_{\theta z}^{(t)} = (\tau_{\theta z}^{(i)} + \tau_{\theta z}^{(r)} + \tau_{\theta z}^{(s)}) - \int_{y_1}^{y_2} \tau_{xz} \cdot (G_{\theta z}^{(i)} + G_{\theta z}^{(r)} + G_{\theta z}^{(s)}) \cdot idy \tag{53}$$

In this paper, we define the DSCF as the ratio of the stress $\tau_{\theta z}^{(t)}$ (induced by total displacement field) to the stress τ_0 (induced by incident wave). For the steady-state SH waves, the DSCF is given by

$$\tau_{\theta z}^{*} = |\tau_{\theta z}^{(t)}/\tau_0| \tag{54}$$

where $\tau_0=\mu k W_0$. The wave number of incident wave can be expressed as the ratio of the diameter of the cavity $2a$ to the wavelength λ of the incident wave, namely,

$$\eta = ka/\pi = \omega a/c_s\pi = 2a/\lambda \tag{55}$$

which represents a dimensionless frequency $\omega a/c_s\pi$.

7 Numerical Examples and Results

With the novel method developed in Secs. 2–6, we can calculate the harmonic dynamic stress field of the infinite wedge with the circular cavity and study the effect of the apex angle of the wedge and the cavity position on the DSFC on the surface of the cavity.

To validate our method developed in this study, the apex angle of the wedge is at first set $\varphi=90$ deg ($2\varphi=180$ deg), by which the wedge problem degenerates to a half-space problem, which is the classical problem solved by Lee and Trifunac [25,26]. Figures 4(*a*) and 4(*b*) illustrate the surface displacement when the incident angle $\alpha=90$ deg and the wave number $\eta=0.5$ and 1.0 at the normalized distance between the vertex and the center of the cavity, $L/a=1.5$ and 5.0, respectively. It can be seen that our predictions agree very well with the numerical results of Lee and Trifunac [25,26]. Then, we set the distance between the cavity and the vertex of the wedge in our problem being large enough (e.g., $L/a=10{,}000$) so that the influence of the cavity on the surface motion can be neglected (we double checked this by selecting different value of L/a), then the problem can be degenerates into the problem solved by Sanchez-sesma [27]. We chose different apex angles of the wedge, $2\varphi=60,75,90,105,120,\ldots,225$ deg, and the incident SH wave comes along the bisector line of wedge with frequency $k=3\pi$. The displacement amplitude of the vertex is illustrated in Fig. 4(*c*). As we can see the predications of our method agree very well with the results of Sanchez-sesma [27].

Figure 5–7 show the DSCF at the surface of cavity at various apex angle $\varphi=90$ deg, $\varphi=75$ deg and 45 deg, respectively, with various incident angle $\alpha=0,45,90$ deg and different distance between the vertex and the center of the cavity $L=10,20,30$ (note that the center of cavity is on the bisector line of wedge angle). We will discuss the condition that the center is biased from the bisector line later, and the wave frequency $\eta=0.1,1.0,2.0$, respec-

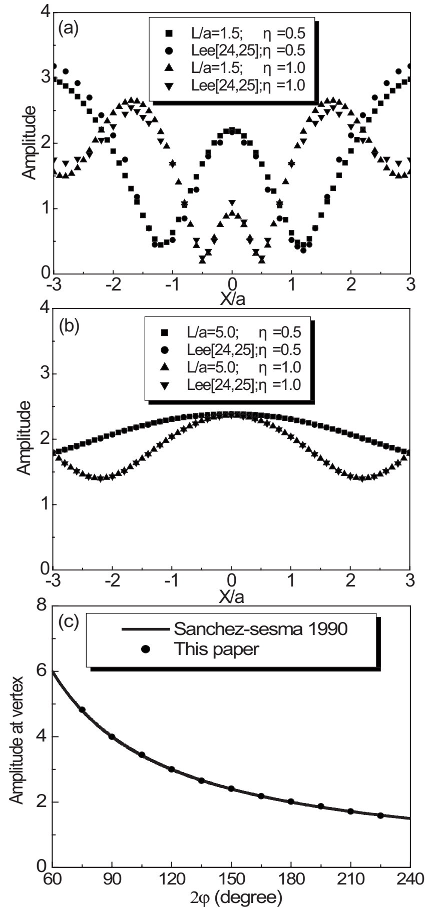

Fig. 4 Verification of our method. ((*a*) and (*b*)) The surface displacement of a half-space predicted by this paper in comparison with the results of Lee and Trifunac [25,26] at *L/a* =1.5 and 5.0, respectively. (*c*) The displacement at vertex of a wedge predicated by this paper in comparison with the results of Sanchez-sesma [27].

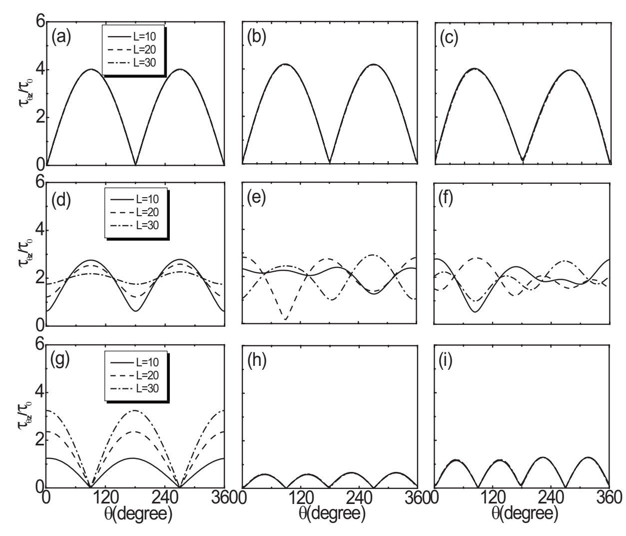

Fig. 5 The DSCF on the cavity at $\varphi=90$ deg, where (*a*) $\alpha=0$ deg, $\eta=0.1$; (*b*) $\alpha=0$ deg, $\eta=1.0$; (*c*) $\alpha=0$ deg, $\eta=2.0$; (*d*) $\alpha=45$ deg, $\eta=0.1$; (*e*) $\alpha=45$ deg, $\eta=1.0$; (*f*) $\alpha=45$ deg, $\eta=2.0$; (*g*) $\alpha=90$ deg, $\eta=0.1$; (*h*) $\alpha=90$ deg, $\eta=1.0$; and (*i*) $\alpha=90$ deg, $\eta=2.0$

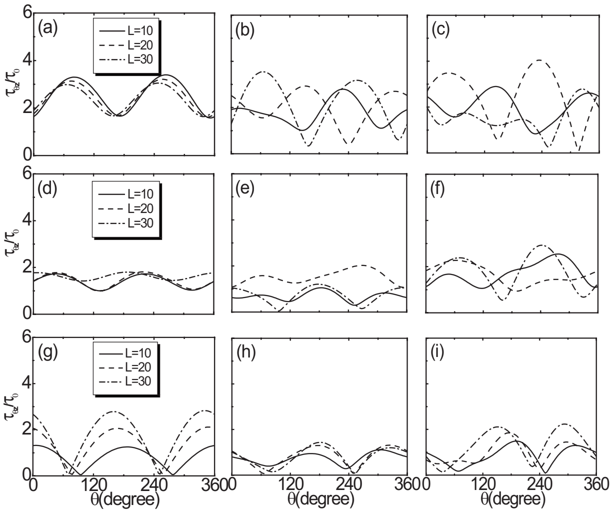

Fig. 6 The DSCF on the cavity at $\varphi=75$ deg, where (*a*) $\alpha=0$ deg, $\eta=0.1$; (*b*) $\alpha=0$ deg, $\eta=1.0$; (*c*) $\alpha=0$ deg, $\eta=2.0$; (*d*) $\alpha=45$ deg, $\eta=0.1$; (*e*) $\alpha=45$ deg, $\eta=1.0$; (*f*) $\alpha=45$ deg, $\eta=2.0$; (*g*) $\alpha=90$ deg, $\eta=0.1$; (*h*) $\alpha=90$ deg, $\eta=1.0$; and (*i*) $\alpha=90$ deg, $\eta=2.0$

tively. For example, Figs. 5(*a*), 5(*d*), and 5(*g*) show the variation of the DSCF on the cavity with different incident angles $\alpha=0,45,90$ deg at a constant incident frequency $\eta=0.1$. Figures 5(*b*), 5(*e*), and 5(*h*) and Figs. 5(*c*), 5(*f*), and 5(*i*) show the corresponding DSCF on cavity at different frequencies $\eta=1.0$ and $\eta=2.0$, respectively. We can see that the influence of the incident angles on the DSCF can be obtained through studying the panels in vertical alignment at constant incident frequencies (e.g., panels a, d, and g; panels b, e, and h; panels c, f, and i in Fig. 5), and in a similar manner, the influence of the incident frequencies on the DSCF can be obtained through studying the panels in horizontal alignment at constant incident angles (e.g., panels a–c; panels d–f; panels g–i in Fig. 5). Figures 6 and 7 are illustrated in the same way as that of Fig. 5.

At low frequency, $\eta=0.1$, for different incidence angles ($\alpha=0,45,90$ deg), and different wedge angles $\varphi=90$ deg, $\varphi=75$ deg and $\varphi=45$ deg, the DSCF around the loop are approximately periodically symmetric, which indicates that the response of wedge at $\eta=0.1$ is similar to a static response, as shown in Figs. 5(*a*), 5(*d*), and 5(*g*), Figs. 6(*a*), 6(*d*), and 6(*g*), and Figs. 7(*a*), 7(*d*), and 7(*g*)). At high frequencies $\eta=1.0$ (Figs. 5, 6, 7(*b*), 7(*e*), and 7(*h*)) and $\eta=2.0$ (Figs. 5, 6, 7(*c*), 7(*f*), and 7(*i*)), the stress concentration factors exhibit dynamic character, losing periodic symmetry. It is also noted that the position change of the cavity ($L=10,20,30$) does not influence the DSCF on the surface of cavity when $\varphi=90$ deg with horizontal incidence $\alpha=0$ deg (see Figs. 5(*a*)–5(*c*)). The underlying mechanism is that the incident wave horizontally penetrates the medium without the disturbance by the reflect wave from the boundary. From Figs. 5–7, we can see that the DSCF around the cavity decreases gradually with the increase in the incident angle of the incident waves at cavity position of $L=10$. It seems that the oblique and vertical incidence induce lower DSCF in comparison with the horizontal incident, which is caused by the scattering and diffraction of the SH-waves by the wedge and internal cavity.

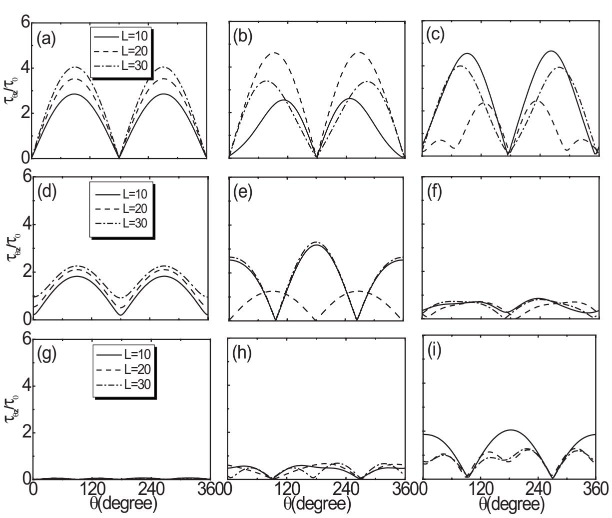

Fig. 7 The DSCF on the cavity at $\varphi=45$ deg, where (*a*) $\alpha=0$ deg, $\eta=0.1$; (*b*) $\alpha=0$ deg, $\eta=1.0$; (*c*) $\alpha=0$ deg, $\eta=2.0$; (*d*) $\alpha=45$ deg, $\eta=0.1$; (*e*) $\alpha=45$ deg, $\eta=1.0$; (*f*) $\alpha=45$ deg, $\eta=2.0$; (*g*) $\alpha=90$ deg, $\eta=0.1$; (*h*) $\alpha=90$ deg, $\eta=1.0$; and (*i*) $\alpha=90$ deg, $\eta=2.0$

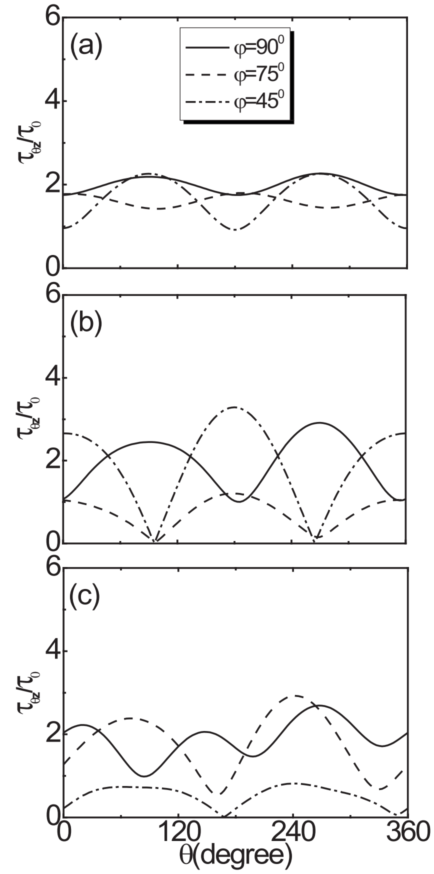

Fig. 8 The DSCF on the cavity at variable wedge angels with $L=30$, $\alpha=45$ deg, where (*a*) $\eta=0.1$, (*b*) $\eta=1.0$, and (*c*) $\eta=2.0$

The influence of wedge angles on the DSCF is studied at cavity position $L=30$ and the incident angle $\alpha=45$ deg, as shown in Fig. 8. We can see that the stress fluctuation on the surface of cavity is smaller at low frequency $\eta=0.1$, and the apex angle has less effect on the stress fluctuation; in contrast, the stress fluctuation is much higher at higher frequency $\eta=1.0$ and 2.0, and the apex angle has significant influence on the stress fluctuation.

Figure 9 shows the effect of the positions of the cavity on DSCF when the center of the cavity is biased from the bisector of the wedge angle at $\varphi=45$ deg in comparison with previous calculations when the center of the cavity is on the bisector. In this calculation, the line OO'' is biased from the bisector by 22.5 deg,

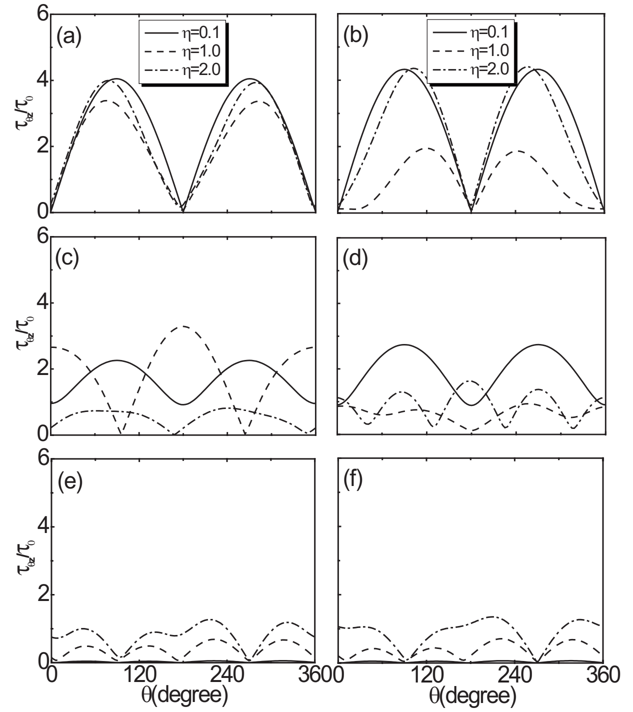

Fig. 9 The influence of the cavity positions on the DSCF when the cavity is biased from the bisector of the wedge angle at $L=30$, $\varphi=45$ deg. ((*a*) and (*b*)) $\alpha=0$ deg, ((*c*) and (*d*)) $\alpha=45$ deg, and ((*e*) and (*f*)) $\alpha=90$ deg, where (*a*), (*c*), and (*e*) show the DSCF when the cavity is on the bisector of the apex angle, while (*b*), (*d*), and (*f*) show the DSCF when the cavity is biased from the bisector.

i.e., the angle between the line OO'' and horizontal surface S changes from 45 deg (see Figs. 9(*a*), 9(*c*), and 9(*e*)) to 22.5 deg (see Figs. 9(*b*), 9(*d*), and 9(*f*)). The incident angles are $\alpha=0,45,90$ deg, the incident frequencies are $\eta=0.1,1.0,2.0$, respectively, and the cavity position is $L=30$. Figures 9(*b*), 9(*d*), and 9(*f*) exhibit several interesting observations: compared with the panel on the left side (Figs. 9(*a*), 9(*c*), and 9(*e*)), the DSCF of the biased cavity becomes higher at the frequencies of $\eta=0.1$ and $\eta=2.0$, but becomes lower at the frequency of $\eta=1.0$.

At last, a quarter space containing a cavity with different cavity position $L=10,1.5,1.45,1.43$ (continuously decreases the distance between the cavity center and apex) are calculated for the incident angle $\alpha=45$ deg and incident frequency $\eta=2.0$, as shown in Fig. 10. We can see that the DSCF increases rapidly as the cavity gets close to the wedge apex, and the DSCF becomes singular when the cavity is close enough to the wedge apex.

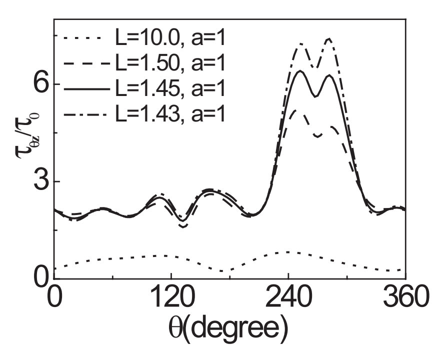

Fig. 10 The influence of the cavity position on the DSCF as the distance between the cavity center and the wedge apex decreases

8 Conclusions

A novel method is developed for studying the antiplane dynamic problem of an infinite wedge with a circular cavity by adopting the Green's function, complex functions, and multipolar coordinates method. This approach allows us to transfer the infinite wedge problem to an equivalent half-space problem by using Green's function method. The analytical expressions for the displacement and stress fields of the wedge are then derived. Based on the solution for the stress field of the wedge, the stress on the surface of the cavity are calculated at different wedge angles, location of the cavity, incident angles, and frequencies of the dynamic load. We find that the wedge angle, cavity location, and incident angle and frequency of the load have significant effect on the DSCF. The DSCFs grow rapidly as the distance between the cavity and wedge apex reduces. When the cavity is close enough to the boundary of the wedge, the DSCF on the loop exhibits singularity. The dynamic stress analysis method for an infinite wedge problem developed in this paper is of practical importance in engineering design, such as dam design and earthquake engineering.

Acknowledgment

This work is supported by the National Natural Science Foundation of China through Grant Nos. 10628205, 10732050, 10502031, and 10872115, the National Basic Research Program of China through Grant Nos. 2004CB619304 and 2007CB936803, and the SRF for ROCS, SEM

References

[1] Shahani, A. R., 1999, "Analysis of an Anisotropic Finite Wedge Under Antiplane Deformation," J. Elast., **56**, pp. 17–32.
[2] Shahani, A. R., 2003, "Mode III Stress Intensity Factors for Edge-Cracked Circular Shafts, Bonded Wedges, Bonded Half Planes and DCB's," Int. J. Solids Struct., **40**, pp. 6567–6576.
[3] Shahani, A. R., 2005, "Some Problems in the Antiplane Shear Deformation of Bi-Material Wedges," Int. J. Solids Struct., **42**, pp. 3093–3113.
[4] Shahani, A. R., 2006, "Model III Stress Intensity Factors in an Interfacial Crack in Dissimilar Bonded Materials," Arch. Appl. Mech., **75**, pp. 405–411.
[5] Tranter, C. J., 1948, "The Use of the Mellin Transform in Finding the Stress Distribution in an Infinite Wedge," Q. J. Mech. Appl. Math., **1**, pp. 125–130.
[6] Williams, M. L., 1952, "Stress Singularities Resulting From Various Boundary Conditions in Angular Corners of Plates in Extension," ASME J. Appl. Mech., **19**, pp. 526–528.
[7] Dempsey, J. P., and Sinclair, G. B., 1979, "On the Stress Singularities in the Plane Elasticity of the Composite Wedge," J. Elast., **9**, pp. 373–391.
[8] Dempsey, J. P., 1981, "The Wedge Subjected to Tractions: A Paradox Resolved," J. Elast., **11**, pp. l–10.
[9] Lévy, M., 1899, "Sur La Legitimite De La Regle Dite Du Trapeze Dans L'etude De La Resistance Des Barrages En Maconnerie," Compt. Rend., **126**, pp. 1235–1240.
[10] Ting, T. C. T., 1984, "The Wedge Subjected to Tractions: A Paradox Re-Examined," J. Elast., **14**, pp. 235–247.
[11] Ting, T. C. T., 1985, "Elastic Wedge Subjected to Antiplane Shear Traction—A Paradox Explained," Q. J. Mech. Appl. Math., **38**, pp. 245–255.
[12] Kargarnovin, M. H., and Shahani, A. R., 1997, "Analysis of an Isotropic Finite Wedge Under Anti-Plane Deformation," Int. J. Solids Struct., **34**, pp. 113–128.
[13] Shahani, A. R., 2007, "On the Anti-Plane Shear Deformation of Finite Wedges," Appl. Math. Model., **31**, pp. 141–151.
[14] Faal, R. T., Fotuhi, A. R., Fariborz, S. J., and Daghyani, H. R., 2004, "Anti-Plane Stress Analysis of an Isotropic Wedge With Multiple Cracks," Int. J. Solids Struct., **41**, pp. 4535–4550.
[15] Faal, R. T., Fariborz, S. J., and Daghyani, H. R., 2007, "Stress Analysis of a Finite Wedge Weakened by Cavities," Int. J. Mech. Sci., **49**, pp. 75–85.
[16] Achenbach, J. D., 1968, "Wedge-Like Waves in a Composite Medium," Int. J. Eng. Sci., **6**, pp. 223–232.
[17] Achenbach, J. D., 1970, "Shear Waves in an Elastic Wedge," Int. J. Solids Struct., **6**, pp. 379–388.
[18] Dermendjian, N., Lee, V. W., and Liang, J. W., 2003, "Anti-Plane Deformations Around Arbitrary-Shaped Canyons on a Wedge-Shape Half-Space: Moment Method Solutions," Earth. Eng. Eng. Vibra., **2**, pp. 281–287.
[19] Liu, G., and Liu, D. K., 2007, "The Ground Motion of an Isosceles Triangular Hill Above a Subsurface Cavity With Incident SH Waves," Acta Mech. Solida Sinica, **28**, pp. 60–66.
[20] Liu, D. K., Gai, B. Z., and Tao, G. Y., 1982, "Applications of the Method of

Complex Functions to Dynamic Stress Concentrations," Wave Motion, **4**, pp. 293–304.
[21] Liu, D., and Han, F., 1993, "The Scattering of Plane SH-Waves by Noncircular Cavity in Anisotropic Media," ASME J. Appl. Mech., **60**(3), pp. 769–772.
[22] Hudson, J. A., 1980, *The Excitation and Propagation of Elastic Waves*, University of Cambridge, Cambridge.
[23] Pao, Y. H., and Mow, C. C., 1973, *Diffraction of Elastic Waves and Dynamic Stress Concentrations*, Crane, Russak & Company Inc., New York.
[24] Lee, V. W., Chen, S., and Hsu, I. R., 1999, "Anti-Plane Diffraction From Canyon Above Subsurface Unlined Tunnel," J. Eng. Mech., **125**, pp. 668–674.
[25] Lee, V. W., 1977, "On the Deformations Near Circular Underground Cavity Subjected to Incident Plane SH-Waves," University of Southern California, Los Angeles, CA.
[26] Lee, V. W., and Trifunac, M. D., 1979, "Response of Tunnels to Incident SH-Waves," J. Eng. Mech., **105**, pp. 643–659.
[27] Sanchez-sesma, F. J., 1990, "Elementary Solutions for Response of a Wedge-Shaped Medium to Incident SH and SV Waves," Bull. Seismol. Soc. Am., **80**, pp. 737–742.

An Invariant Analysis of the Bending of Three Edge-Bonded Dissimilar Plates

K. Aderogba
Department of Mathematics,
University of Lagos,
Lagos, 23401 Nigeria
e-mail: kanmiaderogba@yahoo.com

A representation theorem is proved for the solution of the problem of two perfectly bonded isotropic semi-infinite plates under the influence of an arbitrary vertical load located in the midplane of the interior of one of them. Its function is to show that if the deflection of an unbounded isotropic plate under the influence of an arbitrary vertical load is known, then the corresponding deflections for two perfectly bonded isotropic semi-infinite plates are explicitly determinable, solely, and compactly in terms of the known deflection. Indeed, whatever the nature of the mechanism of loading is, the induced bending moments and shears in the two bonded plates are determinable by the process of differentiation only. A systematic repeated application of the theorem then yields a well-structured series solution when the arbitrary vertical load is arbitrarily located in a compound plate comprising two semi-infinite dissimilar isotropic plates separated by another dissimilar isotropic plate strip of finite breadth. As an application, we determine the effective elastic constants of a compound plate comprising a homogeneous isotropic plate in which a finite number of isotropic parallel plate strips of small breadths are embedded at such distances apart that their interaction effects may be taken as independent of one another. [DOI: 10.1115/1.3130813]

Keywords: isotropic materials, compound plates, bending, effective elastic constants, repeated reflection

1 Introduction

Maxwell [1] showed that if we have a complete theory of electrical images in the case of two dielectric media separated by a flat surface, then the corresponding complete theory of electrical images in the case of three dielectric media separated by two parallel flat surfaces may be systematically constructed by repeatedly applying the known theory for the two media.

It seems, however, that this powerful method is less known in linear elasticity because comparably intricate procedures abound in the literature when considering the effect of an elastic singularity operative in or near a surface layer. This may be attributable to the fact that while the solutions of electrostatic problems are generally representable by harmonic functions, the solutions of linear isotropic elasticity problems are generally representable by biharmonic functions, with the Cartesian coordinates occurring explicitly in the solution.

Nevertheless, Maxwell's method is concise, economical, and generally employable, usually yielding the precise form of the unique dependence of the global solution on only the influencing function and the material properties of the constituents of the compound medium, as well as reducing the rigor and effort required in calculating field components.

This repeated reflection method will therefore be employed in this paper to determine the deflection of a compound plate comprising two dissimilar isotropic semi-infinite plates separated by another dissimilar isotropic plate strip of finite breadth, under the influence of an arbitrary vertical load arbitrarily located in the compound plate. It will therefore require establishing first the complete theory of elastic images in the case of two dissimilar isotropic semi-infinite plates separated by a straight line, under the influence of an arbitrary vertical load located in the interior of one of the two perfectly bonded plates. Although it turns out that the calculation of the required deflections of the two bonded plates requires the two operations of differentiation and integration, the calculation of the desired bending moments and Kirchoff shears requires the process of differentiation only, whatever the nature of the mechanism of loading is.

The general solution subsequently constructed by repeatedly applying the theory thus obtained in the case of two media to the case of three plates separated by two parallel straight lines, is then employed to determine the effective flexural rigidity and Poisson's ratio of a compound plate comprising a homogeneous isotropic plate in which N parallel plate strips of small breadths are embedded, at such distances apart that their interaction effects may be considered as independent of one another. Maxwell [1] used a similar approach to determine the effective resistance of a compound medium consisting of a dielectric medium of resistance k_2 in which identical dielectric small spheres of resistance k_1 are disseminated, whose separate effects do not depend on their interference.

2 Maxwell's Motivating Problem

With a view to indicating the broad lines of the treatment of the elastic compound plate problem, the motivating problem of Maxwell [1] will first be revisited in order to present his solution in a compact well-structured manner, which is invariant, with respect to the choice of the physical nature of the influencing electrical singularity, and which also takes account of the companion problem when the arbitrary influencing singularity is located inside the separating dielectric plate.

Therefore, let x, y, and z be the three-dimensional rectangular Cartesian coordinates, and suppose that the three regions ($|x|<\infty, |y|<\infty, -\infty<z<0$), ($|x|<\infty, |y|<\infty, 0<z<H$), and ($|x|<\infty, |y|<\infty, H<z<\infty$) are occupied by three dielectric media whose specific resistances are k_1, k_2, and k_3, respectively; the

Contributed by the Applied Mechanics Division of ASME for publication in the Journal of Applied Mechanics. Manuscript received February 15, 2008; final manuscript received February 19, 2009; published online July 23, 2009. Review conducted by Anthony Waas.

electrostatic potentials and the electric currents being continuous at the two parallel plane surfaces of separation between the three media.

First, let us suppose that the first medium of resistance k_1 contains an arbitrary influencing singularity, which, if this first medium had been infinitely extended, is characterized by the harmonic electrostatic potential $V\ (x,y,z)$. Then, in the actual case under consideration, the potentials V_1, V_2, and V_3 induced in the three domains $-\infty < z < 0$, $0 < z < H$, and $H < z < \infty$ can be calculated without any complexity by the principle of repeated reflection to yield the solution

$$V_1 = V(x,y,z) - k_{12}V(x,y,-z) + k_{32}(1-k_{12}^2)\sum_{n=1}^{\infty}(k_{12}k_{32})^{n-1}V(x,y,2nH-z)$$

$$V_2 = (1+k_{21})\left[V(x,y,z) + k_{32}\sum_{n=1}^{\infty}(k_{12}k_{32})^{n-1}V(x,y,2nH-z) + \sum_{n=1}^{\infty}(k_{12}k_{32})^{n}V(x,y,2nH+z)\right]$$

$$V_3 = (1-k_{12})(1+k_{32})\left[V(x,y,z) + \sum_{n=1}^{\infty}(k_{12}k_{32})^{n}V(x,y,2nH+z)\right]$$

provided that $k_{ij}=(k_i-k_j)/(k_i+k_j)$, which shows that only two combinations of the resistances k_1, k_2, and k_3, namely, k_{12} and k_{32}, are required to characterize the electrostatics of the compound medium, since $k_{ij}=-k_{ji}$, and that at great distances from the interfaces, the potential V_3 on the other side of the interface plate assumes the form $V_3^{\infty}=(1-k_{12})(1+k_{32})V_0(x,y,z)/(1-k_{12}k_{32})$, where $V_0(x,y,z)$ is the value of the influencing potential V at the origin.

This solution is clearly in complete agreement with that of Maxwell [1] in the special case when the influencing singularity is a point charge E located at the point (0, 0, $-h$) in the first medium, for which $V(x,y,z)=E\cdot[x^2+y^2+(z+h)^2]^{-1/2}$. In this case, we can reduce the series solution to definite integrals by the relation

$$(r^2+z^2)^{-1/2} = \int_0^{\infty} J_0(rt)e^{-t|z|}dt, \quad r^2 = x^2+y^2$$

where J_0 denotes the ordinary Bessel function of zero order. Thus,

$$V_3 = E(1-k_{12})(1+k_{32})\int_0^{\infty} J_0(rt)e^{-t(z+h)}[1-k_{12}k_{32}e^{-2Ht}]^{-1}dt$$

Next, suppose that the arbitrary singularity is operative inside the separating medium of resistance k_2, which, if this medium were infinitely extended, is characterized by the potential $V\ (x,y,z)$. Then, with k_{ij} as previously defined, an application of the principle of images again yields the new solution

$$V_1 = (1+k_{12})\left[V(x,y,z) + k_{32}\sum_{n=1}^{\infty}(k_{12}k_{32})^{n-1}\{V(x,y,2nH-z) + k_{12}V(x,y,z-2nH)\}\right]$$

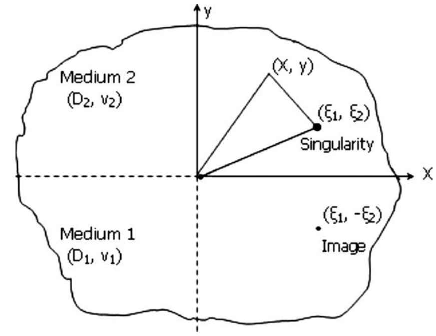

Fig. 1 Singularity in the interior of one of the two joined semi-infinite plates

$$V_2 = V(x,y,z) + k_{12}V(x,y,-z) + k_{32}\sum_{n=1}^{\infty}(k_{12}k_{32})^{n-1}\{V(x,y,2nH-z) + k_{12}V(x,y,z-2nH)\} + \sum_{n=1}^{\infty}(k_{12}k_{32})^{n}\{V(x,y,2nH+z) + k_{12}V(x,y,-2nH-z)\}$$

$$V_3 = (1+k_{32})\left[V(x,y,z) + k_{12}V(x,y,-z) + \sum_{n=1}^{\infty}(k_{12}k_{32})^{n}\{V(x,y,2nH+z) + k_{12}V(x,y,-2nH-z)\}\right]$$

which can again be reduced to definite integrals in particular cases.

We may remark that as the repeated reflection is effected, the images get farther and farther away from the two parallel plane interfaces, and their influence therefore gets less and less.

If the influencing singularity is a point charge E located at the point (0, 0, h) inside the separating plate of resistance k_2, and if we again put $r^2=x^2+y^2$, then proceeding to the limit as $r\to\infty$, we find that

$$V_2 = -E(1+k_{12})\left[1+\frac{(1+k_{12})}{k_{12}(1-k_{12}k_{32})}\right]\log r$$

This shows that the potential V_2 gives rise to a mainly two-dimensional current when the distance from the influencing point charge is a moderate multiple of the thickness of the separating plate.

There is no difficulty whatsoever in generalizing the foregoing introductory analysis to conduction through any number of bonded plane layers separating two other dissimilar media, but the above introductory analysis is all that we require in this paper.

3 A Representation Theorem

In further preparation for the analysis of the problem of three perfectly edge-bonded elastic plates separated by two parallel straight lines, we first establish a solution representation theorem in the case of two elastic plates separated by a single straight line. Its function is to transform the solution for an unbounded plate under the influence of an arbitrary vertical load into the corresponding solution for two perfectly edge-bonded dissimilar semi-infinite isotropic plates.

Let x and y be the two-dimensional rectangular Cartesian coordinates, and suppose that the two domains $(|x|<\infty, -\infty<y<0)$ and $(|x|<\infty, 0<y<\infty)$ are occupied by two dissimilar isotropic plates of elastic moduli (D_1,ν_1) and (D_2,ν_2), respectively, as shown in Fig. 1, a perfect bond being maintained along the interface ($|x|<\infty, y=0$), with D_1 and D_2 standing for flexural rigidities, while v_1 and v_2 designate corresponding Poisson's ratios.

Let an arbitrary vertical load be applied at the point (ξ_1, ξ_2) inside the second plate of moduli (D_2, ν_2), which in an unbounded plate ($|x|<\infty, |y|<\infty$) is characterized by the deflection $W(x,y)$. It is desired to determine the induced deflections $W_1(x,y)$ and $W_2(x,y)$ in the regions $y<0$ and $y>0$, respectively, consistent with the perfect bond continuity conditions

$$W_1 = W_2, \frac{\partial W_1}{\partial y} = \frac{\partial W_2}{\partial y}$$
$$M_2^{(1)} = M_2^{(2)}, {}_*V_2^{(1)} = {}_*V_2^{(2)} \tag{1}$$

at $y=0$, for all x, where M_1 and M_2 are bending moments, while ${}_*V_1$ and ${}_*V_2$ are Kirchoff shears, subscripts 1 and 2 in parentheses are used to distinguish between the regions $y<0$ and $y>0$, respectively. Generally [2],

$$M_1 = -D\left[\nabla^2 W - (1-\nu)\frac{\partial^2 W}{\partial y^2}\right]$$
$$M_2 = -D\left[\nu\nabla^2 W + (1-\nu)\frac{\partial^2 W}{\partial y^2}\right]$$
$${}_*V_1 = -D\frac{\partial}{\partial x}\left[\nabla^2 W + (1-\nu)\frac{\partial^2 W}{\partial y^2}\right] \tag{2}$$
$${}_*V_2 = -D\frac{\partial}{\partial y}\left[(2-\nu)\nabla^2 W - (1-\nu)\frac{\partial^2 W}{\partial y^2}\right]$$
$$\nabla^4 W = 0$$

where ∇^2 stands for the two-dimensional Laplacian operator.

For a bending hot spot located at the point (ξ_1, ξ_2) in an infinite homogeneous plate, $W(x,y)=c_1 \log r_1$, where c_1 is a constant and $r_1^2=(x-\xi_1)^2+(y-\xi_2)^2$, whereas for a concentrated vertical load applied at the same point in an infinite plate $W(x,y)=c_2 r_1^2 \log r_1$, where c_2 is another constant [2]. With $r^2=x^2+y^2$, we may also note the formula

$$2\int\int \log r dy dy = r^2 \log r - \frac{3}{2}(y^2-x^2) + 2x\left[y \tan^{-1}\left(\frac{y}{x}\right) - x \log r\right]$$

which shows that the biharmonic function $r^2 \log r$ is representable in terms of the harmonic functions (y^2-x^2), $\log r$, and $y \tan^{-1}(y/x) - x \log r$. Clearly, therefore, and as first noted by Almansi [3] in his investigation of the general solution of the polyharmonic equation $\nabla^{2n}\Phi=0$, for any positive integer n, if we are given any two-dimensional biharmonic function ψ, then harmonic functions F and G are determinable, such that ψ is representable in at least one of the forms:

$$F + xG, \quad F + yG, \quad F + r^2 G$$

the choice being guided by the boundary-value problem that may be under investigation.

Consequently, in view of the semi-infinite domains of definition of the two materials constituting the present composite plate, we assume that the influencing function $W(x,y)$ due to the presence of an arbitrary singularity at the point (ξ_1, ξ_2) admits the Fourier integral representation,

$$W(x,y) = \int_0^\infty [f(t) + ytg(t)]e^{ty} \cos txdt \tag{3}$$

when $y<\xi_2$, where $f(t)$ and $g(t)$ are known functions of t and ξ_2 being immaterial in the subsequent analysis if $\cos tx$ is replaced by $\sin t(x-\xi_1)$ or by $\cos t(x-\xi_1)$.

Next, guided by Eq. (3) and the regularity requirement that the perturbational part of the desired deflection must vanish as $y \to \infty$, we construct $W_1(x,y)$ and $W_2(x,y)$ as follows:

$$W_1 = \int_0^\infty [F_1(t) + ytG_1(t)]e^{ty} \cos txdt$$
$$W_2 = \int_0^\infty [\{F_2(t) + ytG_2(t)\}e^{-ty} + \{f(t) + ytg(t)\}e^{ty}]\cos txdt \tag{4}$$

where the weighting functions $F_i(t)$ and $G_i(t)$, $i=1,2$, are to be determined in terms of the known functions $f(t)$ and $g(t)$, consistent with the continuity conditions in Eq. (1).

Substitution of Eq. (4) into Eq. (2), and the application of Eq. (1), therefore yield the connections

$$F_1 = f(1-\alpha_{12}) + g\lambda_{12}, \quad G_1 = g(1-\beta_{12})$$
$$F_2 = -f\alpha_{12} + g\lambda_{12}, \quad G_2 = -(2f+g)\alpha_{12} \tag{5}$$

where

$$\alpha_{ij} = [D_i(1-\nu_i) - D_j(i-\nu_j)]/[D_i(1-\nu_i) + D_j(3+\nu_j)]$$
$$\beta_{ij} = [D_i(3+\nu_i) - D_j(3+\nu_j)]/[D_i(3+\nu_i) + D_j(1-\nu_j)] \tag{6}$$
$$\lambda_{ij} = \tfrac{1}{2}(\beta_{ij} - \alpha_{ij})$$

having no summation on any repeated index and being clear that $\alpha_{ij} \neq -\alpha_{ji}$, $\beta_{ij} \neq -\beta_{ji}$.

This completes the analysis of the two-phase plate problem. On noting that the representation in Eq. (3) is equivalent to the results,

$$\int_0^\infty f(t)e^{ty} \cos txdt = W(x,y) - \frac{1}{2}y\int \nabla^2 W(x,y)dy$$
$$\int_0^\infty tg(t)e^{ty} \cos txdt = \frac{1}{2}\int \nabla^2 W(x,y)dy \tag{3'}$$

the substitution of Eq. (5) into Eq. (4) and comparison of the resulting expressions with Eq. (3) yield the desired uniqueness theorem as follows: If the deflection $W(x,y)$ of an unbounded plate ($|x|<\infty, |y|<\infty$), under an arbitrary vertical load applied in the upper region $y>0$ is known, then the required deflections W_1 and W_2 for two perfectly bonded semi-infinite isotropic plates occupying the domains ($|x|<\infty, -\infty<y<0$) and ($|x|<\infty, 0<y<\infty$), respectively, when the same arbitrary vertical load is applied to the upper plate ($|x|<\infty, 0<y<\infty$), are explicitly determinable in terms of the known influencing deflection W in accordance with the relations

$$W_1 = \pounds_{21}(y)W(x,y)$$
$$W_2 = W(x,y) + L_{21}(y)W(x,-y) \tag{7}$$

where the operators $L_{21}(y)$ and $£_{21}(y)$ are defined by

$$L_{21}(y) = -\alpha_{12}\left[1 - 2y\frac{\partial}{\partial y} + y^2\nabla^2\right] + \frac{1}{2}\lambda_{12}\int dy\int \nabla^2\{\ \}dy$$

$$£_{21}(y) = 1 - \alpha_{12} + \frac{1}{2}y(\alpha_{12} - \beta_{12})\int \nabla^2\{\ \}dy + \frac{1}{2}\lambda_{12}\int dy\int \nabla^2\{\ \}dy \tag{8}$$

showing that only two combinations of the elastic moduli (D_1, ν_1) and (D_2, ν_2), namely, α_{12} and β_{12}, are required in the characterization of the deflection of the perfectly joined semi-infinite plates.

As will be apparent from the preceding analysis, the general manner in which the dependence of W_1 and W_2 on W is established is at least as important as the recognition of the uniqueness itself. Moreover, since neither medium has preferred status, the sense of loading is immaterial. Thus, if the loading were applied to the first plate of moduli (D_1, ν_1), then the final result would be

$$W_1 = W(x,y) + £_{12}(y)W(x,-y)$$
$$W_2 = L_{12}(y)W(x,y) \tag{9}$$

where

$$L_{12}(y) = 1 - \alpha_{21} + \frac{1}{2}y(\alpha_{21} - \beta_{21})\int \nabla^2\{\ \}dy + \frac{1}{2}\lambda_{21}\int dy\int \nabla^2\{\ \}dy$$

$$£_{12}(y) = -\alpha_{21}\left[1 - 2y\frac{\partial}{\partial y} + y^2\nabla^2\right] + \frac{1}{2}\lambda_{21}\int dy\int \nabla^2\{\ \}ydy \tag{10}$$

while α_{21}, β_{21}, and λ_{21} are once again defined by Eq. (6). We shall also require the operators

$$L_{23}(y) = -\alpha_{32}\left[1 - 2y\frac{\partial}{\partial y} + y^2\nabla^2\right] + \frac{1}{2}\lambda_{32}\int dy\int \nabla^2\{\ \}ydy$$

$$£_{23}(y) = 1 - \alpha_{32} + \frac{1}{2}y(\alpha_{32} - \beta_{32})\int \nabla^2\{\ \}dy + \frac{1}{2}\lambda_{32}\int dy\int \nabla^2\{\ \}dy \tag{11}$$

whose structures are governed by the operators in Eq. (8). It may be readily verified that the representation theorem (Eq. (7)) reduces to that of Aderogba [4] in the special case when the influencing deflection $W(x,y)$ is harmonic.

Moreover, since it also follows from Eqs. (7) and (8) that

$$\nabla^2 W_1 = (1 - \beta_{12})\nabla^2 W(x,y)$$

$$\frac{\partial^2 W_1}{\partial y^2} = \left[(1 - \alpha_{12})\frac{\partial^2}{\partial y^2} + \frac{1}{4}(\alpha_{12} - \beta_{12})\left(3 + 2y\frac{\partial}{\partial y}\right)\nabla^2\right]W(x,y)$$

$$\nabla^2 W_2 = \nabla^2 W(x,y) - \alpha_{12}\left[\nabla^2 - 2\frac{\partial}{\partial y}\left(2\frac{\partial}{\partial y} - y\nabla^2\right)\right]W(x,-y)$$

$$\frac{\partial^2 W_2}{\partial y^2} = \frac{\partial^2}{\partial y^2}W(x,y) + \frac{1}{4}(\beta_{12} - \alpha_{12})\nabla^2 W(x,-y) - \alpha_{12}\left[\frac{\partial^2}{\partial y^2} - \frac{\partial}{\partial y}\left(1 + y\frac{\partial}{\partial y}\right)\left(2\frac{\partial}{\partial y} - y\nabla^2\right)\right]W(x,-y)$$

the substitution of these expressions into Eq. (2) leads to the conclusion that if we know the deflection when the elastic homogeneous isotropic infinite plate is subjected to an arbitrary vertical load, then the corresponding bending moments and Kirchoff shears for two perfectly bonded isotropic semi-infinite plates can be obtained by differentiation of the known deflection for the infinite plate.

Specifically,

$$M_1^{(1)} = -D_1\left[\left\{1 - \beta_{12} - \frac{1}{4}(1-\nu_1)(\alpha_{12} - \beta_{12})\left(3 + 2y\frac{\partial}{\partial y}\right)\right\}\nabla^2 - (1-\nu_1)(1-\alpha_{12})\frac{\partial^2}{\partial y^2}\right]W(x,y)$$

$$M_2^{(1)} = -D_1\left[\left\{\nu_1(1 - \beta_{12}) + \frac{1}{4}(1-\nu_1)(\alpha_{12} - \beta_{12})\left(3 + 2y\frac{\partial}{\partial y}\right)\right\}\nabla^2 + (1-\nu_1)(1-\alpha_{12})\frac{\partial^2}{\partial y^2}\right]W(x,y)$$

$$_*V_1^{(1)} = -D_1\frac{\partial}{\partial x}\left[\left\{1 - \beta_{12} + \frac{1}{4}(1-\nu_1)(\alpha_{12} - \beta_{12})\left(3 + 2y\frac{\partial}{\partial y}\right)\right\}\nabla^2 + (1-\nu_1)(1-\alpha_{12})\frac{\partial^2}{\partial y^2}\right]W(x,y) \tag{12}$$

$$_*V_2^{(1)} = -D_1\frac{\partial}{\partial y}\left[\left\{(2-\nu_1)(1 - \beta_{12}) - \frac{1}{4}(1-\nu_1)(\alpha_{12} - \beta_{12})\left(3 + 2y\frac{\partial}{\partial y}\right)\right\}\nabla^2 - (1-\nu_1)(1-\alpha_{12})\frac{\partial^2}{\partial y^2}\right]W(x,y)$$

$$M_1^{(2)} = -D_2\left[\left\{\nabla^2 - (1-\nu_2)\frac{\partial^2}{\partial y^2}\right\}W(x,y) - \alpha_{12}\left\{\nabla^2 - 2\frac{\partial}{\partial y}\left(2\frac{\partial}{\partial y} - y\nabla^2\right)\right\}W(x,-y) + \alpha_{12}(1-\nu_2)\left\{\frac{\partial^2}{\partial y^2} - \frac{\partial}{\partial y}\left(1 + y\frac{\partial}{\partial y}\right)\left(2\frac{\partial}{\partial y} - y\nabla^2\right)\right\}W(x,-y) + \frac{1}{4}(1-\nu_2)(\alpha_{12} - \beta_{12})\nabla^2 W(x,-y)\right]$$

$$M_2^{(2)} = -D_2\left[\left\{\nu_2\nabla^2 + (1-\nu_2)\frac{\partial^2}{\partial y^2}\right\}W(x,y) - \nu_2\alpha_{12}\left\{\nabla^2 - 2\frac{\partial}{\partial y}\left(2\frac{\partial}{\partial y} - y\nabla^2\right)\right\}W(x,-y) - \alpha_{12}(1-\nu_2)\left\{\frac{\partial^2}{\partial y^2} - \frac{\partial}{\partial y}\left(1 + y\frac{\partial}{\partial y}\right)\left(2\frac{\partial}{\partial y} - y\nabla^2\right)\right\}W(x,-y) - \frac{1}{4}(1-\nu_2)(\alpha_{12} - \beta_{12})\nabla^2 W(x,-y)\right]$$

$$_*V_1^{(2)} = -D_2\frac{\partial}{\partial x}\left[\left\{\nabla^2 + (1-\nu_2)\frac{\partial^2}{\partial y^2}\right\}W(x,y) - \alpha_{12}\left\{\nabla^2 - 2\frac{\partial}{\partial y}\left(2\frac{\partial}{\partial y} - y\nabla^2\right)\right\}W(x,-y) - \alpha_{12}(1-\nu_2) \times \left\{\frac{\partial^2}{\partial y^2} - \frac{\partial}{\partial y}\left(1 + y\frac{\partial}{\partial y}\right)\left(2\frac{\partial}{\partial y} - y\nabla^2\right)\right\}W(x,-y) - \frac{1}{4}(1-\nu_2)(\alpha_{12} - \beta_{12})\nabla^2 W(x,-y)\right] \tag{13}$$

$$_*V_2^{(2)} = -D_2\frac{\partial}{\partial y}\left[\left\{(2-\nu_2)\nabla^2 - (1-\nu_2)\frac{\partial^2}{\partial y^2}\right\}W(x,y) - \alpha_{12}(2-\nu_2) \times \left\{\nabla^2 - 2\frac{\partial}{\partial y}\left(2\frac{\partial}{\partial y} - y\nabla^2\right)\right\}W(x,-y) + \alpha_{12}(1-\nu_2)\left\{\frac{\partial^2}{\partial y^2} - \frac{\partial}{\partial y}\left(1 + y\frac{\partial}{\partial y}\right)\left(2\frac{\partial}{\partial y} - y\nabla^2\right)\right\}W(x,-y) + \frac{1}{4}(1-\nu_2)(\alpha_{12} - \beta_{12})\nabla^2 W(x,-y)\right]$$

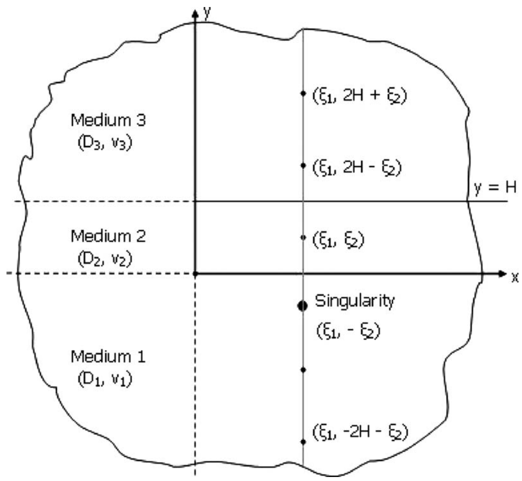

Fig. 2 Singularity outside a plate separating two semi-infinite plates

These relations clearly facilitate the routine calculation of interfacial jump quantities, since local values of moments and shears are of importance in the bending of compound materials.

4 The Three-Phase Compound Plate

Suppose now that three dissimilar plates with moduli $(D_1,\nu_1\}$, $\{D_2,\nu_2)$, and (D_3,ν_3) occupy the regions $(|x|<\infty,-\infty<y<0)$, $(|x|<\infty,0<y<H)$, and $(|x|<\infty,H<y<\infty)$, respectively, as shown in Fig. 2, the three plates being perfectly bonded at the interfaces $(|x|<\infty,y=0)$ and $(|x|<\infty,y=H)$.

First, we suppose that an arbitrary vertical load is applied in the interior of the first medium of moduli (D_1,ν_1), which in an unbounded medium $(|x|<\infty,|y|<\infty)$ is characterized by the deflection $W(x,y)$. Then, repeated application of the representation theorem (Eq. (7)) at the two parallel straight line interfaces immediately yields the formulas

$$W_1 = W(x,y) + \pounds_{12}(y)W(x,-y) + \pounds_{21}(y)\sum_{n=1}^{\infty} L^{(n)}(y)L_{12}(2nH - y)W(x,2nH-y)$$

$$W_2 = L_{12}(y)W(x,y) + \sum_{n=1}^{\infty} L^{(n)}(y)L_{12}(2nH-y)W(x,2nH-y) + L_{21}(y)\sum_{n=1}^{\infty} L^{(n)}(-y)L_{12}(2nH+y)W(x,2nH+y) \tag{14}$$

$$W_3 = \pounds_{23}(H-y)\left[L_{12}(y)W(x,y) + L_{21}(y)\sum_{n=1}^{\infty} L^{(n)}(-y)L_{12}(2nH + y)W(x,2nH+y)\right]$$

for the desired deflections in the three regions $(|x|<\infty,-\infty<y<0)$, $(|x|<\infty,0<y<H)$, and $(|x|)<\infty$, $H<y<\infty)$, respectively, where for any positive integer n,

$$L^{(n)}(y) = L_{23}(H-y)L_{21}(2H-y)\cdots L_{21}[2(n-1)H-y]L_{23}[(2n-1)H-y] \tag{15}$$

Two similar sets of formulas, involving Airy stress function and Love strain function, have been established by Aderogba [5,6] in the case of extensional elasticity. We may also note that if the interface plate of moduli (D_2,ν_2) is very much softer than the other constituents of the compound plate, then it tends to prevent the transmission of singularities from the influencing medium of moduli (D_1,ν_1) to the outer medium of moduli (D_3,ν_3) on the other side of the interface plate, and vice versa. It may also be noted from Eq. (14) that the distant effect in the third medium due to the specification of an arbitrary vertical load in the first medium is characterized by the deflection

$$W_3^{\infty} = \pounds_{23}(y)\left[L_{12}(y)W_0(x,y) + \sum_{n=1}^{\infty}[L_{21}(y)L_{23}(y)]^n L_{12}(y)W_0(x,y)\right] \tag{16}$$

a formula that will be useful in subsequent analysis, where W_0 is the value of W when the singularity is located at the origin.

Next, we suppose that the arbitrary vertical load is applied in the interior of the interface plate of moduli (D_2,ν_2), which in an unbounded plate $(|x|<\infty,|y|<\infty)$ is characterized by the deflection $W(x,y)$. Then, by again repeatedly applying the representation theorem (Eq. (7)) at the two parallel straight line interfaces $(|x|<\infty,y=0)$ and $(|x|<\infty,y=H)$, we arrive at the formulas

$$W_1 = \pounds_{21}(y)\left[W(x,y) + \sum_{n=1}^{\infty} L^{(n)}(y)\{W(x,2nH-y) + L_{21}(2n+1-y)W(x,-2nH+y)\}\right]$$

$$W_2 = W(x,y) + L_{21}(y)W(x,-y) + \sum_{n=1}^{\infty} L^{(n)}(y)[W(x,2nH-y) + L_{21}(2nH-y)W(x,-2nH+y)] + L_{21}(y)\sum_{n=1}^{\infty} L^{(n)}(-y) \times [W(x,2nH+y) + L_{21}(2nH+y)W(x,-2nH-y)] \tag{17}$$

$$W_3 = \pounds_{23}(H-y)\left[W(x,y) + L_{21}(y)W(x,-y) + L_{21}(y)\sum_{n=1}^{\infty} L^{(n)}(-y) \times\{W(x,2nH+y) + L_{21}(2nH+y)W(x,-2nH-y)\}\right]$$

where the operators $L_{ij}(y)$, $\pounds_{ij}(y)$, and $L^{(n)}(y)$ assume their previous values.

The special case of a plate strip $(0<|x|<\infty,\ 0<y<H)$, bonded to two rigid constraints and subjected to an arbitrary vertical load in its interior, may be deduced from Eq. (17) by making $D_1=\infty$, $D_3=\infty$, which leads directly to $W_1=0$, $W_3=0$, while

$$W_2 = W(x,y) + \Delta(y)W(x,-y) + \sum_{n=1}^{\infty}\Delta^{(n)}(y)[W(x,2nH-y) + \Delta(2nH-y)W(x,-2nH+y)] + \Delta(y)\sum_{n=1}^{\infty}\Delta^{(n)}(-y)[W(x,2nH+y) + \Delta(2nH+y)W(x,-2nH-y)] \tag{18}$$

in which

$$\Delta(y) = -1 + 2y\frac{\partial}{\partial y} - y^2\nabla^2 \tag{19}$$

$$\Delta^{(n)}(y) = \Delta(H-y)\Delta(2H-y)\cdots\Delta[2(n-1)H-y]\Delta[(2n-1)H-y]$$

In passing, we may remark, by an examination of Eq. (17), that only four combinations of the elastic moduli (D_1, ν_1), (D_2, ν_2), and (D_3, ν_3), namely, α_{12}, β_{12}, α_{32}, and β_{32}, are required for the determination of the three deflections: W_1, W_2, and W_3 when the singularity acts inside the interface plate of moduli (D_2, ν_2), whereas an examination of Eq. (14) reveals that only six combinations of these elastic moduli are required in the determination of the three deflections when the singularity acts inside the first plate of moduli (D_1, ν_1).

5 Applications

Modern theories of compound media are incomplete unless they include a discussion of the overall properties of such compound media. We therefore return to formulas (14), which represent the solution when an arbitrary vertical load is applied to the first medium of moduli (D_1, ν_1).

Let us suppose that $D_3 = D_1$ and $\nu_3 = \nu_1$, so that the case is that of a plate strip of moduli (D_2, ν_2) embedded in a matrix medium of moduli (D_1, ν_1). Then, by Eq. (16), the dominant distant effect on the other side of the embedded plate strip is

$$W_3^{\infty} = \pounds_{21}(y) L_{12}(y) W_0(x,y) \tag{20}$$

If the influencing deflection $W(x,y)$ arises from a bending hot spot located at the point $(0, -h)$ in the first medium, so that $W(x,y) = K \log r_0$, where $r_0^2 = x^2 + (y+h)^2$, while K is a constant, then Eq. (20) may be approximated to

$$W_3^{\infty} = 4KD_2[D_1(1-\nu_1) + D_2(3+\nu_2\ ]^{-1} \log r \tag{21}$$

where

$$r^2 = x^2 + y^2 \tag{22}$$

If there are N identical small plate strips of moduli (D_2, ν_2) embedded in the matrix medium of moduli (D_1, ν_1), at such distances from one another that their interaction effects may be taken as independent of one another, then if these plate strips are all enclosed within a medium of moduli (D_0, ν_0), which itself is embedded in the matrix medium of moduli (D_1, ν_1), we will have the equivalence relation

$$ND_2/[D_1(1-\nu_1) + D_2(3+\nu_2)] = D_0/[D_1(1-\nu_1) + D_0(3+\nu_0)] \tag{23}$$

On the other hand, if the influencing deflection $W(x,y)$ arises from a concentrated vertical load at the same point $(0, -h)$, then Eq. (20) will similarly lead to the equivalence relation

$$ND_2/[D_1(3+\nu_1) + D_2(1-\nu_2)] = D_0/[D_1(3+\nu_1) + D_0(1-\nu_0)] \tag{24}$$

The solution of the simultaneous Eqs. (23) and (24) is given by

$$D_0 = \frac{D_1 D_2 N}{D_1 + D_2(1-N)}$$
$$\nu_0 = -2 - \nu_1 + (2 + \nu_1 + \nu_2)/N \tag{25}$$

These D_0 and ν_0, therefore, represent the effective flexural rigidity and Poisson's ratio of a compound plate comprising a homogeneous isotropic plate of moduli (D_1, ν_1) in which are embedded N small plate strips, each of moduli (D_2, ν_2), at such distances from one another that their interaction effects may be taken as independent from one another. If $N=1$, then we obtain the expected result $D_0 = D_2$ and $\nu_0 = \nu_2$.

Finally, let us consider the problem in which two isotropic quarter plates of moduli (D_1, ν_1) and (D_2, ν_2) occupy the quarter planes $(0 < x < \infty, -\infty < y < 0)$ and $(0 < x < \infty, 0 < y < \infty)$, respectively, a perfect bond being maintained at the interface $(0 < x < \infty, y=0)$, while the edge $(x=0, |y| < \infty)$ is rigidly clamped. An arbitrary singularity is applied to the upper quarter plate of moduli (D_2, ν_2), which in an unbounded plate $(|x| < \infty, |y| < \infty)$ is characterized by the deflection $W(x,y)$.

Clearly, by virtue of the representation law (Eq. (7)), if $D_1 = D_2$ and $\nu_1 = \nu_2$, then the complete solution for the clamped semi-infinite plate $(0 < x < \infty, |y| < \infty)$ is given by

$$W_*(x,y) = W(x,y) + L(x) W(-x,y) \tag{26}$$

where

$$L(x) = -1 + 2x\frac{\partial}{\partial x} - x^2 \nabla^2 \tag{27}$$

Equation (26), of course, satisfies the clamped conditions

$$W_*(x,y) = 0, \quad \frac{\partial W_*}{\partial x}(x,y) = 0 \tag{28}$$

at the edge $(x=0, |y| < \infty)$.

In the actual case when $(D_1, \nu_1) \neq (D_2, \nu_2)$, the desired complete solution for the two edge-bonded dissimilar quarter plates is given by the representation law (Eq. (7)) in the explicit form

$$W_1 = \pounds_{21}(y)[W(x,y) + L(x) W(-x,y)] \tag{29}$$

for the quarter plate $(0 < x < \infty, -\infty < y < 0)$, and

$$W_2 = W(x,y) + L(x)W(-x,y) + L_{21}(y)[W(x,-y) + L(x)W(-x,-y)] \tag{30}$$

for the quarter plate $(0 < x < \infty, 0 < y < \infty)$, where the operators $L_{21}(y)$ and $\pounds_{21}(y)$ are once again defined by Eq. (8).

This completes the analysis of the problem of two clamped edge-bonded quarter plates, which leads directly to the following conclusion. If the deflection $W_*(x,y)$ of a clamped semi-infinite plate under the influence of an arbitrary vertical load is known, then the corresponding deflections for two clamped edge-bonded dissimilar quarter plates are explicitly determinable, in terms of the known deflection $W_*(x,y)$ for the clamped semi-infinite plate.

6 Closure

It is first proved that at each point of two perfectly bonded isotropic semi-infinite dissimilar plates, the deflection can be determined by applying suitably defined integrodifferential operators on its corresponding value in the isotropic homogeneous plate of infinite extent, whatever be the physical nature of the influencing vertical load. By a systematic repeated application of this basic theorem, we then obtain a new generalized well-structured theorem, which is applicable when an arbitrary vertical load acts in or near a plate of finite breadth that separates two other dissimilar isotropic semi-infinite plates. Specifically, if the deflection of an isotropic homogeneous infinite plate under the influence of an arbitrary vertical load is known, then their corresponding values for two dissimilar isotropic semi-infinite plates separated by a third dissimilar isotropic plate of finite breadth are explicitly determinable by using Maxwell's method of repeated reflection.

The elastic field due to the presence of an arbitrary singularity in a compound semi-infinite solid with a free flat surface can be found by a similar method, the compound solid comprising two transversely isotropic dissimilar layers perfectly bonded to a third dissimilar transversely isotropic semi-infinite homogeneous solid, which should cover many geophysical applications, as discussed by Eshelby [7] when the influencing singularities are dislocations.

References

[1] Maxwell, J. C., 1873, *A Treatise on Electricity and Magnetism*, Vol. 1, Dover, New York, pp. 244–450.
[2] Timoshenko, S., and Woinowsky-Krieger, S., 1959, *Theory of Plates and Shells*, McGraw-Hill, New York.
[3] Fung, Y. C., 1965, *Foundations of Solid Mechanics*, Prentice-Hall, Englewood Cliffs, NJ, pp. 266–269.
[4] Aderogba, K., 1973, "The Thermal Bending of Composite Plates," Int. J. Solids Struct., **9**, pp. 1389–1402.
[5] Aderogba, K., 2003, "An Image Treatment of Elastostatic Transmission From an Interface Layer," J. Mech. Phys. Solids, **51**, pp. 267–279.
[6] Aderogba, K., 2007, "Theory of Images in Plane-Layered Axisymmetric Elastostatics," Int. J. Solids Struct., **44**, pp. 3920–3927.
[7] Eshelby, J. D., 1973, "Dislocation Theory for Geophysical Applications," Philos. Trans. R. Soc. London, Ser. A, **274**, pp. 331–338.

Energy Dissipation in Normal Elastoplastic Impact Between Two Spheres

Yanchen Du
School of Medical Instrument and Food Engineering,
University of Shanghai for Science and Technology,
Shanghai 200093, China

Shulin Wang
School of Energy and Power Engineering,
University of Shanghai for Science and Technology,
Shanghai 200093, China

Elastoplastic deformation occurs widely in engineering impact. Although many empirical solutions of elastoplastic impact between two spheres have been obtained, the analytical solution, verified by means of other methods, to the impact model has not been put forward. This paper proposes a dynamic pattern of elastoplastic impact for two spheres with low relative velocity, in which three stages are introduced and elastic and plastic regions are both considered. Finite element analyses with various parameters are carried out to validate the above model. The numerical results prove to agree with the theoretical predictions very well. Based on this model, the dissipation nature of elastoplastic impact are then analyzed, and the conclusion can be drawn that materials with lower yield strength, higher elastic modulus, and higher mass density have better attenuation and dissipation effects. The study provides a basis to predict the particle impact damping containing plastic deformation and to model the impact damped vibration system enrolling microparticles as a damping agent. [DOI: 10.1115/1.3130801]

Keywords: elastoplastic impact, energy dissipation, analytical model, finite element method

1 Introduction

Conventional particle impact damping (PID) features elastic deformation and momentum exchange, which cannot exhaust most of the vibration energy, but reverberate it among impact partners or mode shapes [1]. Therefore the research of energy dissipation due to plastic deformation in particle impacts plays an important role in improving the performance of PID. Moreover, the simulation of granular flow [2,3] where millions of particles collide with each other also relies on the understanding of binary collision of two spheres. Since finite element analysis (FEA) or iteration methods usually result in a large amount of computation resources occupation and time consumption for millions of impacts to occur in the PID system, to obtain an analytical solution of the elastoplastic impact between two spheres has become a hot research topic in the past two decades. In the PID system, the particle size usually ranges from 200 μm to 20 mm, in which the surface tension could be ignored, unlike that in nanoscale impacts [4].

Johnson [5] summarized the theoretical, numerical, and experimental findings of elastoplastic impact research before 1985 and achieved an expression for the coefficient of restitution, which is valid in impacts at moderate speeds (up to 500 ms^{-1}) on the premise of a fully plastic indentation.

Stronge [6] developed Johnson's theory [5] and divided the impact process into four stages: elastic impact before onset of yield, quasistatic elastoplastic indentation, fully plastic indentation, and elastic unloading from maximum indentation. All relevant formulas have been obtained and the square of coefficient of restitution is expressed as a ratio of recovery kinetic energy to strain energy during compression.

Thornton [7] found that the coefficient of restitution obtained from Stronge's model [6] is larger than unity at low speeds, and he deduced a set of formulas and arrived at an expression of coefficient of restitution only relevant to the ratio of initial velocity to yield velocity. Furthermore, Wu et al. [8] investigated the normal impact of an elastic spherical particle with a substrate, which is assumed to be elastic or elastoplastic, by means of the finite element method.

Zhang and Vu-Quoc [9] modeled the dependence of the coefficient of restitution on the impact velocity in elastoplastic collisions with dynamic FEA, which verified the normal force-displacement (NFD) model presented by Vu-Quoc and Zhang [10] and the counterpart of the force-driven model proposed by Vu-Quoc et al. [11]. The model proposed by Vu-Quoc and Zhang [10] has been validated by experiments [12]. In addition, the companion elastoplastic tangential force-displacement (TFD) model is proposed in Refs. [13,14].

Mesarovic and Fleck [15] performed an accurate numerical study of normal indentation of an elastoplastic half-space by a rigid sphere. Moreover, Mesarovic and Johnson [16] examined the process of decohesion of two adhering elastoplastic spheres following mutual indentation beyond their elastic limit. Their FEA results revealed that, for elastic–perfectly plastic materials, the contact pressure at the end of loading is approximately uniform.

Kogut and Etsion [17] developed a loading model and Etsion et al. [18] developed an unloading model of elastoplastic spherical contact. The dissipated energy due to plastic deformation was discussed and an elastic plastic loading (EPL) index [18] was defined to indicate the plasticity level of the loaded sphere. The dimensionless expressions, obtained from the results of many cases with different materials and geometrical parameters, are applicable to the elastoplastic contact of identical spheres.

More recently, Weir and Tallon [19] found that the coefficient of restitution depends on geometry and history, and Weir and McGavin [4] reported that new regimes will arise at the nanoscale.

With the plastic deformation involved, the impact becomes so complicated that an accurate theoretical solution is difficult to obtain. Despite its approximation, the theoretical model has the advantage of its applicability to the different materials and different spherical sizes, and its foundation to find out the effects of all the primary parameters involved in the impact process. From the above literature review it can be seen that an analytical solution obtained from the theoretical model and verified by means of other methods is still missing. The main goal of this paper is to develop a theoretical model for normal impact of two spherical,

Contributed by the Applied Mechanics Division of ASME for publication in the JOURNAL OF APPLIED MECHANICS. Manuscript received March 3, 2008; final manuscript received March 23, 2009; published online July 23, 2009. Review conducted by Sanjay Govindjee.

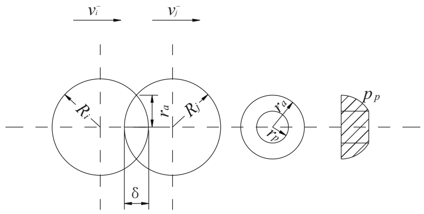

Fig. 1 Schematic of elastoplastic impact between two spheres

isotropic, and perfectly elastoplastic bodies with frictionless surfaces. FEA results will be compared to verify the proposed model. This model is helpful to understand the effect of impact parameters such as velocity, yield strength, elastic modulus, mass density, etc., on the coefficient of restitution, to provide a foundation to predict the performance of PID containing plastic deformation and to model the impact damped vibration system enrolling microparticles as a damping agent [20].

2 Model of Elastoplastic Impact Between Two Spheres

As shown in Fig. 1, the two colliding spheres (sphere i and sphere j) have the following parameters: elastic moduli E_i and E_j, Poisson's ratios ν_i and ν_j, yield strengths σ_{yi} and σ_{yj}, radii R_i and R_j, masses m_i and m_j, mass densities ρ_i and ρ_j, velocities before impact v_i^- and v_j^-, velocities after impact v_i^+ and v_j^+, relative deformation (displacement) δ, contact force P, radius of contact area r_a, and radius of plastic zone in contact area r_p.

2.1 Basis and Assumptions of Model. In this model, we suppose that the two spheres with normal contact are made of the perfectly elastoplastic and isotropic material, which is not extremely soft so that the quasistatic simulation can be applied [9]. Besides, the friction and air resistance are all neglected.

According to the study first made by Johnson [5], the transition point from a purely elastic stage to an elastoplastic one was taken as the onset of yield beneath the contact surface, with the corresponding central contact pressure equal to $1.61\sigma_y$ (σ_y is the smaller yield strength of sphere i and sphere j), which was taken as the mean pressure in the plastic zone by Thornton [7]. FEA shows that the mean pressure in the plastic zone is more than $2\sigma_y$ [9], but less than $2.8\sigma_y$ as indicated by the theoretical model [6].

Stronge [6] pointed out that although the plastically deforming region enlarges as contact pressure increases, it remains confined below the surface for pressures throughout the range $1.1 < p_m/\sigma_y < 2.8$ (p_m is the mean pressure of the contact center), which is termed contained plastic deformation. In this elastoplastic range, the observable permanent indentation of the surface is small because plastic deformation is incompressible and the plastically deforming region is encased within an otherwise elastic body.

In this paper, we propose a new definition of transition point. Since the plastic region is small and fully contained by the material, which remains elastic in the elastoplastic range before the plastic region expands to the contact surface, the collision at a low velocity behaves more like an elastic impact, and thus it is reasonable to combine this range to the elastic compression phase. In this paper, we define the transition point as a point when the center of the contact area reaches yield and the corresponding mean pressure of the plastic region is taken as the contact pressure of rigid punch, which is about $2.57\sigma_y$, since the radius of the contact area is far less than that of the contacting spheres.

To simplify the modeling, we further make the following assumptions.

(1) The geometrical relationship in the elastic compression phase is still valid in the elastoplastic compression phase, as described in Eq. (3).
(2) The pressure distribution in the elastic compression phase is still valid in the elastoplastic compression phase, as described in Eq. (6), with two boundary conditions, that when $r=r_p$, $p(r)=p_p$ and when $r=r_a$, $p(r)=0$.
(3) The relationship between contact force and relative deformation in the elastic resilience phase is similar to that in the elastic compression phase.

Assuming these two spheres collide in a normal direction periodically, we consider the interval between their contact and separation as a period, which can be divided possibly into the following three phases: elastic compression phase (ECP), elastoplastic compression phase (EPCP), and elastic resilience phase (ERP).

2.2 Modeling at the Stage of ECP. This stage begins when these two spheres contact and ends when the center of contact surface comes into yield. Deformation occurring in this phase is mainly elastic so that Hertz's elastic contact theory can be applied in this stage.

According to Hertz's theory [21], we have

$$r_a = \left[\frac{3P\left(\dfrac{1}{E_i^*}+\dfrac{1}{E_j^*}\right)}{4\left(\dfrac{1}{R_i}+\dfrac{1}{R_j}\right)}\right]^{1/3}$$

where $E_i^*=E_i/(1-\nu_i^2)$ and $E_j^*=E_j/(1-\nu_j^2)$.

Let $E^*=E_i^*E_j^*/(E_i^*+E_j^*)$ and $R^*=R_iR_j/(R_i+R_j)$, then r_a can be expressed as

$$r_a = \left(\frac{3PR^*}{4E^*}\right)^{1/3} \tag{1}$$

Also from Hertz's theory, the relative deformation of the two spheres can be given by

$$\delta = \frac{3P\left(\dfrac{1}{E_i^*}+\dfrac{1}{E_j^*}\right)}{4r_a} = \frac{3P}{4E^*r_a} \tag{2}$$

From Eqs. (1) and (2), we obtain

$$r_a^2 = R^*\delta \tag{3}$$

$$P = \tfrac{4}{3}E^*\sqrt{R^*}\,\delta^{3/2} \tag{4}$$

Thus, the equation of motion in the elastic compression phase can be described as [5,6]

$$m^*\frac{d^2\delta}{dt^2} = -\frac{4}{3}E^*\sqrt{R^*}\,\delta^{3/2} \tag{5}$$

where m^* is the equivalent mass of the spheres [7], and $m^*=m_im_j/(m_i+m_j)$.

Assuming the compressive pressure in the elastic contact area is spherically distributed, and can be expressed as from Hertz's theory,

$$p(r) = \left(\frac{p_c}{r_a}\right)\sqrt{r_a^2-r^2}$$

where $p_c=3P/2\pi r_a^2$ is the compressive pressure of the contact center. And considering Eqs. (3) and (4), we have

$$p(r) = \frac{2E^*}{\pi R^*}\sqrt{r_a^2-r^2} \tag{6}$$

At the end of the elastic compression phase, the pressure at the contact center reaches $p_c=p_p=\min(p_{pi},p_{pj})$, because $r_a \ll R_i$ and $r_a \ll R_j$, p_{pi} and p_{pj} can be obtained approximately similar to the impact solution of a rigid flat punch problem [22], where we have

$$p_{pi} = \left(1+\frac{\pi}{2}\right)\sigma_{yi}$$

$$p_{pj} = \left(1 + \frac{\pi}{2}\right)\sigma_{yj}$$

Thus, r_{ae}, the radius of the contact area, and δ_e, the relative deformation, at the end of the ECP can be expressed as

$$r_{ae} = \frac{\pi p_p R^*}{2E^*} \qquad \delta_e = R^*\left(\frac{\pi p_p}{2E^*}\right)^2 \tag{7}$$

Solving Eq. (5) and considering the boundary condition $\dot{\delta}=v_r^-$ when $\delta=0$, we obtain the relative velocity in the ECP as follows:

$$\dot{\delta} = \sqrt{(v_r^-)^2 - \frac{16E^*\sqrt{R^*}}{15m^*}\delta^{5/2}} \tag{8}$$

At the end of the ECP, $\delta=\delta_e$, thus we get

$$\dot{\delta}_e = \sqrt{(v_r^-)^2 - \frac{16E^*\sqrt{R^*}}{15m^*}\delta_e^{5/2}} \tag{9}$$

Integrating Eq. (8), and noticing the initial conditions $\delta=0$ when $t=0$, the relation of δ versus t can be deduced as

$$t = \int_0^{\delta}\left[(v_r^-)^2 - \frac{16E^*\sqrt{R^*}}{15m^*}\delta^{5/2}\right]^{-1/2} d\delta \tag{10}$$

The instant t_e at which the elastic compression phase ended can be expressed as

$$t_e = \int_0^{\delta_e}\left[(v_r^-)^2 - \frac{16E^*\sqrt{R^*}}{15m^*}\delta^{5/2}\right]^{-1/2} d\delta \tag{11}$$

The expressions mentioned above are available in the book by Johnson [5].

2.3 Modeling at the Stage of EPCP. This stage begins at the onset of yield on the contact surface and ends when the relative velocity of these two spheres decelerates to zero. With the increase in the contact force, the central plastic region gradually enlarges and the surrounding elastic boundary also gradually expands. Thus, the contact area can be divided into an inner circular plastic region and an outer annular elastic region surrounding the former. The contact force in the plastic region can be expressed as $\pi r_p^2 p_p$. According to Eq. (6), the total contact force of the annular elastic region can be expressed as

$$P_e = \int_{r_p}^{r_a} \frac{4rE^*}{R^*}\sqrt{r_a^2 - r^2}\,dr = \frac{4E^*(r_a^2 - r_p^2)^{3/2}}{3R^*} = \frac{p_p^3\pi^3(R^*)^2}{6(E^*)^2}$$

In view of Eqs. (3) and (6), the total contact force over the whole contact area can be expressed as

$$P = \frac{p_p^3\pi^3(R^*)^2}{6(E^*)^2} + \pi r_p^2 p_p = \pi R^* p_p \delta - \frac{p_p^3\pi^3(R^*)^2}{12(E^*)^2}$$

Then, the motion equation in the elastoplastic compression phase can be written as

$$m^*\frac{d^2\delta}{dt^2} = -\left[\pi R^* p_p \delta - \frac{p_p^3\pi^3(R^*)^2}{12(E^*)^2}\right] \tag{12}$$

Solving Eq. (12) and considering the initial conditions of $\dot{\delta} = \dot{\delta}_e$ when $\delta=\delta_e$, the relative velocity in the elastoplastic compression phase is

$$\dot{\delta} = \sqrt{\dot{\delta}_e^2 + \frac{\pi^5(R^*)^3 p_p^5}{48m^*(E^*)^4} + \frac{p_p^3\pi^3(R^*)^2}{6m^*(E^*)^2}\delta - \frac{\pi R^* p_p}{m^*}\delta^2} \tag{13}$$

When $\dot{\delta}=0$, that is, at the end of the elastoplastic compression phase, the relative deformation δ_{ep} between the two spheres can be written as

$$\delta_{ep} = \delta_{\max} = \sqrt{\left[\frac{p_p^2\pi^2(R^*)}{6(E^*)^2}\right]^2 + \frac{m^*\dot{\delta}_e^2}{p_p \pi R^*}} + \frac{p_p^2\pi^2 R^*}{12(E^*)^2} \tag{14}$$

In order to obtain the relation of relative deformation δ versus time t, Eq. (13) is integrated. In view of initial conditions $\delta=\delta_e$ when $t=t_e$, we get the relation of δ versus t as follows:

$$t = t_e + \int_{\delta_e}^{\delta}\left[\dot{\delta}_e^2 + \frac{\pi^5(R^*)^3 p_p^5}{48m^*(E^*)^4} + \frac{p_p^3\pi^3(R^*)^2}{6m^*(E^*)^2}\delta - \frac{\pi R^* p_p}{m^*}\delta^2\right]^{-1/2} d\delta \tag{15}$$

The curve of δ versus t can be obtained by numerical integration methods. The instant t_{ep} at which the EPCP ended can be expressed as

$$t_{ep} = t_e + \int_{\delta_e}^{\delta_{ep}}\left[\dot{\delta}_e^2 + \frac{\pi^5(R^*)^3 \sigma_p^5}{48m^*(E^*)^4} + \frac{p_p^3\pi^3(R^*)^2}{6m^*(E^*)^2}\delta - \frac{\pi R^* p_p}{m^*}\delta^2\right]^{-1/2} d\delta \tag{16}$$

2.4 Modeling at the Stage of ERP. This stage begins at an instant right after these two spheres rebounded and ends when they separated completely.

According to Eq. (4), we get the contact force in the ERP

$$P = \tfrac{4}{3}E^*\sqrt{R^*}(\delta - \delta_{res})^{3/2}$$

where δ_{res} is the irreversible plastic relative deformation.

Because the contact force at the end of the EPCP is equivalent to that at the beginning of the ERP, we have

$$\pi R^* p_p \delta_{ep} - \frac{p_p^3\pi^3(R^*)^2}{12(E^*)^2} = \frac{4}{3}E^*\sqrt{R^*}(\delta_{ep} - \delta_{res})^{3/2}$$

From this equation we get

$$\delta_{res} = \delta_{ep} - \left[\frac{3}{4E^*\sqrt{R^*}}\left(\pi R^* p_p \delta_{ep} - \frac{p_p^3\pi^3(R^*)^2}{12(E^*)^2}\right)\right]^{2/3} \tag{17}$$

And the motion in the ERP can be expressed as

$$m^*\frac{d^2\delta}{dt^2} = -\frac{4}{3}E^*\sqrt{R^*}(\delta - \delta_{res})^{3/2} \tag{18}$$

Solving Eq. (18) and considering the initial conditions of $\dot{\delta}=0$ when $\delta=\delta_{ep}$, the relative velocity in the ERP can be expressed as

$$\dot{\delta} = -\sqrt{\frac{16}{15}\cdot\frac{E^*\sqrt{R^*}}{m^*}(\delta_{ep} - \delta_{res})^{5/2} - \frac{16}{15}\cdot\frac{E^*\sqrt{R^*}}{m^*}(\delta - \delta_{res})^{5/2}} \tag{19}$$

It is negative because the direction of relative velocity is opposite to that of the relative deformation in the ERP.

At the end of the ERP, $\delta=\delta_{res}$, thus the relative velocity v_r^+ at the end of the impact process can be expressed as

$$v_r^+ = v_j^+ - v_i^+ = \sqrt{\frac{16E^*\sqrt{R^*}}{15m^*}(\delta_{ep} - \delta_{res})^{5/2}} \tag{20}$$

In order to obtain the relation of relative deformation δ versus time t, we integrate Eq. (19) considering the initial conditions of $\delta=\delta_{ep}$ when $t=t_{ep}$, and then get the relation between δ and t as follows:

$$t = t_{ep} - \int_{\delta_{ep}}^{\delta} \left[\frac{16}{15} \cdot \frac{E^* \sqrt{R^*}}{m^*} (\delta_{ep} - \delta_{res})^{5/2} - \frac{16}{15} \cdot \frac{E^* \sqrt{R^*}}{m^*} (\delta - \delta_{res})^{5/2} \right]^{-1/2} d\delta \qquad (21)$$

The curve of δ versus t can be obtained by numerical integration. When the ERP ended, the instant t_{res} can be expressed as

$$t_{res} = t_{ep} - \int_{\delta_{ep}}^{\delta_{res}} \left[\frac{16}{15} \cdot \frac{E^* \sqrt{R^*}}{m^*} (\delta_{ep} - \delta_{res})^{5/2} - \frac{16}{15} \cdot \frac{E^* \sqrt{R^*}}{m^*} (\delta - \delta_{res})^{5/2} \right]^{-1/2} d\delta$$

2.5 Loss Factor in Impact Process. The effective coefficient of restitution e can be expressed as

$$e = \frac{v_j^+ - v_i^+}{v_i^- - v_j^-} = \frac{v_r^+}{v_r^-} \qquad (22)$$

The energy loss is equivalent to the difference of the total kinetic energy before and after impact. According to the momentum conservation in the impact process we have

$$m_i v_i^- + m_j v_j^- = m_i v_i^+ + m_j v_j^+$$

Substituting Eq. (22) into the equation above, the velocity of these two spheres after their collision can be expressed, respectively, as

$$v_i^+ = v_i^- - \frac{(1+e) m_j (v_i^- - v_j^-)}{m_i + m_j} \qquad (23)$$

$$v_j^+ = v_j^- + \frac{(1+e) m_i (v_i^- - v_j^-)}{m_i + m_j} \qquad (24)$$

According to the definition [23], the loss factor η can be written as

$$\eta = \frac{\left[\frac{1}{2} m_i (v_i^-)^2 + \frac{1}{2} m_j (v_j^-)^2 \right] - \left[\frac{1}{2} m_i (v_i^+)^2 + \frac{1}{2} m_j (v_j^+)^2 \right]}{2\pi \left[\frac{1}{2} m_i (v_i^-)^2 + \frac{1}{2} m_j (v_j^-)^2 \right]} \qquad (25)$$

For equal masses, the loss factor can be written as

$$2\pi\eta = \frac{(1-e^2)(v_i^- - v_j^-)^2}{2[(v_i^-)^2 + (v_j^-)^2]}$$

so for a fixed coefficient of restitution, the loss factor is maximum when $v_i^- = -v_j^-$. The corresponding maximum value is $2\pi\eta_{\max} = 1 - e^2$.

3 Dynamic FEA Simulations

In order to verify the model proposed in this paper, we carry out dynamic FEA. The collision cases of identical spheres (see Sec. 3.1) and different ones (see Sec. 3.2) are both studied.

3.1 Impact Between Identical Spheres. The axisymmetric models are created with the help of PATRAN software from MSC. The fine mesh is adopted in the 0.2R (the radius of colliding sphere) fan-shaped zone near the contact area, and the coarse mesh is used in other regions to save the possible computation time. The numbers before and after the symbol "/" represent, respectively, the number and the bias factor of mesh seed on this side, as shown in Fig. 2. The quadrangular element meshes are obtained with the paver partition method, as shown in Fig. 3.

The FEA simulations are carried out with the MARC MENTAT 2005 from MSC, and the transient contact model with large deformation and the Newton–Raphson iteration method with displacement convergence are adopted. The contact tolerance and time step are taken as 10^{-8} m and 10^{-6} s, respectively. In the simulation cases studied in this section, we assume that the two colliding spheres are identical in geometry and material, and their parameters are chosen as follows: elastic modulus $E_i = E_j = 210$ GPa, Poisson's ratio $\nu_i = \nu_j = 0.25$, yield strength $\sigma_{yi} = \sigma_{yj} = 210$ MPa, $v_i^- = 20$ mm/s and v_j^- varying among -20 mm/s, -15 mm/s, -10 mm/s, -5 mm/s, 0 mm/s, 5 mm/s, 10 mm/s, and 15 mm/s, and $R_i = R_j$ varying among 0.5 mm, 1 mm, 2.5 mm, 5 mm, and 10 mm.

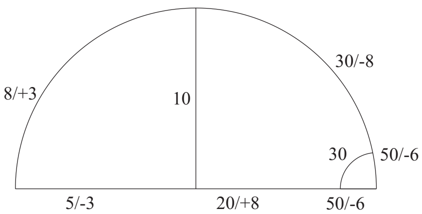

Fig. 2 Schematic of mesh seed parameters

Figure 4 shows the relationship between the relative deformation of two spheres and the duration time in an impact period. It can be seen that the results produced by the FEA simulations agree reasonably well with those obtained from the theoretical model expressed by Eqs. (10), (15), and (21). The deformation in an impact period cannot return to zero, which indicates that the deformation features elastoplasticity.

The velocities of two spheres and the loss factor after their collision are the results we are focused on. Figures 5 and 6 demonstrate the velocities of sphere i and sphere j after their impact, respectively; Fig. 7 indicates the loss factor in the process. It can be seen that the calculated results from Eq. (23) (Fig. 5), Eq. (24) (Fig. 6), and Eq. (25) (Fig. 7) show good agreement with those from FEA simulation. And the loss factor increases considerably when $v_j^- < 0$ (Fig. 7); that is, the energy loss will be enhanced if the spheres move in the opposite direction, which is consistent with the analytical result obtained at the end of Sec. 2.

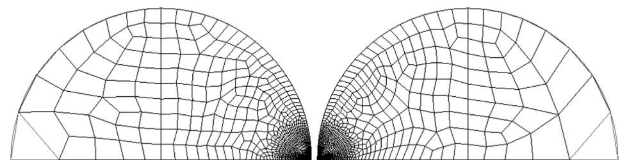

Fig. 3 Schematic of element partition result

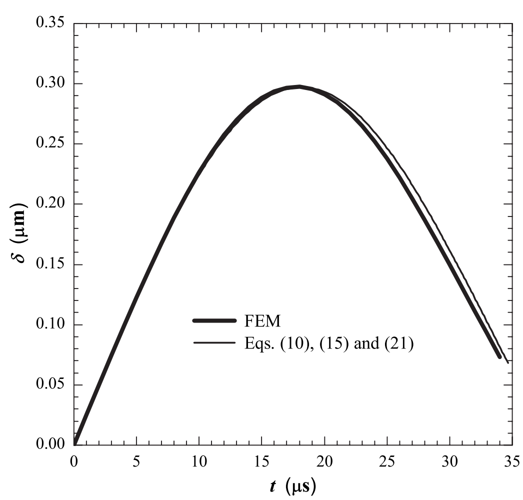

Fig. 4 Curve of relative deformation and impact time in impact process; $v_i^- = 20$ mm/s, $v_j^- = -5$ mm/s, and $R_i = R_j = 2.5$ mm

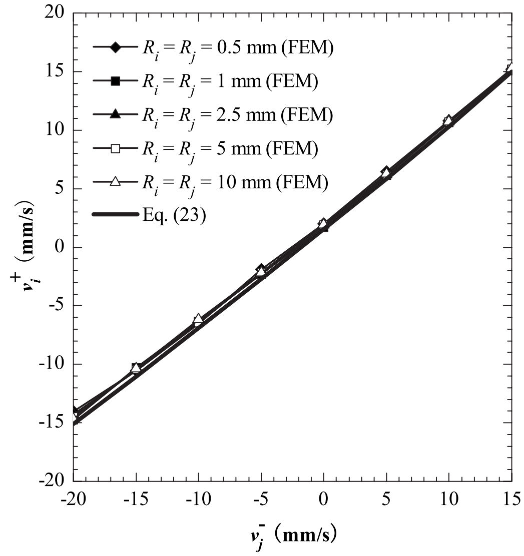

Fig. 5 Velocity of sphere *i* after impact between identical spheres

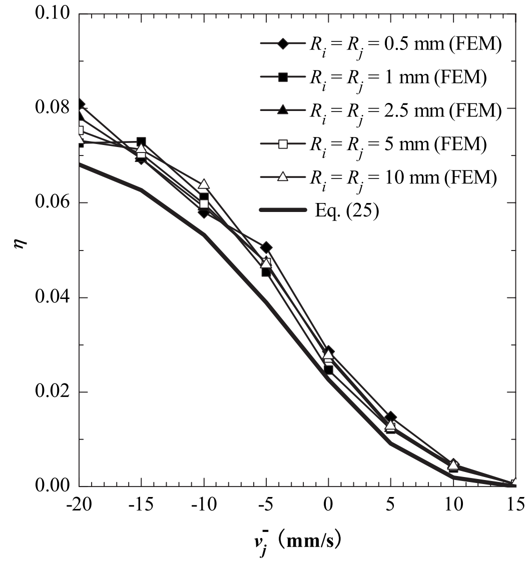

Fig. 7 Loss factor in impact between identical spheres

3.2 Impact Between Different Spheres. In this section, the FEA simulations in the impact cases with different materials or different radii are carried out to calibrate the model proposed in this paper. The method of mesh partition is similar to that used in Sec. 3.1 except that the fan-shaped zone with the fine mesh is defined with the radius of the smaller colliding sphere.

In collision cases with different materials, the parameters are chosen as follows: elastic moduli $E_i=210$ GPa and $E_j=100$ GPa, Poisson's ratios $\nu_i=0.25$ and $\nu_j=0.33$, yield strengths $\sigma_{yi}=210$ MPa and $\sigma_{yj}=100$ MPa, $\upsilon_i^-=20$ mm/s and υ_j^- varying among -20 mm/s, -15 mm/s, -10 mm/s, -5 mm/s, 0 mm/s, 5 mm/s, 10 mm/s, and 15 mm/s, and $R_i=R_j$ varying among 0.5 mm, 1 mm, 2.5 mm, 5 mm, and 10 mm. Figure 8 indicates the effective coefficient of restitution in the impact process. Figures 9 and 10 demonstrate the velocities of sphere *i* and sphere *j* after their impact, respectively; Fig. 11 indicates the loss factor in the impact process.

In collision cases with different radii, the parameters are chosen as follows: elastic modulus $E_i=E_j=210$ GPa, Poisson's ratio $\nu_i=\nu_j=0.25$, yield strength $\sigma_{yi}=\sigma_{yj}=210$ MPa, $\upsilon_i^-=20$ mm/s and υ_j^- varying among -20 mm/s, -15 mm/s, -10 mm/s, -5 mm/s, 0 mm/s, 5 mm/s, 10 mm/s, and 15 mm/s, and $R_i=10$ mm and R_j varying among 2.5 mm, 5 mm, and 10 mm. Figures 12 and 13 demonstrate the velocities of sphere *i* and sphere *j* after their impact, respectively; Fig. 14 indicates the loss factor in the process.

As shown in these figures, the theoretical predictions agree closely with the FEA simulation results from all cases listed above, which further validates the reliability of the proposed model.

4 Energy Dissipation Analysis Based on the Proposed Model

In this section, several primary parameters in the collisions are discussed to show their effect on loss factor on the basis of the

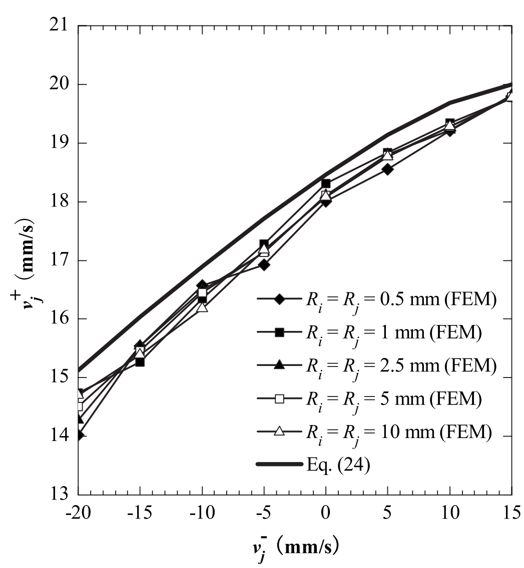

Fig. 6 Velocity of sphere *j* after impact between identical spheres

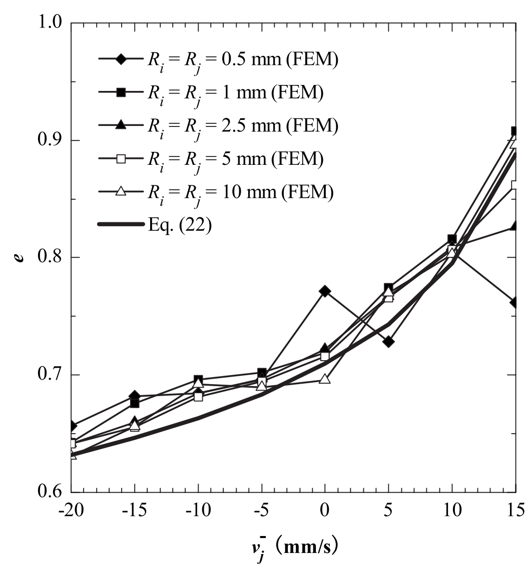

Fig. 8 Effective coefficient of restitution in impact between different material spheres

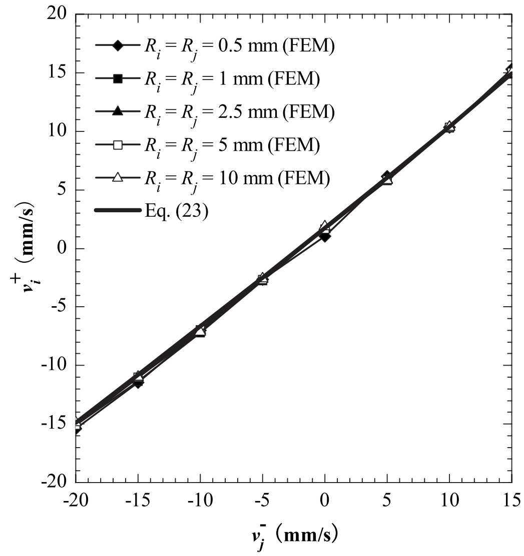

Fig. 9 Velocity of sphere *i* after impact between different material spheres

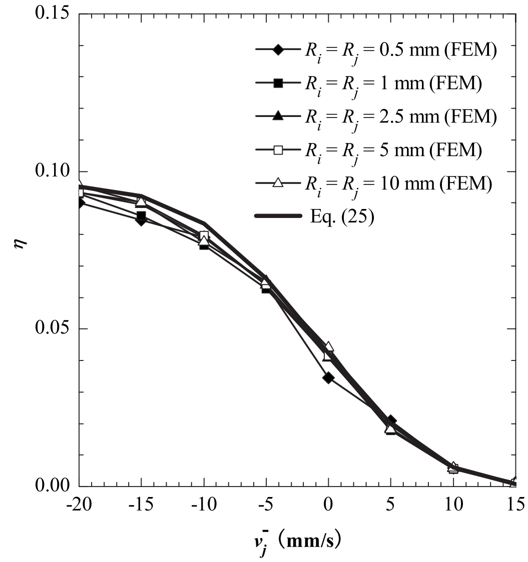

Fig. 11 Loss factor in impact between different material spheres

proposed model. The parameters used in the calculating cases are chosen as the same as those in Sec. 3.1 except for the listed parameters.

4.1 Effect of Impact Velocity on Loss Factor. According to Eq. (25), we obtain the relation between the loss factor and the velocity ratio of two spheres, as shown in Fig. 15. The loss factor obviously increases when $v_j^-/v_i^- > 0$, especially when $v_j^-/v_i^- = -1$, which means when the two spheres have the velocity of the same magnitude but the opposite direction before their impact, the loss factor reaches to its maximum, which is in accordance with the analytical result obtained at the end of Sec. 2. In the range of $v_j^-/v_i^- > 0$, the loss factor decreases with the velocity ratio increasing, and the larger the velocity ratio, the lower the loss factor.

4.2 Effect of Yield Strength and Elastic Modulus of Materials on Loss Factor. The most important material parameters on loss factor are the yield strength and the elastic modulus. According to Eq. (25), Fig. 16 represents the dependence of the loss factor on the yield strength and the elastic modulus.

As shown in Fig. 16, the loss factor increases with the yield strength decreasing. This reflects the fact that the yield strength enables the material to resist plastic deformation. The lower the yield strength, the easier the plastic deformation of the material, and the higher the loss factor. On the other hand, the elastic modulus is the measurement of the material's deforming ability. The higher the elastic modulus, the smaller the elastic deformation to occur before yielding, and the weaker the ability of the material to rebound, which implies more energy loss. This is also verified by the upper curves in Fig. 16.

4.3 Effect of Mass Density on Loss Factor. Figure 17 shows the effect of mass density on the loss factor. Larger density means larger mass and larger impact intensity. Thus the larger the mass density, the higher the loss factor, which is consistent with the experimental results from Panossian [24].

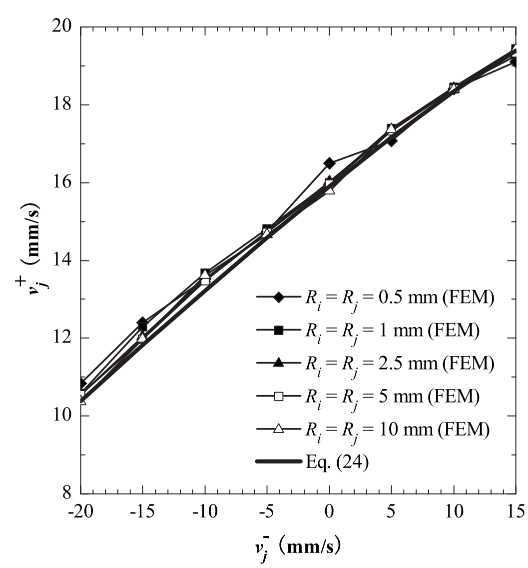

Fig. 10 Velocity of sphere *j* after impact between different material spheres

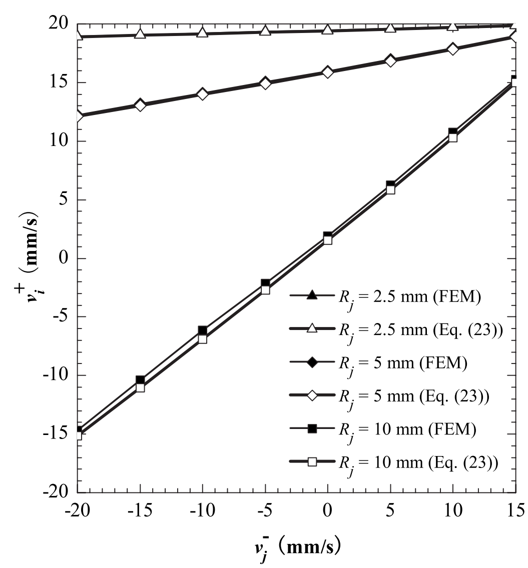

Fig. 12 Velocity of sphere *i* after impact between different radius spheres

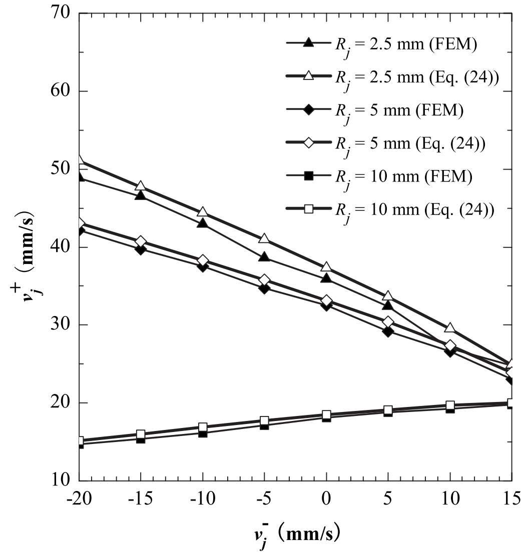

Fig. 13 Velocity of sphere *j* after impact between different radius spheres

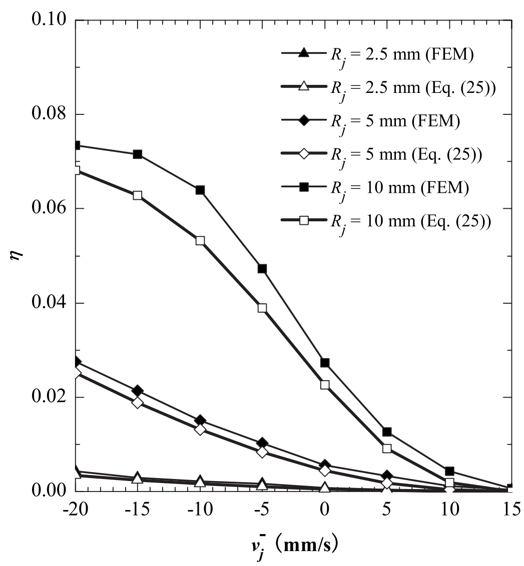

Fig. 14 Loss factor in impact between different radius spheres

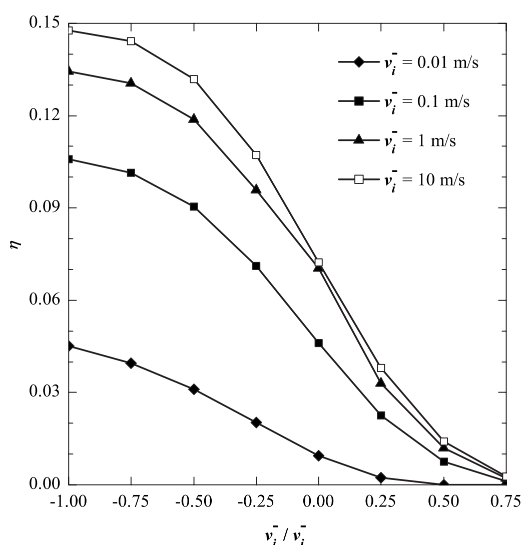

Fig. 15 Loss factor with different impact velocity groups: $R_i = R_j = 2.5$ mm, $E_i = E_j = 210$ GPa, $\nu_i = \nu_j = 0.25$, and $\sigma_{yi} = \sigma_{yj} = 210$ MPa

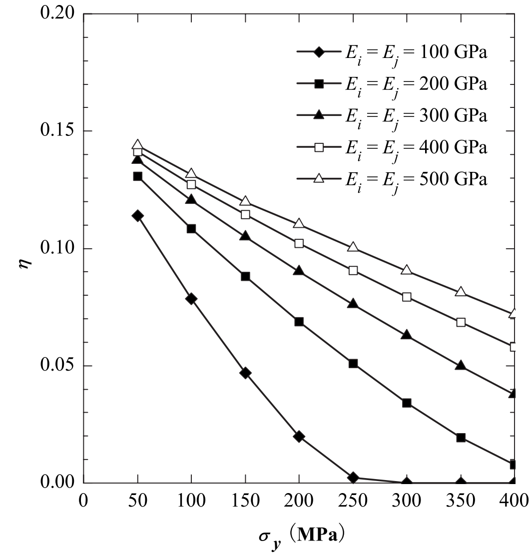

Fig. 16 Loss factor with different material parameters: $\sigma_{yi} = \sigma_{yj} = 50-400$ MPa at interval of 50 MPa, $R_i = R_j = 2.5$ mm, $v_i^- = -v_j^- = 20$ mm/s, and $\nu_i = \nu_j = 0.25$

5 Conclusions

In this paper, we first propose a theoretical model of elastoplastic impact for two spheres with low relative velocity, and verify it with FEA simulations, numerical results of which show good agreement with the predictions of analytical solutions for identical and different spheres. Based on this model, this paper also analyzes the deformation and dissipation nature of the elastoplastic impact system, and concludes that the materials with lower yield strength and higher elastic modulus dissipate more energy in the impact process, which provides a principle to select the material of impact partners in particle impact damper. Furthermore, the materials with larger mass density are shown to be favorable to increase energy dissipation in vibroimpact, which coincides with the observations from Panossian [24]. In a word, the study provides a foundation to predict the performance of particle impact

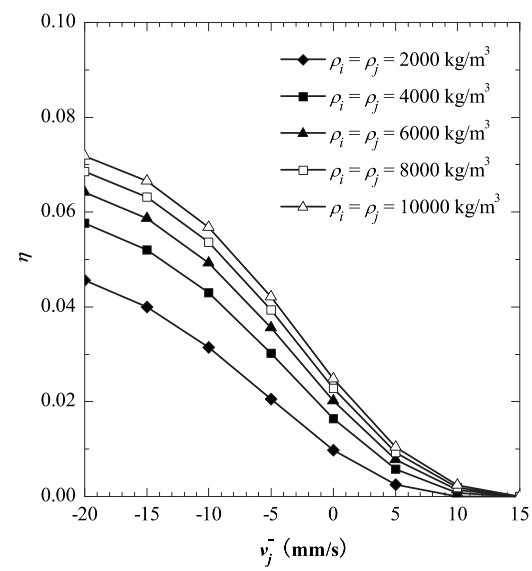

Fig. 17 Loss factor with different mass densities: $v_i^- = 20$ mm/s, $R_i = R_j = 2.5$ mm, $E_i = E_j = 210$ GPa, $\nu_i = \nu_j = 0.25$, and $\sigma_{yi} = \sigma_{yj} = 210$ MPa

damping containing plastic deformation and to model the impact damped system enrolling the microparticles as a damping agent.

Acknowledgment

We thank the support from the National Natural Science Foundation of China (Grant No. 50375100). And we are also grateful to Associate Professor B. Zheng and Dr. X. Wu in the College of Aerospace Engineering and Mechanics, Tongji University, for their valuable suggestions on FEA simulation.

Nomenclature

e = effective coefficient of restitution
E_i and E_j = elastic moduli of sphere i and sphere j
E^* = equivalent elastic modulus of two spheres
E_i^* and E_j^* = equivalent elastic moduli of sphere i and sphere j
m^* = equivalent mass of two spheres
m_i^* and m_j^* = masses of sphere i and sphere j
p_c = compressive pressure of contact center
p_m = mean pressure of contact center
p_p = compressive pressure on the plastic contact area of two spheres
p_{pi} and p_{pj} = limit compressive pressures of sphere i and sphere j
$p(r)$ = contact pressure distribution in the elastic contact area of two spheres
P = contact force
P_e = contact force over the annular elastic area in the elastoplastic compression phase
r_a = radius of contact area
r_{ae} = transition contact radius from ECP to EPCP
r_p = radius of plastic zone in the contact area
R^* = equivalent radius of two spheres
R_i and R_j = radii of sphere i and sphere j
t = impact time from touching to separation of two spheres
t_e, t_{ep}, and t_{res} = respective instants at which elastic compression phase, elastoplastic compression phase, and elastic resilience phase ended since the beginning of contact of two spheres
v_i^- and v_j^- = velocities of sphere i and sphere j before impact
v_i^+ and v_j^+ = velocities of sphere i and sphere j after impact
v_r^- = relative velocity of two spheres before impact
v_r^+ = relative velocity of two spheres after impact
δ = relative deformation of two spheres in impact
$\dot{\delta}$ = relative velocity of two spheres in impact
δ_e and δ_{ep} = respective relative deformations of two spheres at the end of elastic compression phase and elastoplastic compression phase
$\dot{\delta}_e$ = relative velocity of two spheres at the end of elastic compression phase
$\delta_{\max}$ = maximum of relative deformation of two spheres
δ_{res} = plastic relative deformation of two spheres
η = energy loss factor
ν_i and ν_j = Poisson's ratios of sphere i and sphere j
ρ_i and ρ_j = mass densities of sphere i and sphere j
σ_y = minimum yield strength of sphere i and sphere j
σ_{yi} and σ_{yj} = yield strengths of sphere i and sphere j

References

[1] Wang, S., 2003, "New Fine Particle Impact Damping and Its Structure," Tenth International Congress on Sound and Vibration, Stockholm, pp. 1635–1642.
[2] Vu-Quoc, L., Zhang, X., and Walton, O. R., 2000, "A 3-D Discrete Element for Dry Granular Flows of Ellipsoidal Particles," Comput. Methods Appl. Mech. Eng., **187**(3–4), pp. 483–528.
[3] Wu, C.-Y., Dihoru, L., and Cocks, A. C. F., 2003, "The Flow of Powder Into Simple and Stepped Dies," Powder Technol., **134**(1-2), pp. 24–39.
[4] Weir, G., and McGavin, P., 2008, "The Coefficient of Restitution for the Idealized Impact of a Spherical, Nano-Scale Particle on a Rigid Plane," Proc. R. Soc. London, Ser. A, **464**, pp. 1295–1307.
[5] Johnson, K. L., 1985, *Contact Mechanics*, Cambridge University Press, Cambridge, Secs. 6.1–6.4, 11.5, pp. 153–184, 361–366.
[6] Stronge, W. J., 1995, "Theoretical Coefficient of Restitution for Planar Impact of Rough Elastoplastic Bodies," Impact, Waves and Fracture, ASME, Vol. AMD-205, pp. 351–362.
[7] Thornton, C., 1997, "Coefficient of Restitution for Collinear Collisions of Elastic Perfectly Plastic Spheres," ASME J. Appl. Mech., **64**, pp. 383–386.
[8] Wu, C.-Y., Li, L.-Y., and Thornton, C., 2005, "Energy Dissipation During Normal Impact of Elastic-Plastic Spheres," Int. J. Impact Eng., **32**(1–4), pp. 593–604.
[9] Zhang, X., and Vu-Quoc, L., 2002, "Modeling the Dependence of the Coefficient of Restitution on the Impact Velocity in Elasto-Plastic Collisions," Int. J. Impact Eng., **27**, pp. 317–341.
[10] Vu-Quoc, L., and Zhang, X., 1999, "An Elastoplastic Contact Force-Displacement Model in the Normal Direction: Displacement-Driven Version," Proc. R. Soc. London, Ser. A, **455**, pp. 4013–4044.
[11] Vu-Quoc, L., Zhang, X., and Lesburg, L., 2000, "A Normal Force-Displacement Model for Contacting Spheres, Accounting for Plastic Deformation: Force-Driven Formulation," ASME J. Appl. Mech., **67**(2), pp. 363–371.
[12] Plantard, G., and Papini, M., 2005, "Mechanical and Electrical Behaviors of Polymer Particles. Experimental Study of the Contact Area Between Two Particles. Experimental Validation of a Numerical Model," Granular Matter, **7**(1), pp. 1–12.
[13] Vu-Quoc, L., Lesburg, L., and Zhang, X., 2004, "An Accurate Tangential Force-Displacement Model for Granular-Flow Simulations: Contacting Spheres With Plastic Deformation, Force-Driven Formulation," J. Comput. Phys., **196**(1), pp. 298–326.
[14] Zhang, X., and Vu-Quoc, L., 2007, "An Accurate Elastoplastic Frictional Tangential Force-Displacement Model for Granular Flow Simulations: Displacement-Driven Formulation," J. Comput. Phys., **225**(1), pp. 730–752.
[15] Mesarovic, S. Dj., and Fleck, N. A., 1999, "Spherical Indentation of Elastic-Plastic Solids," Proc. R. Soc. London, Ser. A, **455**, pp. 2707–2728.
[16] Mesarovic, S. Dj., and Johnson, K. L., 2000, "Adhesive Contact of Elastic-Plastic Spheres," J. Mech. Phys. Solids, **48**(10), pp. 2009–2033.
[17] Kogut, L., and Etsion, I., 2002, "Elastic-Plastic Contact Analysis of a Sphere and a Rigid Flat," ASME J. Appl. Mech., **69**, pp. 657–662.
[18] Etsion, I., Kligerman, Y., and Kadin, Y., 2005, "Unloading of an Elastic-Plastic Loaded Spherical Contact," Int. J. Solids Struct., **42**, pp. 3716–3729.
[19] Weir, G., and Tallon, S., 2005, "The Coefficient of Restitution for Normal Incident, Low Velocity Particle Impacts," Chem. Eng. Sci., **60**(13), pp. 3637–3647.
[20] Du, Y., Wang, S., Zhu, Y., Li, L., and Han, G., 2008, "Performance of a New Fine Particle Impact Damper," Adv. Acoust. Vib., **2008**, p. 140894.
[21] Gladwell, G. M. L., 1980, *Control Problems in the Classical Theory of Elasticity*, Sijthoff & Noordhoff, Germantown.
[22] Yu, T., 1989, *Plasticity Mechanics*, Higher Education, Beijing.
[23] Rao, S. S., 1990, *Mechanical Vibrations*, 2nd ed., Addison-Wesley, Reading, MA.
[24] Panossian, H. V., 1992, "Structural Damping Enhancement Via Non-Obstructive Particle Damping Technique," J. Vib. Acoust., **114**, pp. 101–105.

The Dynamic Compressive Response of an Open-Cell Foam Impregnated With a Non-Newtonian Fluid

M. A. Dawson

G. H. McKinley

Department of Mechanical Engineering,
Massachusetts Institute of Technology,
Cambridge, MA 02139

L. J. Gibson

Department of Materials Science and Engineering,
Massachusetts Institute of Technology,
Cambridge, MA 02139

The response of a reticulated, elastomeric foam filled with colloidal silica under dynamic compression is studied. Under compression beyond local strain rates on the order of $1\ s^{-1}$, the non-Newtonian, colloidal silica-based fluid undergoes dramatic shear thickening and then proceeds to shear thinning. In this regime, the viscosity of the fluid is large enough that the contribution of the foam and the fluid-structure interaction to the stress response of the fluid-filled foam can be neglected. An analytically tractable lubrication model for the stress-strain response of a non-Newtonian fluid-filled, reticulated, elastomeric foam under dynamic compression between two parallel plates at varying instantaneous strain rates is developed. The resulting lubrication model is applicable when the dimension of the foam in the direction of fluid flow (radial) is much greater than that in the direction of loading (axial). The model is found to describe experimental data well for a range of radius to height ratios ($\sim 1-4$) and instantaneous strain rates of the foam ($1\ s^{-1}$ to $4\times 10^2\ s^{-1}$). The applicability of this model is discussed and the range of instantaneous strain rates of the foam over which it is valid is presented. Furthermore, the utility of this model is discussed with respect to the design and development of energy absorption and blast wave protection equipment. [DOI: 10.1115/1.3130825]

Keywords: foam, lubrication approximation, non-Newtonian, porous media, shear-thickening fluid

1 Introduction

While existing armor is highly advanced and capable of resisting most projectiles [1], advancements toward the development of an armor that efficiently protects against the enormous pressure gradients generated by explosive devices are limited. Blast waves can cause severe damage to the human body as well as to vehicles and structures. Recently, the design of a novel reactive armor to mitigate the effects of blast waves has been explored [2]. This design incorporates open-cell (reticulated) foams filled with shear-thickening, non-Newtonian liquids into existing composite armor. Open-cell foams filled with non-Newtonian liquids have the potential to impede shockwaves, increasing the time it takes for waves to propagate through the foam medium and decreasing the resulting pressure gradient experienced by underlying media (e.g., tissue). As a first step in modeling this nonlinear phenomenon, we analyze the flow of a non-Newtonian fluid (NNF), which has a shear-thickening regime, through an open-cell, elastomeric foam. The flow of both Newtonian and non-Newtonian fluids through open-cell foams has been investigated extensively for a variety of engineering applications, but characterizing the contribution of the fluid to energy absorption under dynamic loading is still a critical area of research. Most of the previous research has focused on the development of complex, often computational, models to describe the contribution of Newtonian fluids in an open-cell foam under impact loading [3–6]. More recent work by Dawson et al. [7] has resulted in the development of tractable models for the contribution of viscous Newtonian flow to the stress-strain response of a low-density, reticulated, fluid-filled foam under dynamic loading. However, comparably little work has been done in the field of non-Newtonian flow through deformable porous media. While a number of authors have studied the pressure drop of general power-law, non-Newtonian fluids through porous media [8–10], a comparable model for the response of a non-Newtonian fluid-filled foam under dynamic compression has not been published.

In this paper, we analyze the response of a NNF-filled, low-density, reticulated, elastomeric foam under dynamic axial compression. The response after the fluid has undergone shear thickening is particularly important since the fluid will nearly always be in this regime for most engineering designs under dynamic loading. Scaling arguments demonstrate that after the shear-thickening transition, the contribution of the foam itself and the contribution of the fluid-structure interaction to the overall response can be neglected. Based on these arguments, a lubrication model for squeezing flow of a non-Newtonian fluid between two parallel plates is developed in which the characteristic dimension of the fluid in the direction of fluid flow (radial) is assumed to be much greater than that in the direction of loading (axial). The corresponding range of instantaneous strain rates of the NNF-filled foam over which this model is applicable is also given. It is anticipated that this model is applicable for nearly all expected instantaneous strain rates caused by either impact loading or blast wave loading. The range of characteristic dimensions of the NNF-filled foam over which this model is valid is also given based on previous research on the applicability of a lubrication model to the stress-strain response of a Newtonian fluid-filled foam under dynamic compression [7]. The lubrication model is analytically tractable, depending only on the characteristic fluid properties, the characteristic radius to height ratio of the NNF-filled foam, and the instantaneous strain rate of the foam. Furthermore, it is independent of all of the parameters of the low-density, elastomeric foam, such as foam grade.

Experimental measurements of the stress-strain response of a

Contributed by the Applied Mechanics Division of ASME for publication in the Journal of Applied Mechanics. Manuscript received March 6, 2008; final manuscript received March 23, 2009; published online July 23, 2009. Review conducted by Nesreen Ghaddar.

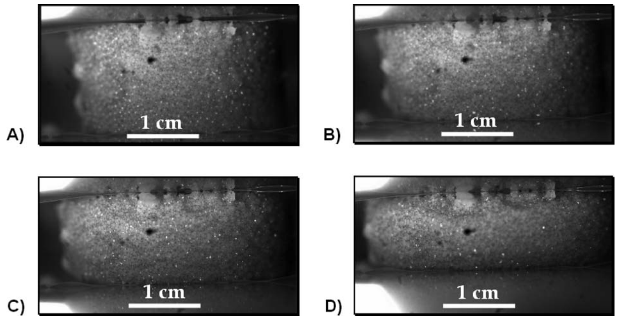

Fig. 1 Images of a 70 pores/in. foam filled with 61% volume fraction silica-based non-Newtonian fluid loaded in axial compression at 250 mm/s. (*a*) $\varepsilon=0$ strain, (*b*) $\varepsilon=0.1$ strain, (*c*) $\varepsilon=0.2$ strain, and (*d*) $\varepsilon=0.3$ strain.

low-density polyurethane foam filled with a colloidal silica non-Newtonian fluid under dynamic loading are presented. The non-Newtonian fluid is comprised of a high volume fraction of nearly monodisperse silica particles suspended in ethylene glycol. Shear thickening is often observed in concentrated colloidal dispersions and is characterized by a dramatic increase in viscosity with increasing shear stress in the fluid [11,12]. Numerous studies have concluded that reversible shear thickening in colloidal suspensions is due to the formation and jamming of clusters of particles (hydroclusters) bound together by hydrodynamic lubrication forces between particles [13–16]. Detailed reviews and quantitative descriptions of the mechanisms for shear thickening of colloidal suspensions are given in Refs. [17–19]. In this paper, the complex behavior of colloidal silica non-Newtonian fluid is discussed and related to the response of the NNF-filled foam. In the range where the model is valid, it is found to be strongly supported by experimental results. Finally, a brief discussion of the engineering applications of non-Newtonian fluid-filled foams and the significance of the model presented in this paper are presented.

2 Analysis

2.1 Model Assumptions. This analysis considers dynamic axial compression of a low-density, elastomeric foam fully saturated with a non-Newtonian power-law fluid between two parallel plates. The fluid is assumed to remain in a cylindrical shape with uniform radius while undergoing deformation, where the radius of the cylinder can be determined by conservation of mass of an incompressible fluid (Fig. 1). In addition, the fluid is assumed to be a power-law fluid with a highly shear-thickening regime, such that the maximum viscosity is several orders of magnitude greater than the minimum viscosity. For known nanoparticle based non-Newtonian fluids, this will result in a maximum viscosity greater than 10^3 Pa s. In this viscosity range, the stress within the fluid is three orders of magnitude greater than that in the foam alone. Furthermore, the characteristic dimension of the colloidal particles in the fluid is several orders of magnitude smaller than the characteristic dimension of the foam pore size. These two observations ensure that the response of the elastomeric foam, as well as the fluid-structure interaction between the foam and the non-Newtonian fluid, can be neglected, so that the system behaves as if the foam were nonexistent. This assumption is supported in Fig. 2 where magnified images of the cells of the foam are shown before loading and during loading. In Fig. 2 it is evident that the foam struts are readily torn apart by the highly viscous fluid flow, supporting the hypothesis that the structural support from the foam and the fluid-structure interaction is negligible. This result is in contrast to the result presented by Dawson et al. [7] for a lower viscosity, Newtonian fluid-filled foam where the structural response of the foam and the fluid-structure interaction are significant. The analysis presented in this paper is also based on a lubrication approximation, which assumes that the ratio of the characteristic radius of the specimen to the characteristic height of the specimen, in this paper referred to as the aspect ratio, is much greater than 1. Dawson et al. [7] gave a detailed analytical description of the applicability of the lubrication approximation to a comparable problem with a Newtonian fluid and demonstrated the rapid convergence of the lubrication model to the exact solution as the aspect ratio increases. They concluded that beyond aspect ratios of 4, the lubrication model can be used to approximate the exact solution; however, even beyond aspect ratios of unity, the lubrication solution is shown to approximate the exact solution to within 10% for most strains. Finally, after the shear-thickening transition, the flow is assumed to be dominated by viscous forces for all instantaneous strain rates of the foam considered in this analysis.

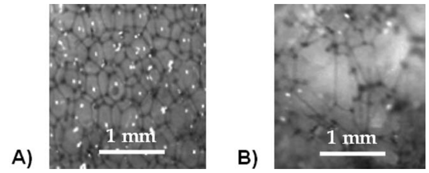

Fig. 2 Optical micrograph of a NNF-filled foam. (*a*) $\varepsilon=0$ strain and (*b*) $\varepsilon=0.4$ strain.

2.2 Fluid Flow in a Rectangular Channel. We first consider a model for pressure driven flow of a power-law fluid through a rectangular channel (Fig. 3) where the length of the channel is L, the width is W, and the height is $2B$ with $2B \ll W \ll L$. The flow is assumed to be incompressible and locally fully developed. The gravitational effects are assumed to be negligible. Since the flow is assumed to be dominated by viscous forces, inertial effects can also be neglected. The following velocity and pressure profiles are assumed:

$$V_z = V_z(x,y)$$

$$V_x = V_y = 0$$

$$P = P(z) \tag{1}$$

where V_x, V_y, and V_z are the velocity components in the horizontal (x), vertical (y), and axial (z) directions, respectively, and P is the local pressure within the fluid. Coupling the equation of continuity with the full Navier–Stokes equations of motion, this problem is readily solved for a power-law fluid where the viscosity η is given by the relation

$$\eta = m(\dot{\gamma})^{n-1} \tag{2}$$

where m is the consistency index, n is the power-law exponent, and $\dot{\gamma}$ is the magnitude of the rate of strain tensor or the shear rate of the fluid. Following Bird et al. [20], the necessary boundary conditions are based on symmetry and no wall-slip at the wall and can be given by

$$\tau_{yz}|_{y=B} = 0$$

$$V_z|_{y=0} = 0 \tag{3}$$

where τ_{yz} is the shear stress in the fluid. Applying these assumptions and boundary conditions, the Navier–Stokes equations of

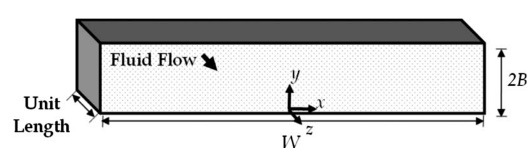

Fig. 3 Model of rectangular channel flow

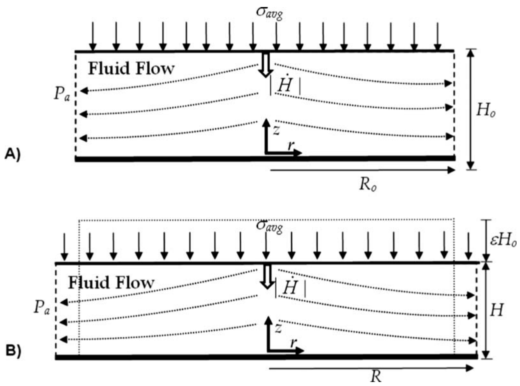

Fig. 4 Lubrication fluid flow model assuming the absence of foam. (*a*) At 0 strain and (*b*) at any given strain ε.

motion in the axial direction can be solved using a lubrication approximation. The resulting flow rate Q, given by Bird et al. [20], is found to be

$$Q = 2WB^2\left(-\frac{B}{m}\frac{\partial P}{\partial z}\right)^{1/n}\frac{1}{\left(\frac{1}{n}+2\right)} \tag{4}$$

2.3 Radial Fluid Flow in a Cylindrical Specimen Squeezed Between Parallel Plates. In the lubrication limit, flow in a rectangular channel can be transformed to radial squeezing flow between two parallel plates where the lower plate is fixed and the upper plate is moving as shown in Fig. 4. As previously discussed, the fluid is assumed to remain in a cylindrical shape with uniform radius while undergoing deformation. By conservation of mass the aspect ratio at any given axial strain ε is given by

$$\frac{R}{H} = \frac{R_o}{H_o}\left[\frac{1}{1-\varepsilon}\right]^{3/2} \tag{5}$$

where R_o is the initial radius of the NNF-filled foam at zero strain, H_o is the initial height at zero strain, R is the radius at any given strain, H is the distance between the plates, and ε is the strain, taken to be positive in compression and given by $(1-H/H_o)$ (Fig. 4). In Fig. 4 P_a is the atmospheric pressure on the free surface, and the magnitude of the velocity of the top plate is given by $|\dot{H}|$, where $\dot{H}$ is the time rate of change in the distance between the two plates. Using the transformations from the two-dimensional, rectangular channel, planar flow problem in Sec. 2.2 to the squeezing flow problem between parallel plates in cylindrical coordinates given by Bird et al. [20], Eq. (4) can be rewritten for the lubrication squeezing flow between parallel plates as

$$Q(r) = \pi r H^2\left(\frac{-H}{2m}\frac{\partial P}{\partial r}\right)^{1/n}\frac{1}{\left(\frac{1}{n}+2\right)} \tag{6}$$

Furthermore, the equation of continuity can be used to find a relation between the volumetric flow rate and the change in height of the fluid giving

$$Q(r) = \pi r^2(-\dot{H}) \tag{7}$$

Combining Eqs. (6) and (7) and solving for the pressure profile give

$$P(r) - P_a = \frac{2m(-\dot{H})^n}{H^{2n+1}}\left(\frac{2n+1}{n}\right)^n\frac{R^{n+1}}{n+1}\left[1-\left(\frac{r}{R}\right)^{n+1}\right] \tag{8}$$

For a power-law fluid σ_{zz} is zero on the surface of the plate by arguments of the equations of motion in the normal direction and mass conservation under a no slip condition. Furthermore, Bird et al. [20] gave the solution for squeezing flow of viscoelastic fluids between parallel disks, accounting for normal stresses using the Criminale-Ericksen-Filbey (CEF) equations. It is evident that the pressure distribution given in Eq. (8) is equivalent to this solution, indicating normal stress effects σ_{zz} on the surface of the plate are negligible. Neglecting inertial effects, a force balance can be used to find an equivalent uniform stress distribution or true stress σ_{avg}, applied to the top compression plate by integrating the pressure field over the radius and dividing by the area of the plate giving

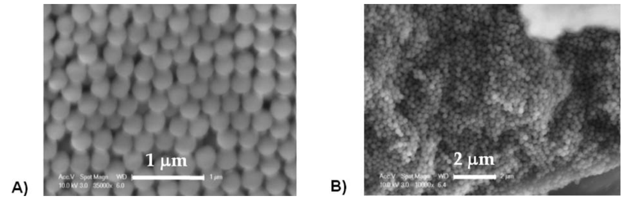

Fig. 5 Scanning electron microscope images of silica particles

$$\sigma_{\text{avg}} = 2\left(\frac{2n+1}{n}\right)^n\frac{m}{n+3}\left(\frac{R_o}{H_o}\right)^{n+1}\left(\frac{-\dot{H}}{H}\right)^n\left(\frac{1}{1-\varepsilon}\right)^{3(n+1)/2} \tag{9}$$

where $-\dot{H}/H$ is the instantaneous strain rate of the NNF-filled foam or the negative of the current rate of change in the height of the foam divided by the current height of the foam. It is important to distinguish the instantaneous strain rate of the foam from the magnitude of the strain rate of the fluid $\dot{\gamma}$, which in this paper is referred to as the local strain rate. In our experiments described below, the fluid flows through an open-cell foam, which introduces a tortuosity to the fluid path. We account for the tortuosity by introducing a constant into Eq. (9).

3 Experimental Methods

3.1 Materials. Specimens of open-cell, flexible, polyester-based polyurethane foams (New Dimension Industries, Moonachie, NJ), with nominal cell diameters of 175 μm, 210 μm, and 235 μm (corresponding to manufacturer specified grades of 90 pores/in., 80 pores/in., and 70 pores/in., respectively) were used in the experiments. The densities of the foams ranged from 0.0318 g/cm^3 to 0.0322 g/cm^3. Based on the manufacturer's value of the density of the solid polyurethane (ρ_s=1.078 g/cm^3), the relative density of the foams was $\rho^*_o/\rho_s \cong 0.030$. The foam was cut into cylindrical specimens with nominal diameter D =25.4 mm and height H_o=12.6 mm. The dimensions of each sample were measured using a digital caliper accurate to within 0.01 mm.

The non-Newtonian fluid consisted of silica nanoparticles (Fuso Chemical Co., Osaka, Japan) suspended in ethylene glycol (VWR, West Chester, PA) at a volume fraction of approximately 61%. The average particle diameter was determined using a scanning electron microscope (XL30 FEG ESEM, FEI/Philips, Hillsboro, OR) as shown in Fig. 5(*a*). The diameters of 100 particles were measured and analyzed using SCION IMAGE analysis software (Scion Corporation, Frederick, MD). The particles are found to be nearly monodisperse (Fig. 5(*b*)) with an average diameter of 293 nm+−31 nm. The density of the silica nanoparticles themselves was taken to be that given by the supplier of 1.95 g/cm^3. The density and viscosity of the ethylene glycol suspending fluid were taken to be ρ=1.11 g/cm^3 and $\mu = 2.1\times10^{-2}$ Pa s at 20°C.

The colloidal silica suspension was first washed with ethylene glycol three times. The washing process began by centrifuging the solution at 2700 g for 4 h using a Sorvall Legend Mach 1.6 Centrifuge (Fisher Scientific, Suwanee, GA). After this centrifuging process, the silica suspension consisted of a sedimented layer and a layer of supernatant, which was subsequently poured off. Ethyl-

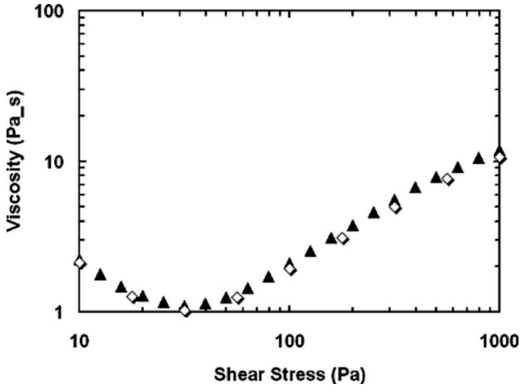

Fig. 6 Steady shear viscosity plotted against shear stress for 48% volume fraction of silica-based non-Newtonian fluid. Gap thickness: 500 μm (▲) and 250 μm (◇).

ene glycol was then added to the remaining sedimented layer and the mixture was resuspended using a VWR digital vortex mixer (VWR, West Chester, PA). In order to determine the volume fraction of the sedimented silica particles after centrifuging and removal of the supernatant, the sediment was dried until no significant change in mass over a 24 h period was detected. Based on this drying experiment, the volume fraction of the sediment was determined to be 69% silica particles by volume. The volume fraction of the sediment after centrifuging and removal of the supernatant was found to be constant to within measures of uncertainty. In the experiments utilized for this paper the sediment was immediately redispersed in ethylene glycol after centrifuging to give a final suspension volume fraction of approximately 61% silica. To redisperse the sediment and create this 61% by volume silica-based NNF, a vortex mixer was used until the sediment appeared to be completely suspended in the fluid. Then the NNF was sonicated for 1 h using an ultrasonic bath. Based on the assumption of ideal mixing, the density of the resulting NNF was estimated to be 1.6 $\mathrm{g/cm^3}$.

3.2 Viscosity of the Silica Suspension. The steady state rheological properties of the colloidal silica suspension or non-Newtonian fluid under shear flow were then measured using a controlled stress rheometer (ARG 2000, TA Instruments, New Castle, DE). The geometry was selected to be a 40 mm aluminum parallel plate geometry with 500 μm gap. Although a cone and plate geometry is preferred for steady state shear properties, the parallel plate geometry is more suitable for use with sandpaper, which is required to reduce slip of a high viscosity fluid. A detailed discussion on the effects of wall slip in rheological measurements can be found in Ref. [21]. In summary, the presence of slip in viscosity measurements is detected by substantial shifts in the viscosity plots with varying gap thickness between the parallel plates (in some cases shifts in the viscosity can be in excess of an order of magnitude). To eliminate slip in the rheological measurements, the parallel plate geometry was covered with a 1000 grit sandpaper, for which the characteristic size of the grit or roughness is of the same order of magnitude as the diameter of the silica particles. The rheological measurements were found to be very similar with gap ranges varying from 250 μm to 1000 μm, indicating that this sandpaper nearly eliminated the effect of wall slip. Figure 6 gives a plot of the viscosity against the shear stress in the silica-based NNF with a volume fraction of approximately 48% measured at gaps of 250 μm and 500 μm. Figure 6 clearly demonstrates in these experiments that there was a negligible change in the viscosity with varying gap thickness, indicating slip was successfully eliminated. All experiments were performed at 22.5°C and controlled with a Peltier temperature control. After loading the sample into the viscometer, the sample was loaded under a preshear stress ramp from 10 Pa to 100 Pa and then allowed to rest for 15 min to eliminate any effects of sample loading. A stress sweep was performed from 10 Pa to a maximum shear stress in the fluid of approximately 15,400 Pa with 10 points/decade, each of which was measured for 60 s. However, for samples with a lower volume fraction of particles than the standard 61% sample, the maximum shear stress value in the fluid could not be achieved due to rate limitations of the rheometer, so the maximum shear stress achievable was recorded. Ascending and descending stress sweeps were performed, and minimal hysteresis was observed, demonstrating the reversibility of the fluid as found by Bender and Wagner [17]. In addition, no yield stress behavior was observed at low stresses. The steady state shear viscosity was measured along with the shear stress in the fluid and local shear rate under controlled stress loading. Because of the complexity of the manufacturing process, determining the exact volume fraction of silica particles is difficult, so small variations in the volume fraction are expected. To assess the sensitivity to variations in the volume fraction of silica and to determine the overall characteristic behavior of high volume fraction silica-based fluids, this procedure was used for a range of volume fractions from 48% to 61%.

3.3 Dynamic Compression Tests on Non-Newtonian Fluid-Filled Foam. Samples of a reticulated, polyurethane foam saturated with the 61% volume fraction silica-based NNF were then prepared. Since even the minimum viscosity of the NNF is large, samples of a reticulated foam were filled by the capillary effect through compression cycles while submerged in a bath of NNF shaken by a vortex mixer. Hager and Craig [22] demonstrated that the deflection of a polyurethane foam compressed to 0.75 strain for a short duration of time is almost completely recoverable. Therefore, an attempt was made not to exceed a strain of 0.75 during the filling process to minimize the microstructural damage caused by the filling process. This filling procedure was carried out until the weight of the fluid-filled foam samples achieved the desired saturated weight expected, based on the density, porosity, and dimensions of the foam as well as the density of the fluid. After saturation, the NNF-filled foam was allowed to recover for 2 h prior to testing, based on data for the recovery of a low-density polyurethane foam presented by Hager and Craig [22].

The compressive true stress-strain response of the NNF-filled foam was measured with the rise direction of the foam parallel to the direction of loading, up to a strain of 0.6 strain and over a range of instantaneous strain rates of the foam from $-\dot{H}/H = 1.0\ \mathrm{s^{-1}}$ to $4\times10^{2}\ \mathrm{s^{-1}}$. For instantaneous strain rates less than $-\dot{H}/H = 50\ \mathrm{s^{-1}}$ an Instron testing machine (Instron Model 1321, Instron Corp., Canton, MA) was used at constant velocities ($-\dot{H} = 12.5$ mm/s, 31.25 mm/s, 62.5 mm/s, 93.75 mm/s, 125 mm/s, and 250 mm/s); for instantaneous strain rates greater than $-\dot{H}/H = 50\ \mathrm{s^{-1}}$ a Dynatup drop-tower (Dynatup 9200 Series, Instron Crop., Canton, MA) was used. The drop-tower impact experiments were arranged to be nearly constant velocity. Data were only collected up to strains of approximately 50%, at which point built in stoppers in the drop tower absorbed the remaining energy. The drop-tower weight was approximately 21.7 kg, resulting in an impact energy that was substantially greater than the energy absorbed by the NNF-filled foam or the energy gained due to potential energy effects. Since the energy of the drop-tower weight was nearly constant, the resulting experiments were nearly constant velocity ($-\dot{H} \approx 0.75$ m/s, 1.00 m/s, 1.25 m/s, 1.50 m/s, 1.75 m/s, 2.00 m/s, 2.25 m/s, 2.50 m/s, 2.75 m/s, and 3.00 m/s). During testing the temperature was maintained at 22.5°C to ensure the fluid properties are consistent. Since the flow is assumed to be instantaneously fully developed, the model presented in this paper is applicable to constant velocity loading.

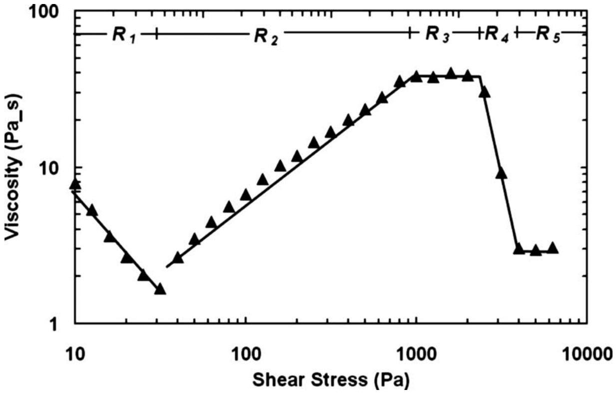

Fig. 7 Steady shear viscosity plotted against shear stress for 50% volume fraction silica-based non-Newtonian fluid

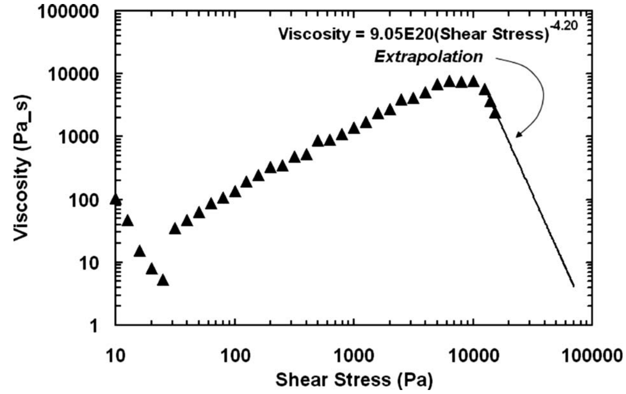

Fig. 8 Steady shear viscosity plotted against shear stress for 61% volume fraction silica-based non-Newtonian fluid

4 Fluid Viscosity Results and Discussion

In Fig. 7 a typical plot of the viscosity against the shear stress in the fluid for a NNF fluid with volume fraction of 50% silica particles is given. The rheological behavior of the fluid under steady state shear viscosity testing in the controlled stress rheometer was consistent for all volume fractions tested, so Fig. 7 is taken to be typical of the behavior for all silica-based, non-Newtonian fluids with the shear-thinning and -thickening regimes discussed in this paper. The viscosity data also correspond well with similar experiments performed by Maranzano and Wagner [18].

Figure 7 also denotes the typical regimes of distinct behavior observed for this class of fluids. At extremely low local strain rates the fluid acts as a shear-thinning fluid (regime R_1). The shear thinning or "yield stress" behavior observed at low shear stresses (or local strain rates) occurs when the particles in an ordered phase begin to orient themselves so that the direction of closest packing of the spheres aligns with the flow velocity, such that the planes containing the closest packing spheres are parallel to the shearing surfaces [23]. Therefore, the three-dimensional ordered phase transforms into a two-dimensional layered phase that permits flow, resulting in a dramatic drop in viscosity. At a critical shear stress (or local strain rate) dramatic shear thickening occurs, evident in regime R_2. The onset of this dramatic shear thickening occurs when the hydrodynamic forces driving particles together exceed the repulsive forces due to interparticle (i.e., electrostatic or steric) potentials and Brownian motion [18], and the particles fail to remain in their ordered state and begin to form three-dimensional clusters of particles. This dramatic shear thickening is evident in Fig. 7 at nearly constant local strain rate. This dramatic shear thickening is often termed "critical shear thickening" as when a discontinuity is observed as shown in Fig. 7. As previously discussed the jamming phenomenon is attributed to shear thickening, but critical shear thickening is only observed for very high volume fractions of solid particles. Following shear thickening, a plateau viscosity is reached (regime R_3). A number of theories have been proposed for this phenomenon, but it is generally accepted that the clusters begin to break down and form a random three-dimensional packing [12]. These first three regimes are characteristic of most non-Newtonian fluids with shear-thickening regimes [12]. However, after the maximum plateau, the fluid is often found to enter one of three stages: fracture, an extended plateau viscosity independent of shear rate, or a shear-thinning regime [12]. This regime of behavior is controlled by particle size distribution, particle content, the volume fraction of particles, particle-particle interactions, and the viscosity of the continuous phase. For the particular fluid discussed in this paper, another shear-thinning regime, R_4, occurs and, finally, for lower volume fraction fluids, a lower plateau viscosity is observed (regime R_5), which is approximately equal to the minimum viscosity previously obtained (Fig. 7). A large body of literature attempts to explain the behavior in all the regimes described [24,17,25,13] but the explanations for some phenomenon are still under dispute, so a detailed description is excluded from this paper. However, the general regimes described here are found to be consistent with this body of literature as seen in Refs. [26,12]. The primary remaining debate is around the shear-thinning regime R_4 and whether or not slip is causing it. In addition to the evidence presented by Hadjistamov [26] and Barnes [12], Hoffman [11] also demonstrated distinct shear-thinning regimes after shear thickening for monodisperse polymeric resin colloids. We believe that much of the recent literature has avoided the debate around this topic by not publishing data in the high stress regime examined in this study. For instance, the maximum shear stresses examined for comparable silica-based non-Newtonian shear-thickening fluids given by Bender and Wagner [17], Fagan and Zukoski [27], Lee et al. [23], and Maranzano et al. [18] range from the order of 100 Pa to the order of 1000 Pa. None of these studies attempts to examine the stress regime approaching and exceeding 1×10^4 Pa, presented in this study. However, more recent studies by Egres and Wagner [28] demonstrated that measurements in this regime are possible. They also showed with a different type of shear-thickening fluid (precipitated calcium carbonate based shear-thickening-fluid (STF)) distinct plateau regimes, corresponding to R_3, followed by, in some cases, what appears to be the beginning of shear-thinning regimes, corresponding to R_4. In addition to this support, the results of the stress-strain response of the NNF-filled foam presented at the end of this paper provide further evidence that the apparent shear-thinning phenomenon in regime R_4 is not caused by slip.

Figure 8 plots the viscosity against the shear stress in the fluid for 61% volume fraction silica/ethylene glycol solution. Limitations in the maximum torque capacity of the viscometer did not allow us to obtain data for the full range of regimes R_4 and R_5. Assuming that the trends in the viscosity of the fluid with 61% volume fraction silica particles are similar to those at lower volume fraction of particles, we can extrapolate the existing R_4 data using a linear regression of the log data (equations shown in the figures). We note that, for lower particle volume fraction based fluids, such as in Fig. 7, the value of the viscosity for the lower plateau (R_5) is similar to that at the minimum of R_1; we expect the transition from R_4 to R_5 to be similar for the fluid with 61% volume fraction of particles. In Fig. 8 an equation for the trend line of the viscosity as a function of the shear stress is given, which can be transformed into an equation for the viscosity as a function of the local shear rate. Using the plateau data and the shear-thinning trend line Fig. 8, the parameters m and n for the power-law model of the 61% volume fraction NNF in regimes R_3 and R_4 can be determined to be $m=7700$ Pa s, $n=1.0$ and $m=10,800$ Pa s, $n=0.19$, respectively.

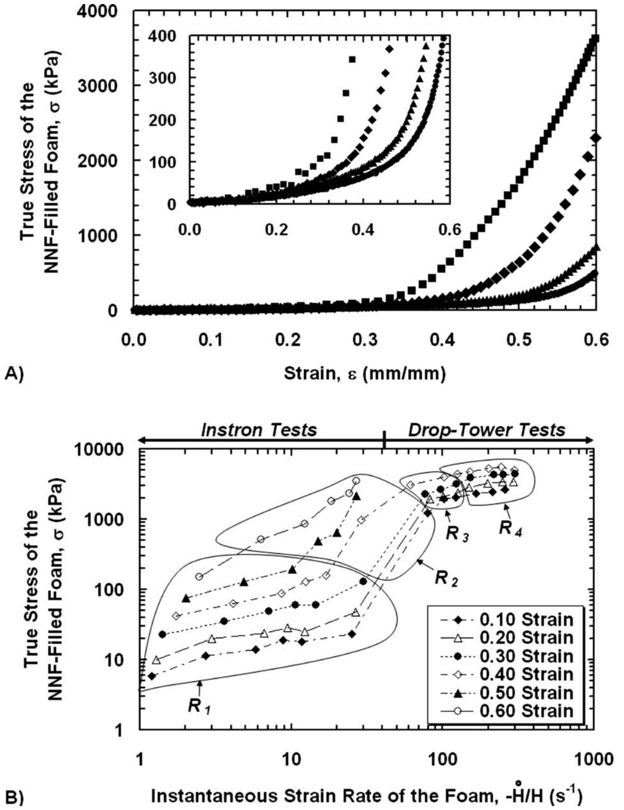

Fig. 9 (a) True stress plotted against strain for a 70 pores/in. foam filled with 61% volume fraction silica-based non-Newtonian fluid. $-\dot{H}=31.25$ mm/s (●), 62.5 mm/s (▲), 125 mm/s (♦), and 250 mm/s (■), corresponding to instantaneous strain rates of 2.5 s^{-1}, 5 s^{-1}, 10 s^{-1}, and 20 s^{-1} at $\varepsilon=0.0$ strain, respectively. (b) True stress plotted against instantaneous strain rate for a 70 pores/in. foam filled with 61% volume fraction silica-based non-Newtonian fluid. Regimes R_1-R_4 correspond to fluid behavior regimes.

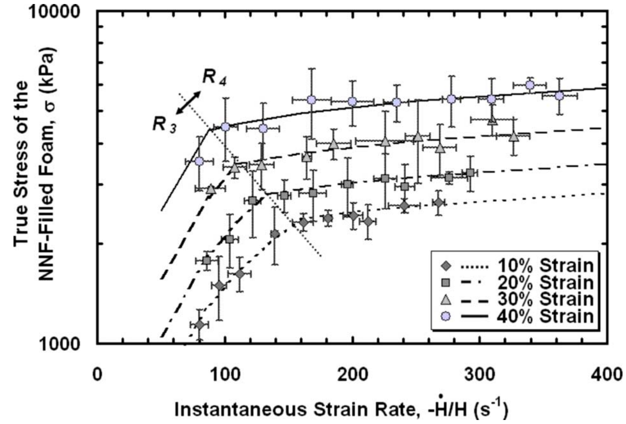

Fig. 10 True stress plotted against instantaneous strain rate for a 70 pores/in. foam filled with 61% volume fraction silica-based non-Newtonian fluid, ranging from 0.10 to 0.40 strain. The model corresponds to regimes R_3 and R_4 of the fluid given by Eq. (10).

5 Fluid-Filled Foam Results and Discussion

A plot of the true stress-strain responses of the 70 pores/in. foam saturated with the 61% volume fraction non-Newtonian fluid loaded at constant velocities ranging from 31.25 mm/s to 250 mm/s is given in Fig. 9(*a*). The dramatic increase in the true stress of the NNF-filled foam with strain is evident. The true stress of the NNF-filled foam is taken to be the load divided by current area, which is calculated based on conservation of mass, as previously discussed. At any given strain, the true stress of the NNF-filled foam and the corresponding instantaneous strain rate of the foam can be determined. The recorded data and Fig. 9(*a*) are used to generate the sample curve of the true stress response of the NNF-filled foam plotted against the instantaneous strain rate of the foam given in Fig. 9(*b*). For instantaneous strain rates less than 50 s^{-1}, strains varying from 0.1 to 0.6 are plotted in increments of 0.1, corresponding to aspect ratios ranging from approximately 1 to 4. For instantaneous strain rates greater than 50 s^{-1} strains varying from 0.1 to 0.4 are plotted, corresponding to aspect ratios ranging from 1 to 2.

The dynamic compressive response of the saturated NNF-filled foam exhibits multiple regimes of behavior similar to the simple shear behavior of the fluid itself given by the previous rheological experiments (Figs. 7 and 8). As shown in Fig. 9(*b*), this behavior corresponds to the first four regimes (R_1–R_4) of the fluid, previously discussed. At low instantaneous strain rates of the foam, the rate of increase in true stress of the NNF-filled foam with instantaneous strain rate is actually less than that of a comparable Newtonian fluid, indicating the viscosity drops with increasing instantaneous strain rate, corresponding to the shear-thinning regime R_1. The onset of the shear-thickening regime, corresponding to R_2, is also evident and, as expected, is found to occur with increasing strain (or aspect ratio) or increasing instantaneous strain rate. Similarly, behaviors corresponding to regimes R_3 and R_4 are also evident. While distinguishing the transition between the upper plateau regime R_3 and the shear-thinning regime R_4 in Fig. 9(*b*) may be difficult at the given scale, the distinction is more apparent in expanded scales provided later in Fig. 10.

In this study, we are primarily interested in modeling the behavior after shear thickening has occurred (R_3 and R_4) since most engineering applications will utilize the NNF in this regime. For example, the expected impact velocities for a helmeted head in a motorcycle accident and a chest covered by standard body armor subjected to a 1 kg trinitrotoluene (TNT) blast wave at a distance of 1 m are on the order of 5 m/s and 10 m/s, respectively. This results in instantaneous strain rates for a 0.01 m thick foam sample of 500 s^{-1} and 1000 s^{-1}, which are clearly beyond the instantaneous strain rate of the foam required for the fluid to transition from regime R_2 to regime R_3 (Fig. 9(*b*)). In addition, our focus was on modeling the behavior in regime R_3 and beyond because analytically modeling the behavior at strain rates less than those of regime R_3 is a complex task, which requires accounting for the fluid-structure interaction and the dramatic variation of the viscosity across the specimen. As previously discussed this problem is avoided for strain rates beyond the transition strain rate between regimes R_2 and R_3, where the effects of the fluid-structure interaction and the foam itself can effectively be neglected.

To compare our model (Eq. (9)) with our data, in the upper plateau regime R_3 and in the shear-thinning regime R_4, we examine data beyond the transition strain rate between regimes R_2 and R_3. Figure 10 shows the true stress response of a 70 pores/in. foam filled with the non-Newtonian fluid under dynamic compression plotted against the instantaneous strain rate of the foam for a range of strains varying from $\varepsilon=0.10$ to $\varepsilon=0.40$ and a range of instantaneous strain rates ranging from $\sim$50 s^{-1} to $\sim$400 s^{-1}. Each point is the average of four data points with error bars corresponding to one standard deviation. The error bars in the true stress direction are quite large as expected since small variations in the volume fraction of the silica particles in the fluid can result in large changes in viscosity but nearly no change in the exponent variable n. Correspondingly, the error bars in the instantaneous strain rate direction arise because changes in the energy absorption of the NNF-filled foam result in changes in the energy of impacting drop tower and thus its velocity. The true stress contribution predicted by the model given by Eq. (9) is plotted in Fig. 10 for both the plateau regime R_3 and the shear-thinning regime R_4, with their corresponding parameters m and n. To fit the true stress model constants C_{Ri} were introduced for each regime (where i corresponds to the regime) into Eq. (9) giving

$$\sigma_{\text{avg}} = 2C_{Ri}\left(\frac{2n+1}{n}\right)^n \frac{m}{n+3}\left(\frac{R_o}{H_o}\right)^{n+1}\left(\frac{-\dot{H}}{H}\right)^n\left(\frac{1}{1-\varepsilon}\right)^{3(n+1)/2} \tag{10}$$

The constants C_{R_3} *and* C_{R_4} given in Eq. (10) were found by establishing a measure of the goodness of fit and finding the value of C_{R_3} and C_{R_4}, which maximizes this measure. The measure for the goodness of fit R^2 is taken to be the sum of the squares of the difference between the experimental values and the average experimental value divided by the sum of the squares of the difference between the experimental values and the predicted values. Based on this measure of the goodness of fit, the empirical constants for regimes R_3 and R_4 are determined to be $C_{R_3}=0.94$ and $C_{R_4}=80$, respectively. These constants can be attributed primarily to two factors. First, as previously discussed, even small variations in the volume fraction of particles can result in large changes in the viscosity curves and thus the observed average true stress. Second, the increased tortuosity of the fluid path in the foam may also play a substantial role since the flow through the foam is not identically in shear flow.

Using the constants C_{R_3} and C_{R_4}, the transition between the plateau regime R_3 and the shear-thinning regime R_4 is found by setting Eq. (10), evaluated with constants (m and n) corresponding to the plateau regime, equal to Eq. (10), evaluated with constants (m and n) corresponding to the shear-thinning regime. The resulting equation governs the transition between R_3 and R_4 and is found to be

$$\left(\frac{-\dot{H}}{H}\right) = \left(\frac{C_{R_4}}{3C_{R_3}}\right)^{1.23}\left(\frac{H_o}{R_o}\right)(1-\varepsilon)^{3/2} \tag{11}$$

Using Eq. (11), for any given initial aspect ratio and strain, the instantaneous strain rate, corresponding to the transition between regimes R_3 and R_4, can be determined. While Eq. (11) is not generalized for all fluids discussed in this paper, it is applicable to the 61% silica-based non-Newtonian fluid, which is the focus of this analysis. Since there is no model for the transition between the shear-thickening regime R_2 and the plateau regime R_3, the onset of the behavior corresponding to R_3 is not predicted in this study; the model was plotted down to an arbitrary instantaneous transition strain rate of the foam selected to be 50 s^{-1}.

The constants C_{R_3} and C_{R_4} are found to be independent of the initial aspect ratio, the strain, and the instantaneous strain rate of the foam as demonstrated in Fig. 10. Furthermore, the constants C_{R_3} and C_{R_4} are also found to be independent of the grade of the foam beyond the shear-thickening transition. An additional study was performed to analyze the effects of varying the pore size of the foam. The true stress response of the NNF-filled foam was compared for 70 pores/in., 80 pores/in., and 90 pores/in. foam both prior to and after shear thickening (regimes R_2 and R_4). Prior to shear thickening, the true stress response is found to be highly dependent on the grade of the foam as demonstrated with Newtonian fluids [7]. Prior to shear thickening, the standard deviation in the true stress response of the three foam grades as a percentage of the average value was found to be 17.7%, which corresponds well with the results presented in Ref. [7]. However, after shear thickening has occurred, the true stress response of the NNF-filled foam is found to be independent of the grade of the foam, with a standard deviation in the true stress as a percentage of the average value of only 2.7%. This finding further supports the evidence shown in Fig. 2 that the fluid-structure interaction is negligible at high loading rates (high stresses) after shear thickening has occurred. Thus, the constants C_{R_3} and C_{R_4} are independent of the grade of the foam beyond the shear-thickening transition.

The need for the introduction of the empirical constants C_{R_3} and C_{R_4} is expected and can primarily be attributed to the fact that small variations in the volume fraction of the silica particles in the fluid can result in large changes in viscosity, corresponding to m in Eq. (10), but nearly no change in the exponent variable n. This effect could readily account for such an apparently large constant while explaining the fact that the true stress scales accurately with all of the parameters in Eq. (10). The need for different empirical constants for each regime (C_{R_3} versus C_{R_4}) can also be seen through this argument. If the actual plateau viscosity is higher than that measured in the rheological experiments, the need for a constant greater than unity is evident for regime R_4. Correspondingly, this effect would necessitate a constant greater than unity in regime R_3 as well; however, since regime R_3 only spans a very short range of local strain rates and local strain rates are expected to vary strongly over the radius of the foam, it is expected that not all of the fluid is accurately modeled by the maximum plateau viscosity (regime R_3). This would result in the model overestimating the average viscosity in the fluid and necessitating a constant less than unity to account for this overestimation. This effect would be less pronounced in the shear-thinning regime R_4 since the range of local strain rates spanned by this regime is much larger than that of R_3. Therefore, the need for different constants for each regime (C_{R_3} versus C_{R_4}) is evident. The effects overall result in a constant for regime R_3, which is on the order of unity, and a constant or regime R_4, which is much greater than unity.

The empirical constants C_{R_3} and C_{R_4} may also indicate that a number of effects, which have been neglected based on the assumptions of the analysis, may be important. For instance, this analysis does not consider the tortuosity in the fluid path in the open-cell foam, which may also contribute to the need for the constants C_{R_3} and C_{R_4}, to be introduced. In addition, this model assumes that the radial velocity is uniform in the z-direction or that the fluid remains in a cylindrical shape as it undergoes deformation. This is a strong assumption as demonstrated in Fig. 1, where little variation in the radius up to 0.30 strain is detectable. However, even small variations in the radius of the NNF-filled foam can result in changes in the local shear rate profile, giving rise to large discrepancies between the predicted viscosity and the actual viscosity in the experiment and thus a discrepancy in the true stress response of the NNF-filled foam. Furthermore, this model uses the lubrication approximation, which assumes that the velocity in the z-direction is much less than the velocity in the r-direction, and the corresponding pressure drop in the z-direction is negligible compared with that in the r-direction. The lubrication approximation technique is known to be a powerful method for solving complex viscous flows. When applied to actual systems the fluid response is often found to converge very rapidly to the lubrication approximation as the ratio of the characteristic radius to the characteristic height is increased. Dawson et al. [7] found that the lubrication approximation for a Newtonian fluid-filled foam under dynamic compression is highly applicable beyond an aspect ratio of 4; however, examining their data shows that even for aspect ratios as small as 1 the lubrication model provides a good approximation. In the experiments presented in this paper the aspect ratios ranged from 1.17 to 3.95. Again, this could result in a small discrepancy in the local shear rate and a large discrepancy in the predicted true stress response of the NNF-filled foam from the model. Moreover, the fluid flow may not be considered entirely shear flow, which would result in a much lower predicted true stress response than actually observed experimentally. In addition, the local shear rate of the fluid may actually differ from that predicted by the model in part due to dependence on the fluid-foam interaction. Although this contribution is expected to be negligible the load response of the NNF-filled foam is three orders of magnitude beyond that of the foam alone, and the characteristic diameter of the particles in the silica suspension is three orders of magnitude smaller than the characteristic pore size of the foam. Lastly, as previously discussed, this model assumes that the flow is dominated by viscous forces. This is an extremely robust assumption for the experiments presented in this analysis, considering the fluid viscosity increases approximately three orders of magnitude and approaches that of "solidlike" behavior after the shear-thickening transition. As previously discussed, the shear-thinning regime R_4 occurs over roughly four orders of magnitude of the local strain rate of the fluid, based on the behavior of fluid with lower volume fractions of particles, which have plateau regimes R_5 at a viscosity corresponding to the minimum viscosity of the fluid. Therefore, it is expected that the shear-thinning regime R_4 would also last several orders of magnitude of the instantaneous strain rate of the NNF-filled foam. Based on this, the fluid maintains an extremely high viscosity with increasing instantaneous strain rate for several orders of magnitude beyond the transition between the shear-thickening regime R_2 and the plateau regime R_3. In the experiments presented in this paper, the maximum Reynolds was Re=0.027, which is much less than unity, demonstrating that the assumption that the flow is dominated by viscous forces is highly applicable. However, for extremely high rate loading scenarios, inertial forces may become more important and this viscous fluid assumption may no longer be valid. Therefore, this model may only provide an order of magnitude estimate beyond loading velocities of ~ 50 m/s (instantaneous strain rates of $\sim 5\times 10^3$ s^{-1}) for samples with similar aspect ratios as those discussed in this paper. As previously discussed, nearly all comparable engineering designs used in dynamic compression, ranging from motorcycle helmets to blast loading protective equipment, would have loading rates applicable to this model.

Overall, the model for the true stress response of a non-Newtonian fluid-filled foam under dynamic compression given by Eq. (10) is strongly supported by experimental results, despite the need for a constant in each regime to account for some of the assumptions of the model. The model is found to describe the experimental results well for a variety of aspect ratios, strains, and instantaneous strain rates of the foam on the order of $-\dot{H}/H = 1.0\times 10^2$ s^{-1}, independent of foam grade for a low-density elastomeric foam. The model is found to fall within one standard deviation of all of the experimental data presented in Fig. 10. A method is also presented to identify the transition instantaneous strain rate between regimes R_3 and R_4, given an initial aspect ratio and strain.

6 Conclusion

A model for the true stress-strain response of a shear-thickening-fluid-filled, reticulated, elastomeric foam under dynamic compression beyond the shear-thickening transition is presented. This model is analytically tractable and useful in developing an understanding of the effects of material design parameters on the response of a NNF-filled foam under dynamic loading. To the authors' knowledge this is the first such analytical model, which explains this complex phenomenon for this selected group of non-Newtonian fluids and may be useful in the development of innovative new products in the field of protective equipment. In particular, this analytical model will be an essential step toward the successful development of a composite armor capable of impeding shockwaves caused by blast loading by providing insight into the energy absorption capabilities and wave propagation characteristics of a NNF-filled foam under dynamic loading.

Acknowledgment

This research was performed while on appointment as a National Defense Science and Engineering Graduate Fellow administered by the American Society for Engineering Education. This material is based on work supported by the National Science Foundation under Grant No. 0408259.

References

[1] Cheeseman, B., and Bogetti, T., 2003, "Ballistic Impact Into Fabric and Compliant Composite Laminates," Compos. Struct., **61**, pp. 161–173.
[2] Bettin, G., and McKinley, G. H., 2005, "High Deformation Rate Behavior of Polymeric Foams Filled With Concentrated Silica Suspensions," Society of Rheology 77th Annual Meeting.
[3] Hilyard, N. C., 1971, "Observations on the Impact Behaviour of Polyurethane Foams; II. The Effect of Fluid Flow," J. Cell. Plast., **7**, pp. 84–90.
[4] Rehkopf, J., Brodland, G., and McNeice, G., 1996, "Experimentally Separating Fluid and Matrix Contributions to Polymeric Foam Behavior," Exp. Mech., **36**, pp. 1–6.
[5] Mills, N., and Lyn, G., 2002, "Modeling Air Flow in Impacted Polyurethane Foam," Cell. Polym., **21**, pp. 343–365.
[6] Schraad, M., and Harlow, F., 2006, "A Multi-Field Approach to Modeling the Dynamic Response of Cellular Materials," Int. J. Mech. Sci., **48**, pp. 85–106.
[7] Dawson, M. A., McKinley, G. H., and Gibson, L. J., 2008 "The Dynamic Compressive Response of Open-Cell Foam Impregnated With a Newtonian Fluid," ASME J. Appl. Mech., **75**(4), p. 041015.
[8] Seguin, M. A., Montillet, A., Brunjail, D., and Comiti, J., 1996, "Liquid-Solid Mass Transfer in Packed Beds of Variously Shaped Particles at Low Reynolds Numbers: Experiments and Model," Chem. Eng. J., **63**, pp. 1–9.
[9] Comiti, J. M., 1989, "A New Model for Determining Mean Structure Parameters of Fixed Beds From Pressure Drop Experiments: Application to Packed Beds With Parallelepipedal Particles," Chem. Eng. Sci., **44**, pp. 1539–1545.
[10] Sabiri, N. E., and Comiti, J. M., 1995, "Pressure Drop in Non-Newtonian Purely Viscous Fluid Flow Through Porous Media," Chem. Eng. Sci., **50**, pp. 1193–1201.
[11] Hoffman, R. L., 1974, "Discontinuous and Dilatant Viscosity Behavior in Concentrated Suspensions. II Theory and Experimental Tests," J. Colloid Interface Sci., **46**, pp. 491–506.
[12] Barnes, H. A., 1989, "Shear-Thickening ('Dilatancy') in Suspensions of Non-aggregating Solid Particles Dispersed in Newtonian Liquids," J. Rheol., **33**, pp. 329–366.
[13] Bossis, G., and Brady, J., 1989, "The Rheology of Brownian Suspensions," J. Chem. Phys., **91**, pp. 1866–1874.
[14] Farr, R. S., Melrose, J. R., and Ball, R. C., 1997, "Kinetic Theory of Jamming in Hardsphere Startup Flows," Phys. Rev. E, **55**, pp. 7203–7211.
[15] Foss, D. R., and Brady, J. F., 2000, "Structure Diffusion and Rheology of Brownian Suspensions by Stokesian Dynamics Simulation," J. Fluid Mech., **407**, pp. 167–200.
[16] Catherall, A. A., Melrose, J. R., and Ball, R. C., 2000, "Shear Thickening and Order-Disorder Effects in Concentrated Colloids at High Shear Rates," J. Rheol., **44**, pp. 1–25.
[17] Bender, J., and Wagner, N., 1996, "Reversible Shear Thickening in Monodisperse and Bidisperse Colloidal Dispersions," J. Rheol., **40**, pp. 899–916.
[18] Maranzano, B. J., and Wagner, N. J., 2001, "The Effects of Particle Size on Reversible Shear Thickening of Concentrated Colloidal Dispersions," J. Chem. Phys., **114**, pp. 10514–10527.
[19] Maranzano, B. J., and Wagner, N. J., 2001, "The Effects of Interparticle Interactions and Particle Size on Reversible Shear Thickening: Hard-Sphere Colloidal Dispersions," J. Rheol., **45**(5), pp. 1205–1222.
[20] Bird, R. B., Armstrong, R., and Hassager, O., 1987, *Dynamics of Polymeric Liquids*, 2nd ed., Wiley, New York.
[21] Yoshimura, A., and Prud'homme, R. K., 1988, "Wall Slip Corrections for Couette and Parallel Disk Viscometer," J. Rheol., **32**(1), pp. 53–67.
[22] Hager, S. L., and Craig, T. A., 1992, "Fatigue Testing of High Performance Flexible Polyurethane Foam," J. Cell. Plast., **28**, pp. 284–303.
[23] Lee, J. D., So, J. H., and Yang, S. M., 1999, "Rheological Behavior and Stability of Concentrated Silica Suspensions," J. Rheol., **43**, pp. 1117–1124.
[24] Hoffman, R. L., 1998, "Explanations for the Cause of Shear Thickening in Concentrated Colloidal Suspensions," J. Rheol., **42**(1), pp. 111–123.
[25] Laun, H. M., Bung, R., and Schmidt, F., 1991, "Rheology of Extremely Shear Thickening Polymer Dispersions," J. Rheol., **35**, pp. 999–1034.
[26] Hadjistamov, D., 1984, *Proceedings of the Ninth International Congress on Rheology*, M. B. Mena, R. Garcfa-Rejon, and C. Rangel, eds., Universidad Nacional Autonoma de Mexico, Acapulco, Mexico, p. 277.
[27] Fagan, M., and Zukoski, C., 1997, "The Rheology of Charged Stabilized Silica Suspensions," J. Rheol., **41**, pp. 373–397.
[28] Egres, R., and Wagner, N., 2005, "The Rheology and Microstructure of Acicular Precipitated Calcium Carbonate Colloidal Suspensions Through the Shear Thickening Transition," J. Rheol., **49**(3), pp. 719–746.

Anisotropic Materials Behavior Modeling Under Shock Loading

Alexander A. Lukyanov
Abingdon Technology Center, Schlumberger,
Research & Development,
Abingdon,
Oxfordshire OX14 1UJ, UK
e-mail: aaluk@mail.ru

In this paper, the thermodynamically and mathematically consistent modeling of anisotropic materials under shock loading is considered. The equation of state used represents the mathematical and physical generalizations of the classical Mie–Grüneisen equation of state for isotropic material and reduces to the Mie–Grüneisen equation of state in the limit of isotropy. Based on the full decomposition of the stress tensor into the generalized deviatoric part and the generalized spherical part of the stress tensor (Lukyanov, A. A., 2006, "Thermodynamically Consistent Anisotropic Plasticity Model," Proceedings of IPC 2006, ASME, New York; 2008, "Constitutive Behaviour of Anisotropic Materials Under Shock Loading," Int. J. Plast., ***24****, pp. 140–167), a nonassociated incompressible anisotropic plasticity model based on a generalized "pressure" sensitive yield function and depending on generalized deviatoric stress tensor is proposed for the anisotropic materials behavior modeling under shock loading. The significance of the proposed model includes also the distortion of the yield function shape in tension, compression, and in different principal directions of anisotropy (e.g., 0 deg and 90 deg), which can be used to describe the anisotropic strength differential effect. The proposed anisotropic elastoplastic model is validated against experimental research, which has been published by Spitzig and Richmond ("The Effect of Pressure on the Flow Stress of Metals," Acta Metall.,* ***32****, pp. 457–463), Lademo et al. ("An Evaluation of Yield Criteria and Flow Rules for Aluminium Alloys," Int. J. Plast.,* ***15****(2), pp. 191–208), and Stoughton and Yoon ("A Pressure-Sensitive Yield Criterion Under a Non-Associated Flow Rule for Sheet Metal Forming," Int. J. Plast.,* ***20****(4–5), pp. 705–731). The behavior of aluminum alloy AA7010 T6 under shock loading conditions is also considered. A comparison of numerical simulations with existing experimental data shows good agreement with the general pulse shape, Hugoniot elastic limits, and Hugoniot stress levels, and suggests that the constitutive equations perform satisfactorily. The results are presented and discussed, and future studies are outlined.* [DOI: 10.1115/1.3130447]

Keywords: anisotropic material, anisotropic plasticity, shock waves, equation of state, stress decomposition

1 Introduction

The investigation of anisotropic material behavior (such as aluminum alloys and composite materials) has found significant interest in the research community due to the widespread application of anisotropic materials in aerospace and civil engineering problems. For example, aluminum alloys are one of the main materials in the construction of modern aircraft and rockets. The strain rate dependent mechanical behavior of anisotropic material (e.g., aluminum alloys) in air and space vehicles is important for applications involving impact. These applications cover a wide range of situations such as crashworthiness and protective armors in air and space vehicles and other applications. Since shock-wave and high-strain-rate phenomena are involved in many physical phenomena, we are interested in understanding the mechanical properties of material under these nontrivial conditions. To describe the anisotropic material response under shock loading the following general aspects need to be investigated: appropriate constitutive equations to describe the strength effect and constitutive equations to describe the equation of state [1].

Several anisotropic yield criteria and their associated yield surfaces have been developed. One of the first yield conditions proposed for the anisotropic material is the quadratic yield criterion proposed by von Mises [2] for plastically incompressible metal crystals with different lattice symmetries. In the theory of anisotropic yield criteria, the most well-known work is Hill's quadratic formulation [2], which contains six parameters specifying the state of anisotropy, but is similar in form to von Mises's criterion for isotropic metals. From the literature review, a general group of anisotropic yield criteria suitable for anisotropic metals can be found. This group includes the yield conditions proposed by Bassani [3], Hosford [4], the yield surface of 4 degree specified by Gotoh [5,6], Arminjon et al. [7], as well as yield surfaces of k degree analyzed by Barlat and Lian [8], Barlat et al. [9,10], Karafillis and Boyce [11], Barlat et al. [12,13], Bron and Besson [14], Darrieulat and Montheillet [15], Stoughton and Yoon [16], Kowalczyk and Gambin [17], Hu [18], Hashiguchi [19], Hu [20,21], and Barlat et al. [22].

The main objectives of the current paper are as follows: (1) to construct the mathematically consistent constitutive equations based on the nonassociated plasticity model suitable for shock-wave propagation in anisotropic materials, (2) to present the description of the anisotropic strength differential effect (SDE) based on the proposed nonassociated plasticity model, and (3) to present the validation of the proposed model against experimental data for different aluminum alloys AA2008 T4, AA2090 T3, AA7108 T1, AA6063 T1, and AA7010 T6. Note that the constitutive equations based on the associated plasticity models suitable for shock-wave propagation were considered in Ref. [1]. It has been proposed that the development of a nonassociative plasticity model is required to accurately describe the yield surface and a thermodynamically consistent evolution of the plastic strain tensor [1,16,23,24].

Contributed by the Applied Mechanics Division of ASME for publication in the Journal of Applied Mechanics. Manuscript received February 9, 2008; final manuscript received February 4, 2009; published online July 27, 2009. Review conducted by Horacio D. Espinosa.

2 Equation of State (Isotropic Case)

Modern, high-resolution methods of monitoring the stress and particle velocity histories in shock waves and equipment have been created [25]; numerous investigations into the mechanical properties of different classes of materials have been undertaken [26–32], and numerous phenomenological as well as microscopic models have been developed [1,27,33–36]. During shock loading, the material undergoes nonlinear behavior; therefore an equation of state (EOS) is required to describe the material's response to these conditions. It is convenient in numerical codes to have an analytical form of the EOS, but such an analytic form is at best an approximation to the true relationship. The EOS for isotropic materials typically defines the pressure as a function of density ρ (or specific volume, ν) and specific internal energy e. A very popular form of equation of state that is used extensively for isotropic solid continua is the Mie–Grüneisen EOS

$$p = f(\rho, e) = P_r(\nu) + \frac{\Gamma(\nu)}{\nu}(e - e_r(\nu)) \tag{1}$$

where ν is the specific volume and $\Gamma(\nu)$ is the Grüneisen gamma defined as

$$\Gamma(\nu) = \nu\left(\frac{\partial p}{\partial e}\right)_\nu \tag{2}$$

Traditionally, Γ is taken to be constant $\Gamma=\Gamma_0$; alternatively, it could have been assumed that $\Gamma_0/\nu_0=\Gamma(\nu)/\nu=\text{const}$ in Eq. (1). Functions $P_r(\nu)$ and $e_r(\nu)$ are assumed to be known functions of ν on some reference curve. Possible reference curves include the shock Hugoniot curve, a standard adiabatic curve (e.g., the adiabatic through the initial state (p_0, ν_0)), the 0 K isotherm, the isobar $p=0$, the curve $e=0$, or some composite curve of one or more of the above curves to cover the complete range of interest in the parameter ν. The most commonly used form of the Mie–Grüneisen equation of state for solid materials, which uses the shock Hugoniot as the reference curve, is given as follows:

$$p = f(\rho, e) = P_H \cdot \left(1 - \frac{\Gamma}{2}\mu\right) + \rho\Gamma e \tag{3}$$

where P_H is the Hugoniot pressure, $\mu=\rho/\rho_0-1$ is the relative change in volume, Γ is the Grüneisen parameter, ρ is the density, e is the specific internal energy, and ν is the current specific volume.

The Rankine–Hugoniot equations for the shock jump conditions can be regarded as defining a relation between any pair of the ρ, p, e, and u_p variables and U [27]. In many dynamic experiments, u_p (the particle velocity directly behind the shock) and U (the velocity at which the shock wave propagates through the medium) are measured. Generally, a shock velocity U is a nonlinear function of particle velocity u_p and it is given by the following relation [26]:

$$U = c + S_1 u_p + S_2\left(\frac{u_p}{U}\right)u_p + S_3\left(\frac{u_p}{U}\right)^2 u_p \tag{4}$$

and Grüneisen's gamma is given by

$$\Gamma = \frac{\gamma_0 + a\mu}{1 + \mu} \tag{5}$$

Therefore, the Grüneisen equation of state with cubic shock velocity as a function of particle velocity defines pressure as

$$p = \frac{\rho_0 c^2 \mu\left[1 + \left(1 - \frac{\Gamma}{2}\right)\mu - \frac{\Gamma}{2}\mu^2\right]}{\left[1 - (S_1 - 1)\mu - S_2\frac{\mu^2}{\mu + 1} - S_3\frac{\mu^3}{(\mu + 1)^2}\right]^2} + (1 + \mu)\cdot\Gamma\cdot E \quad \text{when} \quad \mu > 0 \tag{6}$$

$$p = \rho_0 c^2 \mu + (1 + \mu)\cdot\Gamma\cdot E \quad \text{when} \quad \mu \le 0 \tag{7}$$

where E is the internal energy per initial specific volume, c is the intercept of the $U-u_p$ curve, S_1, S_2, and S_3 are the coefficients of the slope of the $U-u_p$ curve Eq. (4), γ_0 is the Grüneisen gamma, and a is the first order volume correction to γ_0. Parameters c, S_1, S_2, S_3, γ_0, and a represent the material properties, which define its EOS. Parameters have been defined to cover a large number of isotropic materials [26].

3 Equation of State (Anisotropic Case)

In this work, the generalized decomposition of the stress tensor [1,37] is assumed and given by

$$\sigma_{ij} = -p^*\alpha_{ij} + \tilde{S}_{ij}, \quad \alpha_{ij}\tilde{S}_{ij} = 0 \tag{8}$$

where p^* is the total generalized pressure and $\tilde{S}_{ij}$ is the generalized deviatoric stress tensor. It should be noted that in all this work contraction by repeating indices is assumed. Using Eq. (8), the following expression for "pressure" can be obtained:

$$p^* = -\frac{\sigma_{ij}\alpha_{ij}}{\alpha_{kl}\alpha_{kl}} = -\frac{1}{\|\alpha\|^2}\sigma_{ij}\alpha_{ij} \tag{9}$$

where $\|\alpha\|^2=\alpha_{ij}\alpha_{ij}$. Finally using Eqs. (8) and (9), the expression for the generalized deviatoric part of the stress tensor can be rewritten in the following form:

$$\tilde{S}_{ij} = \sigma_{ij} - \alpha_{ij}\cdot\frac{1}{\|\alpha\|^2}\sigma_{kl}\alpha_{kl} \tag{10}$$

For anisotropic materials, the total hydrostatic pressure has been defined [1,37] and given as

$$p^* = p + \frac{\beta_{ij}\tilde{S}_{ij}}{\alpha_{ij}\beta_{ij}}, \quad p = -\frac{\beta_{ij}\sigma_{ij}}{\alpha_{ij}\beta_{ij}} \tag{11}$$

where p is the pressure related to the volumetric deformation, and $\tilde{S}_{ij}$ is the generalized deviatoric part of the stress tensor. The relation (11) is the correct generalized pressure for the elastic regime. To provide an appropriate description of behavior for general anisotropic materials at high pressures, an equation of state for p (pressure related to the volumetric deformation) has to be defined as

$$p^{\text{EOS}} = \begin{cases} \dfrac{\rho_0 c^2 \mu\left[1 + \left(1 - \frac{\Gamma}{2}\right)\mu - \frac{\Gamma}{2}\mu^2\right]}{\left[1 - (S_1 - 1)\mu - S_2\frac{\mu^2}{\mu + 1} - S_3\frac{\mu^3}{(\mu + 1)^2}\right]^2} + (1 + \mu)\cdot\Gamma\cdot E, & \mu > 0 \\ \rho_0 c^2 \mu + (1 + \mu)\cdot\Gamma\cdot E, & \mu \le 0 \end{cases} \tag{12}$$

which also describes correctly the material's behavior at small volumetric strains. Therefore, an appropriate description of general hydrostatic pressure at high pressures has the following form:

$$p^* = p^{\text{EOS}} + \frac{\beta_{ij}\tilde{S}_{ij}}{\alpha_{ij}\beta_{ij}} \tag{13}$$

Note that the methodology described above can be applied for all anisotropic materials and represents a mathematically consistent generalization of the conventional isotropic case. The methodology for calculation of components of the tensor α_{ij} has been previously defined [1,37]. The elements of tensor α_{ij} can be written in the following form:

$$\alpha_{11} = (C_{11} + C_{12} + C_{13})\cdot 3\bar{K}_C, \quad \alpha_{22} = (C_{12} + C_{22} + C_{23})\cdot 3\bar{K}_C, \quad \alpha_{33} = (C_{13} + C_{23} + C_{33})\cdot 3\bar{K}_C \tag{14}$$

$$\bar{K}_C = 1/\sqrt{3 \cdot [(C_{11}+C_{12}+C_{13})^2 + (C_{12}+C_{22}+C_{23})^2 + (C_{13}+C_{23}+C_{33})^2]}$$

$$K_C = \frac{1}{9\bar{K}_C}, \quad \alpha_{ij}\alpha_{ij} = \|\alpha\|^2 = 3 \tag{15}$$

where C_{ij} is the stiffness matrix (written in Voigt notation). The relation (15) describes the norm of tensor α_{ij}, which reduces to Kronecker delta symbol norm in the limit of isotropy. Therefore, the norm of α_{ij} is taken to be $\sqrt{3}$. Furthermore, the following set of equations for the components of the tensor β_{ij} can be written [1,37]):

$$\beta_{11} = (J_{11}+J_{12}+J_{13}) \cdot 3K_S, \quad \beta_{22} = (J_{12}+J_{22}+J_{23}) \cdot 3K_s, \quad \beta_{33} = (J_{13}+J_{23}+J_{33}) \cdot 3K_s$$

$$K_s = 1/\sqrt{3 \cdot [(J_{11}+J_{12}+J_{13})^2 + (J_{12}+J_{22}+J_{23})^2 + (J_{13}+J_{23}+J_{33})^2]} \tag{16}$$

$$\beta_{ij}\beta_{ij} = \|\beta\|^2 = 3$$

where J_{ij} are elements of compliance matrix (written in Voigt notation). To be consistent with the definition of the bulk speed of sound c for isotropic material, the following definition:

$$c = \sqrt{\frac{K_C}{\rho_0}} = c_0 \tag{17}$$

is assumed for anisotropic bulk speed of sound. Here the first generalized bulk modulus K_C is defined according to Eq. (15). Based on methodology previously described, we can conclude that the two fundamental tensors α_{ij} and β_{ij}, which represent the material properties, have been defined. Both of them can be considered as generalizations of the Kronecker delta symbol, which plays the main role in the theory of isotropic material. Using two fundamental tensors α_{ij} and β_{ij}, the definitions of total pressure and pressure corresponding to the volumetric deformation can be defined. In the limit of isotropy, tensors α_{ij} and β_{ij} have the following values $\alpha_{11}=\alpha_{22}=\alpha_{33}=1$ and $\beta_{11}=\beta_{22}=\beta_{33}=1$, and the proposed generalization returns to the traditional classical case where tensors α_{ij} and β_{ij} equal δ_{ij}, and Eqs. (9)–(11) take the following form:

$$p^* = -\frac{\alpha_{ij}\sigma_{ij}}{\alpha_{ij}\alpha_{ij}} = -\frac{\sigma_{kk}}{3}, \quad p = -\frac{\beta_{ij}\sigma_{ij}}{\beta_{ij}\alpha_{ij}} = -\frac{\sigma_{kk}}{3}, \quad p^* = p, \quad S_{ij} = \widetilde{S}_{ij} = \sigma_{ij} - \delta_{ij}\frac{\sigma_{kk}}{3}, \quad K_C = \frac{E}{3(1-2\nu)} = K_S = K \tag{18}$$

Here $p^*=p$ is the conventional hydrostatic pressure and S_{ij} is the conventional deviatoric stress tensor. Also, the two parameters K_c and K_s were considered as the first and second generalized bulk moduli. In the limit of isotropy they reduce to the well-known expression for conventional bulk modulus $K=E/3(1-2\nu)$.

3.1 Thermodynamically Consistent Anisotropic Strength Model. It is important to note Ilyushin's postulate of stability $\oint \boldsymbol{\sigma}: d\bar{\varepsilon}^p \geq 0$ for any isothermal processes [38]. Therefore, the necessary requirement for material at the continuum level is specified by the following condition: The plastic work rate and the rate of change in the effective plastic strain must be positive for all possible modes of plastic deformation. The expression for the plastic dissipation rate (multiplying by temperature) of the anisotropic material can now be considered as follows:

$$\dot{W}_M = \boldsymbol{\sigma}:\dot{\bar{\varepsilon}}^p = (-\alpha_{ij}p^* + \widetilde{S}_{ij})\mathbf{D}^p_{ij} = -p^*\alpha_{ij}\mathbf{D}^p_{ij} + \widetilde{S}_{ij}\mathbf{D}^p_{ij} = Y \cdot \dot{\bar{\varepsilon}}^p \tag{19}$$

where $\dot{W}_M$ is the plastic dissipation rate (multiplying by temperature), $\boldsymbol{\sigma}$ is the stress tensor, $\bar{\varepsilon}^p$ is the plastic strain tensor, $\mathbf{D}^p_{ij}$ is the symmetric part of the plastic velocity gradient tensor, and $\bar{\varepsilon}^p$ is the effective plastic strain. Therefore, the necessary condition for anisotropic plasticity model based on generalized decomposition of the stress tensor can be written as

$$-p^*\alpha_{ij}\mathbf{D}^p_{ij} = 0 \text{ for any } p^* \text{ or } \alpha_{ij}\mathbf{D}^p_{ij} = 0 \text{ and } \widetilde{S}_{ij}\mathbf{D}^p_{ij} = Y \cdot \dot{\bar{\varepsilon}}^p \geq 0 \tag{20}$$

The assumption (20) defines an additional constraint on material behavior and shape of anisotropic plastic potential. Also the assumption (20) can be interpreted as equivalence of plastic dissipation rate of the general anisotropic material and plastic dissipation rate based on the generalized deviatoric part of the stress tensor (similar assumption about the equality of the plastic dissipation rate of general anisotropic material and the equivalent isotropic material has been made by Karafillis and Boyce [11] for their model). Therefore, we have the following set of assumptions for the thermodynamically consistent anisotropic plasticity based on the generalized decomposition of the stress tensors (8)–(10) and (13):

1. $\hat{F}(\widetilde{S}_{ij}, p^*) = Y(\bar{\varepsilon}_p)$

2. $\mathbf{D}_{ij} = \mathbf{D}^e_{ij} + \mathbf{D}^p_{ij}, \quad \mathbf{D}^p_{kk} = 0$ (conventional imcompressibility)

3. $\mathbf{D}^p_{ij} = \dot{\lambda}\dfrac{\partial g(\widetilde{S}_{ij}, \gamma_k)}{\partial \widetilde{S}_{ij}}$ or $\mathbf{D}^p_{ij} = \dot{\lambda}\mathbf{V}_{ijkl}\widetilde{S}_{kl}$ and $\alpha_{ij}\mathbf{D}^p_{ij} = 0$ or $\alpha_{ij}\dfrac{\partial g(\widetilde{S}_{ij}, \gamma_k)}{\partial \widetilde{S}_{ij}} = 0$ (generalized incompressibility) (21)

where the function $\hat{F}(\ )$ describes the shape of the yield surface, $g=g(\widetilde{S}_{ij}, \gamma_k)$ is the plastic potential, γ_k represents a set of state variables, $\widetilde{S}_{ij}$ is the generalized deviatoric stress tensor, $\mathbf{D}^e_{ij}$ is the symmetric part of the elastic velocity gradient tensor, $\mathbf{D}_{ij}$ is the strain rate (symmetric part of velocity gradient), and $\mathbf{V}_{ijkl}$ is the plastic flow matrix. It is also important to note that the generalized incompressible plasticity flow defined by condition $\alpha_{ij}\mathbf{D}^p_{ij}=0$. This condition itself defines special class of plasticity flow.

4 Nonassociated Anisotropic Plasticity Model

4.1 An Anisotropic Yield Function. The objectives of this section are to construct the mathematically consistent yield function of a fully anisotropic material based on generalized decomposition of the stress tensor into generalized spherical part (generalized hydrostatic pressure) and generalized deviatoric stress tensor. Based on research by Spitzig and Richmond [23], Stoughton and Yoon [16], and the aforementioned assumptions specified by Eq. (21), the following yield function is considered:

$$\hat{F}(\widetilde{S}_{ij}) = \Psi(\widetilde{S}_{ij})(1+\chi\bar{p}^*) \leq Y(\bar{\varepsilon}_p), \quad \bar{p}^* = \frac{\sigma_{ij}\alpha_{ij}}{\alpha_{kl}\alpha_{kl}} = \frac{1}{\|\alpha\|^2}\sigma_{ij}\alpha_{ij}, \quad \bar{p}^* = -p^* \tag{22}$$

where $\bar{p}^*$ is the generalized hydrostatic stress and $\Psi(\widetilde{S}_{ij})$ is described by the generalized Hill's yield function

$$\Psi^2(\widetilde{S}_{ij}) = F(\alpha_{33}\widetilde{S}_{yy} - \alpha_{22}\widetilde{S}_{zz})^2 + G(\alpha_{11}\widetilde{S}_{zz} - \alpha_{33}\widetilde{S}_{xx})^2 + H(\alpha_{22}\widetilde{S}_{xx} - \alpha_{11}\widetilde{S}_{yy})^2 + 2N\widetilde{S}^2_{xy} + 2L\widetilde{S}^2_{yz} + 2M\widetilde{S}^2_{xz} \tag{23}$$

The material constants χ, F, G, H, N, L, and M are specified in terms of selected initial yield stresses in uniaxial tension, compression, and equibiaxial tension. It is worth noting that the plasticity model presented in Eq. (23) is naturally independent from the generalized hydrostatic stress $\bar{p}^*=\sigma_{ij}\alpha_{ij}/\alpha_{ij}\alpha_{ij}$ and, therefore, the following equality can be written:

$$\Psi^2(\widetilde{S}_{ij}) \equiv \Psi^2(\sigma_{ij}), \quad \sigma_{ij} = \bar{p}^*\alpha_{ij} + \widetilde{S}_{ij}, \quad \bar{p}^* \neq 0 \tag{24}$$

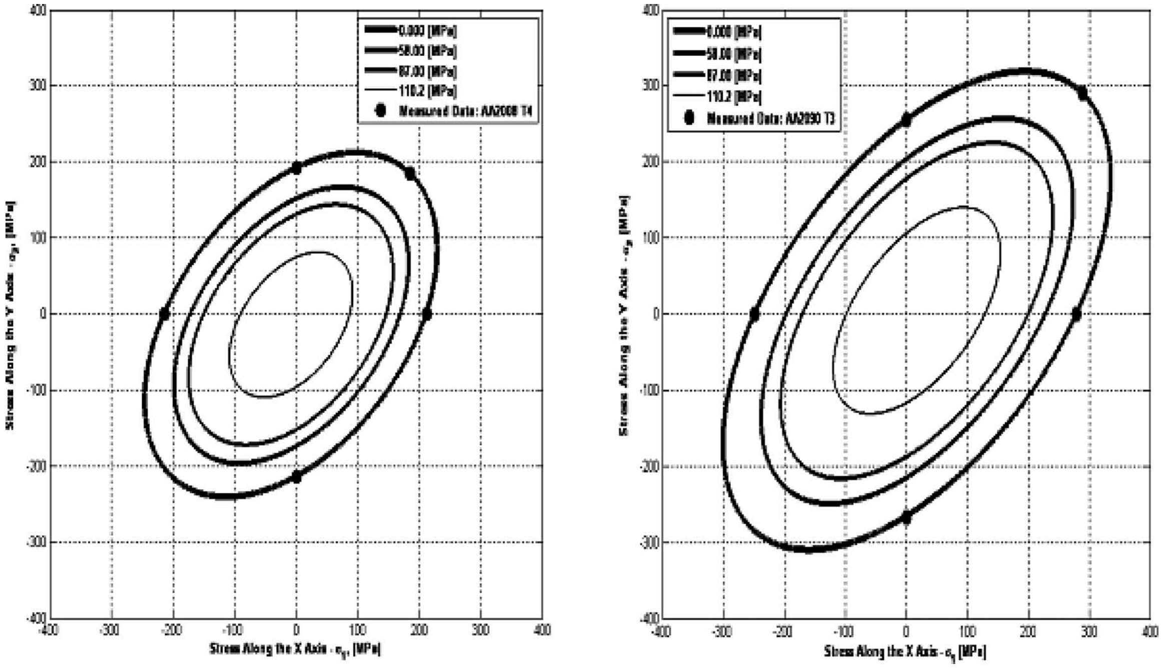

Fig. 1 Contour plots of the proposed yield surface at constant shear stress for the AA2008 T4 and AA2090 T3 alloys, respectively. The numbers in the legend refer to the magnitude of the shear stress in megapascal. The experimental data used to define the proposed yield surface at zero shear stress are also present.

where $\widetilde{S}_{ij}$ is the generalized deviatoric stress tensor and σ_{ij} is the stress tensor.

4.2 The Plane-Stress Condition. In the case of the plane-stress condition, Eqs. (22) and (23) can be written as follows:

$$\hat{F}(\widetilde{S}_{ij}) = \Psi(\widetilde{S}_{ij})(1+\chi\bar{p}^*) \leq Y(\bar{\varepsilon}_p), \quad \bar{p}^* = \frac{1}{\|\alpha\|^2}(\alpha_{11}\sigma_{11}+\alpha_{22}\sigma_{22}) \tag{25}$$

and

$$\Psi^2(\widetilde{S}_{ij}) = F(\alpha_{33}\widetilde{S}_{yy} - \alpha_{22}\widetilde{S}_{zz})^2 + G(\alpha_{11}\widetilde{S}_{zz} - \alpha_{33}\widetilde{S}_{xx})^2 + H(\alpha_{22}\widetilde{S}_{xx} - \alpha_{11}\widetilde{S}_{yy})^2 + 2N\widetilde{S}_{xy}^2 \tag{26}$$

The material constants χ, F, G, H, and N are specified in terms of selected initial yield stresses in uniaxial tension, compression, and equibiaxial tension; this approach similar to that adopted in Ref. [16].

4.3 Calibration of the Yield Function. The aluminum alloys AA2008 T4, AA2090 T3, AA7108 T1, and AA6063 T1 will be used for the calibration process of the proposed yield function. The data for aluminum alloys AA2008 T4 and AA2090 T3 have been taken from the work of Stoughton and Yoon [16]. It is reported that the yield under compression data is normalized to σ_{C0}, so that the scale of the compressive stress cannot be determined [16]. This problem was resolved by arbitrarily setting σ_{C0} to be 1% larger than σ_{T0} (see Ref. [16]). Arbitrarily setting σ_{C0} can lead to anomalous relationships between components of the generalized Kronecker symbol α_{ij}. As a result, more detailed and accurate experimental data are required.

Figure 1 compares the contours of the yield function defined by Eqs. (22) and (23), for various levels of shear stress, and for aluminum alloys AA2008 T4 and AA2090 T3, respectively. Material parameters are presented in Table 1.

The results compare well with the following two sets of experimental data: data dealing with uniaxial compression/tension along the principal directions (rolling and transverse directions), and data associated with equibiaxial tension. It is important to note that none of the experimental data shown on these figures represents a true prediction (see, for example, Ref. [16])—such data points have been used to define the material parameters in the presented plasticity model. In conclusion, the proposed yield function is mathematically consistent, and the plots demonstrate its convexity as well as its flexibility in approximating experimental data.

The experimental results published by Lademo et al. [24] were also used to calibrate the anisotropic plasticity model (yield function). Note that the experimental measurements in Ref. [24] do not include the experimental data for compression and equibiaxial tension. Hence, it is impossible to use an approach like that described above (one based on the yield stress measurements). In the aforementioned paper, a method for the calibration of the proposed yield criteria was based on the yield stresses in the 0 deg, 45 deg, and 90 deg directions, and also the R-ratio in the 0 deg-direction. It has also been assumed that $\chi=0$ for AA7108 T1 and AA6063 T1. The parameters defining the yield surface of AA7108 T1 and AA6063 T1 are presented in Table 2.

A comparison of the measured and predicted values of the yield stress is presented in Fig. 2 for AA7108 T1 and AA6063 T1, respectively.

4.4 Anisotropic Plastic Potential. The system formulated in Eq. (21) includes two restrictions for a plastic potential, these restrictions expressed in terms of the plastic strain rate tensor. The first is the conventional incompressibility restriction, $\mathbf{D}_{kk}^p=0$; and

Table 1 Material properties for AA2008 T4 and AA2090 T3

Material	Yield function parameters
AA2008 T4	$F=0.6945$, $G=-2.9656$, $H=3.7859$, $N=1.5243$, $Y=211.7$ MPa, $\chi(\text{MPa})^{-1}=0.00069$, $\alpha_{11}=0.1001$, $\alpha_{22}=1.2083$, and $\alpha_{33}=1.2369$
AA2090 T3	$F=2.0462$, $G=1.0176$, $H=-1.1570$, $N=2.6306$, $Y=279.6$ MPa, $\chi(\text{MPa})^{-1}=-0.00057$, $\alpha_{11}=1.1907$, $\alpha_{22}=-0.4651$, and $\alpha_{33}=1.1687$

Table 2 Material properties for AA7108 T1 and AA6063 T1

Material	Yield function parameters
AA7108 T1	$F=0.6202$, $G=0.3745$, $H=0.6165$, $N=3.2459$, $Y=291$ MPa, $\chi(\mathrm{MPa})^{-1}=0.0$, $\alpha_{11}=0.9934$, $\alpha_{22}=1.0082$, and $\alpha_{33}=0.9984$
AA6063 T1	$F=1.1545$, $G=-0.2993$, $H=1.1701$, $N=2.4008$, $Y=99.6$ MPa, $\chi(\mathrm{MPa})^{-1}=0.0$, $\alpha_{11}=0.9586$, $\alpha_{22}=1.0509$, and $\alpha_{33}=0.9882$

the second is the generalized incompressibility restriction, $\alpha_{ij}\mathbf{D}_{ij}^{p}=0$, for an anisotropic plastic flow. An application of such assumptions to the modified quadratic Hill's plastic potential is now considered.

1. The modified Hill's function for plastic potential can be written as

$$\hat{F}(\tilde{S}_{yy}-\tilde{S}_{zz})^2+\hat{G}(\tilde{S}_{zz}-\tilde{S}_{xx})^2+\hat{H}(\tilde{S}_{xx}-\tilde{S}_{yy})^2+2\hat{N}\tilde{S}_{xy}^2+2\hat{L}\tilde{S}_{yz}^2 + 2\hat{M}\tilde{S}_{xz}^2=\hat{Y}^2 \tag{27}$$

where $\hat{F}$, $\hat{G}$, $\hat{H}$, $\hat{N}$, $\hat{L}$, and $\hat{M}$ are material constants.

2. The decomposition of strain rate is expressed as follows:

$$\mathbf{D}_{ij}=\mathbf{D}_{ij}^{e}+\mathbf{D}_{ij}^{p}, \quad \mathbf{D}_{kk}^{p}=0 \ \text{(conventional incompressibility)} \tag{28}$$

3. Assumption 2 of Eq. (21) can be expressed via the following set of equations:

$$\begin{gathered}\mathbf{D}_{xx}^{p}=2\dot{\lambda}\cdot\lfloor\hat{H}(\tilde{S}_{xx}-\tilde{S}_{yy})-\hat{G}(\tilde{S}_{zz}-\tilde{S}_{xx})\rfloor\\ \mathbf{D}_{yy}^{p}=2\dot{\lambda}\cdot\lfloor\hat{F}(\tilde{S}_{yy}-\tilde{S}_{zz})-\hat{H}(\tilde{S}_{xx}-\tilde{S}_{yy})\rfloor\\ \mathbf{D}_{zz}^{p}=2\dot{\lambda}\cdot\lfloor-\hat{F}(\tilde{S}_{yy}-\tilde{S}_{zz})+\hat{G}(\tilde{S}_{zz}-\tilde{S}_{xx})\rfloor\\ \mathbf{D}_{xx}^{p}+\mathbf{D}_{yy}^{p}+\mathbf{D}_{zz}^{p}=0\end{gathered} \tag{29}$$

Following the definition of the components of strain rate, the conventional incompressibility of plastic flow is naturally satisfied for the considered plasticity model. However, the generalized incompressibility of plastic flow is not satisfied for this model.

4. Therefore, the following assumption is required:

$$\alpha_{ij}\mathbf{D}_{ij}^{p}=0 \tag{30}$$

As a result, we impose the following restrictions on parameters $\hat{F}$, $\hat{G}$, and $\hat{H}$, the latter representing the parameters of the modified Hill's criterion

$$\begin{gathered}\hat{F}\cdot 0+\hat{G}(\alpha_{11}-\alpha_{33})+\hat{H}(\alpha_{11}-\alpha_{22})=0\\ \hat{F}(\alpha_{22}-\alpha_{33})+\hat{G}\cdot 0+\hat{H}(\alpha_{22}-\alpha_{11})=0\\ \hat{F}(\alpha_{33}-\alpha_{22})+\hat{G}(\alpha_{33}-\alpha_{11})+\hat{H}\cdot 0=0\end{gathered} \tag{31}$$

Note that in the limit of isotropy (in this case, when tensor $\alpha_{ij}\equiv\delta_{ij}$), the system of equations described above in Eq. (31) is trivially satisfied. The aforementioned system has rank 2 and, therefore, we can express its solution in the forms $\hat{F}=A\cdot\bar{F}(\alpha_{ij})$, $\hat{G}=A\cdot\bar{G}(\alpha_{ij})$, and $\hat{H}=A\cdot\bar{H}(\alpha_{ij})$, where $\bar{F}$, $\bar{G}$, and $\bar{H}$ purely depend on the material tensor α_{ij} as follows:

$$\bar{F}(\alpha_{ij})=-\frac{[\alpha_{22}-\alpha_{11}]}{[\alpha_{22}-\alpha_{33}]},\quad \bar{G}(\alpha_{ij})=-\frac{[\alpha_{11}-\alpha_{22}]}{[\alpha_{11}-\alpha_{33}]},\quad \bar{H}(\alpha_{ij})=1 \tag{32}$$

The solution (32) of the system described by Eq. (31) is obtained for those cases in which $\alpha_{11}\neq\alpha_{22}\neq\alpha_{33}$. In all other special cases, the solution can be derived from Eq. (31), which are true in any case including case such as $\alpha_{11}=\alpha_{33}\neq\alpha_{22}$. In general, the solution of the system described by Eq. (31) may be different to the solution (32). Furthermore, in cases of isotropy and special cases of anisotropy where $\alpha_{ij}\equiv\delta_{ij}$, it is reasonable to assume that $\hat{F}=\hat{G}=\hat{H}=A$. Material parameters A, $\hat{N}$, $\hat{L}$, and $\hat{M}$ are defined based on experimental data.

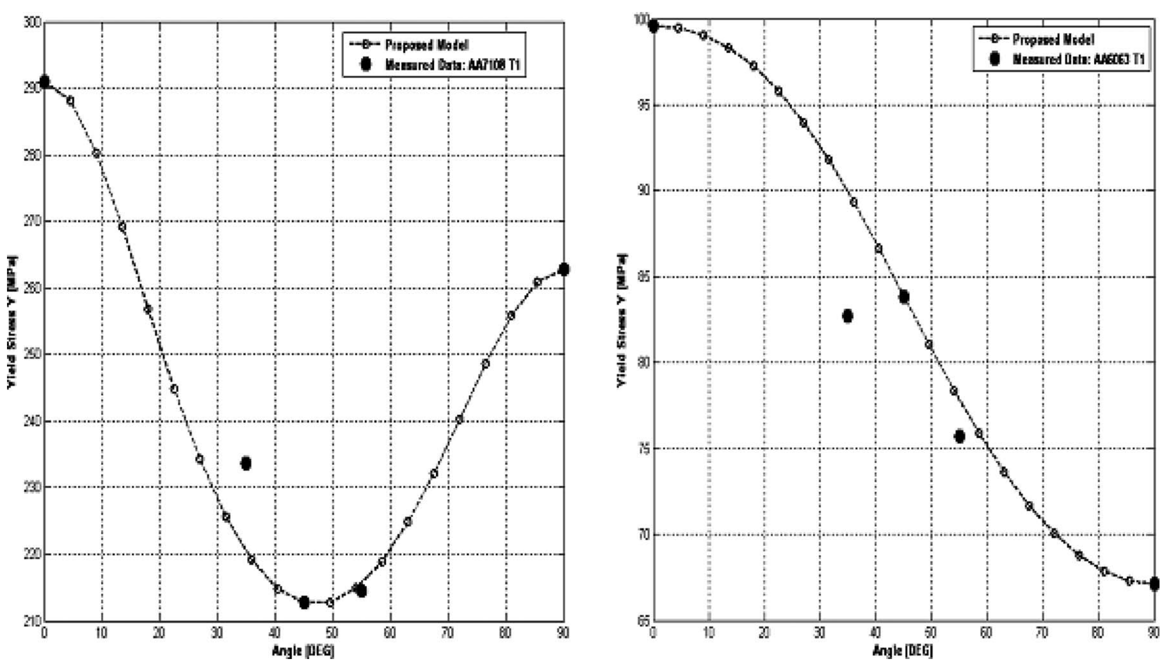

Fig. 2 Distribution of the yield stress versus angle in uniaxial tension for the AA7108 T1 and AA6063 T1 alloys (proposed model). The experimental data used to define the yield surface at zero shear stress are also present.

4.5 Calibration Anisotropic Plastic Flow. The plastic anisotropy of a plane-strain compression/tension process is typically characterized by the Lankford coefficient [39] or R-value, this defined as the ratio of the width plastic strain, ε_W^p, to the through-thickness plastic strain, ε_T^p. Although this simple definition offers at first view an adequate and straightforward means of assessing the in-plane and through-thickness flow and shape anisotropy of sheets, experiments reveal that the R-value carries a significant strain dependence even at very small strains [40–43]). Alternatively, Kocks et al. [41] suggested using the ratio of the width component of the plastic strain rate, $\mathbf{D}^p$, to its through-thickness component. It has also been demonstrated that R varies with the true stress σ (see Ref. [42]). From a thermodynamic perspective, the plastic flow is an irreversible process. Thus, the plastic strains obtained from the tensile test depend not only on the initial and final states (the necked states) but also on the path followed between these states. This fact, noted by Spolidor [42], is not taken into account in the expression for R. Consequently, the appropriate experimental data are required to describe the plasticity flow. The plate-impact test has been developed and successfully used to validate the plasticity model, the equation of state, damage models, and many other constitutive equations. Therefore, the plane shock-wave technique will be used to demonstrate that the proposed nonassociated anisotropic plasticity model (yield function and plastic potential) performs satisfactorily.

5 Numerical Simulation of Anisotropic Elastoplastic Shock-Wave Propagation

The plane shock-wave technique provides a powerful tool for studying different material properties (see, for example, Refs. [26,27]) and assessing a proposed theoretical model by comparing its predictions with experimental data. In this section, plane wave numerical experiments will be used to determine the Hugoniot elastic limit (HEL) (or stress level associated with the elastic precursor wave) and the dynamic compressibility (or bulk modulus) associated with the plastic wave for anisotropic aluminum alloy AA7010 T6.

5.1 Numerical Framework. Plate-impact numerical simulations were performed by solving conventional conservation laws (dealing with mass, linear momentum, and energy) for monopolar media (see Ref. [44]), these coupled with the appropriate constitutive equations. A finite element method (see, for example, Refs. [45–48]) was employed to solve the resulting system. The plates (represented by numerical domains), used in the numerical simulation, are modeled as rectangular bars, as described by Lukyanov [1]. Symmetric planes are applied on all sides of the bars in order to obtain one-dimensional wave propagation along the length of the bar. The mesh resolution is sufficient to resolve all the characteristic of the stress pulse. During the numerical simulation of the plate-impact problem, the stress update including EOS given in Ref. [1] is used, in which the generalized pressure and internal energy are coupled (Mie–Grüneisen EOS is used). The constitutive equations are implemented using a conventional time-centering method (see, for example, Refs. [45,47])

$$\bar{\sigma}_{ij}^{n+1} = \sigma_{ij}^n + [\sigma_{ik}^n \omega_{jk}^{n+1/2} + \omega_{ik}^{n+1/2}\sigma_{kj}^n + (\sigma^\nabla)_{ij}^{n+1/2}]\Delta t^{n+1/2} \quad (33)$$

$$(\sigma^\nabla)_{ij}^{n+1/2} = \mathbf{C}_{ijkl}\mathbf{D}_{kl}^{n+1/2}, \quad \Delta\varepsilon_{kl}^{n+1/2} = \mathbf{D}_{kl}^{n+1/2}\Delta t^{n+1/2} \quad (34)$$

where $\bar{\sigma}_{ij}^{n+1}$ is the trial stress tensor at time t^{n+1} (calculated using elasticity constitutive equations), σ_{ij}^n is the true stress tensor at time t^n, $\omega_{kj}^{n+1/2}$ is the spin tensor (skew-symmetric part of the velocity gradient) at time $t^{n+1/2}$, $\mathbf{D}_{kl}^{n+1/2}$ is the strain rate (symmetric part of the velocity gradient) at time $t^{n+1/2}$, $(\sigma^\nabla)_{ij}^{n+1/2}$ denotes a Jaumann stress rate tensor at time $t^{n+1/2}$, $\mathbf{C}_{ijkl}$ is the elastic stiffness matrix, and $\Delta t^{n+1/2}$ is the time step. During the constitutive model calculations, the stresses and state variables are known at the start of each increment and their values are updated at the end of the increment, according to the change in total strain increment. Using Eq. (33) and the generalized decomposition of the stress tensor specified by Eqs. (8)–(11), the expression for trial generalized deviatoric stress tensor can be written in the form

$$\bar{\bar{S}}_{ij}^{n+1} = \hat{\tilde{S}}_{ij}^n + C_{ijkl}^\alpha d_{kl}^{n+1/2}\Delta t^{n+1/2}, \quad C_{ijkl}^\alpha = \left(C_{ijkl} - \frac{\alpha_{ij}\cdot\alpha_{pq}C_{pqkl}}{\|\alpha\|^2}\right), \quad d_{kl}^{n+1/2} = \mathbf{D}_{kl}^{n+1/2} - \frac{\mathbf{D}_{ii}^{n+1/2}}{3}\delta_{kl} \quad (35)$$

$$(\bar{p}^*)^{n+1} = (\bar{p}^{\mathrm{EOS}})^{n+1} + \frac{\beta_{ij}\bar{\bar{S}}_{ij}^{n+1}}{\alpha_{ij}\beta_{ij}}, \quad (\bar{p}^{\mathrm{EOS}})^{n+1} = P_H^{n+1}\cdot\left(1 - \frac{\Gamma(\nu^{n+1})}{2}\mu^{n+1}\right) + \rho^{n+1}\Gamma(\nu^{n+1})\bar{e}^{n+1} \quad (36)$$

$$\bar{e}^{n+1} = e^n + \nu^{n+1/2}\bar{\bar{S}}_{ij}^{n+1/2}\mathbf{D}_{ij}^{n+1/2}\Delta t^{n+1/2} - \nu^{n+1/2}(\bar{p}^*)^{n+1/2}\mathbf{D}_\alpha^{n+1/2}\Delta t^{n+1/2} - \nu^{n+1/2}Q^{n+1/2}\mathbf{D}_\delta^{n+1/2}\Delta t^{n+1/2} \quad (37)$$

$$\mathbf{D}_\alpha^{n+1/2} = \alpha_{ij}\mathbf{D}_{ij}^{n+1/2}, \quad \mathbf{D}_\delta^{n+1/2} = \delta_{ij}\mathbf{D}_{ij}^{n+1/2}, \quad \nu^{n+1/2} = \tfrac{1}{2}(\nu^{n+1} + \nu^n), \quad (\bar{p}^*)^{n+1/2} = \tfrac{1}{2}[(\bar{p}^*)^{n+1} + (p^*)^n] \quad (38)$$

where $\hat{\tilde{S}}_{ij}^n = \tilde{S}_{ij}^n + (\tilde{S}_{ik}^n\omega_{jk}^{n+1/2} + \tilde{S}_{jk}^n\omega_{ik}^{n+1/2})\cdot\Delta t^{n+1/2}$, in which $\tilde{S}_{ij}^n$ is the true generalized deviatoric stress tensor at time t^n ($\alpha_{ij}\tilde{S}_{ij}^n=0$), $\bar{\bar{S}}_{ij}^{n+1}$ is the trial generalized deviatoric stress tensor at time t^{n+1}, α_{ij} and β_{ij} are the first and second generalized Kronecker symbols, $d_{kl}^{n+1/2}$ is the deviator rate of deformation at time $t^{n+1/2}$, $(\bar{p}^*)^{n+1}$ is the trial generalized hydrostatic pressure at time t^{n+1}, $(\bar{p}^{\mathrm{EOS}})^{n+1}$ is the trial equation of state pressure at time t^{n+1}, $Q^{n+1/2}$ is the artificial bulk viscosity at time $t^{n+1/2}$, ν^{n+1} is the specific volume at time t^{n+1}, and $\bar{e}^{n+1}$ is the trial specific internal energy at time t^{n+1}. Note that the equation of state (36) is linear in internal energy, $\bar{e}^{n+1}$; meanwhile the equation for the specific internal energy (37) is linear in $(\bar{p}^*)^{n+1}$. Thus, Eqs. (36) and (37) can be written in the form (see, for example, Refs. [45,47])

$$(\bar{p}^{\mathrm{EOS}})^{n+1} = A^{n+1} + B^{n+1}\bar{e}^{n+1}, \quad \bar{e}^{n+1} = \hat{e}^{n+1} - \tfrac{1}{2}\nu^{n+1/2}\mathbf{D}_\alpha^{n+1/2}\Delta t^{n+1/2}(\bar{p}^{\mathrm{EOS}})^{n+1} \quad (39)$$

The equation of state pressure $(\bar{p}^{\mathrm{EOS}})^{n+1}$ can be evaluated by solving Eq. (39) as follows:

$$(\bar{p}^{\mathrm{EOS}})^{n+1} = \frac{A^{n+1} + B^{n+1}\hat{e}^{n+1}}{1 + \dfrac{1}{2}B^{n+1}\nu^{n+1/2}\mathbf{D}_\alpha^{n+1/2}\Delta t^{n+1/2}}, \quad \bar{e}^{n+1} = \hat{e}^{n+1} - \frac{1}{2}\nu^{n+1/2}\mathbf{D}_\alpha^{n+1/2}\Delta t^{n+1/2}(\bar{p}^{\mathrm{EOS}})^{n+1} \quad (40)$$

The iterative algorithm for corrections due to anisotropic plasticity flow of the trial generalized deviatoric stress tensor, $\bar{\bar{S}}_{ij}^{n+1}$, generalized pressure, $(p^*)^{n+1}$, and internal energy, $\bar{e}^{n+1}$, is performed when $\hat{F}(\bar{\bar{S}}_{ij}^{n+1},(p^*)^{n+1}) > Y_0$. The iterative algorithm comprises the following system of equations:

$$(\Delta\varepsilon_{kl}^p)^{n+1} = 2\cdot\Delta\lambda^{n+1}\cdot\mathbf{V}_{klpq}\tilde{S}_{pq}^{n+1}, \quad (\Delta\varepsilon_{kl}^e)^{n+1} = \Delta\varepsilon_{kl}^{n+1} - (\Delta\varepsilon_{kl}^p)^{n+1}, \quad (\Delta\varepsilon_{kk}^p)^{n+1} = 0, \quad \alpha_{kl}(\Delta\varepsilon_{kl}^p)^{n+1} = 0 \quad (41)$$

$$(\tilde{S}_{kl}^{n+1})_{i+1} = \bar{\bar{S}}_{kl}^{n+1} - 2\cdot\Delta\lambda_i^{n+1}\cdot\left[C_{klpq}\mathbf{V}_{pqrm} - \frac{\alpha_{kl}\alpha_{pq}}{\|\alpha\|^2}C_{pqwq}\mathbf{V}_{wqrm}\right](\tilde{S}_{rm}^{n+1})_i \quad (42)$$

Table 3 Material properties for AA7010 T6

Functions	Material constants
Yield function	$F=0.6898$, $G=0.2873$, $H=0.6824$, $Y=500.0$ MPa, $\chi(\mathrm{MPa})^{-1}=0.0$, $\alpha_{11}\approx 0.9976$, $\alpha_{22}\approx 1.0029$, and $\alpha_{33}\approx 0.9994$
Plastic potential	$F=0.7694$, $G=1.4843$, $H=-0.5067$, and $Y=500.0$ MPa
EOS	$c_0=\sqrt{K_C/\rho_0}=5154$ m/s, $K_C=74.65$ GPa, $S_1=1.4$, $S_2=0$, $S_3=0$, $\gamma_0=2.0$, and $a=0.48$

$$e_{i+1}^{n+1}=e^n+\nu^{n+1/2}(\tilde{S}_{kl}^{n+1/2})_{i+1}\mathbf{D}_{kl}^{n+1/2}\Delta t^{n+1/2} - \nu^{n+1/2}(p^*)_{i+1}^{n+1/2}\mathbf{D}_{\alpha}^{n+1/2}\Delta t^{n+1/2} - Q^{n+1/2}\mathbf{D}_{\delta}^{n+1/2}\Delta t^{n+1/2} \tag{43}$$

$$(p^{\mathrm{EOS}})_{i+1}^{n+1}=\frac{A_{i+1}^{n+1}+B_{i+1}^{n+1}\hat{e}_{i+1}^{n+1}}{1+\frac{1}{2}B_{i+1}^{n+1}\nu^{n+1/2}\mathbf{D}_{\alpha}^{n+1/2}\Delta t^{n+1/2}}, \quad e_{i+1}^{n+1}=\hat{e}_{i+1}^{n+1} - \frac{1}{2}\nu^{n+1/2}\mathbf{D}_{\alpha}^{n+1/2}\Delta t^{n+1/2}(p^{\mathrm{EOS}})_{i+1}^{n+1} \tag{44}$$

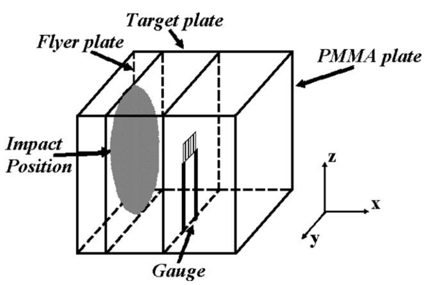

Fig. 3 Schematic of the experimental target assembly

$$(p^*)_{i+1}^{n+1}=(p^{\mathrm{EOS}})_{i+1}^{n+1}+\frac{\beta_{ij}(\tilde{S}_{ij}^{n+1})_{i+1}}{\alpha_{ij}\beta_{ij}} \tag{45}$$

$$\hat{F}((\tilde{S}_{kl}^{n+1})_{i+1},(p^*)_{i+1}^{n+1})-Y_0=0 \tag{46}$$

The algorithm proceeds until the following convergence condition is met: $|\Delta\lambda_{i+1}^{n+1}-\Delta\lambda_i^{n+1}|<|\Delta\lambda_i^{n+1}|\cdot\mathrm{error}$, where $\Delta\lambda_i^{n+1}$ is a scale factor in Eq. (41), obtained for each iteration i at time t^{n+1} by solving the quadratic problem (46) with respect to $\Delta\lambda_i^{n+1}$, and error is a numerical error value, specified initially.

5.2 Shock-Wave Propagation in AA7010 T6 Anisotropic Aluminum Alloy. This section describes the shock-wave propagation in the anisotropic aluminum alloy AA7010 T6 using the yield function and plastic potential proposed in this paper. The parameters for the yield function and plastic potential are presented in Table 3.

The longitudinal and transverse stress histories have been recorded by using stress gauges, placed between target plate and 12 mm polymethyl methacrylate (PMMA) plate, within the target assembly depicted in Fig. 3.

The experimental data for AA7010 T6 presented in this paper correspond to the plate-impact test performed by Bourne and Millett at the Royal Military College of Science (published by De Vuyst et al. [49]) with impact velocities of 450 m/s and 895 m/s. The elastic material properties of AA7010 T6 are taken from De Vuyst et al. [49]. The material properties of aluminum alloy 6082 T6 and PMMA plates are taken from Steinberg [26]. Figures 4 and 5 compare the experimental data with the numerical simulation resulting from the new nonassociated anisotropic plasticity model for the longitudinal and transverse cases.

The experimental values of 0.39 GPa and 0.33 GPa, for the elastic response in the longitudinal and short transverse directions (see Figs. 4 and 5, respectively), correlate well with the modeled values of HEL for the longitudinal and short transverse directions (0.395 GPa and 0.333 GPa, respectively). The associated errors are 1.4% and 0.9%, respectively. Furthermore, the arrival time to

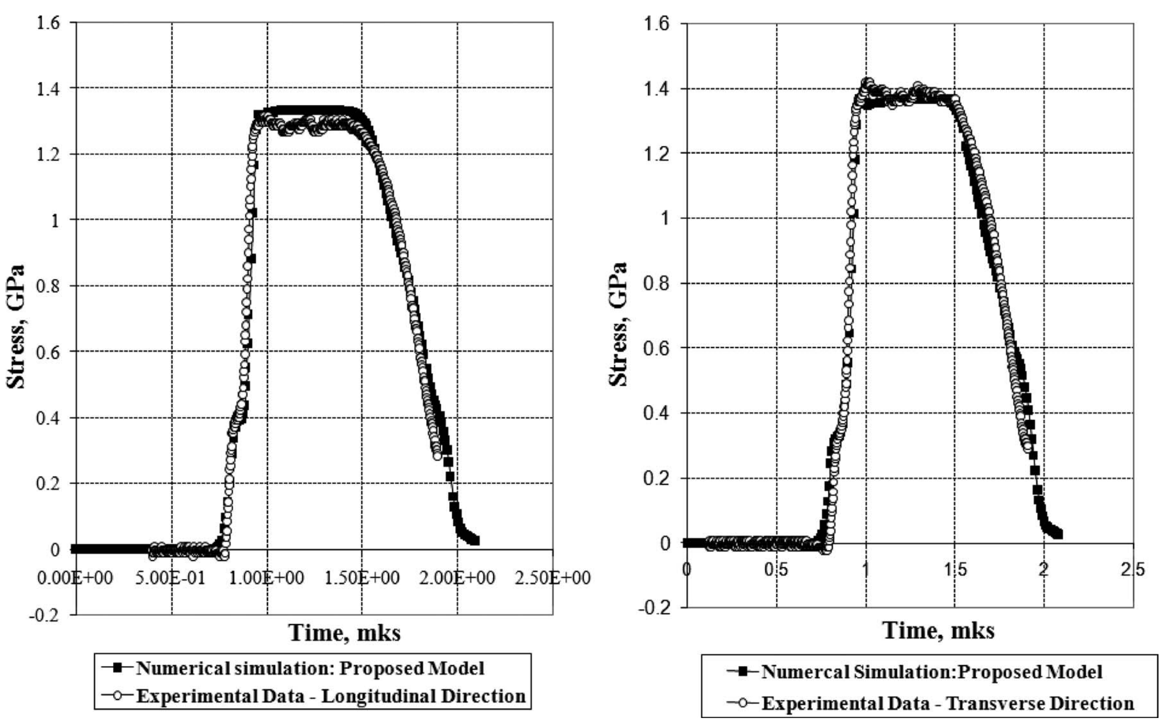

Fig. 4 Back-surface gauge stress traces from plate-impact experiments versus numerical simulation of stress (PMMA) waves for plate-impact test (impact velocity 450 m/s)—target AA7010 T6 for longitudinal and transverse directions, respectively

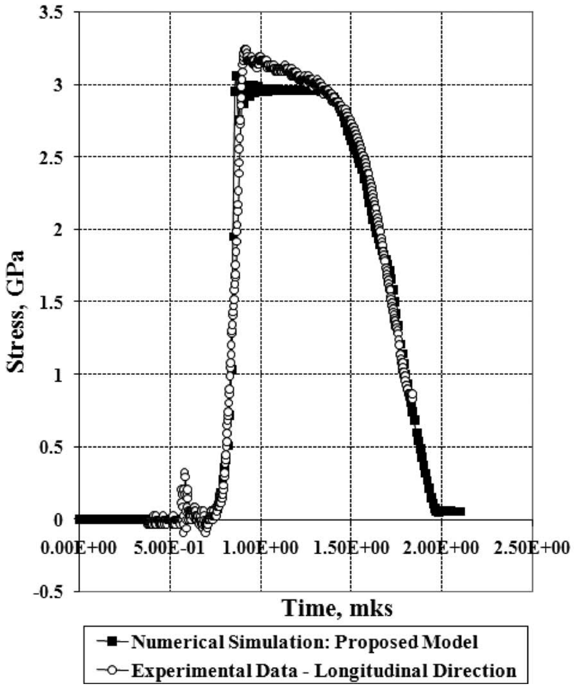

Fig. 5 Back-surface gauge stress traces from plate-impact experiments versus numerical simulation of stress (PMMA) waves for plate-impact test (impact velocity 895 m/s)—target AA7010 T6 for longitudinal and transverse directions, respectively

the HEL and the plastic wave velocity correlate well with experimental data. Further comparison shows that the pulse width and the reloading trace are also in good agreement with the experimental data (see Figs. 4 and 5). The main conclusion obtained from these results is that the nonassociated anisotropic plasticity model, as it stands, is suitable for simulating elastoplastic wave propagation in anisotropic solids. Furthermore, different HELs are obtained when the material is impacted in different directions; excellent agreement with the experimental data demonstrates that the anisotropic plasticity model is adequate.

However, further work is required in the areas of experiment and constitutive modeling, in order to find a better description of anisotropic material behavior.

6 Conclusion

In this work, a thermodynamically and mathematically consistent nonassociated anisotropic plasticity model, based on a generalized decomposition of the stress tensor, is presented. A nonassociated incompressible anisotropic plasticity model based on a generalized pressure sensitive yield function is constructed. It is shown that the proposed formulation of anisotropic plasticity in the case of isotropic materials reduces to Spitzig and Richmond's plasticity model [23] (general pressure sensitive model), which incorporates a pressure independent (von Mises [2]) plasticity model as a particular case, this consistent with the analytical and experimental research in Ref. [23]. The significance of the proposed model includes also the distortion of the yield function shape in tension, compression, and in different principal directions of anisotropy (e.g., 0 deg and 90 deg), which can be used to describe the anisotropic strength differential effect (anisotropic SDE). Based on experimental research, which has been published by Spitzig and Richmond [23], Lademo et al. [24], and Stoughton and Yoon [16], the proposed anisotropic yield function is validated.

Furthermore, the generalized decomposition has allowed the formulation and investigation of a generalized incompressibility constraint, $\alpha_{ij}\mathbf{D}_{ij}^{p}=0$, on the plastic potential, where $\mathbf{D}_{ij}^{p}$ is the plastic strain rate, and α_{ij} is the generalized Kronecker delta symbol [1]. Using the generalized deviatoric stress tensor and generalized incompressibility constraint, $\alpha_{ij}\mathbf{D}_{ij}^{p}=0$, the plastic potential was proposed. The plastic potential has been semi-analytically constructed (that is, the coefficients $\hat{F}$, $\hat{G}$, and $\hat{H}$ in the principals directions have been obtained from Eq. (31). The remaining (generally four) material parameters A, $\hat{N}$, $\hat{L}$, and $\hat{M}$ are defined based on experimental data. Numerical simulations based on the proposed nonassociated anisotropic plasticity model were performed, in order to describe the behavior of the aluminum alloy AA7010 T6 under shock loading conditions. A comparison of the experimental HELs with numerical simulation shows excellent agreement (maximum error is 1.4%). Furthermore, the good agreement of the general pulse shape and Hugoniot stress level suggests that the nonassociated anisotropic plasticity model performs satisfactorily. However, further numerical simulations of the proposed constitutive equations, taking into account more precise anisotropic SDE, are required [16].

Acknowledgment

I thank Professor V. Penjkov and Professor E. Romenski for discussion of this work. Many useful suggestions made by anonymous referees are also greatly appreciated.

References

[1] Lukyanov, A. A., 2008, "Constitutive Behaviour of Anisotropic Materials Under Shock Loading," Int. J. Plast., **24**, pp. 140–167.
[2] Hill, R., 1950, *Mathematical Theory of Plasticity*, Clarendon, Oxford.
[3] Bassani, J. L., 1977, "Yield Characterization of Metals With Transversely Isotropic Plastic Properties," Int. J. Mech. Sci., **19**(11), pp. 651–660.
[4] Hosford, W. F., 1985, "Comments on Anisotropic Yield Criteria," Int. J. Mech. Sci., **27**(7–8), pp. 423–427.
[5] Gotoh, M., 1977, "A Theory of Plastic Anisotropy Based on a Yield Function of Fourth Order (Plane Stress State)—I/II," Int. J. Mech. Sci., **19**(9), pp. 505–512.
[6] Gotoh, M., 1977, "A Theory of Plastic Anisotropy Based on a Yield Function of Fourth Order (Plane Stress State)—I/II," Int. J. Mech. Sci., **19**(9), pp. 513–520.
[7] Arminjon, M., Bacroix, B., Imbault, D., and Raphanel, J., 1994, "A Fourth Order Plastic Potentials for Anisotropic Metals and Its Calculation From Texture Data," Acta Mech., **107**, pp. 33–51.

[8] Barlat, F., and Lian, J., 1989, “Plastic Behavior and Stretchability of Sheet Metals. Part I: A Yield Function for Orthotropic Sheet Under Plane Stress Conditions,” Int. J. Plast., **5**(1), pp. 51–66.
[9] Barlat, F., Lege, D. J., and Brem, J. C., 1991, “A Six-Component Yield Function for Anisotropic Materials,” Int. J. Plast., **7**(7), pp. 693–712.
[10] Barlat, F., Becker, R. C., Hayashida, Y., Maeda, Y., Yanagawa, M., Chung, K., Brem, J. C., Lege, D. J., Matsui, K., Murtha, S. J., and Hattori, S., 1997, “Yielding Description of Solution Strengthened Aluminum Alloys,” Int. J. Plast., **13**(4), pp. 385–401.
[11] Karafillis, A. P., and Boyce, M. C., 1993, “A General Anisotropic Yield Criterion Using Bounds and a Transformation Weighting Tensor,” J. Mech. Phys. Solids, **41**(12), pp. 1859–1886.
[12] Barlat, F., Maeda, Y., Chung, K., Yanagawa, M., Brem, J. C., Hayashida, Y., Lege, D. J., Matsui, K., Murtha, S. J., Hattori, S., Becker, R. C., and Makosey, S., 1997, “Yield Function Development for Aluminum Alloy Sheets,” J. Mech. Phys. Solids, **45**(11–12), pp. 1727–1763.
[13] Barlat, F., Brem, J. C., Yoon, J. W., Chung, K., Dick, R. E., Lege, D. J., Pourboghrat, F., Choi, S.-H., and Chu, E., 2003, “Plane Stress Yield Function for Aluminum Alloy Sheets—Part 1: Theory,” Int. J. Plast., **19**(9), pp. 1297–1319.
[14] Bron, F., and Besson, J., 2004, “A Yield Function for Anisotropic Materials Application to Aluminum Alloys,” Int. J. Plast., **20**(4–5), pp. 937–963.
[15] Darrieulat, M., and Montheillet, F., 2003, “A Texture Based Continuum Approach for Predicting the Plastic Behaviour of Rolled Sheet,” Int. J. Plast., **19**(4), pp. 517–546.
[16] Stoughton, T. B., and Yoon, J. W., 2004, “A Pressure-Sensitive Yield Criterion Under a Non-Associated Flow Rule for Sheet Metal Forming,” Int. J. Plast., **20**(4–5), pp. 705–731.
[17] Kowalczyk, K., and Gambin, W., 2004, “Model of Plastic Anisotropy Evolution With Texture—Dependent Yield Surface,” Int. J. Plast., **20**(1), pp. 19–54.
[18] Hu, W., 2005, “An Orthotropic Yield Criterion in a 3-D General Stress State,” Int. J. Plast., **21**(9), pp. 1771–1796.
[19] Hashiguchi, K., 2005, “Generalized Plastic Flow Rule,” Int. J. Plast., **21**(2), pp. 321–351.
[20] Hu, W., 2007a, “Constitutive Modeling of Orthotropic Sheet Metals by Presenting Hardening-Induced Anisotropy,” Int. J. Plast., **23**, pp. 620–639.
[21] Hu, W., 2007b, “A Novel Quadratic Yield Model to Describe the Feature of Multi-Yield-Surface of Rolled Sheet Metals,” Int. J. Plast., **23**, pp. 2004–2028.
[22] Barlat, F., Yoon, J. W., and Cazacu, O., 2007, “On Linear Transformations of Stress Tensors for the Description of Plastic Anisotropy,” Int. J. Plast., **23**(5), pp. 876–896.
[23] Spitzig, W. A., and Richmond, O., 1984, “The Effect of Pressure on the Flow Stress of Metals,” Acta Metall., **32**, pp. 457–463.
[24] Lademo, O.-G., Hopperstad, O. S., and Langseth, M., 1999, “An Evaluation of Yield Criteria and Flow Rules for Aluminium Alloys,” Int. J. Plast., **15**(2), pp. 191–208.
[25] Bourne, N. K., and Stevens, G. S., 2001, “A Gas Gun for Plane and Shear Loading of Inert and Explosive Targets,” Rev. Sci. Instrum., **72**(4), pp. 2214–2218.
[26] Steinberg, D. J., 1991, “Equation of State and Strength Properties of Selected Materials,” Lawrence Livermore National Laboratory, Report No. UCRL-MA-106439.
[27] Meyers, M. A., 1994, *Dynamic Behavior of Materials*, Wiley, New York.
[28] Zaretsky, E. B., Kanel, G. I., Razorenov, S. V., and Baumung, K., 2005, “Impact Strength Properties of Nickel-Based Refractory Superalloys at Normal and Elevated Temperatures,” Int. J. Impact Eng., **31**(1), pp. 41–54.
[29] Gebbeken, N., Greulich, S., and Pietzsch, A., 2006, “Hugoniot Properties for Concrete Determined by Full-Scale Detonation Experiments and Flyer-Plate-Impact Tests,” Int. J. Impact Eng., **32**, pp. 2017–2031.
[30] Bronkhorst, C. A., Cerreta, E. K., Xue, Q., Maudlin, P. J., Mason, T. A., and Gray, G. T., III, 2006, “An Experimental and Numerical Study of the Localization Behavior of Tantalum and Stainless Steel,” Int. J. Plast., **22**(7), pp. 1304–1335.
[31] Millett, J. C. F., and Bourne, N. K., 2001, “Lateral Stress Measurements in a Shock Loaded Alumina: Shear Strength and Delayed Failure,” J. Mater. Sci., **36**(14), pp. 3409–3414.
[32] Espinosa, H., Mello, M., and Xu, Y., 1997, “A Variable Sensitivity Displacement Interferometer With Application to Wave Propagation Experiments,” ASME J. Appl. Mech., **64**, pp. 123–131.
[33] Gray, G. T., III, Lopez, M. F., Bourne, N. K., Millett, J. C. F., and Vecchio, K. S., 2002, “Influence of Microstructural Anisotropy on the Spallation of 1080 Eutectoid Steel,” *Shock Compression of Condensed Matter-2001*, M. D. Furnish, N. N. Thadhani, and Y. Horie, eds., AIP, Melville, NY, pp. 479–483.
[34] Anderson, C. E., Cox, P. A., Johnson, G. R., and Maudlin, P. J., 1994, “A Constitutive Formulation for Anisotropic Materials Suitable for Wave Propagation Computer Program—II,” Comput. Mech., **15**, pp. 201–223.
[35] Espinosa, H., Lu, H.-C., Zavattieri, P., and Dwivedi, S., 2001, “A 3-D Finite Deformation Anisotropic Visco-Plasticity Model for Fiber Composites,” J. Compos. Mater., **35**(5), pp. 369–410.
[36] Espinosa, H. D., and Zavattieri, P. D., 2003, “A Grain Level Model for the Study of Failure Initiation and Evolution in Polycrystalline Brittle Materials. Part I: Theory and Numerical Implementation,” Mech. Mater., **35**, pp. 333–364.
[37] Lukyanov, A. A., 2006, “Thermodynamically Consistent Anisotropic Plasticity Model,” *Proceedings of IPC 2006*, ASME, New York.
[38] Ilyushin, A. A., 1961, “On the Postulate of Stability,” J. Appl. Math. Mech., **25**, pp. 503–507.
[39] Lankford, W. T., Snyder, S. C., and Bausher, J. A., 1950, “New Criteria for Predicting the Press Performance of Deep Drawing Sheets,” Trans. Am. Soc. Met., **42**, pp. 1197–1232.
[40] Hosford, W. F., 1993, *The Mechanics of Crystals and Textured Polycrystals*, Oxford University Press, Oxford.
[41] Kocks, U. F., Tóme, C. N., and Wenk, H. R., 1998, *Texture and Anisotropy*, Cambridge University Press, Cambridge.
[42] Spolidor, A., 1996, “Determination of Rolling Anisotropy by Extensometry,” J. Mater. Sci., **31**, pp. 5731–5741.
[43] Kitamura, K., Miyazaki S., Iwai, H., and Kohl, M., 1999, “Effect of Rolling Reduction on the Deformation Texture and Anisotropy of Transformation Strain in Ti-50.2at%Ni Thin Plates,” Mater. Sci. Eng., A, **758**, pp. 273–275.
[44] Oden, J. T., 1972, *Finite Elements of Nonlinear Continua*, McGraw-Hill, New York.
[45] Hallquist, J. O., and Whirley, R. G., 1989, “DYNA3D User Manual, Nonlinear Dynamic Analysis in Three Dimensions,” University of California, Lawrence Livermore National Laboratory, Report No. UCID-19592.
[46] Espinosa, H. D., Raiser, G., Clifton, R. J., and Ortiz, M., 1992, “Performance of the Star-Shaped Flyer in the Study of Brittle Materials: Three Dimensional Computer Simulations and Experimental Observations,” J. Appl. Phys., **72**(8), pp. 3451–3457.
[47] Hallquist, J. O., 1998, *LS-DYNA Theoretical Manual*, Livermore Software Technology Corporation, Livermore, CA.
[48] Belytschko, T., Liu, W. K., and Moran, B., 2000, *Nonlinear Finite Elements for Continua and Structures*, Wiley, New York.
[49] De Vuyst, T., Vignjevic, R., Bourne, N. K., and Campbell, J., 2004, “Modelling of Spall in an Anisotropic Aluminium Alloy,” *Space Debris*, Kluwer Academic, Dordrecht, The Netherlands, 2(4), pp. 225–232.

Pointwise Identification of Elastic Properties in Nonlinear Hyperelastic Membranes—Part I: Theoretical and Computational Developments

Jia Lu[1]
e-mail: jia-lu@uiowa.edu

Xuefeng Zhao

Department of Mechanical and Industrial Engineering,
Center for Computer Aided Design,
The University of Iowa,
Iowa City, IA 52242-1527

We present an innovative method for characterizing the distributive elastic properties in nonlinear membranes. The method hinges on an inverse elastostatic approach of stress analysis that can compute the wall stress in a deformed convex membrane structure using assumed elastic models without knowing the realistic material parameters. This approach of stress analysis enables us to obtain the wall stress data independently of the material in question. The stress and strain data collected during a finite inflation motion are used to delineate the elastic property distribution in selected regions. In this paper, we discuss the theoretical and computational underpinnings of the method and demonstrate its feasibility using numerical simulations involving a saclike structure of known material property. [DOI: 10.1115/1.3130805]

Keywords: parameter identification, finite inflation test, nonlinear membrane, inverse method, inverse elastostatics

1 Introduction

This article is the first of a multiple part paper that introduces a new experimental method for delineating the distributive elastic properties in hyperelastic membranes. The method is a nontrivial generalization of the membrane inflation test initially introduced by Rivlin and Saunders [1]. They showed that the stress-strain data collected from the finite inflation of a circularly clamped thin rubber sheet can be used to characterize the specific form of the hyperelastic energy function. Since then, numerous studies have further extended the method and explored the utility in thin-walled biological organs [2–6]. This family of methods hinges on a unique feature of the membrane equilibrium problem, that is, the wall stress can be determined from equilibrium alone, independent of the material parameters (static determinacy). Elastostatic problems having this property are rare in nonlinear elasticity, and the corresponding systems have been almost invariably adapted to design experimental protocols for characterizing the hyperelastic stress-strain relation [1,7,8].

Previously, the finite inflation test has been implemented to axisymmetric problems only, in which the principal stresses are available from the Laplace equation [5]. It is, however, worth noting that the static determinacy is a property that holds not only for axisymmetric membranes but also for a much broader family of membrane systems, in particular, for convex saclike structures that do not have any particular geometric symmetry. In this regard, the potential of the inflation test has not been fully exploited. If equipped with a suitable method for stress analysis, the inflation test may be able to delineate the distributive elastic properties in membrane structures of general convex shape. Such a capability would be highly desirable in biomechanical applications.

Toward the goal of characterizing thin-walled biological soft tissues, we are developing an extended inflation test for identifying the distributive elastic properties in thin membranes. The method is referred to as the pointwise identification method (PWIM). Compared to the axisymmetric inflation test, the key difference lies in the approach of stress analysis. In PWIM, instead of using the analytical solution, which is available only for idealized shapes, the wall stress is computed numerically using a newly devised membrane inverse method [9], a subclass of the finite element inverse elastostatic methods (FEIEMs) discussed in several recent publications [10–15]. The inverse analysis takes as the input a deformed configuration and the corresponding loads and determines the stress in the deformed state assuming that there is a globally attainable stress-free configuration. For a pressurized membrane structure, the inverse method can sharply capture the static determinacy in the wall stress. It has been demonstrated that in the inverse approach the stress can be effectively predicted using assumed material models [9]. In the context of parameter identification, the method enables us to obtain the wall stress independent of the material in question.

In this paper, we discuss the theoretical and computational underpinings of PWIM. The method of inverse stress computation, the cornerstone of PWIM, is presented in Sec. 3. The evaluation of membrane strain depends on what deformation data were recorded; here, we discuss this matter assuming that a deforming mesh is available. Nonlinear regression is utilized to estimate the best fitting parameters once the form of strain energy function is selected. By design, this component is independent of the stress and strain computations and can be modified or improved separately. To evaluate this method, we have performed numerical experiments on a convex membrane of known strain energy function. The numerical experiment is described in Sec. 4 and the results are presented in Sec. 5.

2 Elements of Membrane Theory

2.1 Kinematics. A membrane is a thin material body of which the thickness is much smaller than the other dimensions. Due to thinness, a membrane has negligible resistance to bending

[1]Corresponding author.

Contributed by the Applied Mechanics Division of ASME for publication in the Journal of Applied Mechanics. Manuscript received February 5, 2008; final manuscript received February 4, 2009; published online July 27, 2009. Review conducted by Sanjay Govindjee.

and transverse shear. Thus, it is modeled as a deformable surface that sustains loads by virtue of the wall tension. There are numerous ways to present the membrane equations, but we found the tensorially covariant forms based on convected coordinates to be the most convenient for our exposition. In this representation, the surface is parametrized by surface coordinates $\xi^\alpha(\alpha=1,2)$ in which a pair of coordinates $P=(\xi^1,\xi^2)$ is regarded as the same material point during the deformation. We denoted by $\mathbf{x}=\mathbf{x}(P)$ the position vector of the material point P in a deformed configuration $\mathcal{C}\in\mathbb{R}^3$. The tangent vectors of the coordinate curves

$$\mathbf{g}_\alpha = \frac{\partial \mathbf{x}}{\partial \xi^\alpha} \tag{1}$$

form the basis of the surface tangent space at $\mathbf{x}(P)$. An infinitesimal line element is given by $d\mathbf{x}=\mathbf{g}_\alpha d\xi^\alpha$, and its length is determined from the first fundamental form

$$ds^2 = d\mathbf{x}\cdot d\mathbf{x} = g_{\alpha\beta}d\xi^\alpha d\xi^\beta, \quad g_{\alpha\beta}=\mathbf{g}_\alpha\cdot\mathbf{g}_\beta \tag{2}$$

The summation convention applies to repeated indices. The coefficients $g_{\alpha\beta}$ constitute the components of the surface metric tensor. The contravariant surface basis vectors $\{\mathbf{g}^\alpha,\alpha=1,2\}$ are defined by the relation $\mathbf{g}^\alpha\cdot\mathbf{g}_\beta=\delta^\alpha_\beta$, $\mathbf{g}^\alpha\cdot\mathbf{n}=0$, where $\mathbf{n}$ is the outward unit normal vector of the surface. The dot product $\mathbf{g}^\alpha\cdot\mathbf{g}^\beta$ gives the components $g^{\alpha\beta}$ of a tensor, which is inverse to the metric tensor, i.e., $g^{\alpha\beta}g_{\beta\gamma}=\delta^\alpha_\gamma$. The kinematic variables depend on the configuration in which they are characterized. The position vector, surface basis, contravariant basis, the components of the metric tensor, and the inverse metric tensor on the stress-free reference configuration $\mathcal{C}_0\in\mathbb{R}^3$ (if such a configuration can be identified) are denoted by $\mathbf{X}(P)$, $\mathbf{G}_\alpha$, $\mathbf{G}^\alpha$, $G_{\alpha\beta}$, and $G^{\alpha\beta}$, respectively.

The surface deformation gradient, which maps the surface tangent vectors at $\mathbf{X}(P)$ in $\mathcal{C}_0$ to the tangent vectors at $\mathbf{x}(P)$ in $\mathcal{C}$, is

$$\mathbf{F} = \mathbf{g}_\alpha\otimes\mathbf{G}^\alpha \tag{3}$$

The tensor $\mathbf{F}$, regarded as a linear operator in 3D space, is singular. However, it can be understood as a nonsingular linear operator on vectors lying in the tangent plane at $\mathbf{X}(P)$. In this sense, the inverse deformation gradient $\mathbf{F}^{-1}$ is

$$\mathbf{F}^{-1} = \mathbf{G}_\alpha\otimes\mathbf{g}^\alpha \tag{4}$$

The Cauchy–Green deformation tensor associated with $\mathbf{F}$ is the surface tensor at $\mathbf{X}(P)$ given by

$$\mathbf{C} = \mathbf{F}^T\mathbf{F} = g_{\alpha\beta}\mathbf{G}^\alpha\otimes\mathbf{G}^\beta \tag{5}$$

2.2 Constitutive Equation. The constitutive equation of a hyperelastic membrane is described by a strain energy function (energy density per unit undeformed reference area). The specific form of the energy function can be established in several ways. If the 3D strain energy function of the material is known, the surface energy can be deduced by reduction. Alternatively, one can directly postulate a strain energy that depends on the surface deformation gradient [16,17] and characterize the function form by experiments or some other means. In this work, the second approach is followed. Starting from the assumption $w=w(\mathbf{F})$, the invariant requirement under superposed rigid body motion further requires that $\mathbf{F}$ enter the energy function through $\mathbf{C}$. If the membrane is isotropic, the material isotropy renders

$$w = w(I_1,I_2) \tag{6}$$

where $I_1=\mathrm{tr}\,\mathbf{C}$ and $I_2=\det\mathbf{C}$ are the two principal invariants of tensor $\mathbf{C}$. In our work, it proves to be convenient to express the invariants in tensorially invariant forms

$$I_1 = g_{\alpha\beta}G^{\alpha\beta}, \quad I_2=\frac{g}{G} \tag{7}$$

where g and G are the determinants of the matrices $[g_{\alpha\beta}]$ and $[G_{\alpha\beta}]$, respectively. The fundamental kinetic variable in the membrane theory is the tension

$$\mathbf{t} = \int_{-h/2}^{h/2}\boldsymbol{\sigma}dh = t^{\alpha\beta}\mathbf{g}_\alpha\otimes\mathbf{g}_\beta, \quad t^{\alpha\beta}=t^{\beta\alpha}\approx h\sigma^{\alpha\beta} \tag{8}$$

where $\sigma^{\alpha\beta}$ are the components of the Cauchy stress tensor, and h is the current thickness of the membrane. In the sequel, the tension tensor will also be referred to as the wall stress or simply stress. Properly invariant stress function can be derived with the aid of the *referential* resultant,

$$\mathbf{T} = \mathbf{F}^{-1}(J\mathbf{t})\mathbf{F}^{-T}, \quad J=\sqrt{\frac{g}{G}} \tag{9}$$

which corresponds to the second Piola–Kirchhoff stress $\mathbf{S}$ in the 3D theory. Since $\mathbf{F}^{-1}\mathbf{g}_\alpha=\mathbf{G}_\alpha$, as evidenced in Eq. (4), it is clear that $\mathbf{T}=Jt^{\alpha\beta}\mathbf{G}_\alpha\otimes\mathbf{G}_\beta$. Namely, the components $T^{\alpha\beta}$ differ from $t^{\alpha\beta}$ only by the area factor J. The standard argument involving the balance of mechanical power concludes that

$$\mathbf{T} = 2\frac{\partial w}{\partial\mathbf{C}} = 2\frac{\partial w}{\partial g_{\alpha\beta}}\mathbf{G}_\alpha\otimes\mathbf{G}_\beta \tag{10}$$

It follows that in components $T^{\alpha\beta}=Jt^{\alpha\beta}=2\,\partial w/\partial g_{\alpha\beta}$. For an isotropic membrane, we have

$$Jt^{\alpha\beta} = 2\frac{\partial w}{\partial I_1}G^{\alpha\beta} + 2I_2\frac{\partial w}{\partial I_2}g^{\alpha\beta} \tag{11}$$

In the convected system, the principal invariants of the stress tensor can be computed by

$$J_1 = tr(\mathbf{t}) = t^{\alpha\beta}g_{\alpha\beta}, \quad J_2=\det(\mathbf{t})=\det[t^{\alpha\beta}]\det[g_{\delta\gamma}] \tag{12}$$

Note that these expressions are invariant under the change of surface coordinates.

2.3 Local Stress-Free Configuration. Thin membranes typically collapse when unloaded. They can have multiple stress-free configurations, which may not attain a smooth convex shape. To develop a theoretical framework suitable for parameter identification, it is imperative to have a constitutive description that permits a stressed configuration to be used as the reference. This can be achieved using the notion of *local stress-free configuration*, which associates each infinitesimal material element with a stress-free configuration that can be reached independently of the surrounding material. The stress-free state of the material body is a virtual configuration comprised of the union of the local configurations. The energy function at each material point is characterized with respect to the local stress-free state, whereas the deformation is measured relative to the chosen reference configuration. In this manner, the local stress-free configuration will enter the constitutive law as model parameters. In what follows, we will show that it can be effectively represented by a Riemannian metric tensor endowed to the reference configuration. The essential idea of local configuration was initially contained in Ref. [18] and further expanded in Ref. [19]. This idea has been adapted, in different forms, to describe material inhomogeneity [20,21], finite plasticity [22–25], tissue growth [26,27], residual stress [28,29], and initial strains [30].

With reference to Fig. 1, let $\mathbf{K}^{-1}$ be the local deformation that elastically releases the stress in an infinitesimal surface element at point P and brings the material element to a local stress-free configuration. The map $\mathbf{K}^{-1}$ is defined relative to a reference configuration, which is not necessarily stress-free. With a slight abuse of notation, this reference configuration is still denoted by $\mathcal{C}_0$, and the associated kinematic variables are denoted by capital letters. The local map $\mathbf{K}^{-1}$, regarded as a linear transformation on the

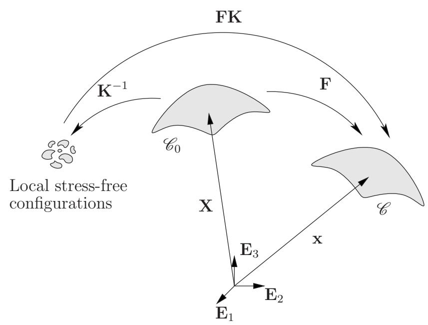

Fig. 1 Schematic illustration of the kinematic map

tangent vectors at $\mathbf{X}(P) \in \mathcal{C}_0$, can be determined if its action on two linearly independent tangent vectors are known. If $(\mathfrak{G}_1 d\xi^1, \mathfrak{G}_2 d\xi^2)$ are the images of the line elements $(\mathbf{G}_1 d\xi^1, \mathbf{G}_2 d\xi^2)$, respectively, we can write $\mathbf{K}^{-1}$ as

$$\mathbf{K}^{-1} = \mathfrak{G}_\alpha \otimes \mathbf{G}^\alpha \tag{13}$$

It should be noted that the tensor $\mathbf{K}^{-1}$ is not the gradient of a global mapping. Moreover, since the local configuration is stress-free, any arbitrary re-orientation remains stress-free, and thus the local configuration $\mathbf{K}^{-1}$ is determined to within a left rotation.

Under the local relaxation, the line element $d\mathbf{X}=\mathbf{G}_\alpha d\xi^\alpha$ is mapped into $\mathbf{K}^{-1}d\mathbf{X}=\mathfrak{G}_1 d\xi^1+\mathfrak{G}_2 d\xi^2$. The relaxed length is given by

$$dS_0^2 = (\mathbf{K}^{-1}d\mathbf{X}) \cdot (\mathbf{K}^{-1}d\mathbf{X}) = d\mathbf{X} \cdot (\mathbf{K}^{-T}\mathbf{K}^{-1})d\mathbf{X} \tag{14}$$

We can interpret the tensor

$$\mathfrak{G} \coloneqq \mathbf{K}^{-T}\mathbf{K}^{-1} = \mathfrak{G}_{\alpha\beta}\mathbf{G}^\alpha \otimes \mathbf{G}^\beta, \quad \mathfrak{G}_{\alpha\beta} = \mathfrak{G}_\alpha \cdot \mathfrak{G}_\beta \tag{15}$$

as a Riemannian metric tensor on $\mathcal{C}_0$ that describes the *unstressed* geometry of material elements. The metric tensor is a local property of the reference configuration; it varies from point to point. The rotation indeterminacy of the local configuration, which presents in $\mathbf{K}^{-1}$, is eliminated in the metric representation.

During a normal deformation $\mathcal{C}_0 \mapsto \mathcal{C}$, the tangent tensor to be used in the constitutive equation is $\mathbf{FK}$, where $\mathbf{F}$ is the regular deformation gradient relative to the reference configuration $\mathcal{C}_0$. Starting from $w=w(\mathbf{FK})$, the invariant requirement renders

$$w = w(\mathbf{K}^T\mathbf{F}^T\mathbf{FK}) \tag{16}$$

The rotational indeterminacy implies $w=w(\mathbf{QK}^T\mathbf{F}^T\mathbf{FKQ}^T)$ for any rotation tensor $\mathbf{Q}$. This condition dictates that the energy function depend on the principal invariants I_1 and I_2 of the tensor $(\mathbf{K}^T\mathbf{F}^T\mathbf{FK})$. A straightforward computation shows

$$\begin{aligned} I_1 &= \mathrm{tr}(\mathbf{K}^T\mathbf{F}^T\mathbf{FK}) = g_{\alpha\beta}\mathfrak{G}^{\alpha\beta} \\ I_2 &= \det(\mathbf{K}^T\mathbf{F}^T\mathbf{FK}) = \frac{g}{\mathfrak{G}}, \quad \mathfrak{G} = \det[\mathfrak{G}_{\alpha\beta}] \end{aligned} \tag{17}$$

It is now clear that the local configuration enters the constitutive equation through the components of the metric tensor $\mathfrak{G}$. This representation is useful for parameter identification. In the case where a global stress-free configuration cannot be attained experimentally, the components $\mathfrak{G}_{\alpha\beta}$ become unknown model parameters, which may be identified pointwise. The pointwisely determined metric may not satisfy the geometric compatibility condition even if a globally compatible stress-free configuration exists.

In closing, it is noted that, although rotational indeterminacy of $\mathbf{K}^{-1}$ renders an isotropic function form, the constitutive approach described here does not preclude anisotropic material. Anisotropic properties can be introduced by the inclusion of appropriate *structural tensors* in the constitutive equation, as suggested by Boehler in Ref. [31]. The ensuing function can be rendered covariant, namely, invariant with respect to the reference frame, as discussed in Ref. [32].

3 Inverse Method of Stress Computation

The inverse elastostatic method is a family of methods for solving finite strain elasticity problems in which a deformed configuration and the corresponding loads are given, while the undeformed configuration and the stress in the deformed state are sought. The inverse problem can be formulated in several ways. Govindjee and Mihalic [10,11] advocated the idea of solving the inverse problem using the standard equilibrium boundary value problem. Following this idea, the present authors' group has derived inverse finite element formulations for stress-resultant shells and membranes [15,9]. The inverse method employed in this paper addresses the following problem: given a deformed configuration of a pressurized membrane and the corresponding pressure, find the stress in the deformed configuration that satisfies the equilibrium equation

$$\frac{1}{\sqrt{g}}(\sqrt{g}t^{\alpha\beta}\mathbf{g}_\alpha)_{,\beta} + p\mathbf{n} = 0 \tag{18}$$

and appropriate boundary conditions. In Eq. (18), $g=\det(g_{\alpha\beta})$, p is the pressure, $\mathbf{n}$ is the unit normal vector of the surface, and $(\ )_{,\beta}$ stands for the derivative with respect to the coordinate ξ^β.

As alluded in Sec. 1, a pressurized membrane structure is statically determinate; the wall stress depends on the load and the deformed geometry only, independent of the material property. For a fully convex membrane with known deformed geometry, Eq. (18) furnishes three partial differential equations that suffice to determine the three components of the stress tensor in a Neumann boundary value problem. In other words, the wall stress in a Neumann problem is completely independent of material models. If a membrane is completely or partially clamped, the boundary constraints will compromise the static determinacy; however, the influence of material behavior exists only in a thin boundary layer. In regions sufficiently distanced from the displacement boundary, the stress is asymptotic to the material-independent, static distribution. This phenomenon has been discussed in several classical papers on membrane mechanics, e.g., Refs. [33,34]. In this case, the membrane structure is said to be effectively static determinate.

In the inverse approach [9], the weak form is formulated directly on the given deformed configuration. The stress distribution in the deformed state is determined by means of finding an inverse motion under an assumed elasticity model. The stress-free configuration so obtained corresponds to a kinematically compatible configuration, which can be brought back to the starting deformed configuration upon the application of the given load, under the assumed material law. Although elasticity is introduced in the computation, the stress solutions so obtained are expected to be practically independent of the material parameters since the deformed configuration is given and utilized in the weak form at the onset. In Ref. [9], it has been demonstrated using a clamped sac that the wall stress is indeed influenced minimally by the material models chosen to perform the computation. Thus, the "static stress" can be effectively predicted despite the introduction of assumed elasticity models and the ignorance of realistic elasticity parameters in the inverse approach.

The details of the inverse membrane element are presented in Ref. [9]. Briefly, the finite element formulation starts with the standard weak form,

$$F \coloneqq \int_\Omega t^{\alpha\beta}\mathbf{g}_\alpha \cdot \delta\mathbf{x}_{,\beta}da - \int_{\partial\Omega_t} \bar{\mathbf{t}} \cdot \delta\mathbf{x}ds - \int_\Omega p\mathbf{n} \cdot \delta\mathbf{x}da = 0 \tag{19}$$

where Ω is the deformed membrane surface, $\partial\Omega_t$ is the boundary upon which the traction $\bar{\mathbf{t}}$ is applied, and $\delta\mathbf{x}$ is any kinematically admissible variation to the current configuration. In the finite element space, the configurations and the variation are approximated by

$$\mathbf{x} = \sum_{I=1}^{\mathrm{Nel}} N_I(\xi^1,\xi^2)\mathbf{x}^I, \quad \mathbf{X} = \sum_{I=1}^{\mathrm{Nel}} N_I(\xi^1,\xi^2)\mathbf{X}^I, \quad \delta\mathbf{x} = \sum_{I=1}^{\mathrm{Nel}} N_I(\xi^1,\xi^2)\,\delta\mathbf{x}^I \tag{20}$$

Here, the superscript I indicates the nodal number, Nel is the total number of nodes in the element, $N_I(\xi^1,\xi^2)$ is the shape function for the Ith node, and the finite element natural coordinates (ξ^1,ξ^2) serve as the convected surface coordinates.

Introducing the matrix forms of stress and strain variables, we may write the finite element equation as

$$\int_\Omega \mathbf{B}^T\mathbf{t}\,da - \mathbf{f}^{\mathrm{ext}} = 0 \tag{21}$$

where $\mathbf{B}$ is the strain-displacement matrix and $\mathbf{f}^{\mathrm{ext}}$ is the external nodal force vector. The explicit expressions for $\mathbf{B}$ and $\mathbf{f}^{\mathrm{ext}}$ can be found in Ref. [9]. In the inverse setting, the constitutive equation (10) is regarded as a function of the referential metric tensor $G_{\alpha\beta}$, which in turn depends on the reference configuration via the relation $G_{\alpha\beta}=(\partial\mathbf{X}/\partial\xi^\alpha)\cdot(\partial\mathbf{X}/\partial\xi^\beta)$. The finite element method (FEM) system, therefore, gives rise to a set of nonlinear algebraic equations for the nodal values of $\mathbf{X}$. In our implementation, these nonlinear equations are solved iteratively using the Newton–Raphson procedure.

Several remarks on the inverse membrane method are as follows.

1. In the context of parameter identification, the inverse method replaces the Laplace equation as the stress solver to provide a static stress solution independent of the material model to be characterized. The ability to compute the static stress in general convex structures, albeit approximately, is the cornerstone of the methodology. It substantially expands the scope of early inflation tests.
2. The inverse method, however, has several limitations. The method does not apply to membranes that have flat or concave regions. If a membrane has a flat or nearly flat surface area, the ensuing finite element system becomes ill conditioned or even singular, reflecting the fact that a flat membrane cannot sustain a transverse load. If the surface is concave, equilibrium requirement may render compressive wall stress, which should be ruled out by stability consideration. Therefore, the inverse method is not a general method for membrane problems. Rather, it should be applied with discretion.
3. The inverse solution may not converge if the material model is not chosen properly. For example, if the material is too compliant, the ensuing reference configuration may revert the original surface curvature thus causing numerical difficulty. Nevertheless, our experience indicated that stiffer material models often lead to converged solution. Once the solution converges, the stress depends minimally on the material parameters.

4 Numerical Experiments

In PWIM, a membrane structure in its entirety will be mounted to a test stand and inflated to several pressure levels. A mesh will be drawn on the surface or a subregion of interest. The positions of the nodes in each deformed configuration will be recorded by a motion acquisition system to establish a deforming mesh that corresponds through all the deformed states. Stress and strain distributions in each configuration will be computed independently. The analysis consists of the following steps.

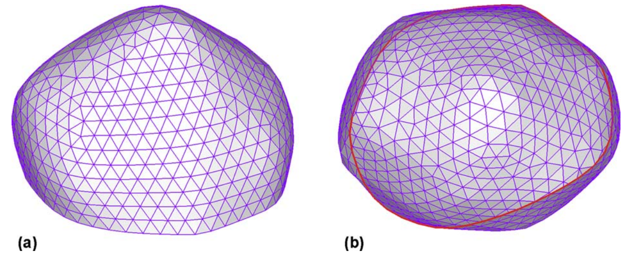

Fig. 2 Undeformed geometry and finite element mesh of the membrane sac: (*a*) perspective view and (*b*) bottom view

1. Computing the stress in each configuration individually using FEIEM.
2. Performing sensitivity analysis to identify regions where the stress is insensitive to material models.
3. Computing the kinematic variables $g_{\alpha\beta}$, $g^{\alpha\beta}$, $\mathbf{g}_\alpha$, and $\mathbf{g}^\alpha$ in each configuration from the recorded surface deformation. If the global stress free configuration is given, compute $G_{\alpha\beta}$ and $G^{\alpha\beta}$ from the reference geometry, and then compute the strain invariants I_1 and I_2. If not, the reference metric tensor will be left as three unknown parameters.
4. Examining the stress-strain property and selecting an appropriate energy function.
5. Obtaining the best fit material parameters at each selected point by nonlinear regression. If the reference configuration is unknown, estimate simultaneously the local metric tensor.

We simulated such an experiment using a numerical model. The membrane structure, shown in Fig. 2, was considered. The mesh was originally constructed from the images of a cerebral aneurysm sac, which is convex but does not have any particular geometric symmetries. We assumed that the wall was described by the strain energy function

$$w_A = \frac{\mu_1}{2}(I_1 - 2\log J - 2) + \frac{\mu_2}{4}(I_1 - 2)^2 \tag{22}$$

with

$$\mu_1 = 0.06521739\ \mathrm{N/mm}, \quad \mu_2 = 0.1521739\ \mathrm{N/mm} \tag{23}$$

This model is referred to as model A in the sequel. The parameters μ_1 and μ_2 are the multiplication of 3D elasticity constants with the wall thickness. Parameters like these are referred to as *effective* elasticity constants. To simulate the clamped boundary constraint typically used in experiments, we assumed that the base of the sac was fixed. Eleven deformed configurations were computed by applying pressures ranging from 60 mm Hg to 110 mm Hg with an interval of 5 mm Hg. This was conducted using the (forward) nonlinear membrane element in FEAP, a nonlinear finite element program originally developed at the University of California, Berkeley [35]. The maximum surface strain, which occurs at 110 mm Hg pressure, is about 10%.

Subsequently, we took these generated deformed configurations as input and applied PWIM to identify the elasticity parameters. The stress distribution in each configuration was computed by the inverse finite element method using a material model, which has the same energy function as model A but ten times elevated material constants. We also computed the stress using 100 times elevated parameters to assess the sensitivity of stress to material parameters.

4.1 Strain Computation. Strain distributions in each configuration were computed with the aid of the finite element interpolation (20). Here, the surface inside an element is parametrized by the finite element natural coordinates. From the finite element interpolation (20),

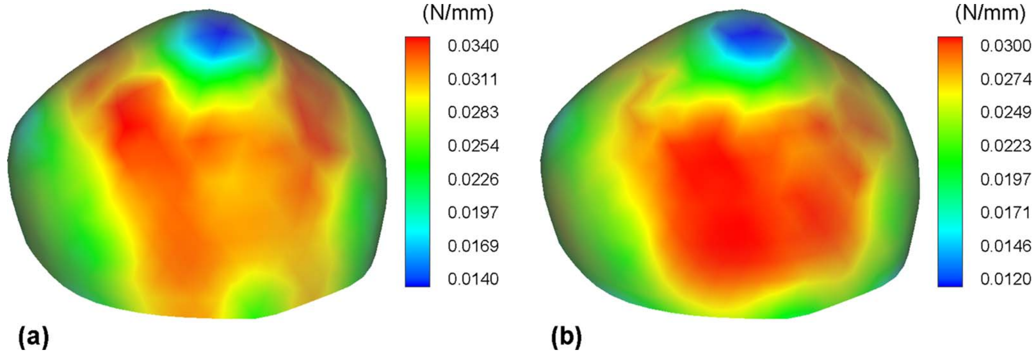

Fig. 3 The distribution of principal stresses in the membrane sac: (*a*) t_1 and (*b*) t_2

$$\mathbf{g}_\alpha = \sum_{I=1}^{\text{Nel}} \frac{\partial N_I}{\partial \xi^\alpha}\mathbf{x}^I, \quad g_{\alpha\beta} = \sum_{I=1}^{\text{Nel}}\sum_{I=J}^{\text{Nel}} \frac{\partial N_I}{\partial \xi^\alpha}\frac{\partial N_J}{\partial \xi^\beta}\mathbf{x}^I\cdot\mathbf{x}^J \tag{24}$$

When the global stress-free reference configuration was given, the quantities $\mathbf{G}_\alpha$, etc., and subsequently the deformation tensor $\mathbf{C}$ and its invariants I_1 and I_2 were computed accordingly.

4.2 Constitutive Regression. As seen in Eq. (11), the stress components are functions of the components of the reference and the current metric tensors, and the elasticity parameters appearing in the constitutive law. As described above, at every integration point in each of deformed configurations, we can obtain the stresses and at least the convected components $g_{\alpha\beta}$ of the current metric tensor. Choosing an appropriate constitutive model, we can express the model stress as functions of the metric tensors and elasticity constants. We denoted the model stress in the ith configuration by

$$^{(i)}t^{\alpha\beta} = t^{\alpha\beta}(\mu, {}^{(i)}g_{\delta\gamma}, G_{\delta\gamma}) \tag{25}$$

where μ stands for the set of elastic parameters. Let $^{(i)}\hat{t}^{\alpha\beta}$ be the "experimental" stress components obtained from the inverse analysis. A logical objective or cost function, which represents the difference between the modeled and observed responses, is

$$\Phi = \sum_{i=1}^{N} ({}^{(i)}t^{\alpha\beta} - {}^{(i)}\hat{t}^{\alpha\beta}){}^{(i)}g_{\alpha\gamma}\,{}^{(i)}g_{\beta\delta}({}^{(i)}t^{\delta\gamma} - {}^{(i)}\hat{t}^{\delta\gamma}) \tag{26}$$

where N is the total number of deformed states. In tensor notation, $\Phi = \Sigma_{i=1}^{N}\|{}^{(i)}\mathbf{t} - {}^{(i)}\hat{\mathbf{t}}\|^2$. If the global stress-free configuration is given, Φ is a function of the material parameters only. Otherwise, Φ depends also on the local metric tensor components $\mathfrak{G}_{\alpha\beta}$, which will be included in the identification. This amounts to adding three additional model parameters to the optimization problem at every regression point. Since $\mathfrak{G}$ is a metric tensor, it is natural to impose the positiveness requirement. In this case, the regression problem can be described as

$$\begin{aligned} &\text{minimize} && \Phi(\mu, \mathfrak{G}_{\alpha\beta}) \\ &\text{subject to} && \mathfrak{G}_{11} > 0, \quad \mathfrak{G}_{22} > 0, \quad \mathfrak{G}_{11}\mathfrak{G}_{22} - \mathfrak{G}_{12}^2 > 0 \\ &\text{and} && \mathbf{l} \le (\mu, \mathfrak{G}_{\alpha\beta}) \le \mathbf{u} \end{aligned} \tag{27}$$

Here, $\mathbf{l}$ and $\mathbf{u}$ are the lower and upper bounds of the regression variables μ and $\mathfrak{G}_{\alpha\beta}$. The parameter identification was performed by a gradient-based, sequential quadratic programming algorithm, SNOPT [36]. As long as the constitutive model is selected, we can compute the analytical gradients of the objective function Φ with respect to the regression variables.

In order to validate the capability of the method, we fitted the obtained stress-strain data to two constitutive models: one is the same model as used in the process of generating the deformed configurations (model A), and the other is a distinct model (model B), which exhibits a similar mechanical behavior to that of model A. Model B has the energy function

$$w_B = \nu_1[\exp(I_1 - 2\log J - 2) - 1] + \frac{\nu_2}{4}(I_1 - 2)^2 \tag{28}$$

where ν_1 and ν_2 are the effective elastic parameters. In the neighborhood of $(I_1, I_2) = (2, 1)$, the two energy functions obviously have similar characteristics. We performed parameter identification under the assumptions of knowing the reference configuration and without knowing the reference configuration. The stress functions of both models and the stress gradients required by the optimization algorithm are recorded in the Appendix.

5 Results

The distribution of the principal stresses predicted from model A at the highest pressure ($p = 110$ mm Hg) is shown in Fig. 3. Figure 4 shows the absolute percentage difference in the principal stresses under drastic changes in elasticity parameters of model A. The upper and lower rows show the percentage difference due to the increase in both material parameters μ_1 and μ_2 by 10 times and 100 times, respectively. Conservatively speaking, the change in the principal stresses is less than 0.15% in the region two layers of elements above the clamped base. In the region near the boundary, the change in principal stresses is relatively large. However, it is below 1%. This analysis allows us to identify the boundary-effect-free regions, where parameter identification is to likely yield reliable results. Later, the sac region excluding five layers of elements from the base is designated as the identification zone. The stress values computed from ten times elevated parameters were used in the parameter regression.

Figure 5 shows the distribution of the identified elasticity parameters (μ_1 and μ_2) of model A, under the condition that the global stress-free configuration is known. In this case, the original mesh is taken to be the reference configuration $\mathcal{C}_0$ and the referential quantities $G_{\alpha\beta}$, etc., are computed from this given geometry. In the dome region (six layers above the boundary) shown in Fig. 5, the identified parameters μ_1 range from 0.06119 N/mm to 0.07010 N/mm, and μ_2 show a narrower range of 0.14986–0.15410 N/mm. Since the stress is computed by FEIEM using a model different from that in the forward computation (ten times of the true elasticity parameters), and hence the acquired stress is not identical to the true stress, the identified parameters are expected to deviate from their true values. The distribution of the identification error (in percentage relative to the true parameters) by knowing the reference metrics are illustrated in Fig. 6. As the figures show, the identification error falls below 8% and 2% for μ_1 and μ_2, respectively.

Figure 7 illustrates the distribution of the identified elasticity parameters of model A without the assumption of known stress-

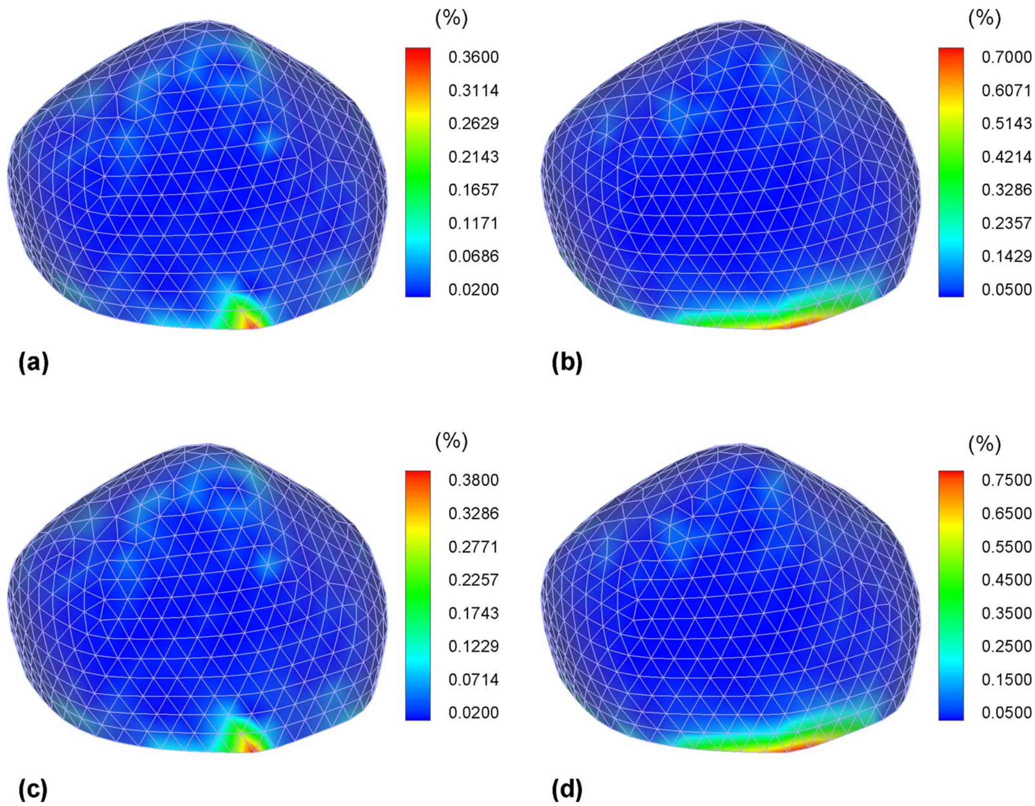

Fig. 4 The percentage difference in principal stresses under the change of elasticity parameters. Upper row: increasing both parameters μ_1 and μ_2 by 10 times: (*a*) t_1 and (*b*) t_2; lower row: increasing both parameters μ_1 and μ_2 by 100 times: (*c*) t_1 and (*d*) t_2.

free configuration. Figure 8 shows the identification error. In the dome region, seven layers of elements away from the boundary, the identified parameters μ_1 ranges from 0.05720 N/mm to 0.07872 N/mm, and μ_2 presents a narrower range of 0.14647–0.15563 N/mm. The percentage error of the identified parameters falls below 15% and 3% for μ_1 and μ_2, respectively. It is evident that in both cases the constant μ_2, which is the leading parameter in this model, is recovered to within a very small error. The identification of constant μ_1 is less accurate but is still within an acceptable range.

Figure 9 shows the distribution of the identified elasticity parameters of model B, with the assumption of the stress-free configuration being given. The distribution of the parameters shows an approximate uniformity in the region, six layers of elements away from the boundary. The ranges of the identified parameters are $0.03052\ \mathrm{N/mm} \le \nu_1 \le 0.03492\ \mathrm{N/mm}$ and $0.14981\ \mathrm{N/mm} \le \nu_2 \le 0.15407\ \mathrm{N/mm}$. Figure 10 shows the distribution of the identified elasticity parameters of model B, without assuming that the stress-free configuration is given. The distribution of the parameters is approximately uniform in the region, seven layers of elements above the boundary. The ranges of the identified parameters are $0.02778\ \mathrm{N/mm} \le \nu_1 \le 0.04037\ \mathrm{N/mm}$ and $0.14524\ \mathrm{N/mm} \le \nu_2 \le 0.15555\ \mathrm{N/mm}$. It is expected that the identified parameters span wider ranges for the case of stress-free configuration being unknown due to the increase in the number of the regression variables.

It is also informative to conduct a statistical analysis in the boundary-effect-free region to examine how well the homogeneity has been identified. Tables 1 and 2 list the means and standard deviations of the identified elasticity parameters for both models over the aforementioned boundary-effect-free regions for both knowing and without knowing the local stress-free configurations. For both models, adding the local reference metric tensor components as three more regression variables generally renders larger

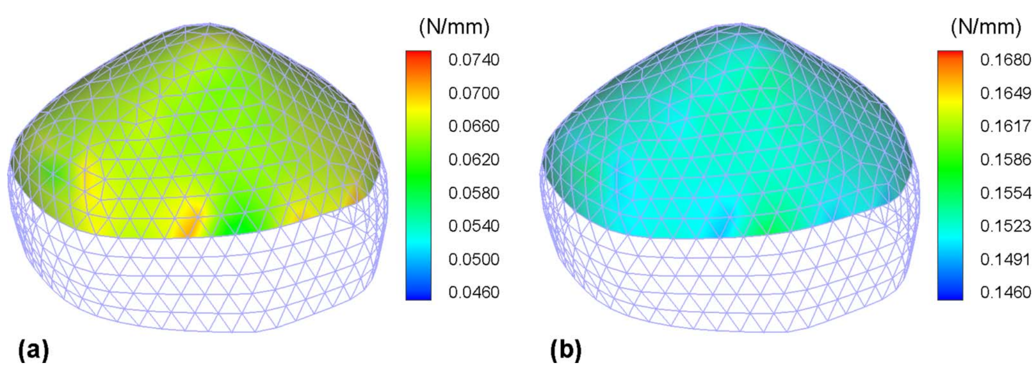

Fig. 5 Identified elasticity parameters of model A knowing the reference metric: (*a*) μ_1 and (*b*) μ_2

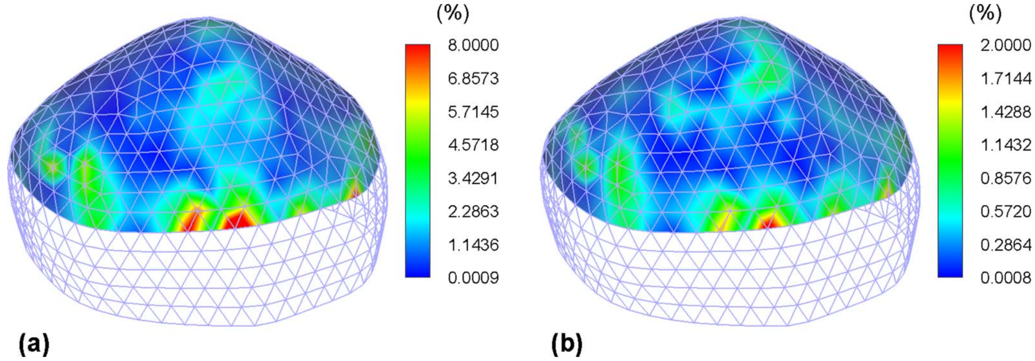

Fig. 6 Absolute values of the relative error (in percentage) between identified elasticity parameters and true parameters of model A knowing the reference metric: (*a*) μ_1 and (*b*) μ_2

standard deviations of identified elasticity parameters. However, the standard deviations of these data, especially those of μ_2 and ν_2, are very small. Hence, we conclude quantitatively that the material homogeneity is satisfactorily recovered.

Figure 11 illustrates the comparison between the stress invariants modeled by model B and the "experimental" stress invariants at a point where a relatively large principal stretch ($\lambda_1 = 1.076$) occurs. The good match between these two curves suggests that model B fits well the stress-strain data generated by model A. It also provides an ad hoc justification for our choice of model B.

6 Discussions and Conclusion

Inspired by the property of static determinacy of the membrane equilibrium problem, we devised a method of pointwise elastic property identification for membranes. The key feature of the method is the utility of FEIEM for the numerical solution of wall stress. For pressurized convex membranes, FEIEM enables us to practically determine the stress distribution using an assumed material model without a priori knowledge of the realistic material parameters. This in turn allows us to acquire the stress and strain data independently and simultaneously at multiple points, and thus to obtain the database necessary for the proposed pointwise identification.

It is instructive to compare the method with commonly used methods for characterizing thin materials, the experiment-based specimen tests [37,38,8,39], and the simulation based parameter identification methods [40,41] such as the inverse finite element method [42,43]. In the specimen tests, material samples are subjected to load protocols designed to create in the specimen central region an approximately uniform stress state, which can be determined from static equilibrium. The strain is obtained directly from the deformation measurement. The elastic property is character-

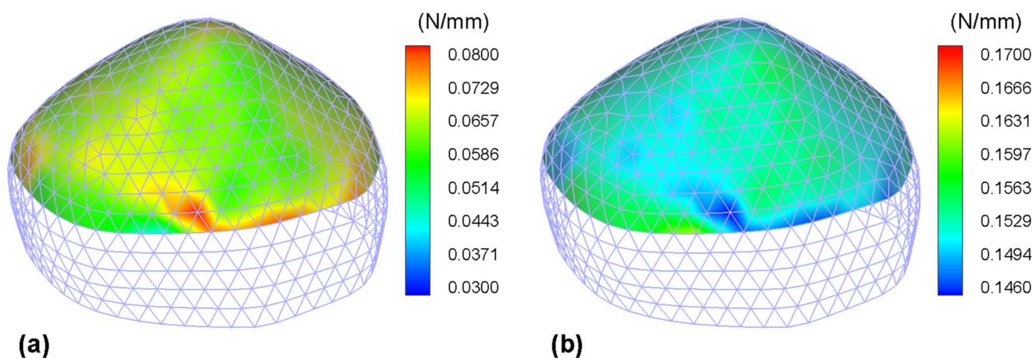

Fig. 7 Identified elasticity parameters of model A without knowing the reference metric: (*a*) μ_1 and (*b*) μ_2

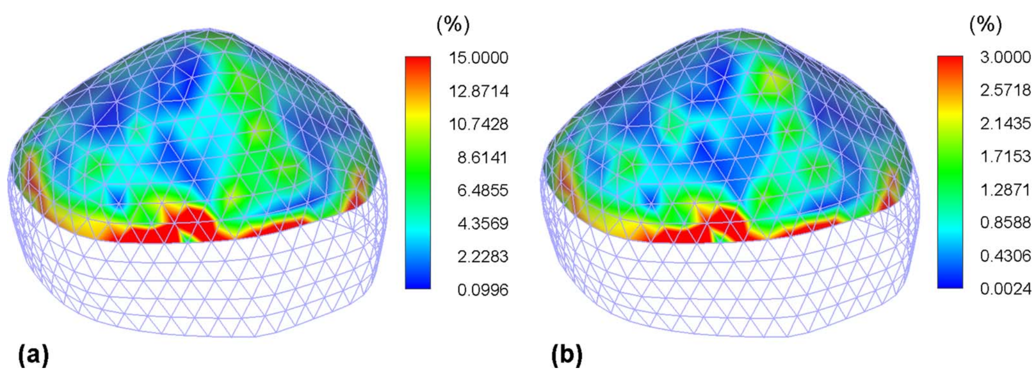

Fig. 8 Absolute values of the relative error (in percentage) between identified elasticity parameters and true parameters of model A without knowing the reference metric: (*a*) μ_1 and (*b*) μ_2

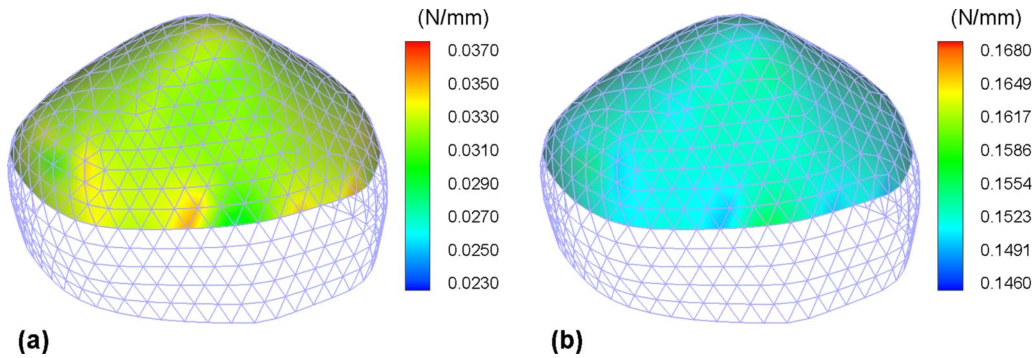

Fig. 9 Identified elasticity parameters of model B knowing the reference metric: (*a*) ν_1 and (*b*) ν_2

ized directly from the stress and strain data. In contrast the parameters are not directly inferred from stress-strain response in inverse finite element methods. These methods are designed for applications where one does not have control over the load or boundary data. Typically, a finite element model with yet unknown parameters is developed for the tested subject. At a given guess of material parameters, the response of the model is predicted. The predicted response, often displacements at selected positions, is compared to the physical measurements; the difference is fed back to an optimization algorithm to adjust the parameters until a satisfactory agreement is achieved. A limitation of these methods is that they cannot effectively deal with heterogeneous properties. It is practically impossible to obtain parameter distribution from indirect regression.

The current method retains the spirit of direct stress-strain regression. It utilizes pointwise stress and strain data acquired from the inflation motion of membranes, as opposed to controlled homogeneous planar deformations. Consequently, the experiment can be rendered nondestructive, and this is one of the distinct features of the method. In comparison to the optimization based approaches [40–43], the present method decouples the stress solution and the parameter regression. This separation not only renders a simpler computation structure but also leads to the possibility of sharply delineating the property map in heterogeneous membranes.

As the specimen test, the availability of direct stress-stain database gives us the advantage of examining the stress-strain properties prior to parameter regression. This feature is valuable to the determination of proper constitutive models for the material. For example, one can examine the co-axial condition between stress and strain to evaluate whether or not the material should be modeled as isotropic (if the material is isotropic, the response satisfies the universal relation $\mathbf{SC}=\mathbf{CS}$, see, e.g., Ref. [44]). The availability of direct stress-strain data to support such a test puts the method in an advantageous position over optimization based methods. In the numerical experiments test conducted here, we did not check the universal relations, since we started with an isotropic energy function and the ensuing stress should satisfy the universal relations to within numerical precision. We will address this approach in the second part of the paper.

Owing to the application of fixed displacement boundary condition and the utility of unrealistic elasticity parameters in FEIEM, there is inevitably a thin boundary layer where the inverse stress solution is not accurate. The boundary layer should be avoided in parameter regression. The same issue exists for the specimen test identification methods albeit in a different manner. The boundary effect in the biaxial testing of planar tissues was studied experimentally by Waldman et al. [45,46] and computationally by Sun et al. [39]. They demonstrated that the gripping methods, e.g., suturing and clamping, or even the number of suture attachments have significant influence over the stress field near the sample edges and even the central region of the sample. This may lead to inaccurate characterization of the material properties. The current method has the advantage of being suture-free. Boundary effect may be alleviated by using a larger mesh area or by employing finer mesh near the boundary.

While the method presents a significant advance in parameter identification, it has some inevitable limitations. First, grounded on the static determinacy of membrane stress, the application is limited to membrane structures. Moreover, the membrane structures must have convex shape in deformed states. An investigation toward the extension to thin-walled shell structures of arbitrary surface characteristics is undertaken in the authors' group. We believe that, in certain situations, the method can be used to identify the in-plane elastic properties of thin-shell structures. Second, like the axisymmetric membrane inflation test, one does not have a complete control over the deformation of the membrane to get a desired deformation protocol, e.g., varying a principal strain while

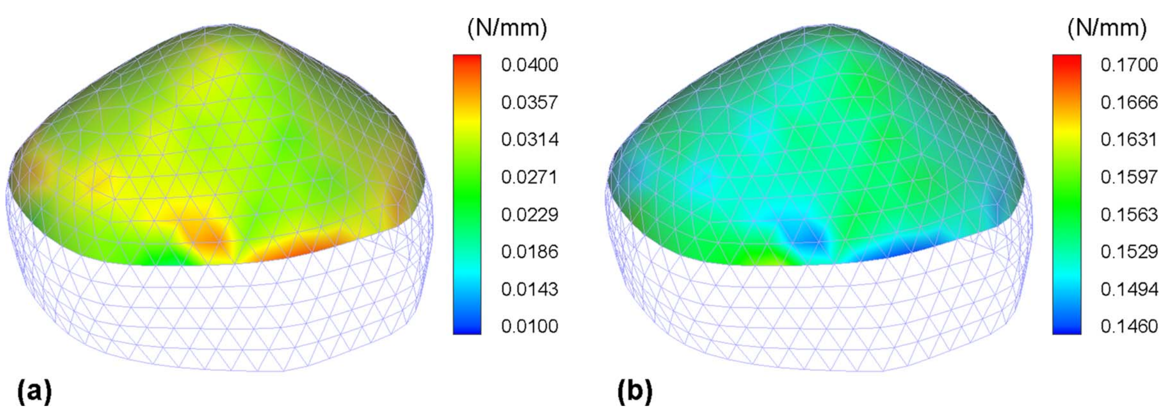

Fig. 10 Identified elasticity parameters of model B without knowing the reference metric: (*a*) ν_1 (*b*) ν_2

Table 1 The means and standard deviations of identified elasticity parameters of model A and model B knowing the reference metric tensor

	Model A		Model B	
	μ_1	μ_2	ν_1	ν_2
Mean (N/mm)	0.06516	0.15208	0.03239	0.15206
SD (N/mm)	0.00113	0.00061	0.00057	0.00061

keeping the other fixed. This may limit the domain of response space that one can examine. Nevertheless, for biological organs, the elastic properties identified by this method may contain enough information about the material behavior in its actual function because the identification is conducted using deformations that closely mimic its motion in the service environment.

In conclusion, we described an innovative method that allows for pointwise identification of local elastic properties in nonlinear membranes and tested the method using numerical experiments. We discussed the theoretical advantages and limitations of the method. The most noteworthy attributes, we believe, are (1) the nondestructive nature and (2) the capability of delineating distributive properties. While some limitations remain, the method opens a new pathway of material parameter identification and holds the promise of noninvasive identification for biological tissues.

Table 2 The means and standard deviations of identified elasticity parameters of model A and model B without knowing the reference metric tensor

	Model A		Model B	
	μ_1	μ_2	ν_1	ν_2
Mean (N/mm)	0.06484	0.15218	0.03132	0.15257
SD (N/mm)	0.00328	0.00143	0.00200	0.00168

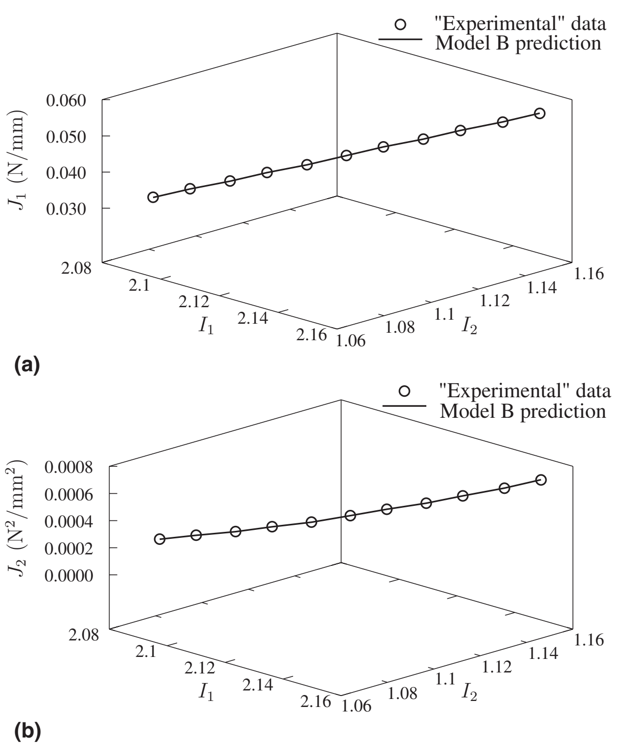

Fig. 11 Comparison between the "experimental" stress invariants and the predictions of model B: (*a*) J_1 and (*b*) J_2

Acknowledgment

This work was supported by the National Science Foundation through Grant No. CMS 03-48194 to the University of Iowa. We thank Dr. Robert E. Harbaugh and Dr. Madhavan L. Raghavan for providing us with the original mesh data of the aneurysm sac.

Appendix: Stress Gradients

When using gradient-based optimization algorithms, one needs to provide the analytical gradients of the objective function with respect to the regression variables. Sections A1 and A2 present the analytical gradients of the stress components with respect to the material parameters and the metric tensor components of the stress-free configuration for models A and B, respectively.

1 Model A. The convected components of the stress tensor are derived as

$$t^{\alpha\beta} = \frac{1}{J}\{[\mu_1 + \mu_2(I_1 - 2)]G^{\alpha\beta} - \mu_1 g^{\alpha\beta}\} \tag{A1}$$

In Eq. (A1), we replace $G^{\alpha\beta}$ with $\mathfrak{G}^{\alpha\beta}$ if the stress-free configuration is unknown, for the purpose of consistency with the notation in Sec. 2.3.

The stress gradients are defined as the partial derivatives of the stress components $t^{\alpha\beta}$ with respect to the regression variables. The stress gradients with respect to the elasticity parameters, μ_1 and μ_2, respectively, are

$$\frac{\partial t^{\alpha\beta}}{\partial \mu_1} = I_2^{-1/2}(G^{\alpha\beta} - g^{\alpha\beta}) \tag{A2}$$

$$\frac{\partial t^{\alpha\beta}}{\partial \mu_2} = I_2^{-1/2}(I_1 - 2)G^{\alpha\beta} \tag{A3}$$

If the stress-free configuration is unknown, the stress gradients with respect to the contravariant reference metric tensor components $\mathfrak{G}^{\alpha\beta}$ are

$$\frac{\partial t^{\alpha\beta}}{\partial \mathfrak{G}^{11}} = -\frac{1}{2}I_2^{-3/2} g\mathfrak{G}^{22}(\gamma\mathfrak{G}^{\alpha\beta} - \mu_1 g^{\alpha\beta}) + I_2^{-1/2}\left(\gamma\frac{\partial \mathfrak{G}^{\alpha\beta}}{\partial \mathfrak{G}^{11}} + \mu_2 g_{11}\mathfrak{G}^{\alpha\beta}\right) \tag{A4}$$

$$\frac{\partial t^{\alpha\beta}}{\partial \mathfrak{G}^{22}} = -\frac{1}{2}I_2^{-3/2} g\mathfrak{G}^{11}(\gamma\mathfrak{G}^{\alpha\beta} - \mu_1 g^{\alpha\beta}) + I_2^{-1/2}\left(\gamma\frac{\partial \mathfrak{G}^{\alpha\beta}}{\partial \mathfrak{G}^{22}} + \mu_2 g_{22}\mathfrak{G}^{\alpha\beta}\right) \tag{A5}$$

$$\frac{\partial t^{\alpha\beta}}{\partial \mathfrak{G}^{12}} = I_2^{-3/2} g\mathfrak{G}^{12}(\gamma\mathfrak{G}^{\alpha\beta} - \mu_1 g^{\alpha\beta}) + I_2^{-1/2}\left(\gamma\frac{\partial \mathfrak{G}^{\alpha\beta}}{\partial \mathfrak{G}^{12}} + 2\mu_2 g_{12}\mathfrak{G}^{\alpha\beta}\right) \tag{A6}$$

where $\gamma = \mu_1 + \mu_2(I_1 - 2)$ and $g = \det(g_{\alpha\beta})$.

2 Model B. The convected stress components of this model are

$$t^{\alpha\beta} = \frac{1}{J}[2\nu_1 \exp(I_1 - 2\log J - 2)(G^{\alpha\beta} - g^{\alpha\beta}) + \nu_2(I_1 - 2)G^{\alpha\beta}] \tag{A7}$$

Likewise, $G^{\alpha\beta}$ will be replaced by $\mathfrak{G}^{\alpha\beta}$ if the stress-free configuration is unknown. The stress gradients with respect to the elasticity parameters are given by

$$\frac{\partial t^{\alpha\beta}}{\partial \nu_1} = 2I_2^{-1/2}\xi(G^{\alpha\beta} - g^{\alpha\beta}) \tag{A8}$$

$$\frac{\partial t^{\alpha\beta}}{\partial \nu_2} = I_2^{-1/2}(I_1 - 2)G^{\alpha\beta} \tag{A9}$$

The stress gradients with respect to the unknown contravariant metric tensor components of the stress-free configuration are

$$\begin{aligned}\frac{\partial t^{\alpha\beta}}{\partial \mathfrak{G}^{11}} = &-\frac{1}{2}I_2^{-3/2}g\mathfrak{G}^{22}[(2\nu_1\xi + \nu_2\eta)\mathfrak{G}^{\alpha\beta} - 2\nu_1\xi g^{\alpha\beta}] \\ &+ I_2^{-1/2}[2\nu_1\xi(g_{11} - I_2^{-1}g\mathfrak{G}^{22})](\mathfrak{G}^{\alpha\beta} - g^{\alpha\beta}) \\ &+ I_2^{-1/2}\left[\nu_2 g_{11}\mathfrak{G}^{\alpha\beta} + (2\nu_1\xi + \nu_2\eta)\frac{\partial \mathfrak{G}^{\alpha\beta}}{\partial \mathfrak{G}^{11}}\right]\end{aligned} \tag{A10}$$

$$\begin{aligned}\frac{\partial t^{\alpha\beta}}{\partial \mathfrak{G}^{22}} = &-\frac{1}{2}I_2^{-3/2}g\mathfrak{G}^{11}[(2\nu_1\xi + \nu_2\eta)\mathfrak{G}^{\alpha\beta} - 2\nu_1\xi g^{\alpha\beta}] \\ &+ I_2^{-1/2}[2\nu_1\xi(g_{22} - I_2^{-1}g\mathfrak{G}^{11})](\mathfrak{G}^{\alpha\beta} - g^{\alpha\beta}) \\ &+ I_2^{-1/2}\left[\nu_2 g_{22}\mathfrak{G}^{\alpha\beta} + (2\nu_1\xi + \nu_2\eta)\frac{\partial \mathfrak{G}^{\alpha\beta}}{\partial \mathfrak{G}^{22}}\right]\end{aligned} \tag{A11}$$

$$\begin{aligned}\frac{\partial t^{\alpha\beta}}{\partial \mathfrak{G}^{12}} = &I_2^{-3/2}g\mathfrak{G}^{12}[(2\nu_1\xi + \nu_2\eta)\mathfrak{G}^{\alpha\beta} - 2\nu_1\xi g^{\alpha\beta}] \\ &+ I_2^{-1/2}[4\nu_1\xi(g_{12} + I_2^{-1}g\mathfrak{G}^{12})](\mathfrak{G}^{\alpha\beta} - g^{\alpha\beta}) \\ &+ I_2^{-1/2}\left[2\nu_2 g_{12}\mathfrak{G}^{\alpha\beta} + (2\nu_1\xi + \nu_2\eta)\frac{\partial \mathfrak{G}^{\alpha\beta}}{\partial \mathfrak{G}^{12}}\right]\end{aligned} \tag{A12}$$

where $\xi = e^{I_1 - 2\log J - 2}$ and $\eta = I_1 - 2$.

References

[1] Rivlin, R. S., and Saunders, D. W., 1951, "Large Elastic Deformations of Isotropic Materials. VII. Experiments on the Deformation of Rubber," Philos. Trans. R. Soc. London, Ser. A, **243A**, pp. 251–288.
[2] Wineman, A., Wilson, D., and Melvin, J. W., 1979, "Material Identification of Soft Tissue Using Membrane Inflation," J. Biomech., **12**, pp. 841–850.
[3] Bylski, D. I., Kriewall, T. J., Akkas, N., and Melvin, J. W., 1986, "Mechanical Behavior of Fetal Dura Mater Under Large Deformation Biaxial Tension," J. Biomech., **19**, pp. 19–26.
[4] Kriewall, T. J., Akkas, N., Bylski, D. I., and Melvin, J. W., 1993, "Mechanical Behavior of Fetal Dura Mater Under Large Axisymmetric Inflation," ASME J. Biomech. Eng., **105**, pp. 71–76.
[5] Hsu, F. P. K., Schwab, C., Rigamonti, D., and Humphrey, J. D., 1994, "Identification of Response Functions for Nonlinear Membranes Via Axisymmetric Inflation Tests: Implications for Biomechanics," Int. J. Solids Struct., **31**, pp. 3375–3386.
[6] Hsu, F. P. K., Liu, A. M. C., Downs, J., Rigamonti, D., and Humphrey, J. D., 1995, "A Triplane Video-Based Experimental System for Studying Axisymmetrically Inflated Biomembranes," IEEE Trans. Biomed. Eng., **42**(5), pp. 442–450.
[7] Storakers, B., 1979, "An Explicit Method to Determine Response Coefficients in Finite Elasticity," J. Elast., **9**, pp. 207–214.
[8] Sacks, M. S., 2000, "Biaxial Mechanical Evaluation of Planar Biological Materials," J. Elast., **61**, pp. 199–246.
[9] Lu, J., Zhou, X., and Raghavan, M. L., 2008, "Inverse Method of Stress Analysis for Cerebral Aneurysms," Biomech. Model. Mechanobiol., **7**, pp. 477–486.
[10] Govindjee, S., and Mihalic, P. A., 1996, "Computational Methods for Inverse Finite Elastostatics," Comput. Methods Appl. Mech. Eng., **136**, pp. 47–57.
[11] Govindjee, S., and Mihalic, P. A., 1998, "Computational Methods for Inverse Deformations in Quasi-Incompressible Finite Elasticity," Int. J. Numer. Methods Eng., **43**, pp. 821–838.
[12] Yamada, T., 1998, "Finite Element Procedure of Initial Shape Determination for Hyperelasticity," Struct. Eng. Mech., **6**(2), pp. 173–183.
[13] Lu, J., Zhou, X., and Raghavan, M. L., 2007, "Inverse Elastostatic Stress Analysis in Pre-Deformed Biological Structures: Demonstration Using Abdominal Aortic Aneurysm," J. Biomech., **40**, pp. 693–696.
[14] Lu, J., Zhou, X., and Raghavan, M. L., 2007, "Computational Method of Inverse Elastostatics for Anisotropic Hyperelastic Solids," Int. J. Numer. Methods Eng., **69**, pp. 1239–1261.
[15] Zhou, X., and Lu, J., 2008, "Inverse Formulation for Geometrically Exact Stress Resultant Shells," Int. J. Numer. Methods Eng., **74**, pp. 1278–1302.
[16] Green, A. E., and Rivlin, R. S., 1964, "On Cauchy's Equation of Motion," Z. Angew. Math. Phys., **15**, pp. 290–292.
[17] Spencer, A. J. M., 1970, "The Static Theory of Finite Elasticity," IMA J. Appl. Math., **6**(2), pp. 164–200.
[18] Truesdell, C., and Noll, W., 1965, "The Non-Linear Field Theories of Mechanics," *Handbuch der Physik*, Vol. Bd. 3/3, S. Flügge, ed., Springer-Verlag, Berlin.
[19] Noll, W., 1972, "A New Mathematical Theory of Simple Material," Arch. Ration. Mech. Anal., **48**, pp. 1–50.
[20] Epstein, M., and Maugin, G. A., 1990, "The Energy-Momentum Tensor and Material Uniformity in Finite Elasticity," Acta Mech., **83**(3–4), pp. 127–133.
[21] Epstein, M., and Maugin, G. A., 1996, "On the Geometrical Material Structure of Anelasticity," Acta Mech., **115**, pp. 119–131.
[22] Maugin, G. A., and Epstein, M., 1998, "Geometrical Material Structure of Elastoplasticity," Int. J. Plast., **14**, pp. 109–115.
[23] Miehe, C., 1998, "A Constitutive Frame of Elastoplasticity at Large Strains Based on the Notion of a Plastic Metric," Int. J. Solids Struct., **35**(30), pp. 3859–3897.
[24] Lu, J., and Papadopoulos, P., 2004, "A Covariant Formulation of Anisotropic Finite Plasticity: Theoretical Development," Comput. Methods Appl. Mech. Eng., **193**, pp. 5335–5358.
[25] Lu, J., 2006, "A Covariant Condition and Related Constitutive Results in Finite Plasticity," ZAMP, **57**, pp. 313–323.
[26] Rodriguez, E. K., Hoger, A., and Mcculloch, A. D., 1994, "Stress-Dependent Finite Growth in Soft Elastic Tissues," J. Biomech., **27**, pp. 455–467.
[27] Taber, L. A., 1995, "Biomechanics of Growth, Remodeling, and Morphogenesis," Appl. Mech. Rev., **48**, pp. 487–545.
[28] Johnson, B. E., and Hoger, A., 1995, "The Use of a Virtual Configuration in Formulating Constitutive Equations for Residually Stressed Elastic Materials," J. Elast., **41**, pp. 177–215.
[29] Hoger, A., 1997, "Virtual Configurations and Constitutive Equations for Residually Stressed Bodies With Material Symmetry," J. Elast., **48**, pp. 125–144.
[30] Olsson, T., Stålhand, J., and Klarbring, A., 2006, "Modeling Initial Strain Distribution in Soft Tissues With Application to Arteries," Biomech. Model. Mechanobiol., **5**, pp. 27–38.
[31] Boehler, J. P., 1979, "A Simple Derivation of Representations for Non-Polynomial Constitutive Equations in Some Case of Anisotropy," Z. Angew. Math. Mech., **59**, pp. 157–167.
[32] Lu, J., and Papadopoulos, P., 2000, "A Covariant Constitutive Description for Anisotropic Non-Linear Elasticity," ZAMP, **51**, pp. 204–214.
[33] Rossettos, J. N., 1966, "Nonlinear Membrane Solutions for Symmetrically Loaded Deep Membranes of Revolution," NASA Technical Report No. NASA TN D-3297.
[34] Wu, C. H., and Peng, D. Y. P., 1972, "On the Asymptotically Spherical Deformation of Arbitrary Membranes of Revolution Fixed Along an Edge and Inflated by Large Pressures—A Nonlinear Boundary Layer Phenomenon," SIAM J. Appl. Math., **23**, pp. 133–152.
[35] Taylor, R. L., 2003, FEAP User Manual, v7.5, Technical report, Department of Civil and Environmental Engineering, University of California, Berkeley.
[36] Gill, P. E., Murray, W., and Saunders, M. A., 2005, "SNOPT: An SQP Algorithm for Large-Scale Constrained Optimization," SIAM Rev., **47**, pp. 99–131.
[37] Lanir, Y., and Fung, Y. C., 1974, "Two-Dimensional Mechanical Properties of Rabbit Skin—I. Experimental System," J. Biomech., **7**, pp. 29–34.
[38] Lanir, Y., and Fung, Y. C., 1974, "Two-Dimensional Mechanical Properties of Rabbit Skin—II. Experimental Results," J. Biomech., **7**, pp. 171–182.
[39] Sun, W., Sacks, M. S., and Scott, M. J., 2005, "Effects of Boundary Conditions on the Estimation of the Planar Biaxial Mechanical Properties of Soft Tissues," ASME J. Biomech. Eng., **127**, pp. 709–715.
[40] Kavanagh, K. T., and Clough, R. W., 1971, "Finite Element Applications in the Characterization of Elastic Solids," Int. J. Solids Struct., **7**, pp. 11–23.
[41] Iding, R. H., Pister, K. S., and Taylor, R. L., 1974, "Identification of Nonlinear Elastic Solids by a Finite Element Method," Comput. Methods Appl. Mech. Eng., **4**, pp. 121–142.
[42] Kyriacou, S. K., Shah, A. D., and Humphrey, J. D., 1997, "Inverse Finite Element Characterization of Nonlinear Hyperelastic Membrane," ASME J. Appl. Mech., **64**, pp. 257–262.
[43] Seshaiyer, P., and Humphrey, J. D., 2003, "A Sub-Domain Inverse Finite Element Characterization of Hyperelastic Membranes Including Soft Tissues," ASME J. Biomech. Eng., **125**, pp. 363–371.
[44] Beatty, M. F., 1987, "A Class of Universal Relations in Isotropic Elasticity," J. Elast., **17**, pp. 113–121.
[45] Waldman, S. D., and Lee, J. M., 2002, "Boundary Conditions During Biaxial Testing of Planar Connective Tissues. Part 1: Dynamic Behavior," J. Mater. Sci. Mater. Med., **13**, pp. 933–938.
[46] Waldman, S. D., Sacks, M. S., and Lee, J. M., 2002, "Boundary Conditions During Biaxial Testing of Planar Connective Tissues. Part II: Fiber Orientation," J. Mater. Sci. Lett., **21**, pp. 1215–1221.

Xuefeng Zhao
Department of Mechanical and Industrial Engineering,
Center for Computer Aided Design,
The University of Iowa,
Iowa City, IA 52242-1527

Xiaolin Chen
Mechanical Engineering Program,
School of Engineering and Computer Science,
Washington State University,
Vancouver, WA 98686

Jia Lu[1]
Department of Mechanical and Industrial Engineering,
Center for Computer Aided Design,
The University of Iowa,
Iowa City, IA 52242-1527
e-mail: jia-lu@uiowa.edu

Pointwise Identification of Elastic Properties in Nonlinear Hyperelastic Membranes—Part II: Experimental Validation

Following the theoretical and computational developments of the pointwise membrane identification method reported in the first part of this paper, we perform a finite inflation test on a rubber balloon to validate the method. The balloon is inflated using a series of pressurized configurations, and a surface mesh that corresponds through all the deformed states is derived using a camera-based three dimensional reconstruction technique. In each configuration, the wall tension is computed by the finite element inverse elastostatic method, and the in-plane stretch relative to a slightly pressurized configuration is computed with the aid of finite element interpolation. Based on the stress-strain characteristics, the Ogden model is employed to describe the material behavior. The elastic parameters at every Gauss point in a selected region are identified simultaneously. To verify the predictive capability of the identified material model, the deformation under a prescribed pressure is predicted using the finite element method and is compared with the physical measurement. The experiment shows that the method can effectively delineate the distributive elastic properties in the balloon wall. [DOI: 10.1115/1.3130810]

Keywords: parameter identification, finite inflation test, nonlinear membrane, inverse method, inverse elastostatics

1 Introduction

In the first paper [1] of this series, we introduced a new experimental method, the pointwise identification method (PWIM), for characterizing the distributive elastic properties in hyperelastic membranes. The method is a nontrivial generalization of the finite inflation test by Rivlin and Saunders [2]. The original inflation test was limited to axisymmetric membrane structures; in our development it is extended to general convex membranes without any geometric symmetry. The cornerstone of PWIM is a nonconventional approach of stress analysis, the finite element inverse elastostatic method [3–8]. This method takes as the input a deformed configuration of an elastic material body and the corresponding load, and determines the stress distribution by way of finding a stress-free configuration. For finitely deforming membranes, the inverse method can effectively compute the wall stress without knowing the realistic material constitutive equation [7,8]. This capability enables us to collect stress data independently of the material in question. With the availability of stress and strain distributions in several deformed states, the local elastic property of the wall can be characterized pointwise at multiple material points. In Ref. [1], we tested this paradigm numerically using a membrane of known material behavior.

In this work, we validate the method through finite inflation tests on a rubber balloon. PWIM has several attributes that are not shared by conventional parameter identification methods. The most noteworthy characteristic, in our opinion, is the capability of delineating the property map, namely, the parameter distributions. This capability is highly desirable in characterizing heterogeneous properties such as in soft tissues. Although admittedly the concept of pointwise identification is best tested with heterogeneous materials; in this paper we focus on a rubber balloon known to be approximately homogeneous. Our emphasis, in part, is placed on verifying the capability of detecting the uniform property distribution of a homogenous material. Further validation with heterogeneous materials will be the subject of a forthcoming paper.

2 Method

2.1 Photogrammetric Surface Reconstruction. Photogrammetry encompasses methods of image interpretation in order to derive the shape and location of an object from one or more photographs of that object [9]. A primary purpose of photogrammetric measurement is the three-dimensional reconstruction of an object in digital form. Photogrammetry works as follows. First, the camera needs to be calibrated, which allows the photogrammetry program to know the detailed description of the camera, including the focal length, imaging scale, image center, and lens distortion. Second, the user takes enough photographs of the object from different perspectives, which can sufficiently characterize its 3D structure. Third, the photographs are imported into the program, and point referencing is then performed to let the program know the corresponding positions in each 2D image space of a point in the 3D space. Finally, the 3D position of all the selected points are computed using mathematical transformation. If applied to a deforming membrane with enough tracking markers on its surface, which sufficiently characterize the geometry feature of membrane, photogrammetry can be used to record the 3D positions of the tracking markers in different deformed states. By identifying a reference configuration, one can obtain the displacements of the tracking markers and hence compute the strains using interpolation.

2.2 Experiments. A finite element mesh, which constitutes 12×12 four-node elements, was drawn by hand using a fine marker pen on the belly region of the balloon surface. Compressed nitrogen gas was used to inflate the balloon. Before testing, the rubber balloon underwent cyclical inflation-deflation (pre-

[1]Corresponding author.

Contributed by the Applied Mechanics Division of ASME for publication in the JOURNAL OF APPLIED MECHANICS. Manuscript received February 5, 2008; final manuscript received February 4, 2009; published online July 27, 2009. Review conducted by Sanjay Govindjee.

conditioning) for ten times to eliminate Mullin's effect. Subsequently, the balloon was inflated to a relatively large size of approximately 200% stretch. After several seconds of waiting for the balloon to reach its stable status, the balloon was deflated in several decrements. At each state, the air pressure inside the balloon was measured by a manometer. In the meantime, four photos were taken from different perspectives using a Nikon D80 digital SLR camera, which was calibrated prior to the test. Since the balloon generally collapses when the net internal pressure is zero, the configuration under a very small pressure ($0.0001\ \text{N/mm}^2$), but still in convex shape, was taken as the approximate stress-free configuration. Fourteen configurations, including the stress-free configuration and thirteen deformed configurations, were recorded.

Taking the photos as input, we used a close-range photogrammetry program, PHOTOMODELER 6 (EOS Systems Inc.) to reconstruct the 3D surface geometry of the meshed region in each configuration. In the process of 3D geometry reconstruction, an important step is the determination of the point-to-point correspondence between the tracking points in different photographs. Due to the difficulty of corresponding the nodes across different photographs automatically, we determined the point-to-point correspondence by manually picking the points.

2.3 Stress Computation. Taking the reconstructed finite element mesh of each deformed configuration, we computed individually the wall tension using the membrane finite element inverse elastostatic method [7,8]. The inverse method leverages the material insensitivity of the stress in membrane structures. It enables us to compute the wall stress using assumed material models [7,1]. In this work, we employed a neo-Hookean type of hyperelastic constitutive model whose strain-energy function is

$$w_{\text{neo-Hookean}} = \frac{\nu_1}{2}(I_1 - 2\log J - 2) + \frac{\nu_2}{4}(I_1 - 2)^2 \tag{1}$$

Here, $I_1 = \text{tr}(\mathbf{C})$ and $J = \sqrt{\det(\mathbf{C})}$, where $\mathbf{C}$ is the right Cauchy–Green deformation tensor, and (ν_1, ν_2) are the effective elastic parameters as defined in Part I of the paper. Without the second term, the energy function corresponds to the classical neo-Hookean material, which is known to suffer a limit-point instability during inflation motions [10]. The second term is introduced as a remedy to stabilize the deformation. For the sake of quick convergence, unrealistic values of the elasticity parameters, $\nu_1 = \nu_2 = 100\ \text{N/mm}$, which rendered a very small deformation, were assumed.

Clamped boundary conditions were applied on the four edges of the mesh. As discussed in Refs. [1,7], clamped boundary (or other types of displacement constraints) compromises the static determinacy. However, for sufficiently curved membranes the influence exists in a thin boundary layer [11,12], and the thickness of which depends inversely on the surface curvature. Outside the boundary layer, the stress is asymptotic to the material-independent static solution. We hypothesize that the boundary layer can be identified numerically by examining the change of stress under varying material parameters. The region in which the stress remains approximately invariant under relatively large change of material parameters is defined as the boundary-effect-free region. Later, the parameter identification will be carried out in the boundary-effect-free region only. This procedure is important to the experiment design, as we need a practical method to identify, and thus to avoid, the boundary layer.

As in the first part, the (Cauchy) tension tensor $\mathbf{t}$ and the referential tension tensor $\mathbf{T}$ are the resultants of the Cauchy stress $\boldsymbol{\sigma}$ and the second Piola–Kirchhoff stress $\mathbf{S}$, respectively,

$$\mathbf{t} = h\boldsymbol{\sigma}, \quad \mathbf{T} = H\mathbf{S} \tag{2}$$

Here, h and H are the current and initial membrane thicknesses, which are related to $h = \lambda_3 H$, where λ_3 is the thickness stretch. Relative to a convected basis, the tension tensors have the form

$$\mathbf{t} = t^{\alpha\beta}\mathbf{g}_\alpha \otimes \mathbf{g}_\beta, \quad \mathbf{T} = T^{\alpha\beta}\mathbf{G}_\alpha \otimes \mathbf{G}_\beta \tag{3}$$

The current basis $\mathbf{g}_\alpha$ is related to the reference basis $\mathbf{G}_\alpha$ pointwise through the relation $\mathbf{g}_\alpha = \mathbf{F}\mathbf{G}_\alpha$, where $\mathbf{F}$ is the deformation gradient. It follows that the components of the tension and the referential tension differ only by the area stretch factor J, i.e., $T^{\alpha\beta} = Jt^{\alpha\beta}$.

In the inverse computation, the tension $\mathbf{t}$ is computed at each Gauss point in a local orthonormal coordinate system, and thus the outputs are the physical components, which we denoted as t_{11}, t_{22}, and $t_{12} = t_{21}$. The principal tensions, which will be used in parameter regression, can be directly computed according to

$$\begin{aligned} t_1 &= \frac{t_{11} + t_{22}}{2} + \frac{\sqrt{(t_{11} - t_{22})^2 + 4t_{12}^2}}{2} \\ t_2 &= \frac{t_{11} + t_{22}}{2} - \frac{\sqrt{(t_{11} - t_{22})^2 + 4t_{12}^2}}{2} \end{aligned} \tag{4}$$

However, the basis vectors defined independently in each configuration do not form a convected basis. The convected components of the stress can be computed through a linear transformation. Let $\{\bar{\mathbf{g}}_\alpha, \alpha = 1, 2\}$ be a set of basis vectors at a point, and let $\{\mathbf{g}_\alpha, \alpha = 1, 2\}$ be the convected basis at the same point (the computation of the convected basis is discussed in Sec. 2.4). The tension tensor $\mathbf{t}$ can be written, in terms of the two sets of basis, as

$$t^{\alpha\beta}\mathbf{g}_\alpha \otimes \mathbf{g}_\beta = \bar{t}^{\alpha\beta}\bar{\mathbf{g}}_\alpha \otimes \bar{\mathbf{g}}_\beta \tag{5}$$

Taking the dot product of both sides of Eq. (5) with $\mathbf{g}^\alpha \otimes \mathbf{g}^\beta$, and letting $Q_\alpha^\beta = \mathbf{g}^\beta \cdot \bar{\mathbf{g}}_\alpha$, we obtain

$$t^{\alpha\beta} = Q_\delta^\alpha \bar{t}^{\delta\gamma} Q_\gamma^\beta \tag{6}$$

2.4 Strain Computation. Based on the measured nodal positions in the reference and deformed configurations, we approximated the position vectors of a point inside the meshed region via the finite element interpolation,

$$\mathbf{X} = \sum_{I=1}^{\text{Nel}} N_I(\xi^1, \xi^2)\mathbf{X}^I, \quad \mathbf{x} = \sum_{I=1}^{\text{Nel}} N_I(\xi^1, \xi^2)\mathbf{x}^I \tag{7}$$

Here, the superscript I is the indicator of the nodal number, Nel is the total number of nodes in the element, and N_I is the shape function for the Ith node. The natural coordinates (ξ^1, ξ^2) serve as the (elementwise) convected surface coordinates. The displacement field is $\mathbf{u} = \mathbf{x} - \mathbf{X}$. It follows that the covariant basis vectors of the reference and current configuration are computed, respectively, as

$$\mathbf{G}_\alpha = \frac{\partial \mathbf{X}}{\partial \xi^\alpha} = \sum_{I=1}^{\text{Nel}} \frac{\partial N_I}{\partial \xi^\alpha}\mathbf{X}^I, \quad \mathbf{g}_\alpha = \frac{\partial \mathbf{x}}{\partial \xi^\alpha} = \sum_{I=1}^{\text{Nel}} \frac{\partial N_I}{\partial \xi^\alpha}\mathbf{x}^I \tag{8}$$

The components of the covariant metric tensors on the reference and current surface, respectively, are given by

$$G_{\alpha\beta} = \mathbf{G}_\alpha \cdot \mathbf{G}_\beta, \quad g_{\alpha\beta} = \mathbf{g}_\alpha \cdot \mathbf{g}_\beta \tag{9}$$

Other geometric entities such as the contravariant basis vectors ($\mathbf{g}^\alpha$ and $\mathbf{G}^\alpha$) and the contravariant metric tensor components ($g^{\alpha\beta}$ and $G^{\alpha\beta}$) are computed in the standard manner, see Ref. [1]. Subsequently, the deformation gradient $\mathbf{F}$ and the right Cauchy–Green deformation tensor $\mathbf{C} = \mathbf{F}^T\mathbf{F}$ are computed at every Gauss point. As presented in Ref. [1], the deformation gradient $\mathbf{F} = \mathbf{g}_\alpha \otimes \mathbf{G}^\alpha$ and $\mathbf{C} = g_{\alpha\beta}\mathbf{G}^\alpha \otimes \mathbf{G}^\beta$. In our implementation, a local orthonormal basis was constructed at every Gauss point in the reference configuration, rendering $G_{\alpha\beta} = \delta_{\alpha\beta}$ and $G^{\alpha\beta} = \delta^{\alpha\beta}$. The components of $\mathbf{C}$ with respect to this basis are the physical components.

The principal stretches λ_1 and λ_2 of the membrane are defined as the eigenvalues of the right stretch tensor $\mathbf{U}$, which is related to the right Cauchy–Green deformation tensor $\mathbf{C}$ through $\mathbf{C} = \mathbf{U}^2$.

Thus, the square stretches λ_1^2 and λ_2^2 are the eigenvalues of $\mathbf{C}$, which are given, in terms of the physical components of $\mathbf{C}$, by

$$\lambda_1^2 = \frac{C_{11}+C_{22}}{2} + \frac{\sqrt{(C_{11}-C_{22})^2+4C_{12}^2}}{2}$$
$$\lambda_2^2 = \frac{C_{11}+C_{22}}{2} - \frac{\sqrt{(C_{11}-C_{22})^2+4C_{12}^2}}{2} \qquad (10)$$

2.5 Isotropy Test. For materials in some symmetry classes, the stress function should satisfy certain *universal relations* [13–17]. For experimentalists, the universal relations are important in determining whether a material belongs to a certain symmetry class. For isotropic elastic materials, the relation

$$\mathbf{SC} = \mathbf{CS} \qquad (11)$$

holds, which implies that the second Piola–Kirchhoff stress tensor $\mathbf{S}$ commutes with the right Cauchy–Green deformation tensor $\mathbf{C}$ in every possible motion. Giving the linear relation between $\mathbf{S}$ and referential tension $\mathbf{T}$, it is clear that $\mathbf{T}$ must satisfy

$$\mathbf{TC} = \mathbf{CT} \qquad (12)$$

This is the universal relation for isotropic membranes.

Utilizing the acquired tension-strain data, we may examine whether $\mathbf{TC}=\mathbf{CT}$ holds. Due to the experimental error, $\mathbf{TC}$-$\mathbf{CT}$ will not be exactly zero even if the material is truly isotropic. We employ the commutator $\mathbf{e}=\mathbf{TC}$-$\mathbf{CT}$ as an isotropy indicator. Due to the symmetry of $\mathbf{T}$ and $\mathbf{C}$, the components $e_{11}=e_{22}=0$, and the only possible nonzero component is e_{12}. We introduce the function $\varepsilon=2|e_{12}|/\sqrt{(\mathbf{TC}):(\mathbf{CT})}$ as a measure of coaxiality. If ε is close to zero for a wide range of stress-strain protocols, we may say the universal relation is satisfied. Obviously, the test alone cannot conclude material isotropy, especially if only limited stress-strain protocols are tested. However, if the universal relation is found to hold true for a rich family of stress-strain protocols, then there is a strong justification to model the material as isotropic.

2.6 Elastic Parameter Identification. The mechanics of rubber elasticity was investigated extensively in the past several decades, and various constitutive models were developed. Among the well-known hyperelastic descriptors, there are mainly two types of energy functions, one in terms of the strain invariants [18,19] and the other in principal stretches [20–23]. Attributing to the limited extensibility of the molecule chain network, the stress-stretch curve shows a characteristic sigmoid shape [24]. Our experimental stress-stretch data displayed the same characteristic as that by Treloar [20]. It was well accepted that Ogden's energy function [22], which contains noninteger powers of the principal stretches, can model the sigmoid shape well within the typical range of experimental stretches. Based on this consideration, we selected the Ogden model to fit our experimental data.

The Ogden model describes the strain-energy function in terms of the principal stretches λ_r $(r=1,2,3)$ in the following form:

$$W = \sum_i \frac{M_i}{\alpha_i}(\lambda_1^{\alpha_i}+\lambda_2^{\alpha_i}+\lambda_3^{\alpha_i}-3) \qquad (13)$$

Here, W is the strain energy per unit reference volume, and M_i and α_i are the elastic parameters. The exponents α_i may take any nonzero real value. The summation on i extends over as many terms as are necessary to characterize a particular material [25]. For membranes, the strain energy per unit reference area is $w=HW$, where H is the reference membrane thickness. Hence, the 2D form of Eq. (13) is

$$w = \sum_i \frac{HM_i}{\alpha_i}(\lambda_1^{\alpha_i}+\lambda_2^{\alpha_i}+\lambda_3^{\alpha_i}-3) \qquad (14)$$

We introduce the effective elasticity parameters $\mu_i=HM_i$ and rewrite Eq. (14) as

$$w = \sum_i \frac{\mu_i}{\alpha_i}(\lambda_1^{\alpha_i}+\lambda_2^{\alpha_i}+\lambda_3^{\alpha_i}-3) \qquad (15)$$

The incompressibility condition $\lambda_1\lambda_2\lambda_3=1$ gives rise to $\lambda_3=(\lambda_1\lambda_2)^{-1}$. Considering that λ_1 and λ_2 are two independent deformation parameters, we may rewrite function (15) as

$$\hat{w}(\lambda_1,\lambda_2) = \sum_i \frac{\mu_i}{\alpha_i}(\lambda_1^{\alpha_i}+\lambda_2^{\alpha_i}+\lambda_1^{-\alpha_i}\lambda_2^{-\alpha_i}-3) \qquad (16)$$

It follows that under the plane stress assumption ($t_3=0$), the principal values of the tension tensor are given by

$$t_1 = \frac{1}{\lambda_2}\frac{\partial\hat{w}}{\partial\lambda_1}, \quad t_2 = \frac{1}{\lambda_1}\frac{\partial\hat{w}}{\partial\lambda_2} \qquad (17)$$

Expanding Eq. (17), we obtain

$$t_1 = \sum_i \mu_i(\lambda_1^{\alpha_i-1}\lambda_2^{-1} - (\lambda_1\lambda_2)^{-\alpha_i-1})$$
$$t_2 = \sum_i \mu_i(\lambda_2^{\alpha_i-1}\lambda_1^{-1} - (\lambda_1\lambda_2)^{-\alpha_i-1}) \qquad (18)$$

It was shown by Ogden [22] that the energy function (15) fits well with the data of a particular rubber material by Treloar [20] if three terms are included. Following this observation, we chose the three-term Ogden model in this work.

The objective function is constructed as

$$\Phi = \sum_{i=1}^{N} w_1({}^{(i)}t_1 - {}^{(i)}\hat{t}_1)^2 + w_2({}^{(i)}t_2 - {}^{(i)}\hat{t}_2)^2 \qquad (19)$$

where N is the number of deformed states recruited into the regression, ${}^{(i)}t_\alpha$ and ${}^{(i)}\hat{t}_\alpha$ $(\alpha=1,2)$ are the predicted and experimental principal tension models (computed from the inverse method) in the ith configuration, and w_1 and w_2 are the weight parameters, the values of which are determined by numerical experiments. To achieve the reported results, we chose $w_1=1.0$ and $w_2=1.5$. Since an approximate global stress-free configuration was obtained, Φ is a function of the unknown elasticity parameters only. The parameter identification problem can be described as

$$\text{minimize} \quad \Phi(\boldsymbol{\mu},\boldsymbol{\alpha}) \quad \text{subject to} \quad \mathbf{l} \le (\boldsymbol{\mu},\boldsymbol{\alpha}) \le \mathbf{u} \qquad (20)$$

Here, $(\boldsymbol{\mu},\boldsymbol{\alpha})=(\mu_1,\mu_2,\mu_3,\alpha_1,\alpha_2,\alpha_3)$ is the vector of elasticity parameters, and $\mathbf{u}$ are the vectors of lower and upper bounds of $(\boldsymbol{\mu},\boldsymbol{\alpha})$.

A practical difficulty in material parameter identification is that multiple sets of parameters may render equally good fits to a given set of stress-strain data due to the presence of local minima or experimental error or regression error [26]. The problem aggravates for highly nonlinear models, as small perturbation in the experimental data may result in a large variation in the ensuing parameters. This issue has a nontrivial implication in membrane identifications. While the 3D energy function parameters are intrinsic properties of the material, the effective properties in the membrane energy function, such as μ_i in Eq. (15), are not. Their values depend on the wall thickness, and thus may vary with the thickness even if the underlying material is intrinsically homogeneous. Due to the numerical nonuniqueness in fitting, a variation in the wall thickness may result in a spurious heterogeneity in the identified intrinsic parameters. To cope with this difficulty, we adopted the following strategy. We first performed regression at a selected point where the response was relatively smooth and determined the parameters α_i and μ_i. Then, based on the consider-

Table 1 The identities and corresponding pressure values of the deformed configurations

Configuration ID	1	2	3	4	5	6	7	8	9	10	11	12	13
Pressure (N/mm^2)	0.00089	0.00134	0.00153	0.00161	0.00167	0.00173	0.00179	0.00184	0.00190	0.00198	0.00208	0.0022	0.00238

ation that the balloon is approximately homogeneous, we applied the values of α_i to all other points and identified the remaining effective parameters μ_i. Although the parameters so obtained are unlikely the global minimizer of the objective function, the (assumed) intrinsic homogeneity is enforced. The regression was performed by a gradient-based, sequential quadratic programming (SQP) algorithm, SNOPT [27].

2.7 Predictive Capability. The usefulness of the identified elastic parameters can be evaluated by examining how well the model derived from a set of experiments can predict the system behavior in a different physical setting [28]. We conducted a forward finite element analysis using the identified material model to predict a deformed configuration, which was not used in the parameter identification. The FEM predictions were compared with the measured deformation. In the forward analysis, we followed the finite element formulation of the Ogden model for membrane problems presented by Gruttmann and Taylor [25] and implemented the element in the nonlinear finite element analysis program (FEAP) [29].

The forward finite element analysis was conducted for the boundary-effect-free region where the parameter identification was carried out. The displacements of the boundary nodes were prescribed according to the recorded nodal positions. The difference between the predicted position $\mathbf{x}$ and measured position $\hat{\mathbf{x}}$ was quantified nodewise with the error measure $e=\|\mathbf{x}-\hat{\mathbf{x}}\|/L$, where L is a characteristic length taken to be 50 mm.

3 Results

3.1 Reconstructed Surfaces and Stress Results. Table 1 lists the 13 deformed configurations and their corresponding pressure values. The largest stretch being around 2.1 occurred in the deformed configuration 13 (the highest pressure). The initial size of a randomly selected element in the stress-free configuration is about $5.3\times 5.3\ mm^2$, whereas in the deformed configuration 13, its size is around $10.6\times 10.6\ mm^2$. Figure 1 shows a typical photo used in the process of 3D geometry reconstruction. Figure 2 shows the reconstructed mesh for the deformed configurations. Two deformed configurations, which were close to other ones, are not shown. Qualitatively, the convexity and smoothness of membrane surfaces were recovered.

Figure 3 shows the finite element mesh and the principal tensions in the 13th state (the highest pressure). It should be noted that the stress solution obtained through the inverse method is largely affected by the geometric features of the surface, e.g., smoothness and curvature. Due to the unavoidable existence of experimental error, the reconstructed membrane surface may have some unphysical local undulations depending on the accuracy of the motion tracking devices. In that case, the stress solution may not converge or has stress concentrations here and there. In order to reduce this artifact, it is imperative that certain surface smoothing processes be conducted prior to stress computation. In this work, we were able to obtain good quality surface meshes from 3D reconstruction without modification for all of the configurations.

3.2 Stress Sensitivity to Material Model. Figure 4 shows the relative difference (in percentage) of the principal tensions under drastic changes in elasticity parameters of the neo-Hookean model. We took the parameters $\nu_1=\nu_2=100\ N/mm$ as the reference values. After varying the two parameters in different ways, we computed the principal tensions using the inverse method and compared them to those computed from the reference parameters. In Fig. 4, the upper row shows the percentage difference in principal stresses when both parameters were magnified ten times, i.e., $\nu_1=\nu_2=1000\ N/mm$. The percentage differences in region 3 layers of elements distanced from the boundary were below 0.05%. Increasing both parameters by 100 times produces a similar difference margin, and we did not report it here. In the lower row, ν_1 was kept unchanged, while ν_2 was increased to five times, i.e., $\nu_1=100\ N/mm$ and $\nu_2=500\ N/mm$. The percentage differences in region 3 layers of elements distanced from the boundary were below 2.8%. The case where ν_1 was increased to five times while ν_2 remained unchanged was also considered and a similar margin of difference was observed.

Throughout all the tests, it appears that the tension solution was affected minimally by proportional variations of the elastic parameters. Changing two parameters unproportionally, however, rendered a relatively larger variation in the tension solution. Nevertheless, the difference was within an acceptable range in region 3 layers of elements distanced from the boundary. This region was identified as the boundary-effect-free region where the parameter identification was performed later.

3.3 Isotropy Test. Figures 5(*a*) and 5(*b*) show the distribution of the coaxiality indicator ε in the lowest and highest pressure states (configurations 1 and 13), respectively. In the boundary-effect-free region defined above, the value of ε was less than 0.58% and 1.07% for configurations 1 and 13, respectively. The values in other states fall into these limits. Allowing for the experimental error, we conclude that the coaxiality condition between the stress and strain tensors was met. Therefore, the material may be modeled as isotropic.

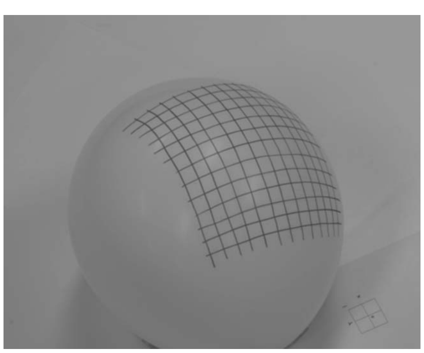

Fig. 1 A photo of the rubber balloon used in the process of 3D geometry reconstruction

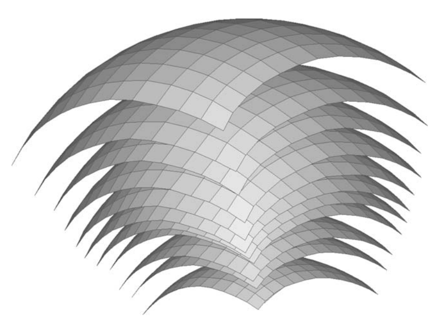

Fig. 2 Reconstructed meshes of the deformed configurations

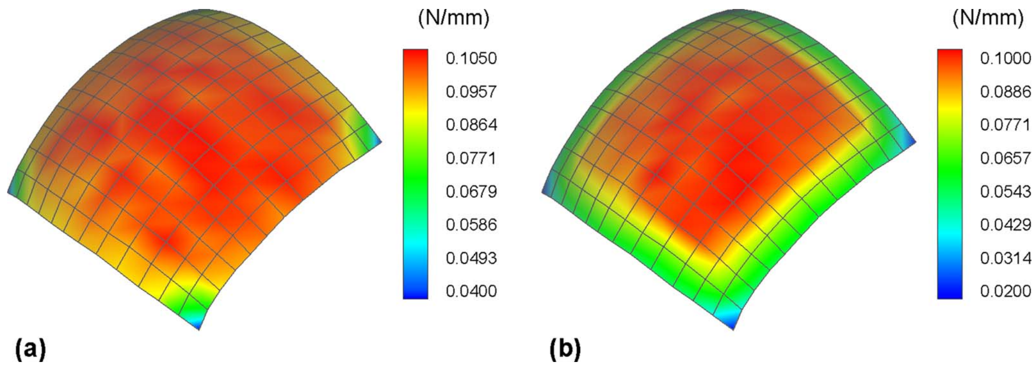

Fig. 3 Distribution of principal tensions in deformed configuration 13: (*a*) t_1 and (*b*) t_2

3.4 Elastic Parameter Identification. As introduced in Sec. 2.6, the parameter identification was accomplished in two steps. First, the regression was performed at a selected Gauss point and all parameters were identified. Second, the identified α_i values were applied to the entire region, and the remaining parameters μ_i were identified at all remaining Gauss points. The identified values of α_i and μ_i at the selected point are listed in Table 2.

The global regression was performed using the states in Table 1 excluding the 11th state ($p=0.00208\ \mathrm{N/mm^2}$), which was reserved for a forward verification. The distributions of the identified parameters μ_i in the whole region are shown in Fig. 6 for the boundary-effect-free region. The ranges, means, and standard deviations of these three parameters are listed in Table 3. Since the standard deviations for all the parameters are relatively small, we may conclude that the material is at least nominally homogeneous.

The intrinsical homogeneity of the material can be checked by inspecting the ratios μ_1/μ_2, μ_1/μ_3, and μ_3/μ_2, which factor out the wall thickness. Since μ_3 is several orders of magnitude smaller than μ_1 and μ_2, we only examine the ratio of μ_1 to μ_2. The distribution of this ratio is illustrated in Fig. 7. Qualitatively seen from the figure, the ratio is approximately uniform over the region. The mean is 3.0309 N/mm, and the standard deviation is 0.1720 N/mm. The result suggests that the intrinsic properties are effectively homogeneous.

Figure 8 illustrates the comparison between the identified model's tension-stretch curves and the experimental data at the point where the initial identification of all six parameters took place. The good match between the model predictions and experimental data indicates that the material's response were modeled successfully by the Ogden model, at least within the stretch range considered in the experiment.

3.5 Predictive Capability. The 11th configuration ($p=0.00208\ \mathrm{N/mm^2}$), which was excluded from parameter identi-

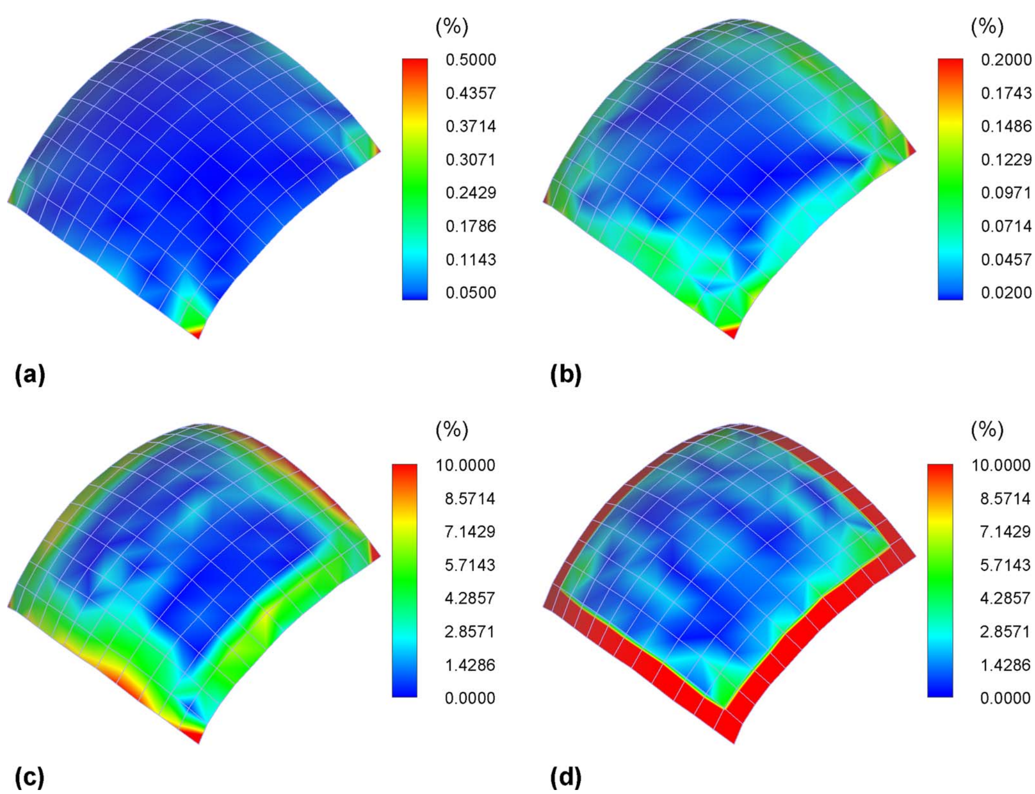

Fig. 4 The percentage difference of principal tensions under the change of elasticity parameters. Upper row: increasing both parameters μ_1 and μ_2 to ten times, (*a*) t_1 and (*b*) t_2; lower row: keeping μ_1 unchanged and increasing μ_2 to five times, (*c*) t_1 and (*d*) t_2.

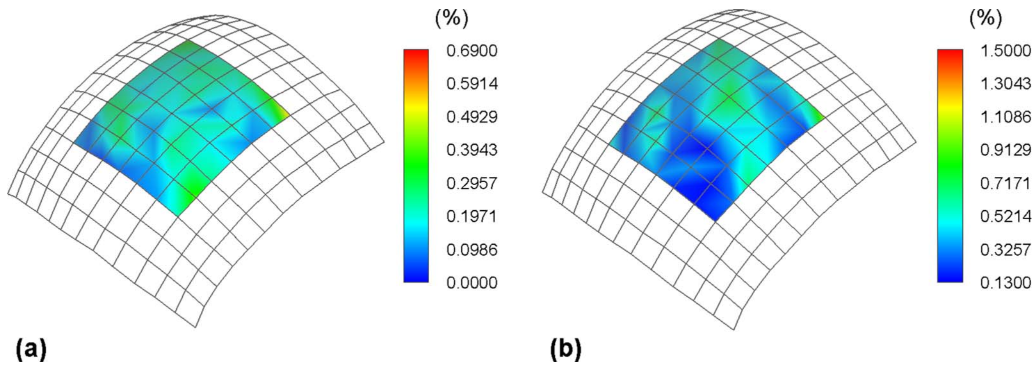

Fig. 5 The distribution of the coaxiality indicator ε (in percentage) in selected configurations: (*a*) configuration 1 and (*b*) configuration 13. Both figures were scaled to fit the canvas for clarity.

fication, was recruited for a forward verification. Figure 9 shows the comparison between the finite element predicted configuration using the identified mean elastic parameters and the experimentally measured configuration. In the left plot, the thick black mesh is the finite element prediction, and the thin gray mesh is the experimental result. The finite element analysis was performed for the boundary-effect-free region where the elastic parameter identification was conducted. Displacement boundary conditions corresponding to the measured nodal positions were applied along the boundary edges. The right plot shows the distribution of the relative error between the predicted and measured nodal positions. As shown in the plots, the computed configuration coincides very well with the experimentally measured one. The position error $e=\|\mathbf{x}-\hat{\mathbf{x}}\|/L$ is less than 0.2% throughout the region.

Table 2 The identified parameters α_i and μ_i for the Ogden model at a selected point

i	α_i	μ_i (N/mm)
1	2.87181	0.05827
2	−1.80776	0.01940
3	−5.76831	-8.477×10^{-5}

4 Discussion and Conclusion

4.1 Advantages and Speculations. The experimental method is designed for delineating the distributive elastic properties in membrane structures. Unlike the traditional specimen tests, which rely on controlled homogeneous deformations, the present method does not require the uniformity of stress and strain in the allowable protocol. Instead, the actual stress and strain generated during a finite inflation motion of a membrane are employed to characterize the distributive properties. To the best knowledge of the authors, this paradigm of parameter identification was not fully

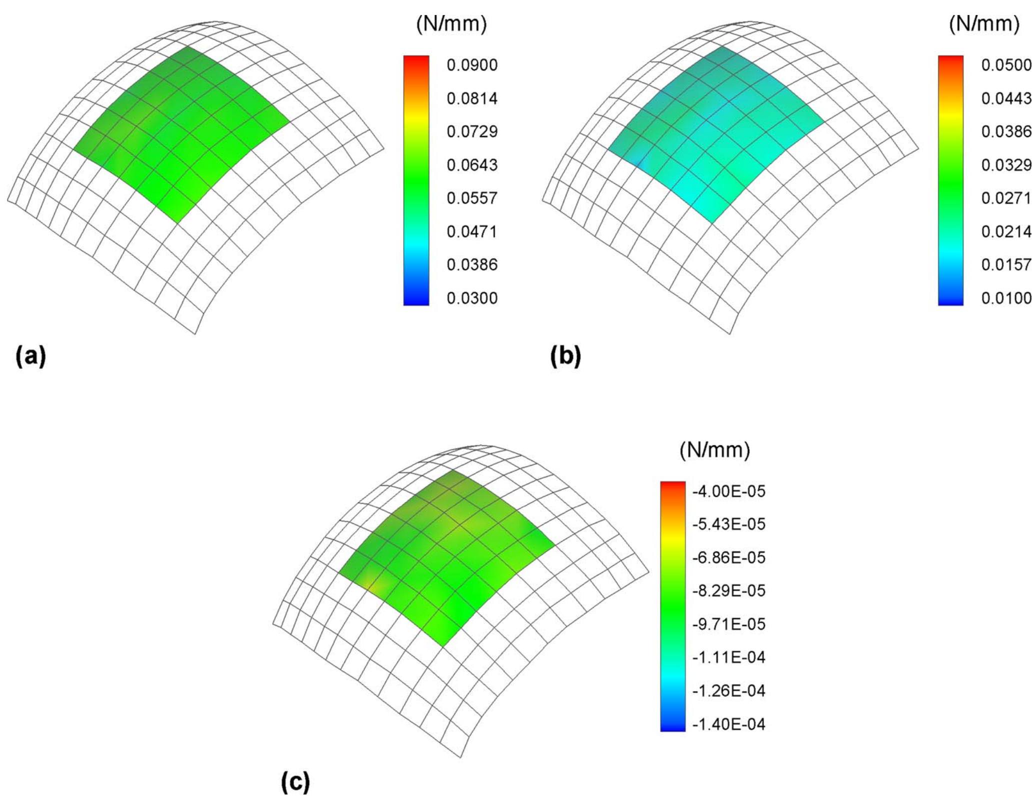

Fig. 6 Identified elasticity parameters of the Ogden model: (*a*) μ_1, (*b*) μ_2, and (*c*) μ_3

Table 3 Ranges, means, and standard deviations of the identified elasticity parameters

	μ_1	μ_2	μ_3
Minimum (N/mm)	0.05470	0.01473	-9.454×10^{-5}
Maximum (N/mm)	0.06453	0.02320	-6.221×10^{-5}
Mean (N/mm)	0.05986	0.01966	-8.154×10^{-5}
SD (N/mm)	0.00239	0.00171	6.923×10^{-6}

explored in the literature. In this paper, we verified experimentally that the method can effectively identify the membrane property and can recover the uniformity of parameters in a known homogeneous rubber balloon. The true value of the method, of course, lies in the potential of delineating the heterogeneous property distribution. So far, there is no effective experimental method that can sharply characterize heterogeneous materials.

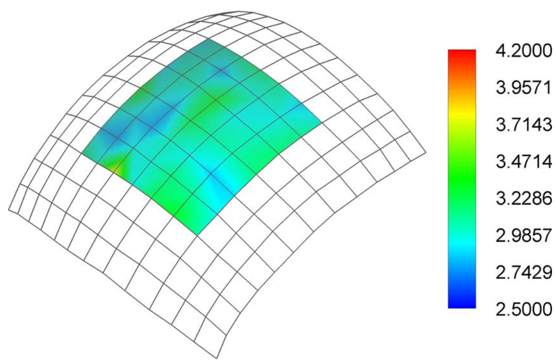

Fig. 7 Distribution of the ratio of μ_1 to μ_2

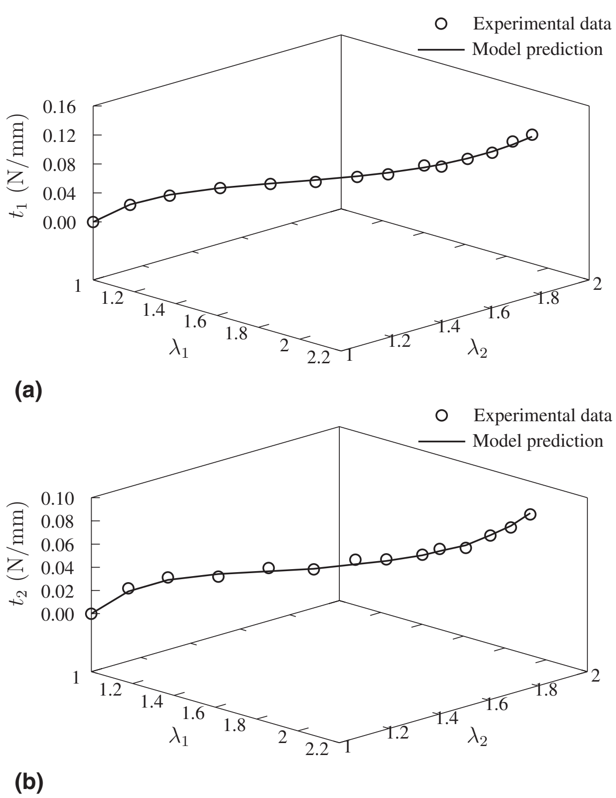

Fig. 8 Comparison between the experimental and the identified tension curves: (*a*) t_1 and (*b*) t_2

In theory, the method is also applicable to anisotropic material. It was demonstrated by Lu et al. [7] for anisotropic materials that the stress solution through the inverse method is also independent of constitutive models and model parameters. However, since anisotropic models contain a symmetry descriptor, which for thin materials is often related to the fiber orientation, the task of property characterization can be much more challenging. In particular, it is unclear whether the symmetry descriptor can be effectively identified from inflation data alone without knowledge of the underlying fiber structure. Research in this direction remains open.

Another noteworthy feature of the method is its nondestructiveness. Due to the elimination of edge force measurement, the membrane does not need to be cut into pieces. The structure in its entirety is tested. This experimental approach provides a framework for designing noninvasive identification methods for thin biological tissues. When augmented with a suitable method for deformation data acquisition, the method may even lead to a noninvasive approach for extracting the in vivo elastic properties of thin living organs.

4.2 Accuracy Issues and Solutions. The accuracy of the method depends critically on the quality of stress and strain data. The former, in turn, is highly sensitive to the surface curvature and thus may be strongly influenced by the inaccurate characterization of the surface geometry. In the present work, a major source of error is the manual node picking. In order to reduce this error, we picked specific corners at the intersection of two lines since it was much easier to determine the position of a sharp corner. The ensuing surface quality for all configurations appeared to be acceptable. If a reconstructed surface has spurious local undulations, it may be necessary to smooth the surface prior to stress computation. Since the strain is computed from the nodal positions via interpolation, its quality is also affected by the aforementioned error. However, the influence on strain accuracy is lesser.

The issue of accuracy can be addressed from several avenues. The first possibility is to use accurate surface data acquisition techniques such as laser scan. Commercial laser scanners can reconstruct solid surfaces to within submicron accuracy. The scanners often output triangulated surface or computer-aided design (CAD) models that can be readily meshed. Second, within the present setting one may increase the mesh density by drawing more nodes on the surface. A finer mesh will capture the surface curvature better and produce more accurate stress results. As a by-product, it will also help sharpening the numerically identified boundary layer. Alternatively, one may use high order elements or other intrinsically smooth approximation methods, such as the meshfree methods [30,31] or the isogeometric method [32]. These methods are more accurate in geometric description, which in turn render more accurate stress solutions.

4.3 Limitations. As discussed in the first part of the paper, the major limitation of this method is that it applies only to thin structures. Strictly speaking, the static determinacy is a property unique to membrane equilibrium, although in some situations the in-plane stress in a shell structure can also be independent of material properties. Hence, this method is limited to membranes and some shell structures.

To some extent, the nondestructiveness of the method limits the range of deformation protocols that one can explore. For instance, one cannot change a principal stretch while maintaining the other one fixed. In this aspect, the individual role of the principal stretches cannot be fully explored. In this regard, the protocols belong to a somewhat restricted subspace in the response surface. The identified material parameters may not accurately reproduce other types of response such as uniaxial tension.

4.4 Concluding Remarks. We conducted experimental validations for the pointwise identification method. We showed that the method can effectively identify the distributions of the elastic parameters of a rubber balloon and can reasonably recover the

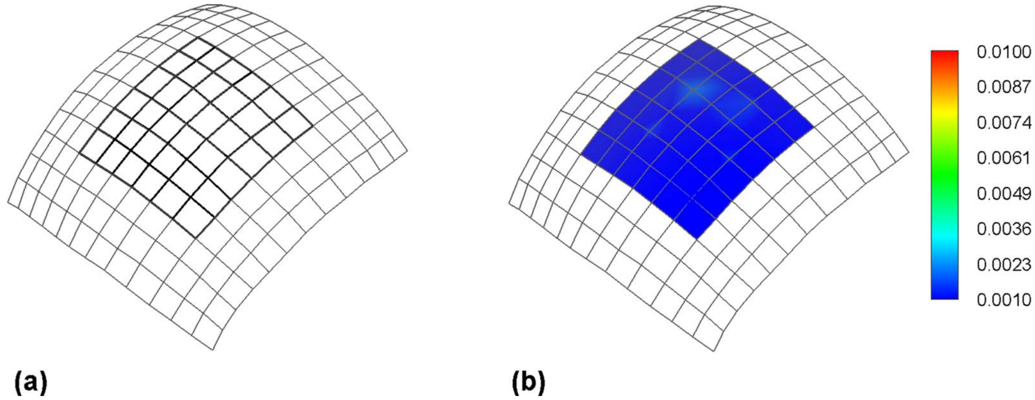

Fig. 9 Comparison between the deformed configuration computed from finite element method using the identified elastic parameters and the experimentally measured configuration. (*a*) Thin gray mesh: experimental (whole domain); thick black mesh: finite element modeled (boundary-effect-free region) and (*b*) distribution of the position error $e = \|\mathbf{x} - \hat{\mathbf{x}}\|/L$.

uniform distribution of properties known to be homogeneous. The derived model can accurately predict the inflation motion at a different pressure. The success of this validation inspires us to further the work, in particular, to validate the method against more complicated constitutive models. The application to heterogeneous materials will be the subject of a forthcoming paper.

Acknowledgment

This work was supported by the National Science Foundation through Grant No. CMS 03-48194 to the University of Iowa. The authors thank Dr. Rahmatalla and Dr. Sultan for their assistance in developing the motion acquisition system.

References

[1] Lu, J., and Zhao, X., 2009, "Pointwise Identification of Elastic Properties in Nonlinear Hyperelastic Membranes—Part I: Theoretical and Computational Developments," ASME J. Appl. Mech., **76**, p. 061013.
[2] Rivlin, R. S., and Saunders, D. W., 1951, "Large Elastic Deformations of Isotropic Materials—VII. Experiments on the Deformation of Rubber," Proc. R. Soc. London, Ser. A, **243**, pp. 251–288.
[3] Govindjee, S., and Mihalic, P. A., 1996, "Computational Methods for Inverse Finite Elastostatics," Comput. Methods Appl. Mech. Eng., **136**, pp. 47–57.
[4] Govindjee, S., and Mihalic, P. A., 1998, "Computational Methods for Inverse Deformations in Quasi-Incompressible Finite Elasticity," Int. J. Numer. Methods Eng., **43**, pp. 821–838.
[5] Lu, J., Zhou, X., and Raghavan, M. L., 2007, "Inverse Elastostatic Stress Analysis in Pre-Deformed Biological Structures: Demonstration Using Abdominal Aortic Aneurysm," J. Biomech., **40**, pp. 693–696.
[6] Lu, J., Zhou, X., and Raghavan, M. L., 2007, "Computational Method of Inverse Elastostatics for Anisotropic Hyperelastic Solids," Int. J. Numer. Methods Eng., **69**, pp. 1239–1261.
[7] Lu, J., Zhou, X., and Raghavan, M. L., 2008, "Inverse Method of Stress Analysis for Cerebral Aneurysms," Biomech. Model. Mechanobiol., **7**, pp. 477–486.
[8] Zhou, X., and Lu, J., 2008, "Inverse Formulation for Geometrically Exact Stress Resultant Shells," Int. J. Numer. Methods Eng., **74**, pp. 1278–1302.
[9] Luhmann, T., Robson, S., Kyle, S., and Harley, I., 2006, *Close Range Photogrammetry: Principles, Techniques and Applications*, Whittles Publishing, Dunbeath, Caithness, Scotland, UK.
[10] Humphrey, J. D., 2002, *Cardiovascular Solid Mechanics: Cells, Tissues, and Organs*, Springer, New York.
[11] Rossettos, J. N., 1966, "Nonlinear Membrane Solutions for Symmetrically Loaded Deep Membranes of Revolution," NASA Technical Report No. NASA TN D-3297.
[12] Wu, C. H., and Peng, D. Y. P., 1972, "On the Asymptotically Spherical Deformation of Arbitrary Membranes of Revolution Fixed Along an Edge and Inflated by Large Pressures—A Nonlinear Boundary Layer Phenomenon," SIAM J. Appl. Math., **23**, pp. 133–152.
[13] Hayes, M., and Knops, R. B., 1966, "On Universal Relations in Elasticity Theory," Z. Angew. Math. Phys., **17**, pp. 636–639.
[14] Beatty, M. F., 1987, "A Class of Universal Relations in Isotropic Elasticity," J. Elast., **17**, pp. 113–121.
[15] Beatty, M. F., 1989, "A Class of Universal Relations for Constrained, Isotropic Elasticity Materials," Arch. Mech., **80**, pp. 299–312.
[16] Pucci, E., and Saccomandi, G., 1997, "On Universal Relations in Continuum Mechanics," Continuum Mech. Thermodyn., **9**, pp. 61–72.
[17] Rivlin, R. S., 2000, "Universal Relations for Elastic Materials," Rendiconti di Matematica e delle sue Applicazioni, Serie VII, **20**, pp. 35–55.
[18] Rivlin, R. S., 1948, "Large Elastic Deformations of Isotropic Materials, IV. Further Developments of the General Theory," Proc. R. Soc. London, Ser. A, **241**, pp. 368–397.
[19] Green, A. E., and Adkins, J. E., 1960, *Large Elastic Deformations and Non-Linear Continuum Mechanics*, Clarendon, Oxford.
[20] Treloar, L. R. G., 1944, "Stress-Strain Data for Vulcanized Rubber Under Various Types of Deformation," Trans. Faraday Soc., **40**, pp. 59–70.
[21] Valanis, K. C., and Landel, R. F., 1967, "The Strain-Energy Function of a Hyperelastic Material in Terms of the Extension Ratios," J. Appl. Phys., **38**, pp. 2997–3002.
[22] Ogden, R. W., 1972, "Large Deformation Isotropic Elasticity—On the Correlation of Theory and Experiment for Incompressible Rubberlike Solids," Proc. R. Soc. London, Ser. A, **326**, pp. 565–584.
[23] Ogden, R. W., 1982, "Elastic Deformation of Rubberlike Solids," *Mechanics of Solids, The Rodney Hill 60th Anniversary Volume*, H. G. Hopkins and M. J. Sewell, eds., Pergamon, Oxford, pp. 499–537.
[24] Treloar, L. R. G., 1976, "The Mechanics of Rubber Elasticity," Proc. R. Soc. London, Ser. A, **351**, pp. 301–330.
[25] Gruttmann, F., and Taylor, R. L., 1992, "Theory and Finite Element Formulation of Rubberlike Membrane Shells Using Principal Stretches," Int. J. Numer. Methods Eng., **35**, pp. 1111–1126.
[26] Sun, W., and Sacks, M. S., 2005, "Finite Element Implementation of a Generalized Fung-Elastic Constitutive Model for Planar Soft Tissues," Biomech. Model. Mechanobiol., **4**, pp. 190–199.
[27] Gill, P. E., Murray, W., and Saunders, M. A., 2005, "SNOPT: An SQP Algorithm for Large-Scale Constrained Optimization," SIAM Rev., **47**, pp. 99–131.
[28] Humphrey, J. D., Strumpf, R. K., and Yin, F. C. P., 1990, "Determination of a Constitutive Relation for Passive Myocardium, II. Parameter-Estimation," ASME J. Biomech. Eng., **112**(3), pp. 340–346.
[29] Taylor, R. L., 2003, FEAP User Manual, V7.5.
[30] Belytschko, T., Liu, W. K., Organ, D., Fleming, M., and Krysl, P., 1996, "Meshless Methods: An Overview and Recent Developments," Comput. Methods Appl. Mech. Eng., **139**, pp. 3–47.
[31] Li, S., and Liu, W. K., 2002, "Meshfree and Particle Methods and Their Application," Appl. Mech. Rev., **55**, pp. 1–34.
[32] Hughes, T. J. R., Cottrell, J. A., and Bazilevs, Y., 2005, "Isogeometric Analysis: CAD, Finite Elements, NURBS, Exact Geometry, and Mesh Refinement," Comput. Methods Appl. Mech. Eng., **194**, pp. 4135–4195.

Derivation of a Damage Sensitive Feature Using the Haar Wavelet Transform

K. Krishnan Nair
Department of Civil and Environmental Engineering,
John A. Blume Earthquake Engineering Center,
Stanford University,
Stanford, CA 94305
e-mail: kknair@stanford.edu

Anne S. Kiremidjian[1]
Professor
Department of Civil and Environmental Engineering,
Stanford University,
Stanford, CA 94305
e-mail: ask@stanford.edu

In this paper, a damage sensitive feature based on the wavelet transform of the vibration signal is derived. The theoretical aspects of wavelet decomposition of vibration signals are presented. It is shown that the energies of the wavelet coefficients at appropriate scales can be used as damage sensitive features. Expressions for the energies of wavelet coefficients using the Haar wavelet basis function are derived for a single degree and a multidegree of freedom system. It is shown that the energies of the wavelet coefficients extracted at higher scales are functions of the physical parameters of the system and the loading function. Finally, the migration of damage sensitive feature vectors with damage is illustrated for the ASCE Benchmark Structure. [DOI: 10.1115/1.3130821]

Keywords: structural safety, damage assessment, data analysis, vibration analysis

1 Introduction

Structural health monitoring (SHM) has been receiving considerable attention in the civil engineering community during the past decade [1–6]. Structural health monitoring consists of the following two steps: (a) diagnosis, which involves damage identification, localization, and quantification; and (b) prognosis, which includes the structure's residual capacity estimation and residual life forecasting [7]. Recent research in damage detection algorithms shows the extensive use of signal processing and pattern classification techniques [8]. Signal processing techniques were introduced for damage diagnosis by Farrar and co-workers [8–10]. Such methods rely on the signatures obtained from the recorded vibration, strain, or other data to extract features that change with the onset of damage. In particular, damage diagnosis algorithms require the tracking of some damage sensitive features. The main focus of this paper is the derivation of a damage sensitive feature using the Haar wavelet transform and establishing a closed form relation with the physical parameters of the structural system.

In the context of SHM, earlier work was carried out in wavelet based system identification of nonlinear structures by Staszewski [11], Ghanem and Romeo [12] and Kijewski and Kareem [13]. Ghanem and Romeo [12] used the discrete wavelet transform to identify the parameters of a time varying system in the presence of noise. Kijewski and Kareem [13] proposed guidelines for selection of wavelet central frequencies, its use in modal separation, and in addition developed a padding scheme to account for end effects. Spanos and Failla [14] reviewed the literature on the applications of wavelet transforms to vibration problem. In the context of this paper, they investigated system identification and damage detection with wavelets. Hou et al. [15] used the wavelet transform to study the sudden jump in the signal when the stiffness of the system is changed.

In recent studies conducted by the authors [16,17], the autoregressive moving average models were used to fit the vibration signals obtained from a sensor. However, these models are valid for stationary signals. Thus, in this study, the continuous wavelet transform is used to decompose the signal to account for nonstationarity. It is important to note that although the application of the model developed in this paper is for stationary signals, it can also be applied to nonstationary signals with appropriate modifications. A damage sensitive feature relating to the energies of the wavelet coefficients of the vibration signal is derived. It is shown that the energies of wavelet coefficients of acceleration signals at higher scales are related to parameters of the physical system and thus are particularly suitable for the purpose of damage detection. In order to illustrate this wavelet based method for damage detection, it is applied to the ASCE Benchmark Structure [18].

The paper is organized as follows. In Sec. 2, the theoretical aspects of wavelet decomposition of vibration signals are discussed. The continuous wavelet transform of a signal is written in terms of the Fourier transform of the signal and the wavelet basis. In Secs. 3 and 4, this framework is used to derive a closed form expression for the energies of the Haar wavelet for a single degree and multiple degree of freedom systems, respectively. The relationship of the damage sensitive feature to physical parameters of the structure such as mode shapes, stiffnesses, and damping ratios is demonstrated. Finally, in Sec. 5, the damage sensitive feature is used to discriminate between a damaged and an undamaged state using vibration signals obtained from the ASCE Benchmark Structure.

2 Properties of the Continuous Wavelet Transform

A wavelet is a function $\psi(t) \in \mathbf{L}^2(\mathfrak{R})$ (the space of square integrable functions) with the following properties [19]:

$$\int_{-\infty}^{\infty} \psi(t)dt = 0$$

$$\|\psi\| = 1 \tag{1}$$

where $\|.\|$ is the $\mathbf{L}^2$ norm. The mother wavelet function $\psi(t) \in \mathbf{L}^2(\mathfrak{R})$ that is dilated/scaled by a and translated by b, denoted by $\psi_{a,b}(t)$, is given as

$$\psi_{a,b}(t) = \frac{1}{\sqrt{a}}\psi\left(\frac{t-b}{a}\right) \tag{2}$$

where $\|\psi_{a,b}\| = 1$. Then the continuous wavelet transform (CWT) of a function $f(t) \in \mathbf{L}^2(\mathfrak{R})$ is given as

[1] Corresponding author.

Contributed by the Applied Mechanics Division of ASME for publication in the Journal of Applied Mechanics. Manuscript received March 4, 2008; final manuscript received March 4, 2008; published online July 27, 2009. Review conducted by Professor Sridhar Krishnaswamy.

$$Wf(a,b) = \int_{-\infty}^{\infty} f(t)\frac{1}{\sqrt{a}}\psi^*\left(\frac{t-b}{a}\right)dt \tag{3}$$

where * represents the complex conjugate. It should be noted that Eq. (3) is a convolution integral.

The main advantage of wavelet analysis over conventional spectral methods such as Fourier methods is that data are localized in both time and scale domains [19]. At lower scales, the wavelet basis function has a smaller support and thus is better able to localize transient phenomena such as discontinuities in the data set. Similarly, at higher scales, the wavelet basis function has a wider support, which helps in identifying long range phenomena.

In the context of this study, it is useful to develop the wavelet transform in terms of the Fourier transform (FT) of a function rather than the function itself. Thus we define the Fourier transform of $f(x) \in \mathbf{L}^2(\Re)$ as [20]

$$F(s) = \int_{-\infty}^{\infty} f(t)\exp(-jts)dt \tag{4}$$

where j is the square root of -1. The inverse Fourier transform (IFT) of $F(s)$ is obtained from

$$f(t) = \frac{1}{2\pi}\int_{-\infty}^{\infty} F(s)\exp(jts)ds \tag{5}$$

The power theorem is applied to obtain [20]

$$\int_{-\infty}^{\infty} f(t)\psi^*_{a,b}(t)dt = \frac{1}{2\pi}\int_{-\infty}^{\infty} F(s)\Psi^*_{a,b}(s)ds \tag{6}$$

where $\Psi(s)$ is the FT of $\psi(t)$.

By substituting Eq. (6) in Eq. (3), it follows that

$$Wf(a,b) = \frac{1}{2\pi}\int_{-\infty}^{\infty} F(s)\Psi^*_{a,b}(s)ds \tag{7}$$

The Fourier transform $\Psi_{a,b}(s)$ of the wavelet function $\psi_{a,b}(t)$ is obtained as follows:

$$\Psi_{a,b}(s) = \int_{-\infty}^{\infty} \psi_{a,b}(t)\exp(-jts)dt = \int_{-\infty}^{\infty} \frac{1}{\sqrt{a}}\psi\left(\frac{t-b}{a}\right)\exp(-jts)dt$$
$$= \sqrt{a}\exp(-jsb)\Psi(as) \tag{8}$$

Thus, substituting Eq. (8) in Eq. (7), Eq. (7) is rewritten as

$$Wf(a,b) = \frac{1}{2\pi}\int_{-\infty}^{\infty} F(s)\sqrt{a}\exp(jsb)\Psi^*(as)ds \tag{9}$$

In this paper, the Haar wavelet basis is considered. A similar analysis with the Morlet wavelet transform can be found elsewhere [21]. A close investigation of the Haar wavelet will provide a physical understanding of wavelet coefficients of an acceleration signal and will provide a basis for correlating these coefficients to damage sensitive features in a pattern classification scheme. The reason that this wavelet bases are investigated is because they have a closed analytical form and provide a systematic derivation of the energies of the wavelet coefficients. This approach can be applied to other wavelet bases; however, they cannot be expressed in a closed mathematical form making it difficult to represent. In Sec. 2.1, we use the Fourier transform of the Haar wavelet basis function to derive the wavelet coefficients of a function $f(t)$.

For the purposes of applying a statistical pattern classification method for damage detection, we define the energy of the wavelet coefficients at appropriate scales as the damage sensitive feature. Thus, the energy of the wavelet coefficients at scale a, E_a, is defined as follows:

$$E_a = \sum_{b=1}^{K} |W\ddot{x}(a,b)|^2 \tag{10}$$

where $W\ddot{x}(a,b)$ is the wavelet coefficient of the acceleration signal at the ath scale and bth time step, K is the number of data points in the signal, and $|\cdot|$ is the absolute value of the quantity. In Secs. 3 and 4, we will derive a closed form expression for the damage sensitive feature using the Haar wavelet transform for single degree of freedom (SDOF) and multiple degree of freedom (MDOF) systems.

In this study, damage detection is carried out by using the energy of the coefficients of the sixth dyadic scale for the Haar wavelet basis function. Selection of these scales has to do with the support of the scaled wavelet basis. The higher scales have a larger support of wavelet basis, thus increasing the likelihood of detecting long term changes. This implies that the wavelet coefficients at higher scales would contain information about vibration modes at lower natural frequencies. In this particular application, ambient vibration data are being analyzed. In such applications, damage detection would generally affect the lower modes because higher modes are unlikely to be excited during ambient vibrations. Thus wavelet coefficients at higher scales would be useful in damage detection. Also, at higher scales, the wavelet coefficients do not pick up a transient phenomenon such as spikes and jumps, thus eliminating problems with noisy data.

Also, at higher scales, the wavelet coefficients do not pick up a transient phenomenon such as spikes and jumps, thus eliminating problems with noisy data.

In Sec. 2.1 we use the Fourier transform of the Haar wavelet basis to derive the wavelet coefficients of a function $f(t)$.

2.1 Haar Wavelet.

The Haar wavelet is defined as follows:

$$\psi(t) = \begin{cases} 1 & \text{for } 0 \le t < 0.5 \\ -1 & \text{for } 0.5 \le t < 1.0 \end{cases} \tag{11}$$

The FT of the Haar wavelet can be shown to be equal to

$$\Psi(s) = \frac{1}{js}\left[1 - \exp\left(-\frac{js}{2}\right)\right]^2 \tag{12}$$

Thus, from Eqs. (9) and (12), the wavelet coefficients using the Haar basis are given as

$$W_Hf(a,b) = \frac{j}{2\pi\sqrt{a}}\int_{-\infty}^{\infty} \frac{F(s)}{s}\exp(jsb)\left[1 - \exp\left(\frac{jas}{2}\right)\right]^2 ds \tag{13}$$

The Haar wavelet and its Fourier transform are shown in Fig. 1.

3 Derivation of the Damage Sensitive Feature Using Wavelet Coefficients of Acceleration Signals for a SDOF System

Consider a single degree of freedom (SDOF) system, with mass m, damping coefficient c, and undamaged stiffness coefficient k, subject to a forcing function $g(t)$ whose equation of motion is given as

$$m\ddot{x} + c\dot{x} + kx = g(t) \tag{14}$$

Taking the Fourier transform of Eq. (14) and applying the derivative rule $F(d^nf(t)/dt^n) = (js)^nF(s)$ the following expression is obtained:

$$(-s^2m + jcs + k)X(s) = G(s) \tag{15}$$

where $X(s)$ and $G(s)$ are the FTs of the displacement and forcing function, respectively. Here, we have made the assumption that the system is linear and the forcing function is stationary. The first assumption is valid, since when we compare the damage with the undamaged system we are looking at an equivalent linear system

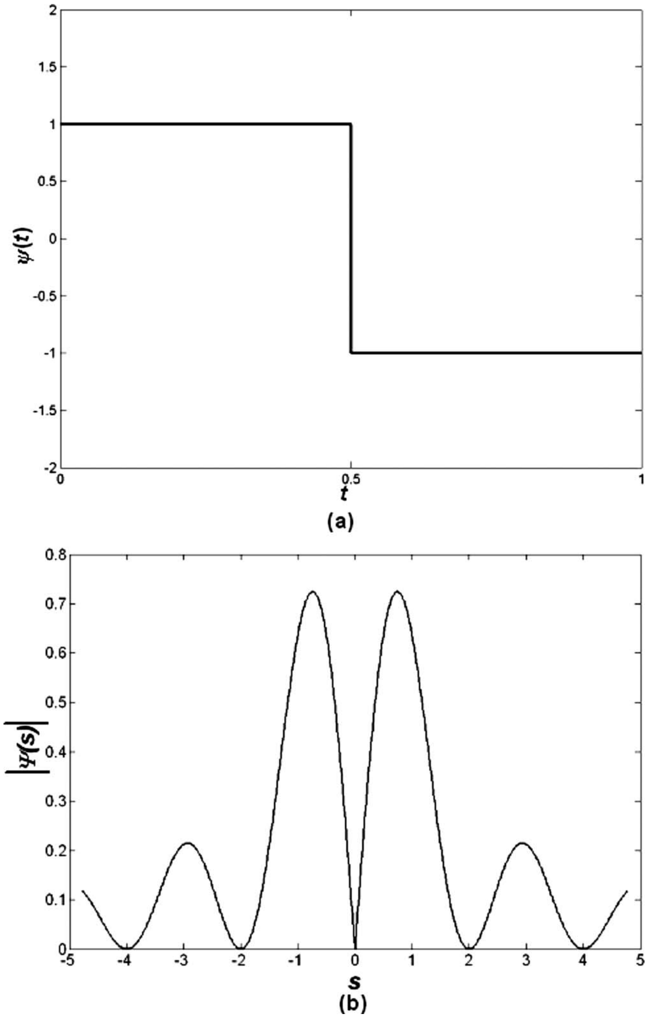

Fig. 1 Haar wavelet: (*a*) Haar basis function and (*b*) its Fourier transform

with reduced stiffness. The second assumption is not always valid in practice; however, we can segment the signal so that each signal is quasistationary.

With these assumptions, we can estimate the FT of the acceleration as

$$\ddot{x}(s) = \mathrm{FT}(\ddot{x}(t)) = -s^2X(s) = \frac{-s^2G(s)}{-s^2m + jcs + k} \tag{16}$$

Using the framework developed in Sec. 2.1 and Eq. (16), expressions for the wavelet transform of acceleration signals are derived next.

3.1 Haar Wavelet Transform of Acceleration Signals. From Eqs. (9) and (16), it can be shown that

$$W\ddot{x}(a,b) = \frac{1}{2\pi}\int_{-\infty}^{\infty} \frac{-s^2G(s)}{(-s^2m + jcs + k)}\sqrt{a}\,\exp(jsb)\Psi^*(as)ds \tag{17}$$

In particular, Haar wavelet coefficients of the acceleration signal can be derived as

$$W_H\ddot{x}(a,b) = \frac{j}{2\pi\sqrt{a}}\int_{-\infty}^{\infty} \frac{-s^2G(s)}{(-s^2m + jcs + k)s}\exp(jsb)\left[1 - \exp\left(\frac{jas}{2}\right)\right]^2 ds \tag{18}$$

In order to solve the above integral, the residue theorem and contour integration is used [22]. The integral I_H is defined as

$$I_H = \int_{-\infty}^{\infty} \frac{sG(s)}{(-s^2m + jcs + k)}\exp(jsb)\left[1 - \exp\left(\frac{jas}{2}\right)\right]^2 ds \tag{19}$$

For an underdamped system, i.e., the damping ratio $\xi = c/2m\omega_n$ is less than 1, the damped natural frequency $\omega_d = \omega_n\sqrt{1-\xi^2}$, ω_n is the natural frequency of the SDOF system, and the poles of Eq. (19), p and q, are calculated as

$$p,q = j\xi\omega_n \pm \omega_n\sqrt{1-\xi^2} \tag{20}$$

The residues of the integral in Eq. (19) are calculated as follows. A function $h(z)$ in the complex variable z is first defined as

$$h(z) = \frac{zG(z)}{(z-p)(z-q)}\exp(jzb)\left[1 - \exp\left(\frac{jaz}{2}\right)\right]^2 \tag{21}$$

It can be proved that $h(z)$ is analytic everywhere in the complex plane except at $z=p$ and $z=q$. Note that $h(z)$ is analytic at $z=0$, since $1-\exp[jaz/2]$ is analytic at $z=0$. Using the residue theorem, it can be shown that

$$I_H = 2\pi j(R_p + R_q) \tag{22}$$

where R_p and R_q are the residues of $h(z)$ evaluated at p and q, respectively. This proof of Eq. (22) is included in Sec. 7. R_p is given as

$$R_p = \lim_{z\to p}(z-p)h(z) = \frac{pG(p)\exp(jpb)\left[1 - \exp\left(\frac{jap}{2}\right)\right]^2}{p-q} \tag{23}$$

Similarly R_q is derived as

$$R_q = \frac{qG(q)\exp(jqb)\left[1 - \exp\left(\frac{jaq}{2}\right)\right]^2}{q-p} \tag{24}$$

Here we assume that the $G(s)$ is defined on the complex plane. Using the residue theorem, it can be shown that

$$W_H\ddot{x}(a,b) = \frac{1}{\sqrt{a}}[R_p + R_q] \tag{25}$$

It is noted the residues R_p and R_q are related to the physical parameters of the system ω_n and ξ, and also on the loading on the SDOF system.

3.2 Damage Sensitive Feature. In this section, the damage sensitive feature is derived for a SDOF system using the Haar basis function. Using the relationship

$$|W_H\ddot{x}(a,b)|^2 = \frac{1}{a}(R_p + R_q)(R_p + R_q)^* = \frac{1}{a}[|R_p|^2 + |R_q|^2 2\,\mathrm{Re}(R_pR_q^*)] \tag{26}$$

where $\mathrm{Re}(\cdot)$ is the real part of the complex quantity, we can conclude that

$$|W_H\ddot{x}(a,b)|^2 \le \frac{1}{a}[|R_p|^2 + |R_q|^2 + 2|R_pR_q^*|] \tag{27}$$

It is noted that $|p| = |q| = \omega_n$. Also, we observe that

$$|\exp(jpb)| = |[\exp(jb\omega_d)\exp(-b\xi\omega_n)]| = \exp(-b\xi\omega_n)$$

$$|\exp(jqb)| = \exp(-b\xi\omega_n) \tag{28}$$

and

$$\begin{aligned}\left|\left[1-\exp\left(\frac{jap}{2}\right)\right]^2\right| &= \left|\left[1-\exp\left(\frac{jap}{2}\right)\right]\right|^2 \\ &= \left|\left[1-\exp\left(\frac{ja\omega_d}{2}\right)\exp\left(\frac{-a\xi\omega_n}{2}\right)\right]\right|^2 \\ &= \left|\left[1-c_1\exp\left(\frac{ja\omega_d}{2}\right)\right]\right|^2\end{aligned} \tag{29}$$

Similarly, it is observed that

$$\begin{aligned}\left|\left[1-\exp\left(\frac{jaq}{2}\right)\right]^2\right| &= \left|\left[1-\exp\left(\frac{ja\omega_d}{2}\right)\exp\left(\frac{a\xi\omega_n}{2}\right)\right]\right|^2 \\ &= \left|\left[1-c_2\exp\left(\frac{ja\omega_d}{2}\right)\right]\right|^2\end{aligned} \tag{30}$$

where $c_1 = 1/c_2 = \exp(-a\xi\omega_n/2)$.

The coefficient c_1 is a decreasing term in a, whereas c_2 is an increasing term in a. Since we consider higher scales to compute the energies, Eqs. (29) and (30) can be approximated as follows:

$$\begin{aligned}\left|\left[1-c_1\exp\left(\frac{ja\omega_d}{2}\right)\right]\right|^2 &= 1+c_1^2-2c_1\cos\left(\frac{a\omega_d}{2}\right) \\ &\approx 1-2c_1\cos\left(\frac{a\omega_d}{2}\right)\end{aligned}$$

$$\left|\left[1-c_2\exp\left(\frac{ja\omega_d}{2}\right)\right]\right|^2 \approx 1+c_2^2 \tag{31}$$

Thus, using Eqs. (28) and (31) we can conclude that

$$|R_p|^2+|R_q|^2 \approx \frac{\exp(-2b\xi\omega_n)\left[|G(p)|^2\left(1-2c_1\cos\left(\frac{a\omega_d}{2}\right)\right)^2+|G(q)|^2(1+c_2^2)^2\right]}{4(1-\xi^2)} \tag{32}$$

In a similar fashion, we can show that

$$|R_pR_q^*| \approx \frac{|G(p)G(q^*)|(1+c_2^2)}{4(1-\xi_2^2)} \tag{33}$$

The expression in Eq. (33) is a constant (i.e., not a function of b) and thus is not included in Eq. (34).

$$|W_H\ddot{x}(a,b)|^2 \approx \frac{\exp(-2b\xi\omega_n)\left[|G(p)|^2\left(1-2c_1\cos\left(\frac{a\omega_d}{2}\right)\right)^2+|G(q)|^2(1+c_2^2)^2\right]}{4a(1-\xi^2)} \tag{34}$$

where $c_1 = 1/c_2 = \exp(-a\xi\omega_n/2)$. For an acceleration signal sampled at $1/\Delta t$ Hz with K data points, the energy at scale a for the Haar basis, E_a^{Haar}, is derived using Eq. (34),

$$E_a^{\text{Haar}} \approx \frac{\left[|G(p)|^2\left(1-2c_1\cos\left(\frac{a\omega_d}{2}\right)\right)^2+|G(q)^2|(1+c_2^2)^2\right]}{4a(1-\xi^2)}\sum_{b=1}^{K}\exp(-2b\xi\omega_n) = \Lambda_{\text{Haar}}(a)\frac{\exp(-2\xi\omega_n\Delta t)[1-\exp(-2K\xi\omega_n\Delta t)]}{1-\exp(-2\xi\omega_n\Delta t)} \tag{35}$$

where

$$\Lambda_{\text{Haar}} = (a)\frac{\left[|G(p)|^2\left(1-2c_1\cos\left(\frac{a\omega_d}{2}\right)\right)^2+|G(q)^2|(1+c_2^2)^2\right]}{4a(1-\xi^2)}$$

Equation (35) consists of Λ_{Haar}, which is a function of c_1 and c_2. Since the damage sensitive feature is obtained at higher scales (i.e., the value of a increases) the value of c_1 is not significant. As the extent of damage increases, the values of c_1 increase and c_2 decreases. In such cases, c_2 will dominate; thus E_a^{Haar} is sensitive to damage at higher scales.

4 Derivation of the Damage Sensitive Feature Using Wavelet Coefficients of Acceleration Signals for a MDOF System

We next consider a structural system with N degrees of freedom (DOFs) with $\mathbf{M}$, $\mathbf{C}$, and $\mathbf{K}$ defined as the mass, damping, and stiffness matrices (of size $N\times N$), respectively. The forcing function is denoted by $\mathbf{g}(t)$. For a proportionally damped system and assuming that the damping ratio in each mode is equal to ξ, the transfer function of the displacement at the kth DOF $x_k(t)$ and the forcing function at the lth DOF, $H_{kl}(s)$, can be derived as [23]

$$H_{kl}(s) = \frac{X_k(s)}{G_l(s)} = \sum_{r=1}^{N}\frac{\phi_{kr}\phi_{lr}}{(\omega_r^2-s^2+2j\xi\omega_r s)} \tag{36}$$

where $X_k(s)$ and $G_l(s)$ are the Fourier transform of the displacement at the kth DOF $x_k(t)$ and the forcing function at the lth DOF $g_l(t)$. Thus, the FT of the acceleration $\ddot{x}_k(t)$ is given as

$$\ddot{x}_k(s)\sum_{r=1}^{N}\frac{-s^2\phi_{kr}\phi_{lr}G_l(s)}{(\omega_2^2-s^2+2j\xi\omega_r s)} \tag{37}$$

where ω_r is the rth modal natural frequency, ϕ_{kr} and ϕ_{lr} are the kth and lth elements of the mass normalized rth mode shape vector ϕ_r. Using similar principles utilized in Sec. 3, the wavelet coefficients of a MDOF system are derived in Sec. 4.1.

4.1 Wavelet Coefficients of Acceleration Signals. With respect to the Haar wavelet, the wavelet coefficient of the acceleration $\ddot{x}_k(t)$ is derived as

$$W_H\ddot{x}_k(a,b)=\frac{j}{2\pi\sqrt{a}}\int_{-\infty}^{\infty}\sum_{r=1}^{N}\frac{-s\phi_{kr}\phi_{lr}G_l(s)}{(\omega_r^2-s^2+2j\xi\omega_r s)}\times\exp(jsb)\left[1-\exp\left(\frac{jas}{2}\right)\right]^2 ds \quad (38)$$

In order to calculate the above integral, we will use principles of contour integration as is done for SDOF systems presented in Sec. 3. Again, the integral I_r for the rth vibration mode is defined as

$$I_r=\int_{-\infty}^{\infty}\frac{-s\phi_{kr}\phi_{lr}G_l(s)}{(\omega_r^2-s^2+2j\xi\omega_r s)}\exp(jsb)\left[1-\exp\left(\frac{jas}{2}\right)\right]^2 ds \quad (39)$$

The poles of Eq. (39), $p_{1,r}$ and $p_{2,r}$, are calculated as

$$p\begin{Bmatrix}1,r\\2,r\end{Bmatrix}=j\xi\omega_r \pm \omega_r\sqrt{1-\xi^2} \quad (40)$$

The function $t(z)$ in the complex variable z is defined as

$$t(z)=\frac{\phi_{kr}\phi_{lr}zG_l(z)}{(z-p_1)(z-p_2)}\exp(jzb)\left[1-\exp\left(\frac{jaz}{2}\right)\right]^2 \quad (41)$$

It can be proven that $t(z)$ is analytic everywhere in the complex plane except at $z=p_{1,r}$ and $z=p_{2,r}$. Using the residue theorem, it can be shown that $I_r=2\pi j(R_{1,r}+R_{2,r})$, where $R_{1,r}$ and $R_{2,r}$ are the residues of $t(z)$ evaluated at $p_{1,r}$ and $p_{2,r}$, respectively. $R_{1,r}$ and $R_{2,r}$ are evaluated as

$$R_{1,r}=\lim_{z\to p_{1,r}}(z-p_{1,r})t(z)=\frac{\phi_{kr}\phi_{lr}p_{1,r}G_l(p_{1,r})\exp(jp_{1,r}b)\left[1-\exp\left(\frac{jap_{1,r}}{2}\right)\right]^2}{p_{1,r}-p_{2,r}} \quad (42)$$

Similarly $R_{2,r}$ can be derived as

$$R_{2,r}=\frac{\phi_{kr}\phi_{lr}p_2G_l(p_{2,r})\exp(jp_{2,r}b)\left[1-\exp\left(\frac{jap_{2,r}}{2}\right)\right]^2}{p_{2,r}-p_{1,r}} \quad (43)$$

Using the residue theorem, it can be shown that

$$W_H\ddot{x}(a,b)=\frac{1}{\sqrt{a}}\left[\sum_{r=1}^{N}R_{1,r}+R_{2,r}\right] \quad (44)$$

Again, we approximate the energy of the Haar wavelet coefficients of acceleration $\ddot{x}_k(t)$ at scale a as $E_{a,k}^{\mathrm{Haar}}\approx 1/a[\sum_{r=1}^{N}|R_{1,r}|^2+|R_{2,r}|^2]$. The rth damped natural frequency $\omega_{d,r}$ is given as $\omega_{d,r}=\omega_r\sqrt{1-\xi^2}$. We define $c_{1,r}=1/c_{2,r}=\exp(-a\xi\omega_r/2)$.

Using similar approximations as in Sec. 3, we obtain the following expression for $E_{a,k}^{\mathrm{Harr}}$:

$$E_a^{\mathrm{Haar}}\approx\sum_{b=1}^{K}\sum_{r=1}^{N}\frac{\phi_{kr}^2\phi_{lr}^2\exp(-2b\xi\omega_r)\left[|G_l(p_{1,r})|^2\left(1-2c_1\cos\left(\frac{a\omega_{d,r}}{2}\right)\right)^2+|G_l(p_{2,r})|^2(1+c_2^2)^2\right]}{4a(1-\xi^2)} \quad (45)$$

Interchanging the summations, we can derive that

$$E_a^{\mathrm{Haar}}\approx\sum_{r=1}^{N}\Lambda_{\mathrm{Haar}}(a,r)\phi_{kr}^2\phi_{lr}^2\frac{\exp(-2\xi\omega_r\Delta t)[1-\exp(-2K\xi\omega_r\Delta t)]}{[1-\exp(-2\xi\omega_r\Delta t)]} \quad (46)$$

where

$$\Lambda_{\mathrm{Haar}}(a,r)=\frac{\left[|G_l(p_{1,r})|^2\left(1-2c_{1,r}\cos\left(\frac{a\omega_{d,r}}{2}\right)\right)^2+|G_l(p_{2,r})|^2(1+c_{2,r}^2)^2\right]}{4a(1-\xi^2)}$$

It is again observed that the energies of the wavelet coefficients for the Haar wavelet basis contain information of the physical system. E_a^{Haar} contains modal information of the system through the kth and lth mass normalized eigenvectors $\boldsymbol{\phi}_k$ and $\boldsymbol{\phi}_l$. As the extent of damage increases and which mode is excited due to the increase in damage, $c_{1,r}$ increases and $c_{2,r}$ decreases. As the value of a increases, the value of $c_{1,r}$ is not significant. In such cases, $c_{2,r}$ will dominate. Thus E_a^{Haar} can be used as an indicator of damage.

Based on the above derivation, it can be concluded that as the stiffness decreases due to damage, the response of the structure will change resulting in changes in the energies based on the wavelet coefficients. Consequently, the damage sensitive feature based on the wavelet coefficients can capture this change in measurements from an undamaged to a damaged structural state.

5 Application

In order to test the validity of the above derived damage sensitive feature, numerically simulated data sets from the ASCE Benchmark Structure are used. The data from the ASCE Benchmark Structure are particularly useful for this purpose because damage was introduced systematically and measurements were obtained after every stage of damage was introduced. The structure is a four story, two-bay by two-bay steel braced frame, illustrated in Fig. 2 [18]. There are 16 sensors (measuring acceleration) in the braced frame, and their placement and direction of measured acceleration are shown in Fig. 3 [18]. Damage is simulated by removing braces in various combinations, resulting in a loss of overall stiffness. The damage patterns (DPs) include the following:

- damage pattern 0: undamaged structure
- damage pattern 1: removal of all braces on the first floor
- damage pattern 2: removal of all braces on the first and third floors
- damage pattern 3: removal of one brace on the first floor
- damage pattern 4: removal of one brace on the first and third floors
- damage pattern 5: damage Pattern 4+loosening of bolts
- damage pattern 6: reduction in the stiffness of a brace to 1/3 of its original value

Damage patterns 6 and 3 are minor, damage patterns 4 and 5 are

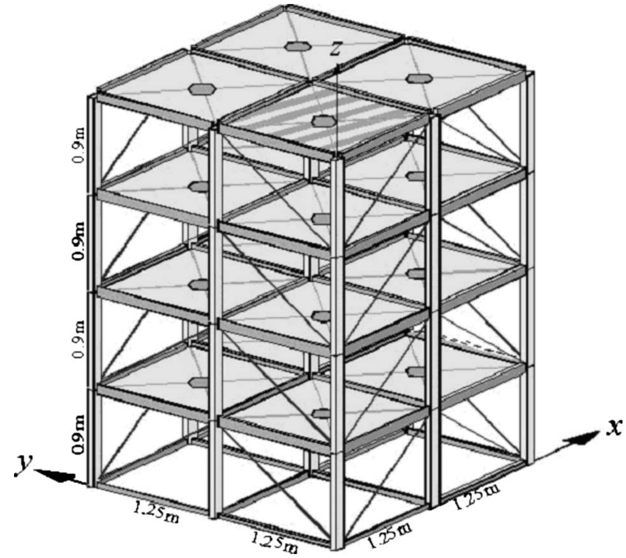

Fig. 2 ASCE Benchmark Structure [18]

moderate, and damage patterns 1 and 2 are major. Additional information on the ASCE Benchmark structure is available at http://cive.seas.wustl.edu/wusceel/asce.shm/benchmarks.htm.

5.1 Damage Detection. Damage detection is performed under the premise that the damage sensitive feature will migrate with the onset of damage. In this study, the damage sensitive feature is defined as the energy of the wavelet coefficients at the sixth dyadic scale for the Haar wavelet (denoted by $\mathbf{E}_6$). It is hypothesized that damage occurs if there is a difference in the mean values of the damage sensitive feature before ($\mu_{\mathrm{DSF,undamaged}}$) and after damage ($\mu_{\mathrm{DSF,undamaged}}$). This can be achieved by using a statistical hypothesis test [16], which is outside the scope of this paper. The reason for choosing the sixth dyadic scale for the Haar wavelet is because this scale is optimal for capturing important characteristics of the signal, which are sensitive to damage for this specific application. In general, one would have to investigate several scales to determine the best candidate for damage detection.

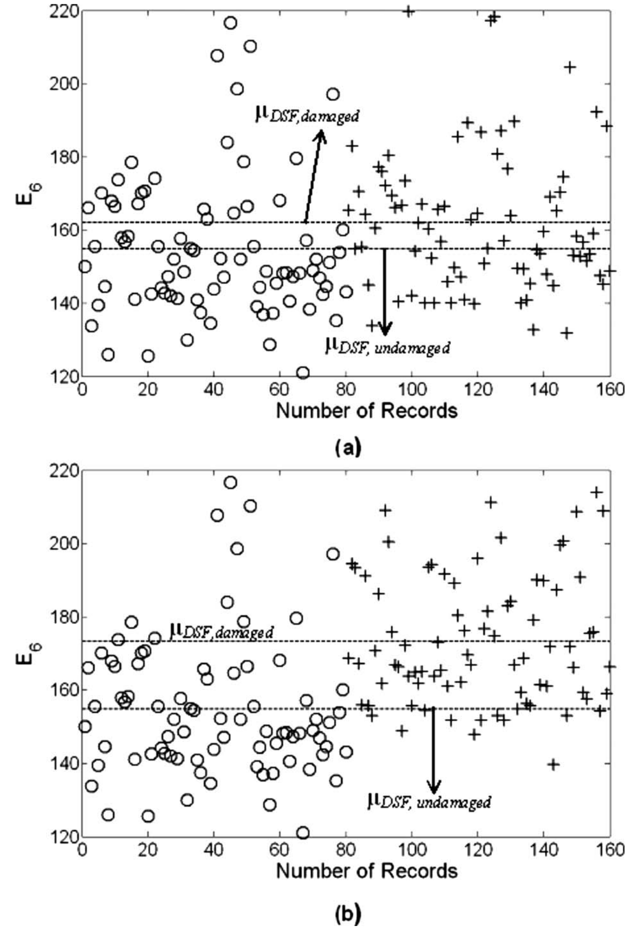

Fig. 4 Migration of the Haar wavelet based damage sensitive feature $\mathbf{E}_6$ for sensor 2 with damage for minor patterns: (*a*) damage pattern 6 and (*b*) damage pattern 3

The data from all 16 sensors were analyzed at each damage state, and damage states 1–6 were identified by all sensors. Although damage states 4 and 5 were identified by all sensors as well, no distinction could be found between these states. It is important to recognize that damage state 4 is the same as damage state 5 but in addition a bolt is loosened in damage pattern 5. This type of damage is very localized and unless the sensor is placed directly on the bolt, the damage state not likely to be detected even by the sensor closes to the loosened bolt. In the following discussion we present the results for representative sensors. These are sensors 2, 3, and 9.

5.1.1 Sensor 2. Figure 4 shows the migration of the features extracted from signals from sensor 2, from an undamaged state to the damaged state for damage patterns 6 and 3. In the case of damage pattern 6 (Fig. 4(*a*)), where the stiffness of a brace is partially reduced on the first floor, it is observed that there is a small separation between the means of $\mathbf{E}_6$. However, this separation is larger for damage pattern 3 (Fig. 4(*b*)), where a brace is removed on the first floor. This difference in the means is significantly larger in the case of major damage patterns 1 and 2 (Fig. 5). It is also noted that the variance of the clouds increases with increase in damage.

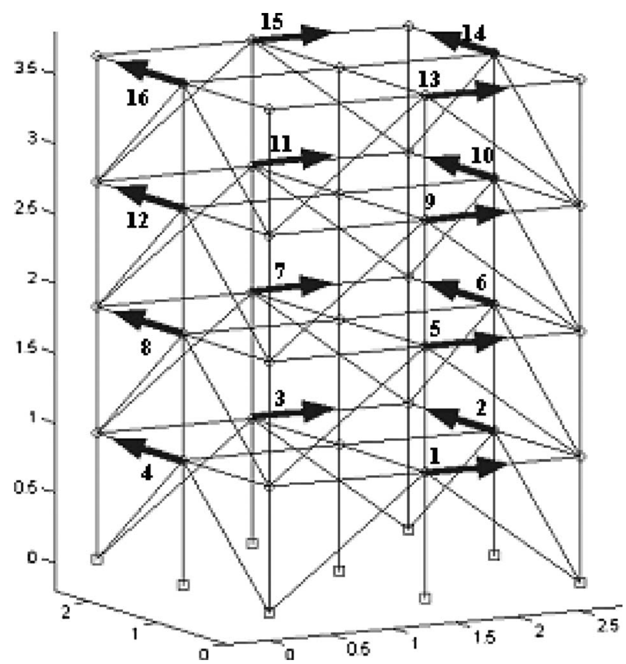

Fig. 3 Placement of sensors and directions of acceleration measurements on the ASCE Benchmark Structure [18]

5.1.2 Sensor 3. Figure 6 illustrates the migration of $\mathbf{E}_6$, extracted from sensor 3 for damage patterns 4 and 5. The means of the damage sensitive feature $\mathbf{E}_6$ for the damaged clouds of dam-

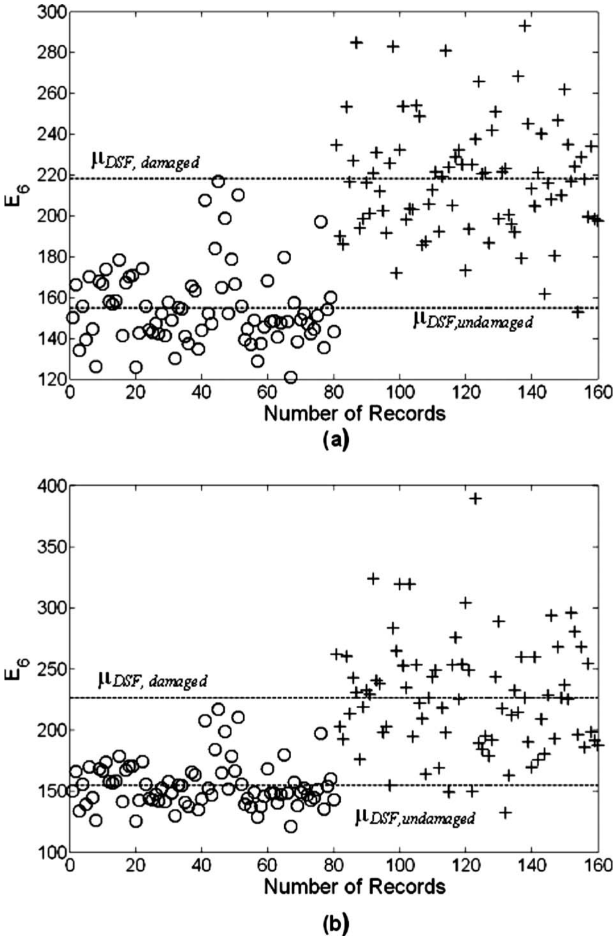

Fig. 5 Migration of the Haar wavelet based damage sensitive feature E_6 for sensor 2 with damage for major patterns: (*a*) damage pattern 1 and (*b*) damage pattern 2

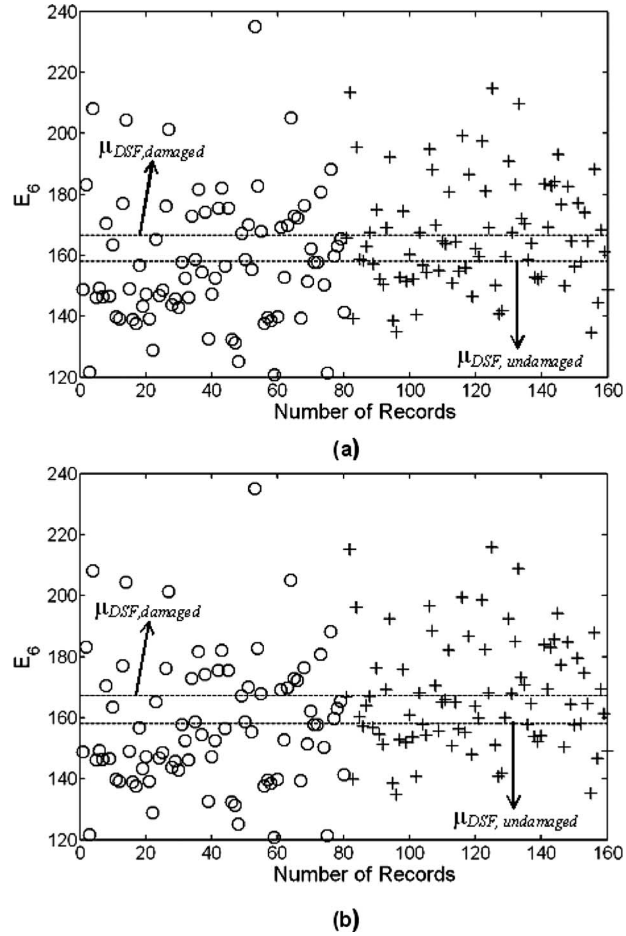

Fig. 6 Migration of the Haar wavelet based damage sensitive feature E_6 for sensor 3 with damage for (*a*) damage pattern 4 and (*b*) damage pattern 5 (undamaged (○); damaged (+))

age patterns 4 and 5 are 166.41 and 166.45, respectively. These results indicate that the change due to bolt loosening was not detected. This result is expected as the damage sensitive feature captures primarily global changes in the structure while bolt loosening will require measurements that capture much more localized material and component behavior.

5.1.3 Sensor 9. Figure 7 illustrates the feature clouds, extracted from sensor 9, for damage patterns 3 and 4. For damage pattern 3, it is observed that there is a very little separation between the clouds because the brace has been removed in the x direction and sensor 9 measures the acceleration in the y direction (Fig. 3). For damage pattern 4, there are two distinct clouds of feature vectors with damage since a brace has been removed from the third storey in the y direction near sensor 9.

For this damage pattern the separation of the clouds can be observed to be small reflecting the fact that indeed this is a small amount of damage introduced to the structure. This shows that the damage sensitive feature is directly related to the amount of damage; however, the quantification of damage with the Haar wavelet appears to be nonconclusive.

6 Conclusions

In this paper, a damage sensitive feature based on the wavelet transform of the vibration signal is derived. The damage sensitive feature is defined as the energy of the wavelet coefficients at higher scales. The theoretical aspects of wavelet decomposition of vibration signals are presented. Expressions for the energies of wavelet coefficients using the Haar wavelet basis function are derived for a single degree and a multidegree of freedom system. The derived damage sensitive feature is applied to various data sets for the ASCE Benchmark Structure.

For a SDOF system, the damage sensitive feature, given in Eq. (35), depends on the natural frequency of the system ω_n, the damping ratio ξ, and the scale a. For the MDOF system, damage sensitive feature, derived in Eq. (46), contains modal information of the system through the kth and lth mass normalized eigenvectors $\boldsymbol{\phi}_k$ and $\boldsymbol{\phi}_l$, natural frequencies, and damping ratios of the system denoted by ω_r and ξ, respectively, under the assumption of proportional damping; and the scale a of the wavelet basis.

The proposed damage sensitive feature is shown to detect damage for the numerically simulated data sets obtained from the ASCE Benchmark Structure. Application of the damage sensitive feature to the ASCE Benchmark simulation experiment demonstrates that the algorithm is able to detect minor, moderate, and major damage patterns. However, loosening of bolts cannot be distinguished when it occurs in conjunction with brace cutting because this damage will have a very localized influence. The difference in the means of the damage sensitive feature is larger for major damage than for moderate and minor damage patterns. With this simple example the damage detection algorithm is used only to illustrate damage detection and not damage quantification or localization. The Haar wavelet is a simple wavelet (Fig. 1) and thus may not be able to capture important details of the vibration signal thus making it useful primarily for damage detection. Other wavelets have been used by the authors, such as the Morlet wavelet to quantify the damage as presented in Ref. [21].

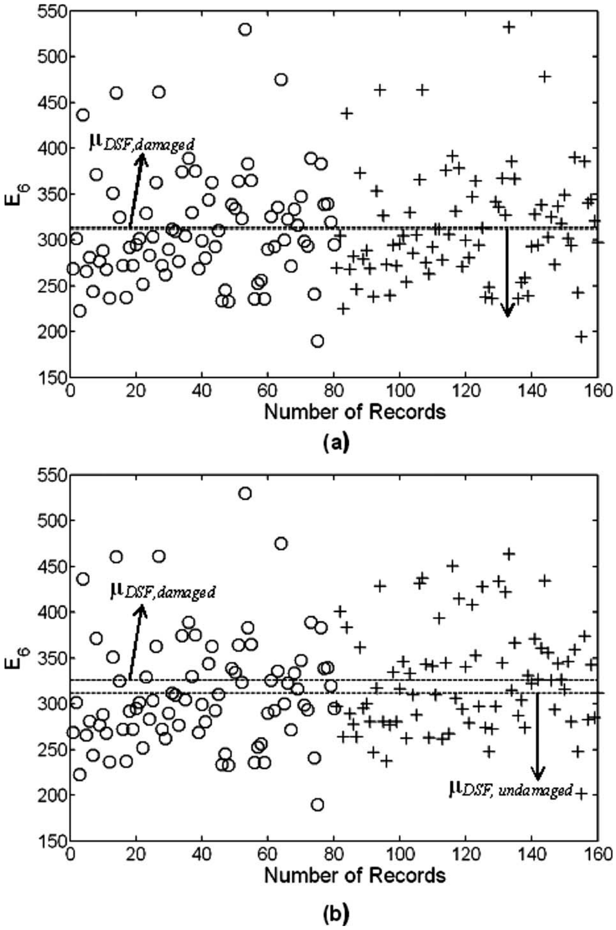

Fig. 7 Migration of the Haar wavelet based damage sensitive feature E_6 for sensor 9 with damage for (*a*) damage pattern 3 and (*b*) damage pattern 4 (undamaged (○); damaged (+))

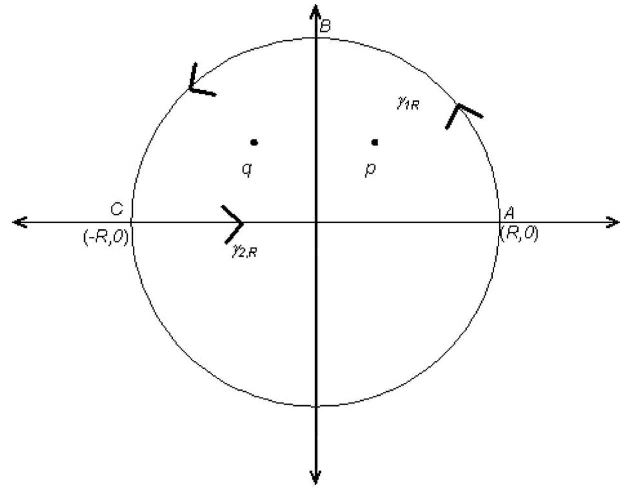

Fig. 8 Illustration of the proof of the contour integration formula

Acknowledgment

This research was partially supported by the John A. Blume Doctoral Fellowship and the NSF-NEESR Grant No. 15BBK16379. The authors would also like to acknowledge the ASCE Benchmark Committee for the data and MATLAB codes. The authors also express their gratitude to Dr. Garo Kiremidjian for help with derivation presented in Sec. 7.

Appendix: Derivation of the Integral I_H

In this appendix, the derivation for the computation of Eq. (19) is given.

Let the path $\gamma_R = \gamma_{1,R} + \gamma_{2,R}$, where Fig. 8 shows that $\gamma_{1,R}$ is the arc *ABC* and $\gamma_{2,R}$ is the arc *CA*. If *R* is sufficiently large, both poles *p* and *q* are within γ_R. By the residue theorem,

$$\int_{\gamma_R} h(z)dz = 2\pi j(R_p + R_q) \tag{A1}$$

where R_p and R_q are poles of the function $h(z)$ and are given by Eqs. (23) and (24), respectively. In this section, we will show that $\lim_{R\to\infty}\int_{\gamma_{2,r}} h(z)dz = 0$. For this purpose, we prove the following Lemma.

LEMMA. *Let* $d > 0$. Then, $\lim_{R\to\infty}\int_0^{\pi}\exp(-dR\sin\theta)d\theta = 0$.

Proof.

$$\int_0^{\pi} \exp(-dR\sin\theta)d\theta = \int_0^{\pi/2} \exp(-dR\sin\theta)d\theta + \int_{\pi/2}^{\pi} \exp(-dR\sin\theta)d\theta \tag{A2}$$

To compute the second integral, make the substitution $\varphi = \pi - \theta$. Thus,

$$\int_{\pi/2}^{\pi} \exp(-dR\sin\theta)d\theta = \int_0^{\pi/2} \exp(-dR\sin\varphi)d\varphi \tag{A3}$$

Thus,

$$\int_0^{\pi} \exp(-dR\sin\theta)d\theta = 2\int_0^{\pi/2} \exp(-dR\sin\theta)d\theta \tag{A4}$$

Now, choose an arbitrarily small $\varepsilon > 0$

$$\int_0^{\pi/2} \exp(-dR\sin\theta)d\theta = \int_0^{\varepsilon} \exp(-dR\sin\theta)d\theta + \int_{\varepsilon}^{\pi/2} \exp(-dR\sin\theta)d\theta \tag{A5}$$

Since the function $\exp(-dR\sin\theta)$ decreases in θ in $[0,\pi/2]$ and $\exp(-dR\sin\theta) \le \exp(-dR\sin\varepsilon)$ in $[\varepsilon,\pi/2]$, we obtain

$$\int_{\varepsilon}^{\pi/2} \exp(-dR\sin\theta)d\theta < \frac{\pi}{2}\exp(-dR\sin\varepsilon) \tag{A6}$$

If *R* is sufficiently large enough, i.e., $R > (1/d\sin\varepsilon)\log(\pi/2\varepsilon)$, then $\int_{\varepsilon}^{\pi/2}\exp(-dR\sin\theta)d\theta < \varepsilon$.

Thus, for any $\varepsilon > 0$, there exists R_ε, such that if $R > R_\varepsilon$, $\int_0^{\pi/2}\exp(-dR\sin\theta)d\theta < \varepsilon$. Hence,

$$\lim_{R\to\infty}\int_0^{\pi} \exp(-dR\sin\theta)d\theta = 2\lim_{R\to\infty}\int_0^{\pi/2} \exp(-dR\sin\theta)d\theta = 0 \tag{A7}$$

■

Now on $\gamma_{2,R}$, $z=R\exp(j\theta)$, and $\theta\in[0,\pi]$ and for any real valued a,

$$|\exp(jaz)| = |\exp(iR\cos\theta)|\exp(-aR\sin\theta) = \exp(-aR\sin\theta) \tag{A8}$$

Furthermore,

$$\left|\left[1-\exp\left(\frac{jaz}{2}\right)\right]^2\right| \leq 1 + 2\left|\exp\left(\frac{jaz}{2}\right)\right| + |\exp(jaz)| = 1 + 2\exp\left(-\frac{a}{2}R\sin\theta\right) + \exp(-aR\sin\theta) \tag{A9}$$

Using the fact that $dz=jR\exp(j\theta)d\theta$, we obtain

$$\left|\int_{\gamma_{2,R}} h(z)dz\right| \leq R\int_0^\pi \frac{|G(z)|\exp(-bR\sin\theta)\left[1+2\exp\left(-\frac{a}{2}R\sin\theta\right)+\exp(-aR\sin\theta)\right]}{|\exp(j\theta)R-p||\exp(j\theta)R-q|}d\theta \tag{A10}$$

Here again, we can approximate

$$|\exp(j\theta)R-p| \geq R\left|\left(1-\frac{p}{R}\right)\right|;|\exp(j\theta)R-q| \geq R\left|\left(1-\frac{q}{R}\right)\right| \tag{A11}$$

Thus, for sufficiently large R, and say for some fixed constant β, e.g., $\beta=0.5$, we get

$$\frac{R^2}{|\exp(j\theta)R-p||\exp(j\theta)R-q|} \leq 4 \tag{A12}$$

Thus, Eq. (A10) maybe rewritten as

$$\left|\int_{\gamma_{2,R}} h(z)dz\right| \leq \frac{4}{R}|G(\exp(j\theta)R)|\left[\int_0^\pi \exp(-bR\sin\theta)d\theta + 2\int_0^\pi \exp\left(-\left[\frac{a}{2}+b\right]R\sin\theta\right)d\theta + \int_0^\pi \exp(-[a+b]R\sin\theta)d\theta\right] \tag{A13}$$

By the Lemma, each of these integrals on the right-hand side of Eq. (A13) has to converge to zero.

Thus

$$\lim_{R\to\infty}\int_{\gamma_{2,R}} h(z)dz = 0$$

Then,

$$\lim_{R\to\infty}\int_{\gamma_R} h(z)dz = \lim_{R\to\infty}\int_{-R}^{R} h(z)dz = I_H \tag{A14}$$

Thus, $I_H=2\pi j(R_p+R_q)$.

■

References

[1] Chang, F.-K., ed., 1997, *Proceedings of the First International Workshop on Structural Health Monitoring*, Stanford University, Stanford, CA/CRC, New York.

[2] Chang, F.-K., ed., 1999, *Proceedings of the Second International Workshop on Structural Health Monitoring*, Stanford University, Stanford, CA/CRC, New York.

[3] Chang, F.-K., ed., 2001, *Proceedings of the Third International Workshop on Structural Health Monitoring*, Stanford University, Stanford, CA/CRC, New York.

[4] Chang, F.-K., ed., 2003, *Proceedings of the Fourth International Workshop on Structural Health Monitoring*, Stanford University, Stanford, CA/CRC, New York.

[5] Chang, F.-K., ed., 2005, *Proceedings of the Fifth International Workshop on Structural Health Monitoring*, Stanford University, Stanford, CA/CRC, New York.

[6] Chang, F.-K., ed., 2007, *Proceedings of the Sixth International Workshop on Structural Health Monitoring*, Stanford University, Stanford, CA/CRC, New York.

[7] Rytter, T., 1993, "Vibrational Based Inspection of Civil Engineering Structure," Ph.D. thesis, Department of Building Technology and Structure Engineering, Aalborg University, Denmark.

[8] Doebling, S. W., Farrar, C. R., Prime, M. B., and Shevitz, D. W., 1996, "Damage Identification and Health Monitoring of Structural and Mechanical Systems From Changes in Their Vibration Characteristics: A Literature Review," Los Alamos National Laboratory, Report No. LA-13070-MS.

[9] Sohn, H., Farrar, C. R., Hunter, H. F., and Worden, K., 2001, "Applying the LANL Statistical Pattern Recognition Paradigm for Structural Health Monitoring to Data From a Surface-Effect Fast Patrol Boat," Los Alamos National Laboratory, Report No. LA-13761-MS.

[10] Sohn, H., and Farrar, C. R., 2001, "Damage Diagnosis Using Time Series Analysis of Vibration Signals," Smart Mater. Struct., **10**(3), pp. 446–451.

[11] Staszewski, W. J., 1998, "Identification of Non-Linear Systems Using Multi-Scale Ridges and Skeletons of the Wavelet Transform," J. Sound Vib., **214**(4), pp. 639–658.

[12] Ghanem, R., and Romeo, F., 2000, "A Wavelet Based Approach for Identification of Linear Time Varying Dynamical Systems," J. Sound Vib., **234**(4), pp. 555–576.

[13] Kijewski, T., and Kareem, A., 2003, "Wavelet Transforms for System Identification: Considerations for Civil Engineering Applications," Comput. Aided Civ. Infrastruct. Eng., **18**, pp. 339–355.

[14] Spanos, P. D., and Failla, G., 2005, "Wavelets: Theoretical Concepts and Vibrations Related Applications," Shock Vib. Dig., **37**(5), pp. 359–375.

[15] Hou, Z. K., Noori, M., and St. Amand, R., 2000, "Wavelet-Based Approach for Structural Damage Detection," J. Eng. Mech., **126**(7), pp. 677–683.

[16] Nair, K. K., Kiremidjian, A. S., and Law, K. H., 2006, "Time Series Based Damage Detection and Localization Algorithm With Application to the ASCE Benchmark Structure," J. Sound Vib., **291**(1-2), pp. 349–368.

[17] Nair, K. K., and Kiremidjian, A. S., 2007, "Time Series Based Structural Damage Detection Algorithm Using Gaussian Mixtures Modeling," ASME J. Dyn. Syst., Meas., Control, **129**(3), pp. 285–293.

[18] Johnson, E. A., Lam, H. F., Katafygiotis, L. S., and Beck, J. L., 2004, "Phase I IASC-ASCE Structural Health Monitoring Benchmark Problem Using Simulated Data," J. Eng. Mech., **130**(1), pp. 3–15.

[19] Mallat, S., 1999, *A Wavelet Tour of Signal Processing*, Academic, New York.

[20] Bracewell, R. N., 1999, *The Fourier Transform & Its Applications*, 3rd ed., McGraw-Hill, New York.

[21] Nair, K. K., and Kiremidjian, A. S., 2009, "A Damage Detection Algorithm Using the Morlet Wavelet Transform," under review.

[22] Kreyzig, E., 1998, *Advanced Engineering Mathematics*, 8th ed., Wiley, New York.

[23] Maia, N. M. M., and Silva, J. M. M., 1998, *Theoretical and Experimental Modal Analysis*, Research Studies, Hertfordshire, England.

Morteza Eskandari-Ghadi
Department of Engineering Science,
Faculty of Engineering,
University of Tehran,
P.O. Box 11155-4563,
Tehran, Iran
e-mail: ghadi@ut.ac.ir,
ghadi@ustmb.ut.ac.ir

Ronald Y. S. Pak
Department of Civil, Environmental and
Architectural Engineering,
University of Colorado,
Boulder, CO 80309-0428
e-mail: pak@colorado.edu

Axisymmetric Body-Force Fields in Elastodynamics of Transversely Isotropic Media

In this paper, a complete elastodynamic solution for axisymmetric problems under axial body-forces in terms of two retarded potential functions in transversely isotropic media is extended to the case of general torsionless axisymmetry. Allowing for both axial and radial distributed internal loads through the use of an extra potential, the new solution retains its completeness via the theory of repeated wave equations. By virtue of its analytical design, the formulation can be reduced to the corresponding elastostatic case by simply suppressing the time-dependence of its potentials as well as the case of isotropy. In the limiting case of the latter material condition, the proposed representation for elastostatic problem degenerates to a recent extension of Love's potential function.
[DOI: 10.1115/1.3130866]

Keywords: potential method, mechanics, transversely isotropy, elastodynamics, elastostatics, axisymmetric, body-force, displacements, stresses, completeness

1 Introduction

One of the characteristics of mechanics of composite materials is anisotropy. Because of this the linear theory of anisotropic elastic media has long been the subject of numerous investigations. Among various possibilities, the case in which the material possesses an axis of elastic symmetry, transversely isotropy, is of most interest. The elastostatic problems of transversely isotropic material have been examined in a number of studies (e.g., Refs. [1–6]). The analytical solution of elastodynamics problems for transversely isotropic material has received even less attention. One of the powerful approaches for dealing with the system of partial differential equations in both elastostatics and elastodynamics is method of potentials. Lekhnitskii [4] considered anisotropic problems characterized by torsionless axisymmetry with the axis of elastic symmetry coincident with the axis of stress symmetry and found the solution of the displacement equations in terms of a single stress function satisfying a fourth-order partial differential equation (see also Ref. [6]). Hu [3] considered the general case of elastostatics problem in transversely isotropic media and generalized Lekhnitskii's solution [4]. Elliott [1] presented a solution of the three-dimensional problems in terms of two potential functions, each satisfying a second-order partial differential equation. He also described an axially symmetric system, where his solution reduces to one potential function satisfying a fourth-order partial differential equation, which itself is Lekhnitskii's potential function [4]. This was observed by Eubanks and Sternberg [2] and described in detail by Wang and Wang [7]. The generalized Elliott solution [1] is related to Lodge [8], called Elliott–Lodge solution (see Ref. [7]), which can be connected to the Lekhnitskii–Hu–Nowacki solution [7].

When an elasticity solution is expressed in terms of potentials, an important question is that of completeness. The literature includes several studies of completeness of the solutions of linear elastostatics problems in the isotropic material in terms of potential functions. There are also a few studies for completeness of the solution in transversely isotropic materials. Eubanks and Sternberg [2] proved that Lekhnitskii's solution [4] in the case of torsionless axisymmetric problems is complete, if the domain of interest is z-convex, where the z-axis is considered parallel to the axis of material symmetry. Wang and Wang [7] proved the completeness of the Lekhnitskii–Hu–Nowacki solution, when the domain is z-convex. They also proved the completeness of the Elliott–Lodge solution under the same conditions.

Some investigations related to the general solution of the elastodynamics problems in linear isotropic elasticity and their completeness can be found in Refs. [9–15]. Recently, Eskandari-Ghadi [16] introduced a complete solution for the general elastodynamics problems in linear transversely isotropic materials in terms of two potential functions. The solution reduces to one for torsionless axisymmetric problems, where, in the cylindrical coordinate system (r,θ,z), the body-force is permitted to have only a component along the axis of material symmetry.

It is the purpose of this paper to present a complete solution of the elastodynamics problems in torsionless axisymmetric transversely isotropic materials under both axial and radial body-forces. As an extension of Ref. [16], the solution is cast in terms of two potential functions, which are governed by two uncoupled inhomogeneous partial differential equations. The issue of completeness is addressed via the theory of repeated wave equations, a generalized form of Boggio's theorem, and the analyticity of the solution with respect to the material parameters of the transversely isotropic media as in Refs. [16,2]. With a direct suppression of the time-dependence of the potentials, the solution is equally applicable to elastostatic problems for transversely isotropic materials, and elastodynamics and elastostatics problems of isotropic materials as well. For the elastostatic case of isotropy, the degenerate formulation converges to Ref. [17]. The governing equation for a pure torsion problem with an angular body-force field can be solved by a direct displacement formulation and will not be elaborated in this communication.

2 Statement of the Problem

Consider the body B at time t in the time interval $(0,t_0)$, where $t_0>0$ can be infinite, to be regular in the sense of Ref. [18]. In a cylindrical coordinate system (r,θ,z), the equations of motion for axisymmetric responses may be written as

$$\frac{\partial\sigma_{rr}}{\partial r}+\frac{1}{r}(\sigma_{rr}-\sigma_{\theta\theta})+\frac{\partial\sigma_{zr}}{\partial z}+b_r=\rho\frac{\partial^2 u}{\partial t^2}$$

Contributed by the Applied Mechanics Division of ASME for publication in the Journal of Applied Mechanics. Manuscript received March 9, 2008; final manuscript received April 3, 2009; published online July 27, 2009. Review conducted by Professor Sridhar Krishnaswamy.

$$\frac{\partial \sigma_{rz}}{\partial r} + \frac{1}{r}\sigma_{rz} + \frac{\partial \sigma_{zz}}{\partial z} + b_z = \rho \frac{\partial^2 w}{\partial t^2} \tag{1}$$

where $\sigma_{ij}(r,z,t)$ and $(i,j=r,\theta,z)$ are the components of stress tensor, ρ is the mass density, $b_i(r,z,t)$ and $(i=r,z)$ are the radial and axial body-force components, and u and w are the radial and axial displacement components. Considering a linear Green-elastic transversely isotropic material whose axis of material symmetry is in the z-direction, the stress-strain relationships can be given in the form of [12]

$$\begin{bmatrix} \sigma_{rr} \\ \sigma_{\theta\theta} \\ \sigma_{zz} \\ \sigma_{rz} \end{bmatrix} = \begin{bmatrix} C_{1111} & C_{1122} & C_{1133} & 0 \\ C_{1122} & C_{1111} & C_{1133} & 0 \\ C_{1133} & C_{1133} & C_{3333} & 0 \\ 0 & 0 & 0 & C_{1313} \end{bmatrix} \begin{bmatrix} \varepsilon_{rr} \\ \varepsilon_{\theta\theta} \\ \varepsilon_{zz} \\ 2\varepsilon_{rz} \end{bmatrix} \tag{2}$$

With the strain-displacement relations as

$$\varepsilon_{rr} = \frac{\partial u}{\partial r}, \quad \varepsilon_{\theta\theta} = \frac{u}{r}, \quad \varepsilon_{zz} = \frac{\partial w}{\partial z}, \quad 2\varepsilon_{rz} = \frac{\partial u}{\partial z} + \frac{\partial w}{\partial r} \tag{3}$$

the equations of motion (1) can be written in terms of displacements as

$$\begin{aligned} &(1+\alpha_1)C_{1212}\left(\frac{\partial^2 u}{\partial r^2} + \frac{1}{r}\frac{\partial u}{\partial r} - \frac{u}{r^2}\right) + \alpha_2 C_{1212}\frac{\partial^2 u}{\partial z^2} \\ &\quad + (C_{1133} + \alpha_2 C_{1212})\frac{\partial^2 w}{\partial r\,\partial z} + b_r = \rho\frac{\partial^2 u}{\partial t^2} \\ &\alpha_2 C_{1212}\left(\frac{\partial^2 w}{\partial r^2} + \frac{1}{r}\frac{\partial w}{\partial r}\right) + C_{3333}\frac{\partial^2 w}{\partial z^2} + (C_{1133} + \alpha_2 C_{1212}) \\ &\quad \times \left(\frac{\partial^2 u}{\partial r\,\partial z} + \frac{1}{r}\frac{\partial u}{\partial z}\right) + b_z = \rho\frac{\partial^2 w}{\partial t^2} \end{aligned} \tag{4}$$

where

$$C_{1313} = \alpha_2 C_{1212}, \quad C_{1111} = (1+\alpha_1)C_{1212} \tag{5}$$

For a positive definite strain energy function, it is required that $C_{1212} > 0$, $\alpha_2 > 0$, and $1+\alpha_1 > 0$.

3 A General Elastodynamic Solution

As noted in Ref. [16], the general solution of the equations of motion (4) in the absence of radial body-forces can be given as

$$\begin{aligned} u(r,z,t) &= -\alpha_3 \frac{\partial^2 F}{\partial r\,\partial z} \\ w(r,z,t) &= (1+\alpha_1)\left(\nabla_r^2 + \frac{\alpha_2}{1+\alpha_1}\frac{\partial^2}{\partial z^2} - \frac{\rho}{(1+\alpha_1)C_{1212}}\frac{\partial^2}{\partial t^2}\right)F \end{aligned} \tag{6}$$

where $\alpha_3 = (C_{1133}+C_{1313})/C_{1212}$, $\nabla_r = \partial^2/\partial r^2 + \partial/r\partial r$, and the potential function F satisfies

$$\left[\Box_1\Box_2 - \delta\frac{\partial^4}{\partial z^2\,\partial t^2}\right]F(r,z,t) = \frac{-1}{\alpha_2(1+\alpha_1)}\frac{b_z(r,z,t)}{C_{1212}} \tag{7}$$

In the above, $\Box_\alpha = \nabla_r^2 + \partial^2/s_\alpha^2/\partial z^2/ - \partial^2/c_\alpha^2/\partial t^2$, $(\alpha=1,2)$, $\delta = (1 - 1/s_2^2)/c_1^2 + (C_{3333}/C_{1111} - 1/s_1^2)/c_2^2$; $c_1^2 = C_{1111}/\rho$ and $c_2^2 = C_{1313}/\rho$, with $s_\alpha^2(\alpha=1,2)$ being the roots of

$$C_{3333}C_{2323}s^4 + (C_{1133}^2 + 2C_{1133}C_{2323} - C_{1111}C_{3333})s^2 + C_{1111}C_{2323} = 0 \tag{8}$$

To ensure the positive definiteness of the strain energy, $s_\alpha^2(\alpha=1,2)$ should not be zero or negative [4,5]. $s_\alpha^2(\alpha=1,2)$ are parameters that may make sense for the amount of anisotropy of the material. For an isotropic material, $s_1^2 = s_2^2 = 1$, and δ is identically zero. In addition, because of the existence of the terms c_1^2 and c_2^2 in the expression for δ, this parameter is small compared with unity even for transversely isotropic material.

To allow for the case of a general nonzero radial body-force field $b_r(r,z,t)$, it is assumed that $b_r(r,z,t)$ is a piecewise continuous function of both variables r and z. Following Ref. [17] for the case of isotropy, one may define an auxiliary radial load potential function $\Theta(r,z,t)$ for the transversely isotropic problem to be a solution of the partial differential equation

$$\frac{\partial^2 \Theta(r,z,t)}{\partial r\,\partial z} = b_r(r,z,t) \tag{9}$$

With the modified definition of the displacement field as

$$\begin{aligned} u(r,z,t) &= -\alpha_3\frac{\partial^2 F(r,z,t)}{\partial r\,\partial z} \\ w(r,z,t) &= \left[(1+\alpha_1)\nabla_r^2 + \alpha_2\frac{\partial^2}{\partial z^2} - \frac{\rho}{C_{1212}}\frac{\partial^2}{\partial t^2}\right]F(r,z,t) \\ &\quad - \frac{1}{\alpha_3 C_{1212}}\Theta(r,z,t) \end{aligned} \tag{10}$$

it can be shown that Eq. (10) satisfies the equations of motion (4) with nonzero axisymmetric body-force densities, provided that Eq. (9) holds and

$$\begin{aligned} &\left[\Box_1\Box_2 - \delta\frac{\partial^4}{\partial z^2\,\partial t^2}\right]F(r,z,t) \\ &\quad = \frac{-1}{\alpha_2(1+\alpha_1)}\frac{b_z(r,z,t)}{C_{1212}} + \frac{1}{\alpha_2\alpha_3 C_{1111}} \\ &\qquad \times \left(\nabla_r^2 + \frac{C_{3333}}{C_{1212}}\frac{\partial^2}{\partial z^2} + \frac{\rho}{C_{1212}}\frac{\partial^2}{\partial t^2}\right)\Theta(r,z,t) \end{aligned} \tag{11}$$

It is clear that a solution by Eq. (10) satisfies, as does Eq. (6), the condition $\mathbf{e}_z.\ \mathrm{curl}[u,0,w]^T = 0$, where $\mathbf{e}_z$ is the unit vector parallel to the z-axis and the superscript T denotes the transpose. The following section addresses the issue of completeness of Eq. (10) for a regular simply connected transversely isotropic solid.

Claim 1: Completeness of the solution (10). Let B be a regular simply connected region in Euclidian space such that a straight line parallel to the z-axis intersects the boundary of B in at most two points. Let $b_r(r,z,t)$ and $b_z(r,z,t)$ be two piecewise continuous functions on B and on an open interval $(0,t_0)$. If $u(r,z,t)$ and $w(r,z,t)$ are the solutions for the equations of motion (4) and analytic with respect to δ in a finite region including 0, then, there exists a function $\Theta(r,z,t)$ of class C^2 on both B and on the interval $(0,t_0)$, which satisfies Eq. (9) and there exists a function $F(r,z,t;\delta)$ and of class C^4 on both B and the interval $(0,t_0)$ that satisfies Eq. (11).

Proof. First, it should be evident that the integration of the partial differential equation (9) is straightforward in an axisymmetric and simply connected domain, yielding

$$\Theta(r,z,t) = \int\int b_r(r,z,t)\,dr\,dz, \quad r \geq 0, \quad r,z \in B \tag{12}$$

and let $u(r,z,t)$ and $w(r,z,t)$ represent the solutions of the wave equations (4). One can write u and w in terms of $F(r,z,t;\delta)$ and $\Theta(r,z,t)$ as Eq. (10) and they will be a solution of the equations of motion provided that F satisfies Eq. (11). The existence of a solution to an equation in the form of Eq. (11) for the domains of interest, however, has been established in Ref. [16]. By virtue of the smoothness hypothesis on $\Theta(r,z,t)$ and $b_z(r,z,t)$, the right-hand side of Eq. (11) is a piecewise continuous function on B and on an open interval $(0,t_0)$, which is written as

$$\bar{b}(r,z,t) = \frac{-1}{\alpha_2(1+\alpha_1)}\frac{b_z(r,z,t)}{C_{1212}} + \frac{1}{\alpha_2\alpha_3 C_{1111}} \times\left(\nabla_r^2 + \frac{C_{3333}}{C_{1212}}\frac{\partial^2}{\partial z^2} + \frac{\rho}{C_{1212}}\frac{\partial^2}{\partial t^2}\right)\Theta(r,z,t) \quad (13)$$

To make the solution for Eq. (11), one may define F_0 to be a solution for

$$\Box_1\Box_2 F_0 = \bar{b}(r,z,t) \quad (14)$$

To find F_0, one may first set $\hat{F}_0(r,z,t)=\Box_2 F_0(r,z,t)$, so that Eq. (14) can be written as

$$\Box_1 \hat{F}_0(r,z,t) = \bar{b}(r,z,t) \quad (15)$$

for which the retarded Newtonian potential (Ref. [19], Art. 83 and Chap. IX)

$$\hat{F}_0(r,z,t) = -\frac{1}{4\pi}\int\int_B\int \frac{\bar{b}(r,z,t-R_1/c_1)}{R_1(r,z;\tilde{r},\tilde{z})}d\tilde{V} \quad (16)$$

With

$$R_1(r,z;\tilde{r},\tilde{z}) = \sqrt{(r-\tilde{r})^2 + s_1^2(z-\tilde{z})^2} \quad (17)$$

is a solution. Since s_1^2 is neither zero nor negative real number, the only singular point in the volume integral (16) is at (r,z). As it can be deduced from Eq. (16) that $\hat{F}_0$ is a C^2 function on $B\times(0,t_0)$, one may define F_0 as

$$F_0(r,z,t) = -\frac{1}{4\pi}\int\int_B\int \frac{\hat{F}_0(r,z,t-R_2/c_2)}{R_2(r,z;\tilde{r},\tilde{z})}d\tilde{V} \quad (18)$$

where $R_2(r,z;\tilde{r},\tilde{z})$ is

$$R_2(r,z;\tilde{r},\tilde{z}) = \sqrt{(r-\tilde{r})^2 + s_2^2(z-\tilde{z})^2} \quad (19)$$

With $\hat{F}_0$ as a solution to Eq. (15), the function F_0 in Eq. (18) can, by virtue of the theory of retarded potentials, be shown to be a solution to $\Box_1\Box_2F_0=\bar{b}$ with the stated smoothness. Next we define $\{F_j\}_{j=1}^{\infty}$ to be the solution of the following set of equations:

$$\Box_1\Box_2 F_j = \frac{\partial^4 F_{j-1}}{\partial z^2\,\partial t^2}, \quad j=1,2,3,\ldots \quad (20)$$

It is seen that F_1 is in the form of F_0, if one replace $\partial^4 F_0/\partial z^2\partial t^2$ instead of $\bar{b}(r,z,t)$ in Eq. (14), and F_2 is in the form of F_0, if one replace $\partial^4 F_1/\partial z^2\partial t^2$ instead of $\bar{b}(r,z,t)$ in Eq. (14), and so on. By virtue of the analyticity of the elasticity solution with respect to δ, one may write $F(r,z,t;\delta)$ in the form of

$$F(r,z,t;\delta) = \sum_{j=0}^{\infty} F_j(r,z,t)\delta^j \quad (21)$$

With $F_j(r,z,t)$ derived by the procedure given above, one may substitute Eq. (20) into Eq. (11) and finds

$$\sum_{j=0}^{\infty}\Box_1\Box_2[F_j(r,z,t)\delta^j] - \delta\sum_{j=0}^{\infty}\frac{\partial^4}{\partial z^2\,\partial t^2}[F_j(r,z,t)\delta^j] = \bar{b}(r,z,t) \quad (22a)$$

or

$$\Box_1\Box_2F_0 + \sum_{j=1}^{\infty}\Box_1\Box_2[\delta^j F_j] - \sum_{j=0}^{\infty}\frac{\partial^4}{\partial z^2\,\partial t^2}[\delta^{j+1}F_j] = \bar{b} \quad (22b)$$

where $\bar{b}(r,z,t)$ is given in Eq. (13). On taking F_0 as a particular solution to Eq. (14), Eqs. (22a) and (22b) can be satisfied if

$$\sum_{j=1}^{\infty}\left\{\left[\Box_1\Box_2F_j - \frac{\partial^4 F_{j-1}}{\partial z^2\,\partial t^2}\right]\delta^j\right\} = 0 \quad (23)$$

This equation is satisfied if $\{F_j\}_{j=1}^{\infty}$ is the solution of Eq. (20). Finally, the smoothness of $F(r,z,t;\delta)$ can likewise be deduced from the smoothness of F_j, which completes the proof. ■

By virtue of Eqs. (10), (2), and (3), the strain-potential and stress-potential relations in terms of $F(r,z,t;\delta)$ are

$$\varepsilon_{rr} = -\alpha_3\frac{\partial^3 F}{\partial r^2\,\partial z}$$

$$\varepsilon_{\theta\theta} = -\frac{\alpha_3}{r}\frac{\partial^2 F}{\partial r\,\partial z}$$

$$\varepsilon_{zz} = \frac{\partial}{\partial z}\left[\alpha_2\frac{\partial^2}{\partial z^2} + (1+\alpha_1)\nabla_r^2 - \frac{\rho}{C_{1212}}\frac{\partial^2}{\partial t^2}\right]F - \frac{1}{\alpha_3 C_{1212}}\frac{\partial\Theta}{\partial z} \quad (24)$$

$$\varepsilon_{rz} = \frac{1}{2}\left[-\alpha_3\frac{\partial^3 F}{\partial r\,\partial z^2} + \left(\alpha_2\frac{\partial^3}{\partial r\,\partial z^2} + (1+\alpha_1)\frac{\partial}{\partial r}\nabla_r^2 - \frac{\rho}{C_{1212}}\frac{\partial^3}{\partial r\,\partial t^2}\right)F - \frac{1}{\alpha_3 C_{1212}}\frac{\partial\Theta}{\partial r}\right]$$

$$\sigma_{rr} = \frac{\partial}{\partial z}\left[-\alpha_3\left(C_{1111}\frac{\partial^2}{\partial r^2} + C_{1122}\frac{1}{r}\frac{\partial}{\partial r}\right)F + C_{1133}\left((1+\alpha_1)\nabla_r^2 + \alpha_2\frac{\partial^2}{\partial z^2} - \frac{\rho}{C_{1212}}\frac{\partial^2}{\partial t^2}\right)F - \frac{C_{1133}}{\alpha_3 C_{1212}}\Theta\right]$$

$$\sigma_{\theta\theta} = \frac{\partial}{\partial z}\left[-\alpha_3\left(C_{1122}\frac{\partial^2}{\partial r^2} + C_{1111}\frac{1}{r}\frac{\partial}{\partial r}\right)F + C_{1133}\left((1+\alpha_1)\nabla_r^2 + \alpha_2\frac{\partial^2}{\partial z^2} - \frac{\rho}{C_{1212}}\frac{\partial^2}{\partial t^2}\right)F - \frac{C_{1133}}{\alpha_3 C_{1212}}\Theta\right] \quad (25)$$

$$\sigma_{zz} = \frac{\partial}{\partial z}\left[\left[(C_{3333}(1+\alpha_1) - \alpha_3 C_{1133})\nabla_r^2 + \alpha_2\frac{\partial^2}{\partial z^2} - \frac{\rho}{C_{1212}}\frac{\partial^2}{\partial t^2}\right]F - \frac{C_{3333}}{\alpha_3 C_{1212}}\Theta\right]$$

$$\sigma_{rz} = C_{1313}\frac{\partial}{\partial r}\left[\left((1+\alpha_1)\nabla_r^2 + (\alpha_2-\alpha_3)\frac{\partial^2}{\partial z^2} - \frac{\rho}{C_{1212}}\frac{\partial^2}{\partial t^2}\right)F - \frac{1}{\alpha_3 C_{1212}}\Theta\right]$$

3.1 Elastodynamic Solution in Isotropic Materials. In the special case of isotropy, the elasticity tensor is described by

$$C_{1111} = C_{3333} = 2\mu + \lambda, \quad C_{1122} = C_{1133} = \lambda, \quad C_{1212} = C_{1313} = \mu \quad (26)$$

where λ and μ are Lame's constants. Using Eq. (26) one may infer that

$$\alpha_1 = \alpha_3 = \frac{\lambda+\mu}{\mu}, \quad \alpha_2 = 1, \quad s_0^2 = s_1^2 = s_2^2 = 1, \quad \delta = 0 \quad (27)$$

$$c_1^2 = \frac{\lambda+2\mu}{\rho}, \quad c_2^2 = \frac{\mu}{\rho} \quad (28)$$

Substituting relations (26)–(28) into Eq. (10) implies

$$u(r,z,t) = -\frac{\lambda+\mu}{\mu}\frac{\partial^2 F(r,z,t)}{\partial r\,\partial z}$$

$$w(r,z,t) = \frac{\lambda+2\mu}{\mu}\left(\nabla_r^2 + \frac{\mu}{\lambda+2\mu}\frac{\partial^2}{\partial z^2} - \frac{\rho}{\lambda+2\mu}\frac{\partial^2}{\partial t^2}\right)F(r,z,t) - \frac{1}{\lambda+\mu}\Theta(r,z,t) \quad (29)$$

where $F(r,z,t)$ satisfies

$$\Box_{i1}\Box_{i2}F(r,z,t) = \frac{-1}{\lambda+2\mu}b_z(r,z,t) + \frac{\mu}{(\lambda+2\mu)(\lambda+\mu)} \times\left(\nabla_r^2 + \frac{\lambda+2\mu}{\mu}\frac{\partial^2}{\partial z^2} + \frac{\rho}{\mu}\frac{\partial^2}{\partial t^2}\right)\Theta(r,z,t) \quad (30)$$

in which for $(\alpha=1,2)$, $\Box_{i\alpha}=\nabla^2-\partial^2/(c_\alpha^2\partial t^2)$ is the wave operator for isotropic material and ∇^2 is the usual three-dimensional Laplace operator. The governing equation for $\Theta(r,z,t)$ does not change and $\Theta(r,z,t)$ is again a solution for Eq. (9).

In the isotropic case, the strain- and stress-potential relations can be found by using Eqs. (24)–(28) as

$$\begin{aligned}
\varepsilon_{rr} &= -\frac{\lambda+\mu}{\mu}\frac{\partial^3 F}{\partial r^2\,\partial z}\\
\varepsilon_{\theta\theta} &= -\frac{\lambda+\mu}{\mu}\frac{1}{r}\frac{\partial^2 F}{\partial r\,\partial z}\\
\varepsilon_{zz} &= \frac{\partial}{\partial z}\left[\frac{\partial^2}{\partial z^2} + \frac{\lambda+2\mu}{\mu}\nabla_r^2 - \frac{\rho}{\mu}\frac{\partial^2}{\partial t^2}\right]F - \frac{1}{\lambda+\mu}\frac{\partial\Theta}{\partial z}\\
\varepsilon_{rz} &= \frac{1}{2}\left[-\frac{\lambda+\mu}{\mu}\frac{\partial^3 F}{\partial r\,\partial z^2} + \left(\frac{\partial^3}{\partial r\,\partial z^2} + \frac{\lambda+2\mu}{\mu}\frac{\partial}{\partial r}\nabla_r^2 - \frac{\rho}{\mu}\frac{\partial^3}{\partial r\,\partial t^2}\right)F - \frac{1}{\lambda+\mu}\frac{\partial\Theta}{\partial r}\right]
\end{aligned} \quad (31)$$

$$\begin{aligned}
\sigma_{rr} &= \frac{\partial}{\partial z}\left[\left(-(\lambda+2\mu)\frac{\partial^2}{\partial r^2} + \lambda\frac{1}{r}\frac{\partial}{\partial r}\right)F + \lambda\left(\frac{\partial^2}{\partial z^2} - \frac{\rho}{\mu}\frac{\partial^2}{\partial t^2}\right)F - \frac{\lambda}{\lambda+\mu}\Theta\right]\\
\sigma_{\theta\theta} &= \frac{\partial}{\partial z}\left[\left(\lambda\frac{\partial^2}{\partial r^2} - (\lambda+2\mu)\frac{1}{r}\frac{\partial}{\partial r}\right)F + \lambda\left(\frac{\partial^2}{\partial z^2} - \frac{\rho}{\mu}\frac{\partial^2}{\partial t^2}\right)F - \frac{\lambda}{\lambda+\mu}\Theta\right]\\
\sigma_{zz} &= \frac{\partial}{\partial z}\left[\left[(3\lambda+4\mu)\nabla_r^2 + \frac{\partial^2}{\partial z^2} - \frac{\rho}{\mu}\frac{\partial^2}{\partial t^2}\right]F - \frac{\lambda+2\mu}{\lambda+\mu}\Theta\right]\\
\sigma_{rz} &= \mu\frac{\partial}{\partial r}\left[\left(\frac{\lambda+2\mu}{\mu}\nabla_r^2 - \frac{\lambda}{\mu}\frac{\partial^2}{\partial z^2} - \frac{\rho}{\mu}\frac{\partial^2}{\partial t^2}\right)F - \frac{1}{\lambda+\mu}\Theta\right]
\end{aligned} \quad (32)$$

4 Reduction for Elastostatics

In the case of linear elastostatics for transversely isotropy, the field functions F and Θ can, unlike some classical dynamic potentials such as Lame's, be taken to be independent of time and the solution (10) can be reduced to

$$\begin{aligned}
u(r,z) &= -\alpha_3\frac{\partial^2 F}{\partial r\,\partial z}\\
w(r,z) &= (1+\alpha_1)\left(\nabla_r^2 + \frac{\alpha_2}{1+\alpha_1}\frac{\partial^2}{\partial z^2}\right)F - \frac{1}{\alpha_3 C_{1212}}\Theta
\end{aligned} \quad (33)$$

where the governing equations for $\Theta(r,z)$ and $F(r,z)$ are, respectively, changed to

$$\frac{\partial^2\Theta(r,z)}{\partial r\,\partial z} = b_r(r,z) \quad (34)$$

$$\nabla_1\nabla_2 F(r,z) = \frac{-1}{\alpha_2(1+\alpha_1)}\frac{b_z(r,z)}{C_{1212}} + \frac{1}{\alpha_2\alpha_3 C_{1111}} \times\left(\nabla_r^2 + \frac{C_{3333}}{C_{1212}}\frac{\partial^2}{\partial z^2}\right)\Theta(r,z) \quad (35)$$

in which the operator ∇_α for $(\alpha=1,2)$ is $\nabla_\alpha=\nabla_r^2+\partial^2/s_\alpha^2\partial z$.

On the basis of the theory of Newtonian potential, the completeness of the elastostatic solution (34) can be readily established. To show the existence of solutions for $\Theta(r,z)$ and $F(r,z)$ it is evident from Eq. (12) that $\Theta(r,z)$ can be given by

$$\Theta(r,z) = \int\int b_r(r,z)drdz, \quad r\geq 0, \quad r,z\in B \quad (36)$$

as a solution to Eq. (33). Denoting the right-hand side of Eq. (34) as

$$\bar{b}(r,z) = \frac{-1}{\alpha_2(1+\alpha_1)}\frac{b_z(r,z)}{C_{1212}} + \frac{1}{\alpha_2\alpha_3 C_{1111}} \times\left(\nabla_r^2 + \frac{C_{3333}}{C_{1212}}\frac{\partial^2}{\partial z^2} + \frac{\rho}{C_{1212}}\frac{\partial^2}{\partial t^2}\right)\Theta(r,z)$$

then F is the solution of $\nabla_1\nabla_2 F=\bar{b}$. With $\nabla_2 F$ denoted as F_1, it is clear that F_1 is governed by

$$\nabla_1 F_1 = \bar{b} \quad (37)$$

A solution of Eq. (37) can be given in terms of the Newtonian potential function [19]

$$F_1(r,z) = -\frac{1}{4\pi}\int\int_B\int \frac{\bar{b}(r,z)}{R_1(r,z;\tilde{r},\tilde{z})}d\tilde{V} \quad (38)$$

where $R_1(r,z;\tilde{r},\tilde{z})$ is given by Eq. (17). Then, $F(r,z)$ is the solution of

$$\nabla_1 F(r,z) = F_1(r,z) \quad (39)$$

which admits

$$F(r,z) = -\frac{1}{4\pi}\int\int_B\int \frac{F_1(r,z)}{R_2(r,z;\tilde{r},\tilde{z})}d\tilde{V} \quad (40)$$

as a solution of $\nabla_1\nabla_2 F=\bar{b}$ with $R_2(r,z;\tilde{r},\tilde{z})$ given by Eq. (19).

The strain and stress components in terms of the potentials Θ and F are identical in form to those in Eqs. (24) and (25).

4.1 Elastostatic Solution for Isotropic Materials. In the limiting case of an isotropic material, the material conditions of Eqs. (26) and (27) reduce the elastostatic displacements in Eq. (33) to

$$\begin{aligned}
u(r,z) &= -\frac{\lambda+\mu}{\mu}\frac{\partial^2 F}{\partial r\,\partial z}\\
w(r,z) &= \frac{\lambda+2\mu}{\mu}\left(\nabla_r^2 + \frac{\mu}{\lambda+2\mu}\frac{\partial^2}{\partial z^2}\right)F - \frac{1}{\lambda+\mu}\Theta
\end{aligned} \quad (41)$$

where the governing equations for $\Theta(r,z)$ and $F(r,z)$ are, respectively, changed to

$$\frac{\partial^2\Theta(r,z)}{\partial r\,\partial z} = b_r(r,z) \quad (42)$$

$$\nabla^2\nabla^2 F(r,z) = \frac{-1}{\lambda+2\mu} b_z(r,z) + \frac{\mu}{(\lambda+2\mu)(\lambda+\mu)} \times \left(\nabla_r^2 + \frac{\lambda+2\mu}{\mu}\frac{\partial^2}{\partial z^2}\right)\Theta(r,z) \tag{43}$$

in which ∇^2 is the usual three-dimensional Laplace operator.

In the same way, one may start from Eq. (29), the general solution for torsionless axisymmetric wave equations in isotropic materials, and eliminate the derivatives with respect to time and get the solution (41).

To show that expressions (41)–(43) coincide with those in Ref. [17] for isotropy, it is sufficient to replace λ and μ with $\nu E/(1+\nu)(1-2\nu)$ and $E/2(1+\nu)$, respectively, to get

$$\begin{aligned} u(r,z) &= -\frac{1}{(1-2\nu)}\frac{\partial^2 F}{\partial r\,\partial z} \\ w(r,z) &= \frac{2(1-\nu)}{(1-2\nu)}\nabla_r^2 F + \frac{\partial^2 F}{\partial z^2} - \frac{2(1+\nu)(1-2\nu)}{E}\Theta \end{aligned} \tag{44}$$

where $\Theta(r,z)$ is the solution of Eq. (42) and

$$\nabla^2\nabla^2 F(r,z) = \frac{-(1+\nu)(1-2\nu)}{E(1-\nu)} b_z(r,z) + \frac{(1+\nu)(1-2\nu)^2}{E(1-\nu)} \times \left(\nabla_r^2 + \frac{2(1-\nu)}{(1-2\nu)}\frac{\partial^2}{\partial z^2}\right)\Theta(r,z) \tag{45}$$

In these expressions ν and E are Poisson's ratio and Young's modulus, respectively. Equations (44) and (45) are exactly the same as the equation given by Simmonds [17] if one replaces F with $(1-2\nu)(1+\nu)F_{\text{Love}}/E$, where F_{Love} is Love's potential function [20].

5 Conclusion

Within the framework of linear Green-elasticity, a complete solution for the elastodynamics and elastostatics problems of torsionless axisymmetric transversely isotropic material with general body-force fields in the vertical and radial directions is presented. By virtue of two potential functions, the problem in a suitably convex domain is shown to be reducible to a fourth-order and second-order inhomogeneous partial differential equations. In the case of isotropy, the solution reduces to the format proposed by Simmonds [17] who did not address the issue of completeness.

References

[1] Elliott, H. A., 1948, "Three Dimensional Stress Distribution in Hexagonal Aeolotropic Crystals," Proc. Cambridge Philos. Soc., **44**, pp. 522–533.
[2] Eubanks, R. A., and Sternberg, E., 1954, "On the Axisymmetric Problem of Elasticity Theory for a Medium With Transverse Isotropy," J. Rat. Mech. Anal., **3**, pp. 89–101.
[3] Hu, H. C., 1953, "On the Three Dimensional Problems of the Theory of Elasticity of a Transversely Isotropic Body," Sci. Sin., **2**, pp. 145–151.
[4] Lekhnitskii, S. G., 1981, *Theory of Elasticity of an Anisotropic Body*, Mir, Moscow.
[5] Michell, J. H., 1900, "The Stress in an Aeolotropic Elastic Solid With an Infinite Plane Boundary," Proc. London Math. Soc., **XXXII**, pp. 247–258.
[6] Nowacki, W., 1954, "The Stress Function in Three Dimensional Problems Concerning an Elastic Body Characterized by Transversely Isotropy," Bull. Acad. Pol. Sci. [Biol], **2**, pp. 21–25.
[7] Wang, M. Z., and Wang, W., 1995, "Completeness and Nonuniqueness of General Solutions of Transversely Isotropic Elasticity," Int. J. Solids Struct., **32**(3/4), pp. 501–513.
[8] Lodge, A. S., 1955, "The Transformation to Isotropic Form of the Equilibrium Equations for a Class of Anisotropic Elastic Solids," Q. J. Mech. Appl. Math., **8**(2), pp. 211–225.
[9] Sternberg, E., and Eubanks, R. A., 1957, "On Stress Functions for Elastokinetics and the Integration of the Repeated Wave Equation," Q. Appl. Math., **15**, pp. 149–153.
[10] Sternberg, E., 1960, "On the Integration of the Equation of Motion in the Classical Theory of Elasticity," Arch. Ration. Mech. Anal., **6**, pp. 34–50.
[11] Sternberg, E., and Gurtin, M. E., 1962, "On the Completeness of Certain Stress Functions in the Linear Theory of Elasticity," Proceedings of the Fourth U.S. National Congress on Applied Mechanics, pp. 793–797.
[12] Gurtin, M. E., 1972, "The Linear Theory of Elasticity," *Handbuch der Physik* (Mechanics of Solids II Vol. Via/2), S. Flügge and C. Truesdell, eds., Springer, Berlin, pp. 1–295.
[13] Stippes, M., 1969, "Completeness of Papkovich Potentials," Q. Appl. Math., **26**, pp. 477–483.
[14] Truesdell, C., 1959, "Invariant and Complete Stress Functions for General Continua," Arch. Ration. Mech. Anal., **4**, pp. 1–29.
[15] Eskandari-Ghadi, M., and Pak, R. Y. S., 2008, "Elastodynamics and Elastostatics by a Unified Method of Potentials for x_3 Convex Domains," J. Elast., **92**(2), pp. 187–194.
[16] Eskandari-Ghadi, M., 2005, "A Complete Solution of the Wave Equations for Transversely Isotropic Media," J. Elast., **81**, pp. 1–19.
[17] Simmonds, J. G., 2000, "Love's Stress Function for Torsionless Axisymmetric Deformation of Elastically Isotropic Bodies With Body Forces," ASME J. Appl. Mech., **67**, pp. 628–629.
[18] Kellogg, O. D., 1953, *Foundation of Potential Theory*, Dover, New York.
[19] Phillips, H. B., 1933, *Vector Analysis*, Wiley, New York.
[20] Love, A. E. H., 1944, *A Treatise on the Mathematical Theory of Elasticity*, Dover, New York.

The *M*-Integral Description for a Brittle Plane Strip With Two Cracks Before and After Coalescence

Hu Yi-Feng

Chen Yi-Heng[1]
e-mail: yhchen2@mail.xjtu.edu.cn

School of Aerospace,
SVL,
Xi'an Jiaotong University,
Xi'an, Shaanxi 710049, P. R. China

In this paper we extend the M-integral concept (Eshelby, J. D., 1956, The Continuum Theory of Lattice Defects, Solid State Physics, F. Seitz and D. Turnbull, eds., Academic, New York, pp. 79–141; Eshelby, J. D., 1970, The Energy Momentum Tensor in Continuum Mechanics, Inelastic Behavior of Solids, M. F. Kanninen, ed., McGraw-Hill, New York, pp. 77–115; Eshelby, J. D., 1975, "The Elastic Energy-Momentum Tensor," J. Elast., ***5****, pp. 321–335; Knowles, J. K., and Sternberg, E., 1972, "On a Class of Conservation Laws in Linearized and Finite Elastostatics," Arch. Ration. Mech. Anal.,* ***44****, pp. 187–211; Budiansky, B., and Rice, J. R., 1973, "Conservation Laws and Energy Release Rates," ASME J. Appl. Mech.,* ***40****, pp. 201–203; Freund, L. B., 1978, "Stress Intensity Factor Calculations Based on a Conservation Integral," Int. J. Solids Struct.,* ***14****, pp. 241–250; Herrmann, G. A., and Herrmann, G., 1981, "On Energy Release Rates for a Plane Cracks," ASME J. Appl. Mech.,* ***48****, pp. 525–530; King, R. B., and Herrmann, G., 1981, "Nondestructive Evaluation of the J- and M-Integrals," ASME J. Appl. Mech.,* ***48****, pp. 83–87) to study the degradation of a brittle plan strip caused by irreversible evolution: the cracks coalescence under monotonically increasing loading. Attention is focused on the change of the M-integral before and after coalescence of two neighborly located cracks inclined each other. The influences of different orientations of the two cracks and different coalescence paths connecting the two cracks on the M-integral are studied in detail. Finite element analyses reveal that different orientations of the two cracks lead to different critical values of the M-integral at which the coalescence occurs. It is concluded that the M-integral does play an important role in the description of the damage extent and damage evolution. However, it only provides some outside variable features. This means that the complete failure mechanism due to damage evolution cannot be governed by a single parameter* M_C *as proposed by Chang and Peng, 2004, "Use of M integral for Rubbery Material Problems Containing Multiple Defects," J. Eng. Mech.,* ***130****(5), pp. 589–598. It is found that there is an inherent relation between the M-integral and the reduction of the effective elastic moduli as the orientation of one crack varies, i.e., the larger the M-integral is, the larger the reduction is. Of great significance is that the M-integral is inherently related to the change of the total potential energy for a damaged brittle material regardless of the detailed damage features or damage evolution. Therefore, this provides a useful and convenient experimental technique to measure the values of M-integral for a damaged brittle material from initial damage to final failure without use of many stain gages (King, R. B., and Herrmann, G., 1981, "Nondestructive Evaluation of the J- and M-Integrals," ASME J. Appl. Mech.,* ***48****, pp. 83–87).*
[DOI: 10.1115/1.3130818]

Keywords: M-integral, damage evolution, brittle material, finite element method, cracks coalescence

1 Introduction

As conventional engineering materials, brittle or quasibrittle materials such as ceramics, concretes, glass, polymethyl methacrylate (PMMA), etc., are still widely used in both civil engineering and mechanical engineering. The structural integrity of the components made of such materials is substantially limited to the growth of a system of distributed defects, e.g., microcrack nucleation, growth, and coalescence, that may induce damage evolution, macrocrack, and final failure. The detailed evolution process from the formation of densely distributed microcracks with random locations and orientations to a macrocrack, to the authors' knowledge, is still not fully understood up to present although some outstanding theories, e.g., the *inner variable theory*, the *effective elastic moduli theory*, and/or the *continuum damage mechanics*, have become popular in the past 20 years (see, e.g., Chaboche [1,2], Krajcinovic [3], Kachanov [4,5], and Ju and Chen [6,7] among many others). As well-known, from the mathematical point of view, the most difficult point is how to introduce some useful and convenient parameters for describing the irreversible damage evolution. For example the simplest one: the detailed process for microcracks coalescence under a monotonically increasing or cyclic loading. These parameters should not only have clear physical meanings but also be easy to measure. However, in gen-

[1]Corresponding author.

Contributed by the Applied Mechanics Division of ASME for publication in the Journal of Applied Mechanics. Manuscript received March 30, 2008; final manuscript received October 30, 2008; published online July 27, 2009. Review conducted by Zhigang Suo.

Fig. 1 The picture after crack coalescence, provided by Professor Chen Zemao (Vice Dean, School of Aerospace, Xi'an Jiaotong University)

eral, the coalescence path between two microcracks could not be known beforehand even in the simplest case where two neighborly microcracks are under consideration. Figure 1 shows a picture provided by Professor Chen Zemao (Vice Dean, School of Aerospace, Xi'an Jiaotong University), in which the coalescence among many surface microcracks can be seen.

Recently, Chen [8,9] proposed an M-integral description to study a cloud of static microcracks in an infinite plane brittle solid subjected to a remote uniform tensile loading. Instead of working in the *Continuum Damage Mechanics* by Chaboche [1,2], his investigation starts from the Eshelby's [10–12] *energy momentum tensor* and the associate invariant integrals [13–15], which have wide applications in fracture mechanics but have little applications in damage mechanics. After performing some lengthy manipulations and numerical calculations, he found that the M-integral plays an important role in the description of damaged brittle materials. For example, the tensile loading direction along which the reduction of the effective elastic modulus due to microcracking becomes maximum, whereas the tensile loading direction along which the reduction of effective elastic modulus due to microcracking becomes minimum is just the direction along which the M-integral becomes minimum. His work implies that a bridge between the invariant integral such as the M-integral and the damage mechanics might be established. Following Chen's [8,9] work, a problem-invariant parameter M_C (the critical value of the M-integral) was proposed by Chang and Chien [16] who suggested a possible fracture parameter for describing the degradation of material and structural integrity caused by irreversible evolution of multiple defects in anisotropic elastic solids. More recently, following Chen's [8,9] work, an energy parameter based on the concept of the M-integral which was proposed by Chang and Peng [17], proved to be capable of describing the fracture behavior of a multidefect mechanical system. They considered the formulation to be suited for fracture analysis in rubbery material problems subjected to large elastic deformation. On one hand, however, all the investigations mentioned above were limited to static cracks or defects without any treatment on the irreversible damage evolutions, say, the coalescence of the two cracks. On the other hand, it is still unclear whether the critical value of the M-integral denoted by M_C could be considered as a material constant or, in other words, whether the complete damage evolution process, say, the coalescence of the two neighborly located microcracks, could be governed by the single parameter M_C.

The goal of this paper is to provide a special investigation for this simplest kind of irreversible damage evolution (i.e., the irreversible coalescence of two microcracks), which is based on the M-integral concept, and to clarify whether the coalescence of the two neighborly located microcracks could be governed by the single parameter M_C. Different orientations of the two cracks are considered, which yield quite different coalescence patterns. Attention is focused on the following four points: (i) the change of the M-integral before and after coalescence of the two neighborly located cracks in a brittle plane strip; (ii) the influence of different coalescence paths on the M-integral before and after coalescence; (iii) the corresponding relationship between the M-integral and the reduction of the effective elastic muduli before and after coalescence; and (iv) the inherent relation between the change of the total potential energy (CTPE) and the M-integral before and after coalescence. Detailed finite element analyses are performed by using the ANSYS program for a strip with two cracks under plane stress deformations.

It is concluded that there is a jump of the M-integral when coalescence of the two cracks occurs. This is because the damage evolution yields the defect-configuration change from one kind of defect-configuration to another, whereas the M-integral just represents this change: the energy release during coalescence. It is found that different coalescence paths have little influence on the value of the M-integral, which can be neglected. Under a certain tensile loading, different orientations of the two cracks yield different values of the M-integral and in turn the critical values of the M-integral are different, at which coalescence occurs, implying that the critical value of the M-integral denoted by M_C is configuration-dependent. In other words, the damage evolution and the complete failure mechanism of a brittle material with many defects cannot be governed by a single parameter M_C as proposed by Chang and Peng [17]. Rather, some defect-configuration parameters should be introduced to modify the apparent dependence on the defect-configurations and damage evolution. By taking different orientations of the two cracks and comparing the calculated values of the M-integral to the reduction of the effective elastic moduli under the same tensile loading, it is concluded that the larger the M-integral is, the larger the reduction is. Of great significance is that under a monotonically increasing loading, the M-integral is inherently related to the change of the total potential energy before, during, and after coalescence for a damaged brittle material regardless of the detailed damage evolution features. This may provide a useful and convenient experimental technique to measure the values of the M-integral for a damaged brittle material during damage evolution until final failure occurs without use of many strain gages [18]. It is concluded that the M-integral does actually play an important role in the description of the damage extent and the damage evolution. However, it only provides some outside variable features (called the outside variable theory) without any consideration of the inner variable features (the so-called inner variable theory). Thus, the present investigation shows a possible way to describe the complete failure mechanism of a brittle material with many defects, i.e., the combination of the outside variable theory with the inner variable theory.

2 Basic Formulations and Finite Element Analyses

The original formulation of the M-integral established by Knowles and Sternberg [19] and Budiansky and Rice [20] is given as follows:

$$M = \oint_C (w x_i n_i - T_k u_{k,i} x_i) ds \tag{1}$$

where w, T_k, u_k, and n_i denote the strain energy density, the tractions, the displacements and the outside normal vector on the selected integral contour C, respectively; the subscript prima $\{\ \}_{,i}$ with $i=1$ or 2 refers to the corresponding differentiation with respect to the coordinates x_1 and x_2, respectively.

Usually, Eq. (1) was used to calculate the crack tip parameters for a single crack as done by Freund [21] without any treatment of damaged brittle materials with many defects. However, from the physical point of view, as the M-integral represents the energy dissipation due to the expansion of defects [20,22], there should be a bridge between the M-integral and the damage extent for static defects in brittle materials. Indeed, Chen [8,9] applied the M-integral analysis for a cloud of static microcracks in an infinite plane elastic solid and proved that the M-integral is twice the CTPE

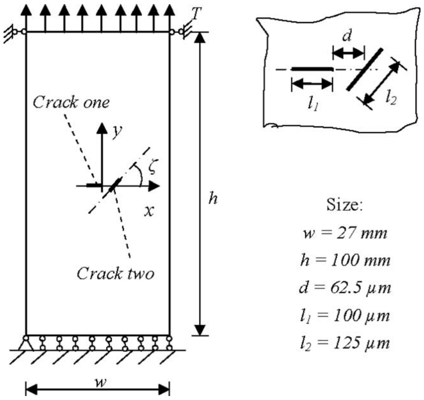

Fig. 2 A brittle strip with two neighborly located cracks before coalescence

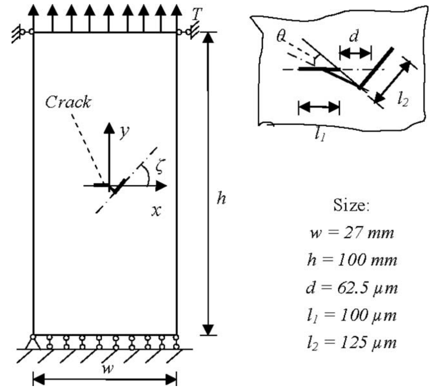

Fig. 3 Detailed configuration for the strip with the two cracks after coalescence

$$M = 2U \tag{2}$$

where U denotes the change of the total potential energy induced from the existence of the many static microcracks.

After performing detailed local-global coordinate transformations, Chen [8,9] emphasized that the M-integral for a cloud of defects is divided into two parts: the net part and the additional part.

$$M = M_N + M_A \tag{3}$$

where the first, M_N, is the summation of the contribution induced from each defect in its local coordinate system and the second, M_A, is the summation of the contribution induced from J_k-integral vector and the global coordinates of each defect center, which accounts for the interacting effects among multidefects. Thus, for a brittle material with finite dimensions, the M-integral might be dependent on the shifts of the global coordinate system. Only when the closed path selected to calculate the M-integral encloses all discontinuities including all defects and the outside boundaries could the M-integral be independent from the shifts of the global coordinate system.

However, Chen's work [8,9] was limited to static microcracks and infinite plane materials without any treatment of the damage evolution and the boundary effects of finite plane materials as shown in Fig. 2. In this section, using finite element analyses, we consider a simplest and basic 2D damage evolution problem: The coalescence between two microcracks in a finite plane brittle strip to clarify the role played by the M-integral before and after coalescence. Figure 2 shows the configuration of the brittle plane strip in which the relative location of the two cracks with respect to the outside boundaries of the strip can be changed by the orientation angle ζ being 11.25 deg, 22.5 deg, 33.75 deg, and 45 deg, respectively. The brittle strip is made of PMMA with the Young's elastic modulus $E=2.565$ Gpa and the Poisson's ratio $\nu=0.332$, and its tensile strength is approximately 40 MPa. The dimensions of the strip are 27 mm$\times$100 mm$\times$3 mm (width$\times$height $\times$thickness) with w, h, d, l_1, l_2, and ζ being the width, the height, the distance between one microcrack tip and the another microcrack center, the lengths of the two microcracks (100 μm and 125 μm, respectively), and the orientation angle of the right microcrack, respectively (Fig. 2). Here, the distance d is always taken to be 62.5 μm. Thus, strong interaction between the two cracks exists. Detailed dimensions of the strip are shown in Fig. 2, which corresponds to the case before coalescence of the two cracks. Alternatively, Fig. 3 shows the configuration after coalescence of the two cracks, provided that the coalescence occurs along the straight connecting line starts from one crack tip and ends at another crack surface or tip, depending on the value of the inclined angle θ. By using the ANSYS program, the schematic finite element meshes before coalescence of the two cracks for the four orientation angles 11.25 deg, 22.5 deg, 33.75 deg, and 45 deg, are shown in Figs. 4(*a*)–4(*d*), respectively. Figures 5(*a*)–5(*d*) show the schematic finite element meshes after coalescence of the two cracks for the four orientation angles 11.25 deg, 22.5 deg, 33.75 deg, and 45 deg, respectively, where the connecting path starts from one crack tip and ends at another crack surface or tip, depending on the value of the inclined angle θ (see Fig. 3). In order to avoid the mesh sensitivity on the results of the M-integral, two kinds of mesh in the ANSYS program adopted in the present calculation: the fine free mesh with more than 12,000 elements and the mapped mesh in the ANSYS program. It is verified that the relative errors induced from the mesh sensitivity are always less than 0.5%. Moreover, in our calculation, the two very flat ellipses with major axis 100 μm and minor axis 5 μm are adopted in Figs. 4(*a*)–4(*d*) and Figs. 5(*a*)–5(*d*). The profiles near each root of all ellipses are approximately similar as we can possibly infer.

It is seen that the coalescence paths determined from the maximum hoop stress criterion indicated by the red marks in Figs. 6(*a*)–6(*d*) for the four orientation angles for the four cases are quite different. Figures 7(*a*)–7(*d*) show the deformation features after the two cracks coalescence. In order to avoid the boundary effect of the strip [8,9], Figs. 8(*a*) and 8(*b*) show four typical integral paths selected for calculating the M-integral before or after coalescence for the strip with the two cracks. In Fig. 8(*a*), path 1 and path 2 are selected within the strip, whereas in Fig. 8(*b*) path 3 and path 4 are selected outside the strip by introducing an imaginary material with much smaller elastic modulus surrounding the strip. As the elastic modulus of the imaginary material tends to zero [8,9], we can account for the boundary effect of the strip on the additional part of the M-integral denoted by M_A on the right hand side of Eq. (2). After using the ANSYS program and performing detailed finite element analyses, we proved in Table 1 (before coalescence) and Table 2 (after coalescence) that the values of the M-integral calculated from the two paths in Fig. 8(*a*) and those from the two paths in Fig. 8(*b*) were approximately the same whenever the coalescence occurs or not, implying that the boundary effect of the plane strip could be neglected. This is because the two cracks with the length of about 100 μm are always located far apart from the boundaries of the strip (several millimeters). Thus, we can focus our attention on the influence of the change of the orientation angle ζ and the coalescence paths between the two cracks on the M-integral before and after coalescence. It should be emphasized that the slopes of the M-integral curves against the loading before and after the coalescence are quite different. That is, the slopes before the coalescence should always be less than those after the coalescence (see Figs. 9–11). Therefore, all the ratio of the M-integral at 4.7 MPa (after coalescence) to the M-integral at 3 MPa (before coalescence) should always be greater than the ratio $(4.7/3)^2=2.4544$ without any doubt. For example, in the case of 11.25 deg the two values of the

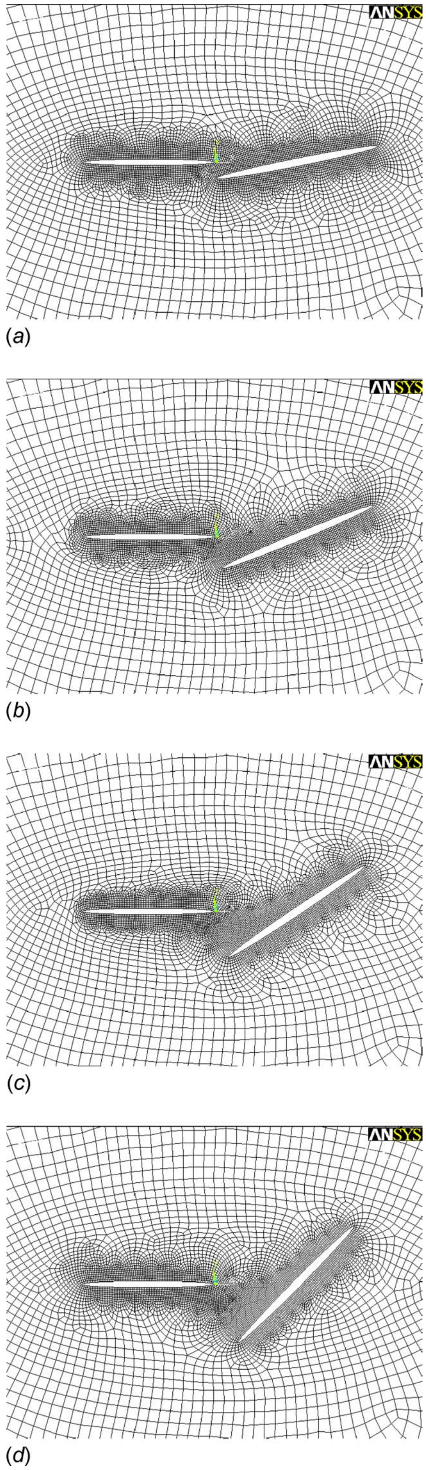

Fig. 4 Finite element meshes before coalescence of the two cracks for the four orientation angles (*a*) 11.25 deg, (*b*) 22.5 deg, (*c*) 33.75 deg, and (*d*) 45 deg

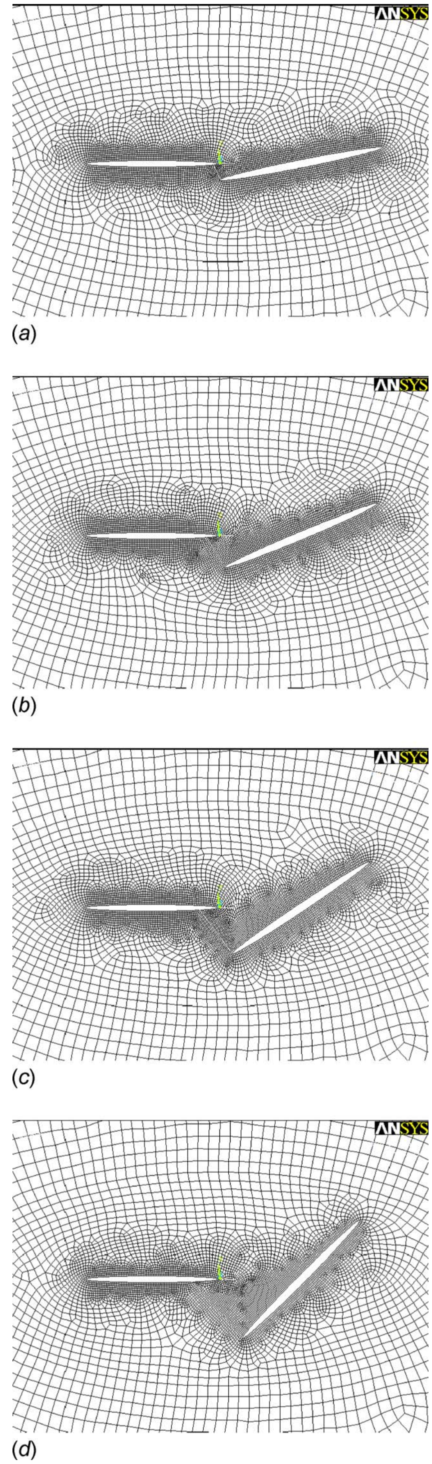

Fig. 5 Finite element meshes after coalescence of the two cracks for the four orientation angles (*a*) 11.25 deg, (*b*) 22.5 deg, (*c*) 33.75 deg, and (*d*) 45 deg

M-integral before and after coalescence are 6.8373 and 1.9131, respectively, with $6.8373/1.9131=3.5740$ larger than the ratio 2.4544. In the cases of 22.5 deg and 33.75 deg, the two values are 6.6420 and 1.6684 with $6.6420/1.6684=3.9811$, and 6.3158 and 1.4168 with $6.3158/1.4168=4.4578$, which are also larger than the ratio $(4.7/3)^2=2.4544$. Physically, this conclusion describes the energy release due to the defect expansion [20] or the change of the defect-configuration from two cracks to one complicated defect.

3 Dependence of the Critical M-Integral Value on the Two Cracks Orientations

In order to clarify whether M_C, as proposed by Chang and Chien [16], is a critical material constant for a brittle material with many cracks, in this section we deal with the possible dependence of the critical M-integral value on the two cracks orientation under monotonically increasing loadings. According to the classical material strength theory, the critical tensile loading at the coalescence

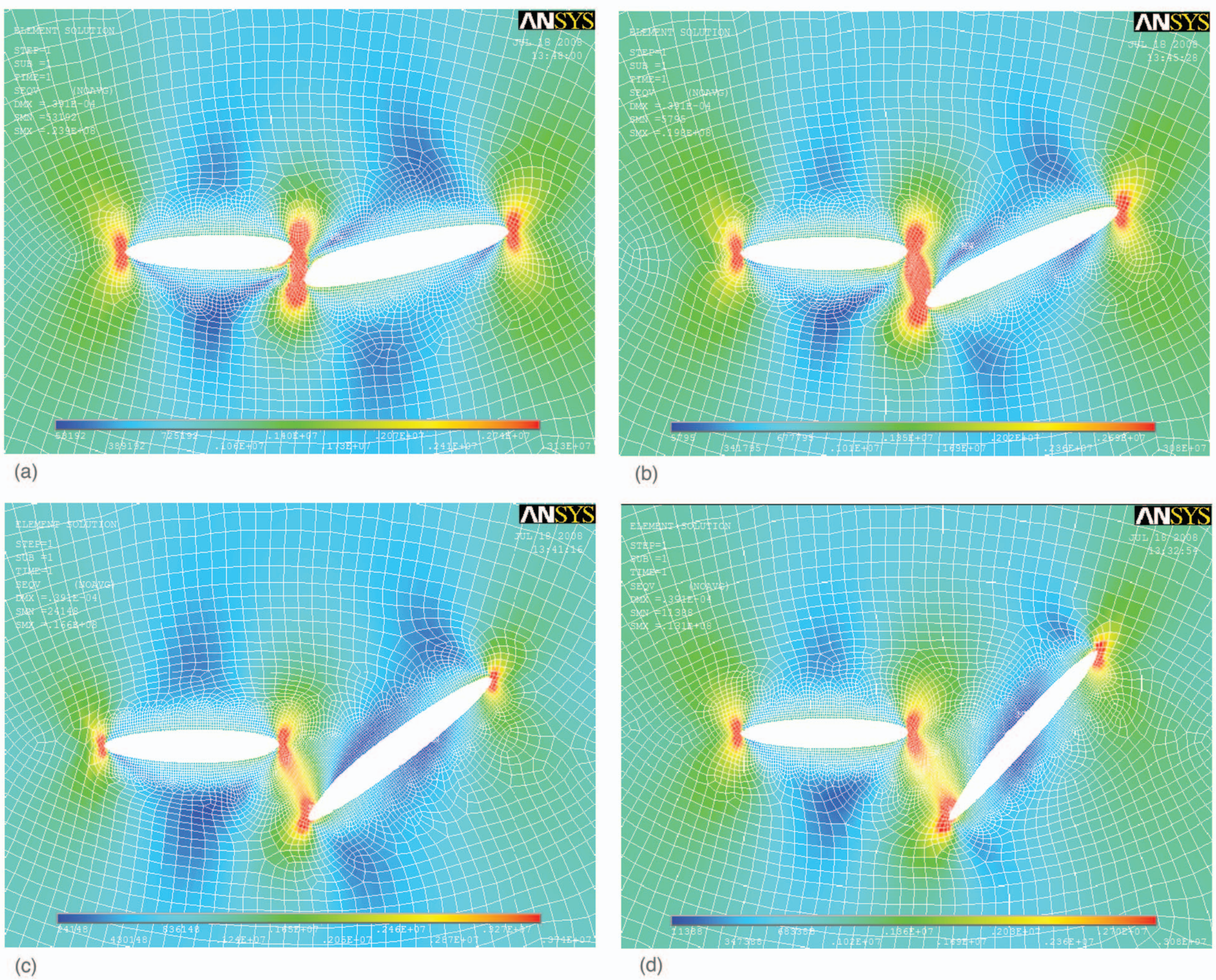

Fig. 6 Finite element analyses for the maximum von-Mises stress along the two cracks (red points) before coalescence for the four orientation angles (*a*) 11.25 deg, (*b*) 22.5 deg, (*c*) 33.75 deg, and (*d*) 45 deg

of two cracks for each of the four orientation angles: 11.25 deg, 22.5 deg, 33.75 deg, and 45 deg, respectively, as listed in Table 3, under which the maximum hoop stress at the red marks in Figs. 7(*a*)–7(*d*) reaches the material strength of 40 MPa. Also, the calculated values of the critical value of the M-integral for each of the four angles are also listed in Table 3.

It is seen from Table 3 that the values of the critical M-integral for the four orientation angles are quite different and the values of the critical tensile loading are quite different either. For example, the minimum critical value of the M-integral is approximately 2.8784 N at 45 deg, whereas the minimum critical value of the tensile loading is approximately 3.8367 MPa at 11.25 deg corresponding to the two cracks nearly perpendicular to the tensile loading direction (see Fig. 2). Obviously, the critical M-integral value does depend on the two cracks orientation as the angle ζ varies. It is concluded that during coalescence between the two cracks the critical value of the M-integral is configuration-dependent and there is no correspondence between the critical values of the M-integral and the critical values of the tensile loading when the orientation angle ζ varies.

What is more, Table 4 shows the critical value of the M-integral and the critical tensile loading at final failure of the strip after coalescence. It is seen that these two parameters, i.e., the critical value of the M-integral and the critical tensile loading, are also quite different when the angle ζ varies. Of great interest is that there is always a jump of the M-integral from coalescence to final failure. Table 4 indicates that the jump is 8.6577, 6.0517, 3.4567, and 2.9213×10^{-4} N for 11.25 deg, 22.5 deg, 33.75 deg, and 45 deg, respectively, implying that the maximum jump of the M-integral occurs at 11.25 deg. It is concluded that the critical value of the M-integral at coalescence or at final failure is always configuration-dependent. In other words, the damage evolution and the complete failure mechanism of a brittle material with many defects cannot be governed by a single parameter M_C as proposed by Chang and Peng [17]. Rather, some defect-configuration parameters should be introduced to modify the apparent dependence on the defect-configurations and damage evolution.

It should be noticed in Table 4 that after coalescence the minimum of the M-integral occurs at orientation angle of 45 deg and the minimum of critical tensile loading is at the angle of 45 deg, too, whereas both maximum critical values of the M-integral and the tensile loading are at 11.25 deg. Thus, an approximate equivalence between the critical value of the M-integral and the critical hoop stress seems existent after coalescence. However, to the authors' knowledge, this might not always be coincidental in general. In fact, after coalescence the two cracks for each of the four orientation angles 11.25 deg, 22.5 deg, 33.75 deg, and 45 deg become a *single complicated defect*. From the phenomenological point of view, the four kinds of the induced complicated defects are quite different (see Figs. 7(*a*)–7(*d*)) and could not be compared to each other (just as the critical values of the M-integral for

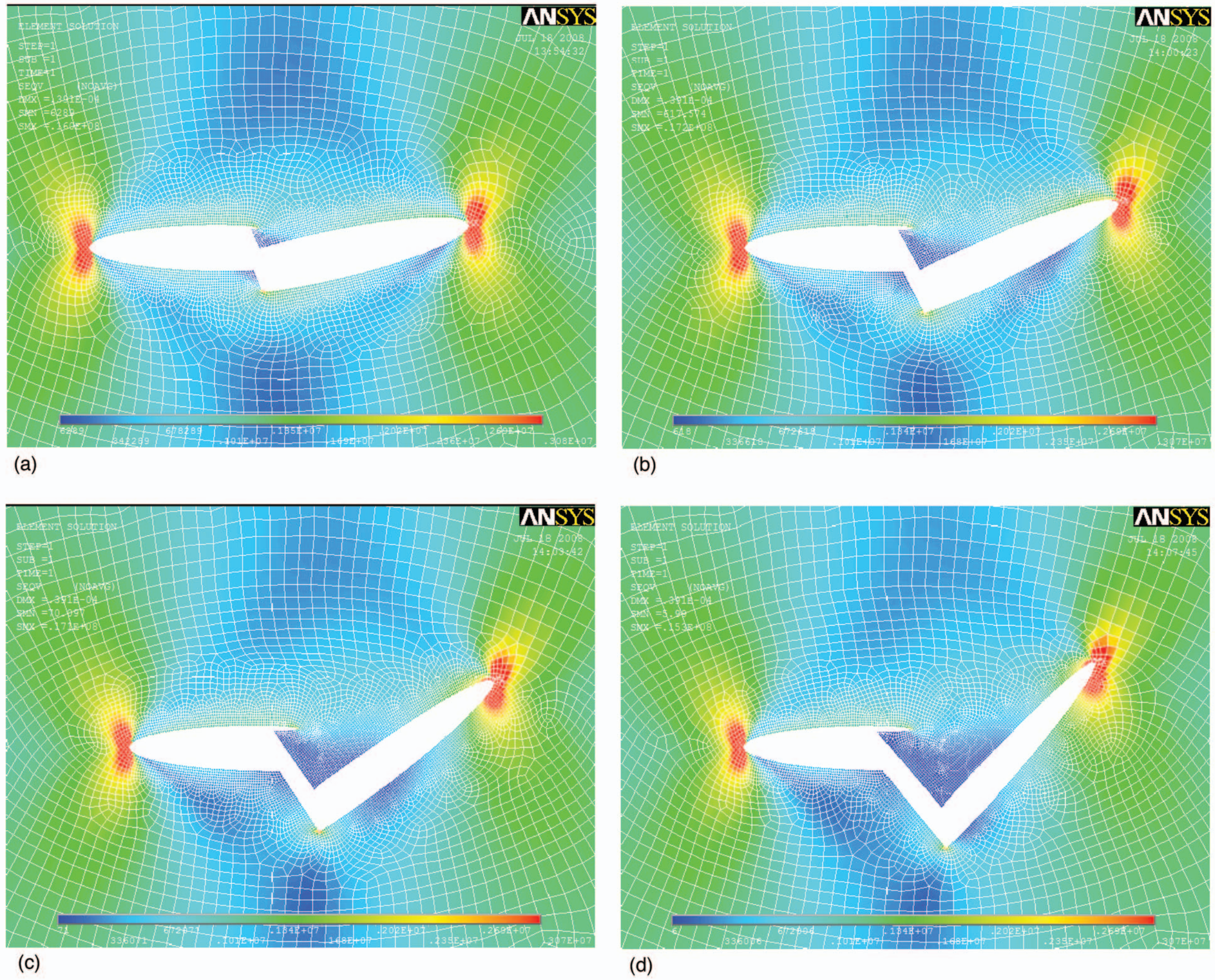

Fig. 7 Finite element analyses for the maximum von-Mises stress along the crack (red points) after coalescence for the four orientation angles (*a*) 11.25 deg, (*b*) 22.5 deg, (*c*) 33.75 deg, and (*d*) 45 deg

a hole and for a crack in an infinite plane could not be compared to each other). It is well-known that the physical meaning of the M-integral is the energy release due to the defect expansion [20] and then the critical values of the M-integral after coalescence for each of the four orientation angles 11.25 deg, 22.5 deg, 33.75 deg and 45 deg should represent the energy release due to the unit expansion of the induced complicated defects. Obviously, the different defects formed after coalescence yield quite different expansion paths in a large region of the strip (just as the kinking or branching of a *single inclined crack* under a tensile loading). At present, generally speaking, it cannot be ensured that the critical values of the M-integral in other cases with many microcracks after coalescence are still corresponding to the critical values of the maximum hoop stress at final failure as shown in Table 4. Moreover, this again verifies that the final failure could not be governed by a single parameter M_C.

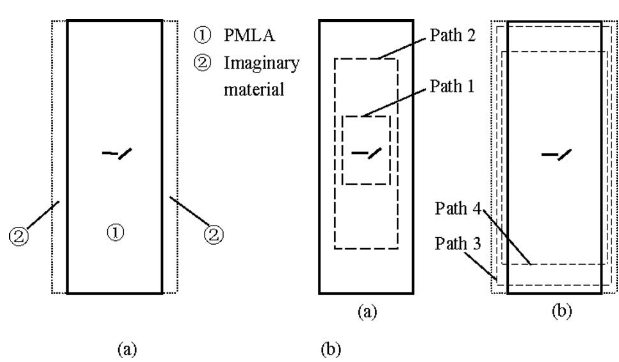

Fig. 8 Four typical closed paths for calculating the *M*-integral before or after coalescence between the two cracks: (*a*) paths 1 and 2 are within the PMLA material and (*b*) paths 3 and 4 are in an imaginary material with infinite small Young's modulus outside the PMLA material

Now, let us study the relationship between the M-integral and the change of the total potential energy for each of the four orientation angles of the two cracks as the coalescence path varies or the angle θ varies (i.e., 10 deg, 20 deg, and 30 deg) with respect to the connecting straight line, respectively. The calculated values of the M-integral under 3 MPa tensile loading (before coalescence) are listed in Table 5. It is seen from Table 5 that the numerical accuracies are very good, always with some relative errors less than 0.5%, which conform a good agreement between the M-integral and twice the CTPE denoted by U. It is found from Table 5 that the inclined coalescence paths have little influence on the values of the M-integral or CTPE, which could be neglected. This indicates that the M-integral as being equivalent to the CTPE presents a phenomenological or outside variable feature regardless of the detailed coalescence paths of the two small cracks. Thus, the results obtained above are confirmed again without any doubt.

Table 1 Calculated values of the *M*-integral and the CTPE under 3 MPa along the four different closed paths before coalescence

Orientation angle ζ (deg)	$M(10^{-4}$ J/m) along path 1	$M(10^{-4}$ J/m) along path 2	$M(10^{-4}$ J/m) along path 3	$M(10^{-4}$ J/m) along path 4	$M_{avg}(10^{-4}$ J/m) average value	$2U(10^{-4}$ J/m)
11.25	1.8909	1.8825	1.8737	1.8835	1.8827	1.9131
22.5	1.6693	1.6666	1.6709	1.6753	1.6705	1.6684
33.75	1.3894	1.3900	1.3855	1.3861	1.3878	1.4168
45	1.1494	1.1456	1.1443	1.1441	1.1459	1.1705

Moreover, the calculated values of the M-integral and twice the CTPE for the four orientation angles 11.25 deg, 22.5 deg, 33.75 deg, and 45 deg, are respectively plotted in Figs. 9–12, where a jump always occurs in each figure at which the maximum hoop stress around the two cracks tips reaches the material strength (40 Mpa) and the coalescence between the two cracks occurs. Physically, this jump represents the energy release during coalescence as a special kind of defect expansion [22]. It is concluded that the curves of the M-integral coincide well with those of twice the CTPE whenever the coalescence occurs or not. In other words, during the damage evolution, this inherent relation still holds although both the M-integral and the CTPE have a jump during coalescence. Perhaps, the jumps of the M-integral before and after coalescence may not be important in the monotonically tensile loading cases, but it may be very important in the cyclic tensile loading cases. Indeed, under the cyclic tensile loading the stress concentration points after coalescence are quite different from those before coalescence and so does the M-integral. It is concluded that the critical values of the M-integral for the four orientation angles are quite different as shown in Table 1 (before coalescence) and Table 2 (after coalescence), imply that the critical values are configuration-dependent. In other words, the detailed process of the damage evolution (i.e., the cracks coalescence) could not be governed by a single parameter M_C as proposed by Chang and Chien [16].

It can be imagined that the present investigation provides a useful experimental technique to measure the values of the M-integral for a damaged brittle material *before, during, and after damage evolution*. That is, instead of directly measuring the M-integral in which a number of strain gages should be placed on a specimen [18], we can measure another parameter CTPE before, during, and after damage evolution without the use of the gages.

4 Relation Between the *M*-Integral and the Reduction of Effective Elastic Moduli

This section deals with the inherent relation between the M-integral and the reduction of the vertical effective elastic modulus due to the two cracks. Calculated values of the M-integral and the calculated values of the vertical effective elastic modulus against the orientation angle of the two cracks, ζ, before and after coalescence are given in Tables 3 and 4, respectively. Here, the vertical effective elastic modulus is calculated by $E_{\text{effect}}=\bar{\sigma}/(\overline{\Delta h}/\text{h})$ with $\bar{\sigma}$ and $\overline{\Delta h}$ denoting the average tensile stress and the average displacement along the top side of the strip as shown in Figs. 2 and 3 and listed in Tables 3 and 4. It is seen in Tables 3 and 4 that the values of the M-integral just show apparently opposite features to those of the reduction of the vertical effective elastic modulus when the orientation angle varies. Indeed, before coalescence the maximum value of the M-integral occurs at 11.25 deg, whereas the minimum value of the vertical effective elastic modulus also occurs at 11.25 deg, which corresponds to the largest reduction of the modulus against the orientation angle. What is more, the minimum value of the M-integral occurs at 45 deg as shown in Table 3, whereas the maximum value of the vertical effective elastic modulus also occurs at 45 deg, which corresponds to the smallest effective modulus reduction against the orientation angle. Table 4 shows the same conclusion as Table 3. That is, the larger the M-integral is, the smaller the vertical effective elastic modulus is or the larger the reduction of the effective elastic modulus is.

It is seen that the modulus differs only in the sixth digit in Tables 3 and 4 when the orientation varies but the M-integral differs quite remarkably with a precision 0.5% as mentioned above. This is because the damage region induced from the two cracks (whenever coalescence occurs or not) is merely around 200 μm and then yields very small reduction of the effective elastic modulus of the strip with 27 mm width, whereas the M-integral represents the energy release induced from the two cracks expansions [20], which should be much more sensitive than the effective modulus when the orientation varies. Of course, the meshing or numerical rounding affects the results should be addressed. We have used both the fine free mesh and the mapped mesh to address the numerical rounding affects on the results. The relative errors could be evaluated and controlled by doubling the free mesh for each of the four orientation angle, which can be automatically induced from the ANSYS program without any difficulty.

Here, an explanation should be given as why the M-integral has a precision of 0.5% and the effective elastic modulus has a precision of 10^{-7}. This is because the output for a plane elastic problem using the ANSYS program is the displacements at all nodes from which the stresses at any point can be calculated by strains from the partial differential methods. Thus, another approximate technique such as the central difference method from the displacements at the neighborly located nodes around the point needed is involved in the ANSYS program. As well-known, the relative errors of the node displacements can be easily controlled by doubling the finite element mesh, whereas the relative errors of the stresses or strains should depend on the approximate technique (e.g., the central difference method). From the error analysis point of view, the

Table 2 Calculated values of the *M*-integral and the CTPE under 4.7 MPa along the four different closed paths after coalescence

Orientation angle ζ (deg)	$M(10^{-4}$ J/m) along path 1	$M(10^{-4}$ J/m) along path 2	$M(10^{-4}$ J/m) along path 3	$M(10^{-4}$ J/m) along path 4	$M_{avg}(10^{-4}$ J/m) average value	$2U(10^{-4}$ J/m)
11.25	6.7692	6.7886	6.7588	6.7803	6.7743	6.8373
22.5	6.5744	6.5922	6.5632	6.5837	6.5784	6.6420
33.75	6.2487	6.2646	6.2365	6.2559	6.2514	6.3158

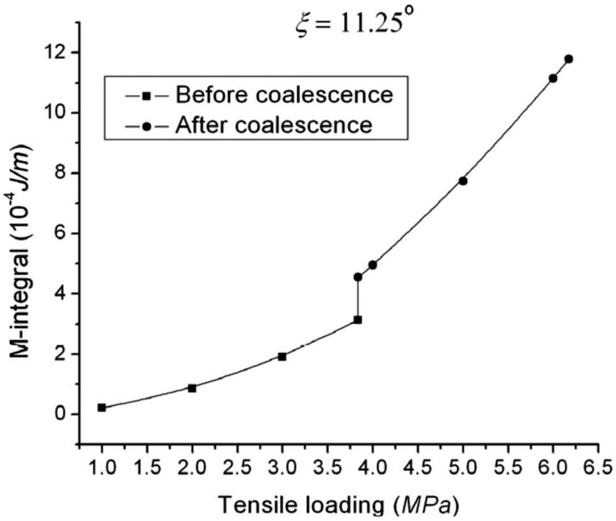

Fig. 9 The calculated curves of the *M*-integral and CTPE denoted by 2*U* for the angle 11.25 deg of the two cracks before and after coalescence

precision of the node displacements is always much higher than the stresses or strains although the ANSYS program provides a good technique to ensure the precision of the stresses or strains. As regards the data of the M-integral and the effective elastic modulus, the precision the M-integral and the precision of the effective elastic modulus for the same damage configuration are quite different. Obviously, the precision of the latter is much higher than the former because the effective elastic modulus can be directly calculated from the average node displacements along the top line of the plane strip and the corresponding tensile loading without any other loss of precision, whereas the precision of the M-integral not only depends on the selected path but also depends on the involving special partial differentials, $u_{k,j}$, (see the second term on the right hand side of Eq. (1)), i.e., the partial differentials of the displacements with respect to the coordinates, which cannot be calculated directly by the ANSYS. Thus, a new complementary program (e.g., the central difference method from the displacements at the neighborly located nodes) should be written to overcome this obstacle. Of course, during performing this

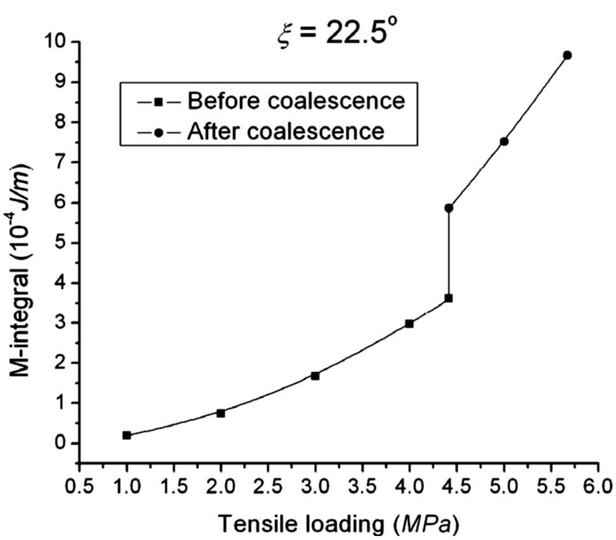

Fig. 10 The calculated curves of the *M*-integral and CTPE denoted by 2*U* for the angle 22.5 deg of the two cracks before and after coalescence

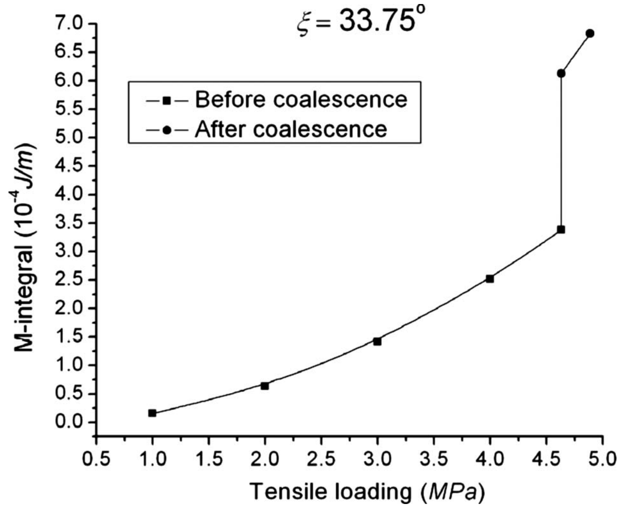

Fig. 11 The calculated curves of the *M*-integral and CTPE denoted by 2*U* for the angle 33.75 deg of the two cracks before and after coalescence

complementary program, some additional errors should unavoidably be induced. This is the reason as why the calculation of the M-integral only has a precision 0.5% mentioned above and the calculation of the effective elastic modulus has a precision 10^{-7} (see Tables 3 and 4).

Finally, it should be emphasized that the M-integral shows an apparent configuration-dependence when the orientation angle ζ of the two cracks varies whatever the coalescence between the two cracks occurs or not. It is proved that the critical value of the M-integral is not a material constant when the orientation angle ζ of the two cracks varies although the M-integral does play an important role in the microcrack damage evolution. How to use the M-integral concept in description of the damage stability and evolution is absolutely important. This topic remains to be further investigated.

5 Conclusions and Remarks

After performing the above numerical analyses, we summarize the following conclusions:

(1) The M-integral plays an important role in description of the damage evolution in brittle materials, for example, the cracks coalescence in brittle materials. Under a monotonically increasing loading, damage evolution always increases the value of the M-integral. For example, there is a jump of the M-integral when coalescence of the two cracks in a plane strip occurs.

(2) The present investigation reveals that the M-integral can provide some outside variable features, called as the outside variable theory, for damaged brittle materials, which might open a new technique or framework to evaluate material damage evolution. Unlike those of the inner variable theory (e.g., the effective elastic moduli theory), the outside variable theory established here and in Chen's [8,9] works provide some phenomenological features of damage and damage evolution in brittle materials.

(3) An inherent relation between the M-integral and the reduction of the effective elastic moduli exists when the orientation angle varies before and after coalescence. That is, for a certain multiple defects configuration, the larger the M-integral is, the larger the reduction of the effective elastic moduli is, whenever the damage evolution occurs or not! When the damage evolution occurs, both the M-integral and the reduction of the effective elastic moduli increase synchronously.

Table 3 The critical tensile loading at coalescence for each of the four orientation angles

Orientation angle (deg)	11.25	22.5	33.75	45
Critical tensile loading σ_{cr}(MPa)	3.836727	4.416336	4.630421	4.704536
Critical value of the M-integral (10^{-4} J/m)	3.1291	3.6155	3.3754	2.8784
Average displacement $\overline{\Delta h}$(10^{-4} m)	1.491110	1.716365	1.799562	1.828361
Effective elastic modulus (GPa) $E_{\text{effect}}=\bar{\sigma}/(\overline{\Delta h}/\text{h})$	2.573068	2.573075	2.573082	2.573089

Table 4 The critical tensile loading at final failure after coalescence for each of the four orientation angles

Orientation angle (deg)	11.25	22.5	33.75	45
Critical tensile loading σ_{cr}(MPa)	6.170965	5.670193	4.888370	4.658115
Critical value of the M-integral (10^{-4} J/m)	11.7868	9.6672	6.8321	5.7997
Jump of the M-integral from coalescence to final failure (10^{-4} J/m)	8.6577	6.0517	3.4567	2.9213
Average displacement $\overline{\Delta h}$(10^{-4} m)	2.398312	2.203688	1.899835	1.810344
Effective elastic modulus (GPa) $E_{\text{effect}}=\bar{\sigma}/(\overline{\Delta h}/\text{h})$	2.573045	2.573047	2.573050	2.573055

(4) The major obstacle is that the critical value of the M-integral is not a material constant when the orientation angle varies before and after coalescence. In other words, even in the present single axis tensile problem, the detailed damage evolution cannot be governed by a single parameter M_C. Rather, it is critical value shows an apparent configuration-dependence when the orientation angle varies. For example, the critical value depends on the relative locations and orientations of the two cracks although it does not depend on the detailed coalescence path connecting the two cracks. Some modifications are needed to combine both the outside variable features and the inner variable features.

(5) The M-integral is inherently related to the change of the total potential energy for a damaged brittle material regardless of the detailed damage feature (i.e., the defect configurational independence). Therefore, this provides a useful and convenient experimental technique to measure the values of the M-integral for a damaged brittle material from initial evolution to final failure without use of the so-called nondestructive evaluation method proposed by King and Herrmann [18] with many strain gages. Detailed experimental data will be given in sequel.

Table 5 Calculated values of the *M*-integral and the CTPE under 3 MPa for three different coalescence paths after coalescence with θ being the inclined angle with respect to the straight connecting path between the two crack tips

Orientation angle (deg)	M-integral or $2U$(10^{-4} J/m)		
	θ=10 deg	θ=20 deg	θ=30 deg
11.25	4.95382	4.95232	4.95246
22.5	4.81160	4.81086	4.81150
33.75	4.57430	4.57456	4.57654
45	4.27438	4.27668	4.28274

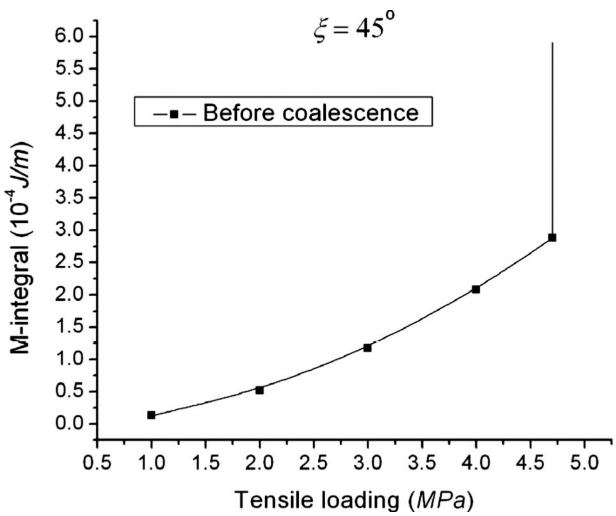

Fig. 12 The calculated curves of the *M*-integral and CTPE denoted by 2*U* for the angle 45 deg of the two cracks before and after coalescence

Acknowledgment

This work was supported by the National Science Foundation of China (Grant No. 10572110) and the Doctorial Foundation of the Chinese Ministry.

References

[1] Chaboche, J. L., 1988, "Continuum Damage Mechanics: Part I-General Concepts," ASME J. Appl. Mech., **55**, pp. 59–64.
[2] Chaboche, J. L., 1988, "Continuum Damage Mechanics: Part II-Damage Growth, Crack Initiation, and Crack Growth," ASME J. Appl. Mech., **55**, pp. 65–72.
[3] Krajcinovic, D., 1989, "Damage Mechanics," Mech. Mater., **8**, pp. 117–197.
[4] Kachanov, M., 1992, "Effective Elastic Properties of Cracked Solids: Critical Review of Some Basic Concepts," Appl. Mech. Rev., **45**, pp. 304–335.
[5] Kachanov, M., 1993, "Elastic Solids of Many Cracks and Related Problems," Adv. Appl. Mech., **30**, pp. 259–428.
[6] Ju, J. W., and Chen, T. M., 1994, "Effective Elastic Moduli of Two-Dimensional Brittle Solids With Interacting Microcracks, Part I: Stationary Models," ASME J. Appl. Mech., **61**, pp. 349–357.
[7] Ju, J. W., and Chen, T. M., 1994, "Effective Elastic Moduli of Two-Dimensional Brittle Solids With Interacting Microcracks, Part II: Evolutionary Damage Models," ASME J. Appl. Mech., **61**, pp. 358–366.
[8] Chen, Y.H., 2001 "M-Integral Analysis for Two-Dimensional Solids With Strongly Interacting Cracks, Part I. In an Infinite Brittle Sold," Int. J. Solids Struct., **38**, pp. 3193–3212.
[9] Chen, Y. H., 2001, "M-Integral Analysis for Two-Dimensional Solids With Strongly Interacting Cracks, Part II. In the Brittle Phase of an Infinite Metal/Ceramic Biomaterial," Int. J. Solids Struct., **38**, pp. 3213–3233.
[10] Eshelby, J. D., 1956, *The Continuum Theory of Lattice Defects, Solid State Physics*, F. Seitz and D. Turnbull, eds., Academic, New York, pp. 79–141.
[11] Eshelby, J. D., 1970, *The Energy Momentum Tensor in Continuum Mechanics, Inelastic Behavior of Solids*, M. F. Kanninen, ed., McGraw-Hill, New York, pp. 77–115.
[12] Eshelby, J. D., 1975, "The Elastic Energy-Momentum Tensor," J. Elast., **5**, pp. 321–335.
[13] Rice, J. R., 1968, "A Path-Independent Integral and the Approximation Analysis of Strain Concentration by Notches and Cracks," ASME J. Appl. Mech.,

35, pp. 297–320.
[14] Rice, J. R., 1968, *Mathematical Analysis in the Mechanics of Fracture*, H. Liebowitz, ed., Academic, New York, vol. 2, pp. 191–311.
[15] Cherepanov, G. P., 1974, *Mechanics of Brittle Fracture Mechanics*, McGraw-Hill, New York, pp. 235–323.
[16] Chang, J. H., and Chien, A. J., 2002, "Evaluation of M-Integral for Anisotropic Elastic Media With Multiple Defects," Int. J. Fract., **114**(3), pp. 267–289.
[17] Chang, J. H., and Peng, D. J., 2004, "Use of M integral for Rubbery Material Problems Containing Multiple Defects," J. Eng. Mech., **130**(5), pp. 589–598.
[18] King, R. B., and Herrmann, G., 1981, "Nondestructive Evaluation of the J- and M-Integrals," ASME J. Appl. Mech., **48**, pp. 83–87.
[19] Knowles, J. K., and Sternberg, E., 1972, "On a Class of Conservation Laws in Linearized and Finite Elastostatics," Arch. Ration. Mech. Anal., **44**, pp. 187–211.
[20] Budiansky, B., and Rice, J. R., 1973, "Conservation Laws and Energy Release Rates," ASME J. Appl. Mech., **40**, pp. 201–203.
[21] Freund, L. B., 1978, "Stress Intensity Factor Calculations Based on a Conservation Integral," Int. J. Solids Struct., **14**, pp. 241–250.
[22] Herrmann, G. A., and Herrmann, G., 1981, "On Energy Release Rates for a Plane Cracks," ASME J. Appl. Mech., **48**, pp. 525–530.

A Slip Damping Model for Plasma Sprayed Ceramics

Peter J. Torvik
Professor Emeritus
Fellow ASME
Air Force Institute of Technology,
1866 Winchester Road,
Xenia, OH 45385
e-mail: torvik@att.net

Ceramic materials applied by air plasma spray are used as components of thermal barrier coatings. As it has been found that such coatings also dissipate significant amounts of energy during vibration, they can also contribute to reducing the amplitude of resonant vibrations. In order to select a coating material for this purpose, or to adjust application parameters for increased dissipation, it is important that the specific mechanism, by which such dissipation occurs, be known and understood. It has been suggested that the dissipative mechanism in air plasma sprayed coatings is friction, along interfaces arising from defects between and within the "splats" created during application. An analysis, similar to that for the dissipation in a lap joint, is developed for an idealized microstructure characteristic of such coatings. A measure of damping (loss modulus) is extracted, and the amplitude dependence is found to be similar to that observed with actual coating materials. A critical combination of parameters is identified, and variations within the microstructure are accounted for by representing values through a distribution. The effective or average value of the storage (Young's) modulus is also developed, and expressed in terms of the parameters of the microstructure. The model appears to provide a satisfactory analytical representation of the damping and stiffness of these materials. [DOI: 10.1115/1.3132182]

Keywords: mechanical properties of materials, damping, friction

1 Introduction

As typically used, the term internal friction is an inclusive term for all types of material damping, regardless of mechanism. However, there appear to be cases in which the mechanism of material damping is truly the Coulomb friction, as in contacts at grain boundaries or in materials constructed from unbonded aggregates. In some cases, the energy dissipation due to frictional losses may be significant. One such case appears to be the dissipation arising in plasma sprayed ceramics as a consequence of relative motion within and between the "splats" resulting from the spraying process.

A distinction should be made between two classes of dissipation due to friction. In the first, the contacting bodies are taken to be rigid, and the same relative displacement is assumed over the entire contact surface. This is referred to as *gross slip*, *sliding*, *or macroslip damping*. In the second class the relative displacement of the contacting bodies varies over the contact region. This type of dissipation due to friction is referred to as *partial slip*, *microslip*, or *slip damping*. While either type can dissipate large amounts of energy, both are subject to such limitations as the dependence on an interfacial contact pressure that may be difficult to evaluate or regulate, and the propensity toward fretting and wear.

In the case of sliding or macroslip damping, the relative displacement across the interface is either zero or the same for all locations in the contact region between two rigid bodies. The energy dissipated per cycle of vibration is proportional to the product of the amplitude and the frictional force.

In the case of slip or microslip damping, the deformation of the contacting surfaces enables the relative displacement between corresponding points across some or the entire interface to vary with the location. A general characteristic of systems incorporating slip damping treated as local Coulomb friction is that the energy dissipated per cycle varies as the third power of the amplitude of the alternating load, and inversely as the interfacial shear stress. The stronger dependence on amplitude occurs because the slipping region itself increases with the level of load. Analyses have been given for the response of contacting spheres to an oscillating tangential force or to a torque about the common diameter [1]. The slip damping generated between a beam and a spar cap [2] and in the lap joint in tension [3] has also been evaluated. The dissipation due to partial debonding of a laminate [4] is also of this class. A thorough discussion of slip damping has been provided by Goodman [5].

Coulomb friction has also been assumed in the related problem of determining the length of the slipping region at the fiber-matrix interface when a crack impinges on the interface. Some deficiencies have been noted. These include that plasticity is neglected [6], that tension and compression are not symmetric [7], and that repeated cycling may change the interfacial shear stress [8]. The hysteresis loops predicted for cyclic loading in a composite with Coulomb friction at the fiber matrix interface have also been compared with experiment [8], but the energy dissipated was not evaluated.

A characteristic force-displacement relationship for a system with slip is shown in Fig. 1. Loading from the undeformed state proceeds along the trajectory *o-a*, with the onset of gross slip at a'. The initial response may be linear or nonlinear, depending on whether the slip begins immediately or at some critical load. A nonlinearity indicates that the specimen is changing in stiffness as slip progresses. If the loading direction is reversed at $a < a'$, unloading occurs along a-o'-b. If the loading direction is reversed at b and then reloaded through b-$0''$-a, a hysteresis loop is formed; the enclosed area of which represents the net work done over the cycle, i.e., the energy dissipated.

2 Damping Characteristics of Plasma Sprayed Ceramics

Recently, there has been a high level of interest in the inherent damping of plasma sprayed ceramics such as alumina, stabilized zirconia, or magnesium-aluminate spinel, when applied as thin coatings to the blades of turbine engines, as components of thermal barrier coatings. A number of studies have shown that the

Contributed by the Applied Mechanics Division of ASME for publication in the Journal of Applied Mechanics. Manuscript received July 18, 2008; final manuscript received April 3, 2009; published online July 27, 2009. Review conducted by Matthew R. Begley.

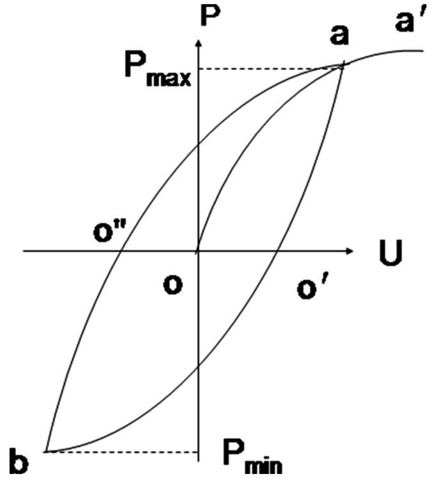

Fig. 1 Force-displacement hysteresis loop with partial slip

damping of such materials increases approximately linear with strain to a critical value (usually 100–200 ppm of interfacial strain) and then remains constant, or diminishes [9].

The splats resulting from the plasma spray process lead to a coating, having internal structure, with the splat orientation nominally parallel to the substrate. Shipton and Patsias [10] examined the microstructure of the plasma sprayed magnesium aluminate spinel by optical and scanning electron microscopy, and found a large population of vertical defects within the splats. The resultant structure (Fig. 2) of the subdivided splats was found to be analogous to an array of ordered parallel sided blocks, of which the thickness and length appear to be only a few micrometers. Friction arising from relative displacements at such interfaces was suggested as the damping mechanism in these materials. This hypothesis was supported by the observation that a spray orientation normal to the substrate led to an improved alignment of interfaces with the axis of strain, and to a higher level of damping. Experiments simulating a coated beam by a vibrating beam with segmented and overlapping cover plates showed a dependence of damping on amplitude similar to that observed for coated beams, as did a computer based simulation employing springs and Coulomb sliders [11].

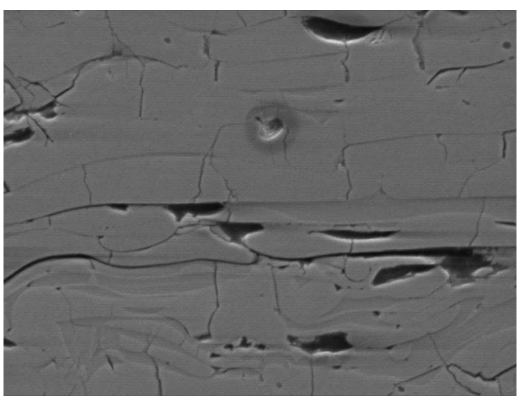

Fig. 2 Microstructure of plasma sprayed MgAl spinel (by Shipton and Patsias [10]; used with permission)

The most relevant measure of the energy dissipation of a material to be used as a thin coating is the loss modulus, E'', related to the energy dissipated, D, by a unit volume undergoing a fully reversed cycle of strain amplitude, ε_0, by

$$E''(\varepsilon_0) = \frac{D(\varepsilon_0)}{\pi\varepsilon_0^2} \tag{1}$$

Values of the material loss modulus extracted from tests are shown in Fig. 3. Values for four specimens of a titania-alumina ceramic (Fig. 3(*a*)) were extracted from the frequency response functions of a base driven cantilever beam, with successively reduced amplitudes of excitation [12]. Values for the loss modulus of yttria stabilized zirconia (Fig. 3(*b*)) are the product of loss factor and storage modulus, as obtained from the decay of free vibrations [13]. Values obtained with electron beam deposition (Fig. 3(*b*)) differ markedly, both quantitatively and qualitatively, from those obtained when the same material was plasma sprayed. Tassini et al. [13] suggested that the structure of plasma sprayed ceramics enabled more relative movement in the loading direction than did the columnar structure obtained with electron beam deposition. This was seen to be consistent with the lower values of storage (Young's) modulus that was also observed.

Although the maximum value of the loss modulus and the strain at which it occurs differs between the two materials, the amplitude dependencies are very similar, at least to a strain of twice for that for maximum damping. In both cases, the loss modulus is seen to rise proportionate to the strain amplitude from a low level, suggesting the presence in the coating of a loss mechanism that is linear in applied load. Further, the effectiveness of this mechanism reaches a limit value at some critical value of load (strain), above which the loss modulus decreases. Increases at higher strains (when present) are presumed to be indicative of the predominance of some other amplitude dependent mechanism. Values of the loss modulus for plasma sprayed ceramic materials, as extracted from other data [9], show similar trends.

3 A Simplified Analysis of Slip Damping

As the microstructure seen in Fig. 2 is suggestive of a laminated material with partial debonding due to vertical cracks in one of the

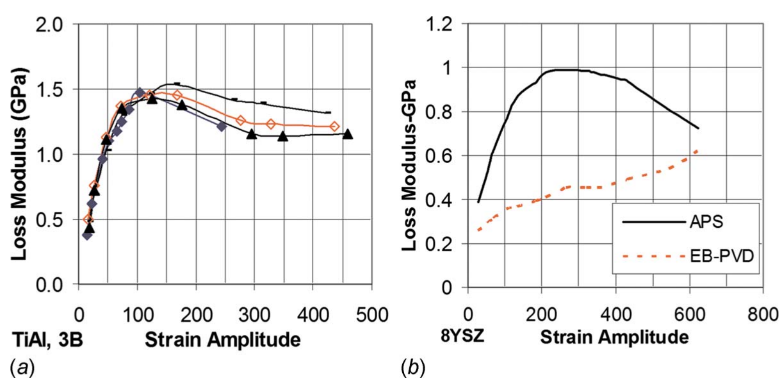

Fig. 3 Loss modulus for ceramic-coatings: (*a*) plasma sprayed titania-alumina and (*b*) 8% yttria stabilized zirconia

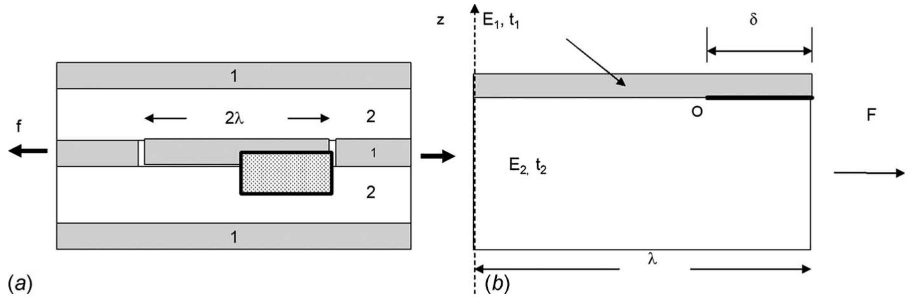

Fig. 4 Unit cell for material with microslip (*a*) location of unit cell and (*b*) detail of unit cell

constituents, a refinement of an analysis previously developed [4] for the evaluation of the resulting damping, due to friction, may be applied. Let the length 2λ of Fig. 4(*a*) be taken as being the representative of the distance between the vertical intrasplat defects, and length $2t_1$ to be the characteristic of the distance between horizontal inta-splat defects, with the resulting block being separated vertically from a similar configuration by a characteristic distance $2t_2$. The vertical plane of symmetry enables the isolation of the unit cell of length λ and thickness t_1+t_2, as shown in Fig. 4(*b*). As relative motion develops only across a load-dependent fraction of the plane separating the two constituents over a length δ from the free end of constituent 2, the phenomenon is one of the microslips.

Unless an identical slipping plane occurs at $z=-2t_2$, the plane at $z=-t_2$ is not truly a plane of symmetry. Additional deformations arising from any resulting shear distribution on this plane are neglected, and the existence of a transverse pressure p, necessary to generate a uniform Coulomb frictional force $\tau=\mu p$, over the slipping region, is presumed. The total load F, carried by a width W of the unit cell is divided between the two constituents. At any F, the load must be divided among the two constituents so as to ensure the same axial strain in the nonslipping region. Thus, the fraction of the load transferred from constituent 2 to constituent 1 over the nonslipping region is RF, where R is a stiffness ratio

$$R = \frac{E_1 t_1}{E_1 t_1 + E_2 t_2} \tag{2}$$

3.1 Initial Loading. At any load $F>0$, slip occurs over some interval $0<x<\delta$, measured from an origin of coordinates at (moving) point 0. Over $\delta-\lambda<x<0$, the two constituents adhere, and displacements and strains must be the same in both constituents. If the shear stress is uniform over the slipping region, the load transferred over the length δ must be $\tau W\delta=RF$. The length of the slipped region as shown in Fig. 4(*b*) at a final load $F=F_{\max}$ is therefore

$$\delta_F = RF_{\max}/(\tau W) \tag{3}$$

For a uniform shear force per unit width $q=\tau W$, the resulting linear variation in axial load may be used to evaluate the displacements u_a at the loaded end of constituent 2, with respect to the plane of symmetry. Since the displacement over an interval Δ with linear variation is the length Δ, times the mean axial force, divided by a stiffness, $B=WE_2t_2$. The result is that

$$u_a = (1-R)F\frac{(\lambda-\delta)}{B} + \frac{[F+(1-R)F]}{2B}\delta \tag{4}$$

For loading to $F<F_{\max}$, at which load the slipped distance $\delta_F=\beta\lambda$ with $0<\beta<1$ does not exceed the half length of the distance between gaps in the interrupted constituent of Fig. 4(*a*), since the slip penetration depth δ is related to the load F, the displacement is

$$u_a = \frac{(RF_{\max})^2}{2Bq}\left[2\frac{(1-R)}{R\beta}\frac{F}{F_{\max}} + \left(\frac{F}{F_{\max}}\right)^2\right] \tag{5}$$

3.2 Unloading. The load distribution for the two constituents at the end of the loading phase is shown as the dashed line of Fig. 5. If, at a load $F_{\max}$, the load is reduced to $F<F_{\max}$, reverse slip begins at the end $x=\delta_F$ and propagates to a depth δ_F-δ along the interface to the point $x=\delta$, also shown in Fig. 5. As the two surfaces remain in adherence for $x<0$, the load transferred to constituent 1 must be reduced from the value of $RF_{\max}$ at the end of the unloading to the new value RF. Thus

$$2\tau W(\delta_F-\delta) = R(F_{\max}-F) \tag{6}$$

and the distribution of axial loads in the two constituents during unloading is shown as the solid lines in Fig. 5. The factor of two

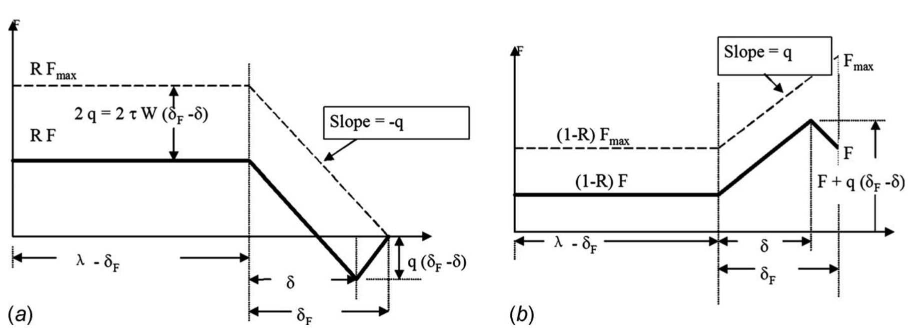

Fig. 5 Distribution of axial forces; loaded and unloading (*a*) constituent 1 and (*b*) constituent 2

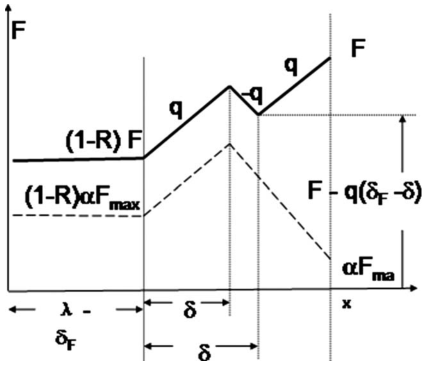

Fig. 6 Load distribution in constituent 2, before and during reloading

arises as the initial distribution of shear must be first reduced to zero, and then further reduced to the negative value.

The displacements at the loaded end of constituent 2, with respect to the plane of symmetry, may be evaluated by noting that the ordinate divided by the stiffness B, is a strain. Consequently, the desired displacement at load F is the area under the heavy line of Fig. 5(*b*), divided by B. But, from Eqs. (3) and (6), the total penetration depth δ_F and the current value δ, are related to the maximum and current values of the load. Making these substitutions, and simplifying

$$u_b = \frac{R^2 F_{\max}^2}{2Bq}\left[\left(1 + \frac{2(1-R)}{\beta R}\right)\frac{F}{F_{\max}} + \frac{1}{2}\left(1 - \left(\frac{F}{F_{\max}}\right)^2\right)\right] \quad (7)$$

When the unloading reaches a value $F=\alpha F_{\max}$ with $-1<\alpha<1$, the reversed slip has taken place to the position determined with Eq. (6)

$$\delta_\alpha = \frac{RF_{\max}}{2q}(1+\alpha) \quad (8)$$

With unloading to $F=0$ (i.e., $\alpha=0$), reversal of slip occurs only on the first half of the original penetration depth δ_F. At $F=-F_{\max}$, reversal occurs over the entire length δ_F.

3.3 Reloading. At the end of the unloading cycle $F=\alpha F_{\max}$, the force in constituent 2 is as shown in the dashed line of Fig. 6. If the loading direction is then reversed and the load is increased, the slip direction is reversed over an interval of distance $\delta_F-\delta$, measured from the free end of the interrupted layer, and the loads become as in the heavy line.

For $0<x<\delta$, no slip occurs. Once again, the change in shear force acting on the interrupted layer must be such as to insure that the strain in the two constituents is the same for $x<0$. Thus, for any load $\alpha F_{\max}<F<F_{\max}$, the slip penetration depth δ, is found from

$$2\tau W(\delta_F - \delta) = R(F - \alpha F_{\max}) \quad (9)$$

$$\delta = \frac{(\alpha+2)RF_{\max} - RF}{2q} \quad (10)$$

The displacement of the loaded end of constituent 2, with respect to the fixed end, is once again the area under the solid line of Fig. 6, divided by B. By using Eqs. (3), (8), and (10) to evaluate the several slip penetration depths in terms of forces, this may be reduced to

$$u_c = \frac{(RF_{\max})^2}{2Bq}\left[\frac{2(1-R)}{R\beta}\frac{F}{F_{\max}} + \frac{(1+2\alpha)}{2} - \alpha\left(\frac{F}{F_{\max}}\right) + \frac{1}{2}\left(\frac{F}{F_{\max}}\right)^2\right] \quad (11)$$

4 Energy Dissipation Due to Slip

4.1 Hysteresis Loop Areas. Having found the displacements at the point of load application, hysteresis loops may be formed, as shown in Fig. 7, and the dissipated energy is evaluated from the area. Hysteresis loops shown are the computed values for $\beta=0.9$ and $R=0.5$.

The ordinates are the ratio $F/F_{\max}$ and the abscissas are a dimensionless displacement, obtained by normalizing the common first factors of Eqs. (5), (7), and (11). The displacement response of Eq. (5) for initial loading to $F=F_{\max}$, is shown as the heavy line in Fig. 7(*a*). The hysteresis loop for a fully reversed cycle as formed with u_b, the displacements of Eq. (7) for the unloading on $F=-F_{\max}$, ($\alpha=-1$), followed by u_c, and the displacements for reloading to $F=F_{\max}$, ($\alpha=-1$), is also given. The reloading curve is seen to asymptotically approach the initial loading trajectory. The hysteresis loops resulting from unloading from $F=F_{\max}$ to $F=0$, ($\alpha=0$), and then reloading to $F=F_{\max}$, are compared in Fig. 7(*b*) with that of the unloading to $-F_{\max}$, ($\alpha=-0.5$), and reloading. The reloading curve does not reach the initial loading curve (Fig. 7(*a*)) until $F=F_{max}$. It is evident that the energy dissipated (area) is much less than for the fully reversed load. As will be seen, the value for load range of N units is N^3 times that for a load range of one unit.

The energy dissipated in a complete cycle from $F_{\max}$ through $\alpha F_{\max}$ with return to $F_{\max}$, may be found by integrating the area within the hysteresis loop as

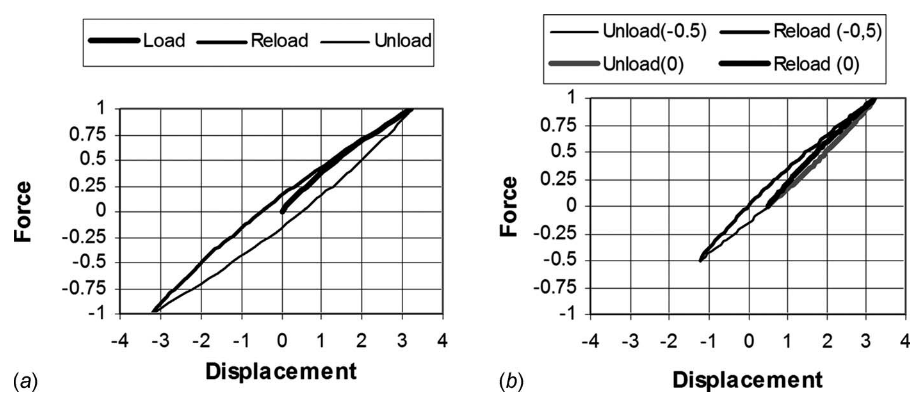

Fig. 7 Hysteresis loops with partial slip (*a*) initial loading; fully reversed load and (*b*) partially reversed loads

$$D_T = \int_{\alpha F_{\max}}^{F_{\max}} (u_b - u_c) dF = F_{\max} \int_{\alpha}^{1} (u_b - u_c) d\left(\frac{F}{F_{\max}}\right) \quad (12)$$

Subtracting the reloading displacement of Eq. (11) from those for unloading in Eq. (7) and integrating leads, after considerable manipulation, to

$$D_T = \frac{R^2}{12Bq}[F_{\max} - \alpha F_{\max}]^3 \quad (13)$$

It is of considerable interest and significance that the dissipation depends only on the total load range, and is independent of the mean value. As noted in previous investigations of slip damping, the dissipation is dependent on the third power of the load range, and inversely as the interface shear. In this analysis, it was assumed that the ends of constituent 1 remain unloaded. If the interruption in this layer closes during compression, less slip and less dissipation will be the result. For an initial gap of zero thickness, opened under the initial loading, the load at which closure in unloading occurs depends on the parameter R, but typically occurs at about $\alpha = -1/2$.

4.2 Dissipation With Partial Slip. The unit damping D, as formed by dividing the energy dissipated D_T, by the volume of the unit cell $W\lambda(t_1+t_2)$, for a fully reversed cycle ($\alpha=-1$), of cyclic stress amplitude $\sigma_0 = F_{\max}/W(t_1+t_2)$, becomes

$$D = \frac{D_T}{W\lambda(t_1+t_2)} = \frac{2}{3}\left[\frac{E_1(t_1+t_2)}{E_1 t_1 + E_2 t_2}\right]^2 \frac{1}{E_2 \tau}[\sigma_0]^3 \frac{t_1^2}{\lambda t_2} \quad (14)$$

If the unit cells within which the slip occurs represent, on average, a volume fraction V_f of the total material, the average value of the unit damping becomes DV_f. A loss modulus based on the nominal amplitude of maximum strain $\varepsilon_0 = \sigma_0/E'$ may then be constructed. If the two constituents of the unit cell have the same modulus $E_1 = E_2 = E$

$$E''(\varepsilon_0) = \frac{D(\sigma_0)}{\pi(\sigma_0/E')^2} V_f = \frac{2}{3\pi}\left[\frac{t_1{}^2}{\lambda t_2}\right]\frac{E'^2}{\tau E} V_f \varepsilon_0 \quad (15)$$

The effective modulus E', is a secant modulus for the material at a cyclic stress of amplitude σ_0, and, in general, will differ from the moduli of the constituents and diminish with increasing applied stress due to the slip-induced lowering of stiffness. Thus, Eq. (15) is consistent with the nearly linear increases at low strains seen in Fig. 3. A development of the relationship between the effective modulus E' and the properties of the unit cell is given in the Appendix.

But the use of Eqs. (14) and (15) is subject to the restraint that the initial penetration depth is less than the half length of the interrupted segment $\delta_F < \lambda$. Thus it is required that the product of the Coulomb friction coefficient μ and the normal pressure p on the interface be such that slip does not occur over the interface, or

$$\frac{RF_{\max}}{\lambda W} = \frac{\sigma_{0-\max} t_1}{\lambda} < \tau \quad (16)$$

The stress, σ_s, or the corresponding strain, $\varepsilon_s = \sigma_s/E'$, at which equality is reached, is driven by an aspect ratio, t_1/λ, and the contact pressure, and is a dominant parameter in the analysis of the energy dissipation due to slip. The value of the loss modulus at the onset of gross slip is

$$E''(\varepsilon_s) = \frac{2}{3\pi}\left(\frac{t_1}{t_2}\right)\left(\frac{E'(\varepsilon_s)}{E}\right) V_f E'(\varepsilon_s) \quad (17)$$

Beyond the limiting value, gross or full slip begins, and the instantaneous rate of dissipation must be as the first power of amplitude over some portion of the cycle, leading to a constant or diminishing loss modulus, as seen in the material properties developed from experimental data, Fig. 3.

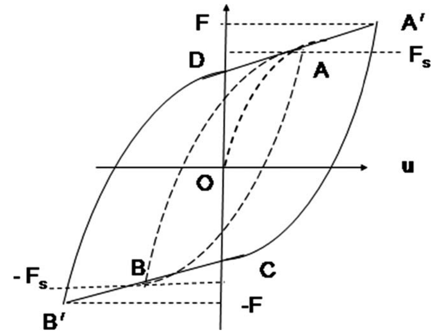

Fig. 8 Hysteresis loop for loading beyond full slip

This formulation of displacements and evaluation of dissipation for loads below gross slip is closely patterned after that developed by Metherell and Diller [3] for the analysis of the lap joint under uniform pressure.

4.3 Dissipation at Loads Beyond Full Slip. For loads F below full slip, substitution of the slip length $\delta = RF/q$ into the displacement for the initial loading as given by Eq. (4) and differentiation, gives that

$$\frac{\partial u_a}{\partial F} = (1-R)\frac{\lambda}{B} + \frac{R^2 F}{qB} \quad (18)$$

and is seen to decrease to λ/B at the force for full slip, at which $\delta = \lambda$ and $F_s = \lambda q/R$. For $F > F_s$, the slope retains the constant value λ/B. The initial loading curve is shown (at exaggerated scale) as the heavy dashed line of Fig. 8; the loading curve for $F > Fs$ with $dF/du = B/\lambda$ is the continuation $A - A'$.

The displacement at initiation of full slip ($F = F_s$, where $RF_s = q\lambda$) is from Eq. (4)

$$u_a(F_s) = \frac{F_s \lambda}{2B}(2-R) \quad (19)$$

and at final load F (point A′)

$$u_a(F) = \frac{F_s \lambda}{2B}(2-R) + (F - F_s)\frac{\lambda}{B} \quad (20)$$

For unloading from $F > F_s$, the force displacement trajectory A′-C is congruent to AB, the unloading curve from F_s. For a fully reversed cycle $F_{\min} = -F$, unloading continues along C-B-B′, parallel to A-A′, and reloading occurs along B′-D-A-A′. Thus, for a fully reversed loading cycle, the hysteresis loop takes the form shown in Fig. 8, as the heavy solid line. The total area of the hysteresis loop is that for the load F_{slip} (light dashed line of Fig. 8), plus the additional area of the parallelogram A′-C-B′-D; the area of which may be evaluated by noting that the area of the parallelogram is that of two congruent triangles, D-A′-C and C-B′-D. After dividing by the cell volume

$$D = \frac{D_T}{W\lambda(t_1+t_2)} = 2\left(\frac{\sigma_0}{\sigma_s} - 1\right)\sigma_s^2 \frac{\lambda t_1}{t_2 E} \quad (21)$$

Adding to this the dissipation per unit volume from Eq. (14), evaluated at gross slip $\sigma_0 = \sigma_s$, at which $\tau\lambda = \sigma_s t_1$, the total energy dissipated per unit volume of the unit cell with $E_1 = E_2 = E$ is

$$D = \left[\left(2\frac{\sigma_0}{\sigma_s} - \frac{4}{3}\right)\right](\sigma_s)^2 \frac{t_1}{Et_2} \quad (22)$$

from which a loss modulus for a material with a volume fraction V_f of slipping cells may be formed as before

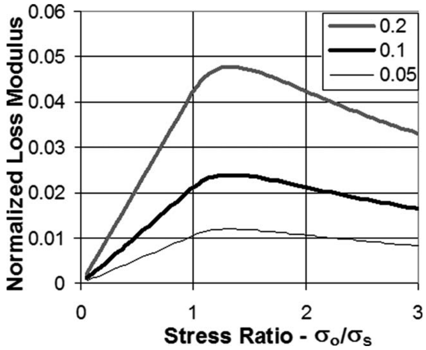

Fig. 9 Loss modulus, single cell

$$E''(\sigma_0) = \frac{D(\sigma_0)}{\pi(\sigma_0/E')^2}V_f = \left[\left(2\left(\frac{\sigma_s}{\sigma_0}\right) - \frac{4}{3}\left(\frac{\sigma_s}{\sigma_0}\right)^2\right)\right]\frac{V_f}{\pi}\frac{E'(\sigma_0)}{t_2 E}E'(\sigma_0) \tag{23}$$

A maximum value is achieved at 4/3 the stress for the gross slip. Such maxima are evident in the properties of ceramics, Fig. 3. Examples of the loss modulus for several values of the thickness ratio t_1/t_2 are shown in Fig. 9, as computed with Eq. (15) for $\sigma_0 \le \sigma_s$, and from Eq. (23) for $\sigma_0 \ge \sigma_s$. Values shown are normalized by division, by $E'^2 V_f/E$.

An evaluation of the effective modulus E' for loads beyond gross slip is given in the Appendix. As the ratio σ_0/σ_s is not identical to the ratio $\varepsilon_0/\varepsilon_s$ due to the softening of the effective modulus, the abscissa of Fig. 9 is not simply proportional to that of Fig. 3.

5 Influence of Variations in Cell Parameters

If an entire volume of material contained a uniform distribution of identical deflects, the unit dissipation and loss modulus for the sample would be the same as that computed from the properties of a single cell. However, variations in such defects may be expected, as is evident in Fig. 2. Since the density, dimension, and orientation of defects enabling slip will vary throughout the material, a distribution, rather than a single value for the critical parameters, is appropriate. But the stress at which full slip in the unit cell first occurs, $\sigma_s = \lambda\tau/t_1$, as computed from Eq. (3) for the case of equal moduli, is a single parameter dependent on the distance between the vertical defects, the interfacial shear stress, and the distance between sliding planes. In consequence, variations in the slip stress serve as a single surrogate variable for variations in any or all of these.

An analogous dependence on a stress parameter occurs in the theory of magnetoelastic damping, for which the dissipation is taken to vary as the third power of applied stress below a critical value, and to have a constant value for stresses above. Smith and Birchak [14] provided a modification to the theory by taking the internal stress, which governs the transition between one relationship for the dissipation to the other, to be a distribution. Although the dissipation at high stress in the present case is linear in stress rather than constant as in magnetoelastic damping, the analysis of Smith and Birchak [14] may be adapted. We assume that the slip stress, σ_s, as used here, is not uniform throughout the material, but may be represented by a simple (square) distribution, having a mean value Σ, with the fraction of elements having slip stress of various values taken to be

$$N(\sigma_s) = \text{constant} \quad \text{for} \quad \Sigma\text{-}\Delta\Sigma < \sigma_s < \Sigma + \Delta\Sigma \tag{24a}$$

$$N(\sigma_s) = 0 \quad \text{for all other values of } \sigma_s \tag{24b}$$

The distribution may then be characterized by Σ, and a single parameter $Z = \Delta\Sigma/\Sigma$. The energy dissipated per unit volume in an "average" unit cell, subjected to a uniform externally applied cyclic stress σ_0, is

$$D = \int D_s N(\sigma_s)d\sigma_s = \frac{1}{2\Delta\Sigma}\int_{\Sigma-\Delta\Sigma}^{\Sigma+\Delta\Sigma} D_s d\sigma_s \tag{25}$$

with the values of dissipation from Eqs. (14) and (22), written in terms of a geometric parameter $\kappa = (2/3)t_1/t_2$ and $\sigma_s = \lambda\tau/t_1$

$$D_s = \frac{\kappa}{E}\left(\frac{\sigma_o^3}{\sigma_s}\right) \quad \text{when} \quad \sigma_0 < \sigma_s \tag{26}$$

$$D_S = \frac{\kappa}{E}[3\sigma_0\sigma_s - 2\sigma_s^2] \quad \text{when} \quad \sigma_0 > \sigma_s \tag{27}$$

But, due to the piecewise representation of the integrand, three cases must be considered.

Case 1. For $0 \le \sigma_0 \le \Sigma - \Delta\Sigma$

$$D = \frac{1}{2\Delta\Sigma}\int_{\Sigma-\Delta\Sigma}^{\Sigma+\Delta\Sigma} \frac{\kappa}{E}\left(\frac{\sigma_0^3}{\sigma_s}\right)d\sigma_s \tag{28a}$$

$$\frac{DE}{\kappa\sigma_0^2} = \frac{1}{2Z}\left(\frac{\sigma_0}{\Sigma}\right)\ln\left\{\frac{1+Z}{1-Z}\right\} \tag{28b}$$

Case 2. For $\Sigma - \Delta\Sigma \le \sigma_0 \le \Sigma + \Delta\Sigma$

$$D = \frac{1}{2\Delta\Sigma}\left[\int_{\Sigma-\Delta\Sigma}^{\sigma_0} \frac{\kappa}{E}(3\sigma_0\sigma_s - 2\sigma_s^2)d\sigma_s + \frac{1}{2\Delta\Sigma}\int_{\sigma_0}^{\Sigma+\Delta\Sigma} \frac{\kappa}{E}\left(\frac{\sigma_0^3}{\sigma_s}\right)d\sigma_s\right] \tag{29a}$$

$$\frac{DE}{\kappa\sigma_0^2} = \frac{3}{4Z}\left[\left(\frac{\sigma_0}{\Sigma}\right) - \left(\frac{\Sigma}{\sigma_0}\right)(1-Z)^2\right] - \frac{1}{3Z}\left[\left(\frac{\sigma_0}{\Sigma}\right) - \left(\frac{\Sigma}{\sigma_0}\right)^2(1-Z)^3\right] + \frac{1}{2Z}\left(\frac{\sigma_0}{\Sigma}\right)\ln\left(\frac{1+Z}{\sigma_0/\Sigma}\right) \tag{29b}$$

Case 3. For $\Sigma + \Delta\Sigma \le \sigma_0$

$$D = \frac{1}{2\Delta\Sigma}\int_{\Sigma-\Delta\Sigma}^{\Sigma+\Delta\Sigma} \frac{\kappa}{E}(3\sigma_0\sigma_s - 2\sigma_s^2)d\sigma_s \tag{30a}$$

$$\frac{DE}{\kappa\sigma_0^2} = 3\left(\frac{\Sigma}{\sigma_0}\right) - \left(\frac{\Sigma}{\sigma_0}\right)^2(2 + 2Z^2/3) \tag{30b}$$

The loss modulus as introduced in Eq. (15) may be computed for each case as

$$E_2''(\varepsilon_0) = \frac{D(\sigma_0)}{\pi(\sigma_0/E')^2}V_f = \left[\frac{2}{3\pi}\frac{t_1}{t_2}\frac{E'}{E}E'V_f\right]\left[\frac{DE}{\kappa{\sigma_0}^2}\right] \tag{31}$$

The first factor on the right is recognized as the loss modulus at the onset of gross slip, Eq. (17). Values of the loss modulus, after scaling by this factor, given in Fig. 10, are for several values of the parameter Z. The abscissa is the ratio of the amplitude of applied cyclic stress to the mean value of the stresses for the onset of gross slip. For $Z \to 0$, the distribution becomes a singularity, the slip stress has a unique value, $\sigma_s = \Sigma$, and the loss modulus becomes that of Fig. 9. Values for $Z = 0$ and $Z = 0.1$ are nearly identical. For any other value of the ratio $Z = \Delta\Sigma/\Sigma$, the maximum value is reduced and the amplitude dependence is slightly weaker. It is of interest to note that, in all cases, the magnitude of the loss modulus does not depend explicitly on the mean slip stress, Σ, but only through the stress ratio, σ_0/Σ. The magnitude of the loss factor near the peak values is dependent on the distribution parameter, but is relatively insensitive to Z at low and high stress ratios.

Although the distribution of defect parameters used here is highly simplistic, it has enabled the capture of the magnitude and the amplitude dependence of the loss modulus (Fig. 10) with a

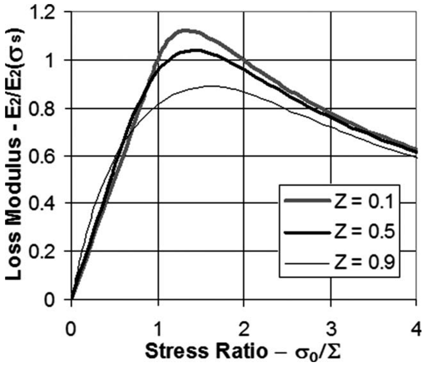

Fig. 10 Influence of distribution parameter on loss modulus (*a*) computed from a slip model, and (*b*) observed, titania-alumina ceramic

modest number of parameters. The general shape is a function only of the distribution parameter Z. The stress for maximum damping is dependent only on the mean slip stress Σ, and weakly on Z. The magnitude is additionally dependent on two factors: One, with a geometric combination $(2/3\pi)V_f(t_1/t_2)$ and the other, having to do with the effective storage (Young's) modulus of the material and the elastic modulus of the constituents.

For the two materials compared in Fig. 3, the loss modulus at twice the strain for maximum damping is about 15% less than the peak value. The decreases with strain in the moduli of Fig. 10 diminish with increasing values of the parameter Z. At twice the stress for peak damping, the loss modulus for $Z=0.9$ has a value about 19% below peak. From this, it is inferred that the range of values of the critical slip parameter σ_s for actual materials must be quite broad, perhaps ranging from less than 10% to more than 190% of the mean value.

6 Summary and Conclusions

The energy dissipation in plasma sprayed ceramics has been previously attributed to friction across interfaces between the splats resulting from the process of application, enabled by large numbers of intrasplat cracks, roughly dividing the sprayed material into a structure containing slipping blocks. Measures of dissipation, such as loss factors and loss moduli, have been found to increase with strain at low strains, suggesting microslip damping. An analysis of the dissipation due to a single slipping block was developed and applied. At a critical value of applied stress, slip takes place over the entire block length, and a transition in the amplitude dependence of the damping measure is seen. As the value of applied stress at the onset of gross or macroslip is dependent on a combination of parameters of the sliding block, and as a sample of real material will contain a large number of nonidentical blocks, a description of the material in terms of a distribution of the critical stresses required for gross slip of the blocks was considered. A simple one-parameter distribution was presumed, and a comparison of predictions with different values of the parameter suggests that observed values of the damping measure correspond best to a broad distribution of stresses for the onset of gross slip.

While the present findings provide some further understanding of damping in plasma sprayed ceramics, some aspects of the observed behavior are not accounted for by this simple model. In particular, a dependence on the prior load history on both long and short term time scales have been noted [13,15]. At some relatively high level of strain, damage may increase the number and/or the dimensions of dissipating sites. It is also likely that a single constant value of the Coulomb friction coefficient is not an adequate representation. For these reasons, values of the critical parameters may change with the history of loading, leading to a dependence of the loss modulus on the history of loading. It should also be noted that the influence of mean stresses were not considered. Such could influence the interface contact pressure, as well as negate the assumption that the vertical defects do not close.

Although the slip damping model is highly idealized as to geometry, the distribution of internal stresses, and the characterization of variations in parameters, the predicted damping measures appear to provide good qualitative agreement with observations. The success of this model, incorporating both microslip and macroslip in providing qualitative predictions of the amplitude dependence of the dissipation, leads further support to the hypothesis of Shipton and Patsias [10], that the damping of plasma sprayed ceramics is predominantly a frictional phenomenon.

Nomenclature

B = stiffness of constituent 2, E_2t_2W
$D(\varepsilon_0)$ = unit damping, energy dissipated per cycle per unit volume
E_1, E_2, E = storage (Young's) modulus of cell constituents
$E'(\varepsilon_0), E''(\varepsilon_0)$ = storage (Young's) and loss modulus for material with microslip
$F, F_s, F_{\max}$ = forces on unit cell
R = stiffness ratio
D_T = total energy dissipated per cycle
V_f = volume fraction of slipping cells
W = width of unit cell
p = normal pressure on interface
q = shear force on interface, per unit length, τW
t_1, t_2 = thickness of constituents of unit cell
u_a, u_b, u_c = displacement of constituent 2
x, z = spatial coordinates
$\delta, \delta_a, \delta_F$ = length of slip region at various loads
Σ = mean value of stresses for gross slip
Z = distribution parameter
α = force ratio during cycle: minimum/maximum
β = dimensionless slip penetration depth, δ/λ
λ = half-length of unit cell
μ = coefficient of Coulomb friction
Σ = mean value of stresses for gross slip
σ_0, ε_0 = average stress and strain in material with microslip
σ_s, ε_s = average stress and strain at gross slip
τ = shear stress on interface, μp

Appendix

The Storage Modulus. The effective or average value of the storage modulus $E'(\varepsilon_0)$, must vary with the amplitude of the applied load, as strain softening will occur in consequence of slip at the interfaces. An amplitude dependent secant modulus for the unit cell, defined as the ratio of the average stress to the average strain $E_0'=\sigma_0/\varepsilon_0$, may be evaluated from the relationships for displacement for constituent 2. The displacement prior to gross slip is given as Eq. (4). The average strain is $\varepsilon_0=u_a/\lambda$; the force is related to the average stress σ_0 by $F=\sigma_0W(t_1+t_2)$. The average stress at gross slip is $\sigma_s=\lambda\tau/t_1$. Using these, the result for equal moduli $E_1=E_2=E$ and $\sigma_0\leq\sigma_s$ is

$$\frac{E}{E_0'} = 1 + \frac{t_1}{2t_2}\frac{\sigma_0}{\sigma_s} \tag{A1}$$

Beyond the gross slip, additional displacements occur. The total displacement for loads beyond the gross slip (Eq. (20)) may be used to find the relationship between the average stress and the average strain. From that ratio, the secant modulus beyond gross slip becomes

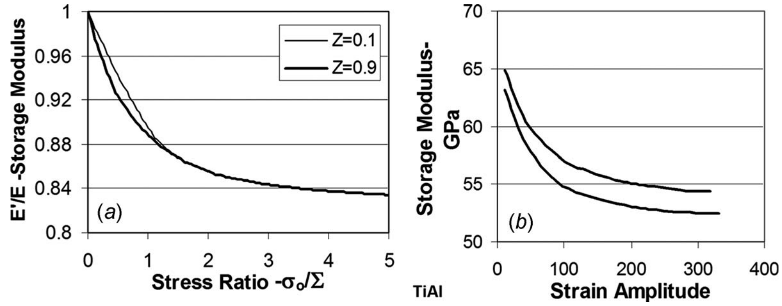

Fig. 11 Storage modulus

$$\frac{E}{E_0'} = 1 + \left(1 - \frac{1}{2}\frac{\sigma_s}{\sigma_0}\right)\frac{t_1}{t_2} \tag{A2}$$

But in general, the properties of all slipping unit cells are not identical. A distribution of parameters may be considered, as done in the evaluation of the loss modulus. Applying the distribution of Eq. (24) to the values of storage modulus for the unit cell below and above the gross slip, Eqs. (32) and (33) leads to the estimates of the storage modulus for the unit cell for any specific value of the geometric parameters t_1/t_2 and V_f, and any specific value of the distribution parameter Z.

But slip may not be occurring in every volume element of width W, length λ, and thickness t_1+t_2. If some length $L=M\lambda$ contains only one slipping block, the ratio of average stress to average strain for the array in the series may be used to determine the effective modulus of that array, in terms of that of the unit cell, with the result that

$$\frac{E}{E_a'} = \left[1 - \frac{1}{M}\left(1 - \frac{E}{E_{0'}'}\right)\right] \tag{A3}$$

Then, if such a line of blocks with one slipping element is surrounded by N^2-1 rows of the same length, but with no slipping blocks, the effective modulus of the MN^2 blocks with one slipping element is found to be

$$\frac{E'}{E} = 1 + V_f\left(1 - \frac{E}{E_{0'}'}\right)\Big/\left[1 - \left(1 - \frac{E}{E_{0'}'}\right)\Big/M\right] \tag{A4}$$

The volume fraction is now $V_f=1/MN^2$. The case of $N=1$ and $V_f=1/M$ corresponds to all blocks in series; parameters $M=1$ and $V_f=1/N^2$ correspond to all blocks in parallel. These limiting cases provide bounds on the stiffness.

The examples given in Fig. 11 were computed from Eq. (35) after evaluating the influence of the distribution of Eq. (24) on the properties of the unit cell. Values shown were found for the arbitrary choices of $V_f=t_1/t_2=0.5$ and $N=M$, with values of the distribution parameter Z corresponding to narrow ($Z=0.1$) and broad ($Z=0.9$) distributions.

Values of the storage modulus for two specimens of an actual ceramic coating, as computed from data given elsewhere [12], are shown in Fig. 11(*b*). The computed results for the broad distribution ($Z=0.9$ of Fig. 11(*a*)) have greater curvature for low values of σ_0/Σ, and therefore, are more representative of the real material, as also suggested by comparisons of the loss modulus. When used with such a broad distribution, the slip model for the plasma sprayed coating material appears to provide a satisfactory characterization of the influence of slip on the stiffness (storage modulus) of the material.

References

[1] Deresiewicz, H., 1974, "Bodies in Contact With Applications to Granular Media," *R. D. Mindlin and Applied Mechanics*, G. Herrman, ed., Pergamon, New York, pp. 105–135.

[2] Pian, T. H. H., and Hallowell, F. C., Jr., 1952, "Structural Damping in a Simple Built-Up Beam," *Proceedings of the First US National Congress of Applied Mechanics*, New York, pp. 97–107.

[3] Metherell, A. F., and Diller, S. V., 1968, "Instantaneous Energy Dissipation in a Lap Joint-Uniform Clamping Pressure," ASME J. Appl. Mech., **35**(1), pp. 123–128.

[4] Torvik, P. J., 1989, "Damping of Layered Materials," *Proceedings of the 30th AIAA/ASME/ASCE/AHS/ASC Structures, Structural Dynamics and Materials Conference*, Reston, VA, pp. 2246–2259, Paper No. AIAA 89-1422.

[5] Goodman, L. E., 2002, "Material and Slip Damping," *Harris' Shock and Vibration Handbook*, 5th ed., C. M., Harris, and A. G., Piersol, eds., McGraw-Hill, New York, pp. 36-1–36-30.

[6] Bao, G., and McMeeking, R. M., 1995, "Thermomechanical Fatigue Cracking in Fiber Reinforced Metal-Matrix Composites," J. Mech. Phys. Solids, **43**(9), pp. 1433–1460.

[7] Dollar, A., and Steif, P. S., 1988, "Load Transfer in Composites With a Coulomb Friction Interface," Int. J. Solids Struct., **24**(8), pp. 789–803.

[8] Pryce, A. W., and Smith, P. A., 1993, "Matrix Cracking in Unidirectional Ceramic Matrix Composites Under Quasi-Static and Cyclic Loading," Acta Metall. Mater., **41**(4), pp. 1269–1281.

[9] Torvik, P. J., 2007, "Integration of Machinery Failure Prevention Technologies Into System Health Management," *A Survey of the Damping Properties of Hard Coatings for Turbine Engine Blades*, Society for Machine Failure Prevention Technology (MFPT), Dayton, OH, pp. 485–506.

[10] Shipton, M., and Patsias, S., 2003, "Hard Damping Coatings: Internal Friction as the Damping Mechanism," *Proceedings of the Eighth National Turbine Engine High Cycle Fatigue Conference*, Monterey, CA, pp. 5e1–5e27.

[11] Green, J., and Patsias, S., 2002, "A Preliminary Approach for the Modeling of a Hard Damping Coating Using Friction Elements," *Proceedings of the Seventh National Turbine Engine High Cycle Fatigue Conference*, Palm Beach Gardens, FL, pp. 7c1–7c9.

[12] Hansel, J., 2008, "Influence of Thickness on Properties of Air Plasma Sprayed Ceramic Blend Coatings," MS thesis, Wright State University, Dayton, OH.

[13] Tassini, N., Lambrinou, K., Mircea, I., Bartsch, M., Patsias, S., and van der Biest, O., 2007, "Study of the Amplitude-Dependent Mechanical Behaviour of Yttria-Stabilised Zirconia Thermal Barrier Coatings," J. Eur. Ceram. Soc., **27**(2–3), pp. 1487–1491.

[14] Smith, G. W., and Birchak, J. R., 1968, "Effect of Internal Stress Distribution on Magnetomechanical Damping," J. Appl. Phys., **39**(5), pp. 2311–2316.

[15] Patsias, S., and Williams, R. J., 2003, "Hard Damping Coatings: Material Properties and F.E. Prediction Methods," *Proceedings of the Eighth HCF Conference*, Monterey, CA, pp. 5d1–5d17.

An Accurate Low Dimension Model for the Waves on Thin Layer Fluid Flowing Down an Inclined Plane

H. Ait Abderrahmane

G. H. Vatistas

Concordia University,
1515 St. Catherine West,
EV-S3.460,
Montreal, QC, H3G 2W1, Canada

*This technical brief deals with the surface instability mode of a liquid film flowing down an inclined plane. A four-equation model that describes the development of the film depth, the flow rate, the free-surface velocity, and the wall shear stress is proposed. The obtained results were found to be in very good agreement with experimental and theoretical results of Liu et al. (1993, "Measurements of the Primary Instability of Film Flow," J. Fluid Mech., **250**, pp. 69–101) and Brevdo et al. (1999, "Linear Pulse Structure and Signalling in Film Flow on an Inclined Plane," J. Fluid Mech., **396**, pp. 37–71).* [DOI: 10.1115/1.3114968]

1 Introduction

Research on thin liquid films flowing along inclined planes or vertical cylinders date back to Nusselt [1]. Since Kapitza and Kapitza's work [2], the problem continues to be the subject of intense research; an exhaustive review is presented in Ref. [3]. A linear stability analysis began with the investigations of Benjamin [4] and Yih [5]. More sophisticated linear analyses based on wave packets and a pseudospectral method are presented in Ref. [6]. In low Reynolds number interval, Benney [7] proposed single nonlinear differential equations for the film thickness. However, Benney's equation failed in capturing all the inertia effects, thus limiting its validity to a narrow region around the critical Reynolds number. For moderate and high Reynolds numbers Skhadov [8] and Lee and Mei [9] proposed a two-equation model using momentum integral method. This technique requires the prescription of a velocity profile, which make the models depend strongly on the initial velocity profile. Skadov's [8] model does not predict the stability threshold and does not feature Hopf bifurcations. However, Lee and Mei [9], who favored the second order terms with respect to long wave parameter, captured the latter bifurcations, but failed to predict the stability threshold. Recently Ruyer-Quil and Maneville [10] derived a four-equation model using the Galerkin method with specific polynomials as test functions. This model involves the film thickness, the flow rate, as well as two corrections to the last parameter; the model predicts correctly the condition for the onset of the instability. It is worth noticing that besides the surface instability mode a thin film of fluid flowing down an inclined plane displays shear instability mode [11]. This instability mode is prevalent when the angle of inclination is very small. Shear mode has wavelengths comparable to the mean film height and travels slower than the mean flow. Developing models able to catch a shear instability mode is an interesting perspective.

We are proposing a model that consists of four equations that describe the evolution of the flow rate $q(x,t)$, film thickness $h(x,t)$, shear stress at the wall $\tau 0(x,t)$, and free-surface velocity $s(x,t)$. The present brief features an alternate formulation of the problem, which is shown to yield results that are comparable to the theoretically more involved methods of Ruyer-Quil and Maneville [10]. The Navier–Stokes equations are reduced using the integral method of Karman–Polhausen and a four-order polynomial to represent the velocity profile. The effectiveness of the proposed model is verified by comparing the obtained results with those of Brevdo et al. [6] and the experimental observations given in Ref. [12].

Contributed by the Applied Mechanics Division of ASME for publication in the JOURNAL OF APPLIED MECHANICS. Manuscript received August 8, 2006; final manuscript received January 30, 2009; published online July 21, 2009. Review conducted by Robert M. McMeeking.

2 Formulation of the Problem

We consider a two-dimensional flow of a thin layer of an incompressible, Newtonian fluid down an inclined plane, making an angle θ with the horizontal, under the action of gravity, as shown in Fig. 1. The upper half space consists of air having a negligible density. The gravitational acceleration is $\boldsymbol{g}=(\boldsymbol{g}\sin\theta, -\boldsymbol{g}\cos\theta)$. The dimensionless governing equations are as follows:

$$u_t + uu_x + wu_z = -p_x + \frac{1}{\mathrm{R}}\left(\varepsilon u_{xx} + \frac{1}{\varepsilon}u_{zz} + \frac{3}{\varepsilon}\right) \tag{1}$$

$$\varepsilon^2(w_t + uw_x + ww_x) = -p_z + \frac{\varepsilon}{\mathrm{R}}\left(w_{zz} - \frac{3}{\varepsilon}\cot\theta\right) \tag{2}$$

$$u_x + w_z = 0 \tag{3}$$

$$z=0: \quad u=w=0 \tag{4}$$

$$z=H(x,t): \quad w = H_t + uH_x \tag{5}$$

$$u_z + \varepsilon\ \mathrm{R}\ PH + \varepsilon^2(w_x - 2u_xH_x) + \frac{\varepsilon^3\ \mathrm{We}\ \mathrm{R}\ H_{xx}H_x}{(1+\varepsilon^2 H_x)^{3/2}} = 0 \tag{6}$$

$$P + \frac{\varepsilon}{\mathrm{R}}(u_zH_x - 2w_z) + \frac{\varepsilon^2\ \mathrm{We}\ H_{xx}}{(1+\varepsilon^2 H_x^2)^{3/2}} = 0 \tag{7}$$

The subscripts x and z indicate partial derivatives of the variables with respect to x and z. The nondimensional equations involve the following fundamental dimensionless numbers: $\mathrm{R}=c_0H_0/\nu$, $\mathrm{We}=\gamma/\rho H_0 c_0^2$, $\mathrm{Fr}=gH_0\cos\theta/c_0^2=3\cot\theta/\mathrm{R}$, and $\varepsilon=H_0/L$, which are the Reynolds, the Weber, the Froude numbers, and a long wave parameter. H_0, L, and $c_0=gH_0^2\sin\theta/3\nu$ are the initial film depth, characteristic length, and Nusselt velocity, respectively. In addition to long wave condition, we assume the following order of magnitude for the Reynolds and Weber numbers: $\mathrm{R}=O(1)$ and $\mathrm{We}=O(\varepsilon^{-2})$.

3 Model

The solution of the problem is approximated via the integral method of Karman–Polhausen, and the following velocity profile is assumed in order to initiate the analysis:

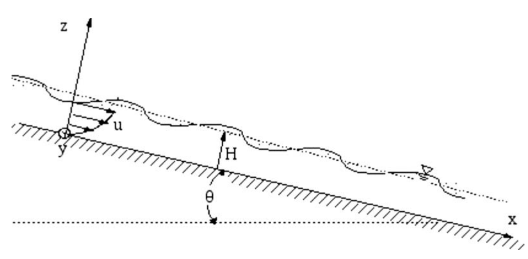

Fig. 1 Schematic of the problem

$$u(x,z,t) = a(x,t)z + b(x,t)z^2 + c(x,t)z^3 + d(x,t)z^4 \quad (8)$$

From the definitions of the velocity at the free surface, the flow rate, the shear stress at the wall, and the free surface, the unknown coefficients $a(x,t)$, $b(x,t)$, $c(x,t)$, and $d(x,t)$ can be related by four equations to the previously mentioned parameters $s(x,t)$, $q(x,t)$, $\tau0(x,t)$, and $\tau_s(x,t)$, respectively,

$$a(x,t) = \tau0(x,t)$$

$$b(x,t) = -\frac{3}{2}\frac{-h(x,t)^2\tau_s(x,t) + 3\cdot\tau0(x,t)\cdot h(x,t)^2 + 8\cdot h(x,t)\cdot s(x,t) - 20\cdot q(x,t)}{h(x,t)^2}$$

$$c(x,t) = \frac{2\cdot(14\cdot h(x,t)\cdot s(x,t) + 3\tau0(x,t)\cdot h(x,t)^2 - 30\cdot q(x,t) - 2\cdot h(x,t)^2\tau_s(x,t)}{h(x,t)^4}$$

$$d(x,t) = -\frac{5}{2}\frac{-12\cdot q(x,t) + \tau0(x,t)\cdot h(x,t)^2 - h(x,t)^2\tau_s(x,t) + 6\cdot h(x,t)\cdot s(x,t)}{h(x,t)^5}$$

Four equations are required to determine the unknown physical quantities $q(x,t)$, $\tau_s(x,t)$, $\tau0(x,t)$, and $h(x,t)$. Combining continuity equation (3) and the kinematic boundary condition (5) along with Leibniz rule we yield to the first equation

$$h_t + q_x = 0 \quad (9)$$

Integrating Eq. (2) from a z-coordinate somewhere in the film to the free surface and using the boundary condition (7) we obtain a pressure. Substituting the expression of the pressure into Eq. (1) and integrating over the entire film thickness with the boundary condition (6), we produce a second required equation. Using the method of moments with a monomial of orders 1 and 2, respectively, we deduce both the third and the fourth equations. The three nonlinear equations are too long to be inserted in this brief note.

4 Linear Stability

The four nonlinear equations are linearized around the basic solution, and we obtain

$$H_t + Q_x = 0 \quad (10)$$

$$-\mathrm{We}\ \varepsilon^3 H_{xxxx} + \frac{\varepsilon^2}{\mathrm{R}}\left(-S_{xxx} + \frac{9}{2}H_{xxx} + 3H_{xxt}\right) + \varepsilon\left(-\frac{15}{7}H_{xt} + \frac{8}{35}S_{xx} - \frac{1}{35}\tau_{xx} - \frac{36}{35}H_{xx}\frac{3}{\mathrm{R}}H_{xx}\cot\theta - H_{tt}\right) + \frac{1}{\mathrm{R}}(\tau_x - 3H_x) = 0 \quad (11)$$

$$\frac{1}{2}\mathrm{We}\ \varepsilon^3 H_{xxxx} + \frac{\varepsilon^2}{\mathrm{R}}\left(\frac{7}{10}S_{xxx} - \frac{61}{20}H_{xxx} - 2H_{xxt} - \frac{1}{60}\tau_{xxx}\right) + \varepsilon\left(\frac{39}{35}H_{xt} - \frac{1}{10}S_{xt} + \frac{3}{160}\tau_{xx} + \frac{1}{120}\tau_{xt} - \frac{137}{560}S_{xx} + \frac{639}{1120}H_{xx} - \frac{3}{2\ \mathrm{R}}H_{xx}\cot\theta + \frac{1}{2}H_{tt}\right) - \frac{1}{\mathrm{R}}(S_x - 3Hx) = 0 \quad (12)$$

$$\frac{1}{3}\mathrm{We}\ \varepsilon^3\cdot H_{xxxx} + \frac{\varepsilon^2}{\mathrm{R}}\left(\frac{61}{105}S_{xxx} - \frac{169}{70}H_{xxx} - \frac{11}{7}H_{xxt} - \frac{1}{70}\tau_{xxx}\right) + \varepsilon\left(\frac{183}{280}H_{xt} - \frac{13}{105}S_{xt} + \frac{1}{80}\tau_{xx} + \frac{1}{140}\tau_{xt} - \frac{13}{56}S_{xx} + \frac{39}{112}H_{xx} - \frac{1}{\mathrm{R}}H_{xx}\cot\theta + \frac{2}{7}H_{tt}\right) - \frac{2}{\mathrm{R}}(S_x + H_t) = 0 \quad (13)$$

The perturbation quantities are expanded in the form of normal modes, and the equations are rescaled in the streamwise direction in order to drop the parameter ε.

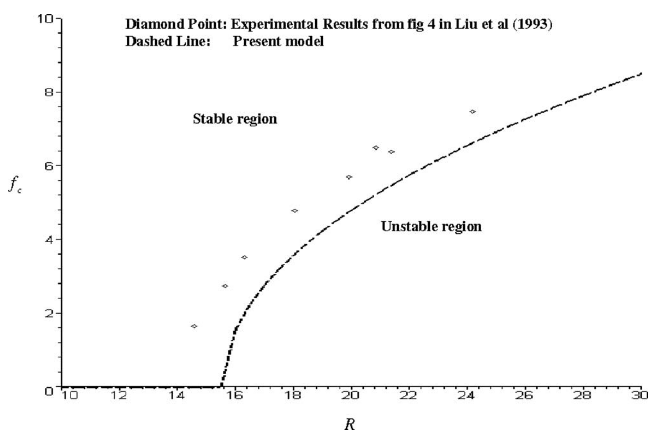

Fig. 2 Cutoff frequency θ=4.6, ν=5.02×10^{-6} m^2 s^{-1}, ρ=1130 kg m^{-3}, and σ=69×10^{-3} N m^{-1}; experimental data from Ref. [12]

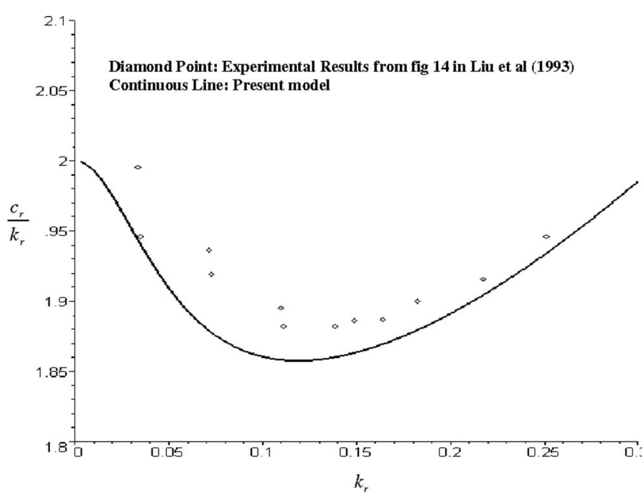

Fig. 3 Phase velocity c_r/k_r as function of wave number k_r: θ=4.6, ν=5.02×10^{-6} m^2 s^{-1}, ρ=1130 kg m^{-3}, and σ=69×10^{-3} N m^{-1}

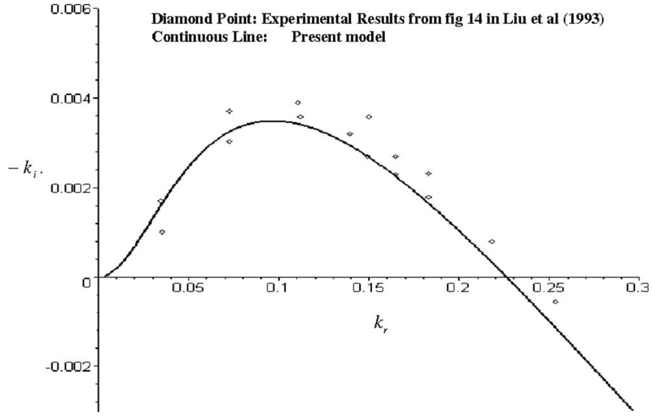

Fig. 4 Spatial growth rate $-k_i$ as function of wave number k_r: $\theta=4.6$, $\nu=5.02\times10^{-6}$ m^2 s^{-1}, $\rho=1130$ kg m^{-3}, and $\sigma=69\times10^{-3}$ N m^{-1}

$$(Q(x,t),H(x,t),\tau(x,t),S(x,t)) \approx (A,B,C,D)\cdot e^{i(k.x-ct)}$$

where A,B,C,D are arbitrary constants, while $c=c_r+i\cdot c_i$ and $k=k_r+i\cdot k_i$ are the complex angular frequency and complex wave number, respectively. Then, the four linear partial differential equations are transformed into four algebraic equations with the four constants A,B,C,D. The condition for a nontrivial solution for the algebraic system leads to the dispersion equation given in the Appendix. In the frame of long waves, the marginal stability condition leads to the threshold of stability $R_c=\frac{5}{6}\cot\theta$ given in Refs. [4,5]. Figure 2 shows the cut-off frequency that separates the stable from the unstable region. A good agreement with observations given in Ref. [12] is amply evident. Furthermore, the celerity of the propagating waves and spatial growth rate are calculated and compared with the experimental results in Figs. 3 and 4, respectively. Here again the agreement is good. It is worth noticing that the similar agreement was found by Brevdo et al. [6], see Figs. 11a, 11b, and 12a in Ref. [6].

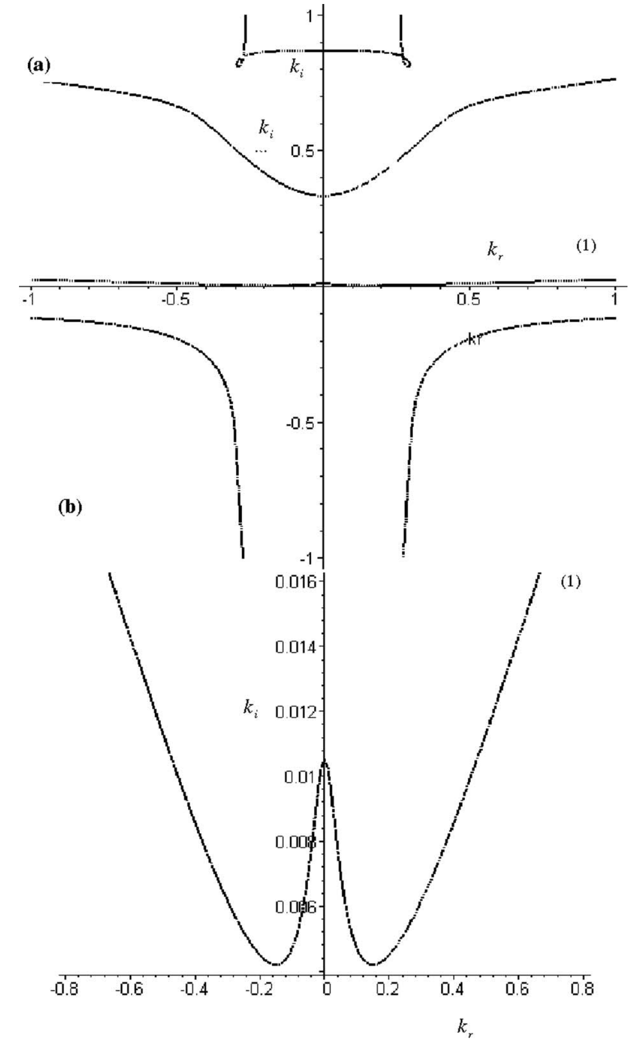

Fig. 5 (*a*) Image of different branches when the growth rate is $c_i=0.02$ and (*b*) close view on the curve (1) R=40

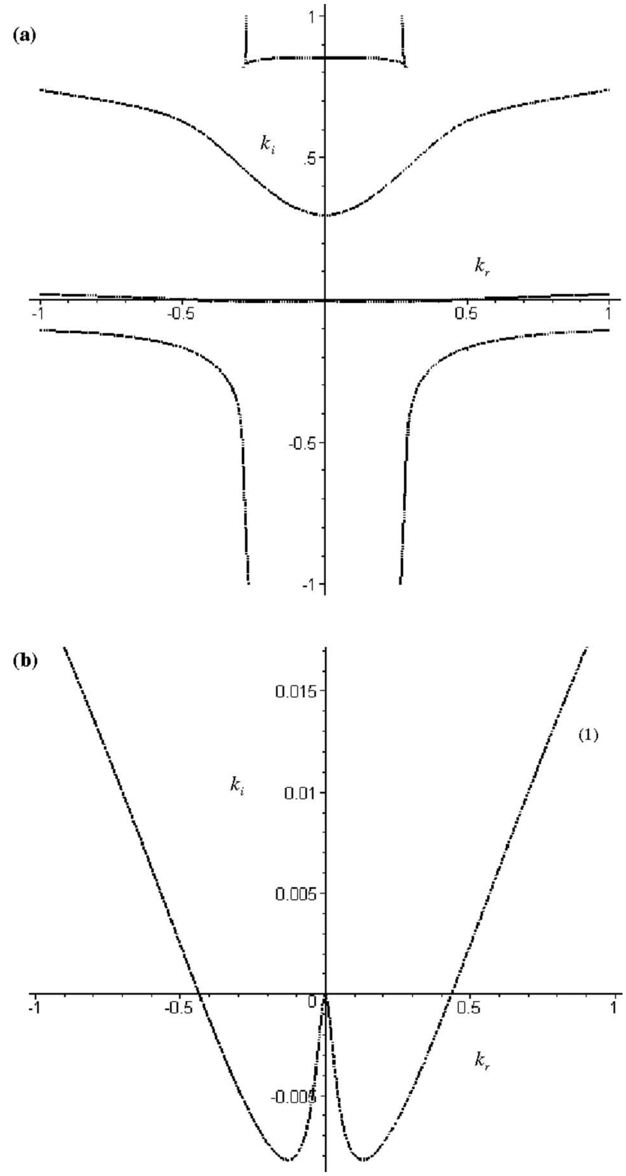

Fig. 6 (*a*) Image of different branches when the growth rate is $c_i=0$ and (*b*) close view on the curve (1) R=40

The accuracy of the proposed model is verified using the formalism of absolute-convective stability based on Briggs' collision criteria. For a given growth rate c_i, the solution of the dispersion relation is displayed in the (k_r,k_i) plane as the oscillation frequency c_r is varied. Similar to Ref. [6], we show through Figs. 5 and 6 the motion of the solution curves when the growth rate is

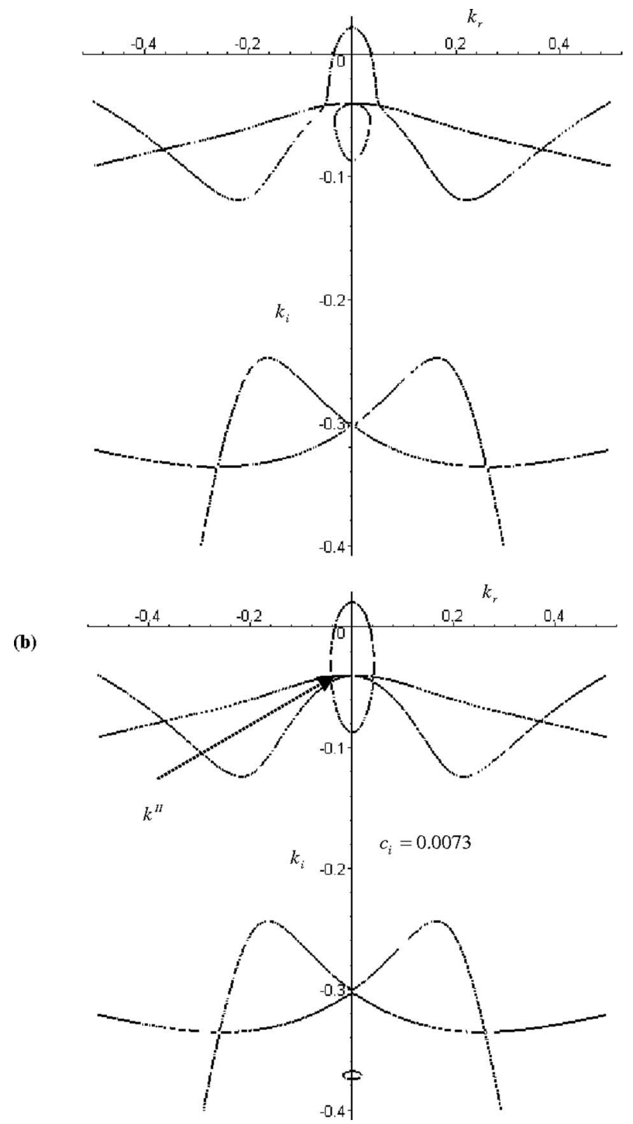

Fig. 7 Pinching process in the complex wave number plane (k_i, k_r) for $V=1.15$, $R=200$, $We=14.18:\theta=4.6$, $\nu=5.02\times10^{-6}$ m^2 s^{-1}, $\rho=1130$ kg m^{-3}, and $\sigma=69\times10^{-3}$ N m^{-1}

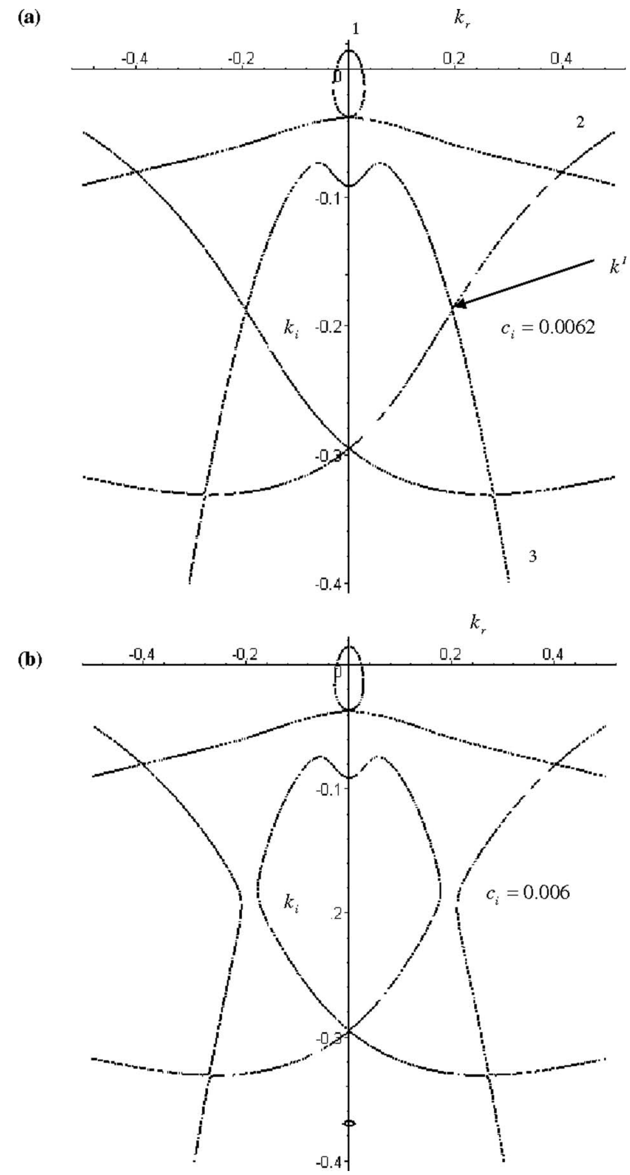

Fig. 8 Pinching process in the complex wave number plane (k_i, k_r) for $V=1.15$, $R=200$, $We=14.18:\theta=4.6$, $\nu=5.02\times10^{-6}$ m^2 s^{-1}, $\rho=1130$ kg m^{-3}, and $\sigma=69\times10^{-3}$ N m^{-1}

decreased from $c_i=0.02$ to $c_i=0$. No pinching of the spatial branches is observed. According to the collision criteria the film flowing down an inclined plane is absolutely stable and convectively unstable, which means that the perturbations are seeped down. The results hold true for Reynolds numbers up to R=200. The resemblance between Figs. 5 and 6 and Figs. 3(a) and 3(c) in Ref. [6] is clear. The agreement between our results and those given by Brevdo et al. [6] is further verified when a reference frame moving at speeds $V=1.15$ and $V=1.16$ with respect to the laboratory is considered. The similitude between our results shown in Figs. 7 and 8 and Fig. 6 in Ref. [6] is encouraging. Figure 7(*a*) shows the three solution branches noted by (1), (2), and (3) for $c_i=0.0075$. The solution (1) is located in the positive k_i half plane. When the growth rate c_i decreases to $c_i=0.0073$ (see Fig. 7(*b*)) the collision of the solution branches (1) and (3) run into the point marked by k_{II}. Decreasing further the spatial growth rate to $c_i=0.0062$, the collision is found between branches (1) and (2) (see Fig. 8(*a*)). This collision point is noted by k_{I}. Figure 8(*b*) shows the solution branches after collision. The positions of the collision point are recovered with remarkable precision. The results are summarized in the following table.

	Collision points	$V=1.15$ *ci*	$V=1.16$ *ci*
Brevdo et al. [6]	I	0.0062	0.0079
Present model	I	0.0061	0.007889
Brevdo et al. [6]	II	0.0073	0.0078
Present model	II	0.00732	0.00779

5 Conclusion

We propose a four-equation model to describe the motion of a liquid film flowing down an inclined plane that involves physical proprieties of the flow only, the flow rate, the film thickness, the shear stress, and the velocity on the free surface. The results obtained were found to follow closely the past experimental observations and the outcome of more encompassing linear analyses.

Appendix: Dispersion Equation

$$
\begin{aligned}
&501{,}760k^8\ \mathrm{We}\ \mathrm{R} + (492{,}800I\ \mathrm{We}\ \mathrm{R}^2 + 752{,}640I)k^7 \\
&+ (1{,}505{,}280 \cot g(\theta) - 564{,}480Ic + 30{,}105{,}600\ \mathrm{We}\ \mathrm{R} \\
&- 1{,}827{,}840\ \mathrm{R} - 121{,}800\ \mathrm{We}\ \mathrm{R}^3 - 501{,}760I\ \mathrm{We}\ \mathrm{R}^2 c)k^6 \\
&+ (15{,}993{,}600I\ \mathrm{We}\ \mathrm{R}^2 - 814{,}464I\ \mathrm{R}^2 \\
&+ 1{,}478{,}400I \cot(\theta)\mathrm{R} + 3{,}958{,}080c\ \mathrm{R} + 246{,}400\ \mathrm{We}\ \mathrm{R}^3 c \\
&+ 8{,}290{,}400I)k^5 + (-1{,}850{,}240c^2\ \mathrm{R} - 1{,}505{,}280I \cot(\theta)c\ \mathrm{R} \\
&+ 47{,}088\ \mathrm{R}^3 + 2{,}841{,}300Ic\ \mathrm{R}^2 - 60{,}211{,}200Ic \\
&- 15{,}052{,}800I\ \mathrm{We}\ \mathrm{R}^2\ c + 90{,}316{,}800 \cot g(\theta) \\
&- 93{,}623{,}040\ \mathrm{R} + 263{,}424{,}000\ \mathrm{We}\ \mathrm{R} - 365{,}400 \cot(\theta)\mathrm{R}^2 \\
&- 125{,}440\ \mathrm{We}\ \mathrm{R}^3\ c^2)k^4 + (-16{,}941{,}960I\ \mathrm{R}^2 \\
&+ 739{,}200 \cot(\theta)\mathrm{R}^2\ c - 345{,}312c\ \mathrm{R}^3 - 3{,}079{,}440Ic^2\ \mathrm{R}^2 \\
&+ 2{,}167{,}603{,}200I + 206{,}713{,}920c\ \mathrm{R} \\
&+ 47{,}980{,}800I \cot(\theta)\mathrm{R})k^3 + (672{,}840c^2\ \mathrm{R}^3 \\
&+ 790{,}272{,}000 \cot(\theta) + 1{,}034{,}880Ic^3\ \mathrm{R}^2 - 96{,}902{,}400c^2\ \mathrm{R} \\
&+ 57{,}539{,}160Ic\ \mathrm{R}^2 - 550{,}368{,}000\ \mathrm{R} - 1{,}512{,}806{,}400Ic \\
&- 376{,}320 \cot(\theta)c^2\ \mathrm{R}^2 - 45{,}158{,}400I \cot(\theta)c\ \mathrm{R})k^2 \\
&+ (2{,}370{,}816{,}000I - 497{,}280c^3\ \mathrm{R}^3 - 56{,}434{,}560Ic^2\ \mathrm{R}^2 \\
&+ 951{,}148{,}800c\ \mathrm{R})k + 16{,}934{,}400Ic^3\ \mathrm{R}^2 \\
&- 361{,}267{,}200c^2\ \mathrm{R} - 790{,}272{,}000Ic + 125{,}440c^4\ \mathrm{R}^3 = 0
\end{aligned}
$$

I is the complex number.

References

[1] Nusselt, W., 1916, "Die obserflachenkondensation des Wasserdampfes," Z. Ver. Dtsch. Ing., **60**, pp. 541–552.

[2] Kapitza, P. L., and Kapitza, S. P., 1949, "Wave Flow of Thin Layers of Viscous Fluid," Zh. Eksp. Teor. Fiz., **19**, pp. 105–120.

[3] Chang, H. C., 1994, "Wave Evolution on a Falling Flow," Annu. Rev. Fluid Mech., **26**, pp. 103–136.

[4] Benjamin, T. B., 1957, "Wave Formation in Laminar Flow Down an Inclined Plane," J. Fluid Mech., **2**, pp. 554–574.

[5] Yih, C. S., 1955, "Stability of Parallel Laminar Flow With a Free Surface," *Proceedings of the Second US Congress on Applied Mechanics*, ASME, New York, pp. 623–628.

[6] Brevdo, L., Laure, P., Dias, F., and Bridges, T. J., 1999, "Linear Pulse Structure and Signalling in Film Flow on an Inclined Plane," J. Fluid Mech., **396**, pp. 37–71.

[7] Benney, D. J., 1966, "Long Waves on Liquid Films," J. Math. Phys., **45**, pp. 150–115.

[8] Shkadov, V. Y., 1967, "Wave Conditions in the Flow of Thin Layer of Viscous Liquid Under the Action of Gravity," Izv. Akad. Nauk SSSR, Mekh. Zhidk. Gaza, **1**, pp. 43–51.

[9] Lee, J. J., and Mei, C. C., 1996, "Stationary Waves on an Inclined Sheet of Viscous Fluid at High Reynolds Number and Moderate Weber Numbers," J. Fluid Mech., **307**, pp. 191–229.

[10] Ruyer-Quil, C., and Maneville, P., 2000, "Improved Modelling of Film Flows Down Inclined Planes," Eur. Phys. J. B, **15**, pp. 357–369.

[11] Floryan, J. M., Davis, S. H., and Kelly, R. E., 1987, "Instabilities of a Liquid Film Flowing Down a Slightly Inclined Plane," Phys. Fluids, **30**(4), pp. 983–989.

[12] Liu, J., Paul, J. D., and Gollub, J. P., 1993, "Measurements of the Primary Instability of Film Flow," J. Fluid Mech., **250**, pp. 69–101.

Characterization of Young's Modulus of Nanowires on Microcantilever Beams

Carmen M. Lilley
e-mail: clilley@uic.edu

Jin He
e-mail: jhe6@uic.edu

Department of Mechanical and Industrial Engineering,
University of Illinois at Chicago,
2039 Engineering Research Facility,
842 W Taylor Street (MC 251),
Chicago, IL 60607

A new approach to measure the elastic modulus of nanowires is presented in this paper using a nanowire and a microcantilever beam composite system. The mechanical behavior of a nanowire-microcantilever beam structure under electrostatic actuation was studied using the finite element method, and a comparison of the resonance frequencies for a nanowire-microcantilever composite beam structure and a microcantilever beam only is presented. The test system can be optimized by introducing arrays of nanowires to increase the resonance frequency difference between the microcantilever beams and the nanowire array microbeam structures.
[DOI: 10.1115/1.3130443]

1 Introduction

Nanowires (NWs) have a wide range of potential applications in opto-electronic nanodevices [1], biological sensors [2], and nano-electronic circuits [3]. As such, there is considerable research interest in measuring the material properties of NWs. For example, Young's modulus is an important mechanical property for designing nanoelectromechanical systems (NEMSs). Experimentally, Young's modulus of a NW was found to have a complex dependence on its cross-sectional size for the size range 10^1-10^2 nm. It should also be noted that careful consideration should be taken in the adoption of Young's modulus as a mechanical property of NWs as a continuum hypothesis may no longer exist [4]. However, for the discussion outlined in this paper, a continuum approach to study overall Young's modulus is still valid because the NW dimensions are large when compared with the continuum cross-sectional limit as proposed in Ref. [4].

Random variations of Young's moduli of silicon NWs and gold NWs were observed with atomic force microscopy (AFM) [5,6] measurements. For silicon NWs, Tabib-Azar et al. [5] measured the range for Young's modulus to vary from 93 GPa to 250 GPa with NW diameters ranging from 140 nm to 200 nm (compared with 185 GPa for bulk silicon in the [111] direction). For gold NWs, Young's modulus is shown to range from 40 GPa to 110 GPa (compared with 78 GPa for bulk gold) with NW diameters ranging from 40 nm to 250 nm [6]. Some researchers attribute these variations to measurement uncertainties of the NW dimensions and the AFM tip. They state that the modulus is independent of cross-sectional size and comparable to the corresponding bulk materials [5–7]. Young's modulus lower than that of the bulk silica was reported when the silica NW size is between 40 nm and 100 nm by resonance frequency measurements [8–10]. However, these lower values are still attributed to factors such as different initial NW shapes [11]. In these experiments, handling, positioning, imaging, gripping, applying, and measuring simultaneously the nanoscale forces and displacements are obstacles to accurately characterize Young's modulus of free-standing NWs. Out-of-plane measurements of NW cross-sectional size generate nontrivial uncertainty in some experiments [5–7,9]. Failure to employ straight NWs, as shown in Refs. [8,10], also makes it difficult to obtain accurate Young's modulus measurements.

Herein, we present an alternative approach to study Young's moduli of various NWs with rectangular cross sections directly fabricated on microcantilevers (MCs) with dimensions in the size range 50–100 nm. The finite element method (FEM) is used to model a NW-MC structure and the MC beam only electrostatically actuated in bending. The dependency of resonance frequency on the MC beam and/or NW geometry sizes, mechanical properties, boundary conditions, and actuation voltage is characterized. Experimentally, this technique can be used to compare the different resonance frequencies between a NW-MC structure and the corresponding MC beam only to numerically calculate overall Young's moduli of the NWs. The essence of this approach is to dramatically reduce difficult nanoscale manipulations and measurements by mechanically testing NWs with a microelectromechanical system (MEMS) device.

2 Modeling Approach

The design and characterization of MC beams as mass sensors [12,13] and as actuators [14,15] were widely researched. Electrostatic actuation of a NW-MC structure can be achieved by applying a voltage V between the structure and a rigid ground plate beneath it (see Fig. 1). Both static and dynamic behaviors of the NW-MC structure can be observed using this actuation method. The resonance frequency for a MC beam will shift when NWs are fabricated on the top surface. The shift in the resonance is a function of the mass loading, the mechanical properties, dimensions, number, and orientation of the NWs. In this paper, the effect of the mass loading on the resonance frequency is considered in the analytical solutions and the FEM simulations by assuming that the mass density is the same as the bulk density [5,8–10]. In addition, the number, orientation, and geometries of the NWs would be known experimentally through metrology measurements with scanning electron microscope (SEM) and AFM imaging. Thus, overall Young's modulus of the NWs can be characterized from the resonance frequency difference if the resonance difference is large enough compared with experimental uncertainties.

Before implementing this approach experimentally, FEM and analytical studies should be performed to predict and analyze the dependence of the resonance frequency on Young's modulus, dimensions, and other factors as previously mentioned for the NW-MC structure and the corresponding MC beam only. An appropriate dimension ratio for the NW and the MC beam is also a prerequisite to obtain an experimentally measurable shift in resonance frequency between a NW-MC structure and a MC beam only. A coupled transducer element TRANS126 and a three dimensional structure solid element SOLID45 provided by commercial software ANSYS were adopted to implement the FEM simulation of the MC beam only and the NW-MC structure under electrostatic actuation [16].

A gold NW fabricated on an aluminum MC beam was selected as the composite system for the following FEM simulations. The dimensions and mechanical properties of the material components were listed in Table 1 and the static and resonance cases are shown in Figs. 2 and 3, respectively. In Fig. 2, the maximum transverse displacements of the MC beam only and the NW-MC structure under different voltages were shown. For a MC beam only, the FEM calculated pull-in voltage V_{PI} (26.0–27.0 V) is consistent with the analytical value of 26.3 V obtained following

Contributed by the Applied Mechanics Division of ASME for publication in the JOURNAL OF APPLIED MECHANICS. Manuscript received February 27, 2007; final manuscript received April 2, 2009; published online July 21, 2009. Review conducted by Sanjay Govindjee.

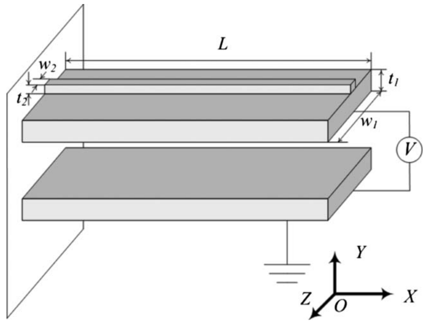

Fig. 1 Schematic illustration of a single NW fabricated on a MC beam surface and under electrostatic actuation (image is not to scale)

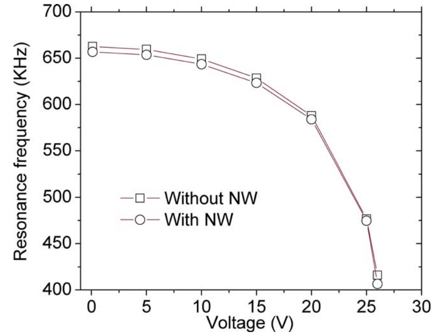

Fig. 3 Resonance frequencies of the MC beam under different voltages and a misalignment angle of 0 deg (circle: NW-MC; square: MC beam only)

the closed-form expressions given by Pamidighantam et al. [17]. As can also be seen in Fig. 2, the displacement of the NW-MC structure is smaller than that of a MC beam only under the same voltage.

The resonance frequencies of the MC beam were influenced by the applied voltage amplitude. The equation of motion for the undamped MC beam under electrostatic actuation is [18]

$$\rho A \frac{\partial^2 u(x,t)}{\partial t^2} + \frac{\partial^2}{\partial x^2}\left(EI_z \frac{\partial^2 u(x,t)}{\partial x^2} \right) = F_m + F_e \tag{1}$$

where F_m is the structural force and F_e is the electrostatic force. The resonance frequency under electrostatic actuation is [18]

$$f = \frac{1}{2\pi}\sqrt{\frac{k_m - k_e}{m}} \tag{2}$$

where k_m and k_e correspond to mechanical and electromechanical stiffnesses, respectively, and m is the MC beam mass. Although k_m is constant for a given MC beam, k_e is proportional to the applied voltage V^2. From Eq. (2), it is observed that the resonance frequency decreases as the applied voltage increases. The resonance frequencies for the NW-MC beam actuated with different applied voltages are presented in Fig. 3. As can be seen, the resonance frequencies for the NW-MC and MC beam only structures actuated with a voltage of $V=5$ V ($V/V_{\mathrm{PI}} \approx 20\%$) will shift approximately to 0.6% from near zero voltage ($V=0.1$ V) actuation.

For a simple cantilever beam vibrating under a mechanical load, the first resonance frequency given by Euler–Bernoulli beam theory is [19]

$$f_{\mathrm{EB}} = \frac{1}{2\pi}\eta^2 \sqrt{\frac{E_1 I_z}{\rho_1 A}} \tag{3}$$

where η is the first solution of $\cos(\eta L)\cosh(\eta L) = -1$, $I_z = w_1 t_1^3/12$ is the moment of inertia of the cross section, and A is the cross section area. Rotational inertia and shear effects were neglected in Eq. (3). Gere and Timoshenko proposed a solution to include these effects and the solution is expressed by the following [20]:

$$f_T = \frac{1}{2\pi}\eta^2 \sqrt{\frac{E_1 I_z}{\rho_1 A}}\left[1 - \frac{1}{2}\eta^2 \frac{I_z}{A}\left(1 + \frac{E_1}{KG}\right)\right] \tag{4}$$

where $G = E/[2(1+\nu)]$ is the shear modulus, and $K = 10(1+\nu)/(12+11\nu)$ is the shear coefficient. The resonance frequencies of the MC beam only calculated with the FEM model and the theoretical formulas are listed in Table 2. From Table 2, it can be seen that the calculated resonance frequency at near zero actuation voltage ($V=0.1$ V) shows close agreement with those calculated from theoretical formulas and the difference is within 1%. In order to lessen the voltage effect on the resonance frequency while considering the design requirements to actuate the beams, an actuation voltage of 5 V was selected and used in the following FEM calculations.

The test system can be optimized by introducing NWs in an array instead of a single NW fabricated on the MC beam. When the dimension ratio of the NW and the MC beam is fixed, employment of a NW array enlarges the resonance frequency difference between the NW array MC structure and the MC beam only. Therefore, the mechanical behavior of a MC beam with a NW array fabricated on the top surface was studied. Figure 4 illustrates the NW array fabricated on the MC beam surface with a 0 deg misalignment angle. As can be seen, the NWs are oriented along the symmetric axis of the MC beam. The resonance frequency of the NW array MC structure can be calculated via the composite beam theory [21] when rotational inertia and shear effects are not taken into account with the following equation:

Table 1 Parameters of a single NW fabricated on the MC beam

	Microcantilever (aluminum)	Nanowire (gold)
Young's modulus (GPa)	$E_1=70$	$E_2=78$
Poisson's ratio	$\nu_1=0.3$	$\nu_2=0.44$
Density (kg/m^3)	$\rho_1=2.7\times10^3$	$\rho_2=19.3\times10^3$
Length (μm)	$L_1=25$	$L_2=25/\cos(\theta)$
Width (μm)	$w_1=2.50$	$w_2=0.10$
Thickness (μm)	$t_1=0.50$	$t_2=0.05$
Initial gap (μm)	$h=1$	
Misalignment angle (deg)	$\theta=0$ to 1	

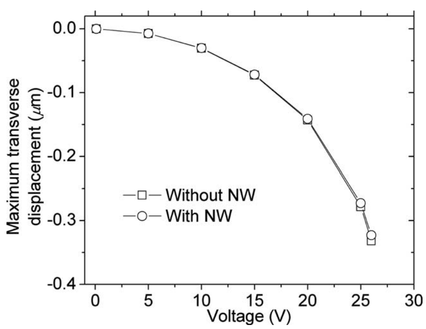

Fig. 2 The maximum transverse displacement of the MC beam under different voltages and with a 0 deg misalignment angle (circle: NW-MC; square: MC beam only)

Table 2 Resonance frequency of the MC beam only

	FEM		Theory	
	Actuation voltage $V=0.1$ V	Actuation voltage $V=5$ V	Euler–Bernoulli beam	Timoshenko beam
Frequency (kHz)	662.74	659.55	658.01	657.86
Relative difference[a]	-	−0.48%	−0.71%	−0.74%

[a]Relative difference is based on the FEM calculated resonance frequency at actuation voltage $V=0.1$ V.

$$f^*_{\mathrm{EB}} = \frac{1}{2\pi}\eta^2\sqrt{\frac{E_1I_{z1}+E_2I_{z2}}{\rho^*A^*}} \tag{5}$$

where I_{z1} and I_{z2} are the moments of inertia about neutral axis of the MC beam and the NW array, respectively, and ρ^* and A^* are the equivalent density and cross section and may be calculated with

$$I_{z1} = \frac{1}{12}w_1t_1^3 + (w_1t_1)\left(h_1 - \frac{1}{2}t_1\right)^2 \tag{6}$$

$$I_{z2} = n\cdot\left[\frac{1}{12}w_2t_2^3 + (w_2t_2)\left(h_2 - \frac{1}{2}t_2\right)^2\right] \tag{7}$$

$$\rho^* = \frac{\rho_1w_1t_1 + n\cdot\rho_2w_2t_2}{w_1t_1 + n\cdot w_2t_2} \tag{8}$$

$$A^* = w_1t_1 + n\cdot w_2t_2 \tag{9}$$

where $h_1=[E_1w_1t_1^2+nE_2w_2t_2(2t_1+t_2)]/[2(E_1w_1t_1+nE_2w_2t_2)]$, $h_2=(t_1+t_2)-h_1$, and n is the number of the NWs on the MC beam.

The theoretical resonance frequencies were calculated for the NW array MC structure using Eq. (5). These frequencies were compared with the FEM calculated resonance frequencies in Fig. 5. As can be seen, the resonance frequency of the NW array MC structure increases with increasing NW thickness t_2 or width w_2 when all other conditions are fixed. It can also be seen that the resonance frequencies calculated from the FEM models show close agreement with those calculated from the theoretical formula. The maximum difference for the two methods is 1.0%.

3 Simulation and Analysis Considerations

The FEM model for a NW array with a misalignment angle of $\theta=1$ deg fabricated on a MC beam is illustrated in Fig. 6. A convergence test for this model was performed and is shown in Fig. 7. The modeling parameters are the same as the NW-MC model parameters listed in Table 1. As can be seen in Fig. 7, the resonance frequency converges as the number of SOLID45 elements approaches approximately 23,000. Therefore, 23,000 elements were used in the following calculations to compare the resonance frequencies of the MC beam only and the NW array MC structure. By measuring the resonance frequencies for these two systems experimentally, we were able to recover overall Young's modulus of the NW material with the FEM models. For example, the resonance frequencies in Fig. 8 were calculated for different overall Young's modulus of gold NWs when the arrays have a misalignment error of $\theta=0$ deg and $\theta=1$ deg. A misalignment error may be possible due to errors in the e-beam patterning of the MC beams on a test die when patterning over large areas.

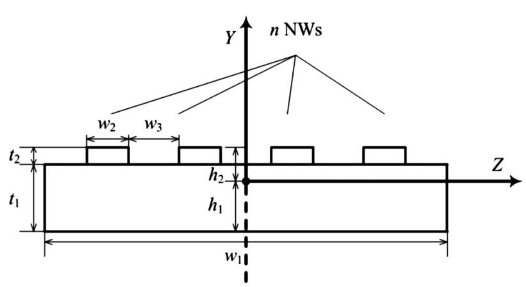

Fig. 4 Schematic illustration of NWs fabricated along the symmetric axis of the MC beam with a 0 deg misalignment

4 Experimental Uncertainty Analysis

An uncertainty analysis of Young's modulus for the NWs as measured with the proposed experimental approach is discussed. The cross section of the NW array MC structure is shown in Fig.

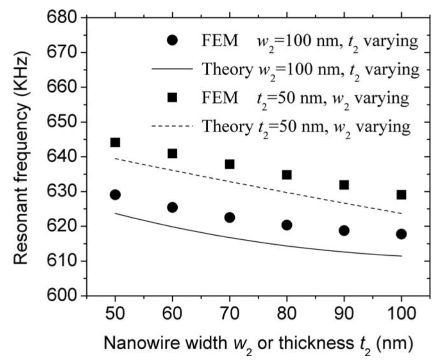

Fig. 5 Dependence of resonance frequencies on the NW-MC structure with an array of ten NWs on the beam surface as a function of varying NW width and thickness. The NWs are fabricated along the symmetric axis of the MC beam and the pitch width is $w_3=100$ nm (circle: FEM, $w_2=100$ nm, t_2 varying; solid line: theory, $w_2=100$ nm, t_2 varying; square: FEM, $t_2=50$ nm, w_2 varying; dash line: theory, $t_2=50$ nm, w_2 varying).

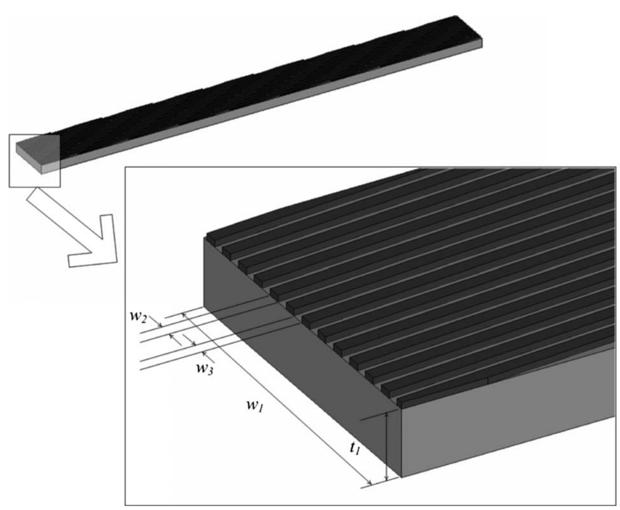

Fig. 6 Schematic illustration of a NW array with a misalignment angle of $\theta=1$ deg fabricated on a MC beam

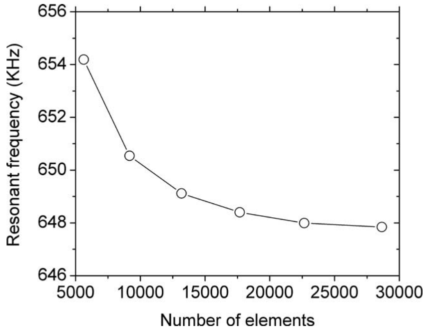

Fig. 7 Convergence test of the NW array MC structure with misalignment angle: $\theta=1$ deg

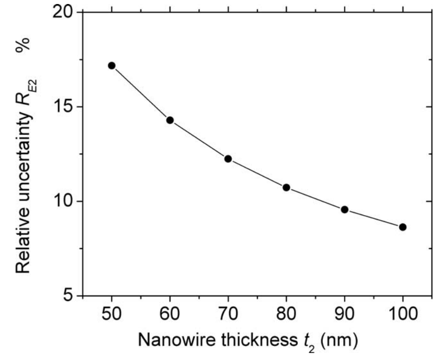

Fig. 9 Variance of the relative uncertainty of NW overall Young's modulus R_{E2} with respect to NW thickness. Ten NWs are fabricated along the symmetric axis of the MC beam. The NW width is $w_2=100$ nm and the thickness t_2 is varying.

4 and the modeling parameters are listed in Table 1. Additional parameters are a misalignment angle of $\theta=1$ deg and the number of NWs is $n=10$. The corresponding equations and explanation for the numerical method of the analysis are given in the Appendix. It should be noted that the calculated uncertainties discussed here are only for systematic uncertainties. The length L, MC beam width w_1, and NW width w_2 can be measured with a SEM using different magnifications to measure at the corresponding scale for each dimension. Using a Hitachi S-3000N SEM instrument as an example, the resolution for measuring L, w_1, and w_2 are approximately 100 nm, 10 nm, and 0.5 nm, respectively. The corresponding relative uncertainties R_L, R_{w1}, and R_{w2} are approximately 0.5% each. The MC beam thickness t_1 and the NW thickness t_2 can be measured with an AFM, which has resolution of 1 nm, which corresponds to the relative uncertainties of $R_{t1}=0.2\%$ and $R_{t2}=2\%$, respectively, for the thickness of the NWs and MC beam measurements. The resonance frequencies of the MC beam only and the NW array MC structure can be measured by microscope scanning vibrometer and the relative uncertainties $R_{f\mathrm{EB}}$ and $R_{f\mathrm{EB}}{}^{*}$ are less then 0.1%. As the resonance frequencies are compared with the FEM results, the uncertainty associated with the FEM results also contribute to the uncertainties of the final results and is less than 1%. As can be seen from Fig. 8, the relative uncertainty for the resonance frequency when there is a 1 deg misalignment angle is 2.5%. Therefore, 2.5% is used for $R_{f\mathrm{EB}}{}^{*}$ and 0.1% is used for $R_{f\mathrm{EB}}$. The relative uncertainty for NW Young's modulus R_{E2} with respect to a change in the NW thickness with the width of 100 nm is shown in Fig. 9. As can be seen, R_{E2} decreases as the NW width w_2 or NW thickness t_2 increases, and the limit for the maximum uncertainty of the NW modulus R_{E2} is 17.2% for the smallest NW ($t_2=50$ nm) considered in Fig. 6, while the uncertainty decreases to 7.5% for the largest NW considered ($t_2=100$ nm). A comparison with other techniques for measuring the modulus of gold NWs is shown in Table 3, which illustrates that the proposed technique is comparable or superior to published results. It can be seen that NW overall Young's modulus uncertainty measured by the proposed experimental approach is well within the range of other experimental methods while improving repeatability and the cost (time and labor) to perform the experiments. Thus this approach provides a viable alternative to measure overall Young's modulus of NWs.

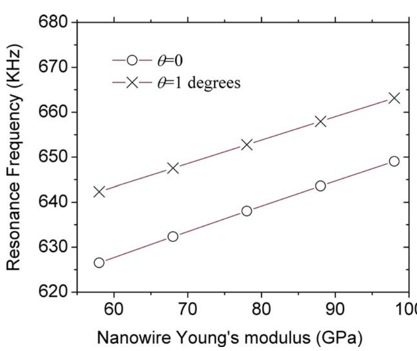

Fig. 8 Resonance frequencies for the NW array MC structure by assuming different NW overall Young's moduli

5 Summary

The dynamic behavior of the MC beam with and without NWs under electrostatic actuation was studied with FEM modeling in this paper. Several factors affect the resonance frequency of the MC structure. If the electrostatic actuation voltage is low compared with the pull-in voltage, the dependence of the resonance frequency on the actuation voltage can be neglected. Introducing a NW array fabricated on the MC beam instead of a single NW significantly increases the resonance frequency difference between the NW-MC structure and the MC-beam only. The NW Young's modulus can be obtained by comparing resonance frequencies of the NW-MC composite structure and the MC-beam only system as measured experimentally to extrapolate the elastic modulus of the NWs with FEM modeling. The proposed design may have applications as a test structure for measuring the elastic properties of bending NWs.

Table 3 Typical uncertainties for NW Young's moduli

Reference	Material	Description	Elastic modulus (GPa)	Relative uncertainty (%)
Tabib-Azar, et al. [5]	Silicon, $D=100-200$ nm, $L\approx 10$ μm	AFM static/dynamic bending	210 ± 40	19.0
Wang, et al. [8]	Silicon oxide, $D=42\pm 2$ nm, $L=11.7\pm 0.2$ μm	TEM[a] dynamic bending	31 ± 5.1	16.5
Dikin, et al. [9]	Silicon oxide, $D=80\pm 5$ nm, $L=17\pm 0.2$ μm	SEM Dynamic bending	43.4 ± 7.0	16.1

[a]TEM is the abbreviation of transmission electron microscopy.

Nomenclature

E_1 = Young's modulus of the MC beam
E_2 = Young's modulus of the NW
h = initial electric gap/anchor height
L = MC-beam length
n = number of NWs on the MC beam
ν_1 = Poisson's ratio of the MC beam
ν_2 = Poisson's ratio of the NW
θ = misalignment angle of the NW
ρ_1 = MC beam density
ρ_2 = NW density
t_1 = thickness of the MC beam/anchor
t_2 = thickness of the NW
V = voltage
V_{PI} = pull-in voltage
w_1 = MC beam/anchor width
w_2 = NW width
w_3 = pitch width

Appendix

For a MC beam only, Eq. (3) can be rewritten as

$$E_1 = \frac{48\pi^2 f_{\mathrm{EB}}^2 \rho_1}{\eta^4 t_1^2} \tag{A1}$$

The relative uncertainty of Young's modulus of the MC beam R_{E1} calibrated from the experiment is

$$R_{E1} = \frac{1}{E_1}\sqrt{\left[\frac{\partial E_1}{\partial t_1}\cdot (R_{t1}t_1)\right]^2 + \left[\frac{\partial E_1}{\partial L}\cdot (R_L L)\right]^2 + \left[\frac{\partial E_1}{\partial f_{\mathrm{EB}}}\cdot (R_{f\mathrm{EB}} f_{\mathrm{EB}})\right]^2} \tag{A2}$$

where R_{t1}, R_L, and $R_{f\mathrm{EB}}$ are the relative measurement uncertainties of the thickness, length, and resonance frequency of the MC beam, and

$$\frac{\partial E_1}{\partial t_1} = -\frac{96\pi^2 f_{\mathrm{EB}}^2 \rho_1}{\eta^4 t_1^3} \tag{A3}$$

$$\frac{\partial E_1}{\partial L} = \frac{192\pi^2 f_{\mathrm{EB}}^2 \rho_1}{\eta^4 t_1^2 L} \tag{A4}$$

$$\frac{\partial E_1}{\partial f_{\mathrm{EB}}} = \frac{96\pi^2 f_{\mathrm{EB}} \rho_1}{\eta^4 t_1^2} \tag{A5}$$

For NW array fabricated on a MC beam, the total relative uncertainty of Young's modulus of the NW R_{E2} is

$$\begin{aligned} R_{E2} = \frac{1}{E_2}\Bigg\{ &\left[\frac{\partial E_2}{\partial t_1}\cdot (R_{t1}t_1)\right]^2 + \left[\frac{\partial E_2}{\partial w_1}\cdot (R_{w1}w_1)\right]^2 + \left[\frac{\partial E_2}{\partial t_2}\cdot (R_{t2}t_2)\right]^2 \\ &+ \left[\frac{\partial E_2}{\partial w_2}\cdot (R_{w2}w_2)\right]^2 + \left[\frac{\partial E_2}{\partial L}\cdot (R_L L)\right]^2 \\ &+ \left[\frac{\partial E_2}{\partial f_{\mathrm{EB}}^*}\cdot (R_{f\mathrm{EB}*} f_{\mathrm{EB}}^*)\right]^2 \Bigg\}^{1/2} \end{aligned} \tag{A6}$$

where R_{w1} is the relative measurement uncertainty of the MC beam width R_{t2}, R_{w2} is the relative measurement uncertainties of the thickness, length of the NW, $R_{f\mathrm{EB}}{}^*$ is the relative measurement uncertainty of the resonance frequency of the NW array MC structure, and R_{E1} is given in Eq. (A2). Due to the difficulty in rewriting Eq. (5) into the explicit function of E_2, Eq. (15) needs to be calculated numerically. Taking $\partial E_2/\partial t_1$ as an example, a small deviation of t_1 is imposed to the thickness of the MC beam denoted as Δt_1 and the thickness becomes $(t_1+\Delta t_1)$. Substituting $(t_1+\Delta t_1)$ into Eq. (5) with all other variables unchanged, the only unknown variable is Young's modulus of NW denoted as $(E_2 + \Delta E_2)$ and the resonance frequency $f_{\mathrm{EB}}{}^*$ becomes a constant. By solving Eq. (5), the deviation ΔE_2 caused by Δt_1 is obtained and thus $\partial E_2/\partial t_1$ is approximated as $\Delta E_2/\Delta t_1$. Other components of Eq. (A6) can be calculated in a similar way.

References

[1] Lou, J., Tong, L., and Ye, Z., 2005, "Modeling of Silica Nanowires for Optical Sensing," Opt. Express, **13**(6), pp. 2135–2140.
[2] Cui, Y., Wei, Q., Park, H., and Lieber, C. M., 2001, "Nanowire Nanosensors for Highly Sensitive and Selective Detection of Biological and Chemical Species," Science, **293**(5533), pp. 1289–1292.
[3] Lieber, C. M., 2003, "Nanoscale Science and Technology: Building a Big Future From Small Things," MRS Bull., **28**(7), pp. 486–491.
[4] Govindjee, S., and Sackman, J. L., 1999, "On the Use of Continuum Mechanics to Estimate the Properties of Nanotubes," Solid State Commun., **110**, pp. 227–230.
[5] Tabib-Azar, M., Nassirou, M., and Wang, R., 2005, "Mechanical Properties of Self-Welded Silicon Nanobridges," Appl. Phys. Lett., **87**(11), pp. 113102.
[6] Wu, B., Heidelberg, A., and Boland, J. J., 2005, "Mechanical Properties of Ultrahigh-Strength Gold Nanowires," Nature Mater., **4**, pp. 525–529.
[7] Heidelberg, A., Ngo, L. T., Wu, B., Phillips, M. A., Sharma, S., Kamins, T. I., Sader, J. E., and Boland, J. J., 2006, "A Generalized Description of the Elastic Properties of Nanowires," Nano Lett., **6**(6), pp. 1101–1106.
[8] Wang, Z. L., Gao, R. P., Poncharal, P., De Heer, W. A., Dai, Z. R., and Pan, Z. W., 2001, "Mechanical and Electrostatic Properties of Carbon Nanotubes and Nanowires," Mater. Sci. Eng., C, **16**, pp. 3–10.
[9] Dikin, D. A., Chen, X., Ding, W., Wagner, G., and Ruoff, R. S., 2003, "Resonance Vibration of Amorphous SiO_2 Nanowires Driven by Mechanical or Electrical Field Excitation," J. Appl. Phys., **93**(1), pp. 226–230.
[10] Wang, Z. L., Gao, R. P., Pan, Z. W., and Dai, Z. R., 2001, "Nano-Scale Mechanics of Nanotubes, Nanowires, and Nanobelts," Adv. Eng. Mater., **3**(9), pp. 657–661.
[11] Silva, E. C. C. M., Tong, L., Yip, S., and Van Vliet, K. J., 2006, "Size Effects on the Stiffness of Silica Nanowires," Small, **2**(2), pp. 239–243.
[12] Lee, J. H., Kim, T. S., and Yoon, K. H., 2004, "Effect of Mass and Stress on Resonance Frequency Shift of Functionalized $Pb(Zr_{0.52}Ti_{0.48})O_3$ Thin Film Microcantilever for the Detection of C-Reactive Protein ," Appl. Phys. Lett., **84**(16), pp. 3187–3189.
[13] Yi, J. W., Shih, W. Y., and Shih, W. H., 2002, "Effect of Length, Width, and Mode on the Mass Detection Sensitivity of Piezoelectric Unimorph Cantilevers," J. Appl. Phys., **91**(3), pp. 1680–1686.
[14] Lishchynska, M., Cordero, N., Slattery, O., and O'Mahony, C., 2005, "Modelling Electrostatic Behaviour of Microcantilevers Incorporating Residual Stress Gradient and Non-Ideal Anchors," J. Micromech. Microeng., **15**, pp. S10–S14.
[15] Lishchynska, M., Cordero, N., and Slattery, O., 2005, "Development of Behavioural Models for Mechanically Loaded Microcantilevers," Analog Integr. Circuits Signal Process., **44**, pp. 109–118.
[16] ANSYS Release 9.0, ANSYS, Inc., http://www.ansys.com.
[17] Pamidighantam, S., Puers, R., Baert, K., and Tilmans, H. A. C., 2002, "Pull-In Voltage Analysis of Electrostatically Actuated Beam Structures With Fixed-Fixed and Fixed-Free End Conditions," J. Micromech. Microeng., **12**, pp. 458–464.
[18] Brusa, E., Bona, F. D., Gugliotta, A., and Soma, A., 2004, "Modeling and Prediction of the Dynamic Behaviour of Microbeams Under Electrostatic Load," Analog Integr. Circuits Signal Process., **40**, pp. 155–164.
[19] Shabana, A. A., 1996, *Vibration of Discrete and Continuous Systems*, Springer-Verlag, New York.
[20] Gere, J. M., and Timoshenko, S. P., 1990, *Mechanics of Materials*, 3rd ed., PWS, Boston.
[21] Thian, S. C. H., Tang, Y., Fuh, J. Y. H., Wong, Y. S., Lu, L., and Loh, H. T., 2006, "Micro-Rapid-Prototyping Via Multi-Layered Photo-Lithography," Int. J. Adv. Manuf. Technol., **29**, pp. 1026–1032.

A Note on the Derivation of Plane-Strain Elastic Green's Functions for Bimaterial Solids

Xi Zhang[1]
CSIRO Petroleum Resources,
Clayton,
Victoria 3168, Australia
e-mail: xi.zhang@csiro.au

*This brief note presents a rigorous proof of the general solutions obtained by Aderogba [1977, "On Eigenstresses in Dissimilar Media," Philos. Mag., **35**, pp. 281–292] for a defect in elastic bimaterial solids. The derivation is based on the fact that some derivative and integral forms of the biharmonic functions are also biharmonic. The associated solutions can be expressed as the linear combinations of these biharmonic functions and their unknown coefficients can be determined by the interface conditions. It is found that the coefficients only depend on the contrasts of material constants across the interface.*
[DOI: 10.1115/1.3112746]

1 Introduction

The solutions to singularities such as point forces, dislocations and their dipoles, and phase transformation dots embedded in bonded elastic dissimilar materials have been investigated by a number of researchers such as Dundurs and Mura [1], Adeerogba [2], and Suo [3], among others. For instance, Dundurs and Mura [1] presented the solutions for dislocations embedded in half plane or in circular inclusions. Suo [3] obtained the universal complex potentials independent of the nature of singularities for the elastic stress and displacement solutions of a bimaterial system, in terms of the solutions of the same singularities in an infinite homogeneous plane. Instead of complex potentials, Adeerogba [2] first gave the universal formulas for Airy stress functions, equivalent to the complex expressions. However, the proof has not been given in his paper. In this note, we will rigorously rederive the formulas given by Adeerogba [2] based on the potential theory. It is anticipated that the same methodology can be applied to the derivations for other media involving interfaces or free surfaces.

2 Problem Formulation

2.1 Elasticity Equations. For a linear elastic solid, the constitutive form for stress σ_{ij} and strain ε_{ij} is

$$2G\varepsilon_{ij} = \sigma_{ij} - \frac{\nu}{1+\nu}\sigma_{kk}\delta_{ij} \tag{1}$$

where G and ν are elastic shear modulus and Poisson's ratio, respectively.

In plane strain, the equilibrium equation is, without the presence of body forces,

$$\sigma_{ij,j} = 0 \tag{2}$$

or the compatibility equation can be expressed as

$$\nabla^2[\sigma_{xx} + \sigma_{yy}] = 0 \tag{3}$$

[1]Corresponding author.

Contributed by the Applied Mechanics Division of ASME for publication in the JOURNAL OF APPLIED MECHANICS. Manuscript received August 13, 2008; final manuscript received February 3, 2009; published online July 27, 2009. Review conducted by Martin Ostoja-Starzewski.

In developing the solution, we can define the Airy stress function Ψ for the stresses as

$$\sigma_{xx} = \frac{\partial^2\Psi}{\partial y^2}, \quad \sigma_{yy} = \frac{\partial^2\Psi}{\partial x^2}, \quad \sigma_{xy} = -\frac{\partial^2\Psi}{\partial x\,\partial y} \tag{4}$$

Substitution of Eq. (4) in the governing equations (3) leads to a biharmonic equation for the Airy stress function

$$\nabla^2(\nabla^2\Psi) = 0 \tag{5}$$

In addition, we can obtain the displacements (u,v) in terms of the stress function, without considering the disagreements pertaining to any rigid body motions, as follows:

$$2Gu = -\frac{\partial\Psi}{\partial x} + (1-\nu)\int \nabla^2\Psi dx \tag{6}$$

$$2Gv = -\frac{\partial\Psi}{\partial y} + (1-\nu)\int \nabla^2\Psi dy \tag{7}$$

2.2 Interface Problems. As for an elastic bimaterial system, the stress and displacement fields in the upper and lower half planes are controlled by their Airy stress functions Ψ^{I} and Ψ^{II}. However, their final forms should depend on the interface conditions. For pure elastic problems, the interface conditions can be obtained by enforcing continuity of normal and tangential displacements and tractions. Therefore, this leads to

$$u^+ = u^- \tag{8}$$

$$v^+ = -v^- \tag{9}$$

$$\sigma^+_{yy} = \sigma^-_{yy} \tag{10}$$

$$\sigma^+_{xy} = -\sigma^-_{xy} \tag{11}$$

On the interface $y_{\mathrm{I}}=y_{\mathrm{II}}=0$, where y_{i} $(i=\mathrm{I},\mathrm{II})$ are local coordinates in the vertical direction for two bonded materials, it can be easily confirmed that the following relations must be satisfied:

$$\frac{\partial^2\Psi^{\mathrm{I}}}{\partial x^2} = \frac{\partial^2\Psi^{\mathrm{II}}}{\partial x^2} \tag{12}$$

$$\frac{\partial^2\Psi^{\mathrm{I}}}{\partial x\,\partial y_{\mathrm{I}}} = -\frac{\partial^2\Psi^{\mathrm{II}}}{\partial x\,\partial y_{\mathrm{II}}} \tag{13}$$

$$\Gamma\left[-\frac{\partial\Psi^{\mathrm{I}}}{\partial x} + (1-\nu^{\mathrm{I}})\int \nabla^2\Psi^{\mathrm{I}}dx\right] = -\frac{\partial\Psi^{\mathrm{II}}}{\partial x} + (1-\nu^{\mathrm{II}})\int \nabla^2\Psi^{\mathrm{II}}dx \tag{14}$$

$$\Gamma\left[-\frac{\partial\Psi^{\mathrm{I}}}{\partial y_{\mathrm{I}}} + (1-\nu^{\mathrm{I}})\int \nabla^2\Psi^{\mathrm{I}}dy_{\mathrm{I}}\right] = -\left[-\frac{\partial\Psi^{\mathrm{II}}}{\partial y_{\mathrm{II}}} + (1-\nu^{\mathrm{II}})\int \nabla^2\Psi^{\mathrm{II}}dy_{\mathrm{II}}\right] \tag{15}$$

where both Ψ^{I} and Ψ^{II} are biharmonic functions, and $\Gamma=G_{\mathrm{II}}/G_{\mathrm{I}}$, ν^{I}, and ν^{II} are Poisson's ratios for the upper and lower planes, respectively.

3 Solution Expressions

In particular, let us consider the case where the defects are located in the upper half plane. The solutions can be sought after the sum of the contributions from the source and its image with respect to the interface between the materials. The source solution in the homogeneous plane is denoted as Ψ^{∞}, but the image solutions cannot be obtained in an easy way because of the stress and displacement coupling on the interface. Following the previous work (i.e., Adeerogba [2]), the Airy stress functions for the upper and lower layers can be expressed as linear combinations of some biharmonic functions. Thus we have

$$\Psi^{\mathrm{I}} = \sum_{i=1}^{4} N_i \bar{\Psi}_i^{\infty}(x, y_{\mathrm{I}}) \tag{16}$$

$$\Psi^{\mathrm{II}} = \sum_{i=1}^{4} M_i \bar{\Psi}_i^{\infty}(x, y_{\mathrm{II}}) \tag{17}$$

where y_i ($i=\mathrm{I},\mathrm{II}$) are local coordinates and, in particular, $y_{\mathrm{I}}=-y_{\mathrm{II}}$; N_i and M_i are undetermined constants and can be determined by the interface conditions. Based on the work presented by Adeerogba [2], the biharmonic functions $\bar{\Psi}_i^{\infty}$ can be expressed as the combinations of the derivative and integral forms of $\Psi^{\infty}(x,y)$. Especially, following Adeerogba [2], those biharmonic functions are chosen as follows:

$$\bar{\Psi}_1^{\infty} = \begin{cases} \Psi^{\infty}(x,y) & \text{in the upper plane} \\ \Psi^{\infty}(x,-y) & \text{in the lower plane} \end{cases} \tag{18}$$

$$\bar{\Psi}_2^{\infty} = \left(1 - 2y\frac{\partial}{\partial y} + y^2\nabla^2\right)\Psi^{\infty}(x,-y) \quad \text{in the upper plane} \tag{19}$$

$$\bar{\Psi}_3^{\infty} = \int dy \int \nabla^2\Psi^{\infty}(x,-y)dy \tag{20}$$

$$\bar{\Psi}_4^{\infty} = y\int \nabla^2\Psi^{\infty}(x,-y)dy \tag{21}$$

From the expression, we know that $M_2 \equiv 0$.

It is easy to prove that $\bar{\Psi}_1^{\infty}$ and $\bar{\Psi}_3^{\infty}$ are biharmonic functions. In addition, applying the Laplacian operator to $\bar{\Psi}_2^{\infty}$ and $\bar{\Psi}_4^{\infty}$ gives

$$\nabla^2\bar{\Psi}_2^{\infty} = \left[-4\frac{\partial^2}{\partial y^2} + 2y\frac{\partial}{\partial y}\nabla^2\right]\Psi^{\infty}(x,-y) + 3\nabla^2\Psi^{\infty}(x,-y) \tag{22}$$

$$\nabla^2\bar{\Psi}_4^{\infty} = \nabla^2\Psi^{\infty}(x,-y) \tag{23}$$

considering the identities

$$\nabla^2(yf) = y\nabla^2 f + 2f'_{y} \tag{24}$$

$$\nabla^2(y^2 f) = 2f + 4yf_{,y} + y^2\nabla^2 f \tag{25}$$

and the fact that if $\Psi^{\infty}(x,y)$ is biharmonic, so is $\bar{\Psi}^{\infty}(x,y)$. It can also be easily proven that these two functions are also biharmonic since

$$\nabla^4\bar{\Psi}_2^{\infty} = \left[-4\frac{\partial^2}{\partial y^2}\nabla^2 + 2y\frac{\partial}{\partial y}\nabla^4 + 4\frac{\partial^2}{\partial y^2}\nabla^2\right]\Psi^{\infty}(x,-y) = 0 \tag{26}$$

$$\nabla^4\bar{\Psi}_4^{\infty} = 0 \tag{27}$$

Therefore the chosen functions are all biharmonic and of course their combinations as given in Eqs. (16) and (17) must meet Eq. (5).

4 Determination of Unknown Constants

We now turn to find out the unknown constants based on the interface continuity conditions. This is equivalent to the determination of these constants by forcing the solutions in Eqs. (16) and (17) to meet the interface conditions (12)–(15). Since the elastic solutions are unique, any forms of Ψ^{I} and Ψ^{II} that meet the interface conditions should be regarded as the exact solutions.

In general, if ψ is harmonic, let us introduce its conjugate φ to construct a complex function

$$f(z) = \psi + i\varphi \tag{28}$$

Then the integral

$$F(z) = u^* + iv^* = \int f(z)dz \tag{29}$$

is also a harmonic function. Therefore, we have

$$u^* + iv^* = \int (\psi dx - \varphi dy) + i(\psi dy + \varphi dx) \tag{30}$$

where u^* and v^* are the real and virtual parts, respectively. Based on Riemann conditions, we have

$$u^*_{,y} = -v^*_{,x} \tag{31}$$

and this leads to the following identity:

$$\int \frac{\partial\psi}{\partial y}dx = -\int \frac{\partial\psi}{\partial x}dy \tag{32}$$

which is very useful in simplifying the complex forms associated with the derivative and integral of $\bar{\Psi}_i^{\infty}$ listed in Eqs. (18)–(21).

For example, based on the above identity, since $\nabla^2\bar{\Psi}^{\infty}$ is harmonic, we have

$$\frac{\partial^2\bar{\Psi}_3^{\infty}}{\partial x^2} = \int dy\frac{\partial}{\partial x}\left(-\int \frac{\partial\nabla^2\bar{\Psi}^{\infty}}{\partial y}dx\right) = -\nabla^2\bar{\Psi}^{\infty} \tag{33}$$

and

$$\frac{\partial\bar{\Psi}_3^{\infty}}{\partial x} = \int dy\left(-\int \frac{\partial\nabla^2\bar{\Psi}^{\infty}}{\partial y}dx\right) = -\int \nabla^2\bar{\Psi}^{\infty}dx \tag{34}$$

$$\frac{\partial\bar{\Psi}_3^{\infty}}{\partial y} = \int dy\int \frac{\partial\nabla^2\bar{\Psi}^{\infty}}{\partial y}dy = \int \nabla^2\bar{\Psi}^{\infty}dy \tag{35}$$

$$\frac{\partial^2\bar{\Psi}_3^{\infty}}{\partial x\,\partial y} = -\int \frac{\partial\nabla^2\bar{\Psi}^{\infty}}{\partial y}dx = \int \frac{\partial\nabla^2\bar{\Psi}^{\infty}}{\partial x}dy \tag{36}$$

In addition

$$\frac{\partial\bar{\Psi}_4^{\infty}}{\partial x} = y\int \frac{\partial\nabla^2\bar{\Psi}^{\infty}}{\partial x}dy = -y\int \frac{\partial\nabla^2\bar{\Psi}^{\infty}}{\partial y}dx \tag{37}$$

$$\frac{\partial\bar{\Psi}_4^{\infty}}{\partial y} = y\int \frac{\partial\nabla^2\bar{\Psi}^{\infty}}{\partial y}dy + \int \nabla^2\bar{\Psi}^{\infty}dy = y\nabla^2\bar{\Psi}^{\infty} + \int \nabla^2\bar{\Psi}^{\infty}dy \tag{38}$$

$$\frac{\partial^2\bar{\Psi}_4^{\infty}}{\partial x\,\partial y} = y\frac{\partial\nabla^2\bar{\Psi}^{\infty}}{\partial x} + \int \frac{\partial\nabla^2\bar{\Psi}^{\infty}}{\partial x}dy \tag{39}$$

$$\frac{\partial^2\bar{\Psi}_4^{\infty}}{\partial x^2} = -y\frac{\partial}{\partial x}\int \frac{\partial\nabla^2\bar{\Psi}^{\infty}}{\partial y}dy = -y\frac{\partial}{\partial x}\nabla^2\bar{\Psi}^{\infty} \tag{40}$$

Therefore, inserting these forms into Eq. (12), it can be rewritten as

$$(N_1+N_2-M_1)\frac{\partial^2\Psi^\infty}{\partial x^2}+(M_3-N_3)\nabla^2\Psi^\infty=0 \quad (41)$$

It must be remembered that on the interface $y_{\mathrm{I}}=y_{\mathrm{II}}=0$; thus we have $\Psi^\infty(x,-y)=\Psi^\infty$. In addition, any differentiation and integral with respect to y should change the sign, e.g.,

$$\frac{\partial\Psi^\infty(x,-y)}{\partial y}=-\frac{\partial\Psi^\infty}{\partial y} \quad (42)$$

$$\int\Psi^\infty(x,-y)dy=-\int\Psi^\infty dy \quad (43)$$

Form the second interface condition (Eq. (13)), we have

$$(N_1+N_2-M_1)\frac{\partial^2\Psi^\infty}{\partial x\,\partial y}+(N_3+N_4+M_3+M_4)\int\frac{\partial}{\partial x}\nabla^2\Psi^\infty dy=0 \quad (44)$$

and based on the third interface condition (Eq. (14)), we have

$$\ell 1\frac{\partial\Psi^\infty}{\partial x}+\ell 2\int\frac{\partial^2}{\partial y^2}\Psi^\infty dx=0 \quad (45)$$

where

$$\begin{aligned}\ell 1=&\Gamma[-N_1^0-N_2^0+N_4^0+(1-\upsilon^{\mathrm{I}})(3N_2^0+2N_4^0+N_1^0)]\\&-[-M_1^0+M_3^0+(1-\upsilon^{\mathrm{II}})(M_1^0+2M_4^0)]\end{aligned} \quad (46)$$

$$\begin{aligned}\ell 2=&\Gamma[N_3^0+(1-\upsilon^{\mathrm{I}})(-N_2^0+2N_4^0+N_1^0)]\\&-[M_3^0+(1-\upsilon^{\mathrm{II}})(M_1^0+2M_4^0)]\end{aligned} \quad (47)$$

In addition, from the fourth interface condition (Eq. (15)), it leads to

$$\ell 3\frac{\partial\Psi^\infty}{\partial y}+\ell 4\int\frac{\partial^2}{\partial x^2}\Psi^\infty dy=0 \quad (48)$$

where

$$\begin{aligned}\ell 3=&\Gamma[-N_1-N_2+N_3+N_4+(1-\upsilon^{\mathrm{I}})(3N_2-2N_4+N_1)]\\&+[M_1+M_3+M_4-(1-\upsilon^{\mathrm{II}})(M_1+2M_4)]\end{aligned} \quad (49)$$

$$\begin{aligned}\ell 4=&\Gamma[N_3+N_4+(1-\upsilon^{\mathrm{I}})(-N_2-2N_4+N_1)]+[M_3+M_4-(1-\upsilon^{\mathrm{II}})\\&\times(M_1+2M_4)]\end{aligned} \quad (50)$$

Without loss of generality, we can define $N_1^0\equiv 1$ for regularization. The conditions $\ell 1=0$ and $\ell 2=0$ can lead to

$$\Gamma[-1-N_2+4(1-\upsilon^{\mathrm{I}})N_2]=-M_1 \quad (51)$$

Based on the first identity of Eq. (44), it gives

$$M_1=1+N_2 \quad (52)$$

and thus we have

$$N_2=\frac{\Gamma-1}{\Gamma k_1+1} \quad (53)$$

Therefore we can get

$$M_1=\frac{\Gamma(k_1+1)}{\Gamma k_1+1} \quad (54)$$

From $\ell 1=0$ and $\ell 3=0$, we have

$$\Gamma[1-4(1-\upsilon^{\mathrm{I}})]N_4+(2M_3+M_4)=0 \quad (55)$$

In addition, considering the other two identities in Eqs. (41) and (44), we have

$$N_3-M_3=0 \quad (56)$$

$$N_3+N_4+M_3+M_4=0 \quad (57)$$

Therefore it gives

$$N_4=0 \quad (58)$$

$$M_4=-2N_3 \quad (59)$$

$$M_3=N_3 \quad (60)$$

Based on

$$\ell 2=0 \quad (61)$$

we have

$$N_3=\frac{(k_2-1)-\Gamma(k_1-1)}{4(\Gamma+k_2)}M_1 \quad (62)$$

It is found that

$$\ell 4=0 \quad (63)$$

is automatically satisfied. Therefore, based on the above constants, all boundary conditions can be met if the Airy stress functions for the upper and lower planes are given by Eqs. (16) and (17). The values of those undetermined constants are exactly the same as those given by Adeerogba [2] for static elasticity. Also, it is found that based on these constants, the interface conditions have been satisfied. Based on the uniqueness of elastic solutions, the stress functions given by Eqs. (16) and (17) can be regarded as the closed-form solutions to the bimaterial problem.

5 Conclusions

In this note, we present the rigorous proof for the construction of Green's functions for singularities in dissimilar material systems in terms of Green's functions in an infinite medium. Although the formulas have been given by Adeerogba [2], here we provide detailed derivations based on some specific features associated with harmonic and biharmonic functions. The formulas have been tested in Ref. [4] for the cases of dislocation dipoles, and the solutions for the dislocation embedded in one medium or on the interface are exactly the same as those by solving a dislocation problem as done by Dundurs and Mura [1]. More importantly, the methodology employed here may be extended to obtain the eigenstress solutions for the defects in other elastic media, such as a half poroelastic plane.

References

[1] Dundurs, J., and Mura, T., 1964, "Interaction Between an Edge Dislocation and a Circular Inclusion," J. Mech. Phys. Solids, **12**, pp. 177–189.

[2] Aderogba, K., 1977, "On Eigenstresses in Dissimilar Media," Philos. Mag., **35**, pp. 281–292.

[3] Suo, Z., 1989, "Singularities Interacting With Interfaces and Cracks," Int. J. Solids Struct., **25**, pp. 1133–1142.

[4] Zhang, X., and Jeffrey, R. G., 2006, "Numerical Studies on Crack Problems in Three-Layered Elastic Media Using an Image Method," Int. J. Fract., **139**, pp. 477–493.

Creeping Flow of Phan-Thien–Tanner Fluids in a Peristaltic Tube With an Infinite Long Wavelength

Abd El Hakeem Abd El Naby[1]
Department of Mathematics,
Faculty of Science,
Mansoura University,
New Damietta, Mansoura 3415, Egypt
e-mail: hakeemnaby@yahoo.com

In this study both linearized and the exponential forms of the Phan-Thien–Tanner model (PTT) are used to simulate the peristaltic flow in a tube. The solutions are investigated under zero Reynolds number and infinitely long wavelength assumptions. Computational solutions are obtained for pressure rise and friction force. The results of the average chyme velocity in the small intestine show that the PTT model is in good agreement with the experimental results, as shown in Table 1. Also, the magnitude of pressure rise and friction force of the exponential PTT model are smaller than in linear PTT model for different values of flow rate. The peristaltic pumping and the augmented pumping are discussed for various values of the physical parameters of interest. The pressure rise and friction force of PTT were compared with other studies in both Newtonian and non-Newtonian cases.
[DOI: 10.1115/1.3132183]

Keywords: peristalsis, non-Newtonian fluid, Phan-Thien–Tanner fluid, uniform geometry

1 Introduction

Peristaltic pumping is a form of material transport that occurs when a progressive wave of area contraction or expansion propagates along the length of a distensible tube containing some material. In physiology, peristalsis is used by the body to propel or mix the contents of a tube as in the ureter, the gastrointestinal tract, the small blood vessels, the bile duct, and other glandular ducts. Since then, slowly relaxing fluctuations cause both shear thinning and viscoelasticity. Also, Phan-Thien–Tanner (PTT) model exhibits both shear thinning and viscoelasticity. So, we consider the chyme in the small intestine as PTT fluids. Where, "viscoelasticity" and "shear thinning" are ordinarily seen only in much more complicated fluids such as polymer solutions.

Recently, a number of investigators studied the peristaltic transport considering different models were proposed in literature. Siddiqui and Schwarz [1] investigated peristaltic flow of a second-order fluid in a tube and used a perturbation method to second-order in dimensionless wave number. El Misiery et al. [2] and Elshehawey et al. [3] studied the peristaltic motion of generalized Newtonian fluid in a uniform and nonuniform channel. While, Abd El Naby and El Misiery [4] studied the effects of an endoscope and generalized Newtonian fluid on peristaltic motion. They were concerned by the Carreau fluid that displays shear thinning which show that the viscosity decreases with increasing shear rate. El Misiery et al. [5] studied the effects of a fluid with variable viscosity and an endoscope on peristaltic motion. Both analytic (perturbation) and numerical for peristaltic transport of a third-order fluid in a circular cylindrical tube were investigated by Hayat et al. [6].

The Phan-Thien–Tanner model found widespread use in the simulation of the flow of polymer solutions and melts. Indeed, it found to be the best simple differential model to represent the elongational properties of polymer solution in entry flows. Even more relevant is the fact that it can also predict accurately the shear properties of those same fluids and these features make it adequate for use in predominantly viscometric flows as given by Quinzani et al. [7]. For example, Azaiez et al. [8] used the linearized form to predict the entry flow through the 4:1 planar contraction. Baloch et al. [9] also used it to simulate both expansion and contraction flows. Oliveira and Pinho [10] studied the analytical solution for fully developed channel and pipe flow of PTT model fluids. They used the linearized and the exponential model to show that the wall shear of PTT fluids is substantially smaller than the corresponding value for a Newtonian or upper-convected Maxwell fluid.

Most of the research on the PTT model had been done in the absence of peristalsis. The purpose of this paper is to study the peristaltic transport of the PTT fluids in presence of peristalsis in a tube. Due to the complexity of the nonlinear equations of motion, we only considered the creeping flow through a uniform tube. The wall of the tube is transversely displaced by an infinite sinusoidal traveling wave of large wavelength. The pressure rise and friction force on the tube have been computed numerically.

2 Phan-Thien–Tanner Model

The constitutive equation for PTT fluids by Phan-Thien and Tanner [11] and Phan-Tien [12] can be written in a general form as

$$f(tr(\tau))\tau + \kappa\tau^{\nabla} = 2\mu D \tag{1}$$

where τ and D are the extra stress and deformation-rate tensors, κ is the relaxation time, μ is a constant viscosity coefficient, and τ^{∇} denotes Oldroyd's upper-convected derivative.

$$\tau^{\nabla} = \frac{\partial\tau}{\partial t} + (v\cdot\nabla)\tau - \tau\cdot\nabla v - (\nabla v)^t\cdot\tau$$

Two forms of the PTT model are in common use, namely, the linearized form given in the original paper Phan-Thien and Tanner [11], where the function of f is

$$f(tr(\tau)) = 1 + \frac{\varepsilon\kappa}{\mu}tr(\tau) \tag{2}$$

and that both forms and the exponential form Phan-Thien [12] with

$$f(tr(\tau)) = \exp\left(\frac{\varepsilon\kappa}{\mu}tr(\tau)\right) \tag{3}$$

In both forms, ε is the natural characteristic of the strained state of the PTT fluid. Moreover, it governs the extensional flow response. Also, PTT model holds for linear viscoelastic behavior at small strains ($\varepsilon < 1$) and it is unsuitable for large strains. Note that the linearized form results from (3) if the trace of the stress tensor is small and that both forms reduce to the well-known upper-convected Maxwell (UCM) model when ε vanishes.

3 Formulation of the Problem

Consider creeping flow of Phan-Thien–Tanner fluids through a uniform tube such that the tube has a sinusoidal wave traveling down its wall. We choose the cylindrical coordinates system $(\bar{R},\bar{Z})$, where the $\bar{Z}$-axis lies along the centerline of the tube and $\bar{R}$ is the distance measured radially. The geometry of the wall surface is described, as in Fig. 1

[1]Present address: Department of Mathematics, College of Teachers, Madina Munawara, Kingdom of Saudi Arabia.

Contributed by the Applied Mechanics Division of ASME for publication in the JOURNAL OF APPLIED MECHANICS. Manuscript received May 15, 2008; final manuscript received October 4, 2008; published online July 27, 2009. Review conducted by Nesreen Ghaddar.

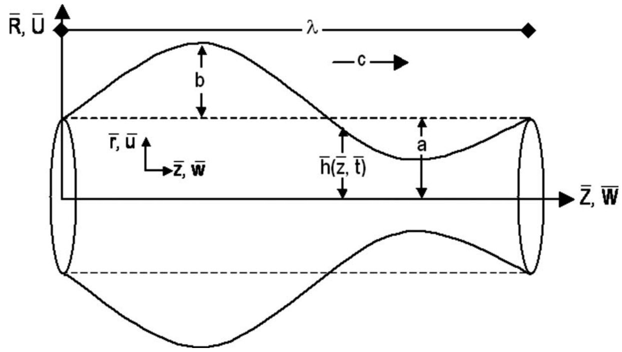

Fig. 1 Peristaltic transport in a uniform tube

$$\bar{h}(\bar{Z},\bar{t}) = a + b \sin\frac{2\pi}{\lambda}(\bar{Z} - c\bar{t}) \tag{4}$$

where a is the radius of the tube, b is the wave amplitude, λ is the wavelength and c is the wave speed, and $\bar{t}$ is the time.

If we choose moving coordinates $(\bar{r},\bar{z})$, which travel in the $\bar{Z}$-direction with the same speed as the wave (wave frame), the tube length is an integral multiple of wavelength, and the pressure difference across the tube is constant, then the flow can be treated as steady. The coordinate frames are related through

$$\bar{z} = \bar{Z} - c\bar{t}, \quad \bar{r} = \bar{R} \tag{5}$$

$$\bar{w}(\bar{r},\bar{z}) = \bar{W}(\bar{R},\bar{Z} - c\bar{t}) - c, \quad \bar{u}(\bar{r},\bar{z}) = \bar{U}(\bar{R},\bar{Z} - c\bar{t}) \tag{6}$$

where $\bar{U},\bar{W}$ and $\bar{u},\bar{w}$ are the velocity components in the radial and axial directions in the fixed and moving coordinates, respectively.

Equations of motion, constitutive equation of Phan-Thien–Tanner fluids, and boundary conditions in the dimensionless form neglecting the wave number (δ) in the moving coordinates reduce to

$$\frac{1}{r}\frac{\partial(ru)}{\partial r} + \frac{\partial w}{\partial z} = 0 \tag{7}$$

$$\frac{\partial P}{\partial z} = \frac{1}{r}\frac{\partial(r\tau_{rz})}{\partial r} \tag{8}$$

$$f\tau_{zz} = 2\mathrm{We}\,\tau_{rz}\frac{\partial w}{\partial r} \tag{9}$$

$$f\tau_{rz} = \frac{\partial w}{\partial r} + \mathrm{We}\,\tau_{rr}\frac{\partial u}{\partial r} \tag{10}$$

$$f = 1 + \varepsilon \mathrm{We}(\tau_{rr} + \tau_{\theta\theta} + \tau_{zz}) \tag{11}$$

$$f = \exp[\varepsilon \mathrm{We}(\tau_{rr} + \tau_{\theta\theta} + \tau_{zz})] \tag{12}$$

where $\mathrm{We}=kc/a$ is the Weissenberg number.

$$\frac{\partial w}{\partial r} = 0, \quad u = 0 \quad \text{for} \quad r = 0 \tag{13}$$

$$w = -1, \quad u = -\frac{dh}{dz} \quad \text{for} \quad r = h = 1 + \phi \sin(2\pi z) \tag{14}$$

where the variables in dimensionless form are as the following:

$$z = \frac{\bar{z}}{\lambda}, Z = \frac{\bar{Z}}{\lambda}, r = \frac{\bar{r}}{a}, R = \frac{\bar{R}}{a}, t = \frac{c\bar{t}}{\lambda}, P = \frac{a^2\bar{P}}{c\lambda\mu}, \delta = \frac{a}{\lambda}, \quad \tau_{ij} = \frac{a\bar{\tau}_{ij}}{\mu c} \quad \text{for } i = j = 1,2,3$$

$$w = \frac{\bar{w}}{c}, W = \frac{\bar{W}}{c}, u = \frac{\lambda\bar{u}}{ac}, U = \frac{\lambda\bar{U}}{ac}, h = \frac{\bar{h}}{a} = 1 + \phi \sin(2\pi z) \tag{15}$$

where ϕ is the amplitude ratio, $\phi = b/a < 1$.

4 Rate of Volume Flow

The instantaneous volume flow rate in the fixed coordinates system is given by

$$\bar{Q} = 2\pi\int_0^{\bar{h}} \bar{W}\bar{R}d\bar{R} \tag{16}$$

where $\bar{h}$ is a function of $\bar{Z}$ and $\bar{t}$. Substituting from Eqs. (5) and (6) into Eq. (16) and integrating, we obtain

$$\bar{Q} = \bar{q} + \pi c\bar{h}^2 \tag{17}$$

where

$$\bar{q} = 2\pi\int_0^{\bar{h}} \bar{w}\bar{r}d\bar{r} \tag{18}$$

is the volume flow rate in the moving coordinates system and is independent of time. Using the dimensionless variables, we find

$$F = \frac{\bar{q}}{2\pi a^2 c} = \int_0^h rwdr \tag{19}$$

The time-mean flow over a period $T=\lambda/c$ at a fixed Z-position is defined as

$$\hat{Q} = \frac{1}{T}\int_0^T \bar{Q}d\bar{t} \tag{20}$$

Using Eq. (17) in Eq. (20) and integrating them, we get

$$\Theta = F + \frac{1}{2}\left(1 + \frac{\phi^2}{2}\right) \tag{21}$$

where

$$\Theta = \frac{\hat{Q}}{2\pi ca^2} \tag{22}$$

5 Linear PTT Model

Neglecting the wave number (δ) implies that $\partial P/\partial r=0$, $\tau_{rr}=0$, and $\tau_{\theta\theta}=0$ and thus the trace of stress tensor becomes τ_{zz}. In this situation, it is easy to verify from the equations of motion that the pressure gradient dP/dz is a function of z only and the integration of the longitudinal momentum equation subjected to the boundary condition $\tau_{rz}=0$ at the symmetry line $r=0$, yields

$$\tau_{rz} = \frac{r}{2}\frac{dP}{dz} \tag{23}$$

With the above simplifications and upon division of the expressions for the two nonvanishing stresses (Eqs. (9) and (10)) the specific function of f cancels out resulting in

$$\tau_{zz} = 2\mathrm{We}\,\tau_{rz}^2 \tag{24}$$

with f given by Eq. (11) using $\tau_{rr}=0$, $\tau_{\theta\theta}=0$, and Eq. (24), we can rewrite Eq. (10) as

$$\frac{\partial w}{\partial r} = \tau_{rz} + 2\varepsilon \mathrm{We}^2\tau_{rz}^3 \tag{25}$$

The solution of Eq. (25) using Eqs. (13), (14), and (23) gives

$$w = -1 + \frac{r^2 - h^2}{4}\frac{dP}{dz} + \frac{\varepsilon \mathrm{We}^2}{16}(r^4 - h^4)\left(\frac{dP}{dz}\right)^3 \tag{26}$$

Substituting from Eq. (26) in Eq. (19) gives

$$\varepsilon \mathrm{We}^2 h^6 \left(\frac{dP}{dz}\right)^3 + 3h^4 \frac{dP}{dz} + 24h^2 + 48F = 0 \quad (27)$$

From the Cardan–Tartaglia formula for the solution of algebraic cubic equation, it can be readily shown that the real solution of Eq. (27) is

$$\frac{dP}{dz} = \frac{-1}{n} + \frac{n}{\varepsilon \mathrm{We}^2 h^2} \quad (28)$$

where $n=(-d+\sqrt{\varepsilon^3 \mathrm{We}^6 h^6 + d^2})^{1/3}$ and $d=12(2F+h^2)\varepsilon^2 \mathrm{We}^4$.

6 Exponential PTT Model

This distribution is obtained in a similar way by inserting the new f function Eq. (12) into Eq. (10) gives

$$\frac{\partial w}{\partial r} = \tau_{rz} \exp(2\varepsilon \mathrm{We}^2 \tau_{rz}^2) \quad (29)$$

Substituting from Eq. (23) in Eq. (29) and using the dimensionless boundary conditions Eq. (14), we obtain

$$w = -1 + \frac{1}{2ds}[\exp(s\, m^2 r^2) - \exp(s\, m^2 h^2)] \quad (30)$$

where

$$m = \frac{1}{2}\frac{dP}{dz}$$

$$s = 2\mathrm{We}^2 \varepsilon$$

Substituting Eq. (30) in Eq. (19) gives

$$2\ s^2 m^3 (2F + h^2) + 1 = \exp(s\, m^2 h^2)(1 - s\, m^2 h^2) \quad (31)$$

This nonlinear equation is not amenable to an analytical solution and therefore numerical methods are required. Equation (31) was solved numerically by using bisection method.

The pressure rise and the friction force on the tube in their non-dimensional forms, are given by

$$\Delta p_\lambda = \int_0^1 \left(\frac{dp}{dz}\right) dz \quad (32)$$

$$F_\lambda = \int_0^1 r^2 \left(-\frac{dp}{dz}\right) dz \quad (33)$$

Substituting Eqs. (28) and (31) in Eqs. (32) and (33) using Eqs. (15) and (21), we obtain the pressure rise and friction force flow rate relationship for the parameters $\{\phi, \varepsilon, \mathrm{We}\}$.

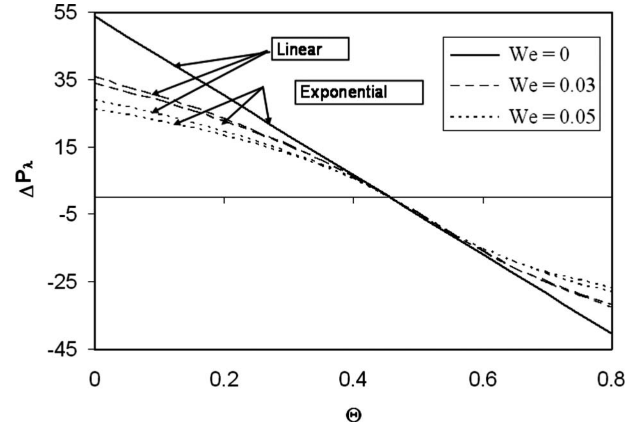

Fig. 2 The pressure rise versus flow rate for ϕ=0.6 and ε =0.5

We noticed that, our results coincide with results obtained by Jaffrin and Shapiro [13] and Barton and Raynor [14] for the Newtonian fluid (We=0 or ε=0).

7 Numerical Results and Discussion

The values of various parameters for the transport of chyme in the small intestine, as reported in Srivastava and Srivastava [15], are c=2 cm/m and a=1.25 cm. In this investigation, it may be noted that the theory of long wavelength and zero Reynolds number remains applicable as the radius of the small intestine, a =1.25 cm, is small compared with the wavelength λ=8.01 cm. The values of the Weissenberg number are {We=0, 0.03, 0.05} while the values of extensional parameter ε are {ε=0.1, 0.25, 0.5} as reported in Azaiez et al. [8] and Hayat et al. [6]. In addition, ε may have an influence on the shear properties, imparting shear thinning to the fluid provided the parameter is not too small has shown no effect of ε when it is of the order of 10^{-2}. It imposes an upper limit to the elongational viscosity and that limit is proportional to the inverse of ε Pinho and Oliveira [16].

The relations between the pressure rise, friction force and the flow rate that are given by Eqs. (32) and (33) are plotted in Figs. 2–6 in the linearized and the exponential PTT model.

In Figs. 2 and 3, the graphs can be divided into two regions, the first region denotes the peristaltic pumping, where $\Theta > 0$ (positive pumping) and $\Delta P_\lambda > 0$ (adverse pressure gradient), which occurs at $\{0 < \Theta \leq 0.457,\ \mathrm{We}=0, 0.03, 0.05\}$. The other region, where $\Theta > 0$ and $\Delta p_\lambda < 0$ (favorable pressure gradient) is called aug-

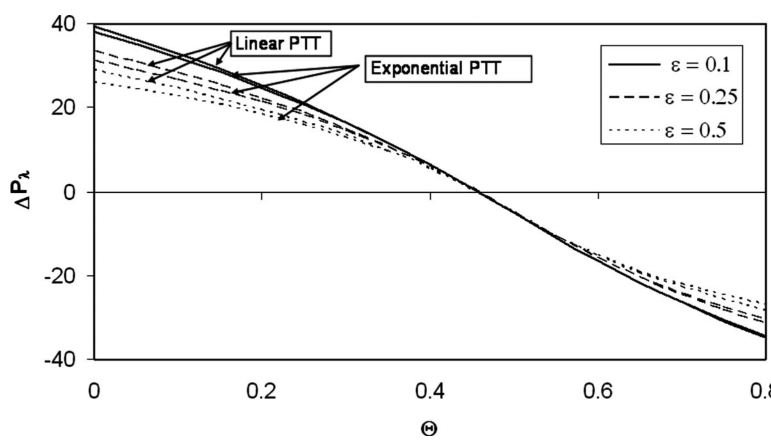

Fig. 3 The pressure rise versus flow rate for ϕ=0.6 and We=0.05

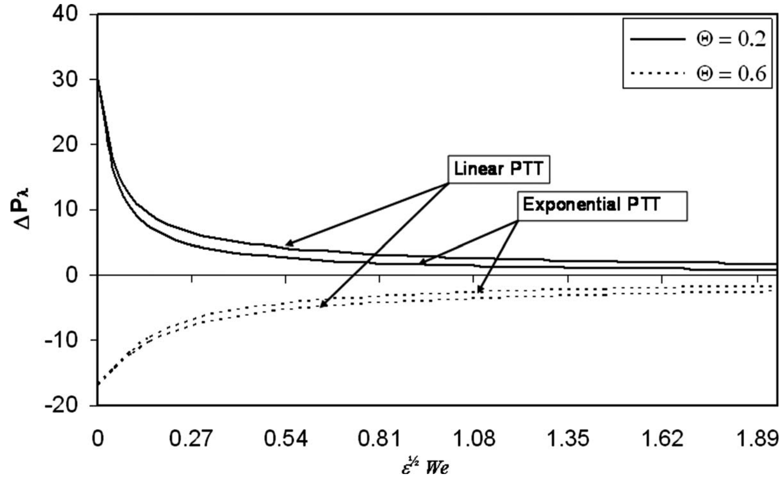

Fig. 4 The pressure rise versus $\varepsilon^{1/2}$ We for ϕ=0.6

mented pumping. It occurs at $\{0.457<\Theta\leq 0.8,\ \mathrm{We}=0, 0.03, 0.05\}$. In the case of peristaltic pumping and augmented pumping, it was noticed that the pressure rise decreases with increasing the Weissenberg number and the extensional parameter for different values of flow rate for the linearized and the exponential PTT model. Moreover, it is independent of the Weissenberg number and the extensional parameter at certain values of flow rate. Maximal adverse pressure gradient occurs at zero flow rate in peristaltic pumping but maximal favorable pressure gradient occurs at $\Theta=0.8$ as shown in Fig. 2. Also, the pressure rise decreases with the increasing flow rate in peristaltic pumping. While, in the case of augmented pumping, the pressure rise increases with the increasing flow rate.

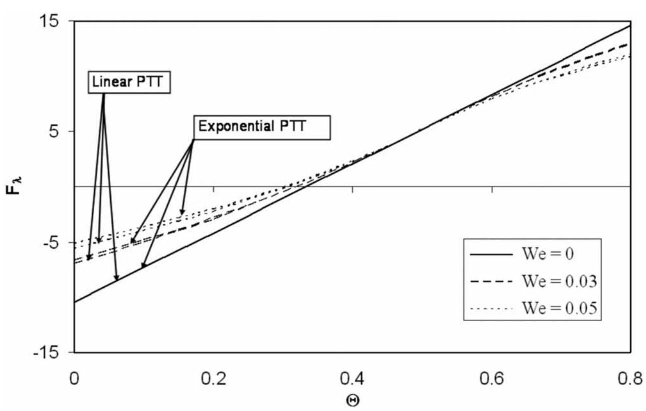

Fig. 5 The friction force versus flow rate for ϕ=0.6 and ε =0.5

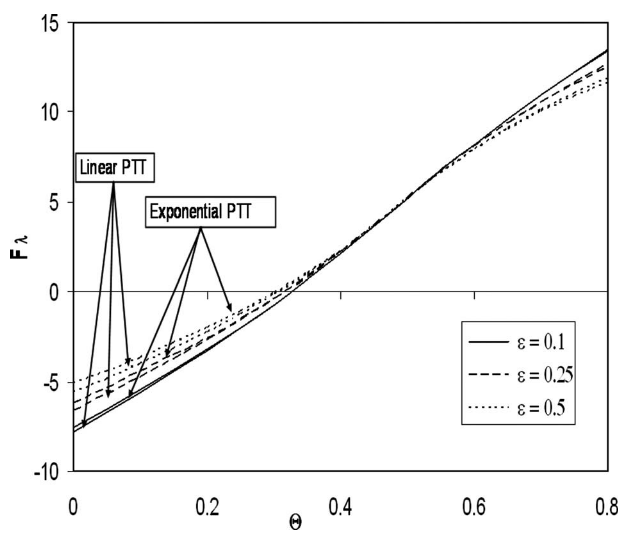

Fig. 6 The friction force versus flow rate for ϕ=0.6 and We =0.05

Figure 4 shows that the pressure rise decreases with the increasing $\varepsilon^{1/2}$We, which characterizes the elasticity and extensibility of the fluid for different values of flow rate. Moreover, the adverse and favorable pressure gradients are symmetric about $\varepsilon^{1/2}$We for different values of flow rate in the linearized and the exponential PTT model. Also, the absolute value of the adverse pressure gradient and favorable pressure gradient has the same value at the parameter $\varepsilon^{1/2}\mathrm{We}=0$ for different values flow rate.

Figures 5 and 6 show that the friction force decreases with increasing the Weissenberg number and the extensional parameter for the exponential and linear PTT model in the forward and backward flow cases, where positive F_λ denotes to the backward flow (reflux phenomena) and when F_λ is negative, it is designated to the forward flow (the flow in the direction wave velocity). Moreover, it is independent of the Weissenberg number and the extensional parameter at certain values of flow rate. In general, Figs. 5 and 6 show that the friction force has an opposite character in comparison to the pressure rise. Furthermore, the pressure rise in the exponential PTT model is smaller than linear PTT model, as shown in Figs. 2, 3, 5, and 6. Comparing our results with Elshehawey and Sobh [18], who used Oldroyd-B fluid, and Abd El Naby [19], who used the Carreau fluid, it was noticed that the exponential PTT model and linear PTT model have the same behavior qualitatively.

We calculated the average chyme velocity in the small intestine for PTT model and compared it with that reported in Srivastava and Srivastava [15] as illustrated in Table 1. The average chyme velocity is calculated for We=0.05 and ϕ=0.6 and Θ is obtained from solving $\Delta P_\lambda=0$ for $r=0$ for different values of ε.

8 Conclusion

From the results of above analysis, it is concluded that the flow field is noticeable by the presence of an incompressible PTT model in a peristaltic tube. More precisely

- the absolute values of pressure rise and friction force decrease with increasing the Weissenberg number and exten-

Table 1 Comparison of average chyme velocity in small intestine

Model	Velocity (cm/m)	Error (%)
Experiment		
Vender et al. [20]	1.016	–
Theory		
Newtonian single-layered ($n=1$)		
Barton and Raynor [14]	1.828	79.92
Newtonian two-layered		
Shukla et al. [17]	2.314	127.75
Newtonian with variable viscosity		
Srivastava et al. [21]	0.934	8.07
Power law		
Srivastava and Srivastava [15]		
$n=0.33$	0.589	41.14
$n=0.50$	1.024	00.78
$n=0.80$	1.688	66.04
Present work (Phan-Thien–Tanner)		
Linear		
$\varepsilon=0.10$	0.792	4.30
$\varepsilon=0.25$	0.969	4.62
$\varepsilon=0.50$	0.963	2.12
Exponential		
$\varepsilon=0.10$	1.015	0.04
$\varepsilon=0.25$	1.022	0.60
$\varepsilon=0.5$	1.033	1.67

This table shows that the PTT model is in good agreement with the experimental results than the other models especially for $\varepsilon=0.1$ for exponential form of PTT model.

sional parameter for different values of flow rate for the linearized and exponential PTT model

- the pressure rise and friction force in the exponential PTT model is smaller than linear PTT model for various values of the physical parameters of interest
- the pressure rise decreases with increasing the elasticity and extensibility of linearized and exponential PTT model for different values of flow rate
- the PTT model is in good agreement with the experimental results than the other models especially at a certain value of extensional parameter

Nomenclature

a = radius of the tube
b = wave amplitude
c = wave speed
D = deformation-rate tensor
f = a function of $tr\ (\tau)$
F = nondimensional volume flow rate in the moving coordinates system
$\bar{h}$ = dimensional wall surface
κ = relaxation time
P = pressure
$\bar{Q}$ = dimensional instantaneous volume flow rate in the fixed coordinates system
$\bar{q}$ = dimensional volume flow rate in the moving coordinates system
$\hat{Q}$ = dimensional time mean flow in the fixed coordinates system
$(\bar{R},\bar{Z})$ = dimensional cylindrical fixed coordinates system
(R,Z) = nondimensional cylindrical fixed coordinates system
$(\bar{r},\bar{z})$ = dimensional cylindrical moving coordinates system
(r,z) = nondimensional cylindrical moving coordinates system
$\bar{t}$ = dimensional time
$(\bar{U},\bar{W})$ = dimensional velocity components in the radial and axial directions, respectively, in fixed coordinates
(U,W) = nondimensional velocity components in the radial and axial directions, respectively, in fixed coordinates
$(\bar{u},\bar{w})$ = dimensional velocity components in the radial and axial directions respectively in moving coordinates
(u,w) = non-dimensional velocity components in the radial and axial directions, respectively, in moving coordinates
$\mathrm{We}=kc/a$ = Weissenberg number
$\delta=a/\lambda$ = wave number
ε = a parameter related to the elongational behavior of the model
Θ = nondimensional time mean flow in the fixed coordinates system
λ = wavelength
μ = constant viscosity coefficient
τ = extra stress tensor
τ^{∇} = Oldroyd's upper-convected derivative
$\phi=b/a$ = amplitude ratio

References

[1] Siddiqui, A. M., and Schwarz, W. H., 1994, "Peristaltic Motion of a Second-Order Fluid in Tubes," J. Non-Newtonian Fluid Mech., **53**, pp. 257–284.
[2] El Misiery, A. M., Elshehawey, E. F., and Hakeem, A. A., 1996, "Peristaltic Motion of an Incompressible Generalized Newtonian Fluid in a Planar Channel," J. Phys. Soc. Jpn., **65**, pp. 3524–3529.
[3] Elshehawey, E. F., El Misiery, A. M., and Abd El Naby, A. E. H., 1998, "Peristaltic Motion of Generalized Newtonian Fluid in a Non-Uniform Channel," J. Phys. Soc. Jpn., **67**, pp. 434–440.
[4] Abd El Naby, A. E. H., El Misiery, A. M., 2002, "Effects of an Endoscope and Generalized Newtonian Fluid on Peristaltic Motion," Int. J. Appl. Math Comput. Sci., **128**, pp. 19–35.
[5] El Misiery, A. M., Abd El Naby, A. E. H., and El Nagar, A. H., 2003, "Effects of a Fluid With Variable Viscosity and an Endoscope on Peristaltic Motion," J. Phys. Soc. Jpn., **72**, pp. 89–94.
[6] Hayat, T., Wang, Y., Siddiqui, A. M., Hutter, K., and Asghar, S., 2002, "Peristaltic Transport of a Third-Order Fluid in Circular Cylindrical Tube," Math. Models Meth. Appl. Sci., **12**, pp. 1691–1706.
[7] Quinzani, L., Armstrong, R. C., and Brown, R. A., 1995, "Use of Coupled Birefringence and LDV Studies of Flow Through a Planar Contraction to Test Constitutive Equations for Concentrated Polymer Solutions," J. Rheol., **39**, pp. 1201–1228.
[8] Azaiez, J., Guenette, R., and Aït-Kadi, A., 1996, "Numerical Simulation of Viscoelastic Flows Through a Planar Contraction," J. Non-Newtonian Fluid Mech., **62**, pp. 253–277.
[9] Baloch, A., Townsend, P., and Webster, M. F., 1996, "On Vortex Development in Viscoelastic Expansion and Contraction Flows," J. Non-Newtonian Fluid Mech., **65**, pp. 133–149.
[10] Oliveira, P. J., and Pinho, F. T., 1999, "Analytical Solution for Fully Developed Channel and Pipe Flow of Phan-Thien–Tanner Fluids," J. Fluid Mech., **387**, pp. 271–280.
[11] Phan-Thien, N., and Tanner, R. I., 1977, "A New Constitutive Equation Derived From Network Theory," J. Non-Newtonian Fluid Mech., **2**, pp. 353–365.
[12] Phan-Thien, N., 1978, "A Nonlinear Network Viscoelastic Model," J. Rheol., **22**, pp. 259–283.
[13] Jaffrin, M. Y., and Shapiro, A. H., 1971, "Peristaltic Pumping," Annu. Rev. Fluid Mech., **3**, pp. 13–36.
[14] Barton, C., and Raynor, S., 1968, "Peristaltic Flow in Tubes," Bull. Math. Biophys., **30**, pp. 663–680.
[15] Srivastava, L. M., and Srivastava, V. P., 1985, "Peristaltic Transport of a Non-Newtonian Fluid Applications to the Vas Deferens and Small Intestine," Ann. Biomed. Eng., **13**, pp. 137–153.
[16] Pinho, F. T., and Oliveira, P. J., 2000, "Analysis of Forced Convection in Pipes and Channels With the Simplified Phan-Thien–Tanner Fluid," Int. J. Heat Mass Transfer, **43**, pp. 2273–2287.
[17] Shukla, J. B., Parihar, R. S., Rao, R. P., and Gupta, S. P., 1980, "Effects of Peripheral-Layer Viscosity on Peristaltic Transport of a Bio-Fluid," J. Fluid

Mech., **97**(2), pp. 225–237.
[18] Elshehawey, E. F., and Sobh, A. M. F., 2001, “Peristaltic Viscoelastic Fluid in a Tube,” Int. J. Math. Math. Sci., **26**, pp. 21–34.
[19] Abd El Naby, A. E. H., 1997, “Some Problems on Peristaltic Motion for Different Fluids,” Ph.D. thesis, Mansoura University, Egypt.
[20] Vender, A. J., Sherman, J. H., and Luciano, D., 1975, *Human Physiology: The Mechanics of Body Function*, Tata McGraw-Hill, India.
[21] Srivastava, L. M., Srivastava, V. P., and Sinha, S. N., 1983, “Peristaltic Transport of a Physiological Fluid Part I Flow in Non-Uniform Geometry,” Biorheology, **20**, pp. 153–166.